BEHAVIOUR OF FIBRE-REINFORCED CONCRETE STRUCTURES UNDER SEISMIC LOADING

A thesis submitted for the degree of

Doctor of Philosophy of the

Imperial College London

by

Sharifah Maszura Binti Syed Mohsin

Structures Section

Department of Civil and Environmental Engineering

Imperial College London

April 2012

To my parents,

for their love and devotion

DECLARATION

The work presented in this thesis was carried out in the Structures Section of the Department of Civil and Environmental Engineering, Imperial College London. I hereby declare that this thesis is the results of my own work and any description of the work of others is acknowledged herein by the reference of the sources.

This thesis is not similar to the one that I have submitted for any degree, diploma or other qualification at any other university. No part of this document has been or is being concurrently submitted for any such degree, diploma or other qualification.

Sharifah Maszura Binti Syed Mohsin

London, April 2012

ABSTRACT

The present research is concerned with the modelling of the structural behaviour of steel fibre-reinforced concrete (SFRC) using non-linear finite-element (FE) analysis. Key structural response indicators such as load-deflection curves, strength, stiffness, ductility, energy absorption and cracking were examined. In particular, the potential for fibres to substitute for a reduction in conventional transverse reinforcement was studied. Such reduction is highly desirables in practice as it helps alleviate reinforcement congestion, often experienced in the seismic detailing of critical regions such as beam-column joints. Thus two key parameters were considered, namely reducing transverse reinforcement while increasing the amount of fibres. The reduction in conventional reinforcement was achieved mainly by increasing stirrups spacing (and also by reducing double-hoop arrangement commonly used in seismic detailing of joints).

The behaviour of SFRC structural elements was studied under both monotonic and reversed-cyclic loadings (the latter used to mimic seismic action). Emphasis was initially focused on the study of available experimental data describing the effect of steel fibres on the post-cracking response of concrete. Consequently the SFRC constitutive model proposed by Lok and Xiao (1999) was selected. The numerical model was calibrated against existing experimental data to ensure the reliability of the FE predictions. Subsequently, further analyses were carried out investigating three main case studies namely, simply supported beams, two-span continuous (i.e. statically-indeterminate) columns, and both exterior and interior beam-column joints. Parametric studies were carried out covering the full practical range of steel fibre dosages and appropriate amounts of reduction in conventional transverse reinforcement. The results show that steel fibres increase the load-carrying capacity and stiffness (thus enhancing response at both the serviceability and ultimate limit states, which are important design considerations). Fibres were found also to improve ductility (as well as altering the mode of failure from a brittle to a ductile one).

ACKNOWLEDGEMENTS

This research work initially was carried out under the supervision of Dr Ali Abbas. In the third year of this research work, Professor Ahmed Elghazouli joined the supervision team followed by Dr Ana Ruiz-Teran. I would like to express my profound gratitude to my supervisors for their insightful supervision, strong support and constant encouragement during the course of this research. Their painstaking and meticulous reading of the manuscript, and their kindness and understanding is very much appreciated.

A special thanks is dedicated to the late Professor Milija Pavlovic, who supervised me in the early stage of my work. His kindness and warm support will always be remembered.

I am also indebted to Dr Demetrios Cotsovos. His constant assistance, expertise and support, transferred during his visit and through the communication tools is acknowledged and will not be forgotten.

I also would like to express my sincere gratitude to the Ministry of Higher Education Malaysia and University of Malaysia Pahang for their financial support and the opportunity given which allowed me to complete my Ph.D research. Without their Fellowship scheme, I will not be able to pursue a Ph.D in Imperial College London.

My thanks also go to Mrs Marilyn Treadaway for her generosity and kindness that has helped me in many ways. Acknowledgment is due to Dr Arash Soleiman for his welcoming assistance despite of his busy schedule. I would like to extend my thanks to the staff of the Department of Civil Engineering and Environmental for their help.

I would also like to express my appreciation to my colleagues Dennis, Hamid, Sotirios, Libin, Razin and so many others who, directly or indirectly have contributed for the successful completion of my studies. To my friends, Kak Ros, Kak Nira, Kak Nad, Feela, Ima, Rashid, Kak Zarina, Hana, Nafisah, Razin, Nazri, Kak Deena, Ustaz Ammar and Ustazah Rohana, I would like to express sincere thanks for the continuous encouragement and supports provided during my studies. Their kindness and

understanding in helping and managing many things have ease the process of the completion of my studies.

To my family, to whom I dedicate this thesis, I would like to express my sincere thanks. I am deeply grateful to my parents for providing me always with endless care, love and encouragement. Above all, I would like to express my deepest gratitude to my fiancé, Anwar for his constant love, understanding and support, throughout the demanding time during my research work.

TABLE OF CONTENTS

ABSTRACT 4
ACKNOWLEDGEMENTS 5
LIST OF FIGURES 15
LIST OF TABLES 35
LIST OF SYMBOLS 40

CHAPTER 1: INTRODUCTION AND OBJECTIVES 46
1.1 Research background 46
1.2 Problem statement 47
1.3 Research aim, objectives and scope 49
1.4 Thesis outline 51

CHAPTER 2: LITERATURE REVIEW 53
2.1 Introduction 53
2.2 Overview of fibres 54
2.2.1 Basic properties and characteristics of SFRC 54
2.2.2 Behaviour of SFRC 56
2.2.3 Crack propagation 57
2.3 Constitutive models for SFRC 60
2.3.1 RILEM TC 162-TDF Recommendations for SFRC 60
2.3.2 Lim et al. (1987) proposed SFRC model 65
2.3.3 Murugappan et al. (1994) proposed SFRC model 67
2.3.4 Lok and Pei (1998) proposed SFRC model 68
2.3.5 Lok and Xiao (1999) proposed SFRC model 71
2.3.6 Barros and Figueiras (1999) proposed SFRC model 72
2.3.7 Barros and Figueiras (2001) proposed SFRC model 74
2.3.8 Barros et al. (2005) proposed SFRC model 75
2.3.9 Tlemat[a,b,c] et al. (2006) proposed SFRC model 76

2.4 Experimental investigation for SFRC under static loading 78
2.4.1 Monotonic loading 78
2.4.1.1 SFRC at the material level 78
2.4.1.2 At the structural level 80
2.4.2 Reversed-cyclic loading 84
2.5 Experimental investigation for SFRC under seismic loading 86
2.6 Summary 88

CHAPTER 3: METHODOLOGY: NON-LINEAR FE ANALYSIS OF SFRC STRUCTURES 91
3.1 Introduction 91
3.2 Constitutive models for SFRC 91
3.2.1 Background 91
3.2.2 Tension model 92
3.2.3 Compression model 93
3.2.4 Conclusions on SFRC constitutive models 93
3.3 Review of material models in ABAQUS software 94
3.3.1 Concrete models available in ABAQUS 95
3.3.1.1 Smeared cracking concrete model 96
3.3.1.2 Brittle cracking concrete model 98
3.3.1.3 Damaged plasticity concrete model 100
3.3.1.4 Concrete model selection 102
3.3.2 Steel model 103
3.3.3 Analysis procedure 104
3.3.3.1 Analysis modules 104
3.3.3.2 Model definition 105
3.3.4 Failure criterion 106
3.4 Seismic design considerations 107
3.5 Scope of case/parametric studies 109
3.5.1 Case study 1: Simply supported beams under monotonic and cyclic loading 110
3.5.2 Case study 2: Two-span continuous columns under monotonic and cyclic loading 111

3.5.3 Case study 3: Beam-column joints under cyclic loading 112
3.6 Summary 113

CHAPTER 4: CASE STUDY 1: SIMPLY SUPPORTED BEAMS UNDER MONOTONIC AND REVERSED-CYCLIC LOADING 114
4.1 Introduction 114
4.2 Case Study 1(a): Calibration with Campione and Mangiavillano (2008) tests 115
4.2.1 Results for beams under monotonic loading (Case Study 1(a)-M) 117
4.2.2 Results for beam under reversed-cyclic loading (Case Study 1(a)-C) 118
4.3 Case Study 1(a)-M: Parametric study on simply supported beams under monotonic loading 120
4.3.1 Load-deflection curves 121
4.3.2 Strength 121
4.3.3 Ductility 127
4.3.4 Cracking pattern 127
4.3.4.1 Principal strain contours 128
4.3.4.2 Principal strain vectors 130
4.3.4.3 Deflected shapes 132
4.3.5 Comparative study with control specimen using non-dimensional ratios 133
4.3.5.1 Strength ratio 134
4.3.5.2 Ductility ratio 135
4.3.5.3 Energy absorption ratio 136
4.3.6 Comparison between FE-based predictions and design calculations 136
4.4 Case Study 1(a)-C: Parametric study on simply supported beams under reversed-cyclic loading 138
4.4.1 Load-deflection curves 139
4.4.2 Strength 139
4.4.3 Ductility 145
4.4.4 Cracking pattern 145
4.4.4.1 Principal strain contours 145
4.4.4.2 Principal strain vectors 148

4.4.4.3 Deflected shapes 150
4.4.5 Comparative study with control specimen using non-dimensional ratios 151
4.4.5.1 Strength ratio 151
4.4.5.2 Ductility ratio 152
4.4.5.3 Energy absorption ratio 152
4.4.5.4 Number of cycles ratio 153
4.5 Case Study 1(b): Calibration with Campione et al. (2006) experimental work 154
4.6 Case Study 1(b): Parametric study on shear failure of simply supported beams under monotonic loading 158
4.6.1 Load-deflection curves 159
4.6.2 Strength 159
4.6.3 Ductility 162
4.6.4 Cracking patterns 163
4.6.4.1 Principal strain contours 163
4.6.4.2 Principal strain vectors 166
4.6.4.3 Deflected shapes 167
4.6.5 Comparative study with control specimen using non-dimensional ratios 169
4.6.5.1 Strength ratio 169
4.6.5.2 Ductility ratio 170
4.6.5.3 Energy absorption 171
4.6.6 Comparison between FE-based predictions and design calculations 172
4.7 Conclusions 174

CHAPTER 5: CASE STUDY 2: TWO-SPAN CONTINUOUS SFRC COLUMN UNDER MONOTONIC AND REVERSED-CYCLIC LOADING 177
5.1 Introduction 177
5.2 Calibration with experimental data 178
5.2.1 Results for column under monotonic loading 181
5.2.2 Results for column under reversed-cyclic loading 183

5.3 Case Study 2(a): Parametric study of SFRC column under monotonic loading 186
5.3.1 Strength 187
5.3.2 Ductility 189
5.3.3 Cracking pattern 193
5.3.3.1 Principal strain contours 194
5.3.3.2 Principal strain vectors 196
5.3.3.3 Deflected shapes 197
5.3.4 Comparative study with control specimen using non-dimensional ratios 198
5.3.4.1 Strength ratio 198
5.3.4.2 Ductility ratio 200
5.3.4.3 Energy absorption ratio 201
5.3.5 Comparison between FE results and analytical calculation 203
5.4 Case Study 2(b): Parametric study analysed under combined axial force and reversed-cyclic loading 205
5.4.1 Strength 205
5.4.2 Ductility 208
5.4.3 Cracking pattern 210
5.4.3.1 Principal strain contours 211
5.4.3.2 Principal strain vectors 213
5.4.3.3 Deflected shapes 214
5.4.4 Comparative study with control specimen using non-dimensional ratios 215
5.4.4.1 Strength ratio 215
5.4.4.2 Ductility ratio 216
5.4.4.3 Energy absorption ratio 217
5.4.4.4 Number of cycles analysed ratio 218
5.5 Conclusions 218

CHAPTER 6: CASE STUDY 3: BEAM-COLUMN JOINTS UNDER REVERSED-CYCLIC LOADING 220
6.1 Introduction 220

6.2 Case Study 3(a): Exterior beam-column joint - Calibration with experimental data (Bayasi and Gebman, 2002) 221
6.2.1 Experimental setup 221
6.2.2 FE analysis input data 222
6.2.3 Results of calibration work 224
6.3 Case Study 3(a): Parametric study on exterior beam-column joint under reversed-cyclic loading 226
6.3.1 Load-deflection curves 227
6.3.2 Strength 227
6.3.3 Ductility 232
6.3.4 Cracking pattern 236
6.3.4.1 Principal stress contours 236
6.3.4.2 Principal strain contours 239
6.3.4.3 Principal strain vectors 241
6.3.4.4 Deflected shapes 242
6.3.5 Comparative study with control specimen using non-dimensional ratio 244
6.3.5.1 Strength ratio 244
6.3.5.2 Ductility ratio 245
6.3.5.3 Energy absorption ratio 246
6.3.5.4 Number of the cycles ratio 247
6.4 Case Study 3(b): Interior beam-column joint - Calibration with experimental data (Filiatrault et al, 1995) 248
6.4.1 Experimental setup 248
6.4.2 FE analysis input data 251
6.4.3 Results of calibration work 253
6.5 Case Study 3(b): Parametric study on interior beam-column joint under reversed-cyclic loading 259
6.5.1 Storey shear-drift curves 261
6.5.2 Strength 266
6.5.3 Ductility 266
6.5.4 Cracking pattern 269
6.5.4.1 Principal stress contours 269

6.5.4.2 Principal strain contours 272
6.5.4.3 Principal strain vectors 274
6.5.4.4 Deflected shapes 275
6.5.5 Comparative study with control specimen using non-dimensional ratios 276
6.5.5.1 Strength ratio 277
6.5.5.2 Ductility ratio 278
6.5.5.3 Energy absorption ratio 279
6.5.5.4 Number of cycles 280
6.6 Conclusions 280

CHAPTER 7: RECOMMENDATIONS FOR DESIGN 283
7.1 Introduction 283
7.2 Case Study 1: Simply-supported beams 284
7.3 Case Study 2: Two-span continuous columns 288
7.4 Case Study 3: Beam-column joints 290
7.5 Summary of design recommendations 293

CHAPTER 8: CONCLUSIONS AND RECOMMENDATIONS 294
8.1 Summary of research work 294
8.2 Summary of conclusions 296
8.3 Recommendations for future work 299

REFERENCES 302

APPENDIX A: MODEL CALIBRATION WORK 310
A.1 Background 310
A.2 Ductile failure: Hughes and Speirs (1982) 311
A.2.1 Experimental data and analysis procedure 311
A.2.2 Discussion of ABAQUS simulation results 312
A.3 Brittle failure: Bresler and Scordelis (1963) 312
A.3.1 Experimental data and analysis procedure 312
A.3.2 Discussion of ABAQUS simulation results 313

A.4 Three-point bending test (tensile failure): Barros et al (2005) 314
A.4.1 Experimental data and analysis procedure 314
A.4.2 Discussion of ABAQUS simulation results 315
A.5 Four-point bending test (tensile failure): Tlemat[a;b] et al (2006) 317
A.5.1 Experimental data and analysis procedure 317
A.5.2 Discussion of ABAQUS simulation results 319
A.6 Three-point bending test (tensile failure): Barros and Figueiras (1999) 321
A.6.1 Experimental data and analysis procedure 321
A.6.1 Discussion of ABAQUS simulation results 323
A.7 Four-point bending test (tensile failure): Trottier and Banthia (1994) 324
A.7.1 Experimental data and analysis procedure 324
A.7.2 Discussion of ABAQUS Simulation Results 325
A.8 Four-point bending test: Cho and Kim (2003) 326
A.8.1 Experimental data and analysis procedure 326
A.8.2 Discussion of ABAQUS simulation results 328
A.9 Four-point bending test: Oh et al (1998) 329
A.9.1 Experimental data and analysis procedure 329
A.9.2 Discussion of ABAQUS simulation results 331
A.10 Four-point bending test: Sharma (1986) 332
A.10.1 Experimental data and analysis procedure 332
A.10.2 Discussion of ABAQUS simulation results 333
A.11 Conclusions 334

APPENDIX B: DESIGN CALCULATION 335
B.1 Shear capacity 335
B.2. Bending moment capacity 338

LIST OF FIGURES

Figure 1.1: Examples of the shapes available for steel fibres 47

Figure 2.1: Types of steel fibres (adapted from Concrete Society, 2007) 55

Figure 2.2: Relationship between (a) Moment-curvature response and (b) Tensile stress-strain behaviour (adapted from Lok and Xiao, 1999) 57

Figure 2.3: Schematic representation of changes in crack geometry and stress fields associated with crack extension (adapted from Kotsovos & Pavlović, 1995) 58

Figure 2.4: The principle of single and multiple cracking. The specimens are loaded in uniaxial tension and the schematic load versus deformation (P-δ) relationship is shown together with the cracking pattern (a) single cracking (or tension softening) (b multiple cracking (or strain hardening) (adapted from RILEM TC 162-TDF, 2002) 59

Figure 2.5: Stress distribution for SFRC sections (adapted from Tlemat et al, 2006) 59

Figure 2.6: Arrangement for standard bending test on small notched beams (adopted from RILEM TC 162-TDF[c] Recommendation, 2003) 61

Figure 2.7: Load-deflection diagram (adapted from RILEM TC 162-TDF Recommendation, 2000) 61

2.8: Stress-strain diagram (RILEM TC 162-TDF Recommendation, 2000) 62

Figure 2.9: Stress-strain diagram and size factor, κ_h (adapted from RILEM TC 162-TDF[a] Recommendation, 2003) 63

Figure 2.10: Geometry and loading of the bending test (adapted from RILEM TC 162-TDF[c] Recommendation, 2003) 65

Figure 2.11: Load – CMOD diagram (RILEM TC 162-TDF[a] Recommendation, 2003) 65

Figure 2.12: Composite stress-strain relations in tension (Lim et al., 1987) 66

Figure 2.13: Composite stress-strain relations in tension (Murugappan et al, 1994) 67

Figure 2.14: Compressive stress-strain relationship for SFRC (Lok and Pei, 1998) 68

Figure 2.15: Tensile stress-strain relationship for SFRC (Lok and Pei, 1998) 69

Figure 2.16: Constitutive stress-strain relationship (Lok and Xiao, 1999) 71
Figure 2.17: Compression stress-strain diagram (Barros and Figueiras, 1999) 73
Figure 2.18: Tensile stress-strain diagram (Barros and Figueiras, 1999) 74
Figure 2.19: Tri-linear softening diagram for hooked-ends SFRC (Barros and Figueiras, 2001) 75
Figure 2.20: Proposed uni-axial tensile stress-strain model for mesh 25 mm (Tlemat[b] et al., 2006) 77
Figure 2.21: Proposed uni-axial tensile stress-strain model (Tlemat[c] et. al, 2006) 78

Figure 3.1: Uniaxial behaviour of plain concrete (adapted from ABAQUS, 2007) 96
Figure 3.2: Tension stiffening model (adapted from ABAQUS, 2007) 96
Figure 3.3: Yield and failure surface in plane stress (adapted from ABAQUS, 2007) 97
Figure 3.4: Shear retention model (adapted from ABAQUS, 2007) 98
Figure 3.5: Rankine criterion in plane stress (adapted from ABAQUS, 2007) 99
Figure 3.6: Post-failure stress-strain curve. (adapted from ABAQUS, 2007) 99
Figure 3.7: Piece-wise linear form of the shear retention model (adapted from ABAQUS, 2007) 100
Figure 3.8: Illustration of the definition of the cracking strain ($\tilde{\varepsilon}_t^{ck}$) used for the definition of tension stiffening data (adapted from ABAQUS, 2007) 100
Figure 3.9: Definition of the compressive inelastic (or crushing) strain ($\tilde{\varepsilon}_t^{in}$) used for the definition of compression hardening data (adapted from ABAQUS, 2007) 101
Figure 3.10: Uni-axial load cycle (tension-compression-tension) assuming default values for the stiffness recovery factors: $w_t = 0$ and $w_c = 1$ (adapted from ABAQUS, 2007) 101
Figure 3.11: Stress-strain relations for steel material 103
Figure 3.12: RC beam modelled using stringer reinforcement (adapted from ABAQUS, 2007) 104
Figure 3.13: Example of boundary conditions for one quarter of a notched beam in (a) 2D and (b) 3D models 105
Figure 3.14: Example of FE mesh refinement sizes for 2D model for (a) fine, (b) 106

medium and (c) coarse meshes
Figure 3.15: Capacity design for unbraced frames: (a) overall view and (b) forces at a beam-column joint, axial forces not shown (adapted from Booth and Key, 2006) 107
Figure 3.16: Simply supported beams case 110
Figure 3.17: Two-span continuous column case 111
Figure 3.18: Beam-column joint case showing (a) exterior and (b) interior joints 112

Figure 4.1: Dimensions and loading arrangement of the beams (adapted from Campione and Mangiavillano, 2008) 115
Figure 4.2: Quarter of the beam modelled in ABAQUS with defined boundary condition along symmetrical (a) front and (b) side views; and (c) FE mesh 116
Figure 4.3: Tensile stress-strain diagram adopted for calibration work of Campione and Mangiavillano (2008) beams 116
Figure 4.4: Loading histories input for (a) monotonic and (b) reversed-cyclic loading 117
Figure 4.5: Load-deflection curves for calibration work in Case Study 1(a)-M 117
Figure 4.6: Kinetic energy plots to determine failure for beams analysed under monotonic loading in Case Study 1(a)-M 118
Figure 4.7: Load-deflection hysteresis loops for calibration work in Case Study 1(a)-C 119
Figure 4.8: Kinetic energy plots to determine failure for beams analysed under monotonic loading in Case Study 1(a)-C 119
Figure 4.9: Tensile stress-strain relations for Case Study 1(a) for different fibre volume fractions (V_f) 120
Figure 4.10: Load-deflection curves for Case Study 1(a)-M beams with $SI = 0\%$ 122
Figure 4.11: Load-deflection curves for Case Study 1(a)-M beams with $SI = 50\%$ 122
Figure 4.12: Load-deflection curves for Case Study 1(a)-M beams with $SI = 100\%$ 122
Figure 4.13: Load-deflection curves for Case Study 1(a)-M beams with $SI = 200\%$ 123
Figure 4.14: Tensile strain in concrete at the mid-span crack opening region at the bottom of the beam ($\varepsilon_{c,c}$) for Case Study 1 (a)-M with $SI = 50\%$ 125
Figure 4.15: Tensile strain in steel bar at the mid-span crack opening region at the bottom of the beam ($\varepsilon_{b,s}$) for Case Study 1 (a)-M beam with $SI = 50\%$ 125

Figure 4.16: Load-deflection curve for Case Study 1 (a) series $SI = 50\%$ (shown up to a deflection of 4 mm) 126

Figure 4.17: Principal strain contours for Case Study 1(a)-M with $SI = 0\%$ for (a) $V_f = 0\%$, (b) $V_f = 1\%$, (c) $V_f = 1.5\%$, (d) $V_f = 2\%$ and (e) $V_f = 2.5\%$ 128

Figure 4.18: Principal strain contours for Case Study 1(a)-M with $SI = 50\%$ for (a) $V_f = 0\%$, (b) $V_f = 1\%$, (c) $V_f = 1.5\%$, (d) $V_f = 2\%$ and (e) $V_f = 2.5\%$ 129

Figure 4.19: Principal strain contours for Case Study 1(a)-M with $SI = 100\%$ for (a) $V_f = 0\%$, (b) $V_f = 1\%$, (c) $V_f = 1.5\%$, (d) $V_f = 2\%$ and (e) $V_f = 2.5\%$ 129

Figure 4.20Principal strain contours for Case Study 1(a)-M with $SI = 200\%$ for (a) $V_f = 0\%$, (b) $V_f = 1\%$, (c) $V_f = 1.5\%$, (d) $V_f = 2\%$ and (e) $V_f = 2.5\%$ 130

Figure 4.21: Principal strain vectors for Case Study 1(a)-M with $SI = 0\%$ for (a) $V_f = 0\%$, (b) $V_f = 1\%$, (c) $V_f = 1.5\%$, (d) $V_f = 2\%$ and (e) $V_f = 2.5\%$ 130

Figure 4.22: Principal strain vectors for Case Study 1(a)-M with $SI = 50\%$ for (a) $V_f = 0\%$, (b) $V_f = 1\%$, (c) $V_f = 1.5\%$, (d) $V_f = 2\%$ and (e) $V_f = 2.5\%$ 131

Figure 4.23: Principal strain vectors for Case Study 1(a)-M with $SI = 100\%$ for (a) $V_f = 0\%$, (b) $V_f = 1\%$, (c) $V_f = 1.5\%$, (d) $V_f = 2\%$ and (e) $V_f = 2.5\%$ 131

Figure 4.24: Principal strain vectors for Case Study 1(a)-M with $SI = 200\%$ for (a) $V_f = 0\%$, (b) $V_f = 1\%$, (c) $V_f = 1.5\%$, (d) $V_f = 2\%$ and (e) $V_f = 2.5\%$ 131

Figure 4.25: Deflected shapes for Case Study 1(a)-M with $SI = 0\%$ for (a) $V_f = 0\%$, (b) $V_f = 1\%$, (c) $V_f = 1.5\%$, (d) $V_f = 2\%$ and (e) $V_f = 2.5\%$ 132

Figure 4.26: Deflected shapes for Case Study 1(a)-M with $SI = 50\%$ for (a) $V_f = 0\%$, (b) $V_f = 1\%$, (c) $V_f = 1.5\%$, (d) $V_f = 2\%$ and (e) $V_f = 2.5\%$ 132

Figure 4.27: Deflected shapes for Case Study 1(a)-M with $SI = 100\%$ for (a) $V_f = 0\%$, (b) $V_f = 1\%$, (c) $V_f = 1.5\%$, (d) $V_f = 2\%$ and (e) $V_f = 2.5\%$ 133

Figure 4.28: Deflected shapes for Case Study 1(a)-M with $SI = 200\%$ for (a) $V_f = 0\%$, (b) $V_f = 1\%$, (c) $V_f = 1.5\%$, (d) $V_f = 2\%$ and (e) $V_f = 2.5\%$ 133

Figure 4.29: Ratio of maximum load to that of the control specimen ($SI = 0\%, V_f = 0\%$) versus steel fibre volume fraction graph for Case Study 1(a)-M 134

Figure 4.30: Ratio of yield load to that of the control specimen ($SI = 0\%, V_f = 0\%$) 134

versus steel fibre volume fraction graph for Case Study 1(a)-M

Figure 4.31: Ratio of ductility ratio to that of the control specimen ($SI = 0\%, V_f = 0\%$) versus steel fibre volume fraction graph for Case Study 1(a)-M 134

Figure 4.32: Ratio of energy absorption to that of the control specimen ($SI = 0\%, V_f = 0\%$) versus steel fibre volume fraction graph for Case Study 1(a)-M 136

Figure 4.33: The loading condition, bending moment (M) and shear force (V) diagram from Case Study 1(a) 136

Figure 4.34: Load-deflection curves for Case Study 1(a)-C for beams with $SI = 0\%$ 139

Figure 4.35: Load-deflection curves for Case Study 1(a)-C for beams with $SI = 50\%$ 140

Figure 4.36: Load-deflection curves for Case Study 1(a)-C for beams with $SI = 100\%$ 140

Figure 4.37: Load-deflection curves for Case Study 1(a)-C for beams with $SI = 200\%$ 140

Figure 4.38: Load-deflection curves for Case Study 1(a)-C beams with $SI = 0\%$ and (a) $V_f = 0\%$, (b) $V_f = 1\%$, (c) $V_f = 1.5\%$, (d) $V_f = 2\%$ and (e) $V_f = 2.5\%$ 141

Figure 4.39: Load-deflection curves for Case Study 1(a)-C beams with $SI = 50\%$ and (a) $V_f = 0\%$, (b) $V_f = 1\%$, (c) $V_f = 1.5\%$, (d) $V_f = 2\%$ and (e) $V_f = 2.5\%$ 142

Figure 4.40: Load-deflection curves for Case Study 1(a)-C beams with $SI = 100\%$ and (a) $V_f = 0\%$, (b) $V_f = 1\%$, (c) $V_f = 1.5\%$, (d) $V_f = 2\%$ and (e) $V_f = 2.5\%$ 143

Figure 4.41: Load-deflection curves for Case Study 1(a)-C beams with $SI = 200\%$ and (a) $V_f = 0\%$, (b) $V_f = 1\%$, (c) $V_f = 1.5\%$, (d) $V_f = 2\%$ and (e) $V_f = 2.5\%$ 144

Figure 4.42: Principal strain contours for Case Study 1(a)-C beams with $SI = 0\%$ and (a) $V_f = 0\%$, (b) $V_f = 1\%$, (c) $V_f = 1.5\%$, (d) $V_f = 2\%$ and (e) $V_f = 2.5\%$ 146

Figure 4.43: Principal strain contours for Case Study 1(a)-C beams with $SI = 50\%$ and (a) $V_f = 0\%$, (b) $V_f = 1\%$, (c) $V_f = 1.5\%$, (d) $V_f = 2\%$ and (e) $V_f = 2.5\%$ 146

Figure 4.44: Principal strain contours for Case Study 1(a)-C beams with $SI = 100\%$ and (a) $V_f = 0\%$, (b) $V_f = 1\%$, (c) $V_f = 1.5\%$, (d) $V_f = 2\%$ and (e) $V_f = 2.5\%$ 147

Figure 4.45: Principal strain contours for Case Study 1(a)-C beams with $SI = 200\%$ and (a) $V_f = 0\%$, (b) $V_f = 1\%$, (c) $V_f = 1.5\%$, (d) $V_f = 2\%$ and (e) $V_f = 2.5\%$ 147

Figure 4.46: Principal strain vectors for Case Study 1(a)-C beams with $SI = 0\%$ and 148

(a) $V_f = 0\%$, (b) $V_f = 1\%$, (c) $V_f = 1.5\%$, (d) $V_f = 2\%$ and (e) $V_f = 2.5\%$

Figure 4.47: Principal strain vectors for Case Study 1(a)-C beams with SI = 50% and (a) $V_f = 0\%$, (b) $V_f = 1\%$, (c) $V_f = 1.5\%$, (d) $V_f = 2\%$ and (e) $V_f = 2.5\%$ 149

Figure 4.48: Principal strain vectors for Case Study 1(a)-C beams with $SI = 100\%$ and (a) $V_f = 0\%$, (b) $V_f = 1\%$, (c) $V_f = 1.5\%$, (d) $V_f = 2\%$ and (e) $V_f = 2.5\%$ 149

Figure 4.49: Principal strain vectors for Case Study 1(a)-C beams with $SI = 200\%$ and (a) $V_f = 0\%$, (b) $V_f = 1\%$, (c) $V_f = 1.5\%$, (d) $V_f = 2\%$ and (e) $V_f = 2.5\%$ 149

Figure 4.50: Deflected shapes for Case Study 1(a)-C beams with $SI = 0\%$ and (a) $V_f = 0\%$, (b) $V_f = 1\%$, (c) $V_f = 1.5\%$, (d) $V_f = 2\%$ and (e) $V_f = 2.5\%$ 150

Figure 4.51: Deflected shapes for Case Study 1(a)-C beams with $SI = 50\%$ and (a) $V_f = 0\%$, (b) $V_f = 1\%$, (c) $V_f = 1.5\%$, (d) $V_f = 2\%$ and (e) $V_f = 2.5\%$ 150

Figure 4.52: Deflected shapes for Case Study 1(a)-C beams with $SI = 100\%$ and (a) $V_f = 0\%$, (b) $V_f = 1\%$, (c) $V_f = 1.5\%$, (d) $V_f = 2\%$ and (e) $V_f = 2.5\%$ 150

Figure 4.53: Deflected shapes for Case Study 1(a)-C beams with $SI = 200\%$ and (a) $V_f = 0\%$, (b) $V_f = 1\%$, (c) $V_f = 1.5\%$, (d) $V_f = 2\%$ and (e) $V_f = 2.5\%$ 151

Figure 4.54: Ratio between the maximum load of each beam and that of the control specimen ($SI = 0\%, V_f = 0\%$) versus steel fibre volume fraction for Case Study 1(a)-C 151

Figure 4.55: Ratio between the ductility ratio of each beam and that of the control specimen ($SI = 0\%, V_f = 0\%$) versus steel fibre volume fraction for Case Study 1(a)-C 152

Figure 4.56: Ratio between the energy absorption of each beam and that of the control specimen ($SI = 0\%, V_f = 0\%$) versus steel fibre volume fraction for Case Study 1(a)-C 153

Figure 4.57: Ratio between the maximum number of cycles obtained before failure of each beam and that of the control specimen ($SI = 0\%, V_f = 0\%$) versus steel fibre volume fraction for Case Study 1(a)-C 154

Figure 4.58: Dimensions, loading arrangement and reinforcement detailing of the beams (adapted Campione et al, 2006) 154

Figure 4.59: Symmetrical half of the beam modelled using ABAQUS with (a) 155

defined boundary conditions at middle-side view (plane of symmetry) and (b) FE mesh

Figure 4.60: Load history input data for Case Study 1(b) 155

Figure 4.61: Tensile stress-strain diagram adopted for calibration work of Campione et al. (2006) beams 156

Figure 4.62: Calibration results for Case Study 1(b) for beams (a) with stirrups (i.e. S) and (b) without stirrups (i.e. NS) analysed under monotonic loading 156

Figure 4.63: Kinetic energy plots to determine failure for calibration work in Case Study 1(b) 157

Figure 4.64: Stress-strain relations in tension for parametric studies of Case Study 1(b) 158

Figure 4.65: Load-deflection curves for Case Study 1(b) with $SI = 0\%$ 160

Figure 4.66: Load-deflection curves for Case Study 1(b) with $SI = 50\%$ 160

Figure 4.67: Load-deflection curves for Case Study 1(b) with $SI = 100\%$ 160

Figure 4.68: Load-deflection curves for Case Study 1(b) with no stirrups (NS) 161

Figure 4.69: Principal strain contours for Case Study 1(b) beams with $SI = 0\%$ and (a) $V_f = 0\%$, (b) $V_f = 1\%$, (c) $V_f = 1.5\%$, (d) $V_f = 2\%$ and (e) $V_f = 2.5\%$ 164

Figure 4.70: Principal strain contours for Case Study 1(b) beams with $SI = 50\%$ and (a) $V_f = 0\%$, (b) $V_f = 1\%$, (c) $V_f = 1.5\%$, (d) $V_f = 2\%$ and (e) $V_f = 2.5\%$ 164

Figure 4.71: Principal strain contours for Case Study 1(b) beams with $SI = 100\%$ and ((a) $V_f = 0\%$, (b) $V_f = 1\%$, (c) $V_f = 1.5\%$, (d) $V_f = 2\%$ and (e) $V_f = 2.5\%$ 165

Figure 4.72: Principal strain contours for Case Study 1(b) beams with no stirrups (NS) and (a) $V_f = 0\%$, (b) $V_f = 1\%$, (c) $V_f = 1.5\%$, (d) $V_f = 2\%$ and (e) $V_f = 2.5\%$ 165

Figure 4.73: Principal strain vectors for Case Study 1(b) beams with $SI = 0\%$ and (a) $V_f = 0\%$, (b) $V_f = 1\%$, (c) $V_f = 1.5\%$, (d) $V_f = 2\%$ and (e) $V_f = 2.5\%$ 166

Figure 4.74: Principal strain vectors for Case Study 1(b) beams with $SI = 50\%$ and (a) $V_f = 0\%$, (b) $V_f = 1\%$, (c) $V_f = 1.5\%$, (d) $V_f = 2\%$ and (e) $V_f = 2.5\%$ 167

Figure 4.75: Principal strain vectors for Case Study 1(b) beams with $SI = 100\%$ and (a) $V_f = 0\%$, (b) $V_f = 1\%$, (c) $V_f = 1.5\%$, (d) $V_f = 2\%$ and (e) $V_f = 2.5\%$ 167

Figure 4.76: Principal strain vectors for Case Study 1(b) beams with no stirrups (NS) 167

and (a) $V_f = 0\%$, (b) $V_f = 1\%$, (c) $V_f = 1.5\%$, (d) $V_f = 2\%$ and (e) $V_f = 2.5\%$

Figure 4.77: Deflected shapes for Case Study 1(b) beams with $SI = 0\%$ and (a) $V_f = 0\%$, (b) $V_f = 1\%$, (c) $V_f = 1.5\%$, (d) $V_f = 2\%$ and (e) $V_f = 2.5\%$ 168

Figure 4.78: Deflected shapes for Case Study 1(b) beams with $SI = 50\%$ and (a) $V_f = 0\%$, (b) $V_f = 1\%$, (c) $V_f = 1.5\%$, (d) $V_f = 2\%$ and (e) $V_f = 2.5\%$ 168

Figure 4.79: Deflected shapes for Case Study 1(b) beams with $SI = 100\%$ and (a) $V_f = 0\%$, (b) $V_f = 1\%$, (c) $V_f = 1.5\%$, (d) $V_f = 2\%$ and (e) $V_f = 2.5\%$ 168

Figure 4.80: Deflected shapes for Case Study 1(b) beams with no stirrups (NS) and (a) $V_f = 0\%$, (b) $V_f = 1\%$, (c) $V_f = 1.5\%$, (d) $V_f = 2\%$ and (e) $V_f = 2.5\%$ 168

Figure 4.81: Ratio between the maximum load and that in the control specimen ($SI = 0\%, V_f = 0\%$) versus steel fibre volume fraction for Case Study 1(b) 169

Figure 4.82: Ratio between the yield load and that in the control specimen ($SI = 0\%, V_f = 0\%$) versus steel fibre volume fraction for Case Study 1(b) 170

Figure 4.83: Ratio between the ductility ratio in each beam and that in the control specimen ($SI = 0\%, V_f = 0\%$) versus steel fibre volume fraction for Case Study 1(b) 170

Figure 4.84: Ratio between the energy absorption in each column and that in the control specimen ($SI = 0\%, V_f = 0\%$) versus steel fibre volume ratio for Case Study 1(b) 171

Figure 4.85: Shear force (V) and bending moment (M) diagrams for Case Study 1(b) 172

Figure 5.1: Dimensions, loading arrangement and reinforcement detailing of the column (adapted from Kotsovos et al, 2007) 178

Figure 5.2: (a) constant axial force and (b) monotonic loading 179

Figure 5.3: (a) constant axial force and (b) reversed-cyclic loading 179

Figure 5.4: Symmetrical half of the column modelled in FE model in ABAQUS 180

Figure 5.5: Tensile stress-strain diagram adopted for calibration work of Kotsovos et al (2007) SFRC columns 180

Figure 5.6: Calibration results comparison for the column analysed under monotonic loading 181

Figure 5.7: Kinetic energy plots to determine failure for the column analysed under 182

monotonic loading

Figure 5.8: Principal (a) stress and (b) strain contour distribution, (c) principal strain direction distribution and (d) deformation shape of the column analysed under monotonic loading 183

Figure 5.9: Calibration results comparison for the column analysed under reversed-cyclic loading 184

Figure 5.10: Kinetic energy figure to determine failure under reversed-cyclic loading 185

Figure 5.11: Principal (a) stress and (b) strain contours, (c) principal strain vectors and (d) deflected shape for the column analysed under monotonic loading 185

Figure 5.12: Tensile stress-strain relations for Case Study 2 for different fibre volume fractions (V_f) 186

Figure 5.13: Load-deflection curve for Case Study 2(a) column with $SI = 0\%$ 188

Figure 5.14: Load-deflection curve for Case Study 2(a) column with $SI = 50\%$ 188

Figure 5.15: Load-deflection curve for Case Study 2(a) column with $SI = 100\%$ 188

Figure 5.16: Principal strain contours and vectors for Case Study 2(a) column with $SI = 0\%$ at at $\delta_y = 9.3\ mm$ for: (a) $V_f = 0\%$, (b) $V_f = 1.5\%$, and (c) $V_f = 2.5\%$ 191

Figure 5.17: Principal strain contours and vectors for Case Study 2(a) column with $SI = 0\%$ at $\delta_{max} = 34.2\ mm$ for: (a) $V_f = 0\%$, (b) $V_f = 1.5\%$, and (c) $V_f = 2.5\%$ 192

Figure 5.18: Principal strain contours and vectors for Case Study 2(a) column with $SI = 0\%$ at $V_f = 39.4\ mm$ for: (a) $V_f = 0\%$, (b) $V_f = 1.5\%$, and (c) $V_f = 2.5\%$ 193

Figure 5.19: Principal strain contours for Case Study 2(a) column with $SI = 0\%$ for (a) $V_f = 0\%$, (b) $V_f = 1\%$, (c) $V_f = 1.5\%$, (d) $V_f = 2\%$ and (e) $V_f = 2.5\%$ 194

Figure 5.20: Principal strain contours for Case Study 2(a) column with $SI = 50\%$ for (a) $V_f = 0\%$, (b) $V_f = 1\%$, (c) $V_f = 1.5\%$, (d) $V_f = 2\%$ and (e) $V_f = 2.5\%$ 195

Figure 5.21: Principal strain contours for Case Study 2(a) column with $SI = 100\%$ for (a) $V_f = 0\%$, (b) $V_f = 1\%$, (c) $V_f = 1.5\%$, (d) $V_f = 2\%$ and (e) $V_f = 2.5\%$ 195

Figure 5.22: Principal strain vectors for Case Study 2(a) column with $SI = 0\%$ for (a) $V_f = 0\%$, (b) $V_f = 1\%$, (c) $V_f = 1.5\%$, (d) $V_f = 2\%$ and (e) $V_f = 2.5\%$ 196

Figure 5.23: Principal strain vectors for Case Study 2(a) column with $SI = 50\%$ for (a) $V_f = 0\%$, (b) $V_f = 1\%$, (c) $V_f = 1.5\%$, (d) $V_f = 2\%$ and (e) $V_f = 2.5\%$ 196

Figure 5.24: Principal strain vectors for Case Study 2(a) column with $SI = 100\%$ for (a) $V_f = 0\%$, (b) $V_f = 1\%$, (c) $V_f = 1.5\%$, (d) $V_f = 2\%$ and (e) $V_f = 2.5\%$ 196

Figure 5.25: Deflected shapes for Case Study 2(a) column with $SI = 0\%$ for (a) $V_f = 0\%$, (b) $V_f = 1\%$, (c) $V_f = 1.5\%$, (d) $V_f = 2\%$ and (e) $V_f = 2.5\%$ 197

Figure 5.26: Deflected shapes for Case Study 2(a) column with $SI = 50\%$ for (a) $V_f = 0\%$, (b) $V_f = 1\%$, (c) $V_f = 1.5\%$, (d) $V_f = 2\%$ and (e) $V_f = 2.5\%$ 198

Figure 5.27: Deflected shapes for Case Study 2(a) column with $SI = 100\%$ for (a) $V_f = 0\%$, (b) $V_f = 1\%$, (c) $V_f = 1.5\%$, (d) $V_f = 2\%$ and (e) $V_f = 2.5\%$ 198

Figure 5.28: Ratio between the maximum load and that in the control column ($SI = 0\%, V_f = 0\%$) versus steel fibre volume fraction graph for Case Study 2(a) 199

Figure 5.29: Ratio between the yielding load and that in the control column ($SI = 0\%, V_f = 0\%$) versus steel fibre volume ratio graph for Case Study 2(a) 199

Figure 5.30: Ratio between the ductility fraction in each column and that in the control column ($SI = 0\%, V_f = 0\%$) versus steel fibre volume fraction graph for Case Study 2(a) 200

Figure 5.31: Ductility ratio in each column versus steel fibre volume fraction graph for Case Study 2(a) 201

Figure 5.32: Ratio between the energy absorption in each column and that in the control column ($SI = 0\%, V_f = 0\%$) versus steel fibre volume fraction graph for Case Study 2(a) 202

Figure 5.33: Ratio between the energy absorption in each column and that in the plain reinforced concrete column ($V_f = 0\%$) versus steel fibre volume fraction graph for Case Study 2(a) 202

Figure 5.34: The loading condition, bending moment (M) and shear force (V) diagram from Case Study 2 (Adapted from: Kotsovos et al, 2007) 203

Figure 5.35: Load-deflection curve for Case Study 2(b), column with $SI = 0\%$ 206

Figure 5.36: Load-deflection curve for Case Study 2(b), column with $SI = 50\%$ 206

Figure 5.37: Load-deflection curve for Case Study 2(b), column with $SI = 100\%$ 206

Figure 5.38: Load-deflection curve for Case Study 2(b) column with $SI = 0\%$ for each fibre fraction: (a) $V_f = 0\%$, (b) $V_f = 1\%$, (c) $V_f = 1.5\%$, (d) $V_f = 2\%$ and (e) 207

$V_f = 2.5\%$

Figure 5.39: Load-deflection curve for Case Study 2(b) column with $SI = 50\%$ for each fibre fraction: (a) $V_f = 0\%$, (b) $V_f = 1\%$, (c) $V_f = 1.5\%$, (d) $V_f = 2\%$ and (e) $V_f = 2.5\%$ 208

Figure 5.40: Load-deflection curve for Case Study 2(b) column with $SI = 100\%$ for each fibre fraction: (a) $V_f = 0\%$, (b) $V_f = 1\%$, (c) $V_f = 1.5\%$, (d) $V_f = 2\%$ and (e) $V_f = 2.5\%$ 209

Figure 5.41: Principal strain contours for Case Study 2(b) column with $SI = 0\%$ for (a) $V_f = 0\%$, (b) $V_f = 1\%$, (c) $V_f = 1.5\%$, (d) $V_f = 2\%$ and (e) $V_f = 2.5\%$ 211

Figure 5.42: Principal strain contours for Case Study 2(b) column with $SI = 50\%$ for (a) $V_f = 0\%$, (b) $V_f = 1\%$, (c) $V_f = 1.5\%$, (d) $V_f = 2\%$ and (e) $V_f = 2.5\%$ 212

Figure 5.43: Principal strain contours for Case Study 2(b) column with $SI = 100\%$ for (a) $V_f = 0\%$, (b) $V_f = 1\%$, (c) $V_f = 1.5\%$, (d) $V_f = 2\%$ and (e) $V_f = 2.5\%$ 212

Figure 5.44: Principal strain vectors for Case Study 2(b) column with $SI = 0\%$ for (a) $V_f = 0\%$, (b) $V_f = 1\%$, (c) $V_f = 1.5\%$, (d) $V_f = 2\%$ and (e) $V_f = 2.5\%$ 214

Figure 5.45: Principal strain vectors for Case Study 2(b) column with $SI = 50\%$ for (a) $V_f = 0\%$, (b) $V_f = 1\%$, (c) $V_f = 1.5\%$, (d) $V_f = 2\%$ and (e) $V_f = 2.5\%$ 214

Figure 5.46: Principal strain vectors for Case Study 2(b) column with $SI = 100\%$ for (a) $V_f = 0\%$, (b) $V_f = 1\%$, (c) $V_f = 1.5\%$, (d) $V_f = 2\%$ and (e) $V_f = 2.5\%$ 214

Figure 5.47: Deflected shapes for Case Study 2(b) column with $SI = 0\%$ for (a) $V_f = 0\%$, (b) $V_f = 1\%$, (c) $V_f = 1.5\%$, (d) $V_f = 2\%$ and (e) $V_f = 2.5\%$ 215

Figure 5.48: Deflected shapesfor Case Study 2(b) column with $SI = 50\%$ for (a) $V_f = 0\%$, (b) $V_f = 1\%$, (c) $V_f = 1.5\%$, (d) $V_f = 2\%$ and (e) $V_f = 2.5\%$ 215

Figure 5.49: Deflected shapesfor Case Study 2(b) column with $SI = 100\%$ for (a) $V_f = 0\%$, (b) $V_f = 1\%$, (c) $V_f = 1.5\%$, (d) $V_f = 2\%$ and (e) $V_f = 2.5\%$ 215

Figure 5.50: Ratio between the maximum load and that in the control column ($SI = 0\%, V_f = 0\%$) versus steel fibre volume fraction graph for Case Study 2(b) 216

Figure 5.51: Ratio between the ductility ratio in each column and that in the control column ($SI = 0\%, V_f = 0\%$) versus steel fibre volume fraction graph for Case 216

Study 2(b)

Figure 5.52: Ratio between the energy absorption in each column and that in the control column ($SI = 0\%, V_f = 0\%$) versus steel fibre volume fraction graph for Case Study 2(b) 218

Figure 5.53: Ratio between the maximum number of cycles before failure in each column and that in the control column ($SI = 0\%, V_f = 0\%$) versus steel fibre volume fraction graph for Case Study 2(b) 218

Figure 6.1: Dimensions and steel reinforcement details for (a) full-scale and (b) ½ - scale exterior beam-column joint (adopted from Bayasi and Gebman, 2002) 222

Figure 6.2: Tensile stress-stain diagram for SFRC adopted for the calibration work of the Bayasi and Gebman (2002) beam-column joints 222

Figure 6.3: Stress-stain diagram for conventional steel reinforcement adopted for the calibration work of the Bayasi and Gebman (2002) beam-column joints 223

Figure 6.4: ABAQUS input data for reversed-cyclic loading 223

Figure 6.5: Load-deflection hysteresis loops for calibration work in Case Study 3(a) 224

Figure 6.6: Kinetic energy graph for calibration work in Case Study 3(a) 225

Figure 6.7: Stress-strain relations in tension for Case Study 3(a) 226

Figure 6.8: Load-deflection curve for Case Study 3(a) for specimens with *SI* = 0% 228

Figure 6.9: Load-deflection curve for Case Study 3(a) for specimens with *SI* = 50% 228

Figure 6.10: Load-deflection curves for Case Study 3(a) for specimens with *SI* = 100% 228

Figure 6.11: Load-deflection curve for Case Study 3(a) for specimens with *SI* = 0% and (a) $V_f = 0\%$, (b) $V_f = 1\%$, (c) $V_f = 1.5\%$, (d) $V_f = 2\%$ and (e) $V_f = 2.5\%$ 229

Figure 6.12: Load-deflection curve for Case Study 3(a) for specimens with *SI* = 50% and (a) $V_f = 0\%$, (b) $V_f = 1\%$, (c) $V_f = 1.5\%$, (d) $V_f = 2\%$ and (e) $V_f = 2.5\%$ 230

Figure 6.13: Load-deflection curve for Case Study 3(a) for specimens with *SI* = 100% and (a) $V_f = 0\%$, (b) $V_f = 1\%$, (c) $V_f = 1.5\%$, (d) $V_f = 2\%$ and (e) $V_f = 2.5\%$ 231

Figure 6.14: Principal strain contours and vectors for exterior joints with $SI = 0\%$ and (a) $V_f = 0\%$, (b) $V_f = 1\%$, (c) $V_f = 2\%$ at $\delta_y = 6.25\ mm$ 234

Figure 6.15: Principal strain contours and vectors for exterior joints with $SI = 0\%$ and (a) $V_f = 0\%$, (b) $V_f = 1\%$, (c) $V_f = 2\%$ at $\delta_2 = 12.5\ mm$ 234

Figure 6.16: Principal strain contours and vectors for exterior joints with $SI = 0\%$ and (a) $V_f = 0\%$, (b) $V_f = 1\%$, (c) $V_f = 2\%$ taken at $\delta_3 = 24.9\ mm$ 235

Figure 6.17: Principal strain contours and vectors for exterior joints with $SI = 0\%$ and (a) $V_f = 1\%$ at $\delta_4 = 49.9\ mm$ 235

Figure 6.18: Principal stress contours for Case Study 3(a) joints with $SI = 0\%$ and (a) $V_f = 0\%$, (b) $V_f = 1\%$, (c) $V_f = 1.5\%$, (d) $V_f = 2\%$ and (e) $V_f = 2.5\%$ 237

Figure 6.19: Principal stress contours for Case Study (a) joints with $SI = 50\%$ and (a) $V_f = 0\%$, (b) $V_f = 1\%$, (c) $V_f = 1.5\%$, (d) $V_f = 2\%$ and (e) $V_f = 2.5\%$ 237

Figure 6.20: Principal stress contours for Case Study 3(a) joints with $SI = 100\%$ and (a) $V_f = 0\%$, (b) $V_f = 1\%$, (c) $V_f = 1.5\%$, (d) $V_f = 2\%$ and (e) $V_f = 2.5\%$ 238

Figure 6.21: Principal strain contours for Case Study 3(a) joints with $SI = 0\%$ and (a) $V_f = 0\%$, (b) $V_f = 1\%$, (c) $V_f = 1.5\%$, (d) $V_f = 2\%$ and (e) $V_f = 2.5\%$ 239

Figure 6.22: Principal strain contours for Case Study 3(a) joints with $SI = 50\%$ and (a) $V_f = 0\%$, (b) $V_f = 1\%$, (c) $V_f = 1.5\%$, (d) $V_f = 2\%$ and (e) $V_f = 2.5\%$ 240

Figure 6.23: Principal strain contours for Case Study 3(a) joints with $SI = 100\%$ and (a) $V_f = 0\%$, (b) $V_f = 1\%$, (c) $V_f = 1.5\%$, (d) $V_f = 2\%$ and (e) $V_f = 2.5\%$ 240

Figure 6.24: Principal strain vectors for Case Study 3(a) joints with $SI = 0\%$ and (a) $V_f = 0\%$, (b) $V_f = 1\%$, (c) $V_f = 1.5\%$, (d) $V_f = 2\%$ and (e) $V_f = 2.5\%$ 241

Figure 6.25: Principal strain vectors for Case Study 3(a) joints with $SI = 50\%$ and (a) $V_f = 0\%$, (b) $V_f = 1\%$, (c) $V_f = 1.5\%$, (d) $V_f = 2\%$ and (e) $V_f = 2.5\%$ 242

Figure 6.26: Principal strain vectors for Case Study 3(a) joints with $SI = 100\%$ and (a) $V_f = 0\%$, (b) $V_f = 1\%$, (c) $V_f = 1.5\%$, (d) $V_f = 2\%$ and (e) $V_f = 2.5\%$ 242

Figure 6.27: Deflected shapes for Case Study 3(a) joints with $SI = 0\%$ and ((a) $V_f = 0\%$, (b) $V_f = 1\%$, (c) $V_f = 1.5\%$, (d) $V_f = 2\%$ and (e) $V_f = 2.5\%$ 243

Figure 6.28: Deflected shapes for Case Study 3(a) joints with $SI = 50\%$ and ((a) $V_f = 0\%$, (b) $V_f = 1\%$, (c) $V_f = 1.5\%$, (d) $V_f = 2\%$ and (e) $V_f = 2.5\%$ 243

Figure 6.29: Deflected shapes for Case Study 3(a) joints with $SI = 100\%$ and (a) 243

$V_f = 0\%$, (b) $V_f = 1\%$, (c) $V_f = 1.5\%$, (d) $V_f = 2\%$ and (e) $V_f = 2.5\%$

Figure 6.30: Ratio of maximum load to that of the control specimen (SI $= 0\%, V_f =$ 0%) versus fibre volume fraction for Case Study 3(a) 244

Figure 6.31: Ratio of yield load to that of the control specimen ($SI = 0\%, V_f = 0\%$) versus fibre volume fraction for Case Study 3(a) 245

Figure 6.32: Ratio of ductility ratio to that of the control specimen ($SI = 0\%, V_f = 0\%$) versus fibre volume fraction for Case Study 3(a) 246

Figure 6.33: Ratio of energy absorption to that of the control specimen ($SI = 0\%, V_f = 0\%$) versus fibre volume fraction for Case Study 3(a) 247

Figure 6.34: Ratio of number of cycles to that of the control specimen ($SI = 0\%, V_f = 0\%$) versus fibre volume fraction for Case Study 3(a) 248

Figure 6.35: Prototype building (Adopted from Filiatrault et al, 1995 248

Figure 6.36: Details of the beam-column joints showing (a) specimens S1 and S3, (b) specimen S2, (c) column cross-section and d) beam cross-section (adopted from Filiatrault et al, 1995) 249

Figure 6.37: Loading arrangement of in cyclic (left) and reversed cyclic (right) loading 250

Figure 6.38: Beam-column joint modelled using ABAQUS with boundary condition and reinforcement details for specimens (a) S1 and S3, (b) S2 and (c) mesh adopted 251

Figure 6.39: Tensile stress-strain diagram for plain and fibre-reinforced concrete adopted in the calibration work for Filiatrault et al (1995) beam-column joints 252

Figure 6.40: Stress-strain diagram for conventional steel reinforcement bars adopted in the calibration work for Filiatrault et al (1995) beam-column joints 252

Figure 6.41: ABAQUS history input for calibration work 253

Figure 6.42: Storey shear-storey drift curves comparison for Specimen S1 254

Figure 6.43: Storey shear-storey drift curves comparison for Specimen S2 254

Figure 6.44: Storey shear-storey drift curves comparison for Specimen S3 254

Figure 6.45: Kinetic energy graph for Specimen S1 256

Figure 6.46: Kinetic energy graph for Specimen S2 256

Figure 6.47: Kinetic energy graph for Specimen S3 256

Figure 6.48: Principal (a) stress contour, (b) strain contour, (c) strain vectors and (d) deflected shape for Specimen S1 257

Figure 6.49: Principal (a) stress contour, (b) strain contour, (c) strain vectors and (d) deflected shape for Specimen S2 258

Figure 6.50: Principal (a) stress contour, (b) strain contour, (c) strain vectors and (d) deflected shape for Specimen S3 258

Figure 6.51: Stress-strain relations in tension for the Case Study 3(b) 260

Figure 6.52: ABAQUS history input for the parametric study in the Case Study 3(b) 261

Figure 6.53: Storey shear-drift curve for Case Study 3(b) joints with single stirrups 262

Figure 6.54 Storey shear-drift curve for Case Study 3(b) joints with $SI = 50\%$ 262

Figure 6.55: Storey shear-drift curve for Case Study 3(b) joints with $SI = 100\%$ 262

Figure 6.56: Storey shear-drift curve for Case Study 3(b) joints with single stirrups and (a) $V_f = 0\%$, (b) $V_f = 1\%$, (c) $V_f = 1.5\%$, (d) $V_f = 2\%$ and (e) $V_f = 2.5\%$ 263

Figure 6.57: Storey shear-drift curve for Case Study 3(b) joints with $SI = 50\%$ and (a) $V_f = 0\%$, (b) $V_f = 1\%$, (c) $V_f = 1.5\%$, (d) $V_f = 2\%$ and (e) $V_f = 2.5\%$ 264

Figure 6.58: Storey shear-drift curve for Case Study 3(b) joints with $SI = 100\%$ and (a) $V_f = 0\%$, (b) $V_f = 1\%$, (c) $V_f = 1.5\%$, (d) $V_f = 2\%$ and (e) $V_f = 2.5\%$ 265

Figure 6.59: Principal strain contour and vectors for joints with $SI = 50\%$ and (a) $V_f = 0\%$, (b) $V_f = 1\%$, (c) $V_f = 2\%$ taken from storey drift at $\Delta_y = 28.6$ mm 267

Figure 6.60: Principal strain contour and vectors for joints with $SI = 50\%$ (a) $V_f = 0\%$, (b) $V_f = 1\%$, (c) $V_f = 2\%$ taken at $\Delta_{max} = 69.4$ mm 268

Figure 6.61: Principal strain contours and vectors for joints with $SI = 50\%$ and ((a) $V_f = 0\%$, (b) $V_f = 1\%$, (c) $V_f = 2\%$taken at $\Delta_u = 100.2$ mm 269

Figure 6.62: Principal stress contours for Case Study 3(b) joints with single stirrups and (a) $V_f = 0\%$, (b) $V_f = 1\%$, (c) $V_f = 1.5\%$, (d) $V_f = 2\%$ and (e) $V_f = 2.5\%$ 270

Figure 6.63: Principal stress contours for Case Study 3(b) joints with $SI = 50\%$ and (a) $V_f = 0\%$, (b) $V_f = 1\%$, (c) $V_f = 1.5\%$, (d) $V_f = 2\%$ and (e) $V_f = 2.5\%$ 271

Figure 6.64: Principal stress contours for Case Study 3(b) joints with $SI = 100\%$ and (a) $V_f = 0\%$, (b) $V_f = 1\%$, (c) $V_f = 1.5\%$, (d) $V_f = 2\%$ and (e) $V_f = 2.5\%$ 271

Figure 6.65: Principal strain contours for Case Study 3(b) joints with single stirrups 272

and (a) $V_f = 0\%$, (b) $V_f = 1\%$, (c) $V_f = 1.5\%$, (d) $V_f = 2\%$ and (e) $V_f = 2.5\%$

Figure 6.66: Principal strain contours for Case Study 3(b) joints with $SI = 50\%$ and (a) $V_f = 0\%$, (b) $V_f = 1\%$, (c) $V_f = 1.5\%$, (d) $V_f = 2\%$ and (e) $V_f = 2.5\%$ 273

Figure 6.67: Principal strain contours for Case Study 3(b) joints with $SI = 100\%$ and (a) $V_f = 0\%$, (b) $V_f = 1\%$, (c) $V_f = 1.5\%$, (d) $V_f = 2\%$ and (e) $V_f = 2.5\%$ 273

Figure 6.68: Principal strain vectors for Case Study 3(b) joints with single stirrups and (a) $V_f = 0\%$, (b) $V_f = 1\%$, (c) $V_f = 1.5\%$, (d) $V_f = 2\%$ and (e) $V_f = 2.5\%$ 273

Figure 6.69: Principal strain vectors for Case Study 3(b) joints with $SI = 50\%$ and (a) $V_f = 0\%$, (b) $V_f = 1\%$, (c) $V_f = 1.5\%$, (d) $V_f = 2\%$ and (e) $V_f = 2.5\%$ 274

Figure 6.70: Principal strain vectors for Case Study 3(b) joints with $SI = 100\%$ and (a) $V_f = 0\%$, (b) $V_f = 1\%$, (c) $V_f = 1.5\%$, (d) $V_f = 2\%$ and (e) $V_f = 2.5\%$ 275

Figure 6.71: Deflected shapes for Case Study 3(b) joints with single stirrups and (a) $V_f = 0\%$, (b) $V_f = 1\%$, (c) $V_f = 1.5\%$, (d) $V_f = 2\%$ and (e) $V_f = 2.5\%$ 275

Figure 6.72: Deflected shapes for Case Study 3(b) joints with $SI = 50\%$ and (a) $V_f = 0\%$, (b) $V_f = 1\%$, (c) $V_f = 1.5\%$, (d) $V_f = 2\%$ and (e) $V_f = 2.5\%$ 276

Figure 6.73: Deflected shapes for Case Study 3(b) joints with $SI = 100\%$ and (a) $V_f = 0\%$, (b) $V_f = 1\%$, (c) $V_f = 1.5\%$, (d) $V_f = 2\%$ and (e) $V_f = 2.5\%$ 276

Figure 6.74: Ratio of maximum storey shear to that of the control joint versus fibre volume fraction graph for Case Study 3(b) 277

Figure 6.75: Ratio of storey shear at yield to that of the control joint versus fibre volume fraction graph for Case Study 3(b) 277

Figure 6.76: Ratio between the ductility ratio of each joint and that of the control joint versus fibre volume fraction for Case Study 3(b) 278

Figure 6.77: Ratio between the energy absorption of each joint and that of the control joint versus fibre volume fraction for Case Study 3(b) 279

Figure 6.78: Ratio between the maximum number of cycles of each joint and that of the control joint versus fibre volume fraction for Case Study 3(b) 280

Figure 7.1: Ductility ratio (μ) in (a) 3D surface and (b) 2D contour diagrams; and Maximum load-carrying capacity (P_{max}) in (c) 3D surface and (d) 2D contour 285

diagrams expressed in terms of r_{sw} and V_f for Case Study 1(a)-M

Figure 7.2: Ductility ratio (μ) in (a) 3D surface and (b) 2D contour diagrams; and Maximum load-carrying capacity (P_{max}) in (c) 3D surface and (d) 2D contour diagrams expressed in terms of r_{sw} and V_f for Case Study 1(a)-C 286

Figure 7.3: Ductility ratio (μ) in (a) 3D surface and (b) 2D contour diagrams; and Maximum load-carrying capacity (P_{max}) in (c) 3D surface and (d) 2D contour diagrams expressed in terms of r_{sw} and V_f for Case Study 1(b) 287

Figure 7.4: Ductility ratio (μ) in (a) 3D surface and (b) 2D contour diagrams; and Maximum load-carrying capacity (P_{max}) in (c) 3D surface and (d) 2D contour diagrams expressed in terms of r_{sw} and V_f for Case Study 2(a) 288

Figure 7.5: Ductility ratio (μ) in (a) 3D surface and (b) 2D contour diagrams; and Maximum load-carrying capacity (P_{max}) in (c) 3D surface and (d) 2D contour diagrams expressed in terms of r_{sw} and V_f for Case Study 2(b) 289

Figure 7.6: Ductility ratio (μ) in (a) 3D surface and (b) 2D contour diagrams; and Maximum load-carrying capacity (P_{max}) in (c) 3D surface and (d) 2D contour diagrams expressed in terms of r_{sw} and V_f for Case Study 3(a) 291

Figure 7.7: Ductility ratio (μ) in (a) 3D surface and (b) 2D contour diagrams; and Maximum load-carrying capacity (P_{max}) in (c) 3D surface and (d) 2D contour diagrams expressed in terms of r_{sw} and V_f for Case Study 3(b) 292

Figure A.1: Dimension and loading condition of specimen C2 (Modified from: Hughes and Speirs, 1982) 311

Figure A.2: Results comparison graph for specimen C2 (Hughes and Speirs, 1982) 312

Figure A.3: Dimension and loading condition of beam OA-1 (Modified from: Bresler and Scordelis, 1963) 313

Figure A.4: Results comparison graph for beam OA-1 (Bresler and Scordelis, 1963) 313

Figure A.5: Dimension and loading condition of the notched beam (Modified from: Barros et al, 2005) 314

Figure A.6: Tensile stress-strain diagram for Barros et al (2005) SFRC beams for RC 65/60 BN (v_f = 0.58%) 315

Figure A.7: Tensile stress-strain diagram for Barros et al (2005) SFRC beams for RC 80/60 BN (with v_f = 0.4%) 315

Figure A.8: Comparison graph for SFRC beam RC 65/60(v_f = 0.58%) 316

Figure A.9: Comparison graph for SFRC beam RC 80/60 (v_f = 0.4%) 317

Figure A.9 (b): Comparison graph for SFRC beam RC 80/60 (v_f = 0.4%) until displacement = 1 mm 317

Figure A.10: Dimension and loading condition of the beams (Modified from: Tlemat[b] et al, 2006) 318

Figure A.11: Tensile stress-strain diagram for ISF-1 with v_f = 6% 319

Figure A.12: Tensile stress-strain diagram for ISF-2 with v_f = 6% 319

Figure A.13: ISF-1 results graph using SC concrete model (v_f = 6%) 320

Figure A.14: ISF-2 results graph using SC concrete model (v_f = 6%) 320

Figure A.15: ISF-1 results graph using BC concrete model (v_f = 6%) 320

Figure A.16: ISF-2 results graph using BC concrete model (v_f = 6%) 321

Figure A.17: Dimension and loading condition of the beams (Modified from: Barros and Figueiras, 1999) 322

Figure A.18: Tensile stress-strain diagram for Barros and Figueiras (1999) ZP 30/.50 SFRC beams (v_f = 0.77%) 322

Figure A.19: Tensile stress-strain diagram for Barros and Figueiras (1999) ZX 60/.80 SFRC beams (v_f = 0.77%) 323

Figure A.20: Comparison graph for specimen ZP 30/.50 (v_f = 0.77%) 323

Figure A.21: Comparison graph for specimen ZX 60/.80 (v_f = 0.77%) 324

Figure A.22: Dimension and loading condition of the beams (Modified from: Trottier and Banthia, 1994) 324

Figure A.23: Tensile stress-strain diagram for Trottier and Banthia (1994) SFRC beams using Lok and Pei (1998) model with v_f = 0.51% 325

Figure A.24: Comparison graph for specimen F1 (v_f =0.51%) using 2D element 325

Figure A.25: Comparison graph for specimen F1 (v_f =0.51%) using 3D element 326

Figure A.26: Dimension and loading condition of SFRC batch SFC-30 (Modified from Cho and Kim, 2003) 326

Figure A.27: Material models values applied into ABAQUS for beam (v_f =1.0%) 327

Figure A.28: Material models values applied into ABAQUS for beam (v_f =1.5%) 327

Figure A.29: Material models values applied into ABAQUS for beam (v_f =2.0%) 328

Figure A.30: Comparison results for beam SFC-30 with v_f =1.0% 328

Figure A.31: Comparison results for beam SFC-30 with v_f =1.5% 329

Figure A.32: Comparison results for beam SFC-30 with v_f =2.0% 329

Figure A.33: Dimension and loading condition of SFRC S0.5V1 and S0.5V2 beams (Oh et al, 2009) 330

Figure A.34: Material models values applied into ABAQUS for beam S0.5V1 (v_f =1.0%) 330

Figure A.35: Material models values applied into ABAQUS for beam S0.5V2 (v_f =2.0%) 331

Figure A.36: Comparison results for beam S0.5V1 with v_f =1.0% 331

Figure A.37: Comparison results for beam S0.5V2 with v_f =2.0% 332

Figure A.38: Beam dimensions and reinforcement detailing (Modified from Sharma, 1986) 332

Figure A.39: Material models values applied into ABAQUS for beam DF3 333

Figure A.40: Comparison results between experimental and numerical simulation for beam DF3 334

Figure B.1: Strut inclination method (Reproduced from Eurocode 2, 2003) 335

Figure B.2: Spreadsheet shear capacity calculation screenshot for the RC beams 337

Figure B.3: Spreadsheet shear capacity calculation screenshot for the SFRC beams 337

Figure B.4: Flexural section analysis for RC beam (Reproduced from Eurocode 2, 2003) 338

Figure B.5: Flexural section analysis for SFRC beam (Reproduced from Concrete Society TR-63, 2007) 339

Figure B.6: Spreadsheet bending moment capacity calculation screenshot for the RC 340

beams
Figure B.7: Spreadsheet bending moment capacity calculation screenshot for the SFRC beam 340

LIST OF TABLES

Table 2.1: SFRC strength classes (adopted from RILEM TC 162-TDF, 2003) 64
Table 2.2: Summary of bond stress values 70
Table 2.3: Ultimate strain and *p* value of SFRC (adopted from Barros and Figueiras, 1999) 73
Table 2.4: Values to define the characteristic points of the softening diagram of SFRC (adopted from Barros and Figueiras, 2001) 75
Table 2.5: New approaches for defining the post cracking σ-ε diagram for SFRC (adopted from Barros et al., 2005) 76
Table 2.6: Factors for the proposed model (adopted from Tlemat et al, 2006) 77

Table 3.1: Stirrups spacing values considered for Case study 1(a) 110
Table 3.2: Stirrups spacing values considered for Case study 1(b) 111
Table 3.3: Stirrups spacing values considered for Case study 2 112
Table 3.4: Stirrups spacing values considered for Case study 3(a) 113
Table 3.5: Stirrups spacing values considered for Case study 3(b) 113

Table 4.1(a): Tensile stress-strain relationship for RC beams with no fibres 116
Table 4.1(b): Tensile stress-strain relationship for SFRC beams with V_f= 1% 116
Table 4.2: Results summary of load-deflection curves for calibration work in Case Study 1(a)-M 118
Table 4.3: Results summary of load-deflection curves for calibration work in Case Study 1(a)-C 119
Table 4.4(a): Tensile stress-strain properties for plain concrete for Case Study 1(a) 120
Table 4.4(b): Tensile stress-strain properties for SFRC for Case Study 1(a) 120
Table 4.5: Summary of the significant values in the load-deflection curves for beams in Case Study 1(a)-M beam with $SI = 0\%$ 123
Table 4.6: Summary of the significant values in the load-deflection curves for beams in Case Study 1(a)-M beam with $SI = 50\%$ 123

Table 4.7: Summary of the significant values in the load-deflection curves for beams in Case Study 1(a)-M beam with $SI = 100\%$ 124

Table 4.8: Summary of the significant values in the load-deflection curves for beams in Case Study 1(a)-M beam with $SI = 200\%$ 124

Table 4.9: FE- and code-based strength predictions for Case study 1(a) $SI = 0\%$ 137

Table 4.10: FE- and code-based strength predictions for Case study 1(a) $SI = 50\%$ 137

Table 4.11: FE- and code-based strength predictions for Case study 1(a) $SI = 100\%$ 137

Table 4.12: FE- and code-based strength predictions for Case study 1(a) $SI = 200\%$ 138

Table 4.13: Results summary from load-deflection curves for Case Study 1(a)-C for beams with $SI = 0$ 141

Table 4.14: Results summary from load-deflection curves for Case Study 1(a)-C for beams with $SI = 50\%$ 142

Table 4.15: Results summary from load-deflection curves for Case Study 1(a)-C for beams with SI $= 100\%$ 143

Table 4.16: Results summary from load-deflection curves for Case Study 1(a)-C for beams with $SI = 200\%$ 144

Table 4.17: Calibration results summary for Case Study 1(b) 157

Table 4.18(a): Tensile stress-strain parameters for plain concrete for Case Study 1(b) 158

Table 4.18(b): Tensile stress-strain parameters for SFRC for Case Study 1(b) 159

Table 4.19: Results summary for Case Study 1(b) for beams with $SI = 0\%$ 161

Table 4.20: Results summary for Case Study 1(b) for beams with $SI = 50\%$ 161

Table 4.21: Results summary for Case Study 1(b) for beams with $SI = 100\%$ 162

Table 4.22: Results summary for Case Study 1(b) for beams with no stirrups (NS) 162

Table 4.23: Bending moment capacity calculated for beams in Case Study 1(b) 172

Table 4.24: FE- and code-based strength predictions for Case Study 1(b) beams with $SI = 0\%$ 173

Table 4.25: FE- and code-based strength predictions for Case Study 1(b) beams with $SI = 50\%$ 173

Table 4.26: FE- and code-based strength predictions for Case Study 1(b) beams with $SI = 100\%$ 173

Table 4.27: FE- and code-based strength predictions for Case Study 1(b) beams with no stirrups 173

Table 5.1: Tensile stress-strain relationship for a SFRC mixture with a fibres volume fraction of 0.4% 180

Table 5.2: Result summary from load-deflection curve under monotonic loading 181

Table 5.3: Relevant values from both the Experimental and FE model as well as the expected values from Eurocode 2, under monotonic loading 181

Table 5.4: Result summary from load-deflection curve under reversed-cyclic loading 184

Table 5.5: Relevant values from both the Experimental and FE model as well as the expected values from Eurocode 2, under reversed-cyclic loading 184

Table 5.6(a): Tensile stress-strain properties for plain concrete for Case Study 2 186

Table 5.6(b): Tensile stress-strain properties for fibre-reinforced concrete for Case Study 2 186

Table 5.7: Result summary from load-deflection curve for Case Study 2(a) column with $SI = 0\%$ 189

Table 5.8: Result summary from load-deflection curve for Case Study 2(a) column with $SI = 50\%$ (* CC is the control column with V_f = 0% and *SI* = 0%) 189

Table 5.9: Result summary from load-deflection curve for Case Study 2(a) column with $SI = 100\%$ (* CC is the control column with V_f = 0% and *SI* = 0%) 189

Table 5.10: Section flexural capacity (M_p) calculated based on Eurocode 2 203

Table 5.11: Comparison of analysis results and calculated values for Case Study 2(a) column with $SI = 0\%$ 204

Table 5.12: Comparison of analysis results and calculated values for Case 204

Study 2(a) column with $SI = 50\%$

Table 5.13: Comparison of analysis results and calculated values for Case Study 2(a) column with $SI = 100\%$ 204

Table 5.14: Result summary from load-deflection curve for Case Study 2(b) column with $SI = 0\%$ 207

Table 5.15: Result summary from load-deflection curve for Case Study 2(b) column with $SI = 50\%$ 207

Table 5.16: Result summary from load-deflection curve for Case Study 2(b) column with $SI = 100\%$ 207

Table 6.1: Summary of key points on tress-strain diagrams adopted for the calibration work of Bayasi and Gebman (2002) beam-column joints 223

Table 6.2: Results summary of load-deflection curve for calibration in Case Study 3(a) 225

Table 6.3(a): Tensile strain-stress properties for plain concrete for Case Study 3(a) 226

Table 6.3(b): Tensile strain-stress relation for SFRC for Case Study 3(a) 226

Table 6.4: Results summary for Case Study 3(a) for specimens with *SI* = 0% 229

Table 6.5: Results summary for Case Study 3(a) for specimens with *SI* = 50% (* CJ is the control joint specimen with V_f = 0% and *SI* = 0%) 230

Table 6.6: Results summary for Case Study 3(a) for specimens with *SI* = 100% (* CJ is the control joint specimen with V_f = 0% and *SI* = 0%) 231

Table 6.7(a): Tensile stress-strain properties for plain concrete 252

Table 6.7(b): Stress-strain properties adopted for the calibration work for Filiatrault et al (1995) beam-column joints 252

Table 6.8: Result summary from storey shear – storey drift curves (Specimen S1) 255

Table 6.9: Result summary from storey shear – storey drift curve (Specimen S2) 255

Table 6.10: Result summary from storey shear – storey drift curves (Specimen S3) 255

Table 6.11(a): Tensile strain-stress properties for plain concrete in Case Study 3(b) 260

Table 6.11(b): Tensile strain-stresses properties for SFRC in Case Study 3(b) 260
Table 6.12: Result summary from storey shear-drift curve for Case Study 3(b) joints with single stirrups 263
Table 6.13: Result summary from storey shear-drift curve for Case Study 3(b) joints with $SI = 50\%$ 264
Table 6.14: Result summary from storey shear-drift curve for Case Study 3(b) joints with $SI = 100\%$ 265

Table 7.1: Relationship between *SI* and r_{sw} 284

Table A.1: Summary of geometry, tensile strength and fibre content for each type of steel fibres (Modified from: Barros et al, 2005) 314
Table A.2: Summary of geometry, tensile strength and volume percentage for each type of fibre (Adapted from: Tlemat[a] et al, 2006) 318
Table A.3: Summary of geometry, tensile strength and fibre content for each type of fibre (Barros and Figueiras, 1999) 322
Table A.4: Summary of geometry, tensile strength and fibre content for F1 steel fibre (Trottier and Banthia, 1994) 324
Table A.5: Summary of geometry and fibre content for F1 steel fibre (Cho and Kim, 2003) 327
Table A.6: Summary of geometry, tensile strength and fibre content for F1 steel fibre (Oh et al, 2009) 330
Table A.7: Summary of geometry, tensile strength, fibre content and concrete strength of the beam (Sharma, 1986) 332

LIST OF SYMBOLS

The following symbols are used in this thesis. They are all defined where they first appear. Where more than one meaning has been assigned to a symbol, the correct definition will be evident from the context.

f_t	the concrete tensile strength
f_{tu}	the post-cracking residual tensile stress
ε_{t0}	the cracking strain
ε_{tu}.	the ultimate (post-cracking) strain
δ	deformation
T1	the tensile zone
C	compressive zone
$f_{eq,i}$.	equivalent flexural strength
b	width of the specimen
h_{sp}	the distance between tip of the notch and top of cross section of the specimen
L	the span length of the specimen
σ_{fc}	ultimate compressive stress
$\varepsilon_{fc,d}$	ultimate compressive strain
γ_C	design safety factor for concrete
$f_{R,I}$	the residual flexural tensile strength
κ_h	size factor
f_{fck}	characteristic compressive strength

$f_{fctm,fl}$	mean flexural tensile strength
$f_{fctk,fl}$	characteristic flexural tensile strength
E_{fcm}	mean secant modulus of elasticity
$CMOD_i$	crack mouth opening displacement
$\delta_{R,I}$	mid span deflection
$F_{R,i}$	residual flexural load
$\eta_0^{'}$	fibre orientation factors
η_0	orientation factor in the elastic range
σ_{tu}	ultimate tensile strength
τ_u	the average ultimate pullout bond strength of fibres
E_{ct}	tensile elastic modulus for SFRC composite
V_m	volume fraction of the matrix
V_f	volume fraction of the fibres
E_{mt}	tensile elastic modulus for the matrix
E_f	Young's modulus of steel fibres
η_l	the ratio of the average fibre stress to the maximum fibre stress
ε_{cr}	first crack strain of the composite
ε_{fp}	strain at the proportional limit for the fibre
ε_{mp}	strain at the proportional limit for the matrix
l_f	fibre length
r	the ratio of fibre cross-sectional area to its perimeter.
l^*	reference length taken as the average crack spacing
f_{cu}	characteristic cube strength
γ_m	partial material safety factor
E_{oc}	initial tangent modulus of the fibrous composites

σ_1	compressive stress
ε_1	compressive strain
ε_1^{**}	failure compressive strain
ε_2^{**}	maximum tensile strain at failure
N_1	defined as number of fibres per unit cross sectional area
f_{ct}	concrete tensile strength
f_{cm}	concrete mean cylinder strength
f_c	compressive strength of concrete
ε_{cu}	ultimate compressive strain
η	fibre orientation factor in a 3 dimensional (3D) case
w_f	fibre weight ratio
ε_{c10}	Strain at peak for plain concrete
f_{ctm}	peak tensile strength
C_f	fibre content
N_f	number of fibres on the fracture surface
$\sigma_{t,p}^u$	the maximum tensile stress for plain concrete
ξ	steel fibre-type factor
σ_t	tensile cracking stress
σ_t^u	ultimate tensile cracking stress
ε_t	plastic tensile strain
ε_t^u	elastic ultimate tensile strain
ρ^{close}	shear modulus (i.e. shear retention factor)
ε_{max}	ABAQUS maximum strain
$\tilde{\varepsilon}_t^{ck}$	cracking strain

$\tilde{\varepsilon}_t^{in}$	the inelastic (crushing) strain
ε_t	total strain
ε_{ol}^{el}	elastic strain corresponding to the undamaged material
w_t	tension stiffness recovery factor
w_c	compression stiffness recovery factor
P	lateral monotonic or reversed-cyclic load
N	axial load
SI	Stirrup spacing increased
P_y	yielding load
$P_{y,0}$	yielding load of the control specimen
P_{max}	maximum load carrying capacity
$P_{max,0}$	maximum load carrying capacity of the control specimen
P_u	ultimate load
δ_y	deflection at yield
δ_{Pmax}	deflection at maximum load
δ_u	ultimate deflection
μ	ductility ratio
$\mu_{,o}$	ductility ratio of the control specimen
E_a	energy absorption
$E_{a,0}$	energy absorption of the control specimen
N_c	number of cycles analysed before failure
$N_{c,0}$	number of cycles analysed by the control specimen before failure
V_{rd}	shear capacity
M_{rd}	bending moment caapcity
P_{sc}	load calculated based on shear capacity

P_{BMC}	load calculated based on bending moment capacity
f_y	the longitudinal reinforcement yield stress
N_u	the compression resistance of the column provided by concrete
f_c	the uniaxial cylinder compressive strength of concrete
P_{ty}	true yield load
P_{1p}	load at formation of the first plastic hinges
P_{2p}	load at formation of the second plastic hinges
P_{sust}	sustained load
δ_{sust}	sustained deflection
μ_{sust}	sustained ductility ratio
R_2	reaction at the intermediate support
M_p	flexural capacity
V_{col}	storey shear force
Δ_{col}	storey drift
P_1	actuator force on the beam due to l_1
P_2	actuator force on the beam due to l_2
l_1	the distance of vertical actuators due to Δ_{B1} from the column centre
l_2	the distance of vertical actuators due to Δ_{B2} from the column centre
Δ_{B1}	the vertical displacements at the loading point P_1
Δ_{B2}	the vertical displacements at the loading point P_2
l_c	total height of the column between supports
Δ_y	yield storey drift
Δ_{max}	storey drift at maximum storey shear
V_{max}	maximum storey shear capacity
V_y	yielding storey shear

Δ_u	ultimate storey drift at failure
V_u	ultimate storey shear
r_{sw}	ratio of the stirrups content
SI	increased in the stirrups spacing
SFRC	steel fibre-reinforced concrete
FEA	finite-element analysis
FE	finite-element
RC	reinforced concrete
NLFEM	non-liner finite-element model
NLFEA	non-linear finite element analysis

CHAPTER 1

INTRODUCTION AND OBJECTIVES

1.1 Research background

The history of fibre-reinforced materials started in ancient Egypt over 2000 years ago with mud bricks reinforced with straw fibres (Crowther, 2009). In more recent times, it has moved to the application of asbestos fibre cement which had been used widely since early 1900s. However, due to the health risks associated with using asbestos, some other alternative fibres were introduced in the 1960s, such as steel, glass, and synthetic fibres such as polypropylene fibres etc. Early investigation into the application of steel fibre-reinforced concrete (SFRC) was carried out by Romualdi and Batson (1963) resulted in its application in the pavement construction. Since then, fibres have become widely adopted in different structural applications, for instance in concrete pipes, pavement slabs, marine and refractory applications (Swamy and Lankard, 1974). More recently, it has been used in suspended slabs (Destree, 2001).

Some of the popular fibres available in the market are steel, carbon, plastic (i.e polypropylene, graphite etc), glass and natural (i.e hemp, kenaf etc) fibres. Amongst these different types, steel fibres are widely used in the reinforced concrete (RC) structures, especially slabs, due to its capability in restraining crack opening; and enhancing the ductility, load-carrying capacity and post-cracking behaviour (Swamy and Lankard, 1974; Hannant, 1978; Swamy, 1984; etc). The present research work focuses on the behaviour of steel fibres and other types are outside the scope of this study.

Steel fibres performance is influenced by several factors such as shape, fibre content and aspect ratio (Sharma, 1986; Trottier and Banthia, 1994; Robins et al., 2002; Khaloo and Afshari, 2005). The combination of these factors contributes to the anchorage mechanism between the fibres and the concrete, also the bond stress that develops between the two materials. Fibres with deformed shapes and/or hooked ends usually behave better than straight ones due to the resulting enhanced bond with concrete.

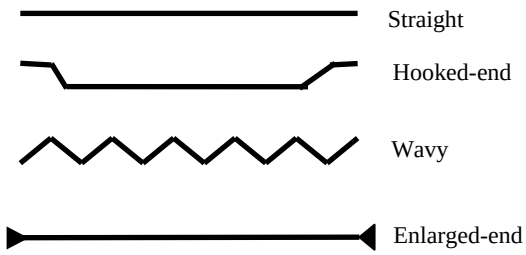


Figure 1.1: Examples of the shapes available for steel fibres

Studies by Trottier and Banthia (1994) and Tlemat et al., (2006) and others confirmed that the anchorage and pull-out behaviour observed is better in fibres with deformed shapes at the ends only (e.g. hooked-end, twin-cone) in comparison to fibres with deformed shapes along their length. Perhaps the most important factor is the amount of fibres provided. If the amount of fibres is increased, this enhances the number of fibres bridging the crack and thus actively restraining crack propagation. Combining these factors with an appropriate aspect ratio value (i.e. ratio of fibre length to diameter) contributes to high energy absorption capacity as well as better pulled out resistance.

Previous experimental research work has demonstrated that steel fibres are capable of increasing the ductility of reinforced concrete structures while reducing steel congestion especially in heavily reinforced regions of beam-column joints (Henager, 1977; Filiatrault et al., 1994). However, limited recommendations (ACI Committee Report, 1988; and Casanova and Rossi, 1997) were made regarding design issues.

1.2 Problem statement

Plain concrete deteriorates rapidly and loses it reliability due to its brittleness and lack of post-peak resistance. Fibres are widely believed to enhance the ductility of concrete, a largely brittle material on its own, and thus improve the structure's ability to

accommodate deformations. This is particularly useful in seismic situations. Furthermore, fibres also improves the energy absorption capacity of the structures (Khaloo and Afhsari, 2005), which is also beneficial in seismic design as there is usually a need for energy dissipation.

One of the main concerns in RC structures is steel congestion, especially for structures designed to accommodate seismic loading. In particular, the beam-column joint region usually is designed to accommodate a high amount of reinforcement. Several studies have been carried out in order to reduce the steel congestion, whilst maintaining the integrity (i.e. loading capacity and ductility) of the structure. One of the potential alternatives is to use steel fibres, which has been examined experimentally by Henager (1977), Jiuru et al (1992), and Filiatrault et al. (1994, 1995). The investigations indicated structural benefits to applying steel fibres as part of the shear reinforcement. This shows potential for reducing the steel congestion, especially in the joint region of RC frames.

Based on the information discussed above with regards to steel fibres properties and their potential to enhance the structural response of the RC structures, it is crucial and beneficial to investigate further and understand the behaviour of SFRC especially under reversed-cyclic and seismic loading conditions. Studies carried out so far (i.e. Filiatrault et al., 1994, 1995; Bayasi and Gebman, 2002) are limited to certain types of structural configuration and only consider a narrow range of fibres ratio due to economical and time constraints. They are also largely experimental studies, which lack the benefit of carrying out full parametric examinations such as one carried out in the present work. Furthermore, limited studies have been carried out to examine any prospective improvement in reducing the congestion of transverse reinforcement (usually provided for shear and confinement purposes) with the introduction of steel fibres.

Therefore, it is of interest to expand previous work to investigate the potential of utilising steel fibres as part of the shear reinforcement, understanding SFRC behaviour considering the full range of fibre dosages and how it can compliment conventional shear reinforcement arrangement. This will result in conclusions and recommendations to help minimise steel congestion, especially the one associated with seismic reinforcement detailing.

In order to achieve the desired seismic performance, it is crucial to ensure that RC structures are designed to behave in a ductile manner. Ductility provides the best assurance against collapse in regions of moderate to high seismicity. This can be achieved by providing adequate lateral strength in the structures. Minimum lateral strength is required even in a very ductile structure to limit yielding and reduce damage caused by moderate frequent earthquakes. Fundamentally, the structure has to be well tied together. In frame structures, strong column and weak beam provide good ductility and is evaluated through capacity design. The latter ensures that the ductile regions yield first and protect the brittle regions from reaching their capacity.

The present research aims to examine the potential for reducing the steel congestion in beam-column joint regions by using SFRC. Parametric and case studies are also carried out in order to propose design recommendations where possible.

The focus of the present study is on reinforced concrete frames (i.e. beams, columns and beams-columns joints), the overall structural responses as well as the local response at critical sections are examined. Conclusions are then made on whether or not steel fibres demonstrate the capability to achieve sufficient strength, stiffness and ductility.

The research work investigates the following key structural issues:

1. Strength: shear force and bending moment capacities at critical sections of beams, columns and beam-column joints (shear behaviour at point of inflection or contra-flexure are studied as well).
2. Stiffness: maximum displacement (e.g. storey drift).
3. Ductility: ratio of maximum displacement / displacement at yield.
4. Plastic hinges formation.
5. Cracking: patterns and locations (potential of cracking at joints will also be studied).

1.3 Research aim, objectives and scope

The overall aim of the present research work is to investigate the behaviour of SFRC structures under reversed-cyclic (i.e. seismic) loading and the potential of fibres in reducing the conventional reinforcement congestion especially in the joint region.

Conclusions and recommendations are made regarding steel fibres potential benefits in enhancing ductility and load carrying capacity of the structures.

The specific objectives of the present work can be classified as follow:

1. To collect and review experimental data (at both material and structural levels) and constitutive models for SFRC under monotonic and reversed-cyclic loading.
2. To implement these constitutive models for SFRC into the finite-elemet (FE) model (ABAQUS version 6.9) and subsequently carry out calibration and validation work using existing experimental data and select the most suitable SFRC material model for the subsequent parametric investigations.
3. To carry out case and parametric studies for SFRC structures (such as beams, columns and beam-column joints) under monotonic and reversed-cyclic loading.
4. To investigate numerically the behaviour of RC structures when steel fibres are added into the mix, especially when this is coupled with a reduction in conventional shear reinforcement as part of the parametric studies.
5. To determine the potential effects of steel fibres on key parameters such as strength, ductility, energy absorption, stiffness and cracking of SFRC structures.
6. To draw conclusions and recommendations for future work.

To facilitate the progress of the current work, the scope of the current work can be explained as follow:

1. Only hooked-end steel fibres are considered, with the fibres properties considered are explained in the respective work.
2. Three types of structures covered in the case studies are simply supported beams, two-span continuous columns, interior and exterior beam-column joints. Experimental data has been collected for each of these case studies which are used initially to validate the FE predictions. Subsequently, further parametric studies are carried out to cover the full range of key parameters such as amount of fibres (i.e. to extend the work beyond the limited scope considered experimentally).

3. In the present study, two parameters are considered for the parametric study, namely steel fibre volume fraction (i.e. ratio between volume of fibres and volume of concrete) and amount of conventional shear reinforcement. Five volume fractions are adopted to represent the practical range of fibre dosages, namely: 0%, 1%, 1.5%, 2% and 2.5%. The conventional shear reinforcement is also reduced by increasing the stirrups spacing by 50% and 100% (and 200% or no stirrups in some cases).

1.4 Thesis outline

This thesis consists of seven chapters which can be categorised into two parts. The first part, which is presented in Chapters 2 and 3 consist of data collection and the means of numerical modelling of selected SFRC structures. The results of the analysis of the SFRC specimens at material and structural levels for calibration purposes are presented on Appendix A. In the second part, encompassing Chapters 4 to 6, the focus is on the behaviour of SFRC structures under various loading conditions and different conventional shear reinforcement arrangements.

Chapter 2 briefly introduces the properties of steel fibres, application and benefits and presents the literature review on the identified SFRC stress-stain relations developed in tension and compression. The last part of the chapter describes some experimental work that have been carried out in order to investigate the potential of steel fibres as alternative shear reinforcement and the response of SFRC structures.

Chapter 3 presents the numerical analysis method adopted for the current study. Brief review of the Finite-element (FE) software package, ABAQUS, the analysis procedure as well as considerations for the SFRC material models which are described and implemented for calibration work (the results of the latter are presented in Appendix A).

Two types of simply supported beams, tested under three or four point bending tests are calibrated, investigated and discussed in Chapter 4. This statically-determinate structure is analysed under two types of loading conditions, i.e. monotonic and reversed-cyclic loading. The three-point beam test was designed to fail in bending, whereas the four-point beam test was designed to observe steel fibres in shear mode of failure. The capabilities of steel fibres in enhancing the strength and ductility of the beams is

analysed by increasing the shear links spacing 50%, 100%, 200% or in critical cases by removing all the stirrups. Behaviour of the SFRC beams is studied, especially the cracking propagations and comparison between the shear and moment capabilities with corresponding code predictions are made.

Chapter 5 presents the studies on statically indeterminate SFRC structural members. Two-span continuous columns were tested under the combined action of a constant axial force and monotonic or reversed-cyclic loading. The effect of steel fibres is observed especially in controlling the crack propagation at the region of contra-flexure and the formation of plastic hinges. Concurrently, the stirrups spacing in the columns were increased by 50% and 100%, and comparison were made to design codes.

The behaviour of beam-column joints under reversed-cyclic loading are investigated in Chapter 6. This case study focuses on the potential for steel fibres to reduce congestion of conventional shear reinforcement. Both exterior and interior beam-column joint case studies were considered. The results suggest steel fibres potential in compensating for reduced conventional shear reinforcement.

Based on the results obtained from the FE analyses, some recommendations for design were suggested in Chapter 7. Two key parameters selected to be discussed in regards of the design proposal are the ductility ratio (μ) and the maximum load carrying capacity (P_{max}).

In the final chapter, a summary of the main findings and conclusions is presented together with the recommendations for future research work.

CHAPTER 2

LITERATURE REVIEW

2.1 Introduction

Reinforced concrete (RC) is a major construction material that has been widely used in many types of engineering structures due to its ability to provide sufficient strength, stiffness, efficiency as well as being cost effective (Kwak and Filippou, 1990). Other desirable properties that RC exhibits include durability, adaptability to different shapes and fire resistance. Although it is generally accepted that concrete is a brittle material, researchers have continuously attempted to introduce ductility into it. One approach is by adding steel reinforcement (both bars and fibres), which provides tensile resistance tension and also offers confinement to the concrete working in compression. There are numerous types of fibres available for commercial use namely steel, glass, synthetic materials (e.g. polypropylene, carbon, nylon) and natural fibres such as hemp and kenaf (Sukontasukkul, 2004).

Fibres are utilised in order to enhance the properties of the inherently weak, brittle and crack-prone cement-based matrices (Johnston, 2001). It is important to reduce the brittleness of plain concrete, to achieve higher tensile or flexural strength, as well as introducing a crack control or closure mechanism thus changing the failure mode to one that includes post-cracking ductility (Hannant, 1978). It is crucial to ensure that adequate mechanical bonding between the matrix and the fibres is achieved. Therefore, the fibres are produced with varying sizes and shapes (e.g. deformed) to provide this anchorage. In fibre-reinforced concrete (FRC), the maximum particle size of the aggregate is restricted to 20 mm to ensure that sufficient bonding is accomplished

(Hannant, 1978). In addition, the post-cracking behaviour of FRC can also affected by the number of fibres across a specific crack, effectiveness of fibre orientation, bond strength and the resistance to fibre pull-out.

Steel fibres are increasingly being used in RC structures. Early studies on steel fibre-reinforced concrete (SFRC) by Romualdi and Batson (1963) showed the implementation of steel fibres in pavement construction. Later, Swamy and Lankard (1974) reported that steel fibres has been widely used in structural applications, some of which are car park, concrete pipes, pavements, marine and refractory applications. An early example of the structural application of SFRC is in the slab in the car park at Heathrow Airport in London (Swamy and Lankard, 1974). Significant improvement to crack resistance, enhancement in post-cracking behaviour, improved ductility of the slab at failure and higher load carrying capacity were achieved by adding SFRC.

Numerous investigations (e.g. Swamy and Al-Ta'an, 1981; Mansur et al., 1986; El-Niema, 1991; Oh et al., 1998; Bayasi and Gebman, 2002; Kotsovos et al., 2007; and Campione and Mangiavillano, 2008) have been published on how steel fibres can enhance the performance of RC structures. This includes experimental work and analytical studies, especially on understanding the behaviour of SFRC. Some of the published work, relevant to the present study, is presented in this chapter. The constitutive models developed to model the behaviour of SFRC as recommended by RILEM TC 162-TDF (2000, 2003) and material models derived purely from experimental work are discussed in section 2.3. In addition, the experimental investigations carried out for SFRC under static monotonic and reversed-cyclic loadings (to mimic seismic loading) are summarised in Section 2.4 and Section 2.5, respectively.

2.2 Overview of fibres

2.2.1 Basic properties and characteristics of SFRC

Steel fibres can be classified according to the production process, shape and material (i.e. steel with low and high carbon contents, stainless steel). The behaviour of steel fibres is characterised by the cross-section shape, aspect ratio, tensile strength, orientation and fibre volume fraction (National Research Council, 2007; Concrete Society, 2007). Figure 2.1 shows some of the shapes available for steel fibres. Plain-

straight and hooked-end steel fibres are commonly used in experimental investigations (e.g. Henagar, 1977; Gefken and Ramey, 1989; Kotsovos et al., 2007; Ozcan et al., 2009 etc). Modulus of elasticity of steel fibres can be assumed to be 200 GPa for steel with low or high carbon contents and 170 GPa for stainless steel (National Research Council, 2007). Smaller fibre volume fractions (i.e. $\leq 2\%$) normally produce post-cracking softening behaviour, whereas, higher fibre volume fractions (i.e. $> 2\%$) may contributed to hardening behaviour, due to multiple cracking occurrences as stated by National Research Council (2007).

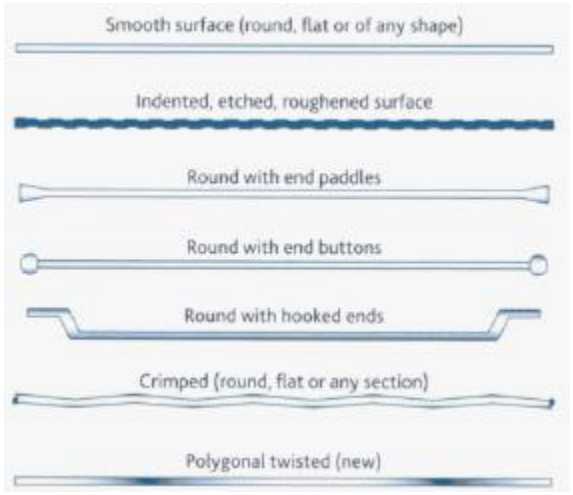


Figure 2.1: Types of steel fibres (adapted from Concrete Society, 2007)

Previous studies (e.g. Sharma, 1986; Trottier and Banthia, 1994; Robins et al., 2002; Khaloo and Afshari, 2005 etc) show that the performance of SFRC is influenced by many factors including the fibre shape, aspect ratio and volume fraction. Deformed steel fibres (i.e. hooked-end, crimped and twin-cone) with appropriate fibre content and aspect ratio require more energy absorption as they undergo the pull-out process, which in turn enhances the toughness characteristic of the FRC (e.g. Narayanan and Darwish, 1987; Lim et al., 1987; Trottier and Banthia, 1994; Robins et al., 2002). Trottier and Banthia (1994) observed that steel fibres with deformed shapes at the end (i.e. hooked-end and twin-cone) produce higher strength and ductility than fibres with a deformed shape along the length (i.e. crimped). Furthermore, most of the experimental work (e.g. Filiatrault et al., 1994, 1995; Bayasi and Gebman, 2002; Campione et al., 2006; and Campione and Mangiavillano, 2008) was carried out using hooked-end steel fibres.

The amount of fibres added in a structure has been a subject of interest due to practical issues such workability of the mixtures and fibre spalling. An appropriate fibre volume fraction is required in order to provide sufficient enhancement in the strength and ductility of SFRC structures. Therefore, based on the studies carried out it is recommended that the fibre volume fractions of steel fibres are limited to 2% (Sharma, 1986; Narayanan and Darwish, 1987; Khaloo and Afshari, 2005), unless enough plasticizer is considered to address the aforementioned concerns (i.e. workability and fibre spalling). Many researchers (i.e. Sharma, 1986; Mansur and Ong, 1991; Oh et al., 1998; Kwak et al., 2002; Campione et al., 2006) studied the effect of fibre content on confinement and enhancement of shear capacity, especially in the absence of conventional shear reinforcement (see Section 2.3.2).

2.2.2 Behaviour of SFRC

Many investigations (i.e. Lok and Pei, 1998; Lok and Xiao, 1999; Barros and Figueiras, 1999; 2001; RILEM TC 162-TDF, 2000; 2003; and Tlemat et al., 2006) proposed that addition of steel fibres may improve the post-cracking behaviour of concrete from a sharp drop, associated with plain concrete, to either tension softening or hardening characteristics depending on the fibre dosage, geometry and bond stress. These suggested constitutive models for SFRC are discussed in Section 2.3.

The effect of the steel fibres on the moment-curvature curve is shown in Figure 2.2 (Lok and Xiao, 1999). It is apparent that the effect of fibres will only take place after the onset of cracking (i.e. after the stress reaches concrete tensile strength f_t). The post-cracking residual tensile stress (f_{tu}) improves the flexural behaviour of the SFRC structure and is governed by the fibre geometry and fibre volume fraction. On the stress-strain diagram, the zone between the origin and the cracking strain (ε_{t0}) represents the region before cracking. The post-cracking zone between the strains ε_{t0} and ε_{t1} is the region where both fibres and concrete between the cracks are resisting the load. Finally, the zone between the strains ε_{t1} and ε_{tu} is the region where the fibres are acting solely until they pull-out (i.e. bond failure) at the ultimate strain ε_{tu}.

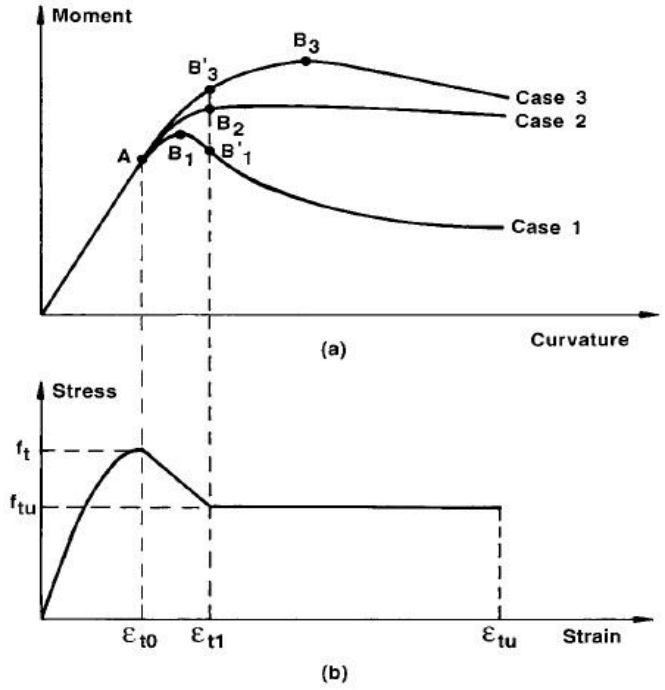


Figure 2.2: Relationship between (a) Moment-curvature response and (b) Tensile stress-strain behaviour (adapted from Lok and Xiao, 1999)

The flexural moment-curvature response obtained can be classified as softening (case 1), idealised elasto-plastic (Case 2), or hardening (Case 3) depending on the fibres pull-out and bridging behaviour. Furthermore, increases in the fibre volume fraction (with the fibre geometry being kept the same) change the pattern of the moment curves from Case 1 to Case 3. The first crack is observed at point A. The ultimate load carrying capacity for the SFRC specimen can be seen from B_1, B_2 and B_3. As the tensile strains in the SFRC stress-strain behaviour are constrained, the crack propagation is controlled and reduced through pull-out resistance of fibres bridging the cracks.

2.2.3 Crack propagation

The failure of plain concrete is governed by the formation of a single crack. Before the initiation of the first crack, the material exhibits linear elastic behaviour. Once the crack initiates, the energy absorption capacity is increased until it is exceeded (Kotsovos and Pavlović, 1995). As the loading continues to increase, the crack expansion is resisted by the aggregate interlock effect in the concrete. Consequently, with any additional energy induced by the applied load, the crack expands more which, subsequently, reduces the

energy capacity of the system further and creates an instable state. Once the energy is released during the fracture processes, the stress and strain concentration at the crack tips orthogonally to the path of the crack extension decreases (Kotsovos and Pavlović, 1995). These fracture processes create voids within the concrete as shown in Figure 2.3. Additionally, as these high tensile stress and strain concentrations reduce, the material is compressed in the direction normal to the crack-extension path, while void formation continues to extend increasing propagation of the crack.

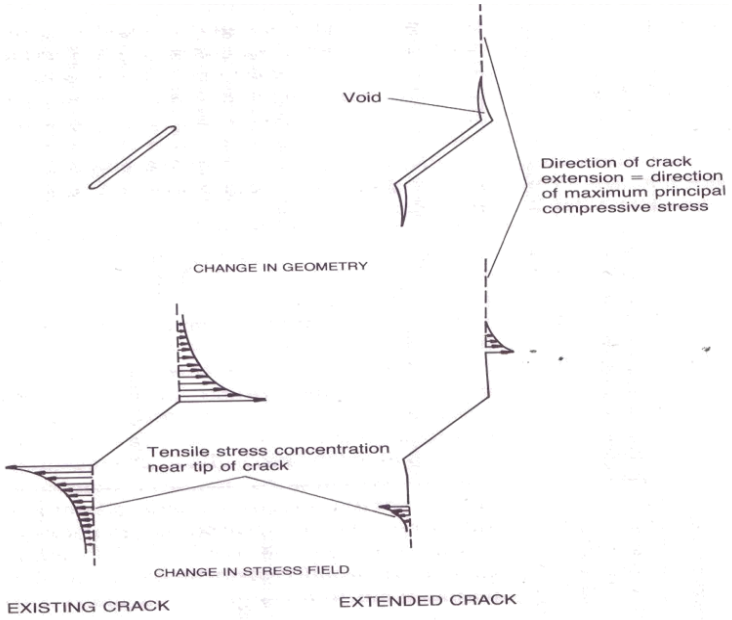


Figure 2.3: Schematic representation of changes in crack geometry and stress fields associated with crack extension (adapted from Kotsovos & Pavlović, 1995)

When a crack is initiated in SFRC elements, the propagation of cracks is controlled by the presence of the fibres in the concrete. Fibres provide crack arresting or bridging effect to resist further cracks opening, during crack propagation. Two potential failure modes (depending on the effectiveness of the fibres in providing crack bridging) are shown in Figure 2.4. According to RILEM TC 162-TDF (2002), failure by a single crack (Figure 2.4(a)) occurs when the first cracking strength is the ultimate strength of concrete and further deformation is governed by the opening of a single crack and fibres pulling out and/or breaking along the edges of the crack. In this case, the fibres are pulled-out or break during crack initiation, or if the maximum load sustained by the fibres exceeded after the formation of the first crack. On the contrary, if the fibres were able to carry more load after the first crack, more cracks will be formed in the nearby

region, which is known as multiple cracking (Figure 2.4(b)). The behaviours are also referred to as tension softening and strain hardening.

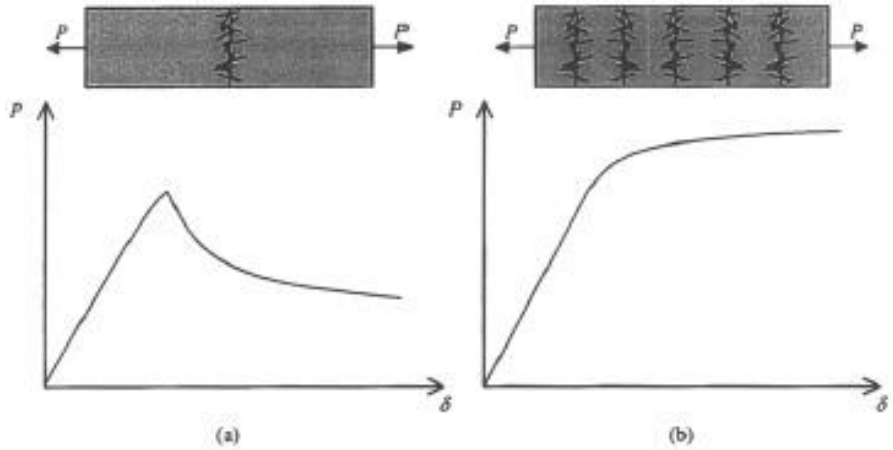


Figure 2.4: The principle of single and multiple cracking. The specimens are loaded in uniaxial tension and the schematic load versus deformation (P-δ) relationship is shown together with the cracking pattern (a) single cracking (or tension softening) (b multiple cracking (or strain hardening) (adapted from RILEM TC 162-TDF, 2002)

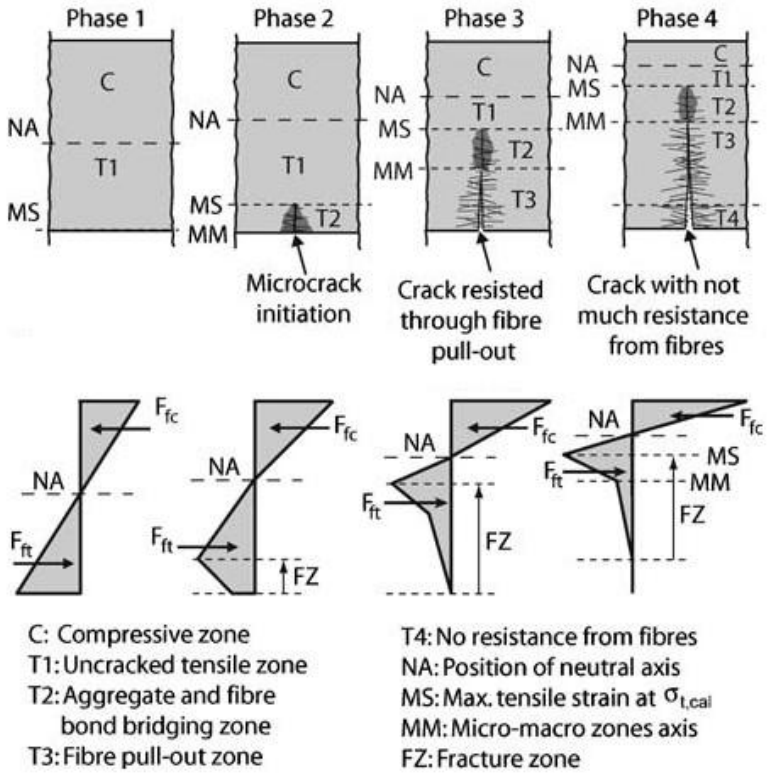


Figure 2.5: Stress distribution for SFRC sections (adapted from Tlemat et al, 2006)

The crack propagation of SFRC is better explained from the stress-strain distribution in a section of the structure (e.g. Tlemat et al., 2006 and Robins et al., 2002) as shown in

Figure 2.5. Similar behaviour was discussed by Hillerborg (1980) and Olesen (2001) using a fictitious crack model in the former and cracked hinge model in the latter for FRC. In Figure 2.5, Phase 1 of the SFRC section shows the condition prior to cracking, thus a linear elastic behaviour was observed. There is no crack in the tensile zone (T1) and the maximum stress is only dependent on the concrete strength and the fibre amount. After crack initiation, it is assumed that the stresses are redistributed across the crack and this is shown in Phase 2 to Phase 3 (see Figure 2.5).

In Phase 2, cracking is initiated after the concrete tensile strength is reached. As the crack starts to propagate, the fibres will continue to sustain the load through bridging effect. When the crack is fully established, a plastic hinge is developed and the behaviour becomes elasto-plastic. Phase 2 ends with the concrete tensile resistance being lost and most of the fibres have exceeded the cracking load (Tlemat et al., 2006).

Phase 3 shows that the crack propagated through the depth of the SFRC section, thus making the un-cracked tensile zone (T1) to be smaller than the compressive zone (C). The fibres are now bridging the opening of the crack at the top of the section. At the same time, the fibre begins to pull-out at the bottom of the section. This pull-out behaviour imposes a crack closure condition until a point in which the fibre is fully pulled-out and this consequently is the final state of Phase 3.

A smaller un-cracked tensile zone can be observed in Phase 4 as the neutral axis moves closer to the compressive zone. A large crack opening develops at the bottom of the section, due to the concrete and fibre failure. The load will be sustained by the part of the section where the fibres are still intact. Phase 4 ends with the failure of the section.

2.3 Constitutive models for SFRC

2.3.1 RILEM TC 162-TDF Recommendations for SFRC

RILEM TC 162-TDF Recommendation (2000) proposed stress-strain relations for SFRC with compressive strengths up to C50/60. The compressive strength is determined by using the method suggested by RILEM TC 162-TDF Recommendation (2000). To understand the post cracking behaviour for SFRC, a series of specimens were studied under compressive and flexural tests. In order to define the values required in the stress-strain relations, the load-deflection resulting from the three-point bending

test (see Figure 2.6) were required to determine the values of equivalent flexural strength, $f_{eq,i}$. The method and related equations are illustrated in Figures 2.7 and 2.8.

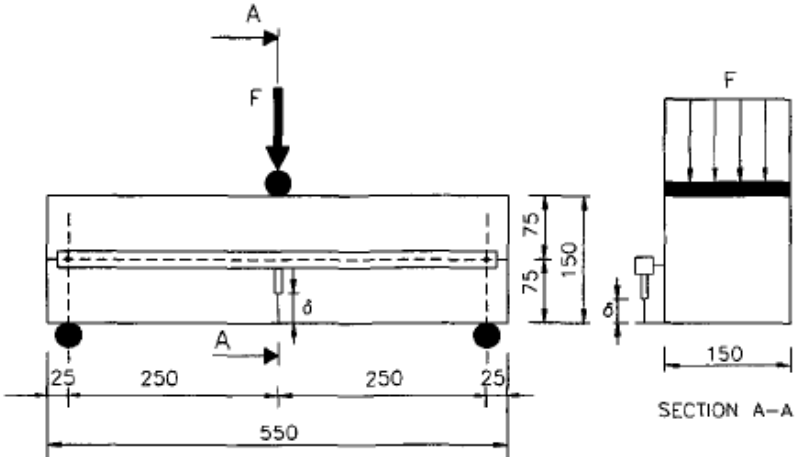


Figure 2.6: Arrangement for standard bending test on small notched beams (adapted from RILEM TC 162-TDF[c] Recommendation, 2003)

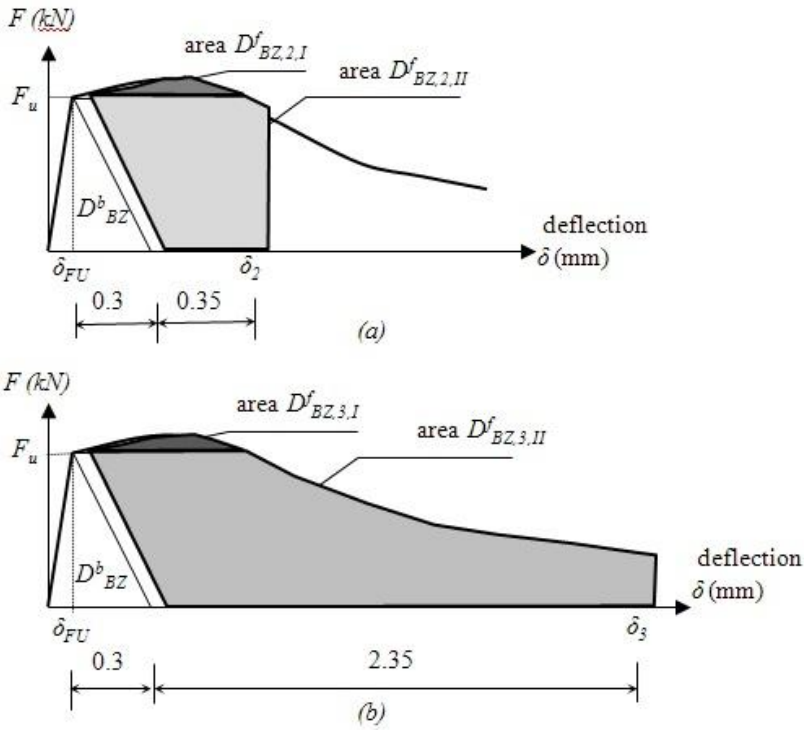


Figure 2.7: Load-deflection diagram (adapted from RILEM TC 162-TDF Recommendation, 2000)

The two different values for equivalent flexural strength, $f_{eq,2}$ and $f_{eq,3}$ were adopted for the analysis. The first value, $f_{eq,2}$ was obtained at total deformation of 0.65mm (see

Figure 2.7 (a) and $f_{eq,3}$ at deformation of 2.65mm (see Figure 2.7 (b)). This deformation is calculated after the elastic range behaviour. The related equations are:

$$f_{eq,2} = \frac{3}{2}\left[\frac{D^f_{BZ,2,I}}{0.65} + \frac{D_{BZ,2,II}}{0.50}\right]\frac{L}{bh^2_{sp}} \text{ (N/mm}^2\text{)} \quad (2.1)$$

$$f_{eq,3} = \frac{3}{2}\left[\frac{D^f_{BZ,3,I}}{2.65} + \frac{D_{BZ,3,II}}{2.50}\right]\frac{L}{bh^2_{sp}} \text{ (N/mm}^2\text{)} \quad (2.2)$$

where b is the width of the specimen (mm), h_{sp} is the distance between tip of the notch and top of cross section (mm) and L is the span length of the specimen (mm). The contribution of steel fibres to the energy absorption capacity was evaluated from the area under load-deflection curve as shown in Figure 2.7. The stress-strain diagram is illustrated in Figure 2.8 below.

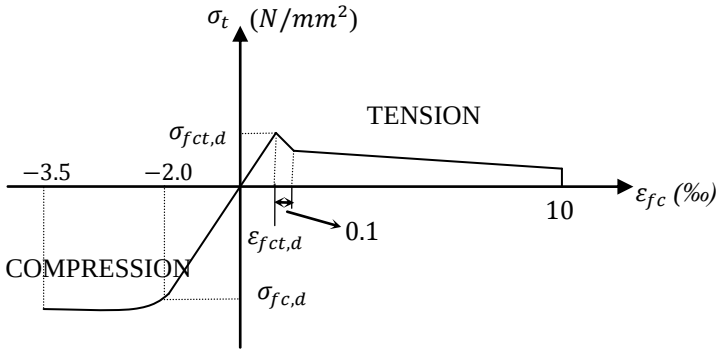


Figure 2.8: Stress-strain diagram (RILEM TC 162-TDF Recommendation, 2000)

In RILEM TC 162-TDF (2000), the compression behaviour of SFRC was assumed to be similar to that of plain concrete but with improved strain values. Therefore, at $\varepsilon_{fc,d} = -2‰$, the ultimate compressive stress was given by $\sigma_{fc} = -0.85 f_{fc,d} = -\frac{0.85 f_{fck}}{\gamma_C}$ (N/mm^2) and the value of $-3.5‰$ was suggested for ultimate strain after failure. The values of equivalent flexural tensile strength, $f_{eq,2}$ and $f_{eq,3}$ calculated before were implemented to define the post cracking stress-strain relations in tension. The values for tensile stress at failure were determined depending on the applied loads on the specimen or structure. For SFRC structure subjected to axial force only, the equation given was:

$$\sigma_{fct,d} = \frac{f_{fctk,ax}}{\gamma_{ct}} \quad \text{(N/mm}^2\text{)} \quad (2.3)$$

when the SFRC structure is subjected to axial force and bending moment, the equation above can be written as:

$$\sigma_{fct,d} = \frac{f_{fctk,ax}(1600-d)}{\gamma_{ct}\cdot 1000} \text{ (N/mm}^2\text{)} \quad (2.4a)$$

For $\frac{1600-d}{1000} \geq 1$ (d in mm) (2.4b)

The values of $f_{eq,2}$ and $f_{eq,3}$ were applied in the equations below to define the tensile stress at the corresponding strain:

At $\varepsilon_{fct.d} + 0.001$, $\sigma_{fct,d} = \frac{0.45}{\gamma_{ct}} f_{eq,2}$ (N/mm^2) (2.5)

At $\varepsilon_{fct.d} = 10‰$, $\sigma_{fct,d} = \frac{0.37}{\gamma_{ct}} f_{eq,3}$ (N/mm^2) (2.6)

In a more recent work on stress-strain relations, RILEM TC 162-TDF (2003), another approach to define the post cracking behaviour of SFRC using the values obtained as residual flexural tensile strength, $f_{R,I}$ was proposed. This method is valid for SFRC with compressive strength up to C50/60. The stress-strain diagram for the compressive and tensile behaviour of SFRC and size factor is defined in Figure 2.9.

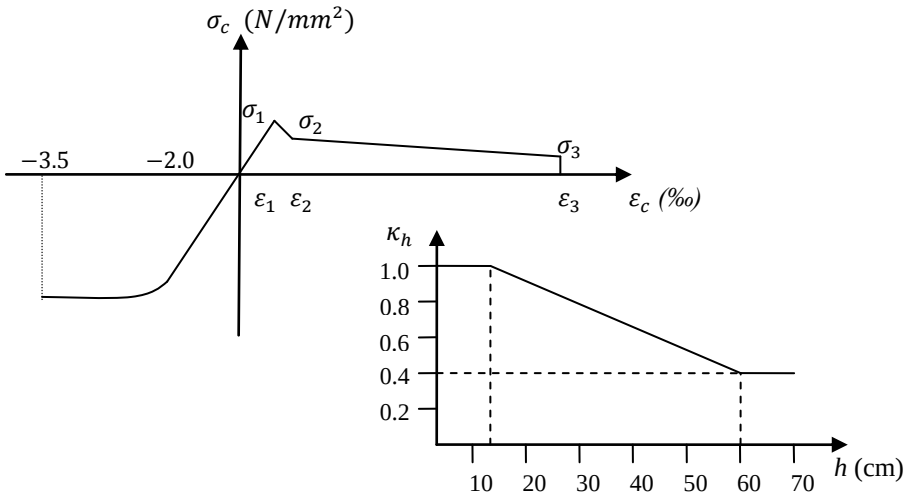


Figure 2.9: Stress-strain diagram and size factor, κ_h (adapted from RILEM TC 162-TDF[a] Recommendation, 2003)

The parameters required to define the stress-strain diagram are as follow:

$$\sigma_1 = 0.7 f_{fctm,fl}(1.6-d) \quad (d \text{ in m}) \text{ (N/mm}^2\text{)} \quad (2.7)$$

$$\sigma_2 = 0.45 f_{R,1} \kappa_h \quad (\text{N/mm}^2) \tag{2.8}$$

$$\sigma_3 = 0.37 f_{R,4} \kappa_h \quad (\text{N/mm}^2) \tag{2.9}$$

$$E_c = 9500(f_{fcm})^{1/3} \quad (\text{N/mm}^2) \tag{2.10}$$

$$\varepsilon_1 = \frac{\sigma_1}{E_c} \tag{2.11}$$

$$\varepsilon_2 = \varepsilon_1 + 0.1‰ \tag{2.12}$$

$$\varepsilon_3 = 25‰ \tag{2.13}$$

$$\kappa_h = 1.0 - 0.6\frac{(h-12.5)}{47.5} \quad |12.5 \leq h \leq 60 \text{ (cm)} \tag{2.14}$$

The value for mean characteristic of flexural tensile strength $f_{fctm,fl}$ can be obtained from Table 2.1, provided the value of characteristic compressive strength f_{fck} is known.

Characteristic compressive strength f_{fck} (cylinders), mean $f_{fctm,fl}$ and characteristic $f_{fctk,fl}$ flexural tensile strength in N/mm^2; mean secant modulus of elasticity E_{fcm} in kN/mm^2							
Strength class of SFRC	C20/25	C25/30	C30/37	C35/45	C40/50	C45/55	C50/60
f_{fck}	20	25	30	35	40	45	50
$f_{fctm,fl}$	3.7	4.3	4.8	5.3	5.8	6.3	6.8
$f_{fctk,fl}$	2.6	3.0	3.4	3.7	4.1	4.4	4.8
E_{fcm}	29	30.5	32	33.5	35	36	37

Table 2.1: SFRC strength classes (adopted from RILEM TC 162-TDF, 2003)

Residual flexural strength $f_{R,1}$ and $f_{R,4}$, are defined at the following crack mouth opening displacement ($CMOD_i$) or mid span deflection ($\delta_{R,i}$) values:$CMOD_1$ = 0.5 mm or $\delta_{R,1}$ = 0.46 mm and $CMOD_4$ = 3.5 mm or $\delta_{R,4}$ = 3.00 mm, respectively. The values for $f_{R,1}$ and $f_{R,4}$ are determined from the following expression:

$$f_{R,i} = \frac{3F_{R,i}L}{2bh_{sp}^2} \ (\text{N/mm}^2) \tag{2.15}$$

with b is the width of the specimen (mm), h_{sp} is the distance between tip of the notch and top of cross section (mm) and L is the span length of the specimen (mm). The

values for $F_{R,i}$ are determined from the experimental load-deflection curve (Figure 2.11), based on its respective $CMOD_i$ or $\delta_{R,i}$. Figure 2.10 shows the geometry and loading condition of the bending test carried out.

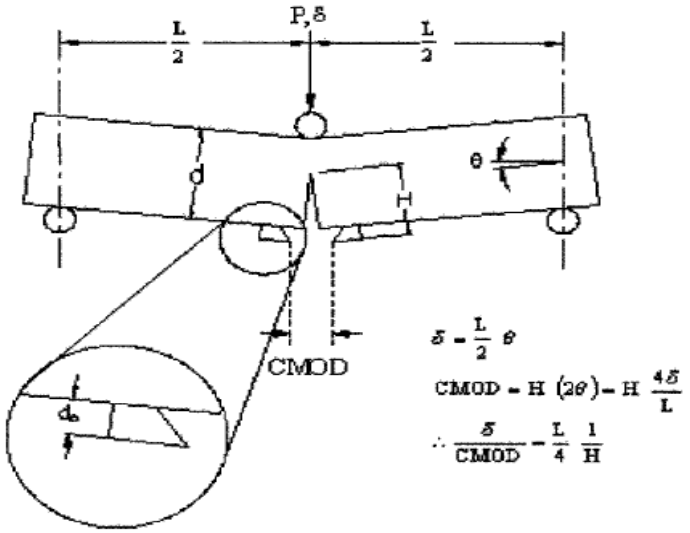


Figure 2.10: Geometry and loading of the bending test (adapted from RILEM TC 162-TDF[c] Recommendation, 2003)

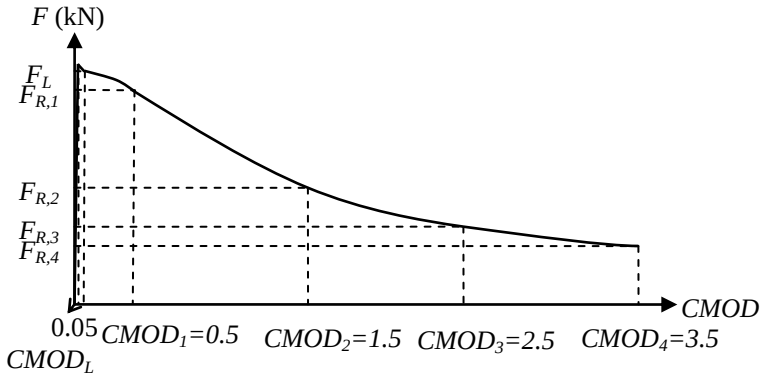


Figure 2.11: Load – CMOD diagram (RILEM TC 162-TDF[a] Recommendation, 2003)

2.3.2 Lim et al. (1987) proposed SFRC model

Lim et al. (1987) proposed tensile stress-strain model to predict the post-cracking behaviour for SFRC. It serves as a generic model, where the fibres properties are defined using related parameters. The parameters involved in defining the curve are fibre volume fractions, fibre configurations (ratio of the cross sectional area to the perimeter of the fibres) and fibre orientation factors ($\eta_0^{'}$). The ultimate tensile strength

σ_{tu} is related to the average ultimate pull-out bond strength τ_u of the fibres. This model is appropriate for studies considering the fibre volume fraction range to be in between 0.5% and 1.5%.

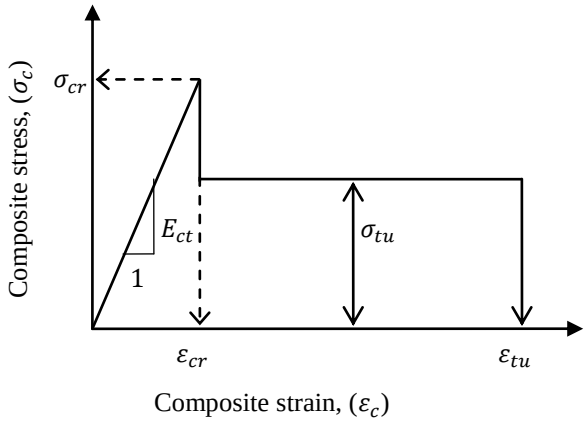


Figure 2.12: Composite stress-strain relations in tension (Lim et al., 1987)

The tensile elastic modulus for SFRC composite (E_{ct}):

$$E_{ct} = E_{mt}V_m + \eta_l\eta_0 E_f V_f \tag{2.16}$$

In which, V_m and V_f are the total volume fraction of the matrix and fibres, respectively; E_{mt} and E_f are the tensile elastic modulus for the matrix and the Young's modulus of steel fibres, respectively; η_l is the ratio of the average fibre stress to the maximum fibre stress, η_0 orientation factor in the elastic range.

The first crack strain of the composite, ε_{cr}, is given by:

$$\varepsilon_{cr} = \eta_l\eta_0' V_f\left(\varepsilon_{fp} - \varepsilon_{mp}\right) + \varepsilon_{mp} \tag{2.17}$$

where η_0' is orientation factor due to fibres realigning across the crack (for the case where $b, h > l_f, \eta_0' = 0.405$), ε_{fp} and ε_{mp} are the strains at the proportional limit for the fibre and matrix, respectively.

The ultimate strength of the composite, σ_{tu}, is given by:

$$\sigma_{tu} = \eta_l\eta_0' V_f l_f \frac{\tau_u}{2r} \tag{2.18}$$

Where l_f is the fibre length, τ_u is the ultimate bond stress, r is the ratio of fibre cross-sectional area to its perimeter.

The post-cracking strain (ε_{tu}) is given by:

$$\varepsilon_{tu} = \omega_u / l^* \quad (2.19)$$

where $\omega_u = l_f/16$ and l^* is a reference length taken as the average crack spacing.

2.3.3 Murugappan et al. (1994) proposed SFRC model

Murugappan et al. (1994) modified constitutive SFRC model proposed by Lim et al. (1987) and applied it for finite element analysis. Murugappan et al. (1994) introduced gradual descending of stress after cracking as the cracking strain increases up to ultimate tensile failure strain (see Figure 2.13), presumably to avoid numerical instability. The residual stress in the concrete matrix was ignored by Lim et al. (1987) since their investigation was based on pre-cracked model, which included an abrupt drop in the stress at the commencement of the post-racking stage was observed.

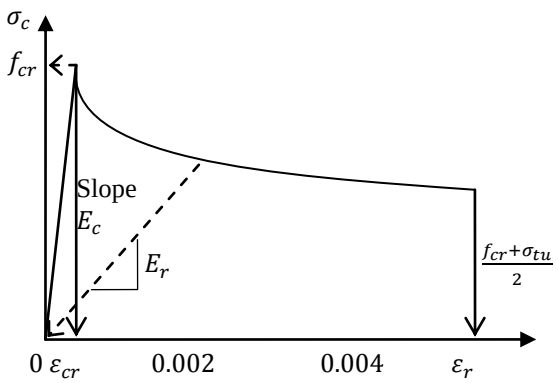


Figure 2.13: Composite stress-strain relations in tension (Murugappan et al., 1994)

$$\sigma_r = \frac{f_{cr}+\beta\sigma_{tu}}{1+\beta} \text{ for } \varepsilon_r > \varepsilon_{cr} \quad (2.20)$$

$$\text{where } \beta = \sqrt{\frac{\varepsilon_r - \varepsilon_{cr}}{0.005}} \quad (2.21)$$

The post-cracking strength σ_{tu} is similar to the equation given in (2.18). The proposed model was used in numerical analyses to replicate the work carried out by Lim et al (1987) on SFRC beams with various span-to-depth ratios ($^a/_d = 1.5 - 3.5$) and fibres volume ratios ($V_f = 0 - 1\%$). The analytical model showed reasonable prediction of the failure mode and ultimate load of the beams.

2.3.4 Lok and Pei (1998) proposed SFRC model

Lok and Pei (1998) investigated the flexural behaviour of SFRC and proposed a generic constitutive model. This model covers both compressive (Figure 2.14) and tensile (Figure 2.15) behaviours. The constitutive model may exhibit strain softening or hardening behaviour depending on the properties of the fibrous concrete. The compressive model for plain concrete as recommended in BS8110 (1985) was adopted for SFRC, since steel fibres have minor effect on the compressive strength (Lok and Pei, 1998). The value for ultimate compressive stress is calculated as:

$$\sigma_{01} = 0.67 f_{cu} / \gamma_m \tag{2.22}$$

where f_{cu} is the characteristic cube strength and γ_m is the partial material safety factor. The ultimate compressive strain is given by:

$$\varepsilon_{01} = 2.4 \times 10^{-4} (f_{cm} / \gamma_m)^{1/2} \tag{2.23}$$

In addition, E_{oc} is defined as initial tangent modulus of the fibrous composites. The compressive stress (σ_1) and strain (ε_1) is given as:

$$\sigma_1 = \sigma_{01} - (\sigma_{01} / (\varepsilon_{01})^2)(\varepsilon_1 - \varepsilon_{01})^2 \tag{2.24}$$

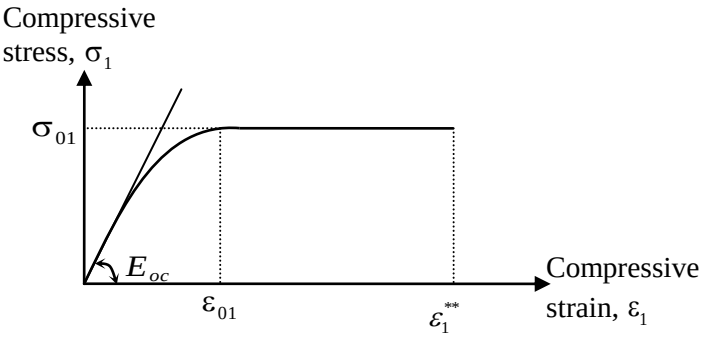


Figure 2.14: Compressive stress-strain relationship for SFRC (Lok and Pei, 1998)

The failure compressive strain ε_1^{**} is taken as 0.0035 (Clarke and Sharma, 1987 cited in Lok and Pei (1998); Swamy and Al-Ta'an, 1981 cited in Lok and Pei (1998)).

Furthermore, there are two stages defined in the tensile stress-strain model, which are the pre-cracking stage (matrix is un-cracked) and the post-cracking stage (matrix is cracked) as shown in Figure 2.15. In the pre-cracking phase the fibres effect was negligible as the beams are assumed to behave in an elastic manner. In the post-

cracking phase, the behaviour is dependent on the fibre volume fraction, bond stress and fibre aspect ratio. Ultimate tensile stress and strain at failure for SFRC are given by σ_{02} and ε_{02}, respectively. The bond stress of the fibres increases gradually and reaches the ultimate value at the end of Process I. The value for the beginning of Process II is calculated based on fibres pull-out or bridging effect. This model uses the assumption that the steel fibres bond perfectly to the concrete matrix and that no slippage occurs at the fibre-matrix interface.

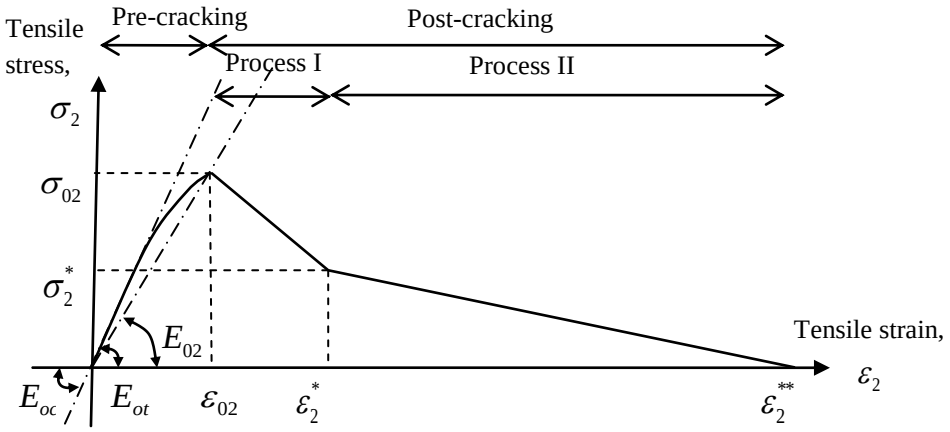


Figure 2.15: Tensile stress-strain relationship for SFRC (Lok and Pei, 1998)

The equations for parameters specified in Figure 2.15 are defined as follows:

$$\sigma_{02} = f_t \tag{2.25}$$

$$\sigma_2^* = \frac{1}{2} v_f \tau_d \frac{L}{d} \tag{2.26}$$

$$\varepsilon_{02} = \frac{\varepsilon_{01}}{\sigma_{01}} \sigma_{02} \tag{2.27}$$

$$\varepsilon_2^* = \tau_d \frac{L}{d} \frac{1}{E_{fp}} \tag{2.28}$$

where the maximum tensile strain after failure ε_2^{**} can be taken as 2 x 10^4 micro-strain (Craig et al., 1987 cited in Lok and Pei, 1998), 1.45 x 10^4 micro-strain (Chuang and Mai, 1987 cited in Lok and Pei, 1998), or 10 x 10^4 micro-strain (Sakai and Nakamura, 1986 cited in Lok and Pei, 1998); E_{fp} is elastic modulus of steel fibres, v_f is fibre volume fraction, τ_d is dynamic bond stress and L/d is the fibre aspect ratio. If the value

for dynamic bond stress is not provided, the values obtained experimentally by other researchers can be applied into the model as illustrated in Table 2.2.

Reference	Notation/bond stress as defined	Values or formula	Origin
Swamy and Mangat (1976)	Bond stress	For straight fibres: 0.82 -2.6 N/mm^2; for hooked-end fibres: 3.7 – 5.3 N/mm^2	Pull-out test
Henagar (1977)	Dynamic bond stress	2.297 N/mm^2 (for deformed fibres, multiplied by 1.1 - 1.2)	Pull-out test
Aveston et al (1974, as cited in Hannant, 1978)	Bond stress	5.4 – 8.3 N/mm^2	Unspecified
Aveston et al (1976, as cited in Hannant, 1978)	Bond stress	3.9 N/mm^2	Unspecified
Hannant (1978)	Average sliding friction bond strength	3.5 N/mm^2	Unspecified
Swamy et al. (1981)	Average bond stress at the first crack Ultimate bond stress	3.57 N/mm^2 4.15 N/mm^2	Modulus of rupture test
Swamy and Al-Ta'an (1981)	Interfacial bond stress between fibre and matrix	For crimped fibres: 2.44 - 2.58 N/mm^2	Modulus of rupture test
Lim et al. (1987a, b)	Ultimate bond stress	For straight fibres: 2.71 -3.05 N/mm^2; for hooked-end fibres: 6.72 - 7.10 N/mm^2	Pull-out test
Soroushian and Lee (1989)	Ultimate bond stress	2.62 - 0.0036 N_1 (N_1 is defined as number of fibres per unit cross sectional area)	Pull-out test
Oh et al. (1998)	Average bond stress	For straight fibres: 4.15 N/mm^2	Pull-out test
Lok and Pei (1998)	Dynamic bond stress	3.5 N/mm^2	Unspecified
Voo and Foster (2003)	Bond shear stress	For hooked-end fibres: 2.5 f_{ct}; and for straight fibres: 1.2 f_{ct} (f_{ct} is the tensile strength, or $f_{ct} = 0.33\sqrt{f_{cm}}$ where f_{cm} is the mean cylinder strength in MPa).	Unspecified

Table 2.2: Summary of bond stress values

Using the proposed constitutive model, a numerical study was conducted on moment-curvature relationship of SFRC by utilising existing experimental data. The predicted curves show good agreement when compared with experimental data (Lim et al, 1987 cited in Lok and Pei, 1998). In addition, it was concluded that (i) good performance was observed when the fibre content and length are high and (ii) the bond stress significantly affect the behaviour of SFRC.

2.3.5 Lok and Xiao (1999) proposed SFRC model

Lok and Xiao (1999) investigated the effect of fibre orientation and proposed the model depicted in Figure 2.16 (the related moment-curvature relation was discussed earlier in Figure 2.2). The compressive stress-strain relations are described as:

$$\sigma = f_c[2(\varepsilon/\varepsilon_{co}) - (\varepsilon/\varepsilon_{co})^2] \qquad (\varepsilon \le \varepsilon_{co}) \tag{2.29}$$

where f_c is compressive strength of concrete.

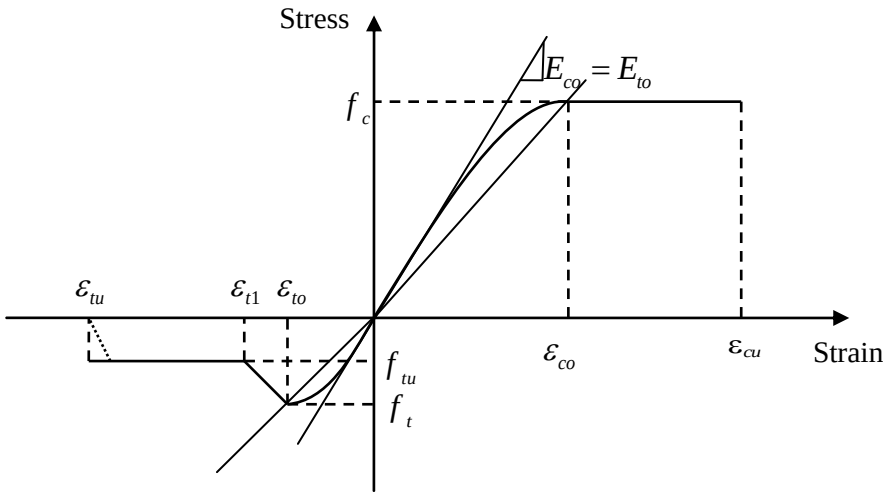


Figure 2.16: Constitutive stress-strain relationship (Lok and Xiao, 1999)

Lok and Xiao (1999) stated that the ultimate compressive strain, ε_{cu} for SFRC at 0.003 may be conservative. They pointed out that Swamy and Al-Ta'an (1981) recommended a value of 0.0035 while Hassoun and Sahebjam (1985 cited in Lok and Xiao, 1999) recommended 0.0035 for concrete reinforced with 1.0% steel fibres ratio and 0.004 for 1.0 to 3.0% fibres ratio. For fibre volume fraction between 0.5 and 2%, Lok and Xiao

(1999) suggested the value of 0.0038. They proposed the following tensile stress-strain relations:

$$\sigma = f_t\left[2\left(\frac{\varepsilon}{\varepsilon_{t1}}\right)-\left(\frac{\varepsilon}{\varepsilon_{to}}\right)^2\right] \qquad (0 \le \varepsilon \le \varepsilon_{to}) \qquad (2.30)$$

$$\sigma = f_t\left[1-\left(\frac{1}{f_{tu}}\right)\left(\frac{\varepsilon-\varepsilon_{to}}{\varepsilon_{t1}-\varepsilon_{to}}\right)\right] \qquad (\varepsilon_{to} \le \varepsilon \le \varepsilon_{t1}) \qquad (2.31)$$

$$\sigma = f_{tu} \qquad (\varepsilon_{t1} \le \varepsilon \le \varepsilon_{tu}) \qquad (2.32)$$

where f_t is the ultimate tensile strength of SFRC, ε_{to} is the corresponding ultimate strain and f_{tu} is the residual strength from the strain ε_{t1} (as depicted in Figure 2.16). These values are defined by Lok and Pei (1998) as:

$$f_{tu} = \eta v_f \tau_d \frac{L}{d} \qquad (2.33)$$

$$\varepsilon_{t1} = \tau_d \frac{L}{d}\frac{1}{E_s} \qquad (2.34)$$

where η is fibre orientation factor in a 3 dimensional (3D) case, taken as 0.50 (Hannant, 1978), or 0.45 (Soroushian and Lee, 1990 cited in Lok and Xiao, 1999). Lok and Xiao (1999) used the value of η as 0.405 for beams and 0.50 for slabs to demonstrate a situation between 3D and 2D random orientations. In addition, v_f is defined as the fibre volume fraction, τ_d is the bond stress interaction between concrete and steel fibres, *L/d* is aspect ratio of the steel fibre and E_s is the elastic modulus of steel fibre.

2.3.6 Barros and Figueiras (1999) proposed SFRC model

Barros and Figueiras (1999) carried out uni-axial compression and bending tests on SFRC at both the material and structural levels to study the post-cracking behaviour of SFRC and subsequently proposed a stress-strain diagram. Two types of steel fibres were used in the study; Dramix ZP 30/.50 (30 mm-long, 0.5 mm diameter) and Dramix ZX 60/.80 (60 mm-long, 0.8 mm diameter). The fibre volume fraction applied in the experimental work ranges between 0% and 0.75%. Based on the uni-axial compression

tests on SFRC cylinder specimens, a compression stress-strain relation was proposed which is given by equation:

$$\sigma_c = f_{cm} \frac{\varepsilon_c / \varepsilon_{cl}}{(1-p-q)+q(\varepsilon_c / \varepsilon_{cl})+p(\varepsilon_c / \varepsilon_{cl})^{(1-q)/p}} \text{ (MPa)} \quad (2.35)$$

with

$$q = 1-p-(E_{cl} / E_{ci}), \qquad p+q \in]0,1[, \qquad (1-q)/p > 0 \quad (2.36)$$

$$E_{cl} = f_{cm} / \varepsilon_{cl} \quad (2.37)$$

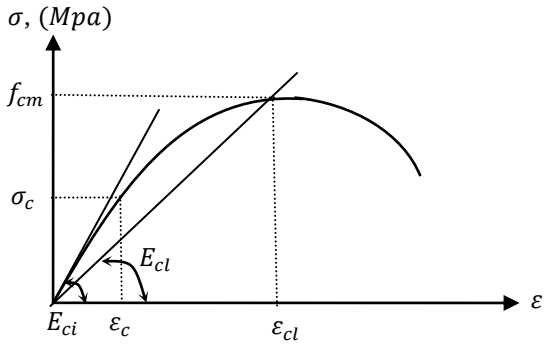


Figure 2.17: Compression stress-strain diagram (Barros and Figueiras, 1999)

The average compression strength, f_{cm}, ultimate strain, ε_{c1} and the ratio between the secant modulus of elasticity and the tangent modulus of elasticity E_{c1} / E_{ci} ($E_{c1,}$ f_{cm}) for each of fiber is expressed as a function of the fiber volume fraction as shown in Figure 2.17. Based on the average compression strength values, the following relationships were suggested in Table 2.3.

Parameters	Fibres type	
	Hooked-end fibres ZP 30/.50	Hooked-end fibres ZX 60/.80
ε_{cl}	$\varepsilon_{c10} + 0.0002W_f$	$\varepsilon_{c10} + 0.00026W_f$
p	$1.0 - 0.919e^{-0.394w_f}$	$1.0 - 0.722e^{-0.144w_f}$

Table 2.3: Ultimate strain and *p* value of SFRC (adopted from Barros and Figueiras, 1999)

Strain at peak for plain concrete, ε_{c10}, was taken as 0.0022 according to CEB-FIP Model Code 1990 (CEB-FIP, 1993 cited in Barros and Figueiras, 1999), with w_f as the fibre weight ratio in the mixture. Both the peak strength, f_{cm} and the tangent Young's

Modulus, E_{ci}, ($E_{ci} = 21500(f_{cm}/10)^{1/3}$) marginally varies with the fibre addition. These values were therefore considered to be equal to those in plain concrete.

Adopting results from 3-point bending tests on notched beams, Barros and Figueiras (1999) assessed the post-peak tensile behaviour of SFRC structures by implementing fracture energy concepts and developed a numerical model. Figure 2.18 shows the correlation of peak tensile strength, f_{ctm} and strain at first cracking, $\varepsilon_{cr.}$ The p_1 parameter is defined in Barros and Figueiras (1995), whilst, p_2 and α parameter are defined in Barros (1995).

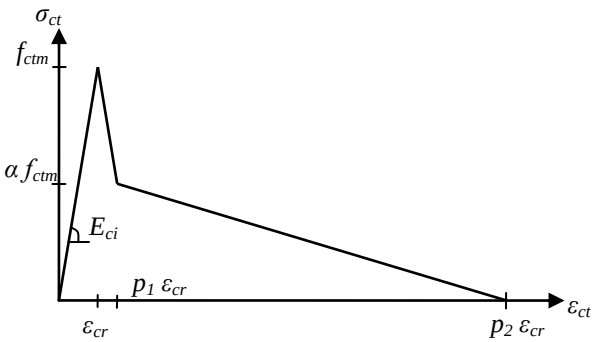


Figure 2.18: Tensile stress-strain diagram (Barros and Figueiras, 1999)

In order to measure the applicability of the model derived and to evaluate the effect of steel fibre reinforcement in thin slabs, Barros and Figueiras (1999) tested slab strips reinforced with ordinary steel wire mesh with different fibre volume fractions under bending (0.38 – 0.75%). The details of the experimental work are explained elsewhere (Barros and Figueiras, 1999). It was observed that the model applied in the simulation showed good agreement of moment-curvature curves when compared to the slabs experimental results. Therefore, Barros and Figueiras (1999) concluded that the stress-strain relations derived are fitted to be applied in the finite element models for the non-linear analysis of SFRC 2-dimensional (i.e. slab) structures.

2.3.7 Barros and Figueiras (2001) proposed SFRC model

Barros and Figueiras (2001) also conducted experiments on notched beams under 4-point bending test (Barros, 1995) and proposed a constitutive model for the non-linear analysis of SFRC slabs. Two types of hooked-end steel fibres, namely Dramix ZP 30/.50 and Dramix ZX 60/.80 were considered in the developed model as applied

previously (Barros and Figueiras, 1999). There were three ranges of fibre ratios considered in this model; 0.38%, 0.56% and 0.75%. Both energy absorption capacity and elasto-plastic behaviour were considered in this model. A smeared crack model was adopted in order to reproduce the concrete cracking behaviour. Based on the experimental results (Barros, 1995) and numerical simulation of the test, a tri-linear diagram was derived to replicate the post-peak behaviour of SFRC in tension as depicted in Figure 2.19, where f_{ct} is the ultimate tensile stress of the SFRC. Note that the linear elastic part of the diagram is omitted for clarity. The characteristic points of the tri-linear softening diagram are specified in Table 2.4.

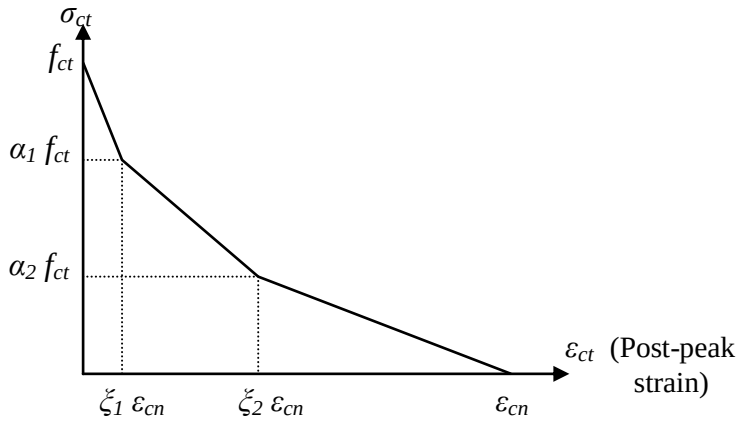


Figure 2.19: Tri-linear softening diagram for hooked-ends SFRC (Barros and Figueiras, 2001)

Parameters	Fibre type					
	ZP 30/.50: fibre content in kg/m^3 (fibre volume fractions)			ZX 60/.80: fibre content in kg/m^3 (fibre volume fractions)		
	30 (0.38%)	45 (0.57%)	60 (0.76%)	30 (0.38%)	45 (0.57%)	60 (0.76%)
ξ_1 (x10^{-3})	7-9	4-6	3-5	3-5	3-5	10-100
α_1	0.35-0.45	0.55-0.65	0.6-0.65	0.4-0.5	0.6-0.7	0.65-0.75
ξ_2 (x10^{-3})	0.2-0.3	0.25-0.35	0.3-0.4	0.15-0.25	0.15-0.25	0.3-0.5
α_2	0.1-0.2	0.15-0.25	0.15-0.25	0.2-0.3	0.25-0.35	0.25-0.35

Table 2.4: Values to define the characteristic points of the softening diagram of SFRC (adopted from Barros and Figueiras, 2001)

2.3.8 Barros et al. (2005) proposed SFRC model

Barros et al. (2005) carried out experimental and numerical work to investigate the SFRC post-cracking behaviour proposed in RILEM TC 162-TDF (2000; 2002; 2003)

recommendations. Two types of steel fibres were adopted in the study; Dramix RC 80/60 BN (F80/60) of 60 mm length and 0.75 mm diameter and Dramix RC 65/60 BN (F65/60) with 60 mm length and 0.92 mm diameter. The steel fibre volume fraction ranges between 0 and 0.56%.

Flexural tests based on RILEM TC 162-TDF (2000; 2002; 2003) recommendations were conducted to evaluate the equivalent strength (f_{eq}) and residual strength (f_R) of SFRC specimens. The results showed a large scatter for f_R, which concludes that f_{eq} is more reliable and appropriate for design purposes. Both f_R and f_{eq} increased linearly with the increase of fibre content (C_f) and number of fibres on the fracture surface (N_f). These values were then applied into the post-cracking relations recommended by RILEM TC 162-TDF (2000; 2002; 2003) for numerical analysis. A cross-sectional layered model for simulating the post cracking SFRC was developed. It was observed that the σ-ε approach recommended by RILEM TC 162-TDF (2000; 2002; 2003), overestimated the stress-strain values. Therefore, inverse analysis was carried out to establish new parameters for determining the post cracking σ-ε diagram of SFRC, as illustrated in Table 2.5.

σ_i (MPa)	ε_i
$\sigma_1 = 0.52 f_{ctm,fl}(1.6-d)$	$\varepsilon_1 = \sigma_1 / E_c$
$\sigma_2 = 0.36 f_{R1}\kappa_h$	$\varepsilon_2 = 1.2$ ‰
$\sigma_3 = 0.27 f_{R4}\kappa_h$	$\varepsilon_3 = 104$ ‰

Table 2.5: New approaches for defining the post cracking σ-ε diagram for SFRC (adopted from Barros et al., 2005)

2.3.9 Tlemat[a,b,c] et al. (2006) proposed SFRC model

Tlemat[b] et al. (2006) proposed a uni-axial tensile stress-strain model based on the experimental work carried out on FRC elements using fibres recycled from chopped tyre wire as well as conventional industrial steel fibres (i.e. twin-cone and hooked-end). The detailed of this work are presented elsewhere (Tlemat[a] et al., 2006). Inverse analysis was carried out to determine the tensile behaviour of constitutive relations of SFRC using experimental data. The simulations were carried out by implementing the beam into a non-linear finite-element software package. The model assumed that the tensile behaviour of SFRC is similar to that of plain concrete but with improved tension

stiffening. The behaviour of the model is summarised into three phases as depicted in Figure 2.20 (related section analysis of the phases was discussed earlier in Figure 2.5).

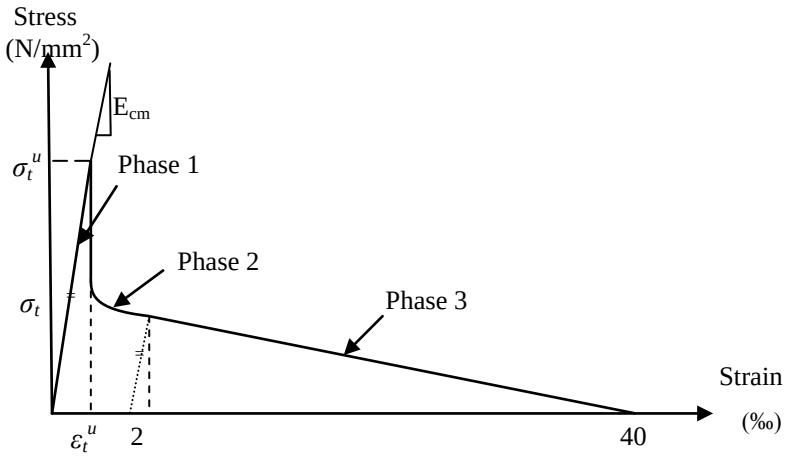


Figure 2.20: Proposed uni-axial tensile stress-strain model for mesh 25 mm (Tlemat[b] et al., 2006)

In Phase 1, the ultimate tensile stress and corresponding strain for SFRC is given by:

$$\sigma_t^u = \sigma_{t,p}^u(1 + 0.32w_f) \quad (\text{N/mm}^2) \tag{2.38}$$

$$\varepsilon_t^u = \sigma_t^u / E_{cm} \tag{2.39}$$

where, $\sigma_{t,p}^u$ is the maximum tensile stress for plain concrete and w_f is the fibre ratio by weight (%). In Phase 2, an exponential stress drop was introduced. The magnitude of the drop depends on the fibre type and is determined by the ξ factor, which has to be determined experimentally. The values of these factors are given in Table 2.6.

Fibre type	ξ Factors
ISF-1 (twin-cone steel fibres)	0.17
ISF-2 (hooked-end steel fibres)	0.19
VSF (virgin steel fibres)	0.20
PRSF (pyrolysed steel fibres)	0.28
SRSF (shredded steel fibres)	0.51

Table 2.6: Factors for the proposed model (adopted from Tlemat et al, 2006)

The tensile stress for strain values in range of $\varepsilon_t^u < \varepsilon < \varepsilon_1$ is given by the relation of:

$$\sigma_t = \sigma_t^u \cdot e^{\xi(\varepsilon_t^u - \varepsilon_1)10^3} \quad (\text{N/mm}^2) \tag{2.40}$$

where ξ is the fibre-type factor (derived based on the fibre influence on the tensile softening) and ε_1 is taken as equal to 2‰. Phase 3 consist of a linear drop of stress to zero at strain, ε equal to 40‰. According to Tlemat[b] et al. (2006), the proposed model in general exhibits good agreement with the experimental results. Moreover, this model is applicable to other types of steel fibres, provided the value of ξ factor is known.

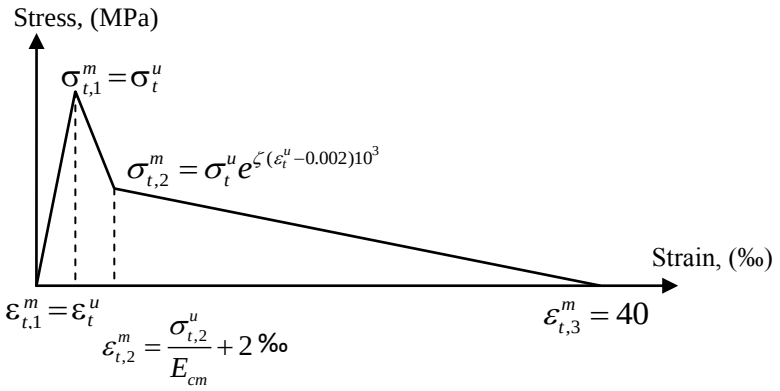


Figure 2.21: Proposed uni-axial tensile stress-strain model (Tlemat[c] et. al, 2006)

Tlemat[c] et al. (2006) also investigated the applicability of tensile stress-strain model proposed by RILEM TC 162-TDF (2000; 2003) guidelines to model the behaviour of SFRC including fibres recovered from used tyres. The tensile stress-strain diagram proposed by the authors (Tlemat[b] et al., 2006) is summarised in Figure 2.21. This figure is a tri-linear diagram based on the one in Figure 2.20 using the same reference points.

The proposed model and the one recommended by RILEM TC 162-TDF (2003) were both applied to simulate the flexural behaviour of prisms reinforced with conventional and recycled steel fibres (Tlemat[a] et. al, 2006). It was concluded that the resistance capacities predicted by the proposed model agreed well with the experimental results, whilst the RILEM TC 162-TDF (2003) model overestimated the resistance capacities.

2.4 Experimental investigation for SFRC under static loading

2.4.1 Monotonic loading

2.4.1.1 SFRC at the material level

Trottier and Banthia (1994) carried out four-point flexural tests to investigate the effect of fibre geometries and matrix strengths on the stiffness of SFRC. The geometries

investigated were hooked-end (60 mm length and 0.8 mm diameter), crimped (60 mm length and 1.0 mm diameter), twin-cone (62 mm length and 1.0 mm diameter) and crescent cross section of crimped steel fibres (52 mm length and 2.3 mm x 0.55 mm) with 0.5% fibre volume fraction. Three different strengths of concrete mixes (normal, medium and high strength concrete) were used in the experiments. Based on the load-deflection curves obtained, for both low and medium strength concrete, hooked-end fibres exhibit the best performance followed by twin-cone fibres. For high strength concrete, better post-peak behaviour was observed for the beam with twin-cone fibres. It was concluded that, steel fibres with deformed ends (i.e. hooked-end and twin-cone) showed higher increases in stiffness, post-peak behaviour and energy absorption.

Robins et al (2002) investigated the pull-out behaviour of hooked-end steel fibres in sprayed concrete tested under flexural loading. Hooked-end steel fibres of 30 mm length and 0.5 mm diameter with volume fractions ranging from 0.5 to 1.0% were considered in the experimental work. Three matrix types were studied considering various fibre embedded lengths and different fibre orientations (with respect of the longitudinal direction). It was concluded that matrix strength, fibre embedment and orientation influence the pull-out behaviour of SFRC. Based on the investigation carried out, the pull-out modes were categorised as (i) hooked-end straightened and consequently pulled out from the matrix, or (ii) the fibre fractured at hook portion. The energy absorption of the SFRC increased for fibre embedment higher than 5 mm. However, as the orientation of the fibre increases, the energy absorption decreases due to the increase in the number of fibre fractures. The optimum fibre orientation is observed at 10-20 degrees, yielding the maximum stiffness value obtained.

A series of experiments were conducted by Barragan et al. (2003) to study and validate the stress-crack opening (σ – w) relations of SFRC obtained from the direct uni-axial tension test proposed in RILEM Recommendations (2001). The specimens tested were notched cylinders. Dramix® RC 80/60 BN hooked-end collated steel fibres with length of 60 mm, diameter of 0.75 mm and fibre content of 0.5% were used. Based on the investigation results, it was concluded that the uni-axial tensile test for SFRC, using the notched cylinders of RILEM Draft Recommendation (2001) is applicable and represent the material response. The proposed equivalent tensile strength (f_{eq}) approach demonstrated the results reasonably, thus can be considered as a reliable concept.

Khaloo and Afshari (2005) tested small concrete slabs with various strengths to investigate the influence of steel fibres length and volume fraction on flexural strength and the energy absorption. Two types of fibres were used, specified in experiment as jc25 and jc35 with lengths of 25 mm and 35 mm and diameter of 0.6 mm and 0.67 mm, respectively. Three different fibre volume fractions; 0.5, 1.0 and 1.5 % were used for both type of fibres. The energy absorption of slabs calculated from the area under load-deflection curves showed enhancement due to more energy required for the fibres to be pulled out. It was concluded that the higher the volumetric percentages of the fibres, the higher the energy absorption required by SFRC slabs to propagate cracks. Based on the results, the authors recommended the use of fibre volume fractions in the range of 0.75-1.75 % and longer fibres.

An investigation was carried out by Tlemat[a] et al. (2006) as explained in section 2.3.2. The results show that the SFRC have a common failure in flexure due to pull-out rather than yielding. It was concluded that the recycled steel fibre is capable of providing impressive resistance against micro-cracking and can be as effective as industrial steel fibres resulting in smaller deflections.

Bencardino et al. (2008) carried out compression tests on cylindrical specimens of SFRC and proposed a compressive stress-strain model for SFRC. Hooked-end steel fibres were used in the investigation. Three ranges of fibre volume fractions were used (1 %, 1.6 % and 3 %). It was concluded that addition of fibres marginally affects the compressive strength of concrete. Additionally, the increase in fibre content improved the post-peak behaviour of load-deflection curve as a more extended softening branch was observed.

2.4.1.2 At the structural level

Swamy and Al-Ta'an (1981) carried out flexural test on SFRC beams to study the deformation pattern and the ultimate strength, when the maximum aggregates size was kept at 20 mm. Crimped steel fibres dimension of 0.5 x 50 mm were used at two different locations, i.e. (i) over the whole depth of the beams or (ii) over the effective tension zone of the beam only. The fibre volume fractions used were 0.5 % and 1.0 %. The test results observed better crack opening control from fibres bridging effect obtained in beams with fibres distributed along the whole depth of the beam as

compared to the fibrous beams at effective tension zone only. The slow cracking propagation reduced the deformation at the first crack for beams with steel fibres resulting to ductile failure. It was concluded that the fibres shows crack opening control capability, thus improving the post-cracking behaviour and increases the stiffness of the beams, leading to less deformation at failure.

Swamy and Bahia (1985) conducted tests on T-beams and rectangular beams to investigate the effectiveness of implementing steel fibres in addition to conventional shear reinforcement. Three parameters were studied: fibre volume fraction (V_f = 0% to 1.2%), percentage of longitudinal steel and amount of web reinforcement. Crimped steel fibres with 50 mm-length and 0.5 mm diameter were adopted for this study. The results show that there was a change in the mode of failure of the beams from diagonal tension to shear compression; however, the amount of fibres was not sufficient to induce flexural failure. Higher load carrying capacity was observed due to the fibres capability in retaining the stiffness of the beams and controlling the crack propagation.

To investigate the effectiveness of steel fibres as shear reinforcement, Sharma (1986) carried out experiments on SFRC beam subjected to combined bending and shear loads. The steel fibres adopted in the test had deformed ends with length of 50 mm, diameter of 0.6 mm and a fibre volume fraction of 0.85%. Two groups of beams were tested; with and without stirrups. In beams without stirrups and fibres, sudden failure was observed. However, for SFRC beams, the crack propagation rate was slower and leads to gradual shear failure. The fibrous beams with stirrups behaved in a ductile manner and produced higher post cracking strength. This study shows that steel fibres are effective in increasing the shear strength, improved ductility and energy absorption as compared to conventionally reinforced concrete beams. The presence of steel fibres in concrete reduces crack propagation, thus allowing for more uniform cracking.

Mansur et al. (1986) studied the effect of steel fibres in beams without stirrups, at various concrete strength, longitudinal reinforcement percentages, fibres volume fraction ($V_f = 0.5, 0.75$ and 1%) and span/effective depth ratio. The hooked-end steel fibres with 30 mm length and 0.5 mm diameter were adopted in the study. Results from the experimental work observed that the mode of failure for beams with no stirrups change from shear failure to flexure failure with addition of fibres. The results show that the critical shear/effective depth ratio of the beams to simulate shear failure

decreased with the increased of the fibre volume fractions. In term of shear resistance, an upward trend was observed for beams with increase of fibre volume fractions.

A series of experiment was carried out by Narayanan and Darwish (1987) to investigate the behaviour of SFRC beams subjected to predominant shear. A 0.3 mm diameter crimped steel fibres with fibre volume fraction between 0.25% and 3% were adopted in this case study. Besides fibre contents, the influence of the aspect ratio of the fibres, concrete strength, amount of longitudinal reinforcement and shear span/effective depth ratio were investigated. The test results show that the addition of fibres facilitates the crack control in the beams and that a higher content of fibres (1%) was able to change the mode of failure from shear to flexure failure.

Additional tests were conducted by El-Niema (1991) to study the behaviour and strength of SFRC beams under shear. Crimped steel fibres with three different aspect ratios of 63.83, 95.75 and 127.7 were adopted in the experimental work. Three fibre volume fractions were utilised; 0.4%, 0.7% and 1.0%. SFRC beams at constant fibre volume fractions showed an increase in stiffness and strength, as the aspect ratio of the fibres were increased. Likewise, similar patterns were observed when the aspect ratio was kept constant and the comparison was made between various fibre volume fractions. Higher fibres content produces higher stiffness and strength as observed from the load-deflection curves. It was established that fibres pull-out and bridging behaviour control the cracking propagation of the beams and enhanced the tensile stiffness and ductility of the SFRC beams. Higher fibres content and aspect ratio increased the first cracking strength of the beams significantly. Higher load is required to produce similar deflection and to pull-out the fibres bridging the crack opening.

Mansur and Ong (1991) investigated the effect of inclusion of steel fibres in reinforced concrete deep beams. Straight but slightly twisted steel fibres, 30 mm long and 0.5 mm wide square in cross section, were mixed with the concrete. Test results show that the addition of fibres improved the cracking propagation and deformation of deep beams, in which, when there is no fibres presence, the cracking propagated rapidly across two-thirds of the beam. However, for fibrous beam with volume fraction of 1.5%, the cracking propagated slower, with fibres bridging the cracks and reducing the rate of crack width opening and extension. It was observed that, the increase in span/depth ratio decreases the shear strength of the deep beams and has effect in the cracking behaviour of the fibrous beams.

A study on the shear behaviour and shear analysis of SFRC under four point bending test was carried out by Oh et al. (1998). The effect of steel fibres as potential shear reinforcement was investigated and two different parameters of fibre volume fractions ($V_f = 0$ to 2%) and amount of stirrups were considered. Round straight steel fibres with a length of 42 mm and a diameter of 0.7 mm were added in the fibrous concrete mix. It was observed that the addition of fibres increases the compressive strength up to 25%. The tensile strength, on the other hand increases substantially more than 100% for fibre volume fraction of 2%. There was a trend of increase in cracking strength and ductility for the fibrous beams, regardless of the amount of the stirrups. A significant increase in the strength and ductility can be observed in beams without stirrups with the mode of failure changing from shear to flexure as the steel fibres content was increased. Better performance in ultimate shear strength and maximum deflection before failure was observed in the SFRC beams as the amount of stirrups was increased up to 75%

Kwak et al. (2002) carried out experimental work on SFRC beams to study the shear strength of the SFRC beams without stirrups. The variables considered were fibre volume fraction ($V_f = 0, 0.5$ and 0.75%), span/depth ratio ($^a/_d$) and concrete strength. Hooked-end steel fibres with length of 50 mm and diameter of 0.8 mm were utilised in the mixtures. It was observed that addition of fibres affect the cracking pattern and changed the failure mode of the beams from shear to flexure failure (for $V_f = 0.5\%$ and $^a/_d = 4$). In terms of the strength, the highest cracking strength and ultimate shear strength were observed from beam with $^a/_d = 2$, thus it shows that increasing the span/depth ratio, decreases the shear strength of the SFRC beams.

An investigation on SFRC short beams was carried out by Cho and Kim (2003) to study the effect of adding steel fibres. Hooked-end steel fibres with a length of 36 mm, a diameter of 0.6 mm and fibre content between 0.5 % and 2.0 % in volume were adopted in the study. The monotonic load test was carried out on the normal strength and high strength RC beams. The results show that the addition of fibres reduces the crack width and changes the mode of failure from shear to flexure failure. Higher strength concrete produced better performance than normal strength concrete and less fibres volume fraction (0.5%) was needed to achieve satisfactory shear resistance as compared to normal strength concrete that require 1% of fibre volume fraction.

A study was carried out by Campione et al. (2006) to analyse the effect of steel fibres in shear strength of RC beams with and without stirrups under four point bending test. The parameters considered were the amount of stirrups, the span/depth ratio and steel fibres content. It was observed that the addition of the fibres improve the ductility of the SFRC beams, even when the stirrups were absent from the beams (Campione et al., 2003; as cited in Campione et al., 2006). It was also found that the increase in span/depth ratio decreases the shear strength of the beams.

2.4.2 Reversed-cyclic loading

Jindal and Hassan (1984) conducted an experimental work to study the effectiveness and behaviour of steel fibres in beam-column joints. Three series of specimens were prepared by incorporating conventional RC joints, SFRC throughout the entire length of the beam and column and SFRC in the joint region only. Circular steel fibres with length and diameter of 25 mm and 0.25 mm, respectively, were utilised at 2% of weight percentage. The specimens were tested under cyclic and/or monotonic loading until failure. It was reported that specimens with steel fibres exhibited better strength and stiffness and failed in a ductile manner.

Gefken and Ramey (1989) investigated the effect of adopting steel fibres reinforcement in the joints with increased hoop spacing tested under reversed-cyclic loading. The joints considered constant lateral reinforcement within the beam and variable lateral reinforcement within the column joint region. Steel fibres used were straight-round with 25 mm length and 0.41 mm diameter (aspect ratio of 60) applied at 2 % volume fraction. Based on the results obtained, it was observed that addition of steel fibres in the joints with increased hoop spacing from 5.1 cm to 8.4 cm improved the joint behaviour. The ductility of fibrous joints showed better or similar performance with the conventional joints with the load bearing capacity increased up to 89%. The energy absorption capacity of the fibrous joint increased between 40% and 110%, as comparison to the conventional joints. Moreover, the crack propagation and damage tolerance in the fibrous joints were appreciably controlled.

Bayasi and Gebman (2002) carried out experiments on conventional and fibrous beam-column joints from actual building structures designed according to the Uniform Building Code (1997). Four joints were constructed which were identical to the

conventional ones but with increased in the hoop spacing by 50% (15.2 cm) and 100% (20.3 cm) and addition of steel fibres in both the beam and column. The steel fibres used in the experimental work had a deformed end with length of 30 mm, a diameter of 0.50 mm and a volume fraction of 2 %. Results indicated that fibrous specimens showed slower deterioration of joint load bearing capacity, higher energy absorption and improved damage tolerance due to the fibre confining action. Fibrous joints showed higher load carrying capacity and ductility due to the confinement provided by fibres together through the anchorage within concrete and its resistance to pull-out.

Two-span continuous RC columns, with and without fibres, were tested by Kotsovos et al (2007) under combined loads of axial forces and monotonic or reversed-cyclic loading. The structures were designed in accordance to Eurocode 2 (2004). Two types of fibre mixes were adopted in this work; FC 30 with 0.32 % volume fraction of 60 mm length and 0.75 mm diameter of steel fibre and FC 60 with 0.64 % volume fraction of 35 mm length and 0.54 mm diameter of steel fibre. Under monotonic loading, the SFRC columns showed a larger number of inclined cracks, with a smaller crack width. Under reversed-cyclic loading, the addition of the steel fibres improved the strength, ductility and controlled the crack propagation of the column. This is true for specimens with concrete strength less than 62 MPa. For specimens with higher concrete strength; there was a reduction in ductility, probably due to insufficient amounts of fibres incorporated with the higher concrete strength mix.

A study was carried out by Campione and Mangiavillano (2008) on SFRC beams to investigate its flexural behaviour under monotonic and reversed-cyclic loading. Several cover thickness and different amount of longitudinal reinforcement were considered. Hooked-end steel fibres with 1% in volume fraction, 30 mm length and of 0.5 mm diameter were added to the fibrous concrete mix. Under monotonic loading, cracking strength and ductility were enhanced with the presence of fibres in the beams. Under reversed-cyclic loading, the addition of fibres increases the shear strength and ductility of the beams. Fibres reduce the crack opening width of the beams due to the pull-out and bridging behaviour which influences the shape of load-deflection curves. Furthermore, the presence of fibres controlled the failure mode of the beams to occur in more ductile manner.

2.5 Experimental investigation for SFRC under seismic loading

Further investigations have also been carried out experimentally to validate the efficiency of using steel fibres in other RC elements. One practical aspect of particular interest is to reduce steel congestion in seismic beam-column joints to ease their construction. A series of experimental work was carried out by Craig et al. (1984) to study the behaviour of SFRC joints. The beam-column joint constructed for the test utilises less hoops than conventional seismic joint as recommended in the code (ACI 318-77, 1977) while the amount of longitudinal steel in compression and tension for the beam were varied. Fibrous concrete in the joint region consisted of 1.5% hooked-end steel fibres with 30 - 50 mm long and 0.5 mm diameter. The reversed-cyclic loading was arranged at a fixed distance from the face of the column to simulate the actual loads that occurred to the beam-column joint during actual earthquake. Based on the test done, the authors reported that the SFRC joints observed better confinement and increased in strength, stiffness, ductility and energy absorption capacities. Steel fibres provide crack arrest mechanism in which the crack width opening were smaller and distributed uniformly, thus maintaining better structural integrity.

Jiuru et al. (1992) reported a research program on the seismic behaviour of SFRC exterior and interior beam-column joints. Steel fibres used were approximately 45 mm long and had diameter of 0.38 mm, with a volume ratio of 1.5 %. The fibrous mixture was casted either within the joint core only or within the joint core and a portion of the beam. The hoops or ties in the beam were kept constant throughout all cases. However, for fibrous joints, the hoops within the joint core were maintained, reduced or eliminated. The joints were tested under combined axial force and displacement controlled reversed-cyclic loading arrangement, which simulated the effect of seismic loading. Experimental results showed that steel fibres improve the joint and beam shear strengths, ductility and energy dissipation capacity of the structures. The fibrous joints exhibited a few diagonal cracks in the beam and a vertical flexural crack near the column face region, whilst moment-shear failure was observed on conventional joints with most of the stirrups of the beam in the plastic hinge region (yielded or nearly yielded). With the introduction of fibres, the ductility of SFRC joints increased up to 46% and energy absorption improved up to 80%.

Filiatrault et al. (1994) tested exterior beam-column joints which was part of a prototype building which was designed following the National Building Code of Canada (1990).

The joints were tested under reversed-cyclic loading with displacement ductility controlled cycles. One specimen without fibres and with a lateral reinforcement following the detailing recommended for seismic design was tested and used as the control specimen. Three other joints, in which, without special seismic detailing recommendation for the spacing of the lateral reinforcement, were tested. Two of them were casted with fibrous concrete in the joint core and in part of the beam and column regions (containing 1.0 % of 30 mm-long, 0.5 mm diameter hooked-end steel fibres and 1.6% of 50 mm long, 0.5 mm diameter hooked-end steel fibres, respectively). The results showed that the energy absorption obtained from fibrous joint with a ratio of 1.6% fibre volume were comparable to the conventional joint with seismic detailing. The joint with 1% fibre volume on the other hand, absorbed about 30% less deformation strain energy. Satisfactory shear strength both in positive and negative flexure, were obtained from the joint with 1.6% fibre volume fraction. Filiatrault et al (1995), extended their work using interior cross-joints instead if exterior T-joints and obtained similar conclusion.

A study was carried out by Lee (2007) to investigate the effect of steel fibres on RC columns under seismic loading. Three parameters were considered; the shear-span-to-depth ratio, the shear reinforcement ratio and the steel fibre volume fraction. Three amount of fibre volume fractions were also adopted at 1%, 1.5% and 2%, using hooked-end steel fibres with length and diameter of 33 mm and 0.55 mm, respectively. It was found that the mode of failure of the columns can be changed from brittle shear failure to ductile flexural failure when the steel fibres were uniformly distributed in the columns. It was observed that the shear strength capacity, the energy dissipation capacity and the ductility of the columns were increased with the increase in the fibre volume fraction. A volume fraction of 1.5% was recommended as the optimum amount of fibre content to improve the strength and ductility capacities of the SFRC columns.

2.6 Summary

Several studies on the behaviour of SFRC were discussed in this chapter. Based on the work reviewed, some conclusions can be made as follows:

- The key factor in the performance of SFRC is the anchorage mechanism and pull-out resistance provided during crack propagation. Several factors that affect the pull-out behaviour are bond strength, the type of fibres, their shape and aspect ratio, fibre orientation and embedment length and fibre volume fraction.
- Based on previous research work (e.g. Lok and Pei, 1998; RILEM TC-162-TDF, 2000; 2003; Bencardino et al, 2008), it is generally agreed that steel fibres have minimal effect on the compressive behaviour of RC. In most of the work, the behaviour of SFRC in compression is assumed to be the same as that for plain concrete (but with an improved ultimate strain value).
- Many researchers (e.g. Lim et al., 1987; Lok and Pei, 1998; RILEM TC-162-TDF, 2002; 2003; Tlemat et al., 2006) suggested that the addition of steel fibres improve the post-cracking behaviour of concrete from the sharp drop associated with plain concrete to either tension softening or tension stiffening. The enhancement in the stress and strain is due to the fibres bridging the cracks and delaying crack propagation through their pull-out resistance.
- The SFRC constitutive models discussed in Section 2.3 can either be classified as either generic (i.e. Lim et al., 1987; Murugappan et al., 1994; Lok and Pei, 1998; Lok and Xiao, 1999; RILEM TC-162-TDF, 2002; 2003) or being applicable only for a specific type of steel fibres (i.e. Barros and Figueiras, 1999; 2001; Tlemat[a,b] et al., 2006).
- In terms of shear behaviour, the addition of steel fibres increase the shear strength, improve the ductility and energy absorption of the SFRC structures and controlled the crack propagation to fail in a ductile manner (e.g. Sharma, 1986; El-Niema, 1991; Filiatrault et al, 1994; 1995; Oh et al., 1998; Kwak et al., 2002, Lee, 2007). Furthermore, sufficient combinations of steel fibres with or without conventional stirrups enhance the energy absorption and change the failure mode of SFRC structures from shear to bending mode of failure. Therefore, it can be concluded that steel fibres show potential as shear reinforcement.
- El-Niema (1991), Oh et al. (1998), Cho Kim (2003) and Lee (2007) concluded that the increase in the fibre volume fractions increased both strength and

stiffness of the SFRC. Fibres shape and geometry have a significant effect on anchorage mechanism provided by the steel fibres. It was observed that deformed shape steel fibres, especially deformed end fibres (i.e. twin-cone and hooked end) provide better capability in increasing the stiffness, post-peak behaviour and energy absorption of the fibrous specimen (Trottier and Banthia, 1994). Moreover, steel fibres with higher aspect ratio provide higher energy absorption (El-Niema, 1991; Khaloo and Afshari, 2005).

Therefore, it can be concluded that investigation carried out for the SFRC exhibits desirable behaviour in which enhancement was observed in the cracking strength, ductility, stiffness and energy absorption. Furthermore, steel fibres controlled the crack propagation and change the mode of failure from brittle to a more ductile manner.

Some work was also carried out to investigate the potential use of fibres as an alternative to shear reinforcement in the RC structures especially under reversed-cyclic and seismic loading (Craig et al., 1984; Gefken and Ramey, 1989; Filiatrault et al., 1994; 1995; Bayasi and Gebman, 2002, Lee, 2007). The studies concluded that steel fibres were able to provide acceptable strength and ductility enhancement that can be comparable with conventional structures even when the stirrups was reduced in SFRC structures. Moreover, the energy absorption of the SFRC structures showed improvement with more controlled crack propagation. This is particularly beneficial in term of seismic design as the structure tends to be congested with shear reinforcement, which causes difficulties in construction work. Some of the crucial factors considered during the investigation can be listed as follow:

1. Range of fibre volume fractions
2. Fibres shape and aspect ratio
3. Ratio of reduction in conventional shear reinforcement
4. The extent of SFRC zone within the structure.
5. Loading and boundary conditions

Nevertheless, the work carried out so far was limited to certain amounts of steel fibres and shear reinforcement ratios. Some experimental work only considered one value of fibre volume fraction (e.g. Gefken and Ramey, 1989; Jiuru et al., 1995; Bayasi and Gebman, 2002) or one case of SFRC structure with reduction in the conventional shear reinforcement (e.g. Craig et al., 1984; Filiatrault et al., 1994, 1995). The work carried

out so far on cyclic behaviour is predominantly experimental and there is hardly any numerical modelling performed. Therefore, the present research work aims to expand this further by means of non-linear FE analysis and critically examine the potential for steel fibres to compensate for reduction in conventional shear reinforcement, particularly under reversed-cyclic loading (which is the key feature in seismic action).

CHAPTER 3

METHODOLOGY: NON-LINEAR FE ANALYSIS OF SFRC STRUCTURES

3.1 Introduction

A summary of the SFRC constitutive models and associated non-linear FE analysis strategies considered in the present research work is presented herein. A discussion of the calibration work carried out between the predictions of the different models and the corresponding existing experimental data is also presented (with full details provided in Appendix A).

3.2 Constitutive models for SFRC

3.2.1 Background

A considerable amount of work has been carried out by different researchers (e.g. Lim et al., 1987, Lok and Pei, 1998; Tlemat et al. 2006) and various tensile stress-strain constitutive models were proposed. Some of these models were discussed in Section 2.3 of Chapter 2. Amongst all the models discussed, only four models are generic (i.e. allowing for different volume fractions, bond stress, aspect ratio etc) and are thus relevant to the present research work. These models were proposed by Lim et al. (1987), Murugappan et al. (1994), Lok and Pei (1998) and Lok and Xiao (1999). Generally, the model proposed by Murugappan et al. (1994) was a modification on the model proposed by Lim et al. (1987). As both models were designed for steel fibres in the range of 0.5% to 1.5%, these models provided insufficient information with regards to the fibres content range requirement intended for the parametric study in the present

work. Furthermore, it should be noted that Lim et al. (1987) model ignored the residual stress developed in the concrete matrix.

As a consequence of the aforementioned issues, the SFRC models proposed by Lok and Pei (1998) and Lok and Xiao (1999) were considered for calibration work. In addition, the models proposed by Tlemat[b] et al. (2006) and Barros and Figueiras (2001) were also considered. The inclusion of these two models and their respective experimental data was useful as one model (Tlemat[b] et al., 2006) allowed for high values of fibre volume fraction (i.e. up to 6%), while the other (Barros and Figueiras, 2001) was applicable only to low fibre amounts (e.g. 0.5%). This wide range was used to examine the capability of the two main models considered (i.e. Lok and Pei, 1998 and Lok and Xiao, 1999) to simulate the behaviour of SFRC with fibres provided in both low and high amounts. This is important since the range considered in the present work was quite varied, with volume fractions between 0.5%~2.5%.

All the aforementioned four models (i.e. Lok and Pei, 1998, Lok and Xiao, 1999 Tlemat[b] et al., 2006 and Barros and Figueiras, 2001) were implanted into the commercially available finite-element software package ABAQUS (2007) as part of the calibration work. The results of the latter were then used to select the best model to be adopted in the subsequent parametric studies. The basic characteristics of the material models and the assumptions made are discussed in the following sections. The details and results of the calibration work were presented in Appendix A.

3.2.2 Tension model

The structural response of SFRC structures is predominantly characterised by its tensile behaviour. Therefore, SFRC behaviour can be effectively modelled using a suitable tensile stress-strain relationship. As mentioned earlier, four constitutive models were considered for the preliminary calibration work (i.e. Lok and Pei, 1998, Lok and Xiao, 1999; Tlemat[b] et al., 2006; and Barros and Figueiras, 2001).

The value for the bond stress (τ_d) for Lok and Pei (1998) and Lok and Xiao (1999) models was assumed based on values summarised in Table 2.2 (Chapter 2). The values of ultimate compressive and tensile strain at failure were taken as -0.0035 and 0.02 (Craig et al., 1987; Lok and Pei, 1998; Lok and Xiao, 1999; Eurocode 2, 1992),

respectively. In addition, if the tensile strength value was not given, the tensile stress was assumed as maximum of 10% of the compressive strength of the concrete.

A minimal conservative modification was made to the Lok and Xiao (1999) model as part of the present research work. The vertical line at the end of the SFRC tensile stress-strain curve proposed by Lok and Xiao (1999) was altered so that the stress decreases gradually to 0 between strain values of 0.018 to 0.02 rather than the original sudden vertical drop (refer to Figure 2.16 in Chapter 2). This alteration was suggested to avoid numerical instability, without affecting the accuracy of the results as the change is insignificant in practical terms. Additionally, the values used to define the material models proposed by Barros and Figueiras (1999) and Tlemat[b] et al. (2006) were taken from the Tables 2.3 and 2.6, respectively.

3.2.3 Compression model

It was concluded in Chapter 2 that the addition of steel fibres has no significant effect on the compressive behaviour of concrete (Bencardino et al., 2008). Therefore for the present work, the SFRC compressive behaviour is assumed to be the same as the one for plain concrete.

3.2.4 Conclusions on SFRC constitutive models

Lok and Pei (1998) and Lok and Xiao (1999) are alike and adopt the same concepts to define the characteristic points on the stress-strain diagram. Lok and Xiao (1999) model, is an improvement of the Lok and Pei (1998) model, considering a user defined value for the orientation factor. Moreover, the shape of the post-cracking tensile stress-strain diagram is similar to the one proposed by RILEM TC 162-TDF Recommendation (2000; 2003) and other researchers (Lim et al., 1987; Murugappan et al., 1994).

Based on the findings of the calibration work carried out (with full details presented in Appendix A), it was found that the results produced by the Lok and Xiao (1999) constitutive model were in best agreement with existing experimental data used in the calibration study. Even in instances where there was a slight difference, the discrepancy was always on the safe side (in design terms) with the model predictions not overestimating actual strength results.

Therefore, the model proposed by Lok and Xiao (1999) was chosen to be used in the present work based on the following reasons. First, the model is applicable for a reasonably wide practical range of fibre volume fractions (i.e. 0.5% to 3.0%), which is similar to the range investigated in the present research work. Secondly, the model is versatile as it allows for definition of different values of aspect ratio (*L/d)* and bond stress (τ_d). Thirdly, the randomness distribution of the steel fibres is considered in the model. Fourthly, the model is capable of exhibiting both tension softening and hardening depending on the amount of fibres provided. Finally, through the calibration work carried out, all predictions were found to agree well with experimental results and to be always on the safe side in terms of its load carrying capacity estimates.

3.3 Review of material models in ABAQUS software

The parametric studies in the present work were carried out using non-linear finite element analysis (NLFEA). To begin with, SFRC material models discussed earlier were validated and calibrated so that only one model was selected for further work. As stated earlier, the present work was carried out using NLFEA software package ABAQUS (2007). A brief review on the software's modeling of RC structures is presented in this section. A more detailed description of the underlying theory and the application of the software can be found elsewhere (ABAQUS, 2007).

To simulate a structure, ABAQUS splits the actual geometry of a structure into a set of finite elements. The discrete portions of the physical structure are represented through these finite elements, which are joined by shared nodes. The collection of finite elements is called a mesh. Mesh density refer to the number of elements used in a particular mesh. Further background on the FE method and modelling in general is available elsewhere (Zienkiewicz and Taylor, 1989; Cook, 1995).

A non-linear structural problem is one in which the structure's stiffness changes as it deforms. Sources of non-linearity in structural mechanics simulations are material (i.e. cracking, yielding), boundary (i.e. sudden change in boundary condition) and geometric (i.e. large deflection in beam). ABAQUS uses the Newton-Raphson method (Zienkiewicz and Taylor, 1989; Cook, 1995) to obtain solutions for non-linear problems

(by applying the load incrementally in small piece-wise linear steps and ensuring convergence).

3.3.1 Concrete models available in ABAQUS

Some of the key points of the material models available in ABAQUS for concrete are discussed in the following sections. The effect of the fibres as reinforcement was adopted in the tension part of the concrete models, either as post-peak tensile strain softening or hardening, thus allowing for fibres behaviour across the crack. Generally, the interaction between steel bars and concrete (and the consequent effect on the concrete model) is considered by modifying some aspects of the plain concrete behaviour, such as the use of tension stiffening. The latter is the increase in stiffness of a cracked RC member due to the development of tensile stresses in the concrete between the cracks (owing to the bond between the steel and the concrete). Thus the stiffness of the member is greater than that based on a cracked plain-concrete section (where concrete in tension is assumed to carry zero stress) and hence the term "tension stiffening". It is usually modelled in NLFEA software by adjusting the post-cracking behaviour so that concrete does not lose its tensile strength suddenly and completely after cracking, but undergoes a gradual loss of tensile strength. The presence of fibres bridging the cracking leads to a significantly more gradual (i.e. ductile) drop from the peak tensile strength. Therefore, the constitutive models for SFRC (see section 3.2 of this chapter) described in terms of tensile stress-strain relations which were incorporated into ABAQUS concrete models by altering the "tension stiffening" part of these models. A full description of the SFRC tensile relations is presented in Section 2.2 of Chapter 2.

Fibres effect on shear response (in a direction parallel to the crack) was also considered by using the "shear retention" part of ABAQUS concrete model. Usually in the NLFEA of RC structures, "shear retention" is used to allow for the effect of aggregate interlock and dowel action. Fibres provide a similar effect and thus can be modelled using this part of the model. The salient features of concrete models available in ABAQUS (from which one was selected and applied in the present research work) are discussed next.

3.3.1.1 Smeared cracking concrete model

In general, the smeared cracking concrete model is designed to simulate the behaviour of concrete subjected to monotonic straining at low confining pressures. It requires the definition of material properties in the uni-axial stress-strain data depicted in Figure 3.1. The compressive behaviour of concrete is modelled as elastic-plastic.

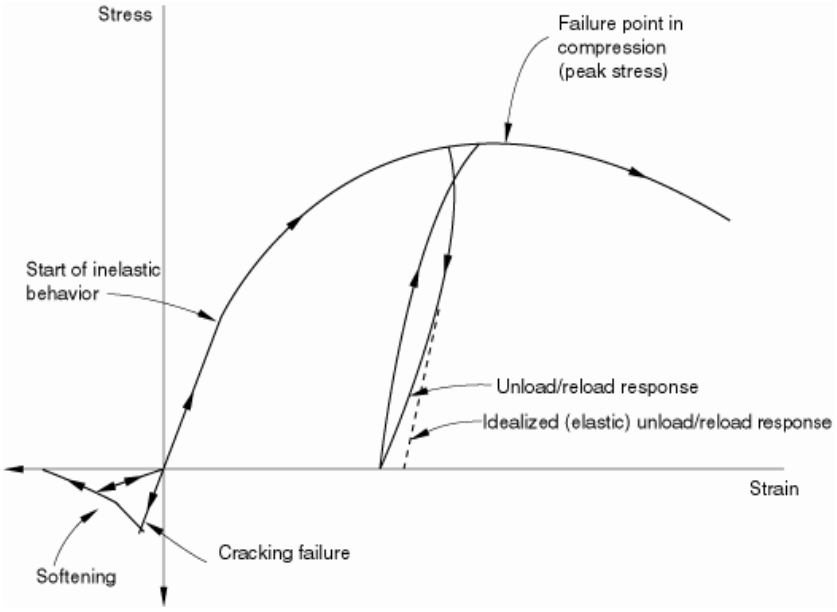


Figure 3.1: Uniaxial behaviour of plain concrete (adapted from ABAQUS, 2007)

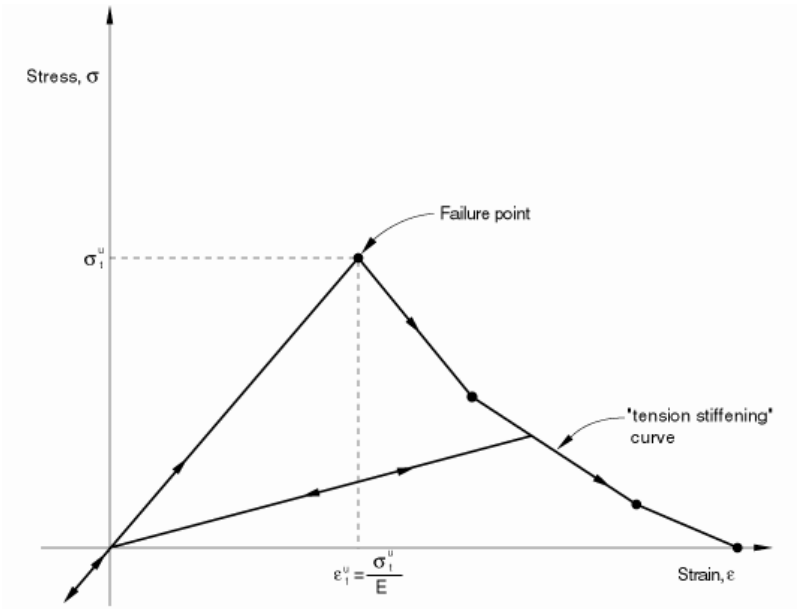


Figure 3.2: Tension stiffening model (adapted from ABAQUS, 2007)

The effect of steel fibres is included through tension stiffening (see Figure 3.2), which is designed to allow for the definition of post-cracking behaviour for cracked concrete and

simulates the reinforcement interaction effect within the concrete. Tensile stress-strain data is given using the values of tensile cracking stress (σ_t) normalised with the ultimate tensile cracking stress (σ_t^u) and its respective plastic tensile strain (ε_t), obtained by deducting the elastic ultimate tensile strain (ε_t^u). The post-cracking tensile stress-strain behaviour is defined based on the material models for SFRC.

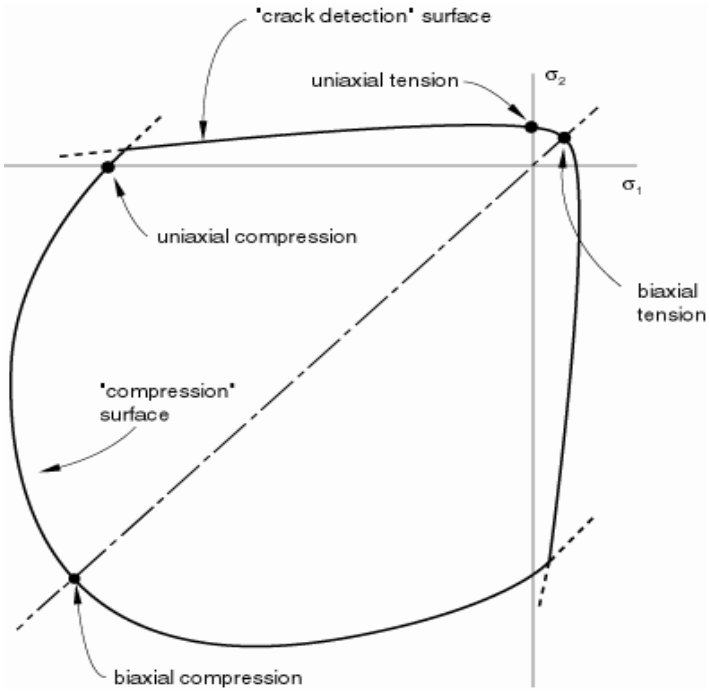


Figure 3.3: Yield and failure surface in plane stress (adapted from ABAQUS, 2007)

Additionally, the relationship between compressive and tensile behaviour is specified in the failure ratio values, in order to allow ABAQUS to define the shape of failure surface as illustrated in Figure 3.3. For the calibration work, only two ratios were defined into ABAQUS. First, the ratio of the ultimate bi-axial compressive stress to the ultimate uni-axial compressive stress and secondly, the absolute value of the ratio of the uni-axial tensile stress at failure to the ultimate uni-axial compressive stress.

Furthermore, the shear stiffness of the concrete decreases when crack is propagated. Figure 3.4 shows one of a standard shear retention graph available in ABAQUS. In order to allow shear retention effects, shear modulus (ρ^{close}), with the value range between 0 and 1 (no shear retention to full shear retention) is classified in the material property. The maximum strain (ε_{max}) is assumed a very large value and is defined by

the user. If the shear retention factor is not specified, ABAQUS/Standard will employ a default response with assumption that the shear response is unaffected by cracking.

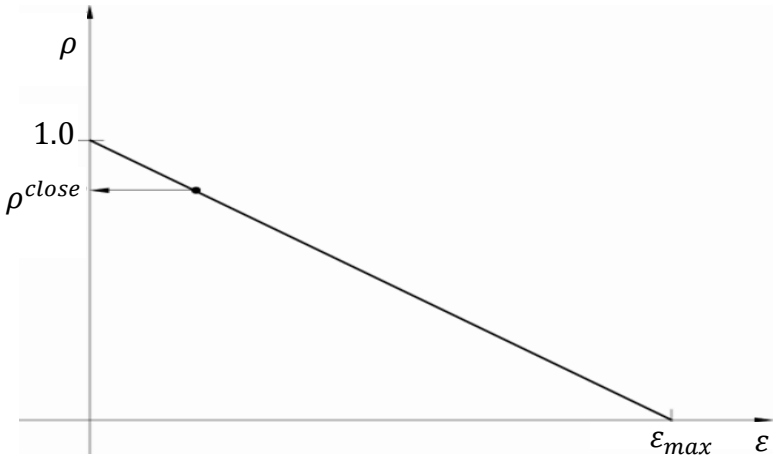


Figure 3.4: Shear retention model (adapted from ABAQUS, 2007)

3.3.1.2 Brittle cracking concrete model

The brittle cracking model is designed to model plain concrete which is dominated by tensile-cracking behaviour. Since the present model focuses on the brittle aspect of concrete behaviour, compressive behaviour has been simplified and assumed to be linear elastic. This is justified, particularly for three dimensional (3D) modelling, as at least one of the three principal stresses needs to be tensile and exceeding the tensile strength to initiate cracking (while the other two principal stresses could be compressive). So the model is capable of modelling concrete behaviour under tension and tension-compression states of stress. Thus the model is applicable to all types of concrete structures. The main attractive feature of the model is that it focuses on the main mechanisms for failure in concrete, namely its brittleness and cracking (predominantly in tension). Thus the simplification made with regards to compressive behaviour is intended to make the solution efficient without affecting its accuracy of mimicking real behaviour of concrete. To make the numerical solution even more efficient, the analysis is usually carried out using the dynamic solver as a quasi-static one (i.e. with a low rate of loading). Therefore in the present study, it was used in conjunction with the explicit dynamic procedure available in ABAQUS/Explicit.

A smeared crack approach is adopted in modelling the brittle behaviour of the concrete. In this approach, ABAQUS includes the presence of the cracks into the calculation of stress and material stiffness. Rankine criterion is incorporated in the brittle cracking

model to detect crack initiation. A crack is formed when the principal tensile stress exceeds the tensile strength of the brittle material. The brittle cracking model requires a failure in tension stress in order to consider failure at a node or region (see Figure 3.5).

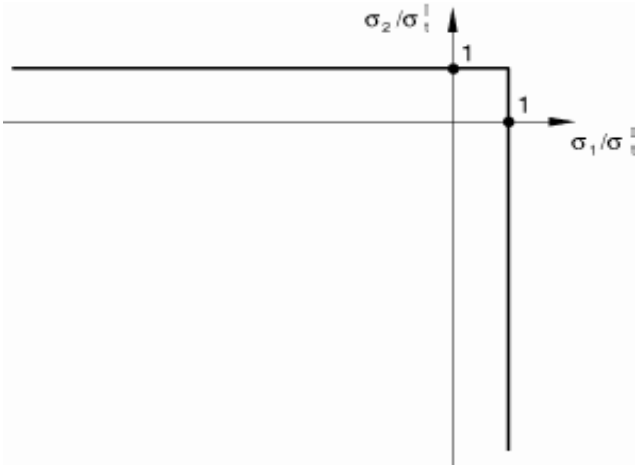


Figure 3.5: Rankine criterion in plane stress (adapted from ABAQUS, 2007)

There are two types of failure mode in this criterion, namely Mode I (tension softening/stiffening) and Mode II (shear softening/retention). Crack initiation is based on Mode I failure, whilst both modes effect the post-cracked behaviour. In Mode II failure, the cracked shear modulus is reduced as the crack opens.

ABAQUS assumes that the first crack is formed when the crack formation complies with Rankine criterion. This model allows crack to close and reopen, which is useful for cyclic analysis, and has memory of all crack directions. The tensile post-failure (i.e. post-cracking) behaviour depicted in Figure 3.6 is specified through a post-failure stress-strain relationship by adopting the values obtained from SFRC material models considered. In addition, the interaction between concrete and reinforcement (including steel fibres) is modelled trough tension stiffening effect.

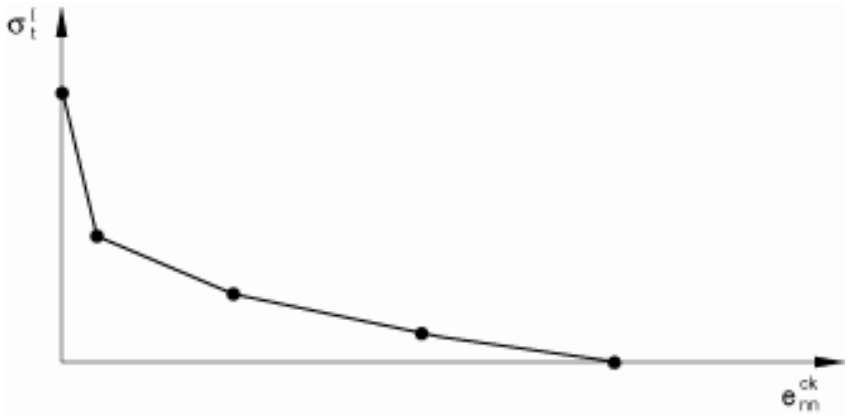


Figure 3.6: Post-failure stress-strain curve. (adapted from ABAQUS, 2007)

The amount of crack opening affects the shear behaviour (in Mode II model). Thus, a shear retention model, as illustrated in Figure 3.7 is defined. Brittle shear is defined to allow shear stiffness in the model.

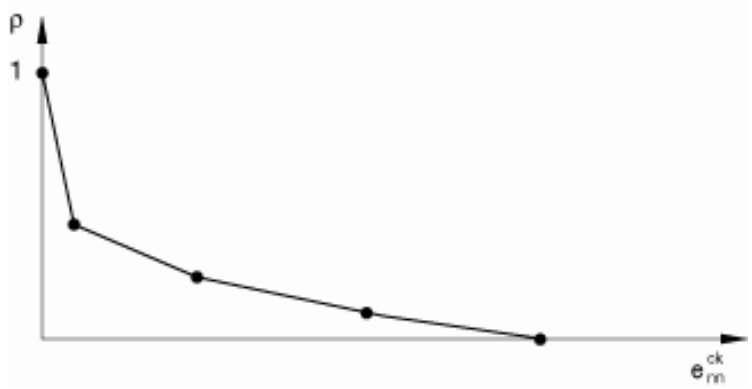


Figure 3.7: Piece-wise linear form of the shear retention model (adapted from ABAQUS, 2007)

3.3.1.3 Damaged plasticity concrete model

This is a continuum plasticity-based damaged model. It applies an isotropic damaged elasticity concept in conjunction with isotropic tensile and compressive plasticity to simulate the inelastic behaviour of concrete. For the calibration work, the post failure behaviour in this model was modelled using tension stiffening by defining strain-softening properties for cracked concrete and the effect of reinforcement (steel fibres and steel reinforcement). Figure 3.8 illustrates the function of cracking strain ($\tilde{\varepsilon}_t^{ck}$), whereas Figure 3.9 defines the inelastic (crushing) strain ($\tilde{\varepsilon}_t^{in}$) adopted in ABAQUS.

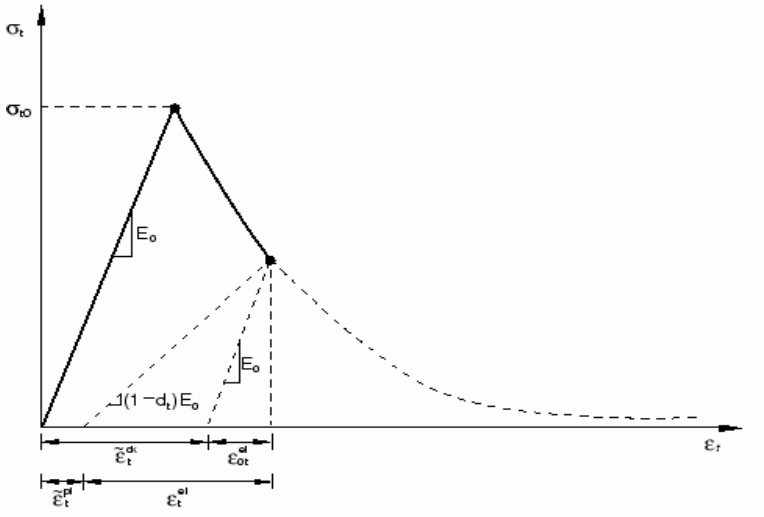


Figure 3.8: Illustration of the definition of the cracking strain ($\tilde{\varepsilon}_t^{ck}$) used for the definition of tension stiffening data (adapted from ABAQUS, 2007)

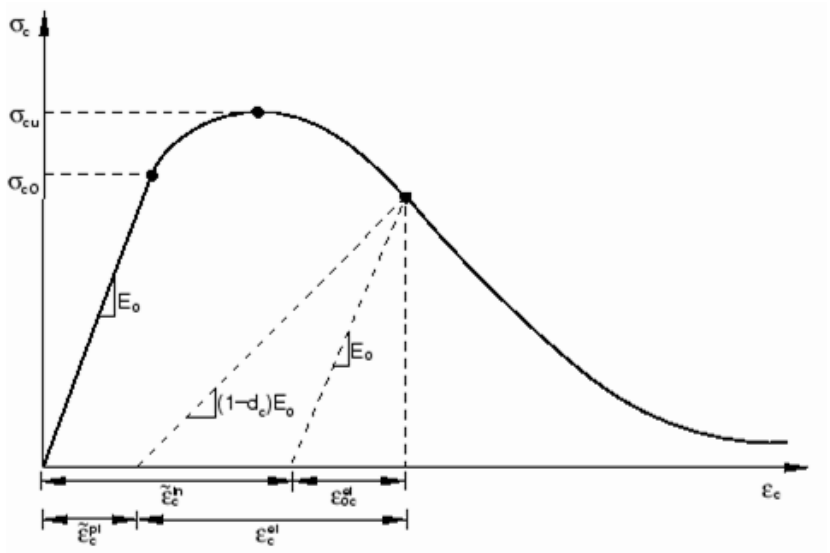


Figure 3.9: Definition of the compressive inelastic (or crushing) strain ($\tilde{\varepsilon}_t^{in}$) used for the definition of compression hardening data (adapted from ABAQUS, 2007)

The data for the strain-softening is defined using the SFRC material models proposed in the Section 3.2 and is applied as cracking strain (which is the total strain minus the elastic strain corresponding to the undamaged material, i.e. $\tilde{\varepsilon}_t^{ck} = \varepsilon_t - \varepsilon_{0l}^{el}$). The cracking strain values will automatically be converted to plastic strain values. The model requires classification as a tabular function in tensile damage and/or crushing damage. If damage is not specified, the model behaves as a plastic model.

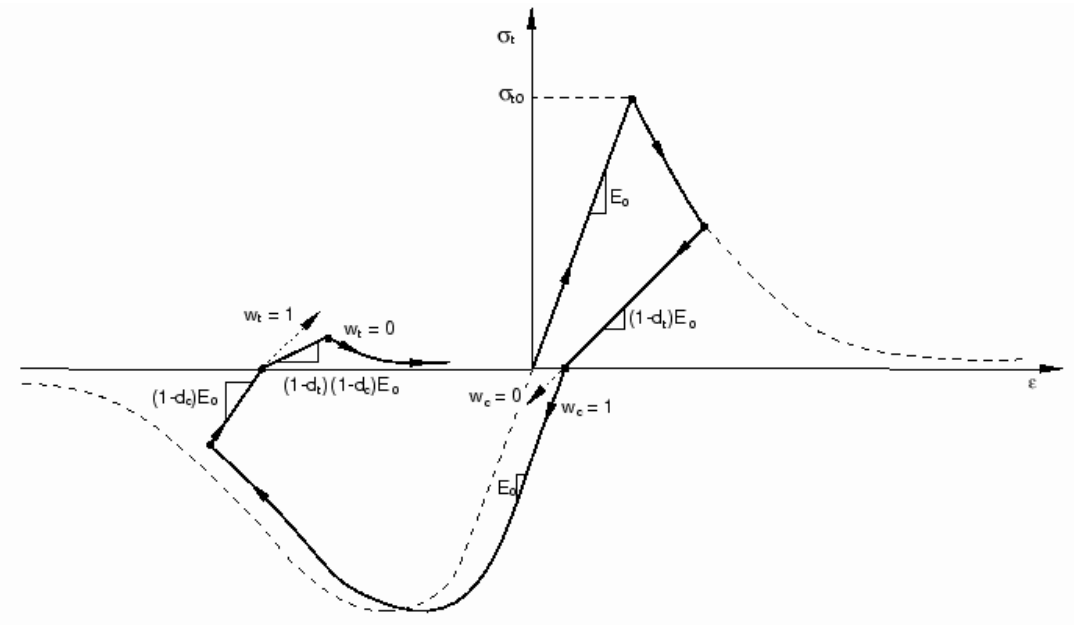


Figure 3.10: Uni-axial load cycle (tension-compression-tension) assuming default values for the stiffness recovery factors: $w_t = 0$ and $w_c = 1$ (adapted from ABAQUS, 2007)

In addition, ABAQUS allows users to define stiffness recovery via the stiffness recovery factor w_t and w_c. ABAQUS (2007) specified that most of the experimental observation in quasi-brittle material, including concrete exhibits that the compressive stiffness is recovered upon crack closure as the load changes from tension to compression, whilst tensile stiffness is not recovered as the load changes, once crushing micro-cracks developed. Figure 3.10 illustrated this load cycle behaviour with the default used by ABAQUS of $w_t = 0$ and $w_c = 1$.

3.3.1.4 Concrete model selection

Based on the calibration work performed (see Appendix A), the brittle cracking model was found to be the most appropriate for carrying out the parametric studies. This model was selected due to the reasons explained below.

- The smeared cracking model was not applicable to the present work as it could only be employed for analysing cases in static monotonic loading at low confining pressures only (the present study includes investigations of SFRC behaviour under reversed-cyclic loading).
- The brittle cracking model is a reasonably-accurate one as the crack initiation and propagation in beams, columns and beam-columns joints is strongly influenced by the tensile characteristics of the concrete. Furthermore, as the present NLFEA is carried out using 3D modelling, at least one principal stress is required to be tensile to trigger cracking (this is the salient feature of concrete behaviour which is predominantly brittle) and this is well captured by the brittle cracking model. So although the model assumes elastic behaviour in compression for efficiency purposes, this does not seem to affect accuracy as the predictions are in good agreement with experimental data (refer to Appendix A).
- Furthermore, the brittle cracking model focuses on the important fundamental parameters affecting concrete behaviour (i.e. brittleness and cracking). This basic yet profound and focused approach allows one to develop a more fundamental understanding of aspects affecting the structural response of SFRC.
- Damage plasticity has the advantage of allowing for stiffness recovery effects for modelling cyclic loading. However, when this model was used, unsatisfactory results were obtained during calibration work presented in

Appendix A. Moreover, there are too many parameters involved in this model, which might become disadvantageous as each set of parameters needs to be calibrated carefully for the given problem (so simply using the defaults values could lead to inaccurate predictions). This requires more extensive and detailed experimental data (compared to the other models which focus on less but more fundamental parameters).

- The sheer number of parameters in the damage plasticity model makes the solution sensitive to any change in these numerous factors. This leads to greater uncertainty with regards to which solution to be adopted. More importantly, it makes it difficult to distinguish between the effects of the many parameters in order to arrive at a fundamental understanding of structural behaviour.

Therefore, the brittle cracking model was adopted for the present research work in order to examine the underlying structural response of SFRC. Once this aim is achieved and the present study is concluded, the work could be extended in future to include more parameters leading to a more refined understanding.

3.3.2 Steel model

In the present study, the steel properties for longitudinal bar and shear reinforcement were modelled using a standard metal plasticity model. The stress-strain relation adopted in ABAQUS is illustrated in the figure below. The model employs isotropic hardening in which the yield stress increases (or decreases) in all stress directions as plastic straining occurs (ABAQUS, 2007).

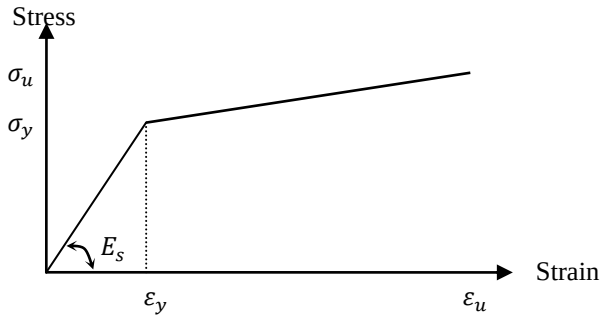


Figure 3.11: Stress-strain relations for steel material

In the present work, the steel properties of longitudinal bar and transverse shear reinforcement were modelled as truss elements (referred to as “stringers” in ABAQUS

element library), which were assigned on the edges of the 3D solid elements used to model concrete. An example of steel stringers created extruded along a concrete beam is given in Figure 3.12. In the mesh module, the stringer was assigned as a 2-node linear 3-D truss (T3D2). The solid element assigned to the concrete is an 8-noded linear brick with reduced integration (C3D8R). The concrete and bar elements share the same nodes.

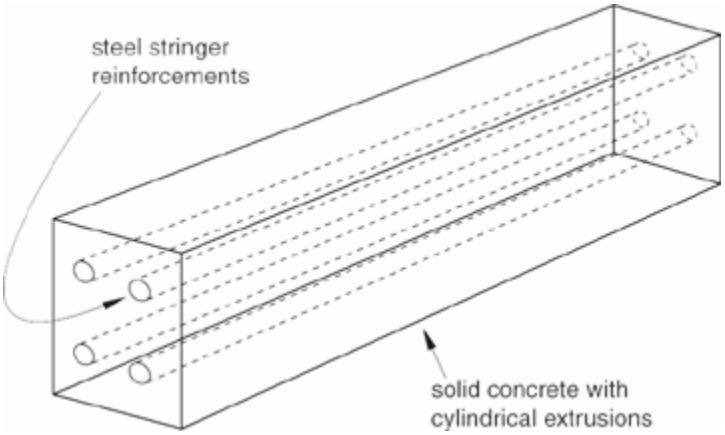


Figure 3.12: RC beam modelled using stringer reinforcement (adapted from ABAQUS, 2007)

3.3.3 Analysis procedure

3.3.3.1 Analysis modules

There are two types of analysis modules offered by ABAQUS, namely standard and explicit. ABAQUS/Standard is applicable to solving linear and non-linear problems, which include static and dynamic analysis. ABAQUS/Explicit is practical at solving dynamic and quasi-static problems, as it requires fewer system resources than the implicit procedure. In the present work, for calibration and validation purposes (see Appendix A), both analysis modules were used.

Abaqus/Explicit uses two routines for solving a structural problem: Riks procedure and Explicit dynamic. In Riks method, loading is assumed proportional, where all load magnitudes vary with a single scalar parameter and the response is reasonably smooth without sudden divergences. Riks method is based on the Newton method and normally has a finite radius of convergence. ABAQUS uses modified Riks method, in which the increment size is limited by moving a given distance along the tangent line to the current solution point. The explicit, dynamic procedure is capable of executing a large

number of small time increments efficiently. In this method, each increment is rather inexpensive as an explicit central-difference time integration rule is utilised, where there is no solution for set of simultaneous equations. Small increments allow the solution to proceed without iteration and without requiring tangent stiffness matrices to be formed. In addition, it is crucial to define amplitude references for boundary conditions and loads applied during a dynamic response step.

For the present work, the Riks procedure was used in conjunction with the smeared cracking concrete model. Whereas for the brittle cracking and damage plasticity concrete models, the Explicit dynamic procedure was adopted. Analysis was carried out by ensuring a quasi-static loading condition, in which the dynamic effect calculated by the energy ratio (ratio of kinetic energy to the strain energy) was less than 0.5%.

Based on the results observed in Appendix A, ABAQUS/Explicit module in conjunction with Explicit dynamic analysis procedure and brittle cracking concrete model and steel model discussed earlier were applied for the case and parametric studies.

3.3.3.2 Model definition

The 2D model was adopted only for the analysis of SFRC at the material level. The remaining calibration work at structural level (with steel reinforcement), was carried out using 3D elements. Similarly, 3D models were adopted in the subsequent case and parametric studies. Example of a quarter of the beams model in 2D and 3D features is shown in Figure 3.13.

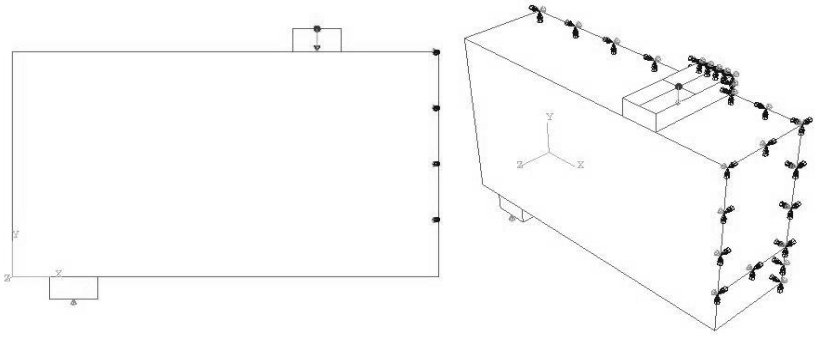


Figure 3.13: Example of boundary conditions for one quarter of a notched beam in (a) 2D and (b) 3D models

A mesh sensitivity analysis was carried out in order to select the best mesh size to be used. As stress-strain relations were used throughout the present work, the results

obtained from ABAQUS were likely to be mesh dependent (with a fine mesh results in a narrower crack width). Thus, the calibration work carried out against experimental data was really crucial in selecting the best mesh size that will accurately represent the true structural response. Figure 3.14 shows three different FE mesh sizes from a 2D model.

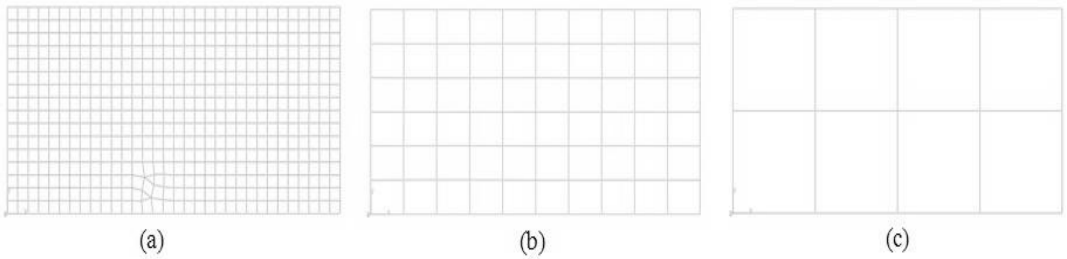


Figure 3.14: Example of FE mesh refinement sizes for 2D model for (a) fine, (b) medium and (c) coarse meshes

In order to avoid pre-mature failure due to localised stress concentrations and to mimic actual experimental arrangements, steel plates (similar size to those used in the experiments) were added in the beam modelled at the support and loading area. In addition, the *Poisson's ratio* value for concrete and steel for the present calibration work and subsequent analysis was taken as 0.15 and 0.3, respectively. The load was applied as displacement based method (DBM) to minimise convergence problems. In the present work, in order to allow for degradation in shear stiffness due to crack propagation the shear modulus was reduced in a linear fashion from full shear retention (i.e. ρ_{close} = 1.0, see Figure 3.4) at the cracking strain by 50% (i.e. to ρ_{close} = 0.5) at the ultimate tensile strain. Taking advantage of the symmetrical arrangement of the simply supported beams considered, only one quarter of the beam was modelled in ABAQUS for the calibration studies presented in Appendix A.

3.3.4 Failure criterion

ABAQUS uses the failure criteria associated with each model (smeared cracking, brittle cracking and damaged plasticity). As additional failure criterion, failure was considered to occur once a sudden high jump in the kinetic energy was identified. This high kinetic energy was due to the excessive and sudden movements of the structure indicating the

presence of extensive/wide cracks which impair structural integrity. This was then confirmed by examining both the deformed shape and cracking pattern of the structure.

3.4 Seismic design considerations

A crucial consideration in designing an earthquake resistant building is to ensure that the structure meets its "performance objectives". Possible performance objectives upon the event of an earthquake are that the structure remains operational, available for immediate occupancy, life safety and collapse prevention (Booth and Key, 2006). These broadly comply with the performance objectives of Part 1, Eurocode 8 (2004) where the structure should satisfy the requirement of *local* collapse prevention (to protect life under a rare seismic action) and *damage limitation* (to reduce the property loss). A reasonable combination of strength and ductility detailing is required in order to achieve the *collapse prevention* performance level (Fardis et al., 2005). Whereas, by restraining the overall lateral displacement or deformation of a system (i.e. providing adequate stiffness) to a level that is acceptable for the structures integrity, the *damage limitation* performance level is attained (Fardis et a.l, 2005).

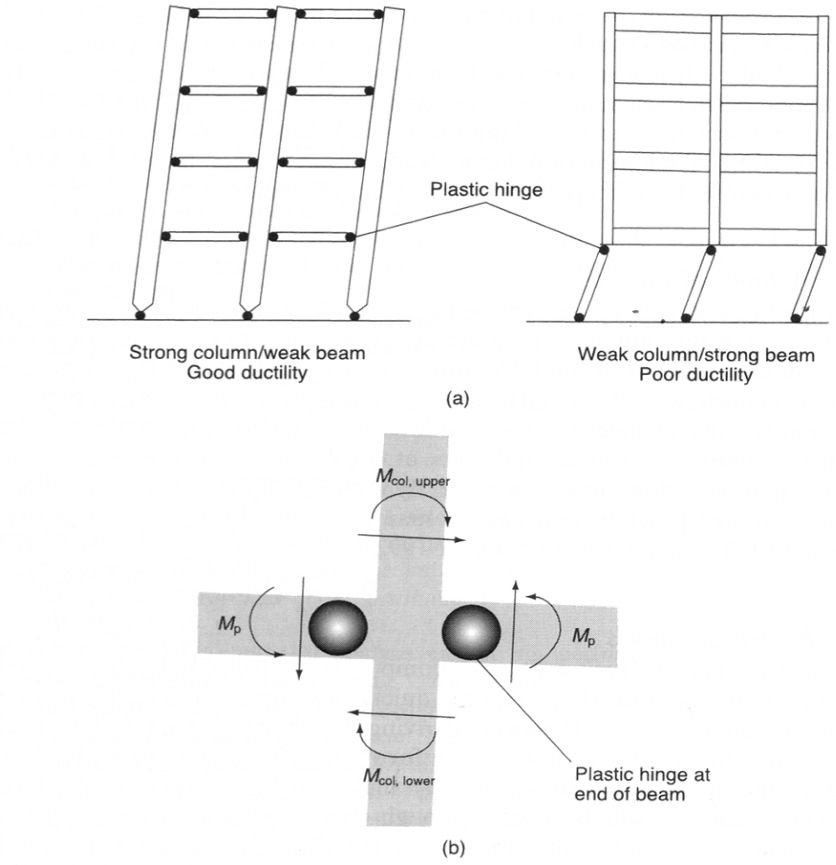


Figure 3.15: Capacity design for unbraced frames: (a) overall view and (b) forces at a beam-column joint, axial forces not shown (adapted from Booth and Key, 2006)

In order to achieve a satisfactory seismic performance, it is important that seismic design for the building follows verification as specified in design codes. For instance, the global displacement ductility demand should be distributed as uniformly as possible throughout the building to prevent a soft-storey mechanism or weak columns/strong beams (see Figure 3.15(a)). In capacity design, columns are designed to be well protected against yielding (except at their base), whereas the middles of the beams are not expected to yield (Booth and Key, 2006). The main plasticity is designed to develop at the ends of the beams, where plastic hinges form as shown in Figure 3.15(b).

Designing the beam and column to the satisfactory seismic detailing inevitably results in steel congestion, especially in the joint region. This leads to construction difficulties resulting in high costs. Thus, researchers are looking into other potential options to reduce the steel congestion, while retaining structural integrity (i.e. strength and ductility). Previous research work (i.e. Henager, 1977; Gefken and Ramey, 1989; Bayasi and Gebman, 2002) attempted to reduce the steel congestion in seismic joint regions by utilising steel fibres into the concrete mix, while increasing the hoop spacing inside the joint region. The experimental results showed that there was significant improvement to the damage tolerance and energy absorption capacity, apart from reducing the steel reinforcement congestion. It was calculated that steel fibres demonstrates its potential as an alternative to shear reinforcement particularly, if these fibres are combined with stirrups, even at a lesser amount as compared to those recommended in design codes for conventional reinforcement.

However, previous work only considered a limited amount of fibre volume fraction (e.g. Craig et al., 1984; Jiuru et al., 1992; Filiatrault et al., 1995) and reduction in conventional shear reinforcement (e.g. Filiatrault et al., 1994; Lee, 2007). The work was predominantly experimental with hardly any numerical investigations carried out. Therefore, the present research work was planned to examine the behaviour of steel fibres in RC structures and their potential to substitute conventional transverse shear reinforcement. Three main case studies considered are analysed under monotonic and reversed-cyclic loading (the latter to mimic seismic action). The present work was carried out covering different structural forms such as simply supported beams, statically-indeterminate columns and both internal and external beam-column joints. The scope of the present study is discussed next.

3.5 Scope of case/parametric studies

The present work is focused on the finite-element modelling of SFRC structures under monotonic and reversed-cyclic loading (the latter to mimic seismic action). Three case studies have been fully investigated covering; simply supported beams (Case Study 1), two-span continuous columns (Case Study 2) and interior and exterior beam-column joints (Case Study 3). For each case study, a parametric study was carried out considering two parameters: the amount of conventional transverse shear reinforcement and the fibre volume fraction. The amount of shear reinforcement was reduced by increasing the spacing between the stirrups. The stirrup spacing increase (SI) values considered were 0%, 50% and 100% (200% and specimens without stirrups were also considered in some case studies). The fibre volume fractions (V_f) considered were 0%, 1%, 1.5%, 2% and 2.5%.

For the parametric studies, only the SFRC material model proposed by Lok and Xiao (1999) was considered (which was the conclusion of the calibration investigations that preceded the parametric studies). The analysis was carried out adopting the brittle cracking concrete model in ABAQUS, as reasonable comparison were obtained with experimental results as discussed in Appendix A (and reasons explained in Section 3.3).

The aim of the case studies and associated parametric investigations was to (i) determine the effect of the addition of steel fibres on both the load carrying capacity and ductility and (ii) determine the potential reduction in shear reinforcement. This is practically desired as it can lead to a reduction in conventional reinforcement congestion in critical regions, particularly the one associated with seismic detailing. Both the overall and local structural responses at critical sections were examined. The work investigated key structural behaviour and design parameters such as load-deflection curves, strength (i.e. shear force and bending moment capacities), stiffness (which is relevant to storey drift), ductility (i.e. ratio of ultimate displacement to the displacement at yield), plastic hinges formation and cracking patterns. Comparisons were then made between the results obtained from FE analyses and those recommended by the design codes. The comparison was made by employing the method recommended by Eurocode 2 (2004) for RC structures without fibres, whilst for SFRC structures the recommendations made by the Concrete Society TR-63 (2007) were adopted. Conclusions were made on potential of steel fibres to satisfy code

requirements of strength and ductility. The main case studies that were investigated are discussed next.

3.5.1 Case study 1: Simply supported beams under monotonic and cyclic loading

Case Study 1 focused on the behaviour of SFRC simply supported beams (i.e. statically determinate structures). Two types of beams and loading arrangements were considered. A 3-point test was considered for Case Study 1(a) (Figure 3.16(a)), whilst a 4-point test (Figure 3.16(b)) was analysed in Case Study 1(b).

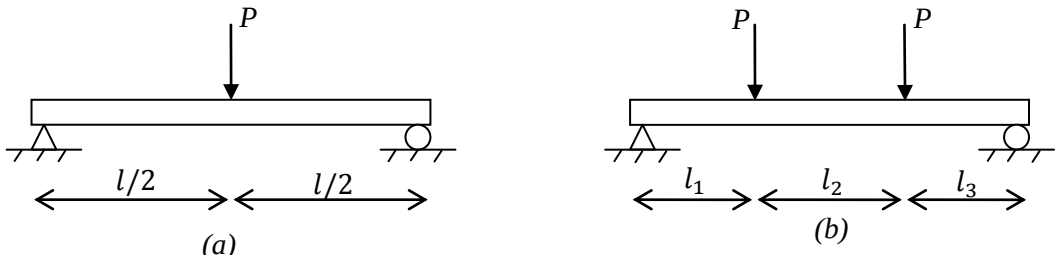


Figure 3.16: Simply supported beams case

Case Study 1(a) was based on the Campione and Mangiavillano (2008) experimental work on simply supported SFRC beams with amount of fibres content in volume, $V_f = 1\%$. Their results have been used to calibrate and validate the FE model used in this parametric analysis. The beams were tested under static monotonic and reversed-cyclic loading. The beams were originally designed to fail in bending. In this particular case, additional reduction of the conventional shear reinforcement was carried out by increasing the spacing between the stirrups by 200% to study the behaviour in such a severe case. The spacing increases (SI) of conventional transverse stirrups considered are summarised in Table 3.1. It should be recalled that the fibre volume fractions (V_f) considered in all case studies were 0%, 1%, 1.5%, 2% and 2.5%.

Stirrups spacing (mm)	Spacing increase (mm)	SI (%)
50	0	0
75	25	50
100	50	100
150	100	200

Table 3.1: Stirrups spacing values considered for Case study 1(a)

Stirrups spacing (mm)	Spacing increase (mm)	SI (%)
135	0	0
200	65	50
270	135	100
-	-	No Stirrups

Table 3.2: Stirrups spacing values considered for Case study 1(b)

Case study 1(b) was based on the specimens tested by Campione et al (2006). The SFRC beams were designed with reduced shear reinforcement in order to induce a shear mode of failure (beams without transverse stirrups were thus studied as well). The beams were tested under monotonic loading. The SI values considered are summarised in Table 3.2. The results for Case Study 1 are discussed in Chapter 4 of this thesis.

3.5.2 Case study 2: Two-span continuous columns under monotonic and cyclic loading

The use of two-span elements was chosen because experimental data on the behaviour of statically-indeterminate beams is limited in comparison to that available for simply supported structural elements. Furthermore, the study of statically-indeterminate structural elements provides a more severe case for studying the structural behaviour of SFRC, since it allows the examination of key parameters such plastic hinge formation, ductility characteristics, redistribution of internal forces and the structural modelling of points of contra-flexure, which cannot be investigated by only considering statically determinate structures. Case Study 2 was based on the specimens tested by Kotsovos et al (2007) in their experimental work on two-span continuous columns under combined axial forces (representing gravity loads) and monotonic or reversed-cyclic loading (representing seismic forces). The general layout of the column is shown in Figure 3.17, where a lateral (P) monotonic or reversed-cyclic load was applied at the middle of one of the column spans in addition to the horizontal axial load (N). Comparisons with code predictions were carried out.

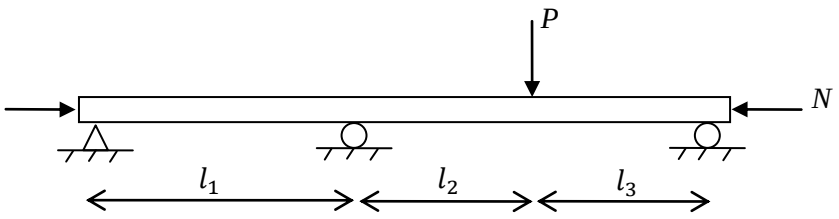


Figure 3.17: Two-span continuous column case

Stirrups spacing (mm)	Spacing increase (mm)	SI (%)
40 & 140	0	0
60 & 210	20 & 70	50
80 & 280	40 & 140	100

Table 3.3: Stirrups spacing values considered for Case study 2

The SI values considered are summarised in Table 3.3. The results of calibration work and parametric studies for this case study are presented in Chapter 5 of this thesis.

3.5.3 Case study 3: Beam-column joints under cyclic loading

In Case study 3, two types of beam-column joints were considered. Case study 3(a) was based on the exterior joint tested by Bayasi and Gebman (2002) under reversed-cyclic loading as shown in Figure 3.18(a). In this joint, the reversed-cyclic loading was applied at the free end of the beam. Parametric studies were carried out with the SI values summarised in Table 3.4.

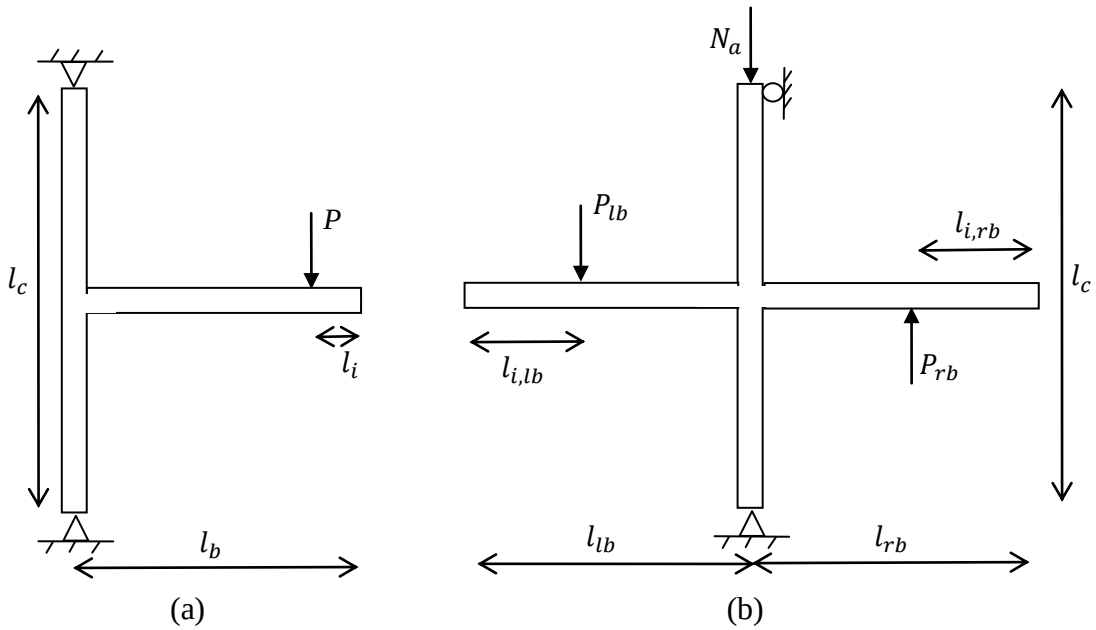


Figure 3.18: Beam-column joint case showing (a) exterior and (b) interior joints

The interior beam-column joint tested by Filiatrault et al. (1995) was considered as the basis for Case Study 3(b) as depicted in Figure 3.18(b). For this particular case, an additional parametric study was considered in which the reduction of the amount of shear reinforcement has been carried out by reducing the hoops area from a double-stirrups to arrangement (commonly used in seismic detailing of columns) to a single-

stirrup one. Table 3.5 shows the stirrups spacing properties for Case Study 3(b). Axial force was applied on the column first (to mimic gravity loads) and was kept constant during the seismic excitation on the beams. Chapter 6 presents the calibration and parametric analysis results for the SFRC beam-column joints.

Stirrups spacing (mm)	Spacing increase (mm)	SI (%)
102	0	0
152	50	50
203	101	100

Table 3.4: Stirrups spacing values considered for Case study 3(a)

Stirrups spacing in the column (mm)	Spacing increase (mm)	Stirrups spacing in the beam (mm)	Spacing increase (mm)	SI (%)
85	0	100	0	Single stirrups
127.5	42.5	150	50	50
170	85	200	100	100

Table 3.5: Stirrups spacing values considered for Case study 3(b)

3.6 Summary

This chapter presents a brief review of the NLFEM, ABAQUS software, initial calibration work (see Appendix A) in order to select appropriate models for subsequent case studies and associated parametric investigations. Based on the findings of the calibration work, it was concluded that the SFRC constitutive model proposed by Lok and Xiao (1999) was to be adopted, together with the brittle cracking concrete model and a steel elastic-plastic model. The present work was carried out using quasi-static analyses in ABAQUS/Explicit. The scope of case and parametric studies was also summarised in the present chapter.

CHAPTER 4

CASE STUDY 1: SIMPLY SUPPORTED BEAMS UNDER MONOTONIC AND REVERSED-CYCLIC LOADING

4.1 Introduction

This chapter presents the results of two case studies on SFRC simply supported beams examined by means of non-linear FE analysis using ABAQUS (refer to Chapter 3 for a description of the models used). The first part of the investigation, Case Study 1(a), is focused on beams under both monotonic and reversed-cyclic loads. Initially, the FE models were calibrated using experimental results by Campione and Mangiavillano (2008). The latter were designed with full shear reinforcement. The second part of the work, Case Study 1(b), was based on SFRC beams initially calibrated based on the experimental work of Campione et al. (2006) under monotonic loading (the beams were designed with reduced shear reinforcement in order to incorporate a shear mode of failure). The experimental work examined the effect of adding fibres (to beams with and without transverse stirrups), especially to substitute the loss in conventional shear reinforcement. However, the fibre content and extent of shear reinforcement reduction considered were limited. The present research work, on the other hand, covers the full practical range of fibre contents and amount of stirrups in the beams. The experimental data was useful in providing a benchmark to validate the FE results against and once this calibration was concluded, full parametric studies were subsequently carried out.

4.2 Case Study 1(a): Calibration with Campione and Mangiavillano (2008) tests

A summary of the experimental work and results of the calibration work for Case Study 1(a) is presented. Campione and Mangiavillano (2008) investigated the flexural behaviour of conventionally reinforced and fibrous concrete beams under monotonic and reversed-cyclic loading. Two SFRC beams and one conventionally reinforced concrete (RC) beam, i.e. without fibres, were selected for this case study. The dimensions of the beams, longitudinal steel and shear reinforcement are given in Figure 4.1. The fibres used in the tests had a 30 mm length, 0.5 mm thickness and a volume fraction V_f = 1%. One of the SFRC beams was tested under static monotonic loading and the other under reversed-cyclic loading. In addition, the RC beam without fibres was loaded under static monotonic loading. The yield and ultimate stress of steel were respectively 467 MPa and 546 MPa for the longitudinal reinforcement, 520 MPa and 620 MPa for the transverse reinforcement. The concrete compressive strength for the RC and the SFRC beams were 32.50 MPa and 36.19 MPa, respectively. All the beams had a 5 mm cover. For both static monotonic and reversed-cyclic loading cases, the beams were subjected to a point load which was applied at the mid-span section.

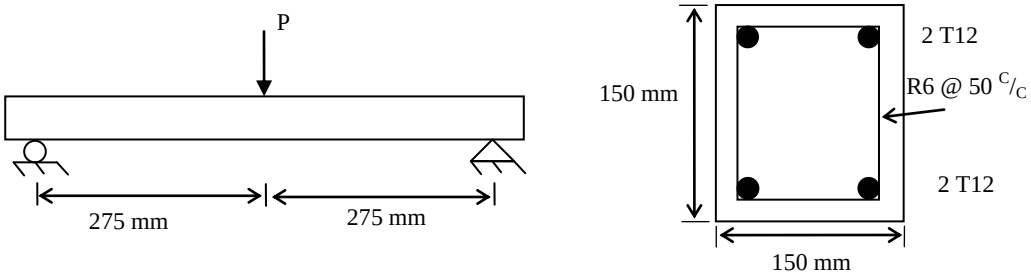


Figure 4.1: Dimensions and loading arrangement of the beams (adapted from Campione and Mangiavillano, 2008)

3D non-linear FE analyses were carried out using ABAQUS (with models described in Chapter 3) and the ensuing numerical results were calibrated using the respective experimental data. Taking advantage of the symmetrical arrangement of the specimens, only a quarter of the beam was modelled (i.e. 275 mm long, 150 mm high and 75 mm wide). A schematic of the beam model with a roller boundary condition along the symmetrical planes and the FE mesh used is depicted in Figure 4.2. To mimic experimental conditions and avoid premature localised failure, steel plates of 10 mm thickness and 20 mm width extending across the breadth of the beam were added at the support and loading points.

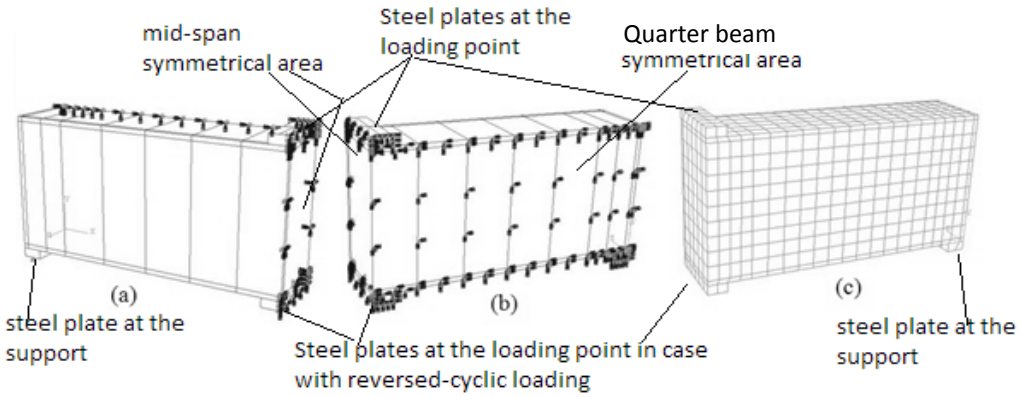


Figure 4.2: Quarter of the beam modelled in ABAQUS with defined boundary condition along symmetrical (a) front and (b) side views; and (c) FE mesh

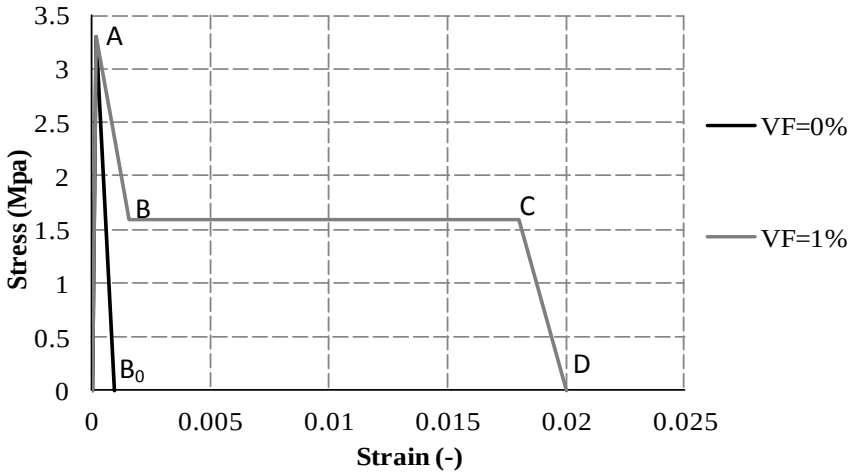


Figure 4.3: Tensile stress-strain diagram adopted for calibration work of Campione and Mangiavillano (2008) beams

Point	Strain (‰)	Stress (MPa)
Origin	0	0
Peak tensile stress (A)	0.195	3.31
Ultimate tensile strain (B_0)	1	0

Table 4.1 (a): Tensile stress-strain relationship for RC beams with no fibres

Point	Strain (‰)	Stress (MPa)
Origin	0	0
Peak tensile stress (A)	0.195	3.31
Beginning of plateau (B)	1.590	1.59
End of plateau (C)	18	1.59
Ultimate tensile strain (D)	20	0

Table 4.1(b): Tensile stress-strain relationship for SFRC beams with V_f = 1%

Figure 4.3 shows the tensile stress-strain relations for concrete applied into the FE model, and the key values are summarised in Table 4.1. The loading was applied using a displacement-based method. The input data for both loading types is shown in Figure 4.4. Based on the initial sensitivity analysis, a mesh comparison elements of 15 mm width was adopted as it yielded the most satisfactory agreement with experimental data.

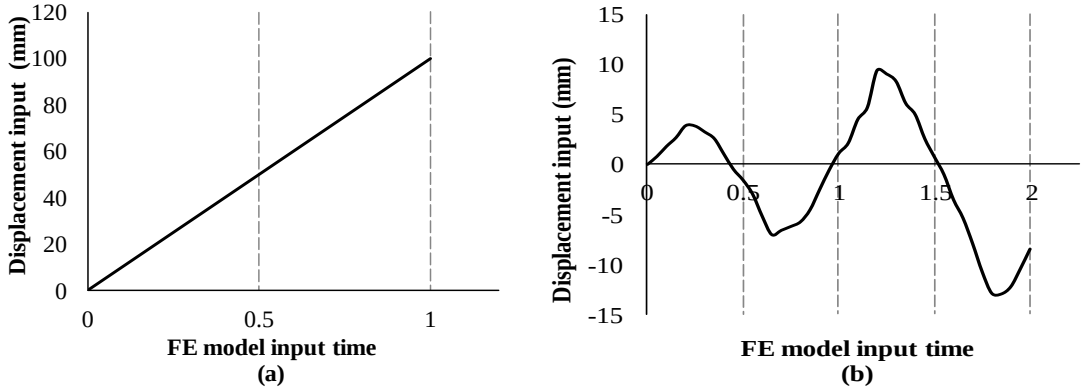


Figure 4.4: Loading histories input for (a) monotonic and (b) reversed-cyclic loading

4.2.1 Results for beams under monotonic loading (Case Study 1(a)-M)

Figure 4.5 shows a comparison between the load-deflection curves based on experimental and numerical results. Good agreement between the two sets of data can be observed in terms of strength and ductility with the FE results being slightly stiffer than the experimental data (albeit the results being the same for the part before yield). The load at yield (P_y), maximum or peak load (P_{max}) and ultimate load at failure (P_u) and their respective deflections δ_y, δ_{Pmax} and δ_u are given in Table 4.2. The ductility ratio (μ) defined as $\mu = \delta_u/\delta_y$ is also included in the table.

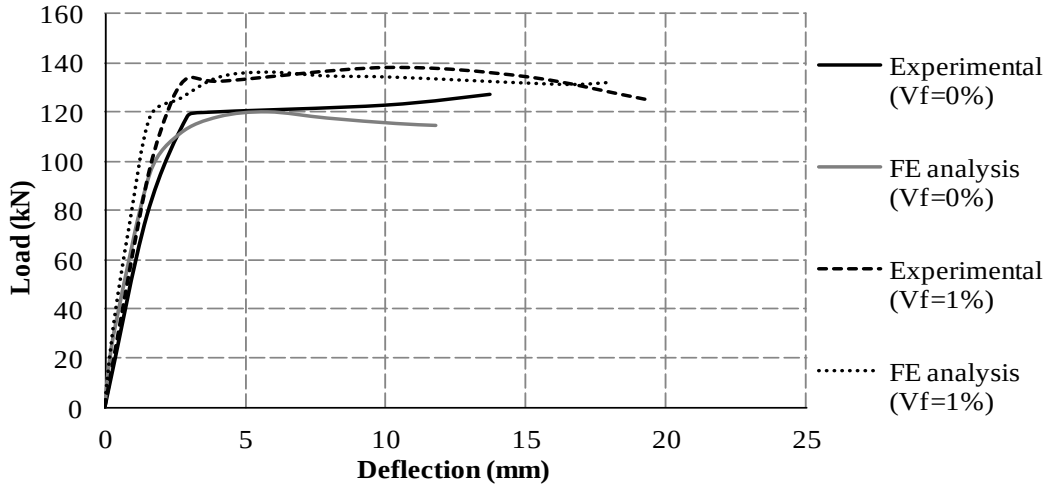


Figure 4.5: Load-deflection curves for calibration work in Case Study 1(a)-M

Beam	P_y (kN)	δ_y (mm)	P_u (kN)	δ_u (mm)	P_{max} (kN)	δ_{Pmax} (mm)	$\mu = \frac{\delta_u}{\delta_y}$
Experimental (Vf=0%)	100.0	2.15	127.4	13.74	127.4	13.74	6.39
FE analysis (Vf=0%)	95.41	1.6	115.0	11.77	120.48	5.80	7.37
Experimental (Vf=1%)	122.5	2.15	125.1	19.3	138.8	10	8.98
FE analysis (Vf=1%)	117.95	1.6	132.2	18.1	136.36	5.81	11.31

Table 4.2: Results summary of load-deflection curves for calibration work in Case Study 1(a)-M

The failure point of the FE analysis is determined by a number of factors, such as the deformed shape and the kinetic energy of the beam, or an abrupt termination of the analysis due to divergence. For the calibration work, the failure point was determined based on the sudden high jump in the kinetic energy, depicted in Figure 4.6, which indicates that extensive/wide cracks occurred impairing the structural integrity.

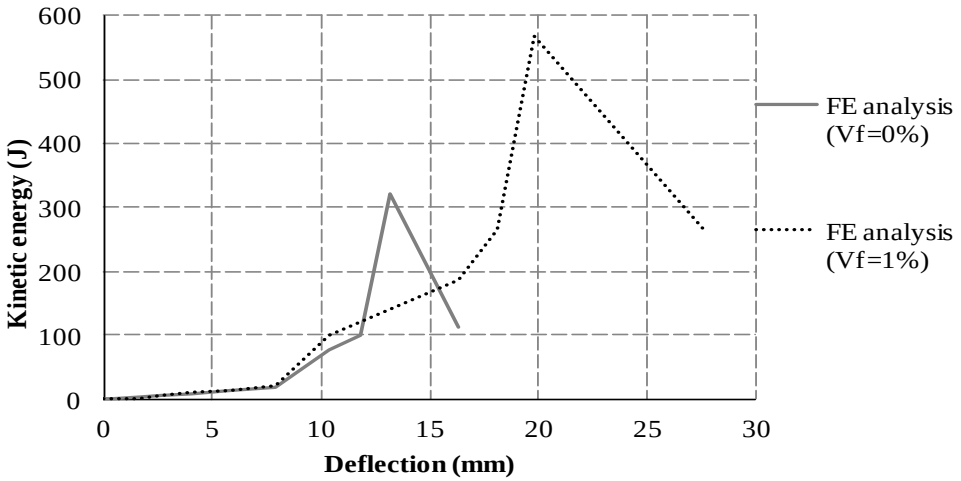


Figure 4.6: Kinetic energy plots to determine failure for beams analysed under monotonic loading in Case Study 1(a)-M

4.2.2 Results for beam under reversed-cyclic loading (Case Study 1(a)-C)

The FE results for SFRC beams ($V_f = 1\%$) analysed under reversed-cyclic loading are presented in Figure 4.7 with the key values summarised in Table 4.3. The data show reasonable agreement with experimental results. The numerical results show a failure point slightly earlier than the one found experimentally. However, the difference is small and the FE results are on the safe side (it could also be argued that the additional small part in the experimental data has started after the onset of failure and thus should

be discounted). The FE failure point was defined based on an examination of the kinetic energy levels depicted in Figure 4.8 (sudden jump was taken to denote failure).

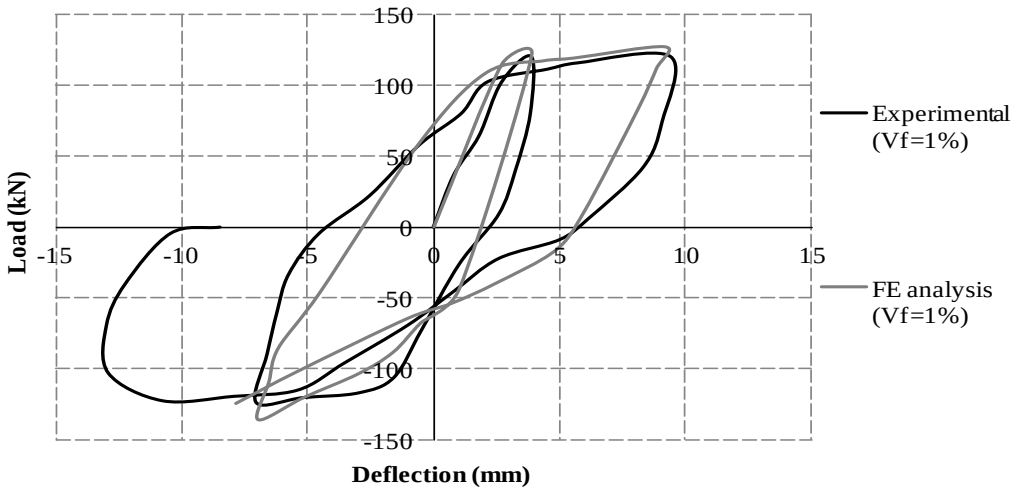


Figure 4.7: Load-deflection hysteresis loops for calibration work in Case Study 1(a)-C

Column	N_c (kN)	P_y (kN)	δ_y (mm)	P_u (kN)	δ_u (mm)	P_{max} (kN)	δ_{Pmax} (mm)	$\mu = \frac{\delta_u}{\delta_y}$
Experimental	2.0	101.8	2.7	120.0	9.41	120.0	9.41	3.49
FE analysis	1.67	114.6	2.7	126.71	9.17	126.71	9.17	3.40

Table 4.3: Results summary of load-deflection curves for calibration work in Case Study 1(a)-C

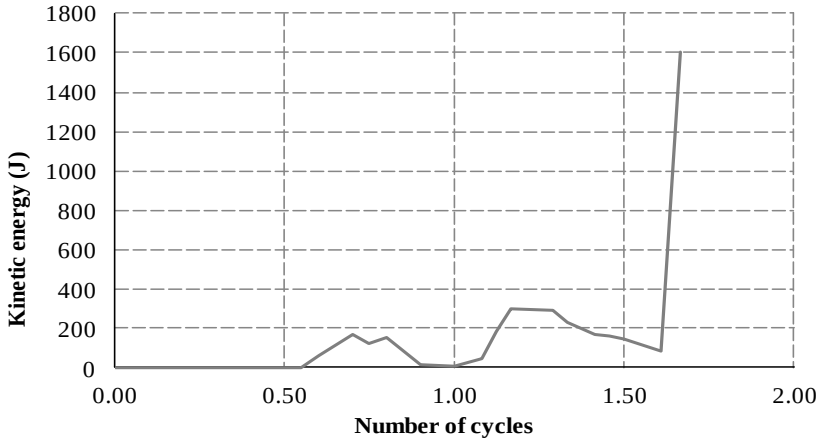


Figure 4.8: Kinetic energy plots to determine failure for beams analysed under monotonic loading in Case Study 1(a)-C

4.3 Case Study 1(a)-M: Parametric study on simply supported beams under monotonic loading

Parametric studies were carried out on simply supported beams under monotonic loading, i.e. Case Study 1(a)-M, and subsequently under cyclic loading, i.e. Case Study 1(a)-C. The present section presents the results for Case Study 1(a)-M.

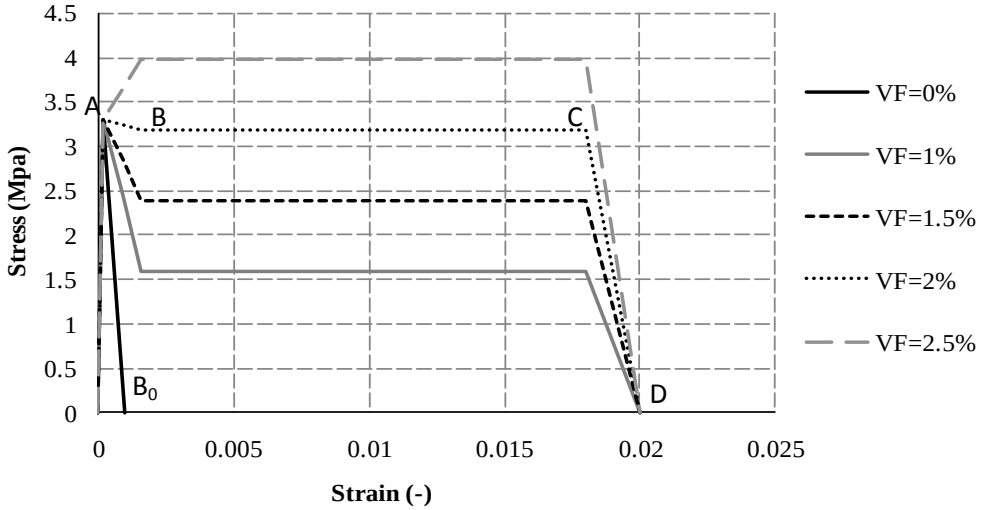


Figure 4.9: Tensile stress-strain relations for Case Study 1(a) for different fibre volume fractions (V_f)

Point	Strain (‰)	Stress, V_f =0.0% (MPa)
Origin	0	0
Peak tensile stress (A)	0.195	3.31
Ultimate tensile strain (B_0)	1.0	0

Table 4.4(a): Tensile stress-strain properties for plain concrete for Case Study 1(a)

Point	Strain (‰)	Stress, V_f=1.0% (MPa)	Stress, V_f=1.5% (MPa)	Stress, V_f=2.0% (MPa)	Stress, V_f=2.5% (MPa)
Origin	0	0	0	0	0
Peak tensile stress (A)	0.195	3.31	3.31	3.31	3.31
Beginning of plateau (B)	1.59	1.59	2.39	3.18	3.98
End of plateau (C)	18	1.59	2.39	3.18	3.98
Ultimate tensile strain (D)	20	0	0	0	0

Table 4.4(b): Tensile stress-strain properties for SFRC for Case Study 1(a)

The spacing between the transverse stirrups was increased from the original values used in the experimental and calibration work discussed earlier and fibres were added as a replacement to the loss in conventional shear reinforcement. The spacing increase (SI) values considered were $SI = 0\%,\ 50\%,\ 100\%$ and 200% (so for instance if the original spacing is 50 mm, $SI = 50\%$ will represent an increase of 25 mm to a new spacing of 75 mm). Five amounts of steel fibres (i.e. volume fractions $V_f = 0\%,\ 1\%,\ 1.5\%,\ 2\%$ and 2.5%) were added and analysed to examine their potential to compensate for the reduction in conventional shear reinforcement. The tensile stress-strain relations for SFRC adopted is given in Figure 4.9 and summarised in Table 4.4. The loading was applied gradually to failure using the displacement-based data defined in Figure 4.4a. The ensuing FE analysis results are discussed next.

4.3.1 Load-deflection curves

The load-deflection curves for Case Study 1(a)-M are presented in the Figures 4.10 to 4.13, for the beams with $SI = 0\%$ to $SI = 200\%$. Key structural response parameters were indentified and summarised in Tables 4.5 to 4.8, namely: the load at which the longitudinal reinforcement yields in tension (P_y) and its corresponding deflection (δ_y), the maximum load (P_{max}) representing the load-carrying capacity and related deflection (δ_{max}), the ultimate load (P_u) representing the residual strength (taken as the minimum of the load at failure or 85% of the maximum load to ensure its practical usefulness) and associated deflection (δ_u) and the ductility ratio (μ) defined as $\mu = \delta_u/\delta_y$. For comparison purposes, the beam with no increase in spacing between stirrups and without fibres (i.e. $SI = 0\%$ and $V_f = 0\%$) is taken as the control beam specimen (*CB*).

4.3.2 Strength

The load-deflection curves show that the beam without fibres has less stiffness and maximum (i.e. peak) load-carrying capacity than those with fibres (with the increase in fibre content resulting in a gradual increase in both stiffness and strength).

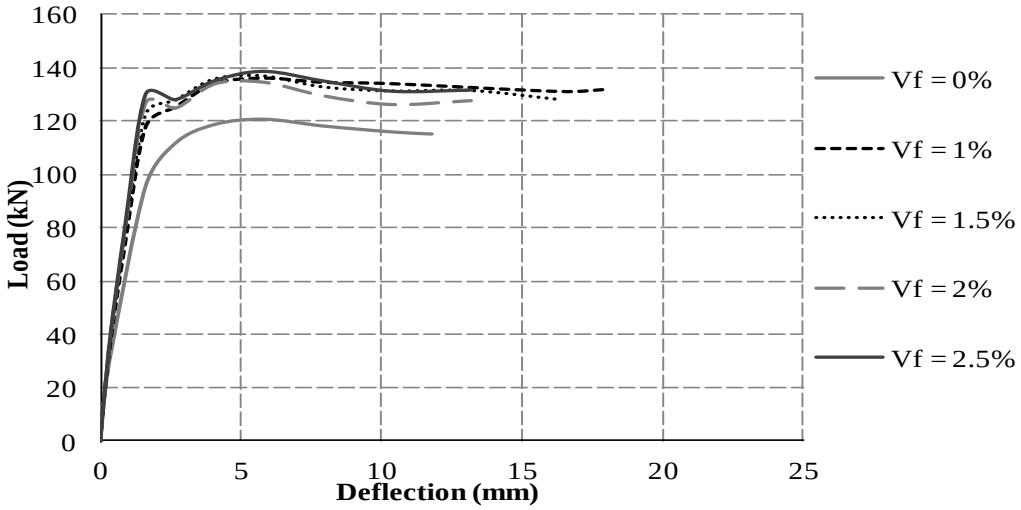


Figure 4.10: Load-deflection curves for Case Study 1(a)-M beams with $SI = 0\%$

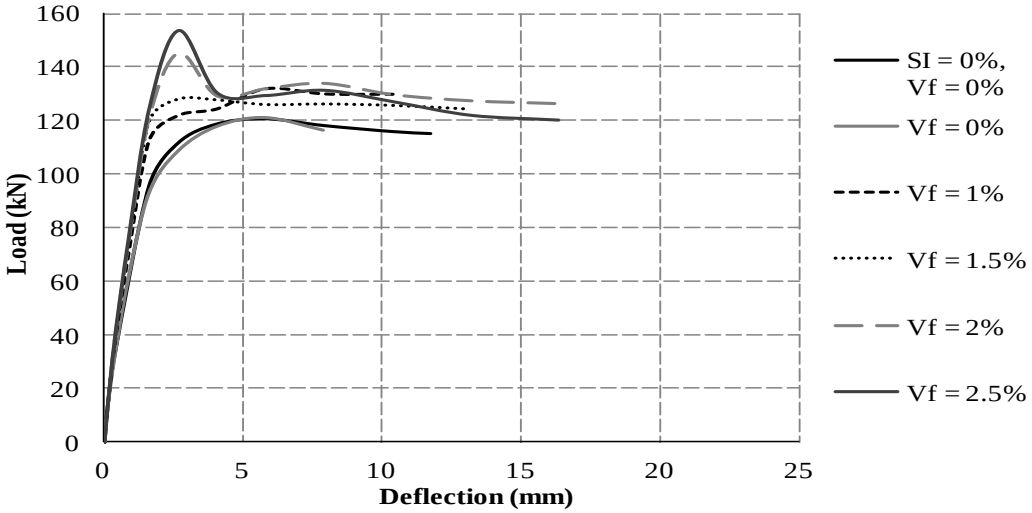


Figure 4.11: Load-deflection curves for Case Study 1(a)-M beams with $SI = 50\%$

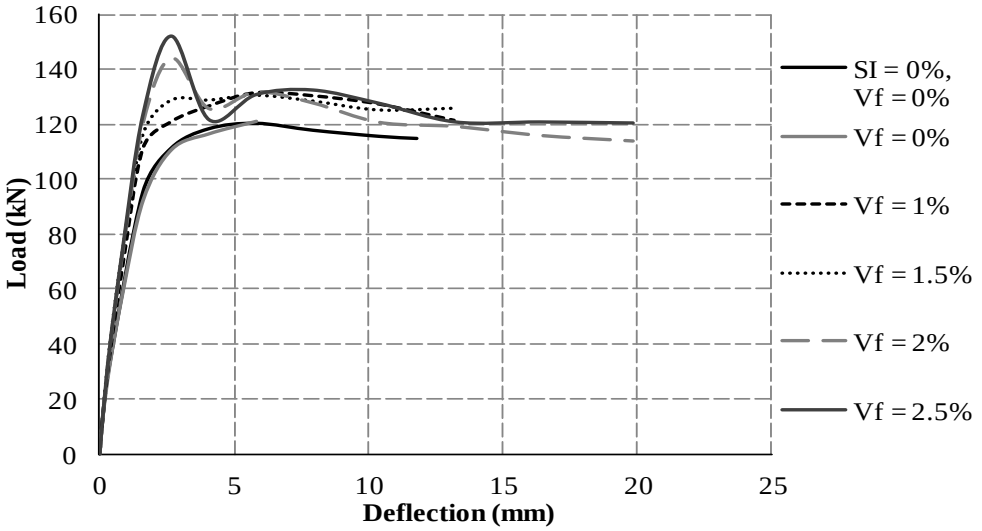


Figure 4.12: Load-deflection curves for Case Study 1(a)-M beams with $SI = 100\%$

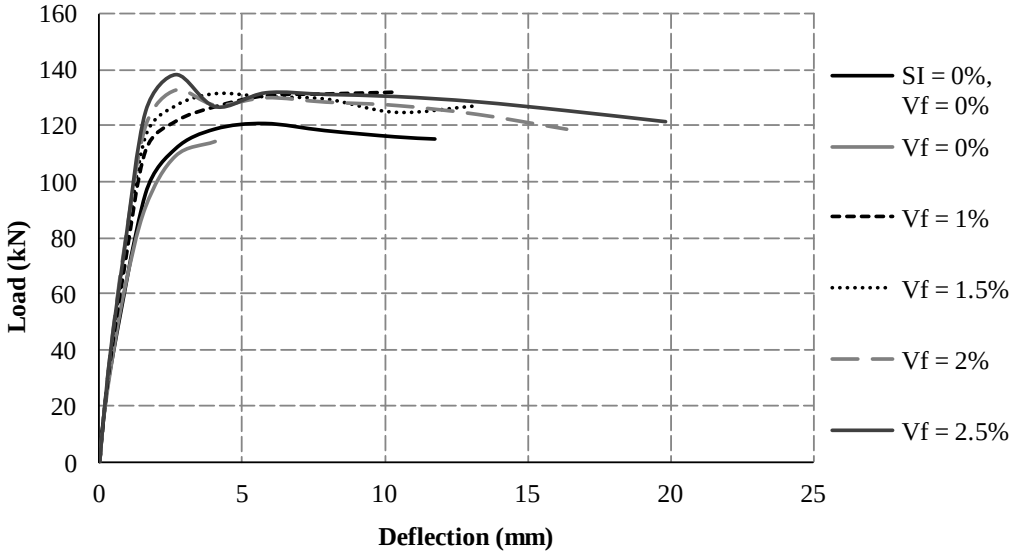


Figure 4.13: Load-deflection curves for Case Study 1(a)-M beams with $SI = 200\%$

V_f (%)	P_y (kN)	δ_y (mm)	P_u (kN)	δ_u (mm)	P_{max} (kN)	δ_{Pmax} (mm)	$\mu = \frac{\delta_u}{\delta_y}$
0	95.41	1.6	115.0	11.77	120.48	5.80	7.37
1	117.95	1.6	132.2	18.1	129.88	3.37	11.31
1.5	122.57	1.6	128.20	16.34	131.94	3.37	10.21
2	126.70	1.6	127.62	13.19	134.52	5.81	8.24
2.5	130.07	1.6	131.69	13.19	138.72	5.81	8.24

Table 4.5: Summary of the significant values in the load-deflection curves for beams in Case Study 1(a)-M beam with $SI = 0\%$

V_f (%)	P_y (kN)	δ_y (mm)	P_u (kN)	δ_u (mm)	P_{max} (kN)	δ_{Pmax} (mm)	$\mu = \frac{\delta_u}{\delta_y}$
0 (CB)	95.41	1.6	115.0	11.77	120.48	5.8	7.37
0	92.88	1.6	116.28	7.91	120.97	5.8	4.94
1	112.36	1.61	129.58	10.38	127.89	4.94	6.45
1.5	119.56	1.61	124.16	13.2	128.95	3.37	8.20
2	121.12	1.61	126.39	16.34	133.2	2.14	10.15
2.5	124.26	1.61	130.45	10.0	138.86	2.14	6.21

Table 4.6: Summary of the significant values in the load-deflection curves for beams in Case Study 1(a)-M beam with $SI = 50\%$

V_f (%)	P_y (kN)	δ_y (mm)	P_u (kN)	δ_u (mm)	P_{max} (kN)	δ_{Pmax} (mm)	$\mu = \frac{\delta_u}{\delta_y}$
0 (CB)	95.41	1.6	115.0	11.77	120.48	5.8	7.37
0	92.4	1.6	121.22	5.8	119.0	5.0	3.63
1	111.4	1.61	121.7	13.2	126.9	4.06	8.20
1.5	116.48	1.61	126.1	13.21	129.08	4.06	8.20
2	120.35	1.61	122.49	9.5	132.3	2.14	5.90
2.5	123.49	1.61	129.04	9.1	137.87	2.14	5.65

Table 4.7: Summary of the significant values in the load-deflection curves for beams in Case Study 1(a)-M beam with $SI = 100\%$

V_f (%)	P_y (kN)	δ_y (mm)	P_u (kN)	δ_u (mm)	P_{max} (kN)	δ_{Pmax} (mm)	$\mu = \frac{\delta_u}{\delta_y}$
0 (CB)	95.41	1.6	115.0	11.77	120.48	5.8	7.37
0	90.8	1.6	114.28	4.06	114.28	4.06	2.54
1	111.3	1.61	132.12	10.38	124.34	3.37	6.45
1.5	116.16	1.61	126.96	13.21	129.16	3.37	8.21
2	120.14	1.6	118.95	16.36	130.25	3.37	10.23
2.5	124.87	1.6	121.22	19.82	132.00	3.37	12.39

Table 4.8: Summary of the significant values in the load-deflection curves for beams in Case Study 1(a)-M beam with $SI = 200\%$

The load-carrying capacity (P_{max}) and load at yield (P_y) in the beams with $SI = 0\%$ improved by up to 15% and 36%, respectively, higher than the beam without fibres. The increases in P_{max} for SFRC beams with $SI = 50\%$, 100% and 200% were up to 14 ~ 16%. In addition, the increase in P_y was up to 35% on average. The enhancement to strength and stiffness is useful for both ultimate- and serviceability-limit states often used in structural design.

Furthermore, for beams with higher fibre content (i.e. V_f = 2% ~ 2.5%) P_{max} was observed with initial relative peak (or "necking") pattern. The "necking" was more noticeable in beams with higher reduction in conventional shear reinforcement. For instance, in the beam with $SI = 50\%$ the peak trend is depicted in Figure 4.11. In order to understand this behaviour, further plots in terms of the tensile strains versus deflection, taken at the mid-span of the beam were constructed as depicted in Figures 4.14 and 4.15 (for comparison purposes, only three beams: $V_f = 0\%$, $V_f = 1.5\%$ and $V_f = 2.5\%$ were considered). Two strain values were taken at the crack opening region

at the bottom of the beam, one at concrete ($\varepsilon_{c,c}$) as depicted in Figure 4.14 and the other at the bottom longitudinal steel bar ($\varepsilon_{b,s}$) as shown in Figure 4.15.

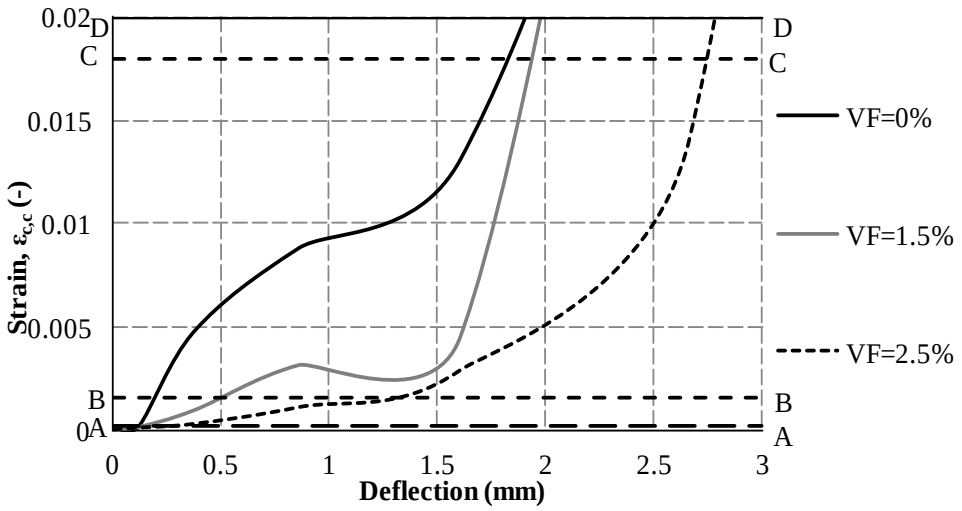


Figure 4.14: Tensile strain in concrete at the mid-span crack opening region at the bottom of the beam ($\varepsilon_{c,c}$) for Case Study 1 (a)-M with $SI = 50\%$

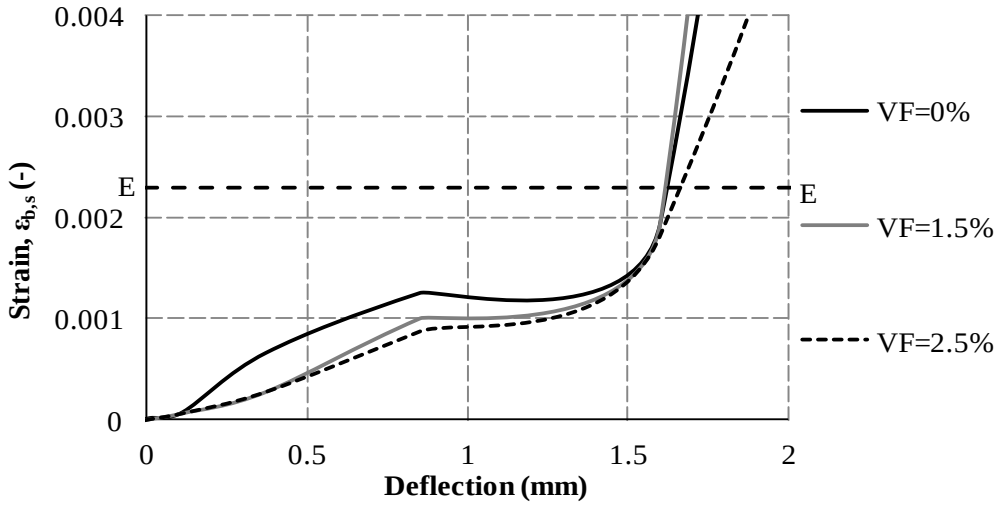


Figure 4.15: Tensile strain in steel bar at the mid-span crack opening region at the bottom of the beam ($\varepsilon_{b,s}$) for Case Study 1 (a)-M beam with $SI = 50\%$

The key points A, B, C, and D from the tensile stress-strain relations (see Figure 4.9) are denoted on Figure 4.14 (horizontal lines at each strain level have been included). Point E which indicates the yield of steel bars (equal to 2.3‰) has been included in Figure 4.15. Once the corresponding deflections have been identified from Figures 4.14 and 4.15, points A to E are then represented in Figure 4.16.

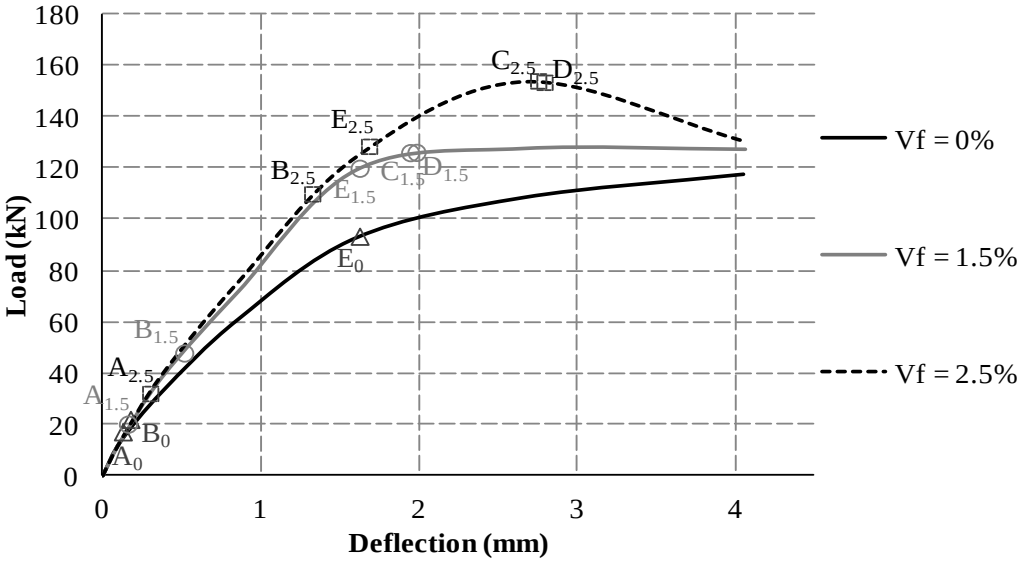


Figure 4.16: Load-deflection curve for Case Study 1 (a) series $SI = 50\%$ (shown up to a deflection of 4 mm)

For the RC beam without fibres ($V_f = 0\%$), the ultimate tensile strain of plain concrete is the lowest and the steel yield (Point E) was reached after concrete cracked in tension. However for SFRC beams, the steel yields before the ultimate tensile (i.e. pull-out) strain of fibrous concrete (Point D) is reached. The steel bars continue to deform beyond the yield point while the SFRC maintains the residual stresses between Points B and C,D (see Figure 4.9). This leads to more stresses in the tension zone being sustained by steel bars and fibrous concrete (as compared to beams with less or no fibres). Therefore, in order to maintain equilibrium the stresses in the compression zone will increase as well. Once Point C is reached, the fibrous concrete stresses drop immediately to zero at Point D (refer to the constitutive model depicted in Figure 4.9). The sudden drop from C to D is more pronounced for beams with higher fibre content (i.e. V_f = 2% ~ 2.5%), which are characterised by "strain hardening". Consequently, the stresses in tension drop drastically and a significant amount of stresses in compression is lost as well and this sudden change results in the peaked or "necking" behaviour observed for P_{max} on the load-deflection curves (e.g. Figure 4.11). For beams with smaller fibre content (i.e. V_f = 0% ~ 1.5%), there is "strain softening" and thus the drop from point C to D is not as high leading to a "smooth" rather than a "peaked" response.

Figure 4.16 depicts the load-deflection curves with points E (steel bar yield), B (start of steel fibres acting without concrete contribution and C,D (ultimate strain of fibres representing pull-out failure). The curves show that for beams without fibres (i.e. V_f =

0%), the yield of steel bars is associated with a large change in stiffness and indicates the beginning of the plateau trend on the load-deflection curve. For SFRC beams with V_f = 1.5% and 2.5%, points C,D occurred at the peak load confirming that fibres at the bottom tensile soffit of the beam have failed in pull-out at that stage. For beams with V_f = 1.5% and 2.5%, points C,D occurred at some margin from the steel bars yield point E confirming the "strain hardening" and "peaked" response discussed above.

4.3.3 Ductility

The ductility was determined using the ultimate deflection (δ_u). The value of the latter was taken at the ultimate load (P_u), which represents the (post-peak) residual strength at failure. The increase in ductility is accompanied by a softening load-deflection response. Therefore, to ensure the practical usefulness of these ductility levels, the residual strength (associated with the ultimate deflection at these ductility levels) was limited to a minimum of 85% the load-carrying capacity (i.e. $P_u \geq 0.85P_{max}$). The residual strength was found to be sufficiently high (i.e. >~85%) in all cases studied, suggesting that the softening is not significant. For design purposes, it is important to maintain the residual strength at an acceptable level in order to utilise the ensuing increase in ductility.

The ductility of the beams can be determined based on the ductility ratio (μ) which shows that the addition of fibres enhances the ductility ratio of the SFRC beams considerably. Nevertheless, there is a critical fibre volume fraction at which, addition of fibres beyond this value does not increase the ductility of the beams. In the beams with full conventional shear reinforcement, all SFRC beams were observed to have higher μ than the RC beam without fibre. A further comparative study of the beams responses and that of the control beam specimen (CB) is provided in a subsequent section of the present chapter where the optimum fibre contents for ductility are discussed.

4.3.4 Cracking pattern

This section presents the FE-based principal strain contours and vectors under monotonic loading. The results depicted in the figures were taken at failure and give an indication of crack formation and patterns.

4.3.4.1 Principal strain contours

Figures 4.17 to 4.20 show the principal strain contours for the beams analysed in Case Study 1(a)-M at failure. The principal strain range was selected between an ultimate tensile strain of 0.001 (i.e. cracking strain for beams without fibres) or 0.02 (i.e. pull-out strain for SFRC beams) and an ultimate compressive strain of -0.0035. The regions where the ultimate tensile strain is exceeded was highlighted in grey to denote tensile failure, while the regions of compressive failure where depicted in black. It was observed that the failure of the beams was characterised by tensile cracking at the mid-span of the beam (i.e. at the section where the lateral load (*P*) was applied). The crack formation regions covered a higher area for the beam without fibres. On the other hand, for SFRC beams the pull-out failure region was limited to a narrow zone under the load where the bending moment is highest.

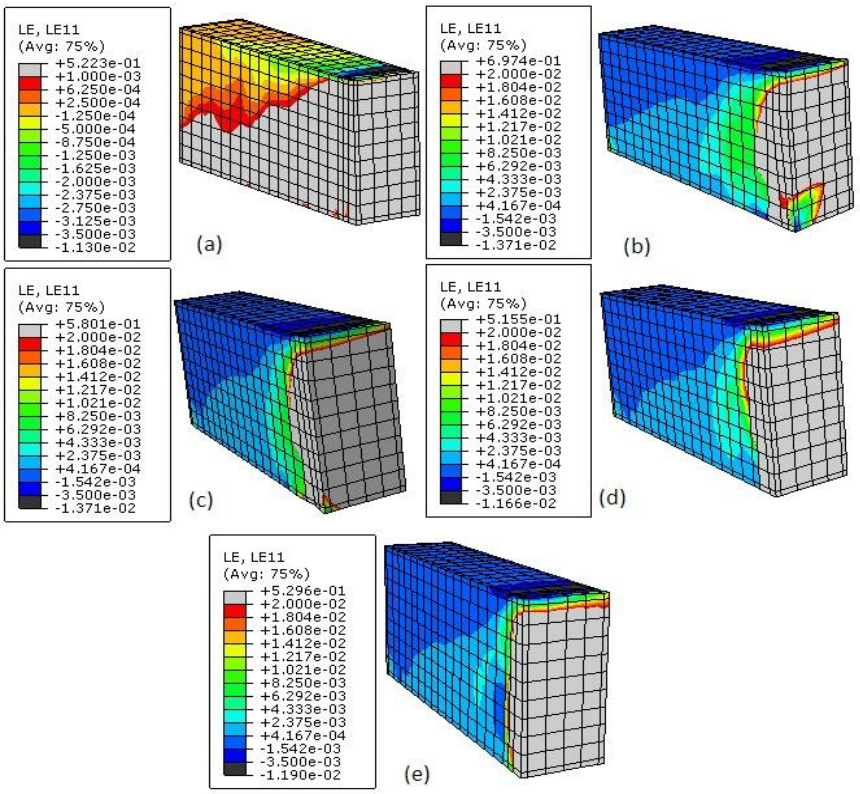


Figure 4.17: Principal strain contours for Case Study 1(a)-M with $SI = 0\%$ for (a) $V_f = 0\%$, (b) $V_f = 1\%$, (c) $V_f = 1.5\%$, (d) $V_f = 2\%$ and (e) $V_f = 2.5\%$

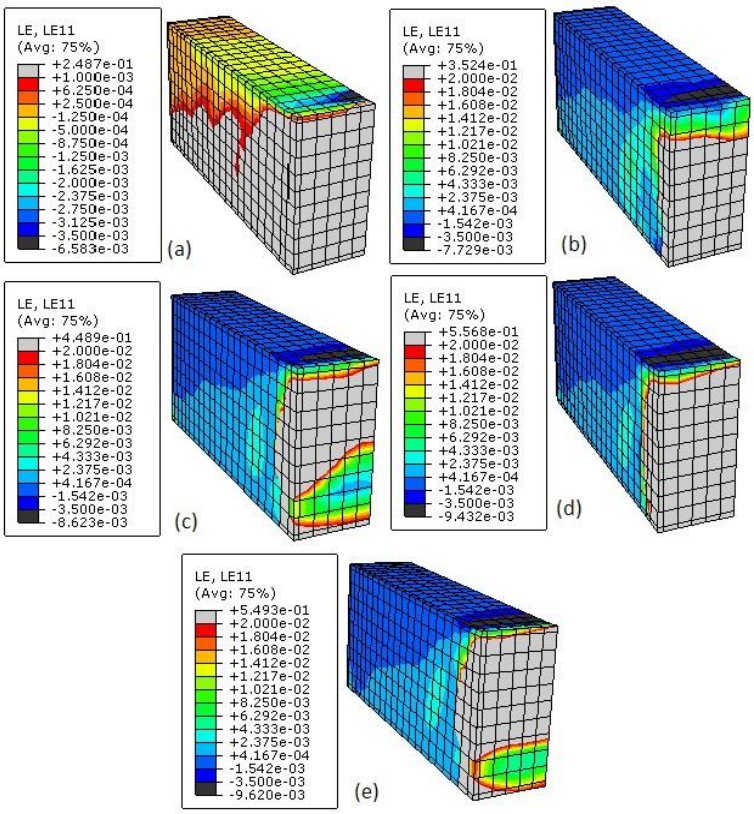


Figure 4.18: Principal strain contours for Case Study 1(a)-M with $SI = 50\%$ for (a) $V_f = 0\%$, (b) $V_f = 1\%$, (c) $V_f = 1.5\%$, (d) $V_f = 2\%$ and (e) $V_f = 2.5\%$

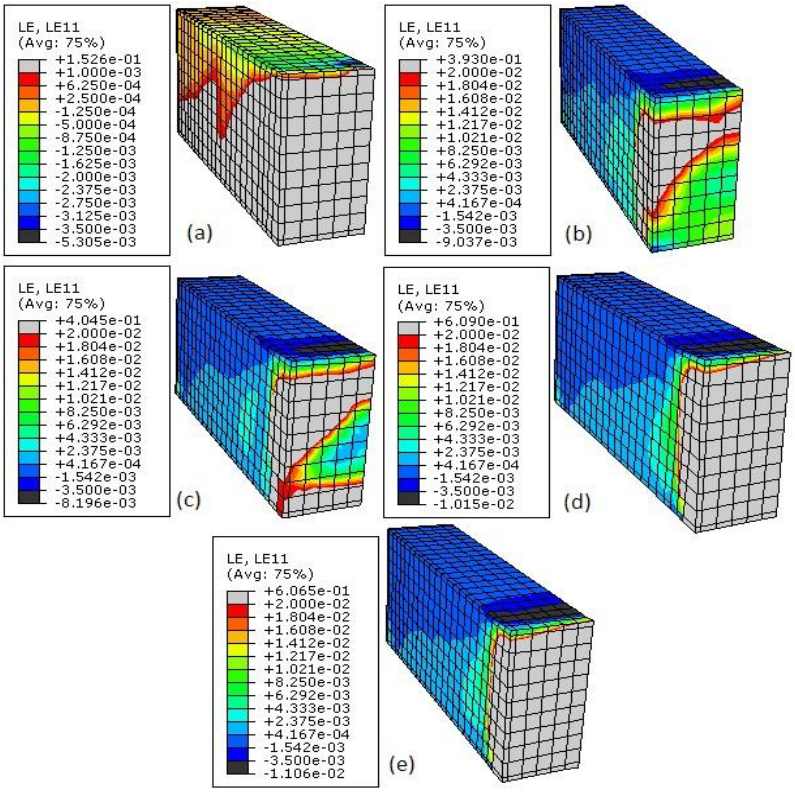


Figure 4.19: Principal strain contours for Case Study 1(a)-M with $SI = 100\%$ for (a) $V_f = 0\%$, (b) $V_f = 1\%$, (c) $V_f = 1.5\%$, (d) $V_f = 2\%$ and (e) $V_f = 2.5\%$

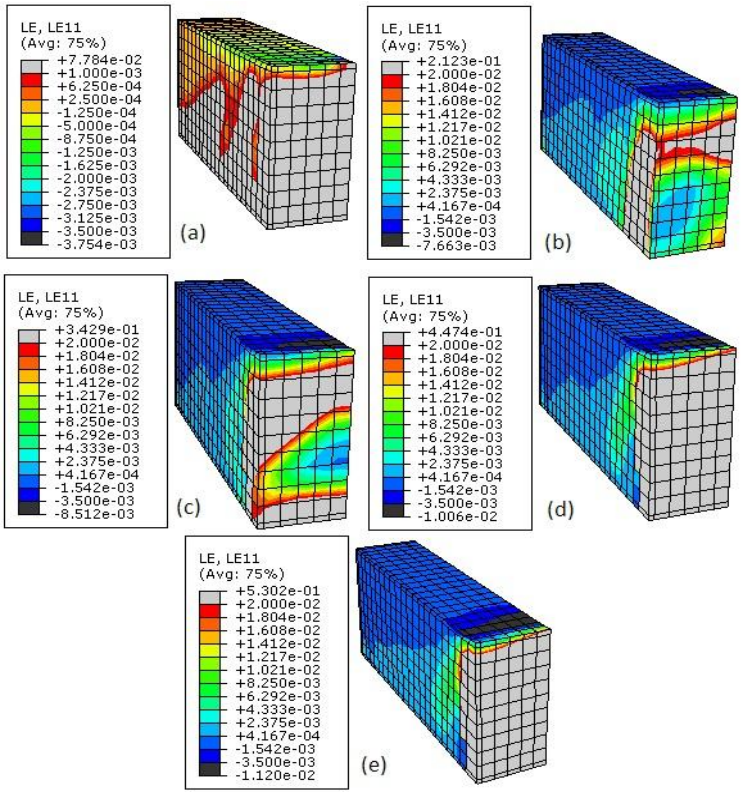


Figure 4.20Principal strain contours for Case Study 1(a)-M with $SI = 200\%$ for (a) $V_f = 0\%$, (b) $V_f = 1\%$, (c) $V_f = 1.5\%$, (d) $V_f = 2\%$ and (e) $V_f = 2.5\%$

4.3.4.2 Principal strain vectors

The principal strain vectors for beams with $SI = 0\%$, $SI = 50\%$, $SI = 100\%$ and $SI = 200\%$ are presented in Figures 4.21, 4.22, 4.23 and 4.24, respectively. From these figures, it can be seen that the cracks at failure occurred at the mid-span of the beams. This was located at the bottom of the beam under the applied lateral load (P).

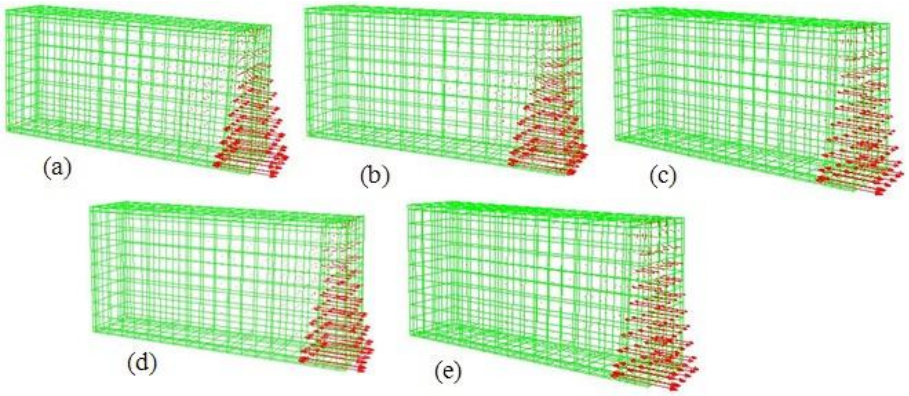


Figure 4.21: Principal strain vectors for Case Study 1(a)-M with $SI = 0\%$ for (a) $V_f = 0\%$, (b) $V_f = 1\%$, (c) $V_f = 1.5\%$, (d) $V_f = 2\%$ and (e) $V_f = 2.5\%$

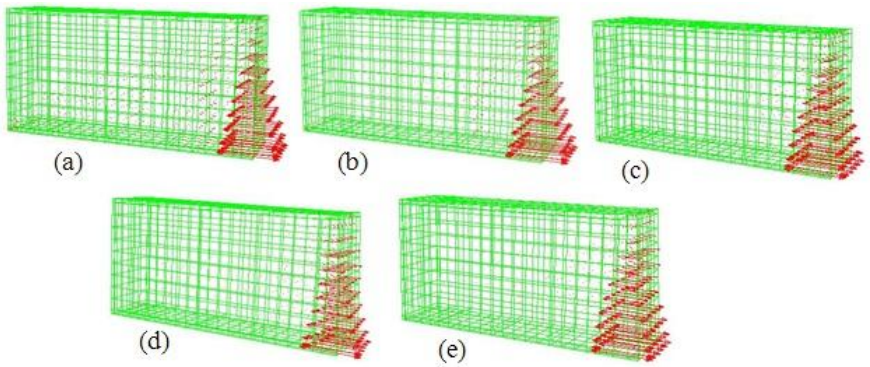


Figure 4.22: Principal strain vectors for Case Study 1(a)-M with $SI = 50\%$ for (a) $V_f = 0\%$, (b) $V_f = 1\%$, (c) $V_f = 1.5\%$, (d) $V_f = 2\%$ and (e) $V_f = 2.5\%$

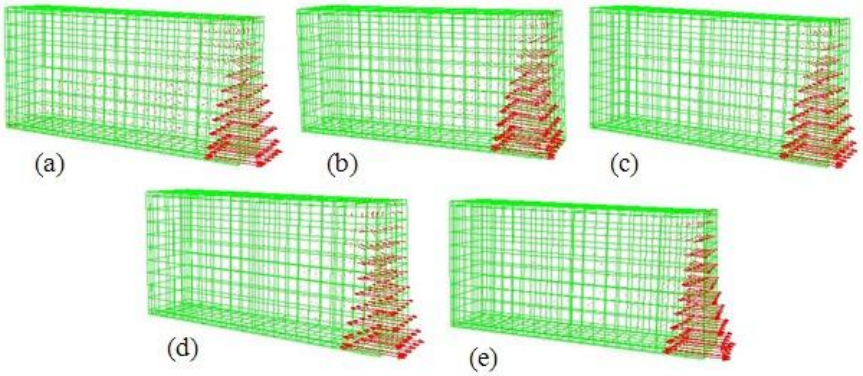


Figure 4.23: Principal strain vectors for Case Study 1(a)-M with $SI = 100\%$ for (a) $V_f = 0\%$, (b) $V_f = 1\%$, (c) $V_f = 1.5\%$, (d) $V_f = 2\%$ and (e) $V_f = 2.5\%$

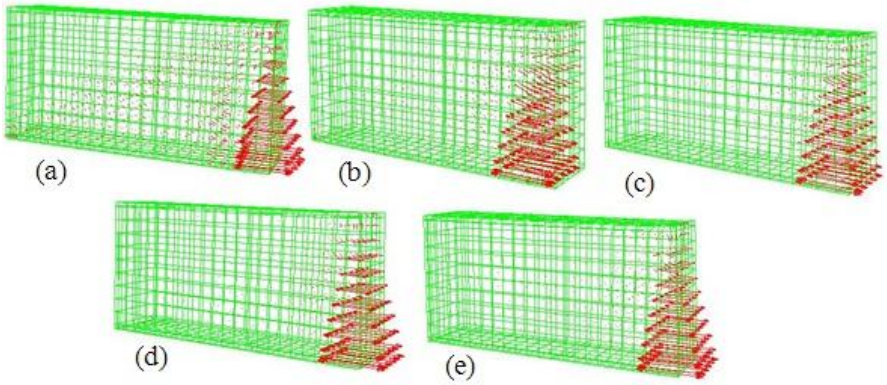


Figure 4.24: Principal strain vectors for Case Study 1(a)-M with $SI = 200\%$ for (a) $V_f = 0\%$, (b) $V_f = 1\%$, (c) $V_f = 1.5\%$, (d) $V_f = 2\%$ and (e) $V_f = 2.5\%$

Based on the cracking pattern presented here, it can be concluded that the failure of the beams analysed in Case Study 1(a)-M was in a bending mode.

4.3.4.3 Deflected shapes

A schematic of the deflected shapes for the beams analysed in Case Study 1(a)-M at failure is given in Figures 4.25 to 4.28. The results show similar patterns with a big deflection at the beam's mid-span. The deformations observed are consistent with the cracking patterns discussed earlier.

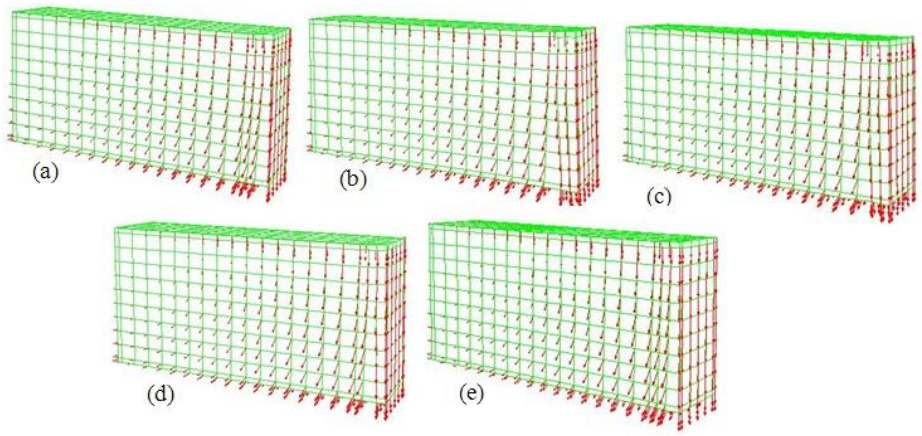


Figure 4.25: Deflected shapes for Case Study 1(a)-M with $SI = 0\%$ for (a) $V_f = 0\%$, (b) $V_f = 1\%$, (c) $V_f = 1.5\%$, (d) $V_f = 2\%$ and (e) $V_f = 2.5\%$

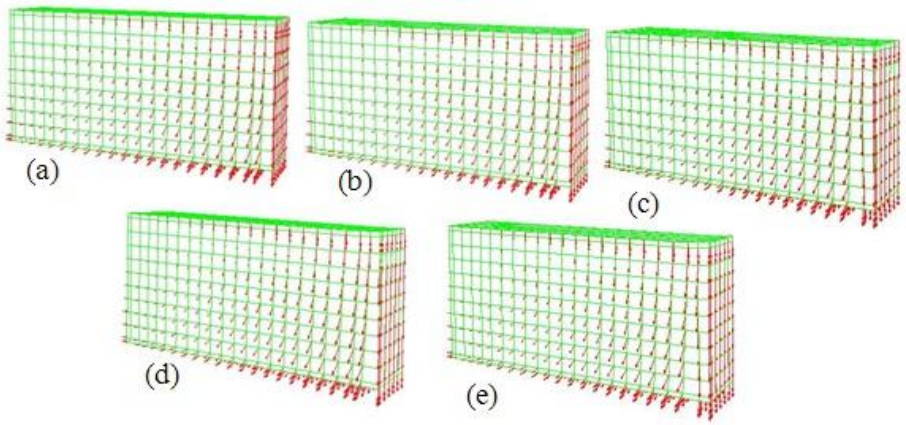


Figure 4.26: Deflected shapes for Case Study 1(a)-M with $SI = 50\%$ for (a) $V_f = 0\%$, (b) $V_f = 1\%$, (c) $V_f = 1.5\%$, (d) $V_f = 2\%$ and (e) $V_f = 2.5\%$

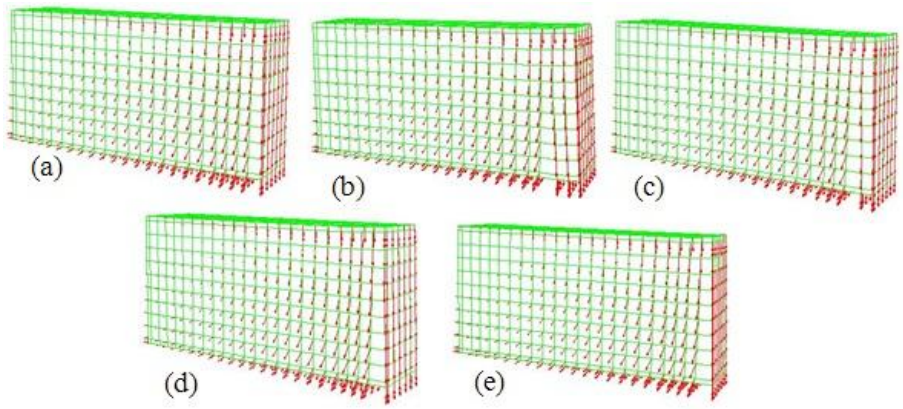


Figure 4.27: Deflected shapes for Case Study 1(a)-M with $SI = 100\%$ for (a) $V_f = 0\%$, (b) $V_f = 1\%$, (c) $V_f = 1.5\%$, (d) $V_f = 2\%$ and (e) $V_f = 2.5\%$

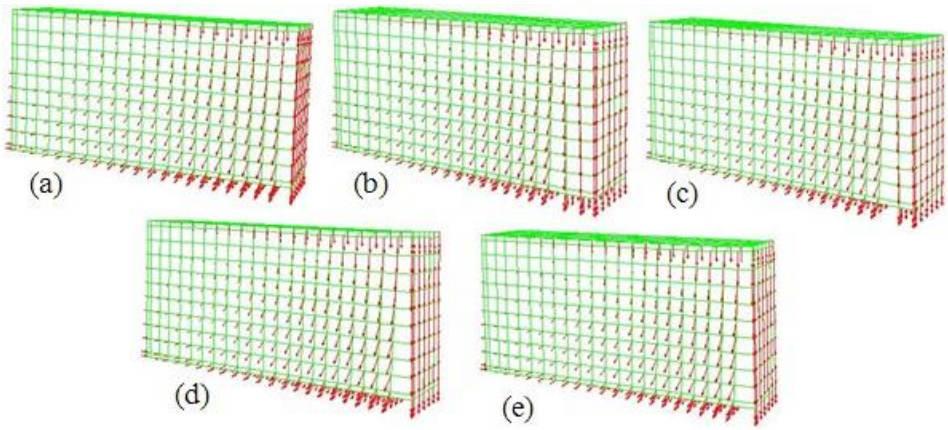


Figure 4.28: Deflected shapes for Case Study 1(a)-M with $SI = 200\%$ for (a) $V_f = 0\%$, (b) $V_f = 1\%$, (c) $V_f = 1.5\%$, (d) $V_f = 2\%$ and (e) $V_f = 2.5\%$

4.3.5 Comparative study with control specimen using non-dimensional ratios

This section presents the overall comparison made between the beams analysed with various fibre dosages and increased stirrup spacing and the control beam specimen (i.e. the beam with no fibres and full conventional shear reinforcement). The values of strength, ductility and energy absorption were normalised by dividing them by the corresponding values of the control specimen. Thus, overall conclusions were made on the potential of fibres to compensate for reduction in conventional shear reinforcement.

4.3.5.1 Strength ratio

The ratio between the maximum load in each beam and that in the control beam (i.e. $P_{max}/P_{max,0}$) is presented in Figure 4.29. The results show that an increase in fibre content leads to an enhancement in strength.

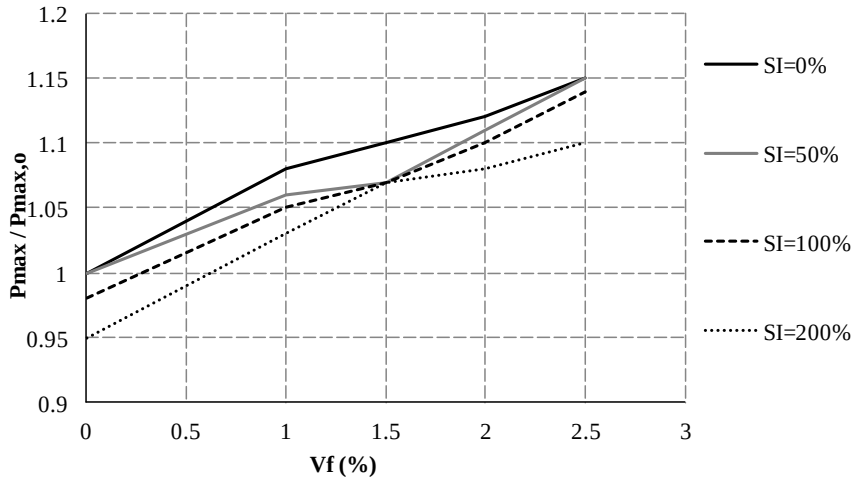


Figure 4.29: Ratio of maximum load to that of the control specimen ($SI = 0\%, V_f = 0\%$) versus steel fibre volume fraction graph for Case Study 1(a)-M

Figure 4.30 depicts the ratio between yield load of each beam to that of the control specimen (i.e. $P_y/P_{y,0}$). There is a consistent upward trend suggesting that the yield load increases as the fibre content is raised.

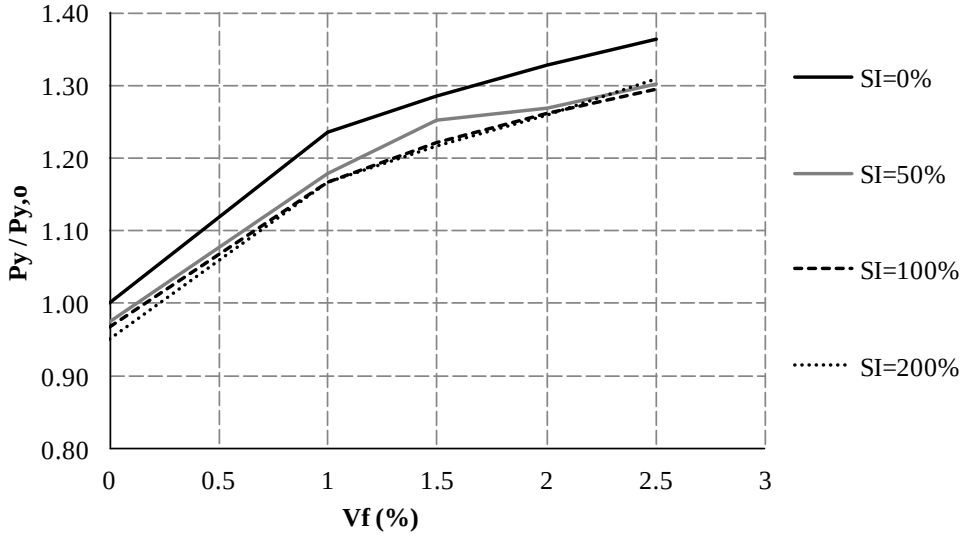


Figure 4.30: Ratio of yield load to that of the control specimen ($SI = 0\%, V_f = 0\%$) versus steel fibre volume fraction graph for Case Study 1(a)-M

4.3.5.2 Ductility ratio

The ductility ratios of all beams analysed under monotonic loading were normalised by dividing them by the counterpart ratio of the control beam (i.e. μ/μ_0) and the results were plotted against the change in fibre volume fraction as shown in Figure 4.31. For the beam with $SI = 0\%$, the ductility ratio reaches a maximum with fibre volume fraction of 1%. If the amount of the conventional shear reinforcement is reduced ($SI = 50\%$, $SI = 100\%$ and $SI = 200\%$) and fibres are added in optimum amounts, the ductility gradually increases by up to 11% ~ 68% compared to the control specimen. The minimum amount of fibres required in order to restore ductility ratio higher than that associated with the control specimen is $V_f = 1\%$ for beams with $SI = 100\%$ and $V_f = 1.5\%$ for beams with $SI = 50\%$ and 200%.

It can be concluded that ductility is enhanced as more fibres are added, however a threshold seems to exist beyond which additional fibres lead to less rather than more ductility. This can be explained by noting that as the fibre content is increased, the beam becomes stiffer and deflects less (this largely due to the fibres role in bridging across cracks and limiting their opening). This is similar to the "over-reinforced" behaviour associated with RC design where too much reinforcement leads to a reduction – rather than an increase – in ductility.

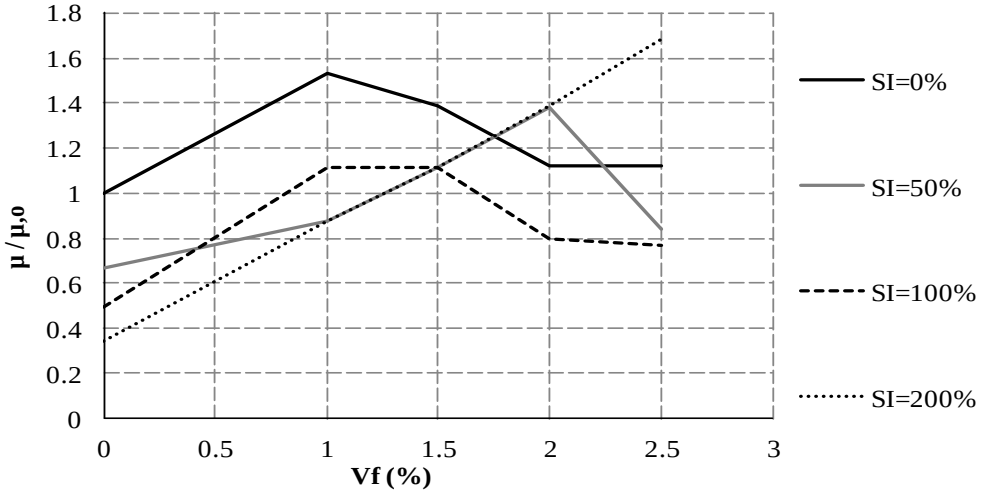


Figure 4.31: Ratio of ductility ratio to that of the control specimen ($SI = 0\%, V_f = 0\%$) versus steel fibre volume fraction graph for Case Study 1(a)-M

4.3.5.3 Energy absorption ratio

The ratio between the energy absorption (E_a) in each beam and that in the control beam ($E_{a,o}$) is given in Figure 4.32. The energy absorption was calculated based on the area under the load-deflection curves. The trend is similar to the one for ductility discussed above confirming its findings.

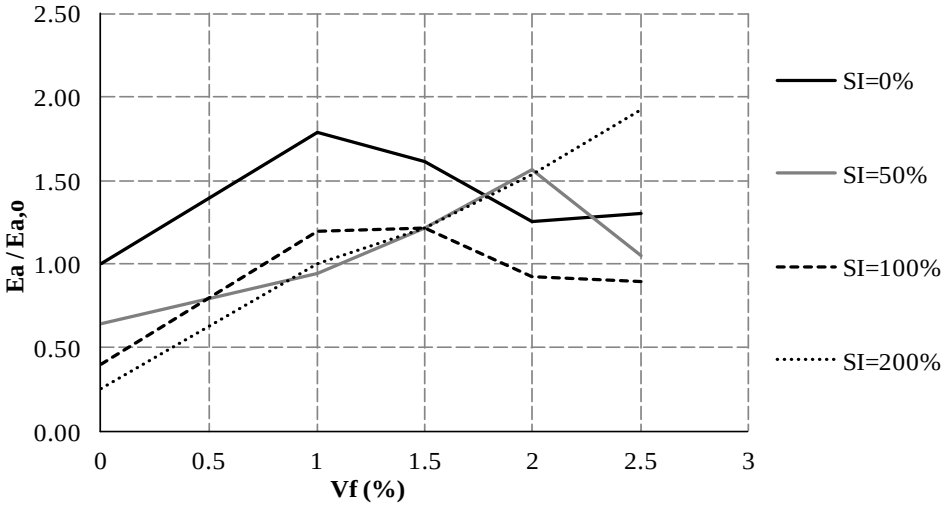


Figure 4.32: Ratio of energy absorption to that of the control specimen ($SI = 0\%, V_f = 0\%$) versus steel fibre volume fraction graph for Case Study 1(a)-M

4.3.6 Comparison between FE-based predictions and design calculations

In this section the results obtained from the FE analyses were compared to those calculated based on Eurocode 2 (2004) and TR-63 (2007). Adopting a rectangular compressive stress block and using the equations recommended by Eurocode 2 (2004), the shear and flexural capacities of RC sections were calculated as V_{rd} and M_{rd}, respectively. An additional tensile stress block was added to calculate the V_{rd} and M_{rd} values for SFRC sections, as suggested by the Concrete Society TR-63 (2007). Brief descriptions of the equations and calculation procedure were given in Appendix B.

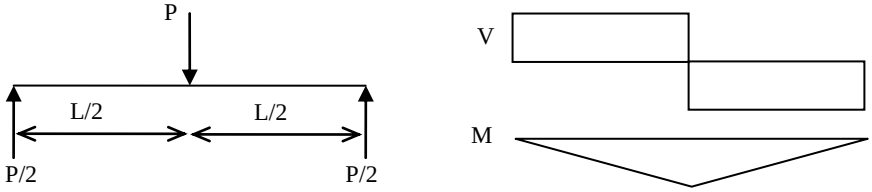


Figure 4.33: The loading condition, bending moment (M) and shear force (V) diagram from Case Study 1(a)

The shear and bending moment capacities of the beam calculated (i.e. V_{rd} and M_{rd}) are given in Tables 4.9 to 4.12, as well as the corresponding loads that would lead to the failure in shear (P_{sc}) and bending (P_{BMC}). A schematic of the shear force and bending moment diagrams used to determine these loads is depicted in Figure 4.33. The minimum of these two loads (P_{SC} and P_{BMC}) was then used to determine the load-carrying capacity and predict mode of failure. A comparison between the FE-based load-carrying capacity (P_{max}) and its analytical counterpart (P_{SC} or P_{BMC}) is also included. In this manner, conclusions can be made on the numerical predictions in the light of Eurocode and TR-63 design-based calculations.

V_f (%)	V_{rd} (kN)	M_{rd} (kNm)	P_{max} (kN)	P_{SC} (kN)	P_{BMC} (kN)	$\frac{P_{max}}{P_{BMC}}$	*Failure mode*
0	98.17	13.85	120.48	196.33	100.72	1.20	bending
1	113.67	15.81	129.88	227.34	114.97	1.13	bending
1.5	120.96	16.80	131.94	241.92	122.15	1.08	bending
2	128.25	17.77	134.52	256.50	129.22	1.04	bending
2.5	135.54	18.72	138.72	271.07	136.14	1.02	bending

Table 4.9: FE- and code-based strength predictions for Case study 1(a) $SI = 0\%$

V_f (%)	V_{rd} (kN)	M_{rd} (kNm)	P_{max} (kN)	P_{SC} (kN)	P_{BMC} (kN)	$\frac{P_{max}}{P_{BMC}}$	*Failure mode*
0	73.64	13.85	120.97	147.28	100.72	1.20	bending
1	89.14	15.81	127.89	178.29	114.97	1.11	bending
1.5	96.43	16.80	128.95	192.87	122.15	1.06	bending
2	103.72	17.77	133.20	207.44	129.22	1.03	bending
2.5	111.01	18.72	138.86	222.02	136.14	1.02	bending

Table 4.10: FE- and code-based strength predictions for Case study 1(a) $SI = 50\%$

V_f (%)	V_{rd} (kN)	M_{rd} (kNm)	P_{max} (kN)	P_{SC} (kN)	P_{BMC} (kN)	$\frac{P_{max}}{P_{BMC}}$	*Failure mode*
0	61.38	13.85	119.0	122.75	100.72	1.18	bending
1	76.88	15.81	126.9	153.76	114.97	1.10	bending
1.5	84.17	16.80	129.08	168.34	122.15	1.06	bending
2	91.46	17.77	132.30	182.92	129.22	1.02	bending
2.5	98.75	18.72	137.87	197.49	136.14	1.01	bending

Table 4.11: FE- and code-based strength predictions for Case study 1(a) $SI = 100\%$

V_f (%)	V_{rd} (kN)	M_{rd} (kNm)	P_{max} (kN)	P_{SC} (kN)	P_{BMC} (kN)	$\frac{P_{max}}{P_{BMC}}$	*Failure mode*
0	49.11	13.85	114.28	98.22	100.72	1.13	shear
1	64.62	15.81	124.34	129.23	114.97	1.08	bending
1.5	71.91	16.80	129.16	143.81	122.15	1.06	bending
2	79.19	17.77	130.25	158.39	129.22	1.01	Bending
2.5	86.48	18.72	132.00	172.97	136.14	0.97	Bending

Table 4.12: FE- and code-based strength predictions for Case study 1(a) $SI = 200\%$

Tables 4.9 to 4.12 showed a summary of the values obtained from the FE analysis and the values calculated based on Eurocode 2 (2004) and Concrete Society TR-63 (2007) for beams with $SI = 0\%$, 50%, 100% and 200%. Comparison between the results calculated for P_{SC} and P_{BMC} showed that all beams failed in a bending mode except for the beam with $V_f = 0\%$ and $SI = 200\%$, which failed in a shear mode. This is logical as this case contains the least amount of shear reinforcement and no fibres. It is interesting to see that the addition of fibres has led to a change in the failure mode from a brittle one (i.e. shear) to a more ductile one (i.e. bending), which is desired in design. Furthermore, the results obtained from the FE analysis and the corresponding values calculated based on Eurocode 2 (2004) and Concrete Society TR-63 (2007) show good correlation (i.e. P_{max}/P_{BMC} is 0.97 ~ 1.20) confirming the validity of the FE-based results, with the latter being more economical than the code estimates. This also confirms the fibres potential to compensate for a reduction in shear reinforcement.

4.4 Case Study 1(a)-C: Parametric study on simply supported beams under reversed-cyclic loading

Parametric studies were carried out on simply supported beams under reversed cyclic loading. The loading history adopted for the present case is the same as the one used in the calibration work (see Figure 4.4b). The constitutive model for SFRC used is defined in Figure 4.9 and Table 4.4. The ensuing FE analysis results are discussed next.

Similarly to the investigation of beams under monotonic loading (i.e. Case Study 1(a)-M), the spacing between the transverse stirrups was increased (with $SI = 0\%$, 50%, 100% and 200%) and different amounts of steel fibres (i.e. volume fractions $V_f = 0\%$,

1%, 1.5%, 2% and 2.5%) were analysed to examine their potential to compensate for the reduction in conventional shear reinforcement.

4.4.1 Load-deflection curves

The FE-based load-deflection curves obtained for Case Study 1(a)-C, analysed under reversed-cyclic loading are presented in Figures 4.34, 4.35, 4.36 and 4.37 for the beams with $SI = 0\%$, 50%, 100% and 200%, respectively. For clarity, the curves were reproduced for each fibre volume fraction value as depicted in Figures 4.38 to 4.41. Key load values and their respective deflections are summarised in Tables 4.13 to 4.16.

4.4.2 Strength

It can be seen that addition of steel fibres to the beams improved its load-carrying capacity (i.e P_{max}). The enhancement evident in all beams with different *SI* values with more fibres consistently leading to higher strength. The curves also show that the fibres enhance stiffness. This is because the fibres bridge the cracks and control their opening leading to reduced deflections compared to beams with less fibre content (conversely higher loads were required in order to produce the same deflections). The larger the amount of fibres in the concrete, the higher the number of fibres bridging the cracks and controlling their opening. The enhancement to strength and stiffness is useful for both ultimate- and serviceability-limit states often used in structural design.

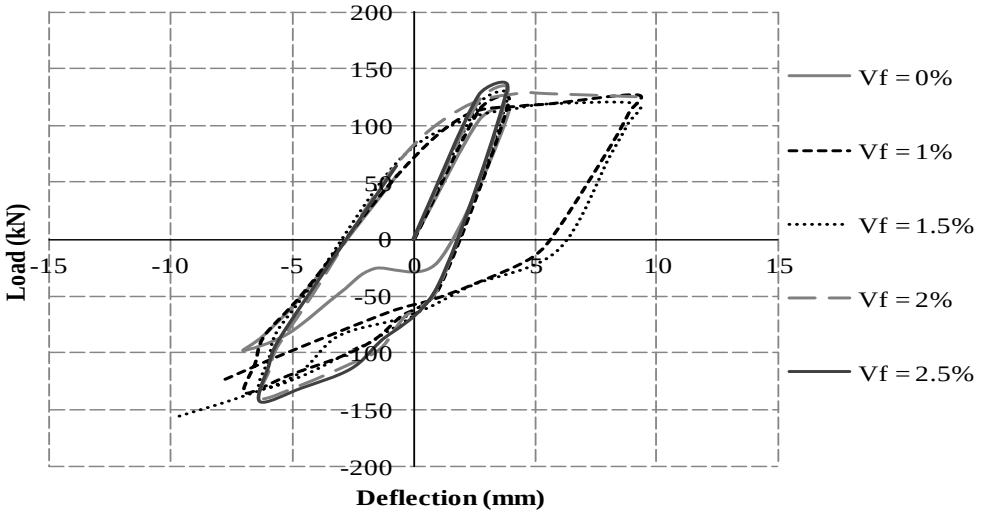


Figure 4.34: Load-deflection curves for Case Study 1(a)-C for beams with $SI = 0\%$

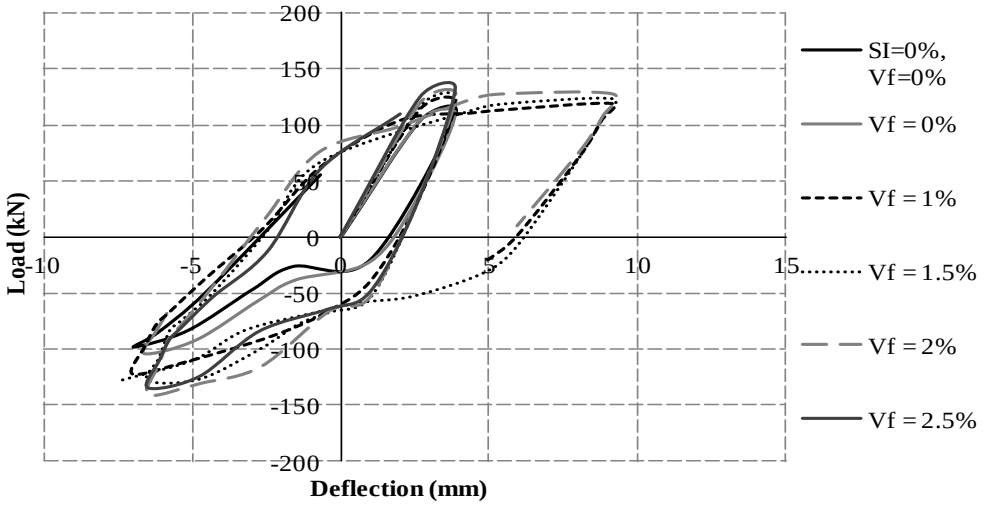


Figure 4.35: Load-deflection curves for Case Study 1(a)-C for beams with $SI = 50\%$

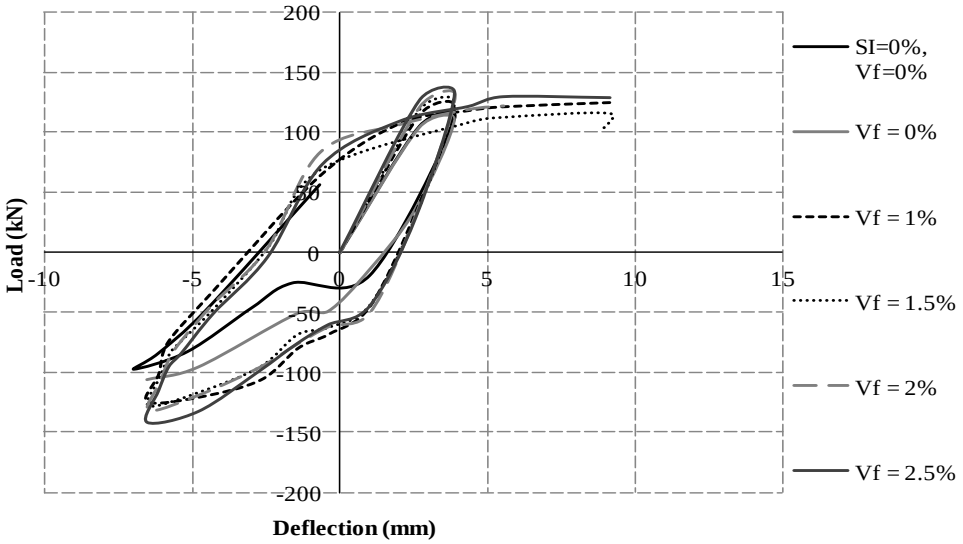


Figure 4.36: Load-deflection curves for Case Study 1(a)-C for beams with $SI = 100\%$

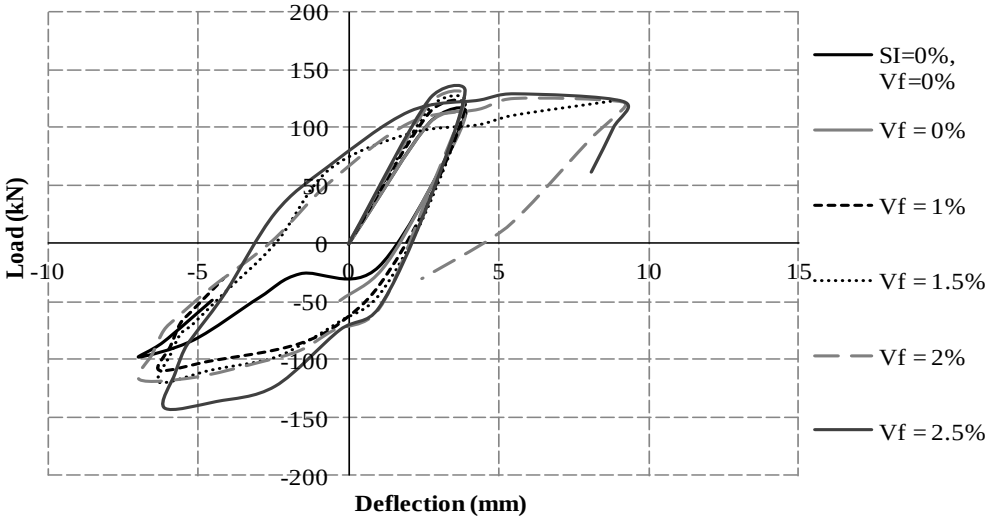


Figure 4.37: Load-deflection curves for Case Study 1(a)-C for beams with $SI = 200\%$

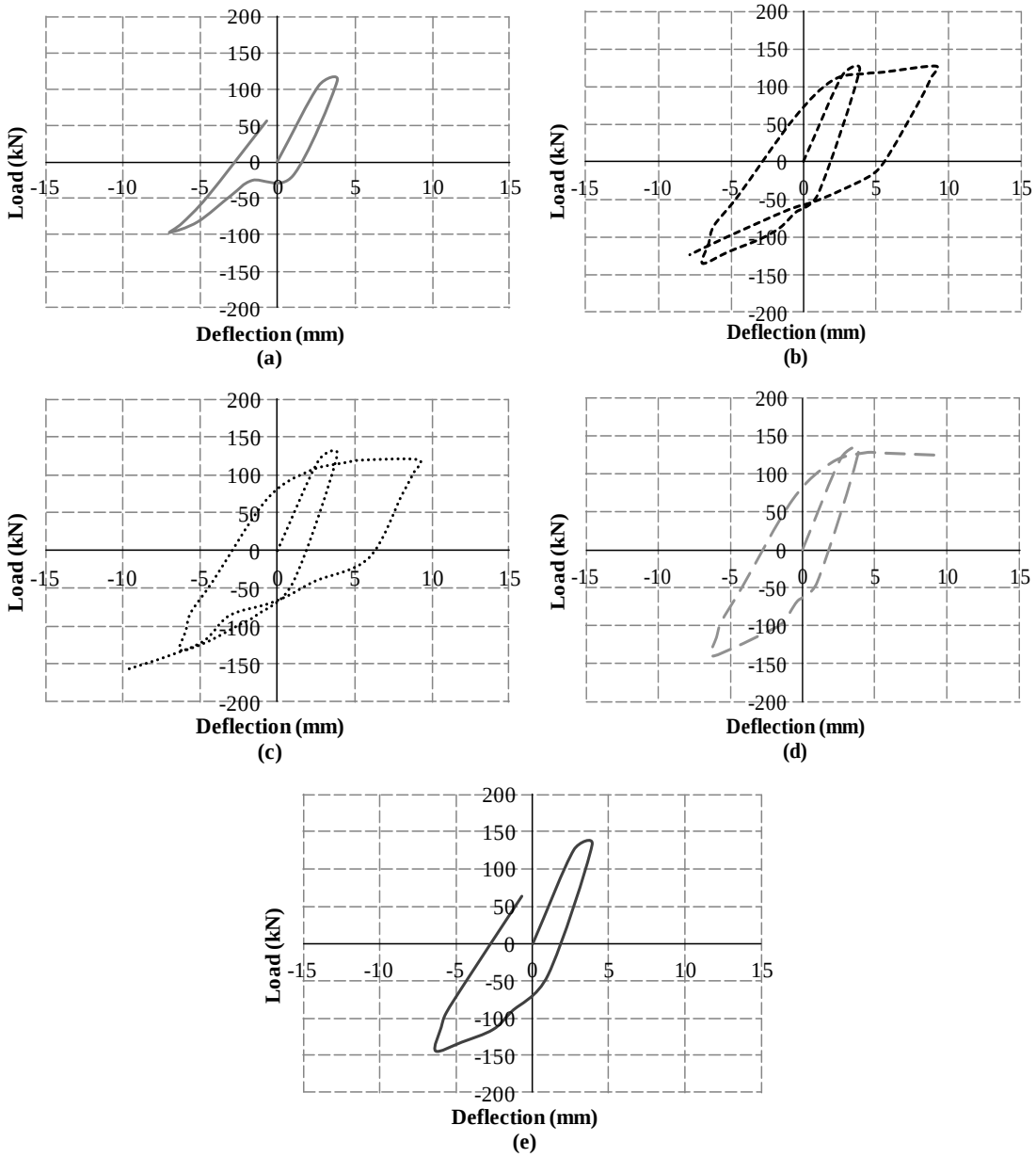


Figure 4.38: Load-deflection curves for Case Study 1(a)-C beams with $SI = 0\%$ and (a) $V_f = 0\%$, (b) $V_f = 1\%$, (c) $V_f = 1.5\%$, (d) $V_f = 2\%$ and (e) $V_f = 2.5\%$

V_f (%)	N_c	P_y (kN)	δ_y (mm)	P_u (kN)	δ_u (mm)	P_{max} (kN)	δ_{Pmax} (mm)	$\mu = \frac{\delta_u}{\delta_y}$
0	0.95	105.0	2.7	111.2	3.89	111.2	3.89	1.44
1	1.67	114.6	2.7	126.71	9.17	126.71	9.17	3.40
1.5	1.72	119.9	2.7	120.0	9.17	128.66	3.89	3.40
2	1.21	122.3	2.7	125.3	9.17	130.4	3.89	3.40
2.5	0.95	126.7	2.7	133.1	3.89	133.1	3.89	1.44

Table 4.13: Results summary from load-deflection curves for Case Study 1(a)-C for beams with $SI = 0\%$

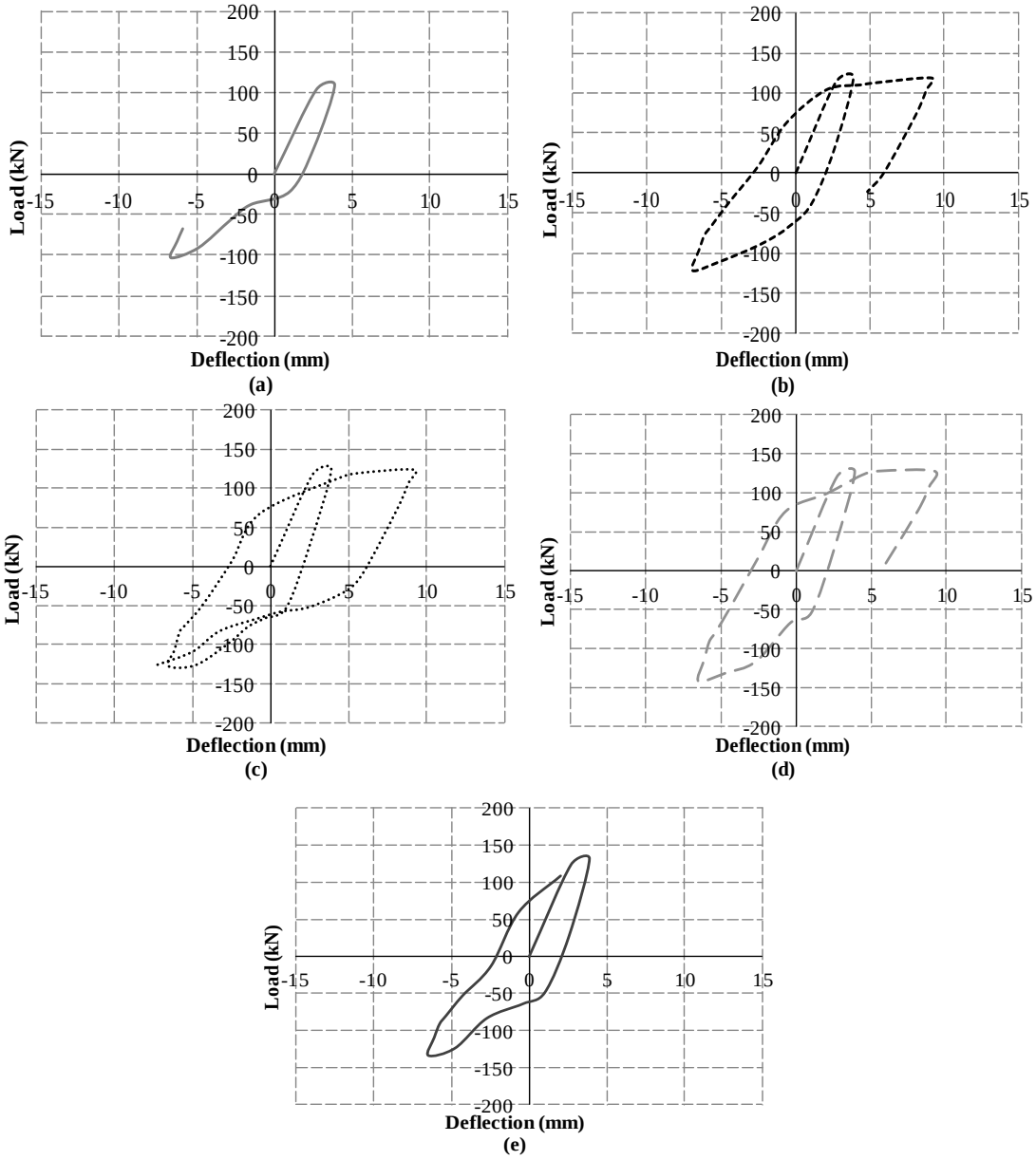


Figure 4.39: Load-deflection curves for Case Study 1(a)-C beams with $SI = 50\%$ and (a) $V_f = 0\%$, (b) $V_f = 1\%$, (c) $V_f = 1.5\%$, (d) $V_f = 2\%$ and (e) $V_f = 2.5\%$

V_f (%)	N_c	P_y (kN)	δ_y (mm)	P_u (kN)	δ_u (mm)	P_{max} (kN)	δ_{Pmax} (mm)	$\mu = \frac{\delta_u}{\delta_y}$
0 (*CB*)	0.95	105.0	2.7	111.2	3.89	111.2	3.89	1.44
0	0.80	103.9	2.7	110	3.89	110	3.89	1.44
1	1.38	113.7	2.7	118.9	9.17	122.52	3.89	3.4
1.5	1.67	117.8	2.7	123.8	9.15	124.83	3.89	3.39
2	1.33	121	2.7	128.4	9.16	128.4	5.54	3.39
2.5	1.08	124.6	2.7	4.7	4.3	132.8	3.89	1.59

Table 4.14: Results summary from load-deflection curves for Case Study 1(a)-C for beams with $SI = 50\%$

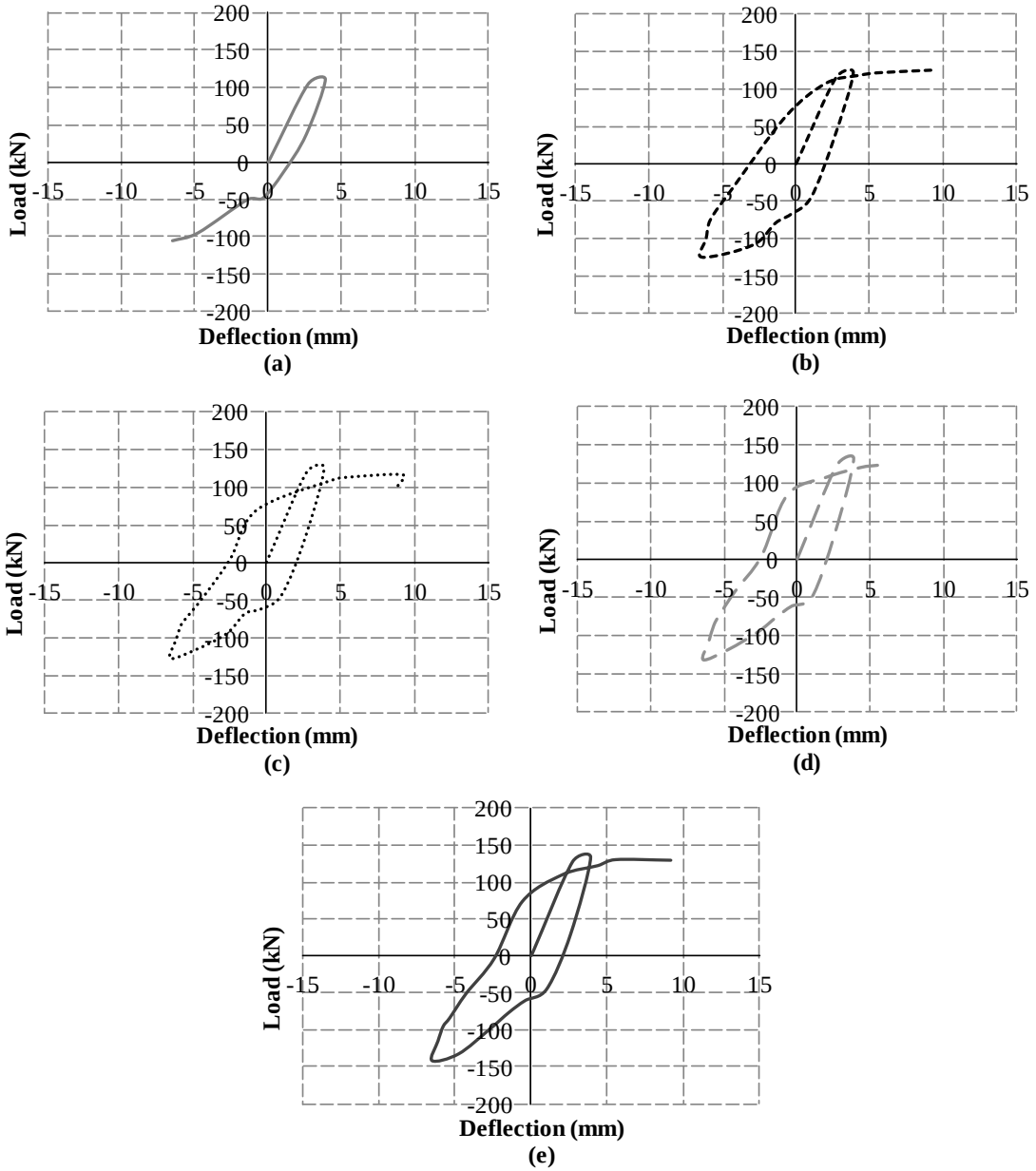


Figure 4.40: Load-deflection curves for Case Study 1(a)-C beams with $SI = 100\%$ nd (a) $V_f = 0\%$, (b) $V_f = 1\%$, (c) $V_f = 1.5\%$, (d) $V_f = 2\%$ and (e) $V_f = 2.5\%$

V_f (%)	N_c	P_y (kN)	δ_y (mm)	P_u (kN)	δ_u (mm)	P_{max} (kN)	δ_{Pmax} (mm)	$\mu = \frac{\delta_u}{\delta_y}$
0 (*CB*)	0.95	105.0	2.7	111.2	3.89	111.2	3.89	1.44
0	0.7	104.3	2.7	111	3.89	111	3.89	1.44
1	1.21	114.8	2.7	125	9.17	122.14	3.89	3.4
1.5	1.25	119.5	2.7	116.4	9.17	123.6	3.49	3.4
2	1.15	121.9	2.7	121.5	9.15	128.2	3.49	3.39
2.5	1.15	126.9	2.7	129	9.15	131.0	3.49	3.39

Table 4.15: Results summary from load-deflection curves for Case Study 1(a)-C for beams with SI = 100%

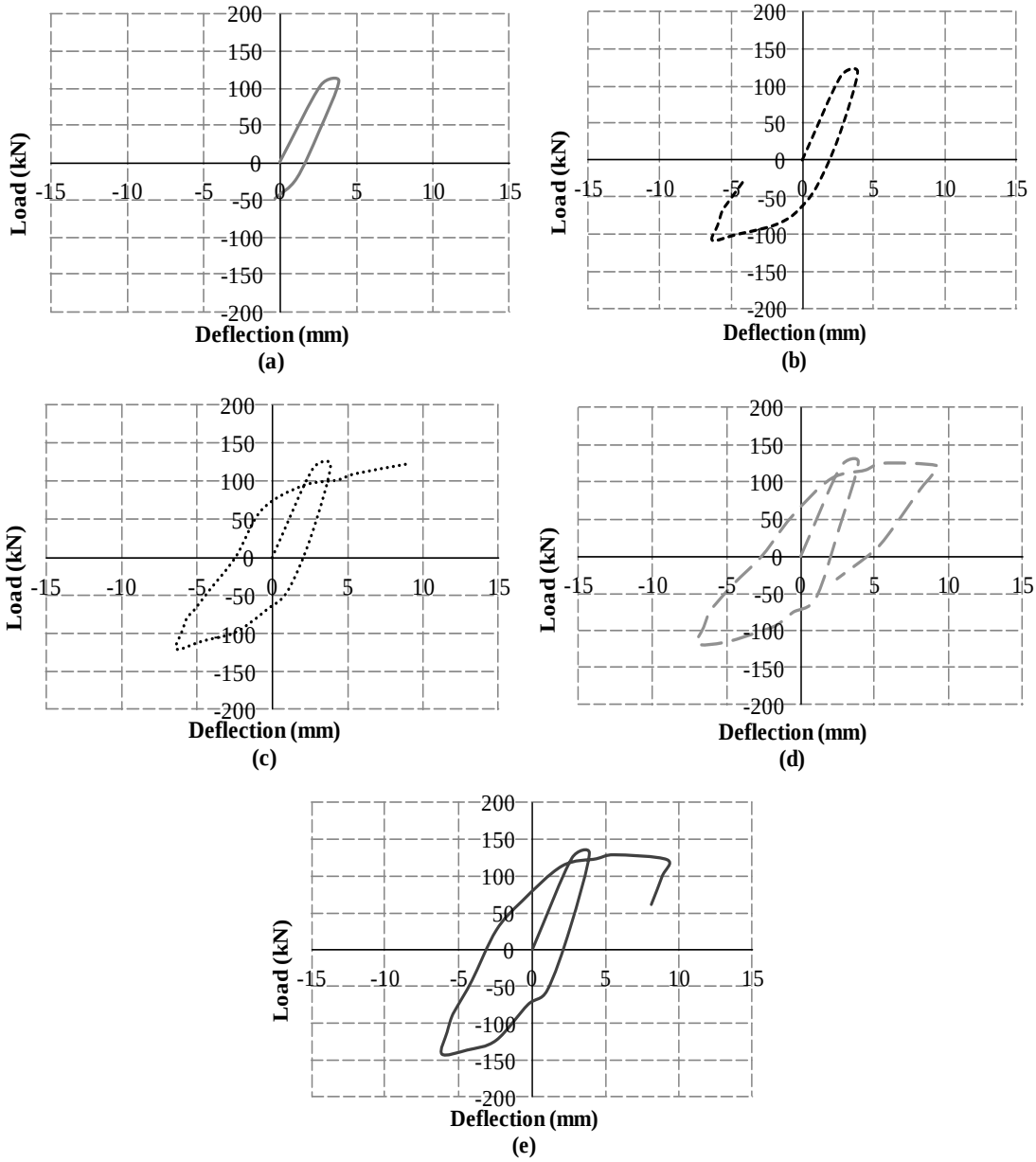


Figure 4.41: Load-deflection curves for Case Study 1(a)-C beams with $SI = 200\%$ and (a) $V_f = 0\%$, (b) $V_f = 1\%$, (c) $V_f = 1.5\%$, (d) $V_f = 2\%$ and (e) $V_f = 2.5\%$

V_f (%)	N_c	P_y (kN)	δ_y (mm)	P_u (kN)	δ_u (mm)	P_{max} (kN)	δ_{Pmax} (mm)	$\mu = \frac{\delta_u}{\delta_y}$
0 (*CB*)	0.95	105.0	2.7	111.2	3.89	111.2	3.89	1.44
0	0.5	104.5	2.7	110.5	3.89	110.5	3.89	1.44
1	0.9	113.3	2.7	119.5	3.89	119.5	3.89	1.44
1.5	1.21	117.1	2.7	124	9.14	122.6	3.89	3.39
2	1.46	120.3	2.7	121.7	9.15	126.8	3.89	3.39
2.5	1.3	124.9	2.7	122.7	9.17	129.6	3.49	3.4

Table 4.16: Results summary from load-deflection curves for Case Study 1(a)-C for beams with $SI = 200\%$

In general, a similar pattern was also observed for the yield load (P_y) in the SFRC beams as P_y increased when the fibre dosage was raised. The data shows that the enhancement was up to ~20% compared to the original specimen with not fibres.

4.4.3 Ductility

Ductility in the present case seems to follow a trend similar to the one observed earlier with beams under monotonic loading, namely that it increases as more fibres are added up to a certain threshold beyond which additional fibres reduce rather enhance ductility. The ductility of the beams can also be measured based on the number of cycles (N_c) obtained before failure. The beam with no reduction in shear reinforcement and no fibres modelled using ABAQUS failed at 0.95 load cycles. From Tables 4.13 to 4.16, it is apparent that all SFRC beams failed at a higher N_c value (except the beam with $SI = 0\%$ and $V_f = 2.5\%$ which failed at 0.95 load cycles). The N_c data confirms the trend associated with ductility as it indicates that providing fibres in excess of an optimum amount leads to less rather than more ductility. The optimum amounts are identified as part of a further study into the effect of fibres on ductility provided in a subsequent section of this chapter.

4.4.4 Cracking pattern

This section presents the principal strain contours and vectors, and deflected shapes of the beams analysed under reversed-cyclic loading. The data presented herein was taken at failure. The graphs helped indicate the cracking pattern.

4.4.4.1 Principal strain contours

Principal strain contours for the beams in Case Study 1(a)-C are depicted in Figures 4.42 to 4.45. The contour intervals were selected so that the tensile strains exceeding 0.002 (i.e. cracking formation strain) for beams without fibres and 0.02 (i.e. fibres pull-out strain) for SFRC beams where highlighted in grey. Similarly, compressive strains exceeding concrete ultimate strain (i.e. -0.0035) was denoted in black.

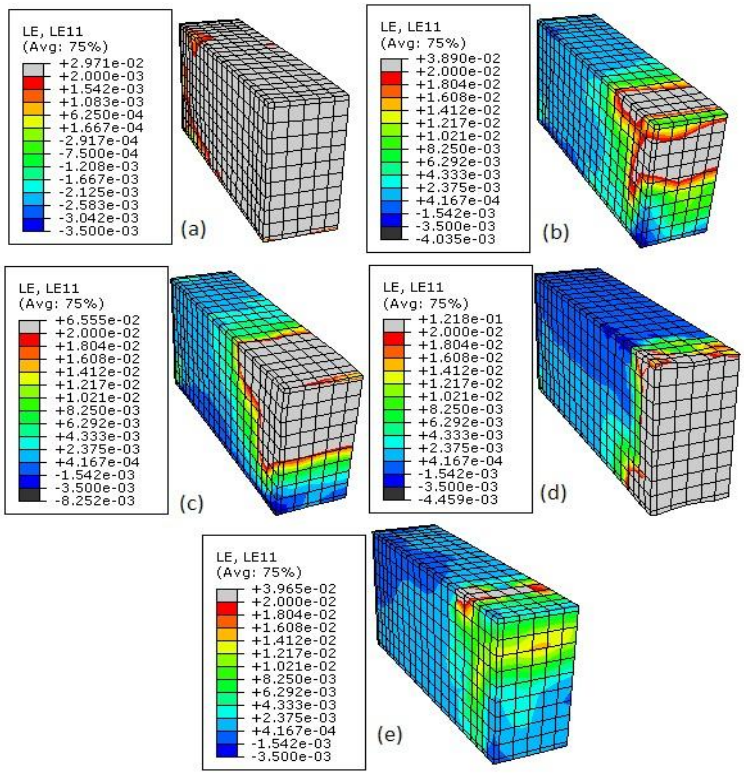


Figure 4.42: Principal strain contours for Case Study 1(a)-C beams with $SI = 0\%$ and (a) $V_f = 0\%$, (b) $V_f = 1\%$, (c) $V_f = 1.5\%$, (d) $V_f = 2\%$ and (e) $V_f = 2.5\%$

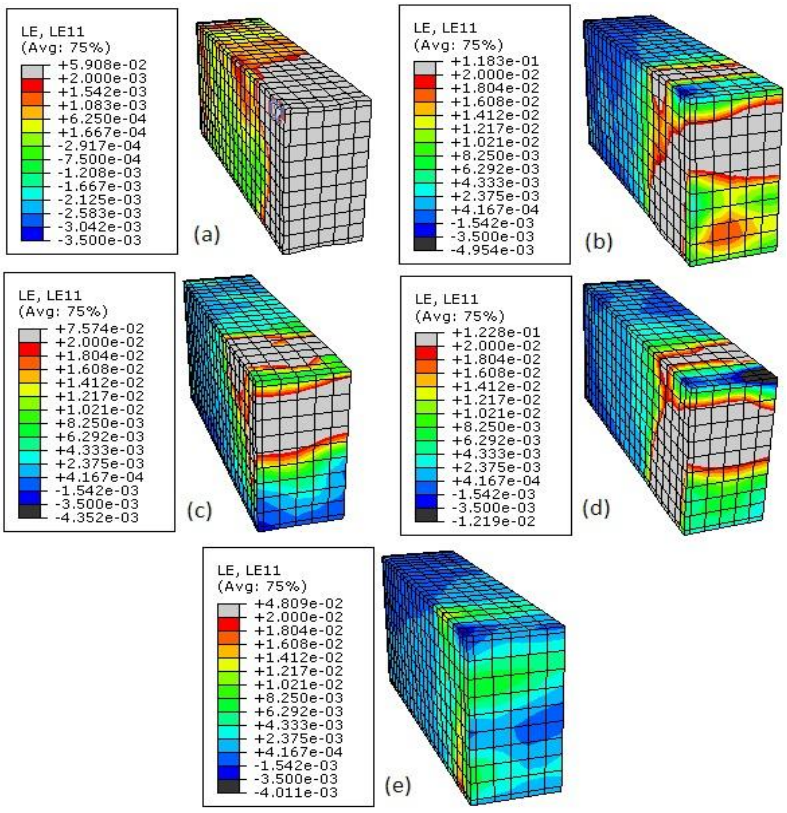


Figure 4.43: Principal strain contours for Case Study 1(a)-C beams with $SI = 50\%$ and (a) $V_f = 0\%$, (b) $V_f = 1\%$, (c) $V_f = 1.5\%$, (d) $V_f = 2\%$ and (e) $V_f = 2.5\%$

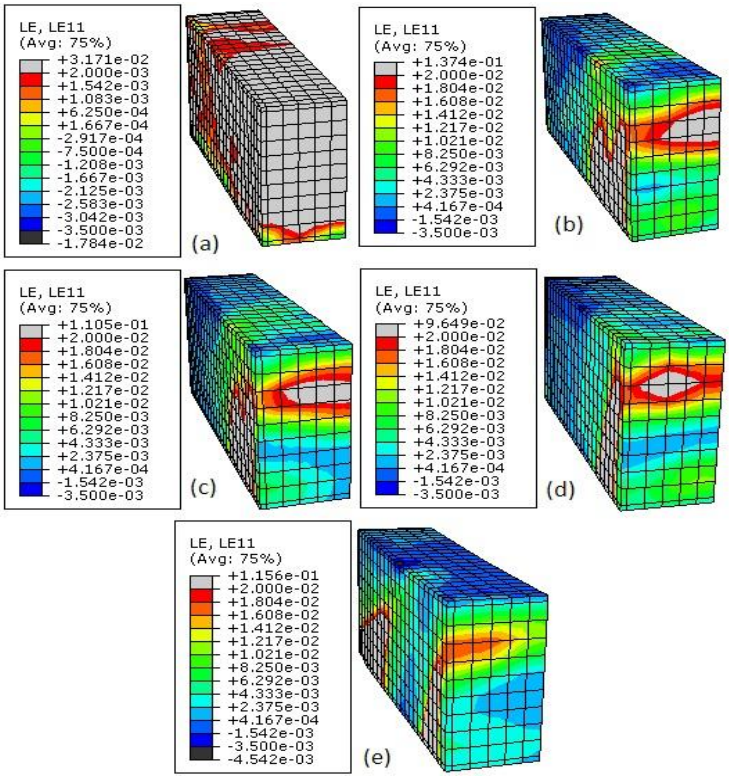


Figure 4.44: Principal strain contours for Case Study 1(a)-C beams with $SI = 100\%$ and (a) $V_f = 0\%$, (b) $V_f = 1\%$, (c) $V_f = 1.5\%$, (d) $V_f = 2\%$ and (e) $V_f = 2.5\%$

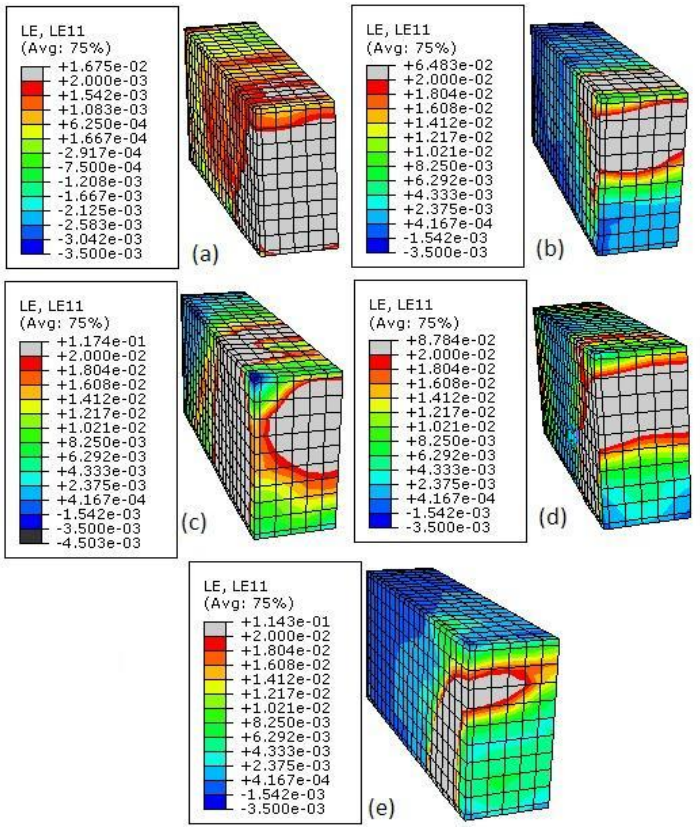


Figure 4.45: Principal strain contours for Case Study 1(a)-C beams with $SI = 200\%$ and (a) $V_f = 0\%$, (b) $V_f = 1\%$, (c) $V_f = 1.5\%$, (d) $V_f = 2\%$ and (e) $V_f = 2.5\%$

The contours show that the addition of steel fibres led to a reduction in the zones affected by pull-out failure, which became limited to a narrow range under the applied load (i.e. at mid-span). This indicates that the fibres help control crack propagation. The figures also show that the fibres are effective in controlling the cracks even when the stirrups spacing was increased (the adverse effect of such increase can be seen as well).

4.4.4.2 Principal strain vectors

The principal strain vectors for the beams with $SI = 0\%$ are given in Figure 4.46, which shows that the addition of fibres led to reduced cracks in the beams. The beam without fibres failed with higher strain along the beam span, whereas the SFRC beams failed with the strains more concentrated at the mid-span of the beams.

The principal strain vectors for the beams with the reduction in the conventional shear reinforcement (see Figures 4.47 to 4.49) produced a similar trend to the beams with $SI = 0\%$, except for a few beams such as the one with $V_f = 2.5\%$ and $SI = 100\%$ which failed with strain vectors indicating a diagonal crack pattern extending from the support towards the middle of the beam span. Similarly, the beams with $V_f = 1.5\%$ and 1.5% with $SI = 200\%$ failed with strains vectors depicting a crack pattern covering a large area of the beam and not limited to a local zone near the load or supports.

The preceding results demonstrate the severity of cracking under reversed-cyclic loading and the potential of steel fibres to control crack opening and propagation.

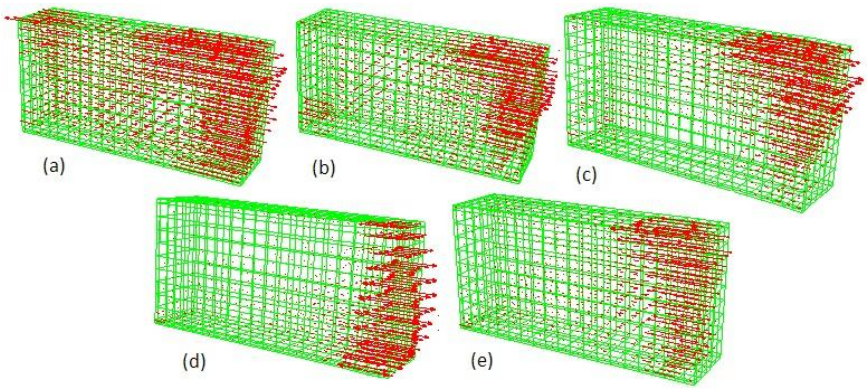


Figure 4.46: Principal strain vectors for Case Study 1(a)-C beams with $SI = 0\%$ and (a) $V_f = 0\%$, (b) $V_f = 1\%$, (c) $V_f = 1.5\%$, (d) $V_f = 2\%$ and (e) $V_f = 2.5\%$

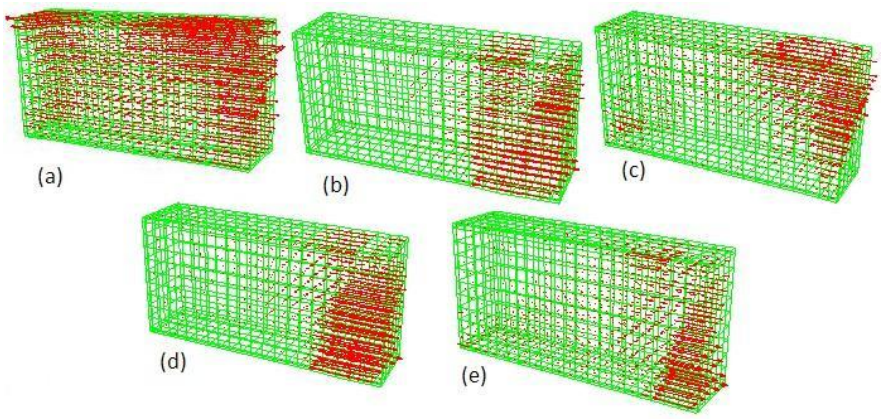


Figure 4.47: Principal strain vectors for Case Study 1(a)-C beams with SI $= 50\%$ and (a) $V_f = 0\%$, (b) $V_f = 1\%$, (c) $V_f = 1.5\%$, (d) $V_f = 2\%$ and (e) $V_f = 2.5\%$

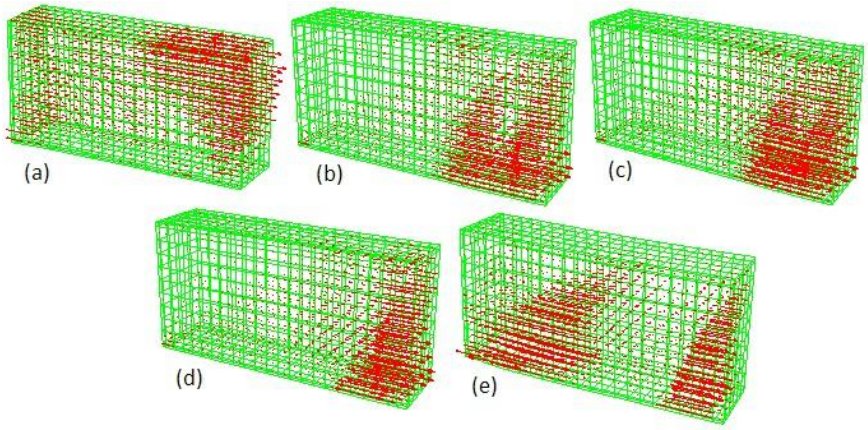


Figure 4.48: Principal strain vectors for Case Study 1(a)-C beams with $SI = 100\%$ and (a) $V_f = 0\%$, (b) $V_f = 1\%$, (c) $V_f = 1.5\%$, (d) $V_f = 2\%$ and (e) $V_f = 2.5\%$

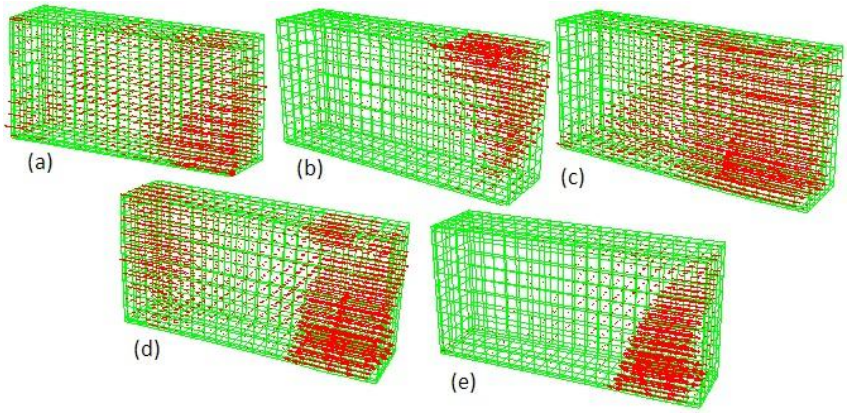


Figure 4.49: Principal strain vectors for Case Study 1(a)-C beams with $SI = 200\%$ and (a) $V_f = 0\%$, (b) $V_f = 1\%$, (c) $V_f = 1.5\%$, (d) $V_f = 2\%$ and (e) $V_f = 2.5\%$

4.4.4.3 Deflected shapes

The FE-based deformed shapes of the beams analysed in Case Study 1(a)-C are depicted schematically in Figures 4.50 to 4.53, which were taken at failure. The deformation was related to the direction of the cyclic load (i.e. upward or downward) and load level at failure.

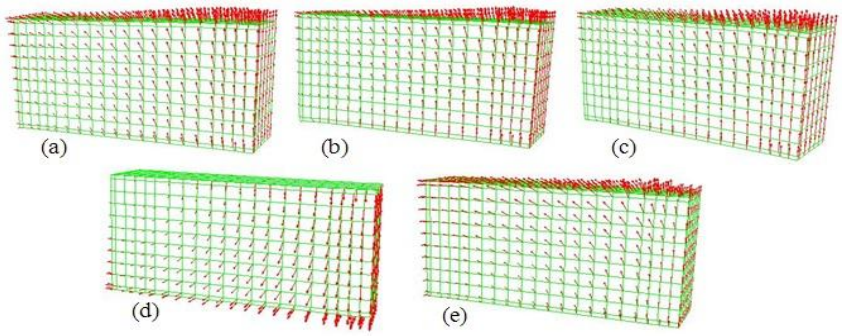


Figure 4.50: Deflected shapes for Case Study 1(a)-C beams with $SI = 0\%$ and (a) $V_f = 0\%$, (b) $V_f = 1\%$, (c) $V_f = 1.5\%$, (d) $V_f = 2\%$ and (e) $V_f = 2.5\%$

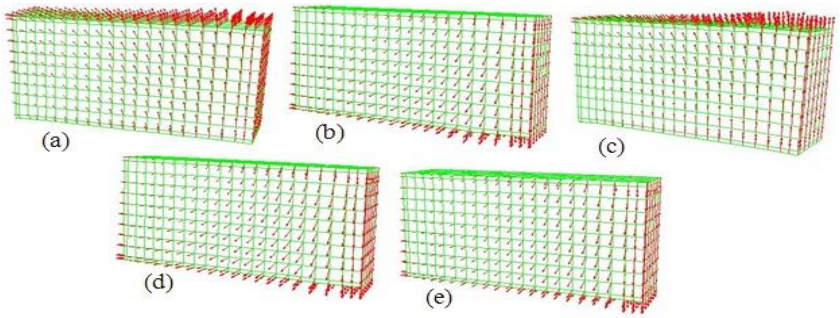


Figure 4.51: Deflected shapes for Case Study 1(a)-C beams with $SI = 50\%$ and (a) $V_f = 0\%$, (b) $V_f = 1\%$, (c) $V_f = 1.5\%$, (d) $V_f = 2\%$ and (e) $V_f = 2.5\%$

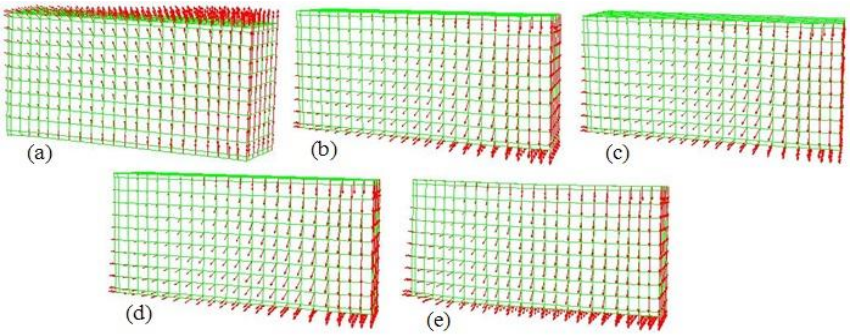


Figure 4.52: Deflected shapes for Case Study 1(a)-C beams with $SI = 100\%$ and (a) $V_f = 0\%$, (b) $V_f = 1\%$, (c) $V_f = 1.5\%$, (d) $V_f = 2\%$ and (e) $V_f = 2.5\%$

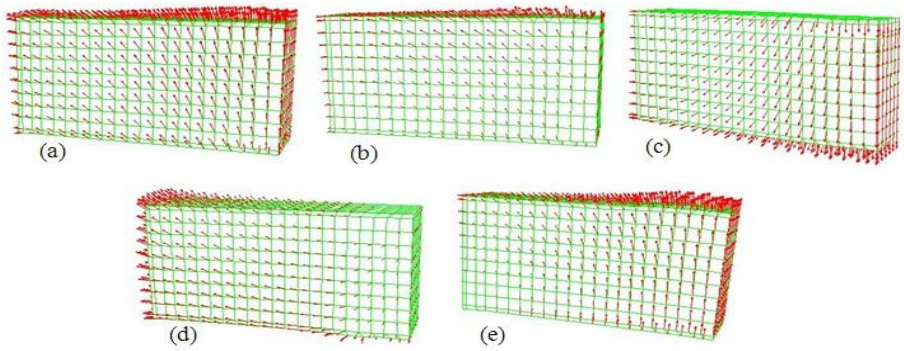


Figure 4.53: Deflected shapes for Case Study 1(a)-C beams with $SI = 200\%$ and (a) $V_f = 0\%$, (b) $V_f = 1\%$, (c) $V_f = 1.5\%$, (d) $V_f = 2\%$ and (e) $V_f = 2.5\%$

4.4.5 Comparative study with control specimen using non-dimensional ratios

An overall comparison was made between the beams analysed with various fibre dosages and increased stirrup spacing and the control beam specimen (CB), i.e. the beam with no fibres and full conventional shear reinforcement. The values of strength, ductility, energy absorption and number of cycles were normalised by dividing them by the corresponding values of the control specimen.

4.4.5.1 Strength ratio

There is an upward trend observed for the strength ratio for all beams as evident in Figure 4.54.

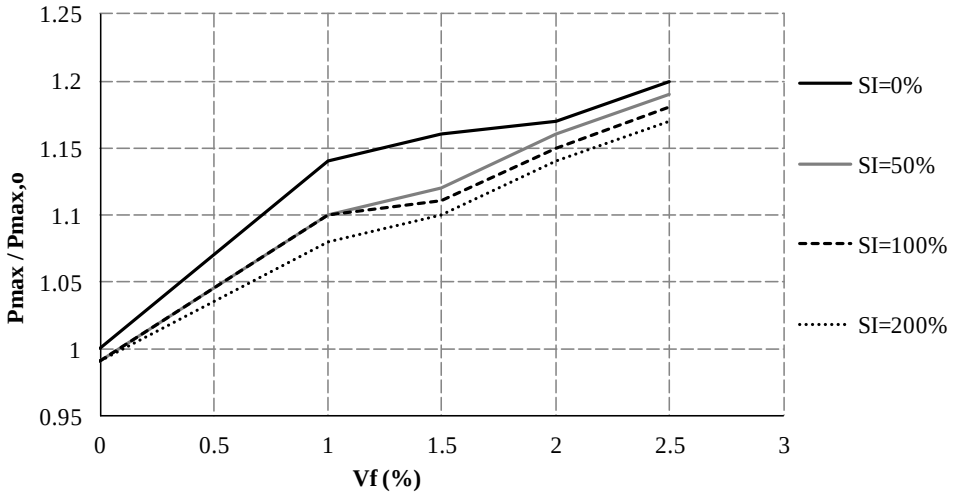


Figure 4.54: Ratio between the maximum load of each beam and that of the control specimen ($SI = 0\%, V_f = 0\%$) versus steel fibre volume fraction for Case Study 1(a)-C

The addition of fibres consistently leads to an enhancement in strength (the enhancement was by up to ~20% compared to the beams without fibres).

4.4.5.2 Ductility ratio

The ratio between the ductility ratio in each beam and that in the control beam is depicted in Figure 4.55. It is clear that fibres improve ductility if provided within certain optimum amounts (as excessive fibres will lead to a decrease in ductility as discussed earlier). The optimum fibre volume fractions was 1% for all beams except for the one with $SI = 200\%$ which required fibres at $V_f = 1.5\%$.

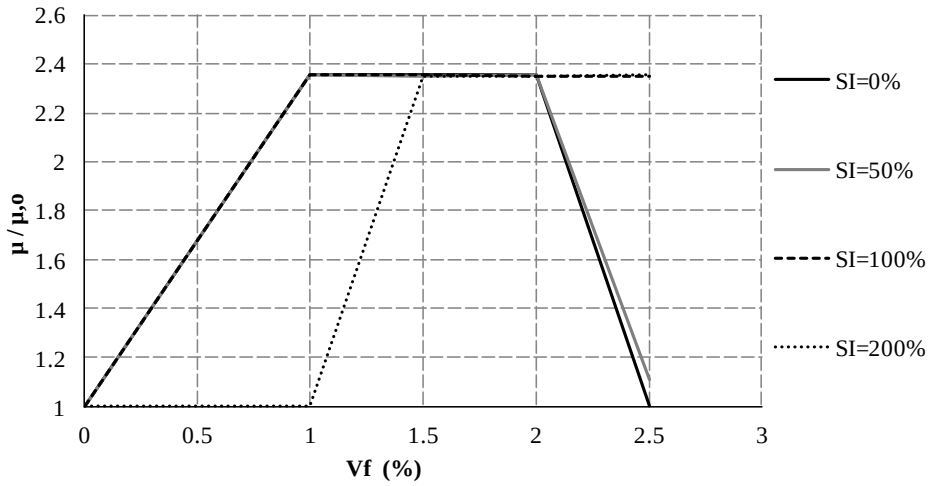


Figure 4.55: Ratio between the ductility ratio of each beam and that of the control specimen ($SI = 0\%, V_f = 0\%$) versus steel fibre volume fraction for Case Study 1(a)-C

The increase in ductility ratio was higher than double that associated with the control specimen, which is significant particularly for cyclic-loading conditions (which is a key feature in seismic action). This indicates the potential for fibres to enhance the structural response under cyclic/seismic loads. Energy absorption is another important consideration under such conditions and is discussed next.

4.4.5.3 Energy absorption ratio

The data for energy absorption ratio for the beams normalised to that in the control specimen is presented in Figure 4.56. There is an upward trend observed in the energy absorption ratio up to $V_f = 1.5\%$ for beam with $SI = 0\%$, 50%, and 100%, and $V_f = 2\%$ for beam with $SI = 200\%$. This confirms that optimum fibre contents should

be observed when adding fibres to enhance ductility and energy absorption. Furthermore, it can be seen that the energy absorption ratio for all SFRC beams (with $V_f = 1.5\%\sim2\%$) were 3.5~5 times higher than the energy absorption levels associated with the control specimen. This indicates the significant potential for fibres to improve the structural response under cyclic/seismic loads and their potential to reduce transverse reinforcement (and thus lessen any congestion due to such reinforcement, which is a common issue in seismic detailing).

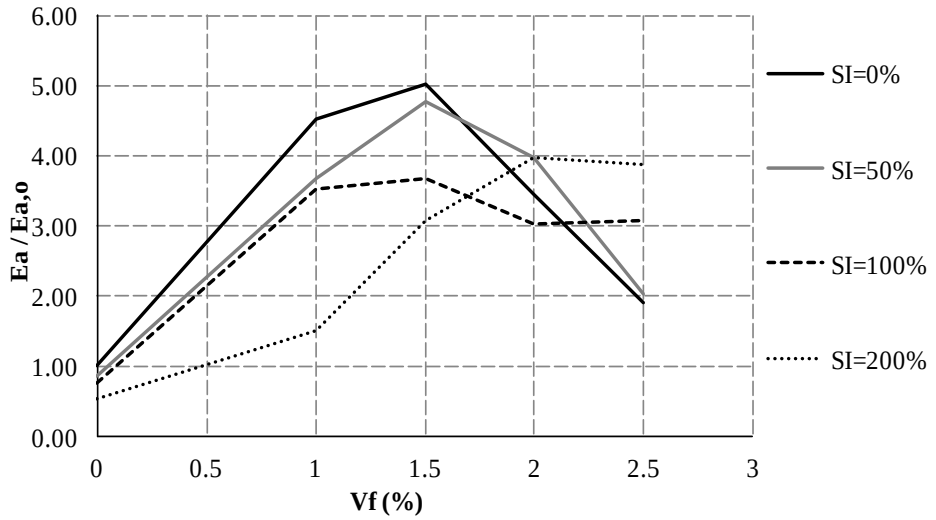


Figure 4.56: Ratio between the energy absorption of each beam and that of the control specimen ($SI = 0\%, V_f = 0\%$) versus steel fibre volume fraction for Case Study 1(a)-C

4.4.5.4 Number of cycles ratio

Figure 4.57 presents the ratio between the number of cycles obtained in each beam (N_c) and that in the control beam ($N_{c,0}$). The highest number of cycles ratio for the beams with $SI = 0\%, 50\%$, and 100% were found with $V_f = 1.5\%$, while for the beams with $SI = 200\%$ this was obtained with $V_f = 2\%$. These results confirm the preceding findings of ductility and energy absorption parametric studies, particularly in terms of improving the structural response under cyclic/seismic loads.

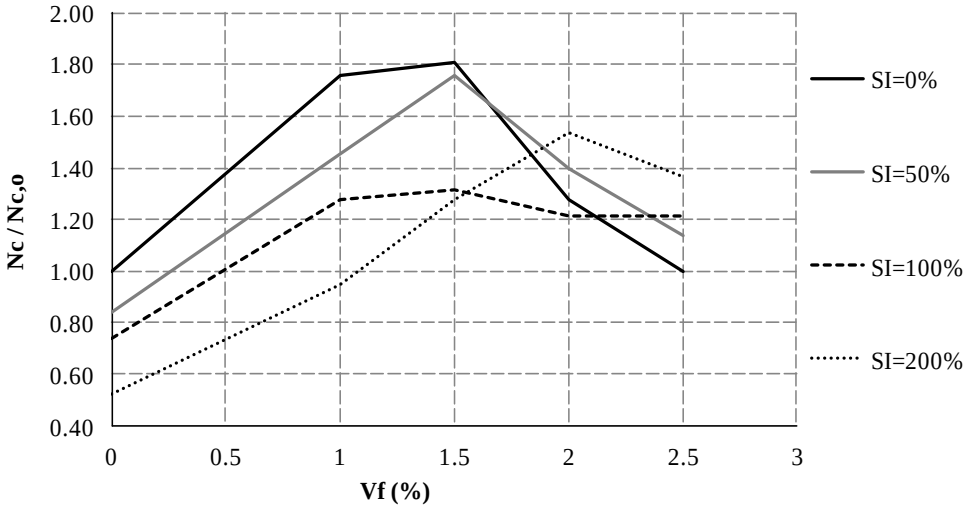


Figure 4.57: Ratio between the maximum number of cycles obtained before failure of each beam and that of the control specimen ($SI = 0\%, V_f = 0\%$) versus steel fibre volume fraction for Case Study 1(a)-C

4.5 Case Study 1(b): Calibration with Campione et al. (2006) experimental work

A series of SFRC simply supported beams with and without stirrups were tested under monotonic loading by Campione et al. (2006) to study their shear behaviour. Steel fibres were added to investigate whether or not fibres can partially or fully substitute transverse stirrups and retain the same level of shear resistance.

Two SFRC beams tested by Campione et al. (2003, 2006), were selected to be calibrated and then adopted for the ensuing parametric studies for the present Case Study 1(b). The beams dimensions and reinforcement and loading arrangements are shown in Figure 4.58.

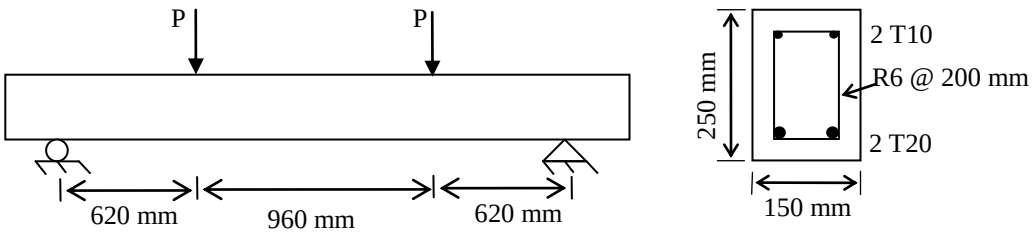


Figure 4.58: Dimensions, loading arrangement and reinforcement detailing of the beams (adapted Campione et al, 2006)

One of the beams was reinforced with stirrups while the other was without any stirrups. The concrete compressive strength was 41.2 MPa, whilst the tensile strength was

assumed to be 9% (i.e. 3.7 MPa) of the compressive strength. The yield stress for main bars and stirrups were 610 MPa and 510 MPa, respectively. Steel fibres used were hooked-end with 30 mm length and 0.5 mm the diameter added at a volume fraction of $V_f = 1\%$. The beams selected for calibration work had a shear span to effective depth ratio of $a/d = 2.8$, where a is the shear span and d is the effective depth of the beam.

Taking advantage of the symmetrical conditions at the mid-span of the beam (see Figure 4.59), for FE analysis purposes only half of the beam was modelled using ABAQUS. The mesh adopted has an element size of 20 mm. Elastic steel plates with 20 mm thickness were added at the support and loading region to mimic the experimental work and help avoid premature localised failure.

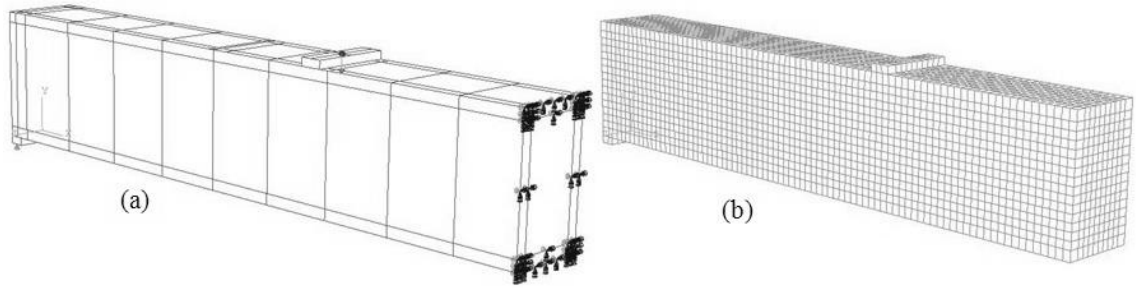


Figure 4.59: Symmetrical half of the beam modelled using ABAQUS with (a) defined boundary conditions at middle-side view (plane of symmetry) and (b) FE mesh

The load was applied gradually using a displacement-based method and the input data is given in Figure 4.60. The tensile stress-strain relation adopted for the calibration work is presented in Figure 4.61 with the key parameters defined in Table 4.18 (b).

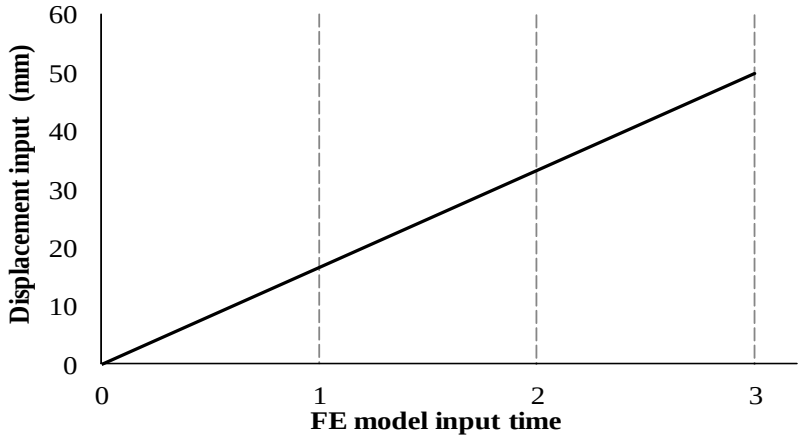


Figure 4.60: Load history input data for Case Study 1(b)

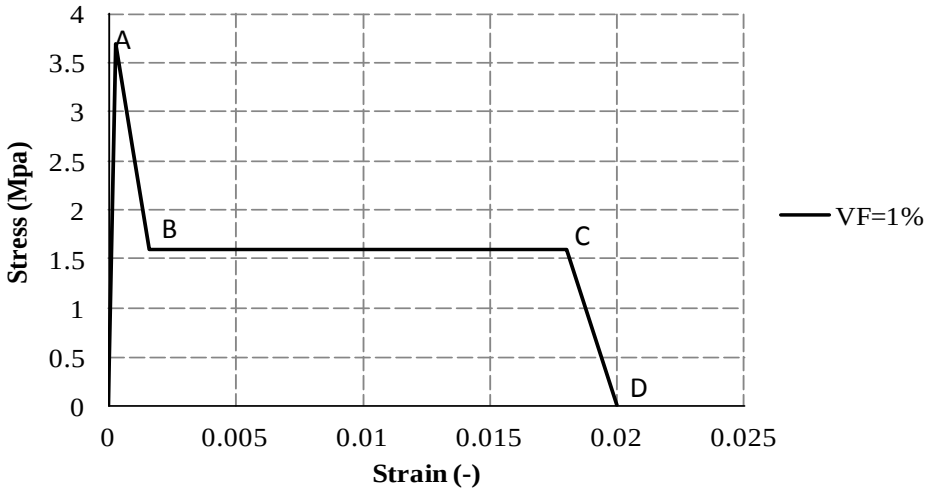


Figure 4.61: Tensile stress-strain diagram adopted for calibration work of Campione et al. (2006) beams\

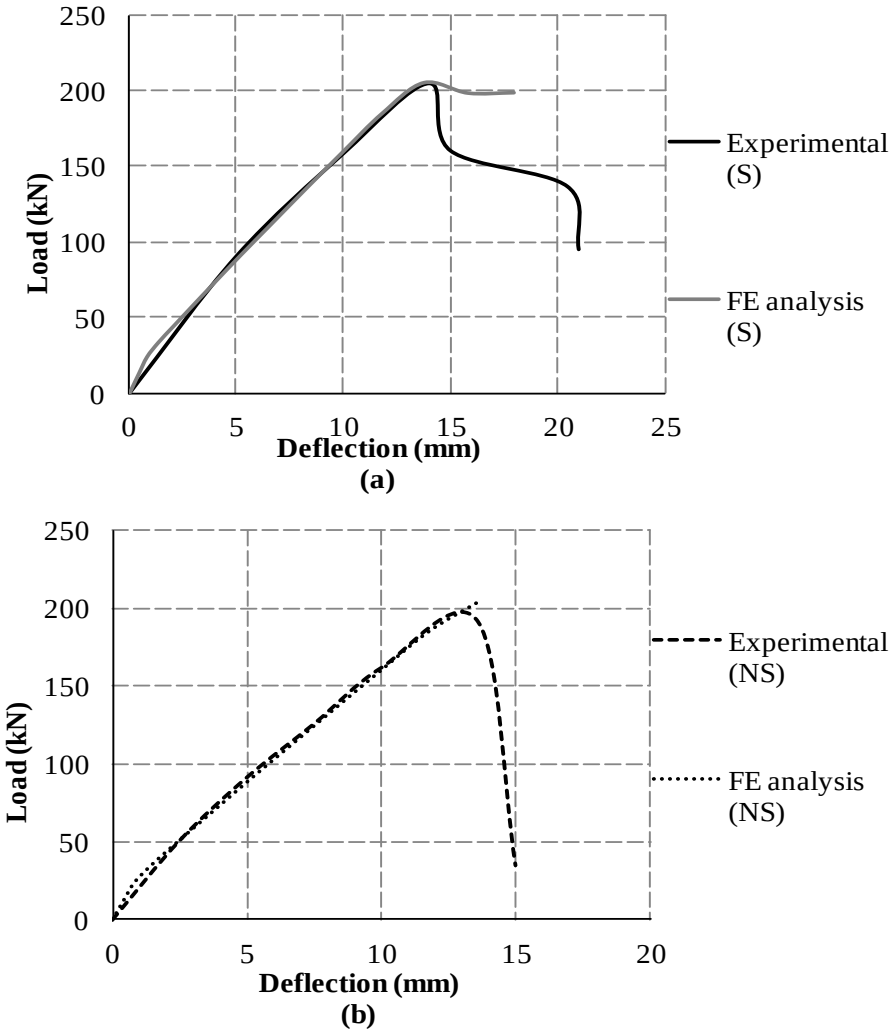


Figure 4.62: Calibration results for Case Study 1(b) for beams (a) with stirrups (i.e. S) and (b) without stirrups (i.e. NS) analysed under monotonic loading

A comparison between the experimental and numerical results is presented in Figure 4.62 for both beams with and without stirrups (denoted by symbols S and NS, respectively). The key values are summarised in Table 4.17. There is good agreement between the two sets of data.

Beam	P_y (kN)	δ_y (mm)	P_u (kN)	δ_u (mm)	P_{max} (kN)	δ_{Pmax} (mm)	$\mu = \frac{\delta_u}{\delta_y}$
Experimental (S)	205.0	14.0	174.25	15.0	205.0	14.0	1.07
FE analysis (S)	205.77	13.76	199.14	17.97	205.77	13.76	1.31
Experimental (NS)	191.8	13.6	191.8	13.6	191.8	13.6	1
FE analysis (NS)	205.44	13.75	205.44	13.75	205.44	13.75	1

Table 4.17: Calibration results summary for Case Study 1(b)

FE-based kinetic energy results are depicted in Figure 4.63 and a sudden large increase in energy was taken to indicate failure (i.e. presence of large/extensive cracks that impair structural integrity).

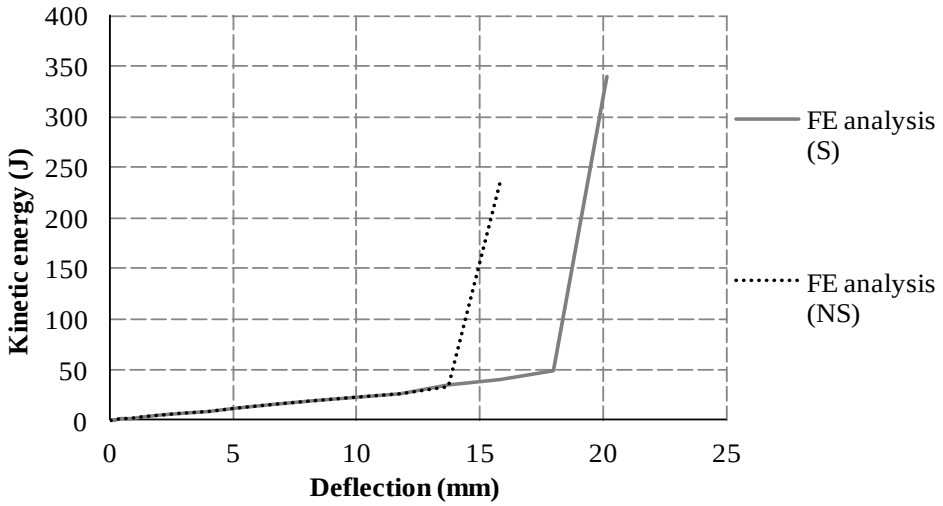


Figure 4.63: Kinetic energy plots to determine failure for calibration work in Case Study 1(b)

4.6 Case Study 1(b): Parametric study on shear failure of simply supported beams under monotonic loading

Following the calibration work, parametric studies were carried out incorporating two key parameters, the increase in spacing between shear stirrups (SI) and steel fibres volume fraction (V_f). The beams were modelled with reduced shear reinforcement in order to induce a shear mode of failure. It is interesting to examine whether or not the addition of fibres has led to a more ductile mode of failure. Therefore, beams considered with $SI = 0\%, 50\%, 100\%$ and with no stirrups (NS). This was coupled with fibres provided at $V_f = 0\%$, 1%, 1.5%, 2% and 2.5%.

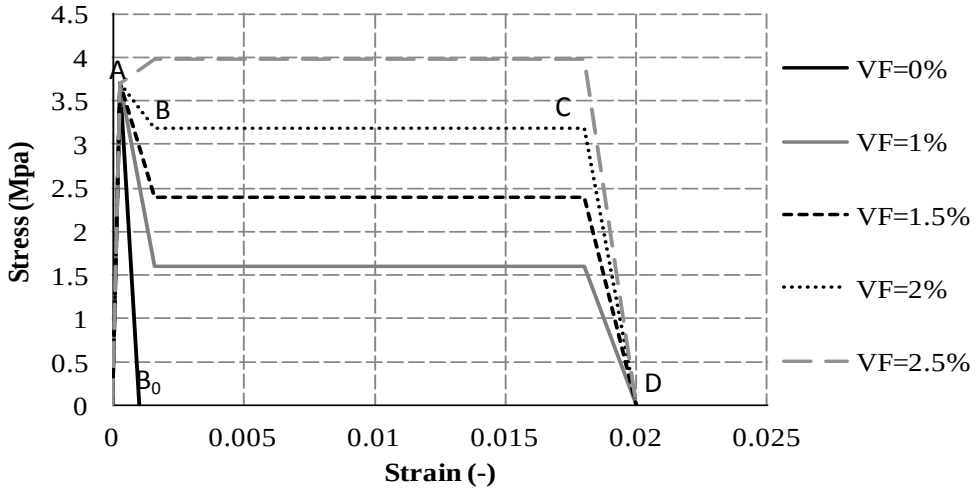


Figure 4.64: Stress-strain relations in tension for parametric studies of Case Study 1(b)

The tensile stress-strain diagram for SFRC beams is shown in Figure 4.64, and the key points on the curves are summarised in Table 4.18 (a) and (b). Beams with different stirrup spacing and fibre contents were analysed under monotonic loading applied gradually as defined in Figure 4.60. The results are discussed next.

Point	Strain (‰)	Stress, V_f=0.0% (MPa)
Origin	0	0
Peak tensile stress (A)	0.247	3.70
Ultimate tensile strain (B_0)	1.0	0

Table 4.18(a): Tensile stress-strain parameters for plain concrete for Case Study 1(b)

Point	Strain (‰)	Stress, V_f=1.0% (MPa)	Stress, V_f=1.5% (MPa)	Stress, V_f=2.0% (MPa)	Stress, V_f=2.5% (MPa)
Origin	0	0	0	0	0
Peak tensile stress (A)	0.247	3.70	3.70	3.7	3.70
Beginning of plateau (B)	1.59	1.59	2.39	3.18	3.98
End of plateau (C)	18	1.59	2.39	3.18	3.98
Ultimate tensile strain (D)	20	0	0	0	0

Table 4.18(b): Tensile stress-strain parameters for SFRC for Case Study 1(b)

4.6.1 Load-deflection curves

The load-deflection curves for Case Study 1(b) with increased in stirrup spacing of $SI = 0\%$, $SI = 50\%$, $SI = 100\%$ and no stirrup (NS) are presented in Figures 4.65, 4.66, 4.67 and 4.68, respectively. In addition, a summary of the key load values and their respective deflections is provided in Tables 4.19, 4.20, 4.21 and 4.22. The load-deflection curves show that the beam without fibres failed early confirming a brittle mode of failure associated with shear strength deficiency. In contrast, there is a gradual increase in strength and ductility as the fibres content is increased. The stiffness has also increased noticeably in comparison to the case without fibres, indicating that SFRC beams deflect less than their counterparts without fibres. This suggests that there are clear benefits of adding fibres at both the serviceability and ultimate limit states, which are important design considerations.

4.6.2 Strength

The load-deflection curves show that the load-carrying capacity of the beams increased as more fibres was added. The beam without fibres and $SI = 0\%$ failed at a maximum load (P_{max}) of 197.27 kN and ultimate deflection (δ_u) of 17.97 mm. This beam was considered as the reference beam and was named the control beam specimen (*CB*) to be compared with the remaining beams in the parametric studies. The increase in the P_{max} of the SFRC beams compared to that in the control specimen was up to an average of 16% in all beams with different stirrup arrangements.

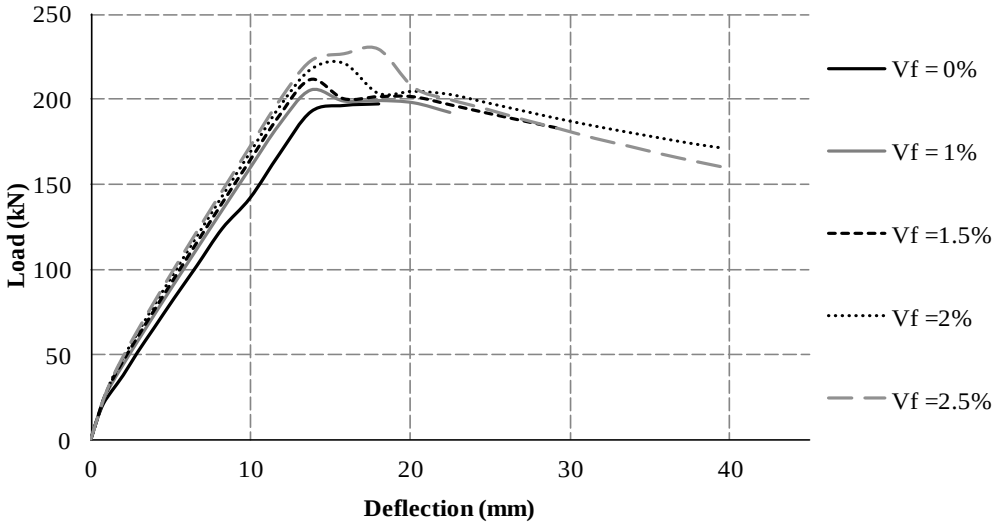


Figure 4.65: Load-deflection curves for Case Study 1(b) with $SI = 0\%$

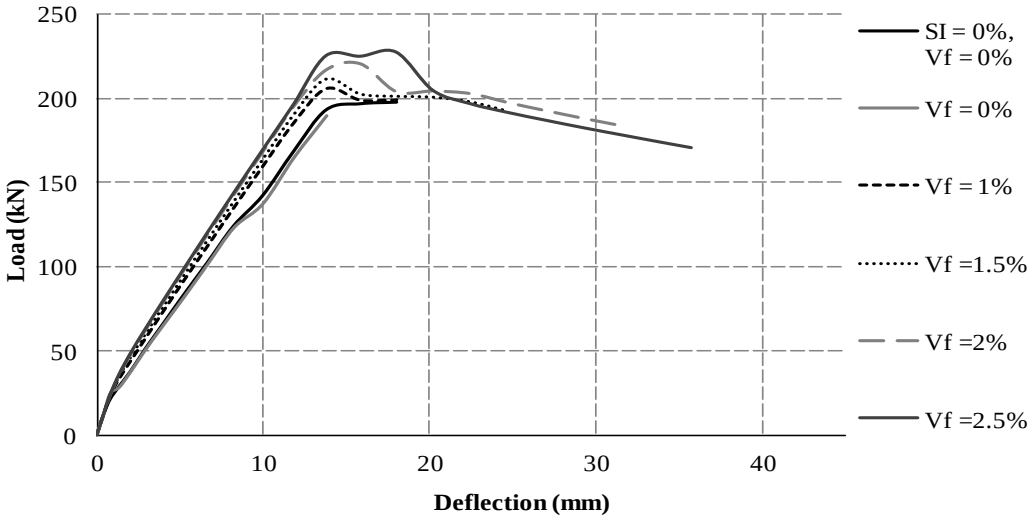


Figure 4.66: Load-deflection curves for Case Study 1(b) with $SI = 50\%$

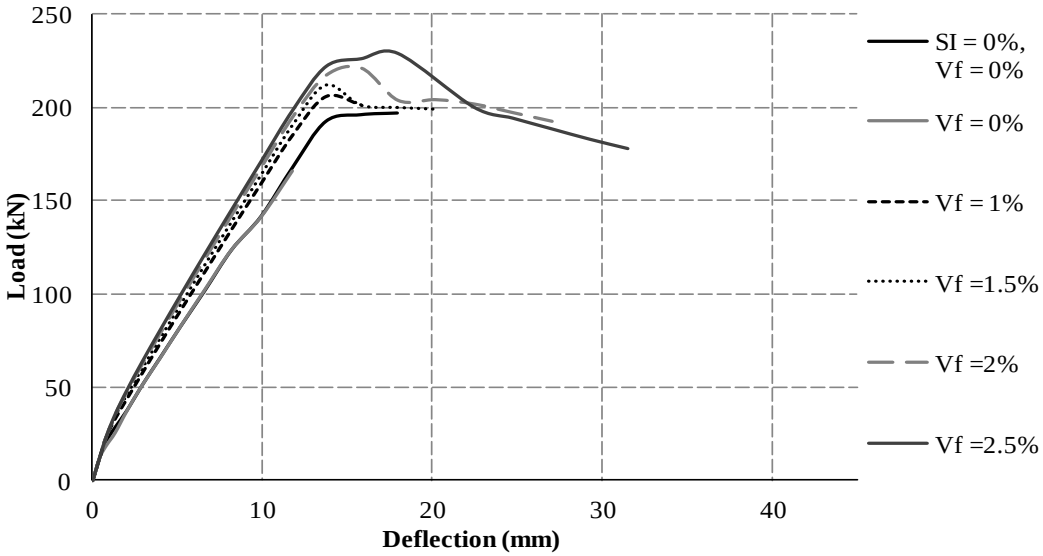


Figure 4.67: Load-deflection curves for Case Study 1(b) with $SI = 100\%$

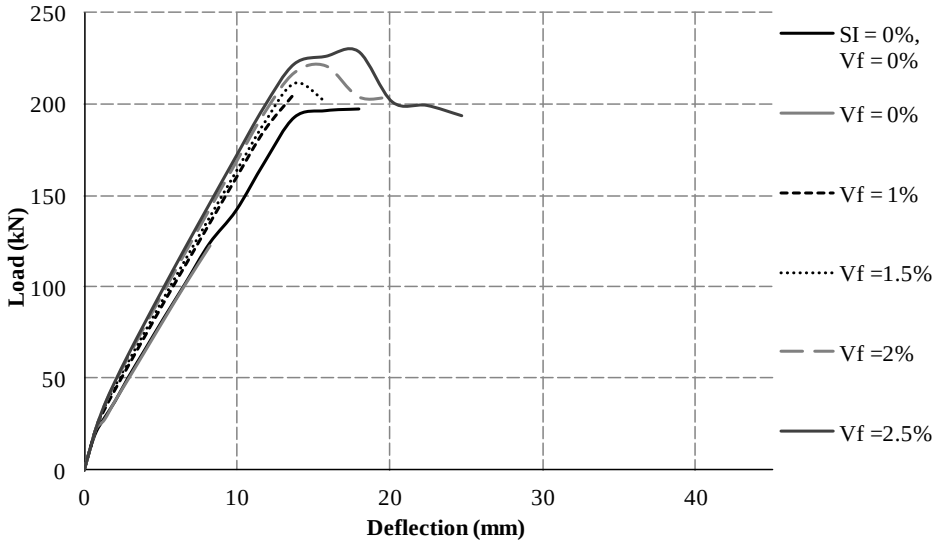


Figure 4.68: Load-deflection curves for Case Study 1(b) with no stirrups (NS)

V_f (%)	P_y (kN)	δ_y (mm)	P_u (kN)	δ_u (mm)	P_{max} (kN)	δ_{Pmax} (mm)	$\mu = \frac{\delta_u}{\delta_y}$
0	192.77	13.76	197.27	17.97	197.27	17.97	1.31
1	205.78	13.76	192.58	22.46	205.76	13.76	1.63
1.5	211.69	13.76	182.9	29.3	211.69	13.76	2.13
2	217.12	13.76	187.63	29.0	220.74	15.82	2.11
2.5	222.26	13.76	194.83	24.5	229.21	17.98	1.78

Table 4.19: Results summary for Case Study 1(b) for beams with $SI = 0\%$

V_f (%)	P_y (kN)	δ_y (mm)	P_u (kN)	δ_u (mm)	P_{max} (kN)	δ_{Pmax} (mm)	$\mu = \frac{\delta_u}{\delta_y}$
0 (CB)	192.77	13.76	197.27	17.97	197.27	17.97	1.31
0	189.94	13.76	189.94	13.76	189.94	13.76	1
1	205.77	13.76	199.14	17.97	205.77	13.76	1.31
1.5	211.59	13.76	192.36	24.73	211.59	13.76	1.8
2	217.03	13.76	187.62	30.0	220.73	15.82	2.18
2.5	222.23	13.76	193.15	25.3	227.23	17.96	1.84

Table 4.20: Results summary for Case Study 1(b) for beams with $SI = 50\%$

V_f (%)	P_y (kN)	δ_y (mm)	P_u (kN)	δ_u (mm)	P_{max} (kN)	δ_{Pmax} (mm)	$\mu = \frac{\delta_u}{\delta_y}$
0 (CB)	192.77	13.76	197.27	17.97	197.27	17.97	1.31
0	165.58	11.8	165.58	11.8	165.58	11.8	1
1	205.65	13.76	201.16	15.82	205.65	13.76	1.15
1.5	211.68	13.76	198.8	20.2	211.68	13.76	1.47
2	217.09	13.76	192.32	27.03	220.75	15.82	1.96
2.5	222.3	13.76	194.82	24.5	229.2	17.97	1.78

Table 4.21: Results summary for Case Study 1(b) for beams with $SI = 100\%$

V_f (%)	P_y (kN)	δ_y (mm)	P_u (kN)	δ_u (mm)	P_{max} (kN)	δ_{Pmax} (mm)	$\mu = \frac{\delta_u}{\delta_y}$
0 (CB)	192.77	13.76	197.27	17.97	197.27	17.97	1.31
0	122.74	8.2	122.74	8.2	122.74	8.2	1
1	205.44	13.75	205.44	13.75	205.44	13.75	1
1.5	211.49	13.75	200.91	15.81	211.49	13.75	1.15
2	216.9	13.75	203.71	20.18	220.61	15.81	1.47
2.5	222.18	13.75	194.78	24.3	229.15	17.96	1.77

Table 4.22: Results summary for Case Study 1(b) for beams with no stirrups (NS)

In addition, the load at yield (P_y) increased by up to 15% higher than that in the control beam. The enhancement to shear strength due to fibres confirms their potential to substitute for a reduction in conventional transverse reinforcement. The steel fibres extend across diagonal shear cracks (induced by tensile principal stresses) and contribute to shear capacity by resisting these diagonal tension stresses.

4.6.3 Ductility

The ductility of the beams can be determined from the ultimate deflection at failure (δ_u). The latter is associated with the ultimate load, which was taken as the minimum of the load at failure or 85% of the maximum load (i.e. $P_u \geq 0.85P_{max}$). This is because of the post-peak "softening" trend observed on the load-deflection curves and thus a practical limit is put on the residual strength (i.e. P_u) to be adopted. The increases of δ_u in the SFRC beams compared to that in the control specimen was up to 63%, 67%, 50% and 12%, for the beams with $SI = 0\%, 50\%, 100\%$ and no stirrups, respectively. The results show that the addition of fibres enhances the ductility of the beams, even in the

beams with no stirrups (albeit the enhancement in the latter is considerably less than the case with stirrups indicating the severity of shear reinforcement reduction when stirrups were completely removed).

4.6.4 Cracking patterns

The principal strain contours and vectors and deflected shapes at failure were studied and the data provided insight into cracking formation and patterns.

4.6.4.1 Principal strain contours

Figures 4.69 to 4.72 depict the principal strain contours for the beams analysed in Case Study 1(b). The strain contours were arranged so that grey areas denote zones where the strains exceed 0.001 (i.e. tensile cracking strain) for beams without fibres and 0.02 (i.e. fibres pull-out strain) for SFRC beams. Black contour regions where used to highlight areas where the compressive strain is higher than that of concrete (i.e. -0.0035).

The figures show that the fibres led to a reduction in crack formation and propagation. Pull-out failure of fibres occurred at limited zones. These zones in the SFRC beams were not at the same location, however they always occurred in a region between the lateral point load (*P*) and the beam mid-span. This is because the bending moment is constant along this region and there is no single peak moment to induce a fixed failure point. More than one small crack formed in this region. Throughout the analysis, only one of these small cracks developed earlier will continue to propagate into a large one. This led to a different location for the single main crack at failure in the beams.

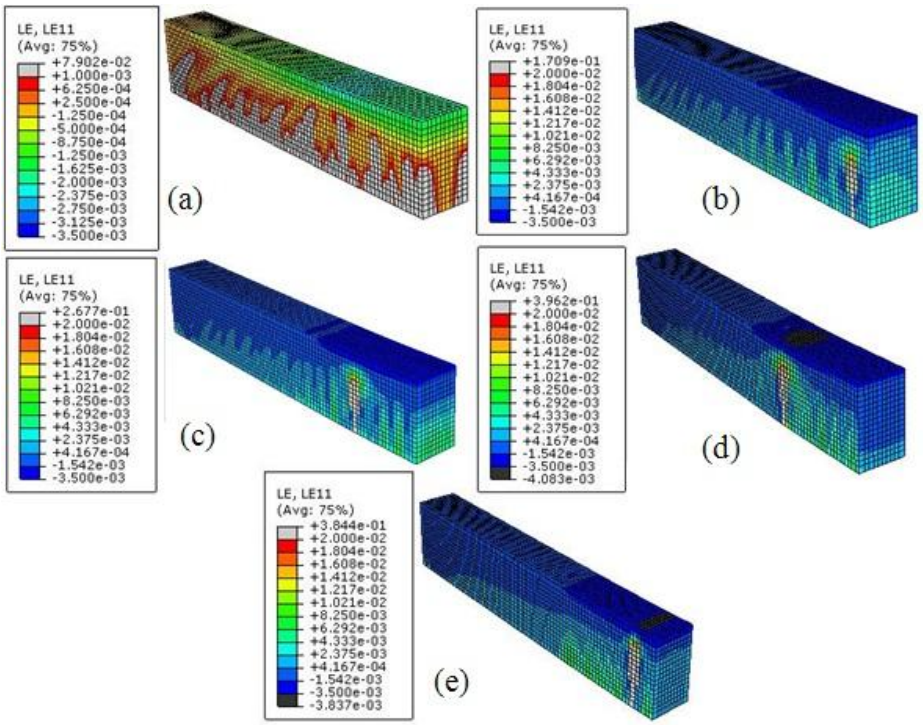


Figure 4.69: Principal strain contours for Case Study 1(b) beams with $SI = 0\%$ and (a) $V_f = 0\%$, (b) $V_f = 1\%$, (c) $V_f = 1.5\%$, (d) $V_f = 2\%$ and (e) $V_f = 2.5\%$

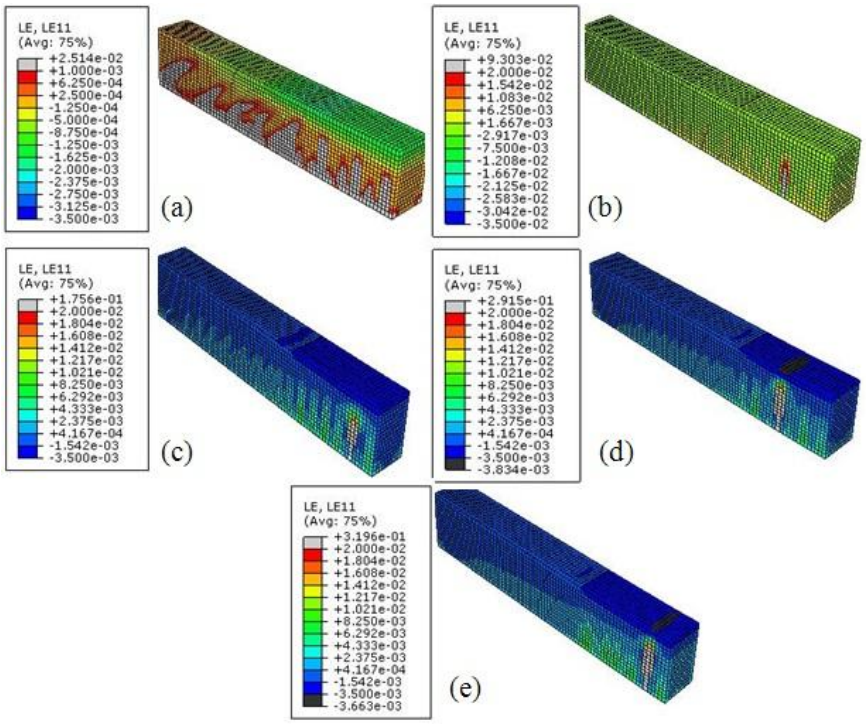


Figure 4.70: Principal strain contours for Case Study 1(b) beams with $SI = 50\%$ and (a) $V_f = 0\%$, (b) $V_f = 1\%$, (c) $V_f = 1.5\%$, (d) $V_f = 2\%$ and (e) $V_f = 2.5\%$

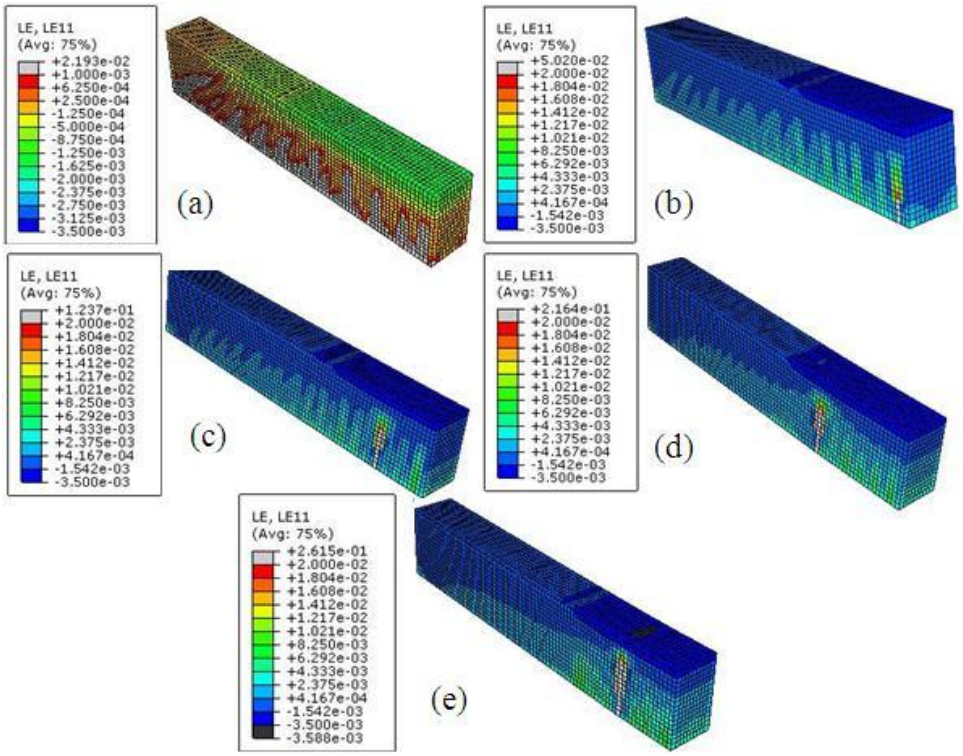


Figure 4.71: Principal strain contours for Case Study 1(b) beams with $SI = 100\%$ and (a) $V_f = 0\%$, (b) $V_f = 1\%$, (c) $V_f = 1.5\%$, (d) $V_f = 2\%$ and (e) $V_f = 2.5\%$

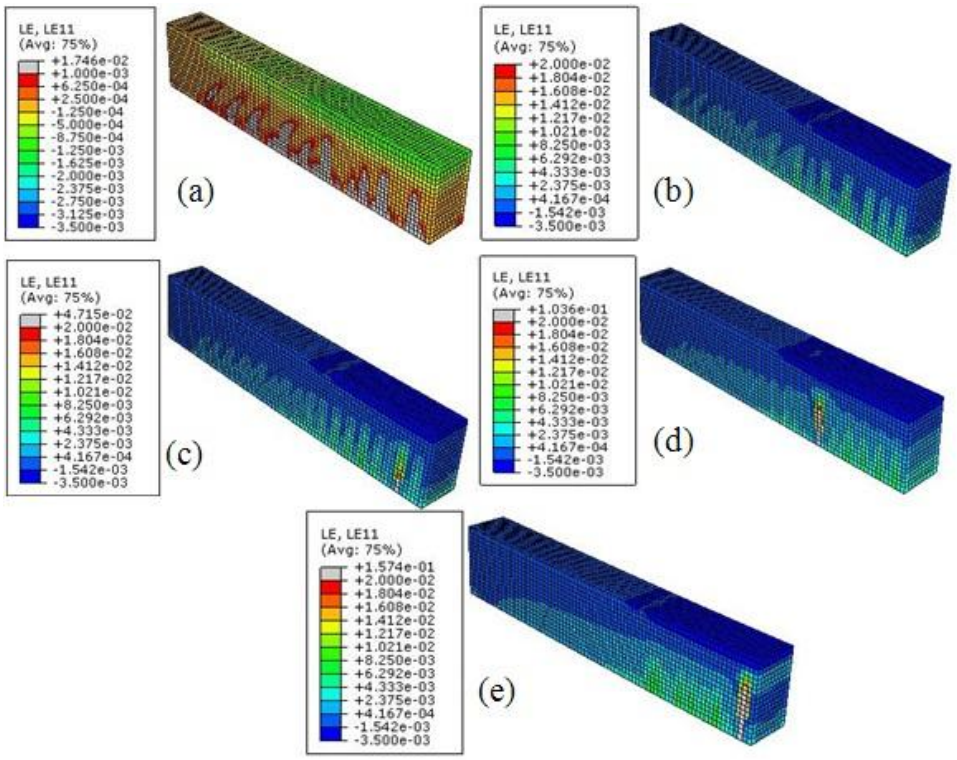


Figure 4.72: Principal strain contours for Case Study 1(b) beams with no stirrups (NS) and (a) $V_f = 0\%$, (b) $V_f = 1\%$, (c) $V_f = 1.5\%$, (d) $V_f = 2\%$ and (e) $V_f = 2.5\%$

4.6.4.2 Principal strain vectors

The principal strain vectors for the beams with $SI = 0\%, 50\%, 100\%$ and no stirrups are presented in Figures 4.73, 4.74, 4.75 and 4.76, respectively. It is interesting to note that viewing the beams in each different stirrup arrangement, from $V_f = 0\%$ to $V_f = 2.5\%$ depicts the principal strain vectors showing the change in the mode of failure. This indicates the effectiveness of steel fibres in bridging and controlling cracks.

In the beams without fibres, the concentration of principal strain vectors was high indicating a crack pattern that is diagonal and covers the whole of the beam. The diagonal pattern in the beams without fibres deteriorated as the stirrups spacing was increased. The diagonal pattern is characteristic of a shear (and brittle) mode of failure. The addition of fibres, on the other hand, led to a change in crack patterns which became more concentrated in limited regions near the beam mid-span, which indicates a flexural (and ductile) failure mode. It is interesting to note that for beams with no stirrups, the addition of fibres by up to $V_f = 1\%$ did not seem to alter the failure mode to the desired ductile one. This highlights the severity of the reduction in shear reinforcement when the stirrups were removed completely, which required higher amounts of fibres (i.e. $V_f \geq 1.5\%$) in order to improve the crack pattern and hence the failure mode. These findings were confirmed by comparing the FE predictions to design code estimates as discussed in subsequent section of this chapter. Thus it can be concluded that steel fibres have the potential to substitute for a reduction in conventional transverse shear reinforcement.

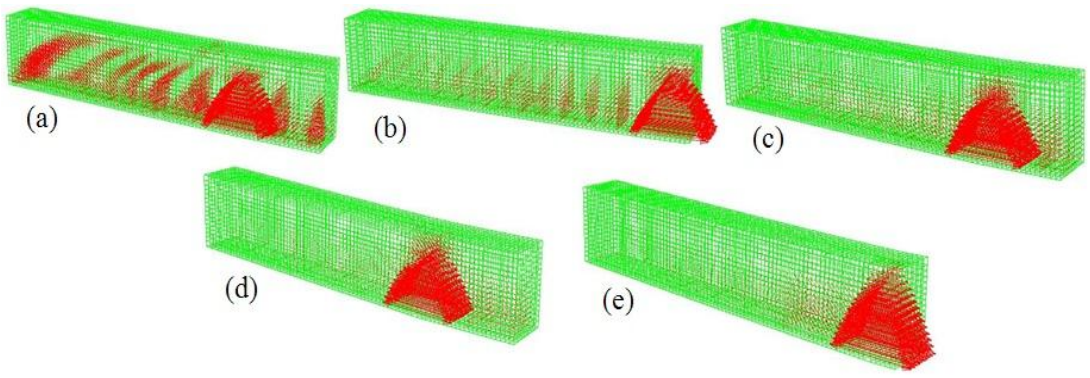


Figure 4.73: Principal strain vectors for Case Study 1(b) beams with $SI = 0\%$ and (a) $V_f = 0\%$, (b) $V_f = 1\%$, (c) $V_f = 1.5\%$, (d) $V_f = 2\%$ and (e) $V_f = 2.5\%$

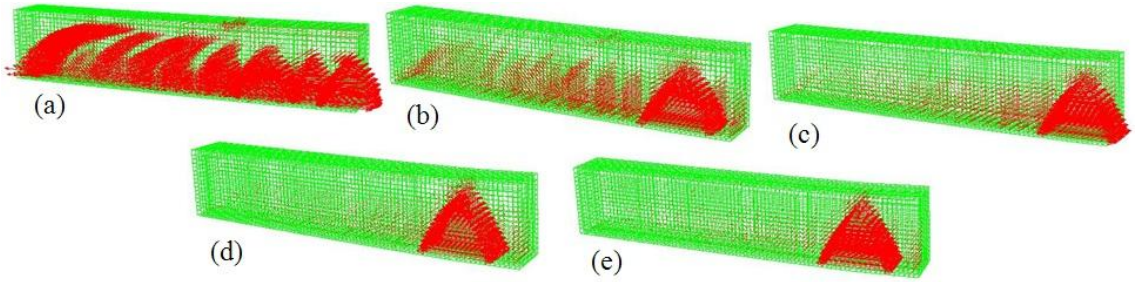


Figure 4.74: Principal strain vectors for Case Study 1(b) beams with $SI = 50\%$ and (a) $V_f = 0\%$, (b) $V_f = 1\%$, (c) $V_f = 1.5\%$, (d) $V_f = 2\%$ and (e) $V_f = 2.5\%$

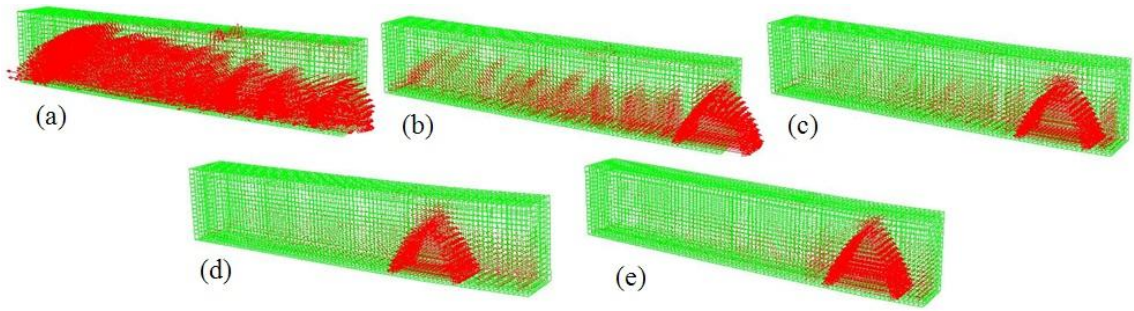


Figure 4.75: Principal strain vectors for Case Study 1(b) beams with $SI = 100\%$ and (a) $V_f = 0\%$, (b) $V_f = 1\%$, (c) $V_f = 1.5\%$, (d) $V_f = 2\%$ and (e) $V_f = 2.5\%$

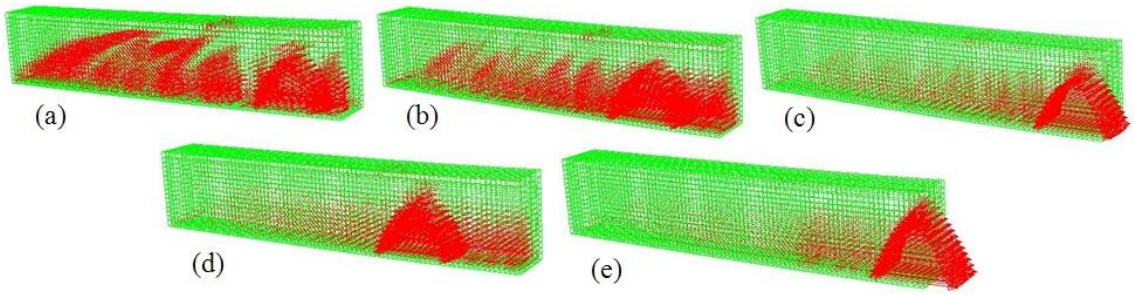


Figure 4.76: Principal strain vectors for Case Study 1(b) beams with no stirrups (NS) and (a) $V_f = 0\%$, (b) $V_f = 1\%$, (c) $V_f = 1.5\%$, (d) $V_f = 2\%$ and (e) $V_f = 2.5\%$

4.6.4.3 Deflected shapes

Deflected shapes of the beams analysed in Case Study 1(b) are depicted schematically in Figures 4.77 to 4.80 and they are consistent with the support and loading conditions.

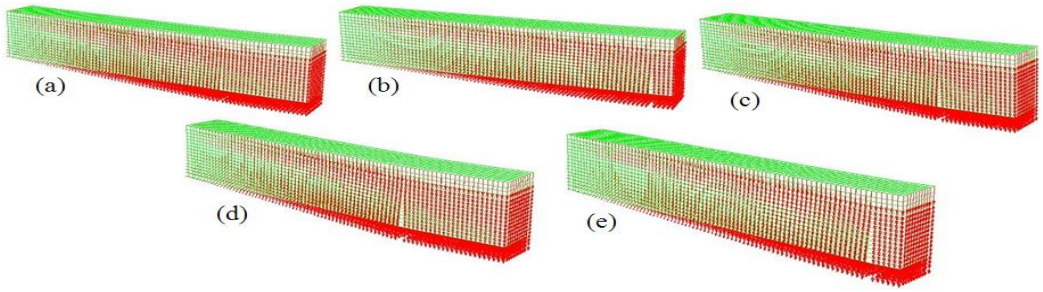


Figure 4.77: Deflected shapes for Case Study 1(b) beams with $SI = 0\%$ and (a) $V_f = 0\%$, (b) $V_f = 1\%$, (c) $V_f = 1.5\%$, (d) $V_f = 2\%$ and (e) $V_f = 2.5\%$

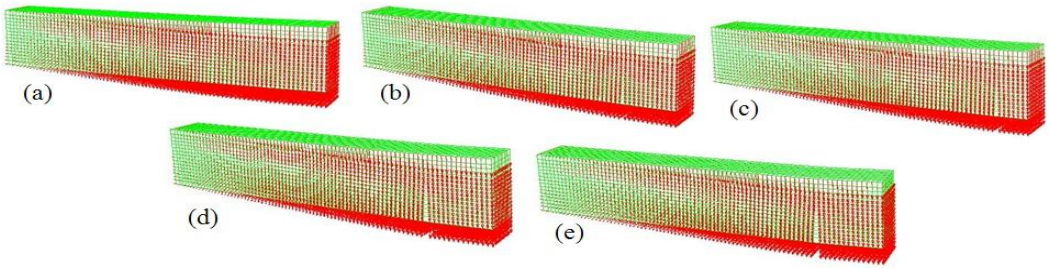


Figure 4.78: Deflected shapes for Case Study 1(b) beams with $SI = 50\%$ and (a) $V_f = 0\%$, (b) $V_f = 1\%$, (c) $V_f = 1.5\%$, (d) $V_f = 2\%$ and (e) $V_f = 2.5\%$

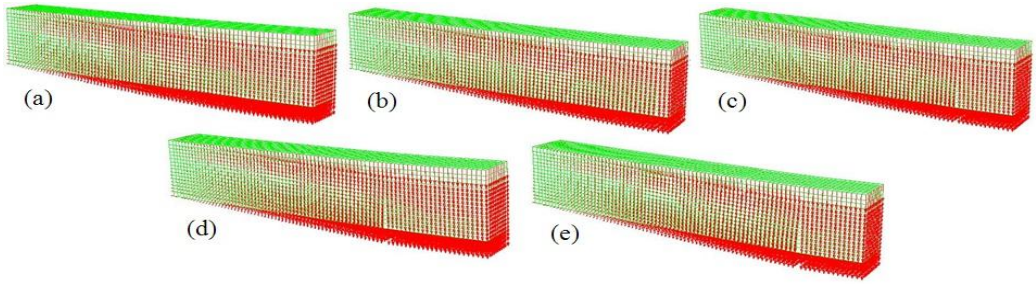


Figure 4.79: Deflected shapes for Case Study 1(b) beams with $SI = 100\%$ and (a) $V_f = 0\%$, (b) $V_f = 1\%$, (c) $V_f = 1.5\%$, (d) $V_f = 2\%$ and (e) $V_f = 2.5\%$

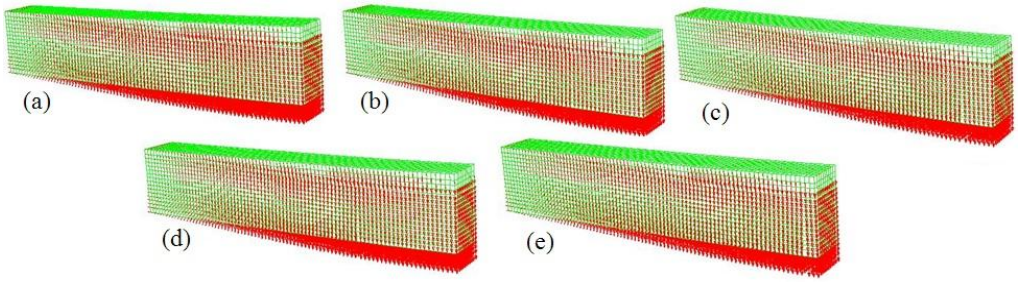


Figure 4.80: Deflected shapes for Case Study 1(b) beams with no stirrups (NS) and (a) $V_f = 0\%$, (b) $V_f = 1\%$, (c) $V_f = 1.5\%$, (d) $V_f = 2\%$ and (e) $V_f = 2.5\%$

4.6.5 Comparative study with control specimen using non-dimensional ratios

This section discusses the overall comparison made between the beams analysed with various fibre dosages and increased stirrup spacing and the control beam specimen (i.e. the beam with no fibres and full conventional shear reinforcement).

4.6.5.1 Strength ratio

The ratios between the maximum load (P_{max}) and yield load (P_y) for each beam and that in the control beam specimen are given in Figures 4.81 and 4.82, respectively. Similar pattern were observed from these two figures. Beams without fibres (i.e. $V_f = 0\%$) showed a decrease in both maximum and yield ratios as the stirrups spacing were increased. Inclusion of steel fibres, on the hand, improved both ratios consistently. The increase in both $P_{max}/P_{max,0}$ and $P_y/P_{y,0}$ ratios was by up to ~15%. Adding fibres at $V_f = 1\%$ seemed to restore the strength level of the control specimen, with more fibres enhancing the strength further.

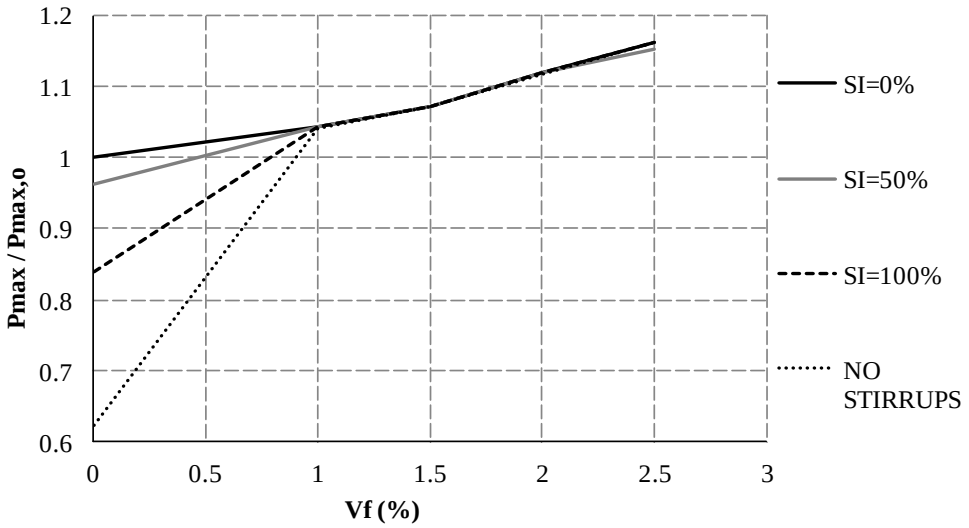


Figure 4.81: Ratio between the maximum load and that in the control specimen ($SI = 0\%, V_f = 0\%$) versus steel fibre volume fraction for Case Study 1(b)

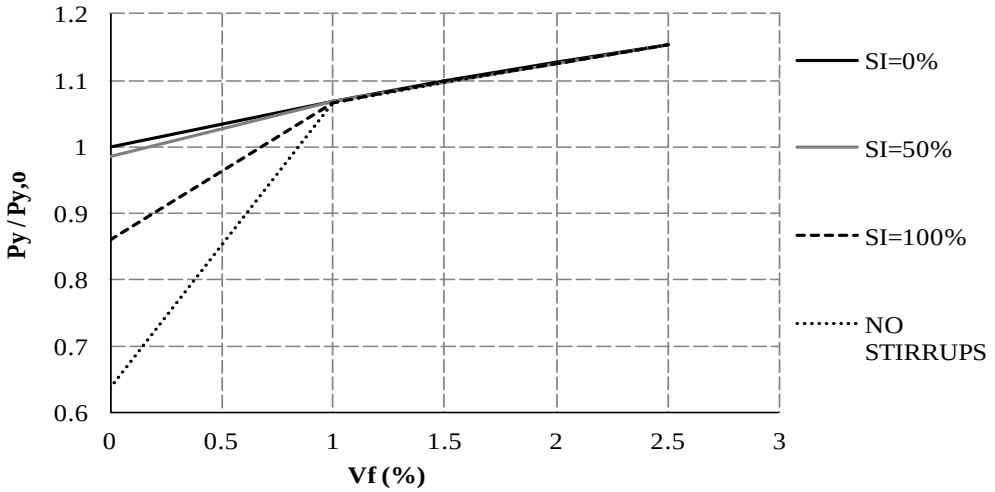


Figure 4.82: Ratio between the yield load and that in the control specimen ($SI = 0\%, V_f = 0\%$) versus steel fibre volume fraction for Case Study 1(b)

4.6.5.2 Ductility ratio

Figure 4.83 presents the results for the ratio between ductility ratio for each beam and that in the control beam plotted against fibre volume fraction. There was a substantial increase in the ductility ratio especially for beams without increase in stirrups spacing (i.e. $SI = 0\%$) by up to 61% at $V_f = 2\%$. Similarly to Case Study 1(a), it was also found that there is an optimum fibre content beyond which adding more fibres leads to less rather more ductility. The optimum fibre contents (i.e. thresholds) were found to be $V_f = 1.5\%,\ 2\%,\ \ 2\%$ and 2.5% for the beams with $SI = 0\%, 50\%, 100\%$ and no stirrups, respectively.

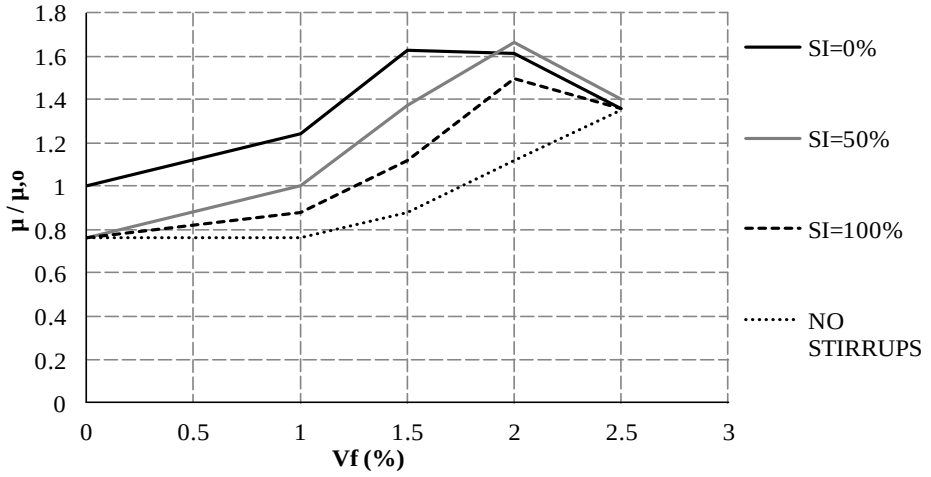


Figure 4.83: Ratio between the ductility ratio in each beam and that in the control specimen ($SI = 0\%, V_f = 0\%$) versus steel fibre volume fraction for Case Study 1(b)

Furthermore, as the spacing between stirrups was increased, the ductility ratio decreased. The minimum fibre volume fraction required to produce ductility ratios comparable to that associated with the control specimen was found to be $V_f = 1\%$, 1.5% and 2% for the beams with $SI = 50\%, 100\%$ and no stirrups, respectively. This shows that when the stirrups spacing was increased, a higher amount of fibres was required to retain the same ductility provision. It is important to note that even for the extreme case when all stirrups were completely removed from the beam (i.e. no stirrups), the addition of steel fibres still had the capability to restore adequate ductility levels (albeit at a higher fibre content of $V_f = 2\%$ as stated above confirming the severity of conventional shear reinforcement reduction).

4.6.5.3 Energy absorption

The energy absorption ($E_a/E_{a,o}$) ratio calculated for Case study 1(b) beams are presented in the Figure 4.84. The results confirm the ductility patterns observed in the preceding section. There was a gradual increased in the $E_a/E_{a,o}$ ratio as the amount of steel fibres was raised up to a certain threshold beyond which energy absorption decreased (this was found to be at $V_f = 2\%$ for all beams except for the one without stirrups). The enhancement in energy absorption was more than double the levels associated with the control specimen, which is a significant improvement.

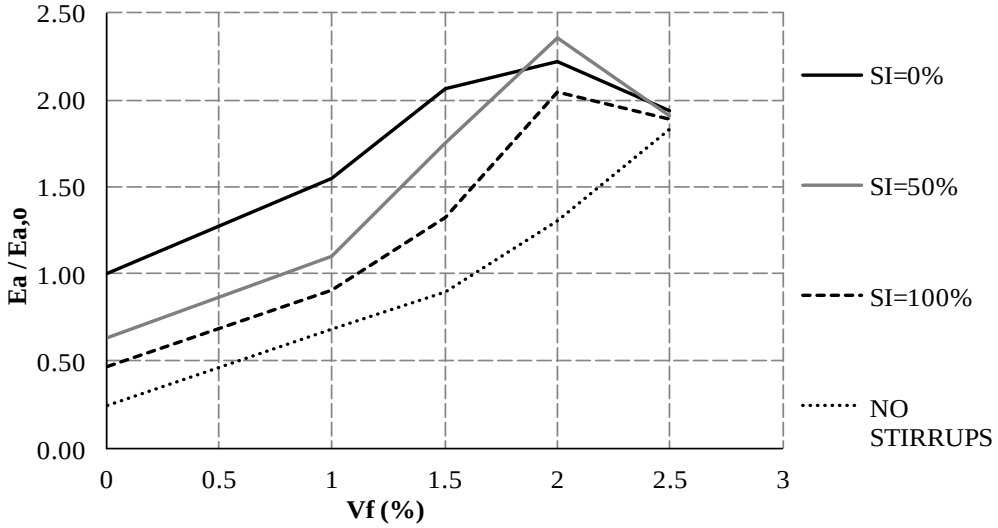


Figure 4.84: Ratio between the energy absorption in each column and that in the control specimen ($SI = 0\%, V_f = 0\%$) versus steel fibre volume ratio for Case Study 1(b)

4.6.6 Comparison between FE-based predictions and design calculations

This section discusses the comparison between the FE results and those calculated according to Eurocode 2 (2004) for conventional RC sections (i.e. without fibres) and Concrete Society TR-63 (2007) for SFRC beams. The shear (V_{rd}) and bending moment (M_{rd}) capacities were calculated first and then the lateral loads corresponding to shear (P_{SC}) and bending (P_{BMC}) modes of failure were determined. Figure 4.85 shows a schematic of the bending moment and shear force diagrams used to calculate the loads.

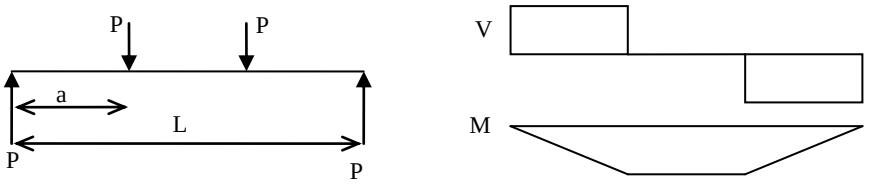


Figure 4.85: Shear force (V) and bending moment (M) diagrams for Case Study 1(b)

The minimum of the two loads (P_{SC} and P_{BMC}) was used to determine the load-carrying capacity and predict the mode of failure. A comparison between the FE-based load-carrying capacity (P_{max}) and its analytical counterpart (P_{SC} or P_{BMC}) is also included. Thus, conclusions can be made on the numerical predictions in the light of Eurocode and Concrete Society TR-63 design-based calculations (see Appendix B).

The values calculated for M_{rd} are given in Table 4.23 and they are not affected by the amount of shear stirrups in the beams. Tables 4.24 to 4.27 presents the V_{rd} values calculated as well as the ratio between the strength predicted by FE analyses and design guidelines and the ensuing failure mode.

V_f (%)	M_{rd} (kNm)
0	70.40
1	71.61
1.5	72.19
2	72.77
2.5	73.34

Table 4.23: Bending moment capacity calculated for beams in Case Study 1(b)

V_f (%)	V_{rd} (kN)	P_{max} (kN)	P_{SC} (kN)	P_{BMC} (kN)	$\frac{P_{max}}{P_{BMC}}$	*failure mode*
0	64.58	197.27	129.16	171.72	1.15	shear
1	117.90	205.76	235.80	174.64	1.18	bending
1.5	127.53	211.69	255.06	176.08	1.20	bending
2	137.16	220.74	274.32	177.50	1.24	bending
2.5	146.79	229.21	293.58	178.88	1.28	bending

Table 4.24: FE- and code-based strength predictions for Case Study 1(b) beams with $SI = 0\%$

V_f (%)	V_{rd} (kN)	P_{max} (kN)	P_{SC} (kN)	P_{BMC} (kN)	$\frac{P_{max}}{P_{BMC}}$	*failure mode*
0	54.19	189.94	108.38	171.72	1.11	shear
1	101.83	205.77	203.66	174.64	1.18	bending
1.5	111.46	211.59	222.92	176.08	1.20	bending
2	121.09	217.03	242.16	177.50	1.22	bending
2.5	130.72	222.23	261.44	178.88	1.24	bending

Table 4.25: FE- and code-based strength predictions for Case Study 1(b) beams with $SI = 50\%$

V_f (%)	V_{rd} (kN)	P_{max} (kN)	P_{SC} (kN)	P_{BMC} (kN)	$\frac{P_{max}}{P_{BMC}}$	*failure mode*
0	48.60	165.58	97.2	171.72	0.96	shear
1	93.18	205.65	186.38	174.64	1.18	bending-shear
1.5	102.81	211.68	205.62	176.08	1.20	bending
2	112.44	217.09	224.88	177.50	1.22	bending
2.5	122.07	222.3	244.14	178.88	1.24	bending

Table 4.26: FE- and code-based strength predictions for Case Study 1(b) beams with $SI = 100\%$

V_f (%)	V_{rd} (kN)	P_{max} (kN)	P_{SC} (kN)	P_{BMC} (kN)	$\frac{P_{max}}{P_{BMC}}$	*failure mode*
0	32.61	122.74	65.22	171.72	0.71	shear
1	68.45	205.44	136.90	174.64	1.18	shear
1.5	78.08	211.49	156.16	176.08	1.20	shear
2	87.71	220.61	175.42	177.50	1.24	Shear/bending
2.5	97.34	229.15	194.68	178.88	1.28	bending

Table 4.27: FE- and code-based strength predictions for Case Study 1(b) beams with no stirrups

The results obtained show that steel fibres increase the load-carrying capacity of the beams. Reasonable agreement with code predictions confirms the validity of the FE-

based results, with the latter being more economical than the code estimates (the FE-based load-carrying capacity values (P_{max}) for SFRC beams were up to 18~28% higher than their code-based counterparts (P_{BMC}), largely because the numerical results are based on 3D modelling compared to the code simplified 1D sectional analysis).

The conventionally RC beams (i.e. without fibres) were initially designed with reduced shear reinforcement in order to induce a shear mode of failure. It is interesting to see that the addition of fibres has led to a change in the failure mode from a brittle one (i.e. shear) to a more ductile one (i.e. bending), which is desired in design. This is true even for the case with severe conventional shear reduction when stirrups were completely removed as the brittle failure mode was reversed to a ductile one with fibres added at $V_f = 2\%$~2.5%. For the rest of the beams the addition of fibres, even at 1%, changed the mode failure of the beam from shear to bending. It can be concluded that steel fibres increase the load-carrying capacity of the beams and ensures a more ductile structural response (thus avoiding a brittle shear mode of failure), which is desired in design.

4.7 Conclusions

Two case studies on SFRC simply supported beams were examined by means of non-linear FE analysis. The first part of the investigation, Case Study 1(a), is focused on beams under both monotonic and reversed-cyclic loads. The study allowed investigating the flexural behaviour of the beams as they were initially designed with sufficient conventional transverse reinforcement to avoid shear failure. The second part of the work, Case Study 1(b), was based on SFRC beams designed with reduced shear reinforcement in order to incorporate a shear mode of failure (beams without transverse stirrups were studied as well). The spacing between shear stirrups was increased in both case studies and fibres were added as a substitute to the loss in shear reinforcement.

Based on the findings of the studies, it can be concluded that the addition of steel fibres consistently enhances the load-carrying capacity. The strength increase was by up to ~15% for beams under monotonic loading and ~20% for the ones under cyclic loading, compared to the original control specimen (i.e. with no increase in stirrups spacing and no fibres). Furthermore, fibres were found to increase stiffness leading to reduced deflections (at the same level of loading compared to beams with less or without fibres).

This shows that there are clear benefits of adding fibres at both the serviceability and ultimate limit states, which are important design considerations. The addition of steel fibres also led to a reduction in crack formation and propagation. It has also improved the structural response by altering the failure mode from a brittle shear mode to a flexural ductile one, which is desired in design (this was more pronounced in Case Study 1(b) as it initially had less conventional shear reinforcement).

As the fibre amount was increased, ductility also improved. Interestingly, it was found that the increase in ductility seems to reduce if excessive amounts of fibres are provided. This suggests that there is an optimum amount of fibres that can be added to enhance ductility. This is similar to the situation experienced when the beam main flexural reinforcement is increased beyond a certain threshold (i.e. "over-reinforced"), which leads to increase in strength but reduction in ductility. A similar pattern was observed for energy absorption, which alongside ductility, is an important design consideration under both monotonic and cyclic loads (the latter being the key feature in seismic action, thus indicating the potential benefits of fibres for the structural response to such loading). The increase in ductility is accompanied by a softening load-deflection response. However, the residual strength was found to be sufficiently high (i.e. >85%) in all cases studied, suggesting the softening is not significant.

For Case Study 1(a)-M, i.e. under monotonic loading, the optimum amounts of fibre content for the beams with $SI = 0\%,\ 50\%,\ 100\%$ and 200% were found to be $V_f = 1\%,\ 2\%,\ 2\%$ and 2.5% respectively. In this parametric study, all beams showed crack occurred at the mid-span of the beam indicating flexural failure (except the beam with $SI = 200\%$ and no fibres which failed in shear).

For Case Study 1(a)-C, i.e. under reversed-cyclic loading, the optimum fibre volume fractions was $V_f = 1\%$ for all beams except the ones with $SI = 200\%$ which required fibres at $V_f = 1.5\%$. Energy absorption and the number of cycles obtained before failure were also studied under cyclic loading and the results showed a similar trend to the one associated with ductility. Based on the principal strain contours and vector, it was found that the cracks occurred mostly in the mid-span of the beam, with the cracking pattern under cyclic loading being more intensive than that under monotonic loading, especially in the beams with $SI = 200\%$.

For Case Study 1(b), the optimum fibre contents were found to be $V_f = 1.5\%, 2\%, 2\%$ and 2.5% for the beams with $SI = 0\%, 50\%, 100\%$ and no stirrups, respectively. It is important to note that even for the extreme case when all stirrups were completely removed from the beam (i.e. no stirrups), the addition of fibres still had the capability to restore adequate ductility levels (albeit at a higher fibre content of $V_f = 2\%$ confirming the severity of conventional shear reinforcement reduction).

Flexural and shear capacities were also calculated using analytical expressions given in Eurocode 2 (2004) for conventional RC sections (i.e. without fibres) and Concrete Society TR-63 (2007) for SFRC beams. These were compared with the strength values obtained from the non-linear FE analyses (the latter were initially calibrated and verified against existing experimental data). This comparative study has confirmed the validity of the FE-based results (with the latter being more economical than the code estimates) and has thus confirmed the potential for fibres to compensate for a reduction in conventional shear reinforcement.

In summary, it can be concluded that steel fibres increase the load-carrying capacity of the beams and ensures a more ductile structural response (thus avoiding a brittle shear mode of failure), which is desired in design. It also leads to an increase in ductility, energy absorption and the number of cycles achieved before failure, with associated optimum/threshold fibre contents determined. Strength enhancements due to fibres were confirmed by comparing to design code predictions (with the numerical results being more economical). Fibres also limit crack propagation as well as reducing degradation effects under reversed-cyclic loading (thus enhancing seismic response).

CHAPTER 5

CASE STUDY 2: TWO-SPAN CONTINUOUS SFRC COLUMN UNDER MONOTONIC AND REVERSED-CYCLIC LOADING

5.1 Introduction

This chapter presents and discusses the non-linear FE analysis carried out on a two-span continuous column under combined constant axial force and static monotonic or reversed-cyclic loading (as part of the case studies summarised in Section 3.2). Two columns investigated experimentally by Kotsovos et al (2007) are selected herein. The numerical model was calibrated against this set of existing experimental data to ensure the reliability of its predictions. Parametric studies were subsequently carried out using the full practical range of steel fibre dosages.

An interesting feature of this work is the consideration of statically indeterminate SFRC columns (under both monotonic and cyclic loadings). Most of SFRC specimens studied in the literature are focused on determinate beams and information on statically indeterminate beams is sparse.

A key issue assessed is whether the use of steel fibres can result in a significant reduction in conventional reinforcement without compromising ductility and strength requirements. In this respect, the spacing between stirrups was relaxed while steel fibres were added to see whether or not the loss of strength can be compensated for in this way. This is particularly useful in situations where the shear reinforcement required can lead to congestion of stirrups, for instance in seismic design (the critical factor in the latter is the cyclic nature of the load, which is examined in this chapter). The FE investigations provided insight into how the steel fibres can help reduce the amount of

conventional shear reinforcement. A summary of the experimental setup together with a discussion of the results of the FE analyses is presented next.

5.2 Calibration with experimental data

Twelve two-span continuous columns were tested by Kotsovos et al (2007). The parameters considered were concrete strength, longitudinal and shear reinforcement properties and specimen with fibrous concrete. The columns were cast and tested as horizontal members. Therefore the axial force was applied horizontally and the lateral monotonic or reversed-cyclic displacement was vertically applied. In the present FE work, only two columns with similar steel reinforcement and material properties but different loading types (i.e. monotonic and cyclic) were selected for the calibration work. These columns are referred to in the experimental work as D16-FC30-M and D16-FC30-C with the properties as shown in Figure 5.1.

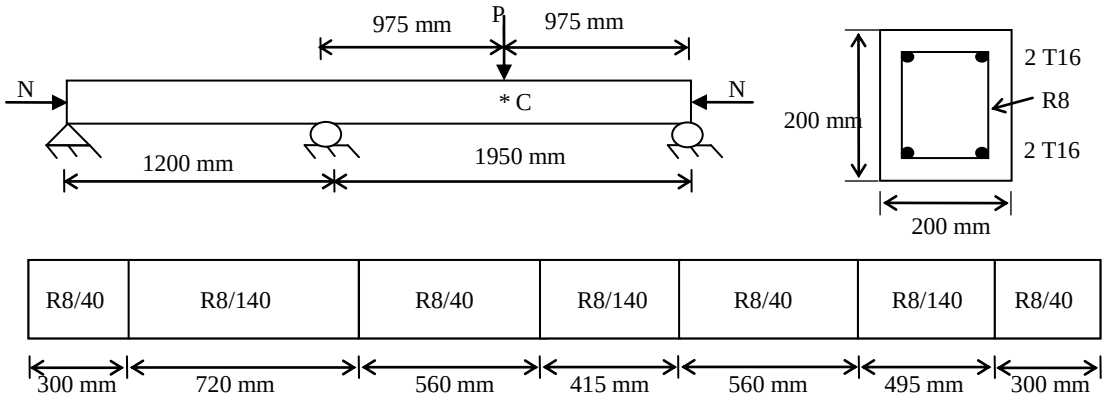


Figure 5.1: Dimensions, loading arrangement and reinforcement detailing of the column (adapted from Kotsovos et al, 2007)

The concrete compressive strength for specimen FC30 was approximately 37 MPa. In addition, the longitudinal reinforcement has a yield stress (f_y) of 555 MPa, whilst, the transverse reinforcement has a yield stress of 470 MPa. The modulus of elasticity for steel (E_s) is 200 GPa. The axial force (N) applied at the column ends is equivalent to:

$$N \approx 0.2N_u = 0.2\, f_c bh. \tag{5.1}$$

where $N_u = f_c bh$ is the compression resistance of the column provided by concrete, f_c is the uniaxial cylinder compressive strength of concrete, and b and h are the cross-

sectional dimensions of the column. Once the axial force is introduced, the lateral monotonic or reversed-cyclic displacement (*P*) was applied at location C in Figure 5.1 (the load and deflection taken to plot the load versus deflection curves are taken at point C as well). The loading history adopted in the FE analyses for both monotonic and cyclic forces is defined in Figures 5.2 and 5.3, respectively.

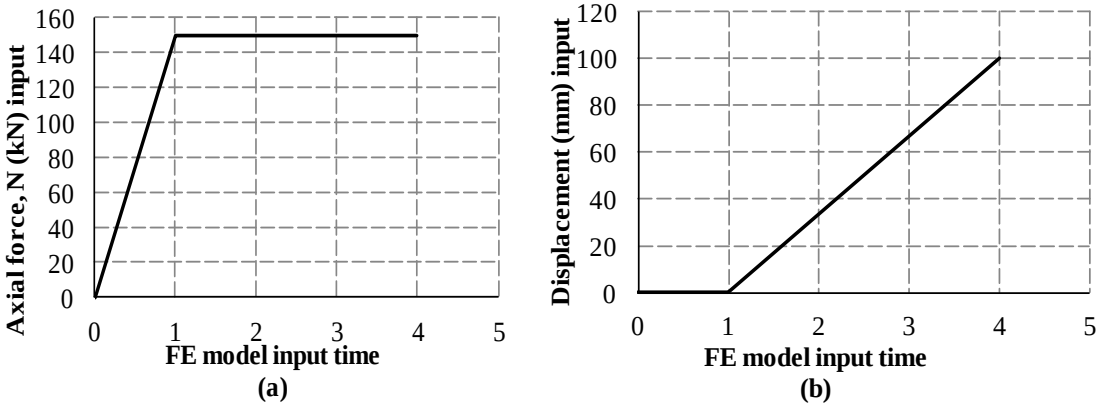


Figure 5.2: (a) constant axial force and (b) monotonic loading

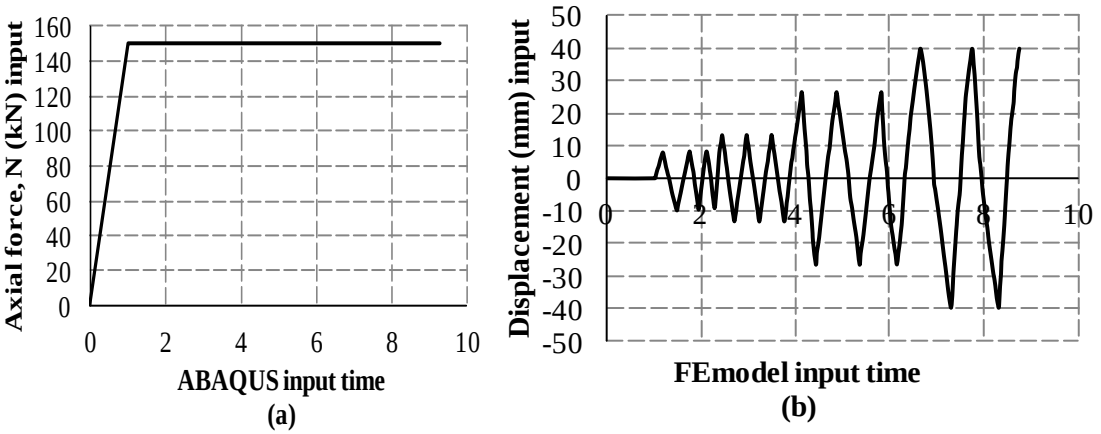


Figure 5.3: (a) constant axial force and (b) reversed-cyclic loading

Calibration work is carried out via FE models in ABAQUS version 6.9 to simulate and reproduce the response of the column to compare with its respective experimental results. To reduce the analysis time, only half of the column was modelled as the specimen is symmetrical about the Y-axis as depicted in Figure 5.4.

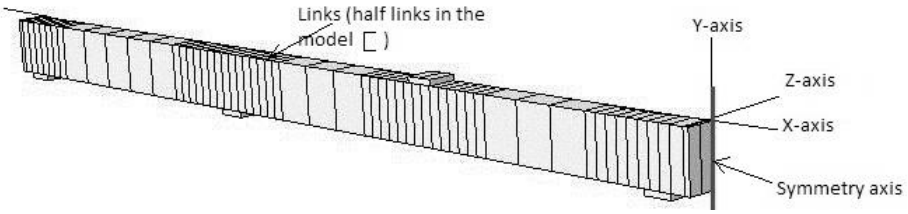


Figure 5.4: Symmetrical half of the column modelled in FE model in ABAQUS

Figure 5.5 shows the tensile stress-strain relation adopted for the analysis carried out with fibre volume fraction V_f = 0.4%. Steel plates of 20-mm thick and 100-mm wide are added to the column at the loading and support locations (this is to mimic experimental setup and also avoid premature localised failure).

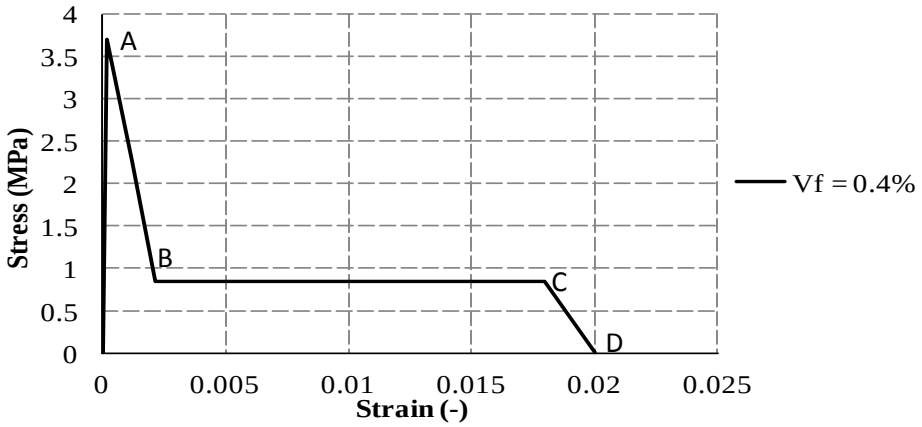


Figure 5.5: Tensile stress-strain diagram adopted for calibration work of Kotsovos et al. (2007) SFRC columns

Point	Stress (MPa)	Strain (‰)
0	0	0
Peak tensile stress (A)	3.70	0.215
Beginning of plateau (B)	0.85	2.120
End of plateau (C)	0.85	18
Ultimate cracking strain (D)	0	20

Table 5.1: Tensile stress-strain relationship for a SFRC mixture with fibres volume fraction of 0.4%

Quasi-static FE analysis was carried out using ABAQUS dynamic solver. To ensure that no significant dynamic effects occur as a result, the energy ratio (kinetic energy / strain energy) was checked at each load step to ensure that it is smaller than 0.5%. Based on the sensitivity analyses a mesh size of 30 mm was selected for the present case as it produces the best agreement to the experimental results.

5.2.1 Results for column analysed under monotonic loading

Figure 5.6 shows the load-deflection curves comparison for the SFRC column analysed under monotonic loading. Good agreement with experimental work can be seen for the column up to a deflection of 40 mm, whereas after this deflection point, the load predicted by FE model is up to 5% higher than the load obtained from experimental results. The load at yield (P_y), maximum load (P_{max}) and ultimate load of the column at failure (P_u), and their respective deflections δ_y, δ_{Pmax} and δ_u are given in Table 5.2.

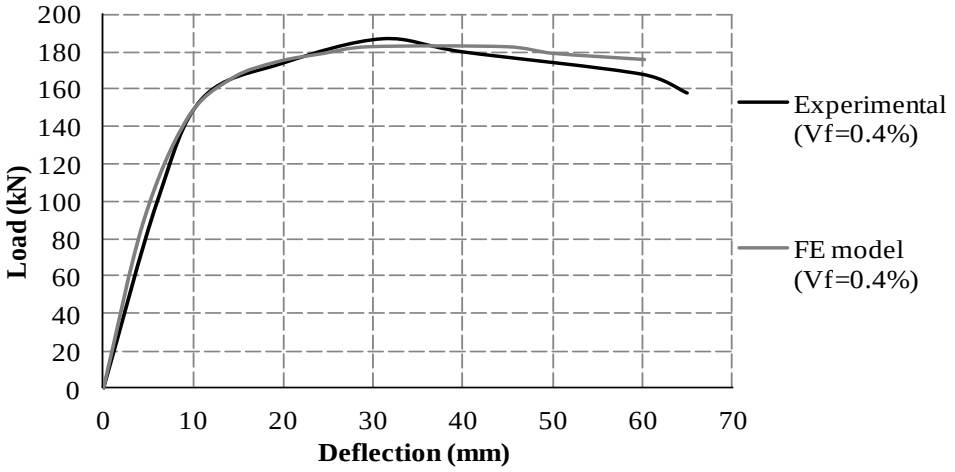


Figure 5.6: Calibration results comparison for the column analysed under monotonic loading

Column	P_y (kN)	δ_y (mm)	P_u (kN)	δ_u (mm)	P_{max} (kN)	δ_{Pmax} (mm)	$\mu = \frac{\delta_u}{\delta_y}$	$\frac{P_{max}}{P_y}$
Experimental	155.0	11	158	65.5	187	31.1	6.0	1.21
FE model	144.3	9.7	174.1	60.3	182.9	44.7	6.2	1.33

Table 5.2: Result summary from load-deflection curve under monotonic loading

	FE and Experimental results			Values calculated based on Eurocode 2					
Column	P_{max}	δ_{Pmax}	δ_{sust}	P_{ty}	$P_y = P_{1p}$	P_{2p}	$\frac{P_{max}}{P_{2p}}$	δ_y	$\mu_{sust=\frac{\delta_{sust}}{\delta_y}}$
Experimental	187.0	31.1	65.5	109	149	171	1.09	11	6.0
FE model	182.9	44.7	60.3	111.5	148.6	170.8	1.07	9.7	6.2

Table 5.3: Relevant values from both the Experimental and FE model as well as the expected values from Eurocode 2, under monotonic loading

A comparison of the experimental results, FE analysis predictions and the corresponding values calculated from Eurocode 2 (2004) are presented in Table 5.3.

The parameters in the table are defined as follows: the load at true yield (P_{ty}), load at formation of the first (P_{1p}) and second (P_{2p}) plastic hinges. From Figure 5.6, it can be seen that there is a slight softening trend on the load-deflection curve beyond the peak value of the load. To ensure that the residual strength and corresponding deflections are still of practical value, a sustained load (P_{sust}) has been defined as being equal to 85% of the maximum (i.e. peak) load, i.e. $P_{sust} = 0.85P_{max}$. The corresponding deflection (δ_{sust}) was also determined and included in Table 5.3. In addition, a sustained ductility ratio (μ_{sust}) was also calculated and included in the Table. From the two tables, good agreement can be seen between the Experimental results, FE data and analytical calculations.

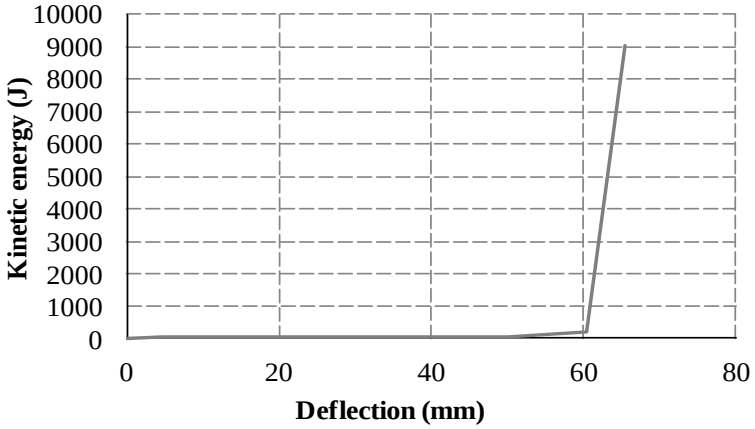


Figure 5.7: Kinetic energy plots to determine failure for the column analysed under monotonic loading

In order to confirm the failure of the structure, the kinetic energy of the column is plotted versus the deflection in Figure 5.7. A clear sudden jump can be observed when the deflection is 60.3 mm, indicating that the failure occurs at that point.

Figure 5.8 illustrates the principal stress contours, principal strain contours and vectors, and deflected shape of the column at failure. In order to observe crack patterns, the range of principal stresses has been selected between a maximum tensile stress of 3.7 MPa and a compressive stress of -37 MPa in the concrete (i.e. these two values correspond to the tensile and compressive strength of concrete used). Similarly, the principal strain range was selected between an ultimate tensile strain of 0.02 and an ultimate compressive strain of -0.0035. It is observed that the maximum principal stresses and strains are concentrated at the intermediate support (R_2) and under lateral loading (P) regions. The grey colour in Figure 5.8(b) and red arrows vectors in Figure

5.8(c) indicate the crack pattern in the column. The deflected shape of the column is given in the Figure 5.8(d) with the forces and support reactions annotated for convenience. The preceding column results indicate a failure in bending and this is confirmed by the experimental results.

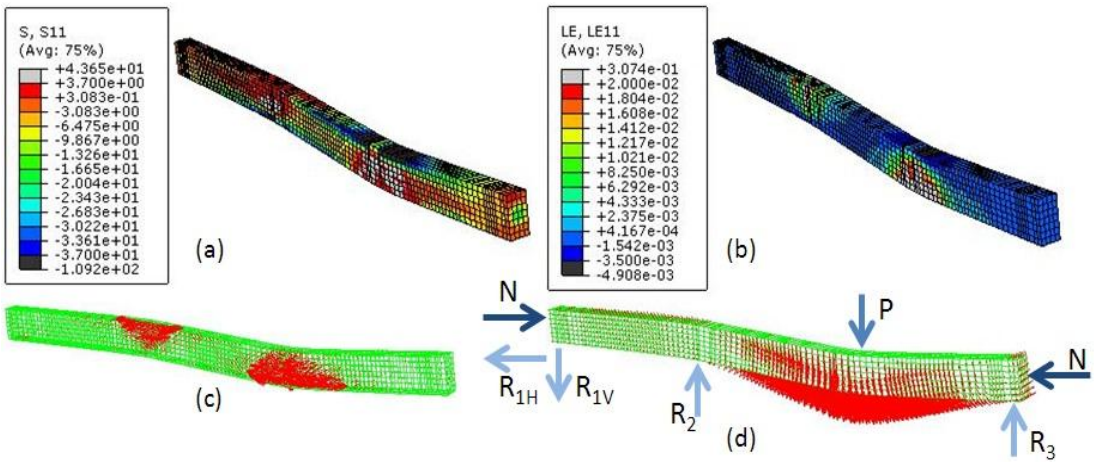


Figure 5.8: Principal (a) stress and (b) strain contours, (c) principal strain vectors and (d) deflected shape of the column analysed under monotonic loading

5.2.2 Analysis results for column under reversed-cyclic loading

A comparison between experimental data and FE predictions for the SFRC columns subject to reversed-cyclic loading is presented in Figure 5.9. Good agreement between the two sets of data was found as the loads obtained from the FE model show less than 10% discrepancy with their experimental counterparts. A summary of key values from the load-deflection hysteresis loop is presented in Table 5.4. In addition, Table 5.5 provides a comparison with the values calculated based on Eurocode 2 (2004).

Reasonable agreement can be observed from both tables, with the ratios calculated varying by less than 7%. Thus, this confirms the validity of the FE model to simulate the behaviour of this structure under reversed-cyclic loading.

The column failed at 9.25 cycles in the FE model. This was determined due to the significant sudden jump in the kinetic energy as evident in Figure 5.10 indicating the presence of large/extensive cracks.

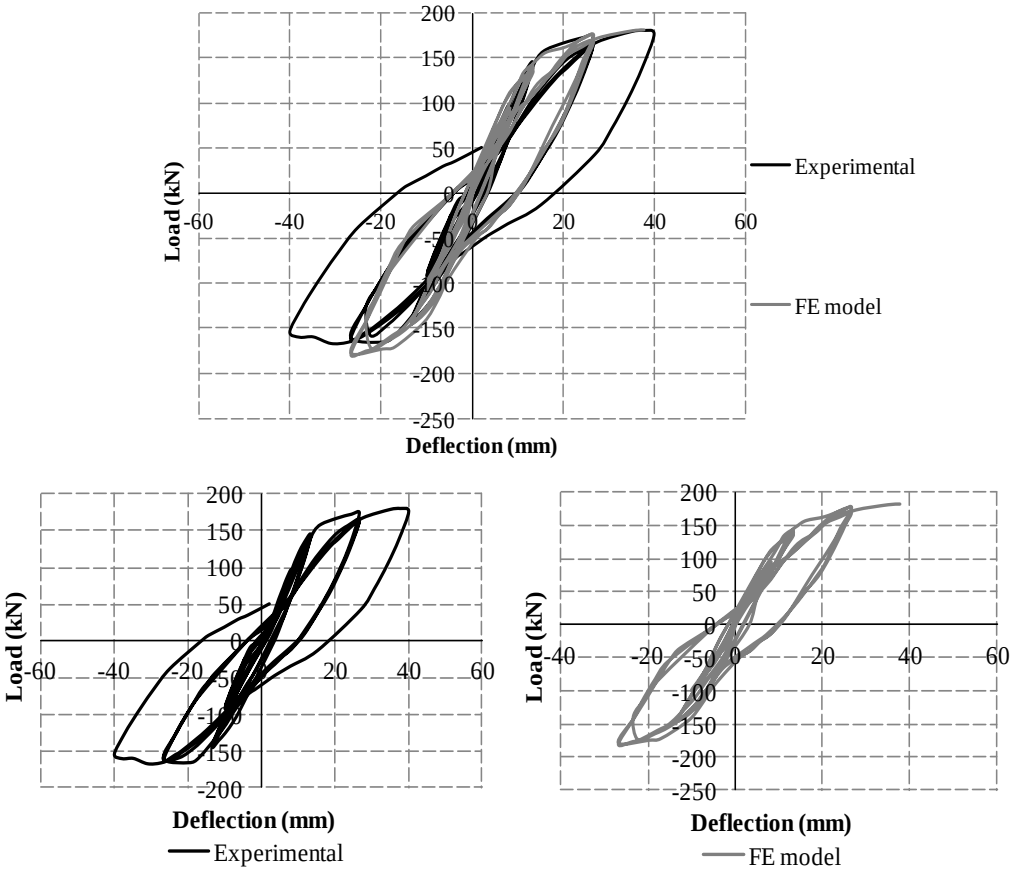


Figure 5.9: Calibration results comparison for the column analysed under reversed-cyclic loading

Column	P_y (kN)	δ_y (mm)	P_u (kN)	δ_u (mm)	P_{max} (kN)	δ_{Pmax} (mm)	$\mu = \frac{\delta_u}{\delta_y}$	$\frac{P_{max}}{P_y}$
Experimental	97.1	8.0	177.2	40.1	183.0	37.7	5.0	1.89
FE model	94.6	8.0	181.5	37.7	181.5	37.7	4.7	1.92

Table 5.4: Result summary from load-deflection curve under reversed-cyclic loading

	Evaluated			Expected values from Eurocode 2					
Column	P_{max}	δ_{Pmax}	δ_{sust}	P_{ty}	$P_y = P_{1p}$	P_{2p}	$\frac{P_{max}}{P_{2p}}$	δ_y	μ_{sust}
Experimental	183.0	37.7	40.1	109.0	149.0	171.0	1.07	11.0	3.65
FE model	181.5	37.7	37.7	111.5	148.6	170.9	1.06	9.7	3.89

Table 5.5: Relevant values from both the Experimental and FE model as well as the expected values from Eurocode 2, under reversed-cyclic loading

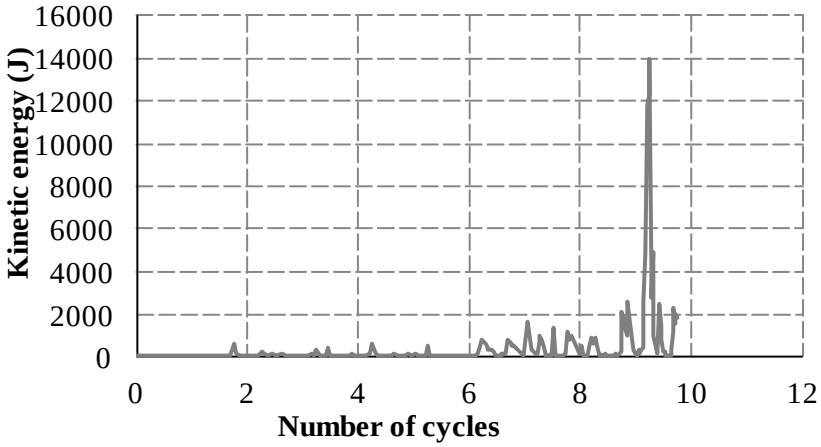


Figure 5.10: Kinetic energy figure to determine failure under reversed-cyclic loading

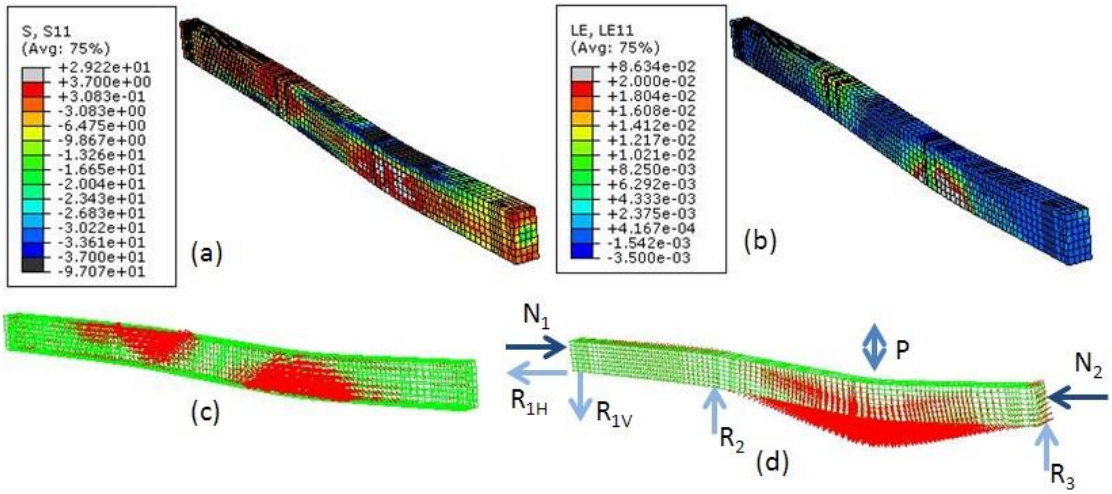


Figure 5.11: Principal (a) stress and (b) strain contours, (c) principal strain vector and (d) deflected shape for the column analysed under reversed-cyclic loading

The cracking pattern obtained at failure is presented in Figure 5.11. The higher stress concentrations are observed at the point where the load *P* is applied, at the mid-span of the first column span and at the intermediate support. Cracks developed in these regions, where steel fibres bridging and restraining these cracks are now being pulled out. From the cracking pattern and deflected shape of the column (see Figure 5.11), it can be observed that this column fails in bending at the section where the load P is applied. This agrees with the experimental observation.

5.3 Case Study 2(a): Parametric study of SFRC column under monotonic loading

The parametric studies were carried out by increasing the spacing between stirrups by *SI* = 0%, 50% and 100%. The fibre volume fraction was increased (by V_f = 0%, 1%, 1.5%, 2% and 2.5%) to see whether or not fibres can compensate for the reduction in shear reinforcement. The tensile stress-strain relations for each fibre volume fraction are depicted in Figure 5.12 and summarised in Tables 5.6(a) and (b).

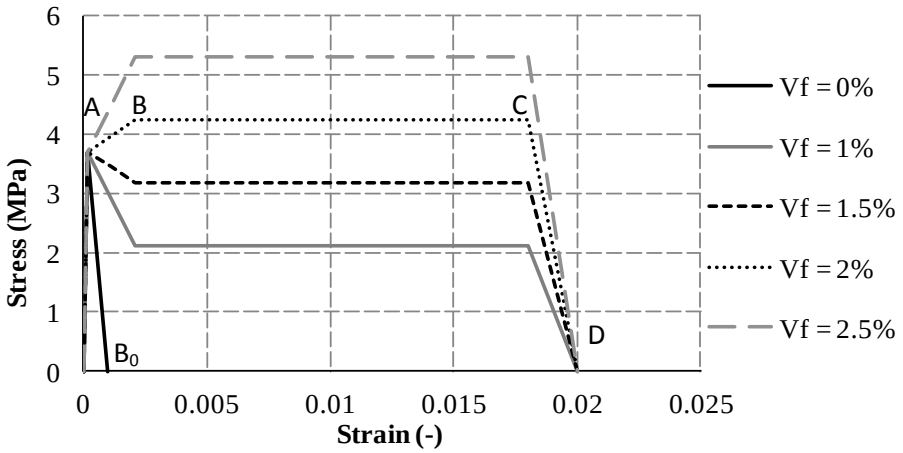


Figure 5.12: Tensile stress-strain relations for Case Study 2 for different fibre volume fractions (V_f)

Point	Strain (‰)	Stress, V_f = 0.0% (MPa)
Origin	0	0
Peak tensile stress (A)	0.215	3.70
Ultimate cracking strain (B_0)	2.0	0

Table 5.6(a): Tensile stress-strain properties for plain concrete for Case Study 2

Point	Strain (‰)	Stress, V_f = 1.0% (MPa)	Stress, V_f = 1.5% (MPa)	Stress, V_f = 2.0% (MPa)	Stress, V_f = 2.5% (MPa)
Origin	0	0	0	0	0
Peak tensile stress (A)	0.215	3.70	3.70	3.7	3.70
Beginning of plateau (B)	2.12	2.12	3.18	4.24	5.30
End of plateau (C)	18	2.12	3.18	4.24	5.30
Ultimate cracking strain (D)	20	0	0	0	0

Table 5.6(b): Tensile stress-strain properties for fibre-reinforced concrete for Case Study 2

Columns with different fibre content and stirrup spacing were considered and analysed under monotonic and reversed-cyclic loading using the loading histories summarised in

Figures 5.2 and 5.3, respectively. The analysis results obtained from the monotonic loading case are discussed in this section, whereas the results of the reversed-cyclic loading case are presented in Section 5.4.

5.3.1 Strength

The load-deflection curves for specimens with increased stirrup spacing of $SI = 0\%$, $SI = 50\%$ and $SI = 100\%$ are presented in Figures 5.13, 5.14 and 5.15. Additionally, a summary of the key load and deflection results is provided in Tables 5.7, 5.8 and 5.9.

From the figures, it can be seen that the increase in the amount of fibres provided has led to an increase in load-carrying capacity (P_{max}). Comparing the strength of each SFRC column to the strength of the column with no fibres, it shows that the load-carrying capacity has increased with an average of 13.1%. In addition, the value of the load at yield (P_y) for the SFRC columns increased gradually up to an average of 23.5% in comparison to the yield load of columns with no fibres. This shows the effectiveness of fibres in bridging the crack opening, thus enhancing the load at yield of the columns.

Taking the column with conventional reinforcement and no fibres ($V_f = 0\%$) with a stirrup spacing increase of $SI = 0\%$ as the reference or control column (CC), further comparisons were made with columns with varying fibre content and stirrup spacing. From Figures 5.15 and 5.16, and Tables 5.8 and 5.9, it is observed that the strength properties of the SFRC columns with stirrup spacing increase of $SI = 50\%$ and $SI = 100\%$, portray better performance than the control column. The values of P_y and P_{max} obtained are also higher than the corresponding values for the control column, even at fibres volume ratio as low as 1%.

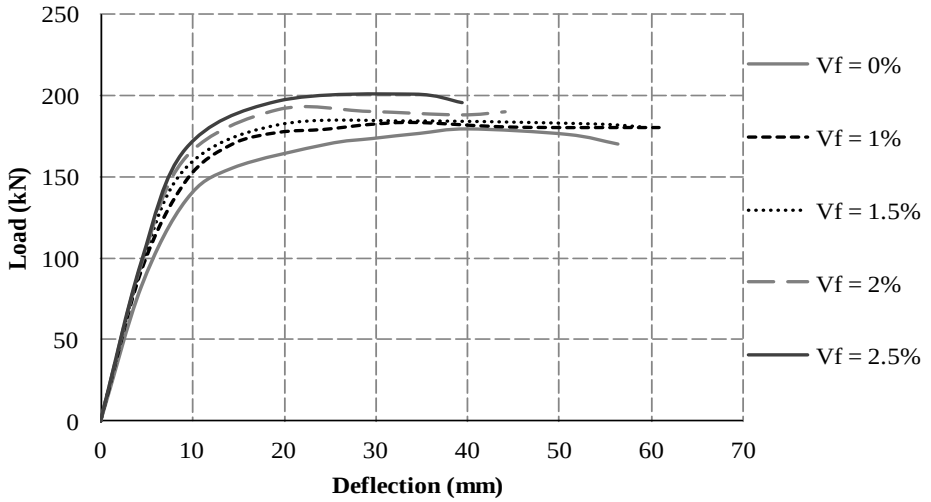


Figure 5.13: Load-deflection curve for Case Study 2(a) column with $SI = 0\%$

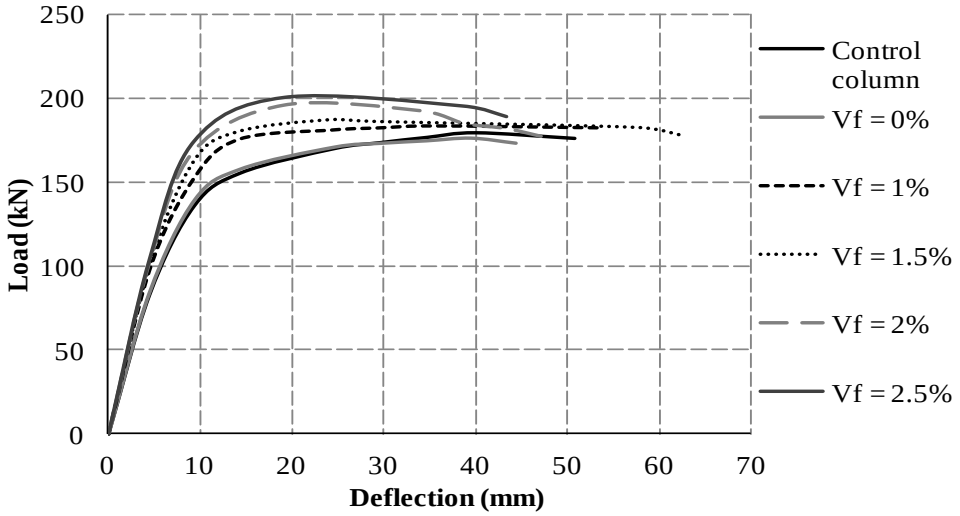


Figure 5.14: Load-deflection curve for Case Study 2(a) column with $SI = 50\%$

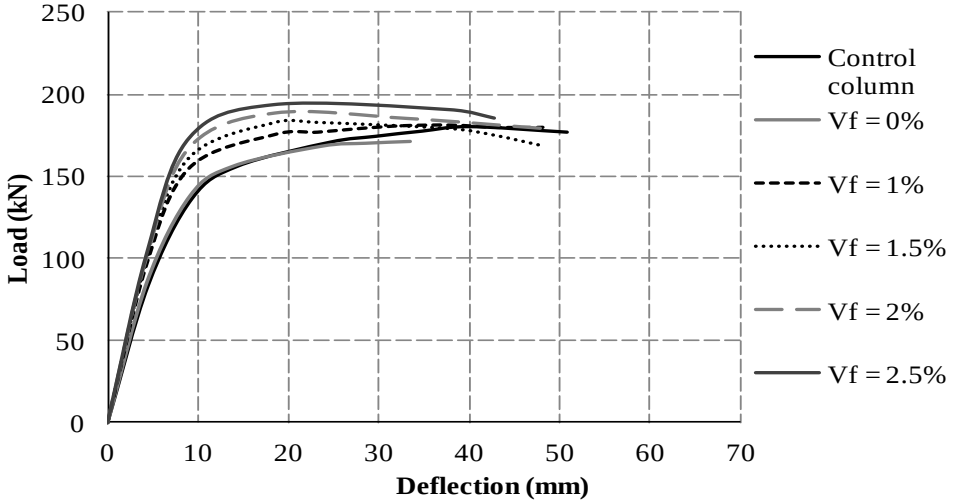


Figure 5.15: Load-deflection curve for Case Study 2(a) column with $SI = 100\%$

V_f (%)	P_y (kN)	δ_y (mm)	P_u (kN)	δ_u (mm)	P_{max} (kN)	δ_{Pmax} (mm)	$\mu = \frac{\delta_u}{\delta_y}$
0	136.3	9.36	170.6	56.4	179.9	40.1	6.03
1	147.6	9.34	180.1	60.9	183.2	50.4	6.52
1.5	155.9	9.32	180.7	59.3	184.6	34.3	6.36
2	162.1	9.3	190.0	44.1	192.0	24.6	4.74
2.5	167.3	9.3	195.5	39.4	200.7	34.2	4.24

Table 5.7: Result summary from load-deflection curve for Case Study 2(a) column with $SI = 0\%$

V_f (%)	P_y (kN)	δ_y (mm)	P_u (kN)	δ_u (mm)	P_{max} (kN)	δ_{Pmax} (mm)	$\mu = \frac{\delta_u}{\delta_y}$
CC	136.3	9.36	170.6	56.4	179.9	40.1	6.03
0	139.4	9.4	173.0	44.4	176.1	39.5	4.72
1	152.62	9.33	182.5	53.7	182.5	29.5	5.76
1.5	162.85	9.32	177.7	62.5	183.7	19.2	6.71
2	168.4	9.32	175.8	48.2	192.3	34.0	5.17
2.5	174.3	9.31	189.2	43.4	200.6	19.2	4.66

Table 5.8: Result summary from load-deflection curve for Case Study 2(a) column with $SI = 50\%$ (CC is the control column with V_f = 0% and *SI* = 0%)

V_f (%)	P_y (kN)	δ_y (mm)	P_u (kN)	δ_u (mm)	P_{max} (kN)	δ_{Pmax} (mm)	$\mu = \frac{\delta_u}{\delta_y}$
CC	136.3	9.36	170.6	56.4	179.9	40.1	6.03
0	137.9	9.12	170.8	33.4	170.8	33.4	3.66
1	155.4	9.04	180.3	48.1	181.6	38.0	5.32
1.5	161.6	9.02	169.4	47.7	183.1	23.3	5.29
2	167.6	9.01	179.4	47.8	188.7	18.4	5.31
2.5	173.1	9.00	185.4	42.8	193.6	18.4	4.76

Table 5.9: Result summary from load-deflection curve for Case Study 2(a) column with $SI = 100\%$ (CC is the control column with V_f = 0% and *SI* = 0%)

5.3.2 Ductility

The ductility of the columns can be analysed by means of examining the ultimate deflection δ_u and the ductility ratio μ. An upward trend in both parameters is observed with the increase in fibre volume fractions. However, this pattern is only true up to a certain *critical* fibre volume ratio; the higher the spacing between the stirrups, the higher the *critical* fibre volume ratio. In this parametric study, the highest ductility ratio

is obtained for the column with $V_f = 1\%$ for $SI = 0\%$, $V_f = 1.5\%$ for $SI = 50\%$, and $V_f = 2\%$ for $SI = 100\%$.

Furthermore, for every *SI* value there is a certain fibre volume fraction for which the ductility of the SFRC column is comparable to that associated with the original control specimen (i.e. with no fibres and full conventional shear reinforcement). This is significant from a practical viewpoint as it indicates that fibres provided at certain amounts can compensate for the decrease in ductility due to a reduction in shear reinforcement. This fibre volume fractions are 1.5% for $SI = 50\%$ and between 1.5% and 2% for the SI $= 100\%$.

It is interesting to note that increasing the fibre content beyond 1.5% ~ 2% has actually led to a reduction (rather than an increase) in ductility. The reduction in ductility is more pronounced in the case of specimens where fibres were added in addition to full conventional shear reinforcement, i.e. SI = 0% (the response became less ductile even when fibre provision exceeded V_f = 1%). This suggest that a situation similar to the one experienced when main flexural reinforcement is increased beyond a certain threshold (i.e. over-reinforced) which leads to an increase in strength but a reduction in ductility. This will be investigated further under cyclic loading to confirm this trend.

The principal strains taken at the same levels of deflection given by δ_y, δ_{max} and δ_u for the fibre volume ratio of 2.5%, are illustrated in Figures 5.16, 5.17 and 5.18, respectively. The columns considered for the comparison are taken from the column with $SI = 0\%$, with fibre volume ratio of $V_f = 0\%$, $V_f = 1.5\%$ and $V_f = 2.5\%$.

In order to observe crack patterns, the maximum and minimum principal strains contours at yield point for the columns has been selected between a 0.001 and -0.0035, respectively (i.e. these two values correspond to the ultimate tensile and compressive strain of concrete used), as shown in Figure 5.16. Cracking formation has occurred in all the columns, as marked by the grey region in the principal strain contour. At this stage, it can be observed that the extent of this grey region decreases as the fibre volume fraction increases. Furthermore, the number of cracks are higher in the columns with a higher fibre volume fraction, as indicated by the strain vectors, but the crack opening width is smaller. This indicates that the steel fibres are restraining the crack opening width by means of the fibres resistance to the pull-out behaviour. Therefore, for high

fibre volume fractions, a higher load is required in order to produce a similar amount of column deflection (i.e. increase stiffness).

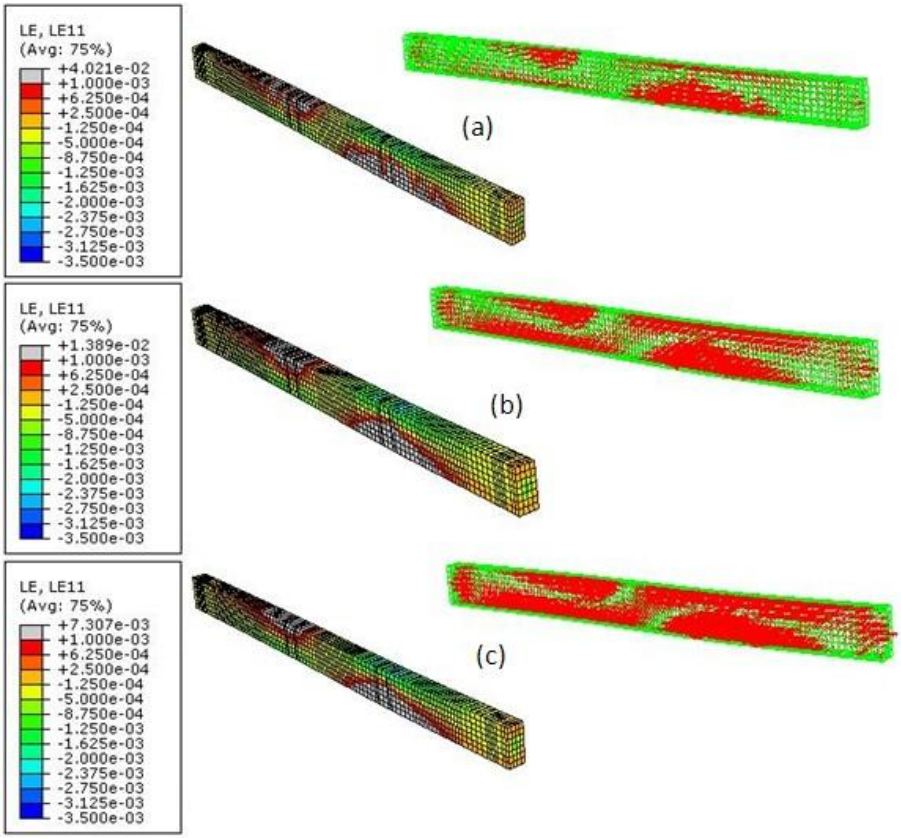


Figure 5.16: Principal strain contours and vectors for Case Study 2(a) column with $SI = 0\%$ at $\delta_y = 9.3\ mm$ for: (a) $V_f = 0\%$, (b) $V_f = 1.5\%$, and (c) $V_f = 2.5\%$

The SFRC column reaches the maximum load bearing capacity, due to the progression of the pull-out failure mechanisms due to loss of anchorage. Once the fibres fail, the load carrying capacity reduces, the cracks opening propagates and the ductility of the column is affected, depending on both the number of cracks and width of crack opening. A higher dosage of fibres contributes to a higher initial load carrying capacity, but once the maximum load is reached, cracks propagate rapidly, thus affecting the capability of the column to sustain further loads with the increase of the deflection. Thus, for instance in the column $V_f = 2.5\%$, the fibres are pulled out rapidly, increasing the crack opening width, which is evident from the higher maximum principal strain value observed in Figure 5.17 (c). In addition, steel fibres in the nearby regions will continue to bridge the crack opening causing the columns to deflect less. However, the maximum principal strain values continue to increase with the increase in loading, until the column losses its integrity and fails, as shown in Figure 5.18. In this figure, the

ultimate tensile cracking strains for columns with no fibres and with fibres are 0.001 and 0.02, respectively. In contrast, the compressive cracking strain value for both types of the columns (with and without fibres) is kept as -0.0035.

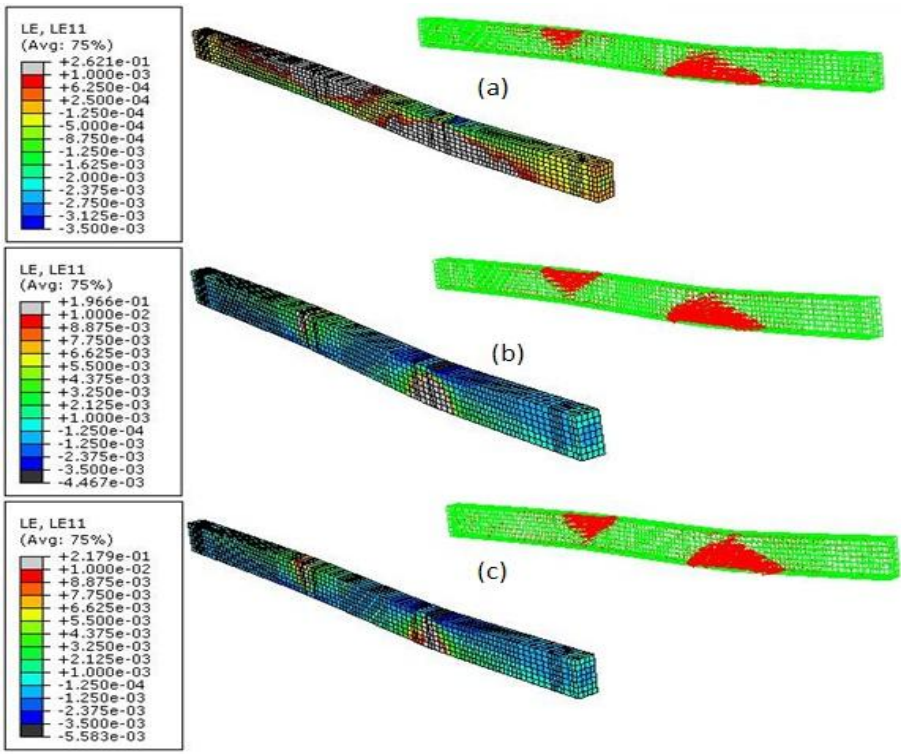


Figure 5.17: Principal strain contours and vectors for Case Study 2(a) column with $SI = 0\%$ at $\delta_{max} = 34.2\ mm$ for: (a) $V_f = 0\%$, (b) $V_f = 1.5\%$, and (c) $V_f = 2.5\%$

As can be observed in Figure 5.17, the maximum principal strain contour (highlighted in grey colour) obtained shows that the lowest strain value is observed in the column with $V_f = 1.5$. Furthermore, for this column, the cracks propagation develops in a more gradual and uniform pattern. This is reasonable as this is the column with the highest stiffness and ductility. On the other hand, for the column with $V_f = 2.5\%$, the maximum principal strain is higher, indicating that after the peak load the fibres in the regions near cracks (shown in grey contour) continue to restrain the crack opening.

It is crucial to understand that, even though the maximum principal strain contour for column with $V_f = 0\%$ produced the highest principal strain value, the ductility of this column is better than the one with $V_f = 2.5\%$. The reason for this behaviour is that, the cracking formation of the column with $V_f = 0\%$ is more uniform and failure is characterised by multiple cracks rather than a single crack, thus allowing for a higher

deflection as the load increases. Accordingly, the failure for column $V_f = 0\%$ is observed with lower load but a higher deflection, in comparison to column $V_f = 2.5\%$.

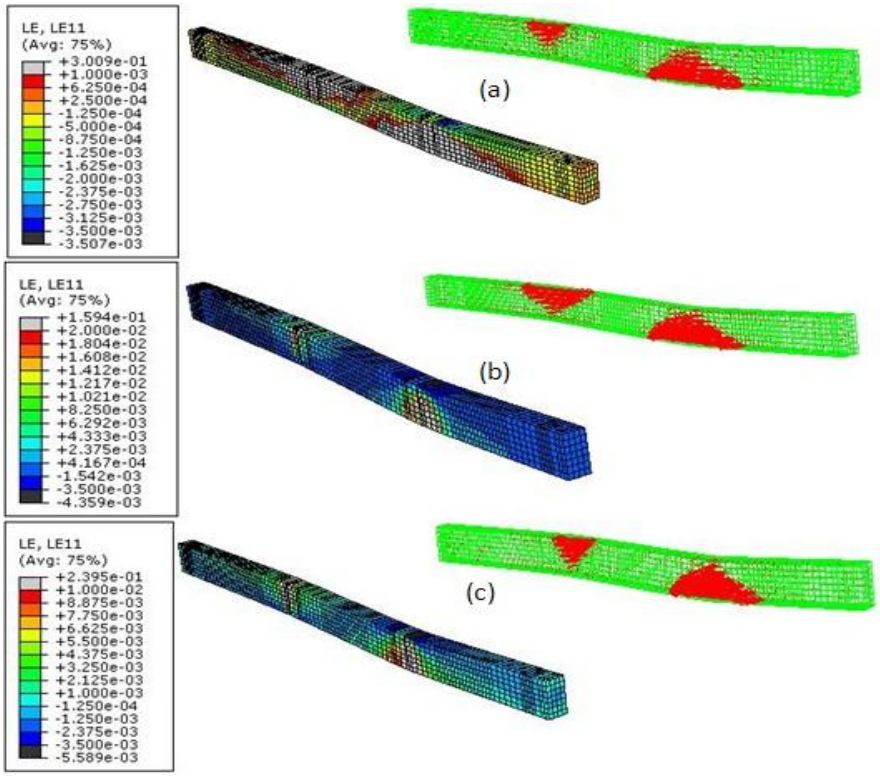


Figure 5.18: Principal strain contours and vectors for Case Study 2(a) column with $SI = 0\%$ at $\delta_u = 39.4\ mm$ for: (a) $V_f = 0\%$, (b) $V_f = 1.5\%$, and (c) $V_f = 2.5\%$

In conclusion, the addition of steel fibres improves the strength of the columns consistently. A similar trend is observed with regards to the stiffness and ductility of the SFRC columns. A critical threshold was found beyond which the addition of more fibres led to a less ductile response. This is similar to "over-reinforced" behaviour in conventional RC design.

5.3.3 Cracking pattern

This section discusses the cracking pattern for Case Study 2(a) columns analysed under monotonic loading. The model presented in the figures for each column is taken at its respective ultimate load (P_u) and deflection (δ_u), i.e. at failure.

5.3.3.1 Principal strain contours

Figures 5.19 to 5.21 present the principal strain contour for the columns analysed in the Case Study 2(a) at failure. The principal strain range was selected between an ultimate tensile strain of 0.001 (column without fibres) or 0.02 (SFRC column) and an ultimate compressive strain of -0.0035. From these figures, it is observed that the failure of the columns is characterised by tensile cracking at two regions: (i) the top of the section at intermediate support and (ii) the bottom of the section where the lateral load (*P*) is applied. The crack regions, represented in grey contour colour, cover a higher area for the column $V_f = 0\%$, and larger stirrups spacing increased.

The addition of fibres improves the crack propagation, where the maximum principal strain is found to concentrate more at the location of the intermediate support is and where the lateral loading is applied, and not throughout these spans.

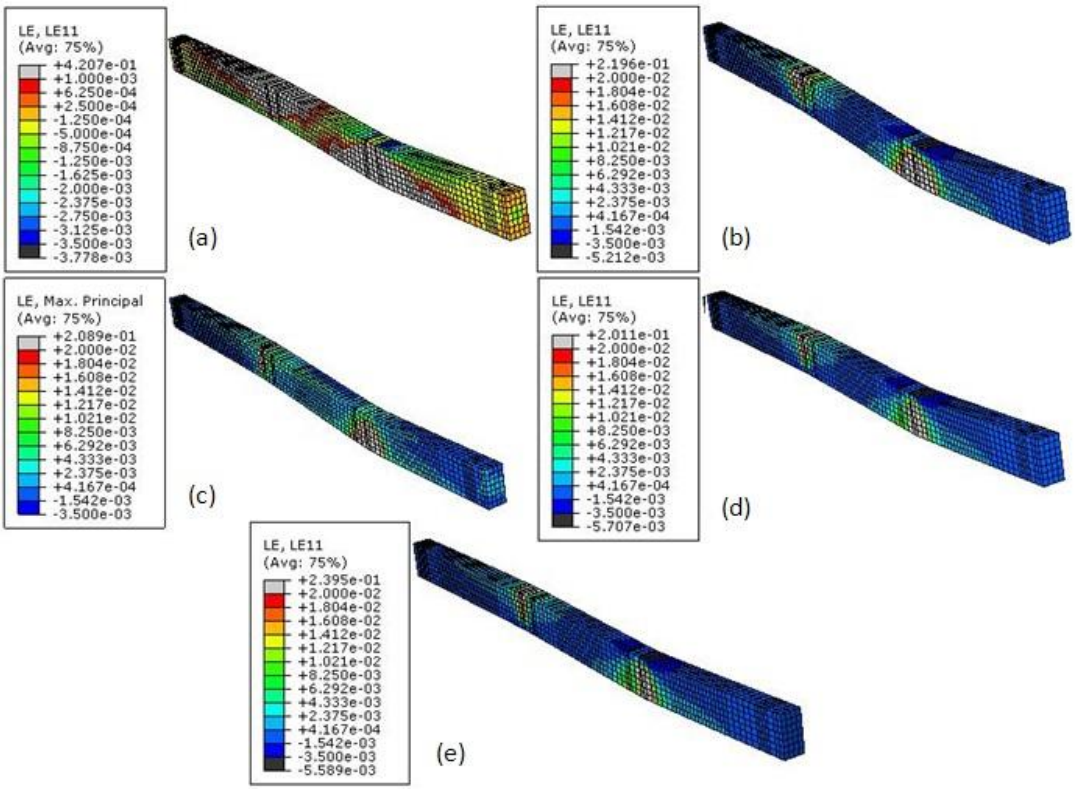


Figure 5.19: Principal strain contours for Case Study 2(a) column with $SI = 0\%$ for (a) $V_f = 0\%$, (b) $V_f = 1\%$, (c) $V_f = 1.5\%$, (d) $V_f = 2\%$ and (e) $V_f = 2.5\%$

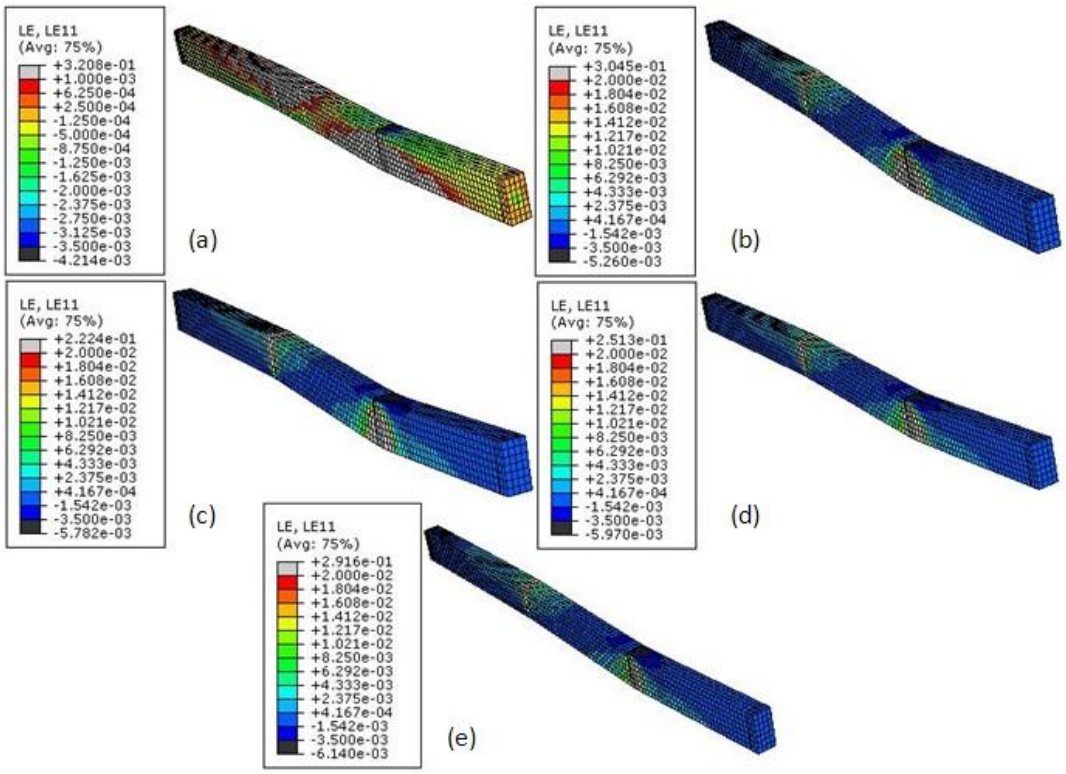


Figure 5.20: Principal strain contours for Case Study 2(a) column with $SI = 50\%$ for (a) $V_f = 0\%$, (b) $V_f = 1\%$, (c) $V_f = 1.5\%$, (d) $V_f = 2\%$ and (e) $V_f = 2.5\%$

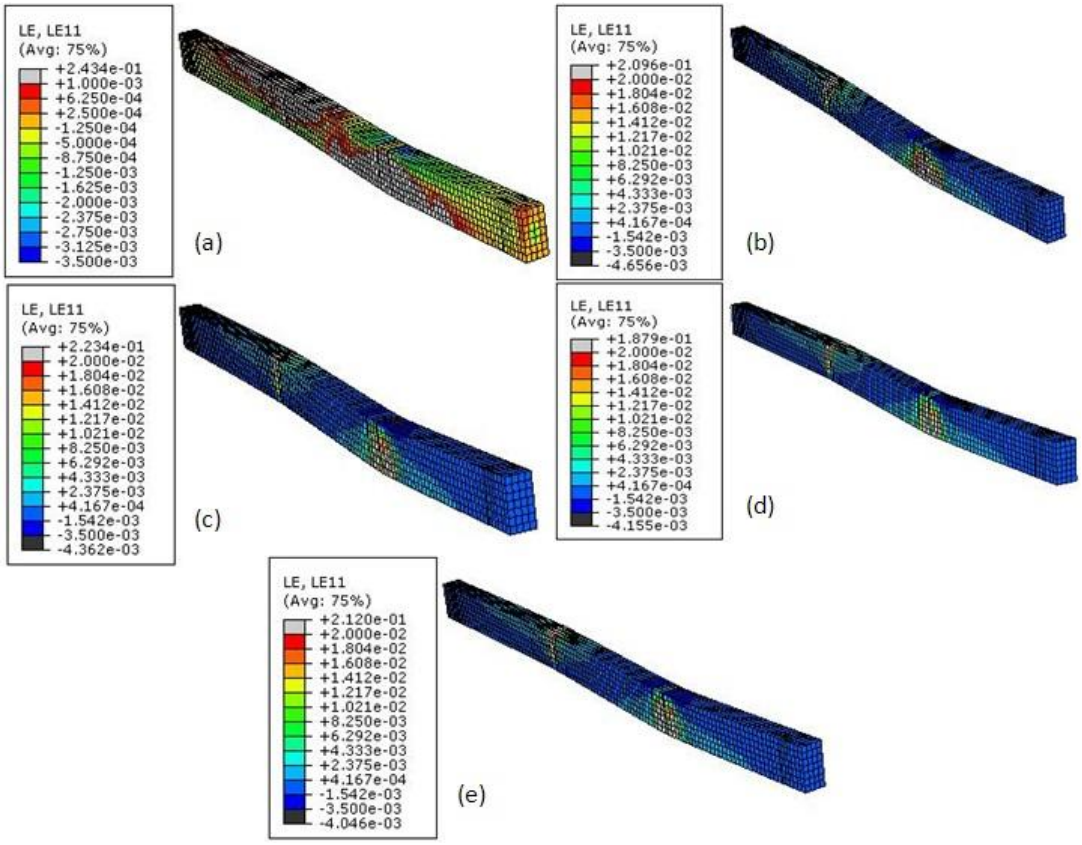


Figure 5.21: Principal strain contours for Case Study 2(a) column with $SI = 100\%$ for (a) $V_f = 0\%$, (b) $V_f = 1\%$, (c) $V_f = 1.5\%$, (d) $V_f = 2\%$ and (e) $V_f = 2.5\%$

5.3.3.2 Principal strain vectors

The principal vectors for column with $SI = 0\%$, $SI = 50\%$ and $SI = 100\%$ are given in Figures 5.22, 5.23 and 5.24, respectively. The cracks at failure for all columns are depicted clearly at the top of the section of the intermediate support and bottom of the section whereof the lateral load (P) is applied. There is a slight principal strain vectors at the column's span between these two regions for the column with no fibres, indicating some cracks propagated in this span, especially in the column with $SI = 100\%$.

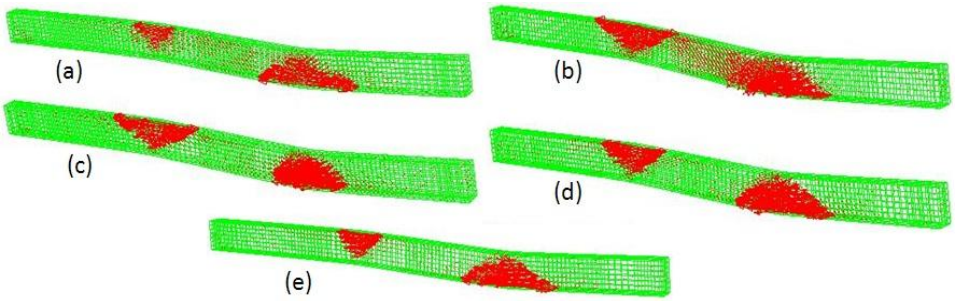


Figure 5.22: Principal strain vectors for Case Study 2(a) column with $SI = 0\%$ for (a) $V_f = 0\%$, (b) $V_f = 1\%$, (c) $V_f = 1.5\%$, (d) $V_f = 2\%$ and (e) $V_f = 2.5\%$

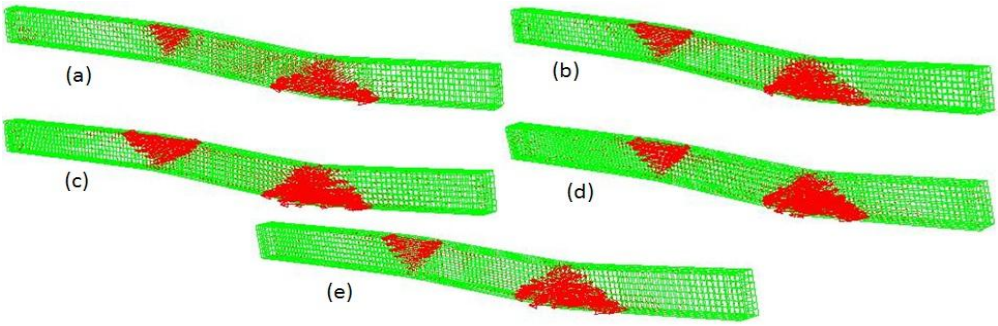


Figure 5.23: Principal strain vectors for Case Study 2(a) column with $SI = 50\%$ for (a) $V_f = 0\%$, (b) $V_f = 1\%$, (c) $V_f = 1.5\%$, (d) $V_f = 2\%$ and (e) $V_f = 2.5\%$

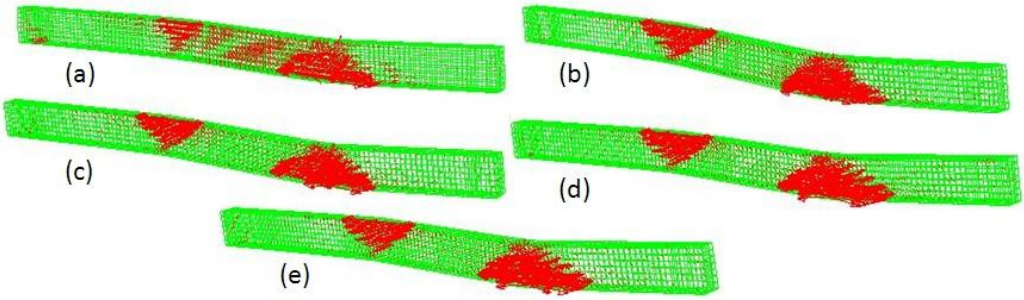


Figure 5.24: Principal strain vectors for Case Study 2(a) column with $SI = 100\%$ for (a) $V_f = 0\%$, (b) $V_f = 1\%$, (c) $V_f = 1.5\%$, (d) $V_f = 2\%$ and (e) $V_f = 2.5\%$

The strain vectors depict crack developed at the span between the intermediate support and the section where lateral load (*P*) is applied (see Figure 5.24 (a)). Thus it can be concluded that in this particular column with no fibres for the column with $SI = 100\%$, the cracking pattern suggested a bending-shear failure. However, inclusion of steel fibres, even at a fibre volume ratio of 1% improves the crack propagation and changes the mode of failure of the SFRC columns from shear to bending failure. Based on the cracking pattern observed in these figures, it can be concluded that all columns show a bending mode of failure, except for the column with no fibres in the most critical with $SI = 100\%$.

5.3.3.3 Deflected shapes

The main deformation of the columns occurs in the span where the lateral load (*P*) is applied, as evident in Figures 5.25, 5.26 and 5.27. Based on these figures, it can be concluded that, the failure occur with a big crack formation at the mid-span of the columns' second span (under the section where the lateral load is applied). The deformed shape of the beams is consistent with the location of the maximum principal strain contour and strain vectors. Thus, it can be concluded that, for all columns analysed under monotonic loading, the failure was attributed to a bending mode of failure, except for column $V_f = 0\%$ (column with $SI = 100\%$), in which the failure was attributed to a shear-bending failure .

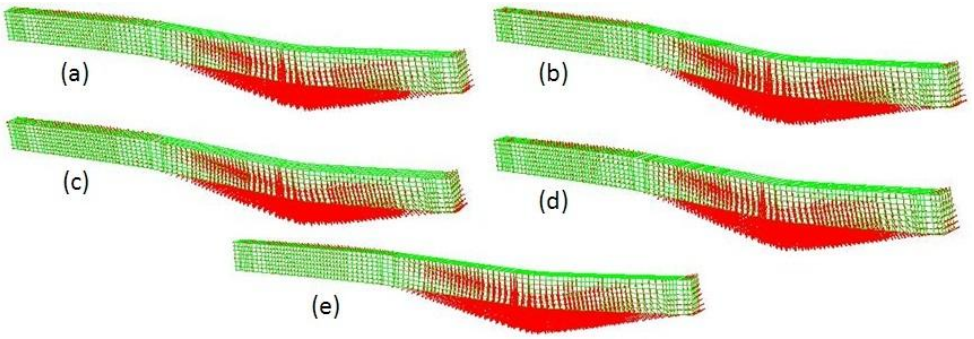


Figure 5.25: Deflected shapes for Case Study 2(a) column with $SI = 0\%$ for (a) $V_f = 0\%$, (b) $V_f = 1\%$, (c) $V_f = 1.5\%$, (d) $V_f = 2\%$ and (e) $V_f = 2.5\%$

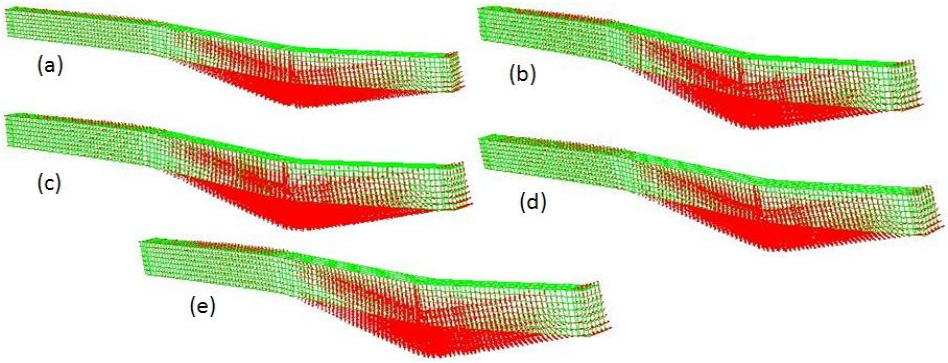


Figure 5.26: Deflected shapes for Case Study 2(a) column with $SI = 50\%$ for (a) $V_f = 0\%$, (b) $V_f = 1\%$, (c) $V_f = 1.5\%$, (d) $V_f = 2\%$ and (e) $V_f = 2.5\%$

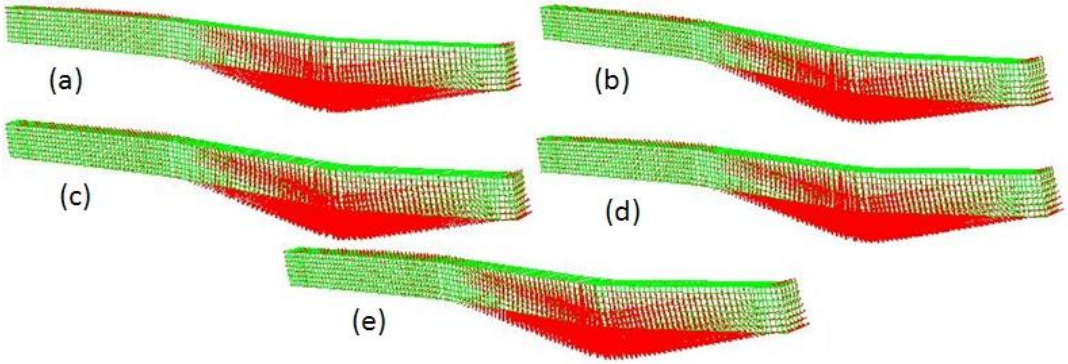


Figure 5.27: Deflected shapes for Case Study 2(a) column with $SI = 100\%$ for (a) $V_f = 0\%$, (b) $V_f = 1\%$, (c) $V_f = 1.5\%$, (d) $V_f = 2\%$ and (e) $V_f = 2.5\%$

5.3.4 Comparative study with control specimen using non-dimensional ratios

In this section, an overall comparison is made between the control specimen (i.e. the one with no fibres and full conventional shear reinforcement) and the columns with various fibre dosages and reduced stirrup spacing. The values of the strength, ductility and energy absorption were normalised by dividing them by the corresponding values of the control specimen. In this manner, overall conclusions were made on the potential of fibres to compensate for reduction in conventional reinforcement.

5.3.4.1 Strength ratio

The ratio between the maximum load (P_{max}) of each column and that for the control column $(P_{max,o})$ is shown in Figure 5.28. There is an upward trend in the $P_{max}/P_{max,o}$ ratio as observed from the figure for all columns as the fibre percentages are increased. However, for the maximum load ratio, columns with $SI = 100\%$ provided lower values than the other two *SI* values in all fibre volume ratios considered. In addition, the

maximum load ratio for columns with $SI = 50\%$ is higher than those with $SI = 0\%$ when fibre ratios are equal or higher than 1.5%. Based on this figure, it can be concluded that the maximum load ratio increases consistently with the increase of the fibre volume ratios. In columns with the smallest amount of stirrups, the maximum load ratio is lower than in the other different columns (compared at the same fibre dosage). However, it is important to note that the $P_{max}/P_{max,o}$ ratio for all SFRC columns is higher than in the $P_{max}/P_{max,o}$ ratio for the control column, when fibres are provided with a ratio of 1%. This indicates that the fibres at this dosage compensate for the loss of strength due to reduction in conventional shear reinforcement.

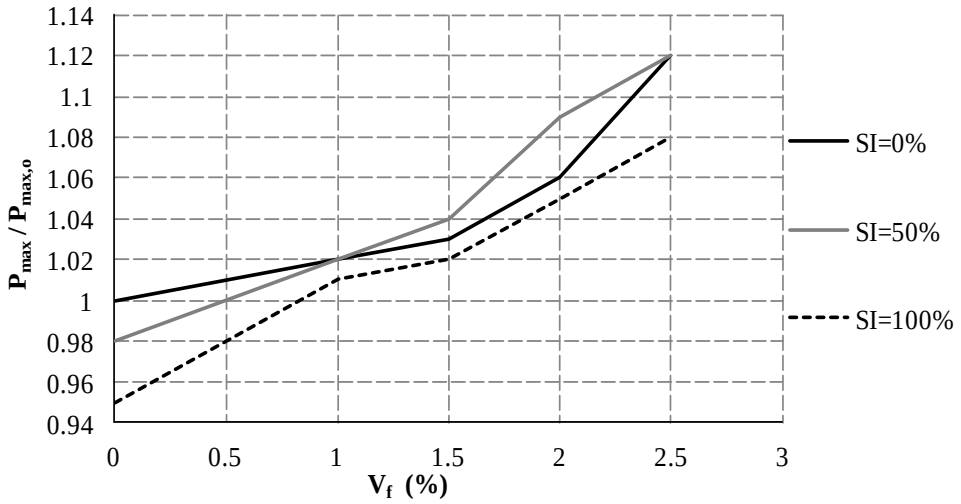


Figure 5.28: Ratio between the maximum load and that in the control column ($SI = 0\%, V_f = 0\%$) versus steel fibre volume fraction graph for Case Study 2(a)

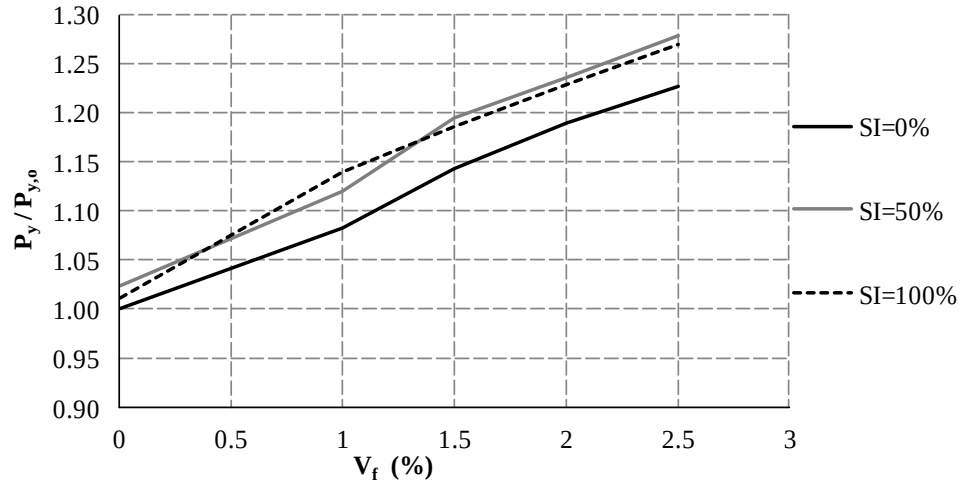


Figure 5.29: Ratio between the yielding load and that in the control column ($SI = 0\%, V_f = 0\%$) versus steel fibre volume fraction graph for Case Study 2(a)

The ratio between the yield load of each column (P_y) and that for the control column ($P_{y,o}$) is shown in Figure 5.29. Similar pattern (upward trend) is observed in the $P_y/P_{y,o}$ ratio as the fibre percentages are increased. Furthermore, the $P_y/P_{y,o}$ ratio for SFRC specimens with an increase in stirrup spacing is higher than those with original stirrup spacing ($i.e. SI = 0\%$). This again indicates that the fibres have the potential to compensate for reduction in conventional reinforcement.

5.3.4.2 Ductility ratio

The ductility ratios of all columns were normalised by dividing them by the ductility ratio of the control specimen $i.e. (\mu/\mu_o)$ and the results were plotted against the change in fibre volume fraction as depicted in Figure 5.30. Although there is an improvement observed in the ductility with the inclusion of steel fibres, the enhancement is limited to a certain ratio of fibres. This optimum ratio of fibres was observed in all specimens (i.e. for columns with $SI = 0\%$, 50% and 100%, the optimum fibre volume fractions are 1%, 1.5% and 2%, respectively). The addition of steel fibres above these fibre dosages reduced the ductility ratio, with the worst ductility ratio performance for SFRC columns with $V_f = 2.5\%$, as can be seen in the Figure 5.30. This can be explained by recalling that a higher fibre ratio leads to a stiffer column that deflects less.

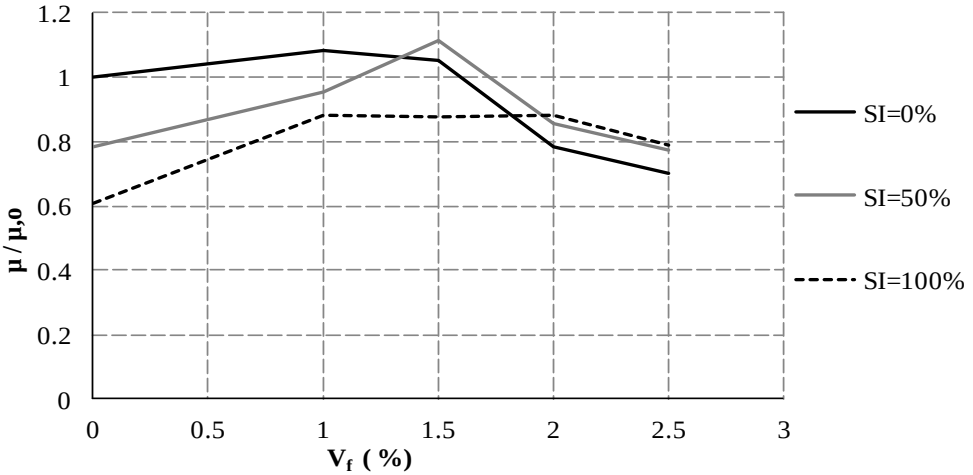


Figure 5.30: Ratio between the ductility ratio in each column and that in the control column ($SI = 0\%, V_f = 0\%$) versus steel fibre volume fraction graph for Case Study 2(a)

Moreover, it is interesting to see that the ductility ratios in the columns with $SI = 100\%$, between $V_f = 1\%$ and $V_f = 2\%$ are similar. In conclusion, for the columns with

an increased in the stirrups spacing, only column $V_f = 1.5\%$ from the columns with $SI = 50\%$ shows better performance in term of ductility than the control column, whereas, the remaining columns perform with a smaller ductility ratio than that in the control column. This suggests that, in terms of ductility, the fibres have potential to replace conventional reinforcement if the reduction in the latter is not very severe (i.e. *SI* not more than 50%). Nevertheless, adding fibres (even at high dosages such as *Vf* = 2.5%) will lead to ductility ratios μ higher than at least ~4, as presented in Tables 5.7 to 5.9 and Figure 5.31, which will be very useful in practice.

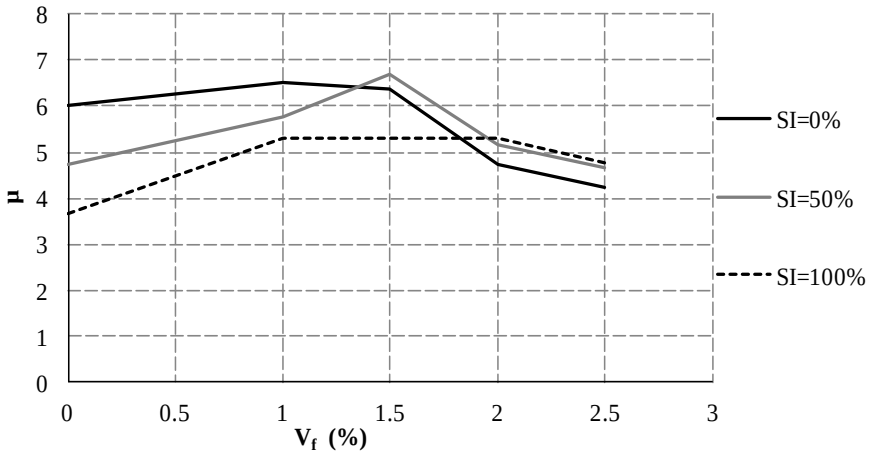


Figure 5.31: Ductility ratio in each column versus steel fibre volume fraction graph for Case Study 2(a)

5.3.4.3 Energy absorption ratio

The ratio between the energy absorption (E_a) in each column and that in the control column ($E_{a,o}$), is represented in Figure 5.32. In columns with $SI = 0\%$, the energy absorption ratio increases by up to 15%, but decreased by 25% when the fibre volume fractions exceeded 1.5%. In columns with increased in stirrups spacing, only $V_f = 1.5\%$ (with $SI = 50\%$) leads to a ratio larger than 1. The trend in the energy absorption figure is very similar to the one for ductility discussed in 5.3.4.2 above.

The preceding results show that fibres can compensate for reduction in energy absorption levels due to increase in stirrups spacing if the increase is within *SI* = 50%. However, this should not be interpreted to indicate that fibres do not improve the energy absorption. To illustrate this, a further comparison was made but now the energy absorption ratio for every SFRC column is normalised by that for its counterpart column without fibres (i.e. $V_f = 0\%$) as shown in Figure 5.33. From the figure, it is

clear that the energy absorption for SFRC columns increased significantly up to 61% and 77% for $SI = 50\%$ and $SI = 100\%$, respectively. This indicates that the energy absorption of the SFRC columns increased due to steel fibres, even when the stirrup spacing was increased.

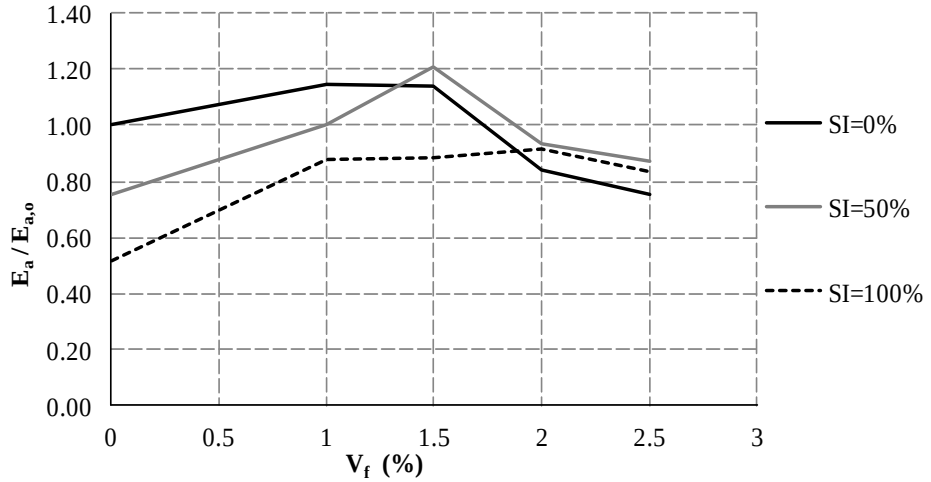


Figure 5.32: Ratio between the energy absorption in each column and that in the control column ($SI = 0\%, V_f = 0\%$) versus steel fibre volume fraction graph for Case Study 2(a)

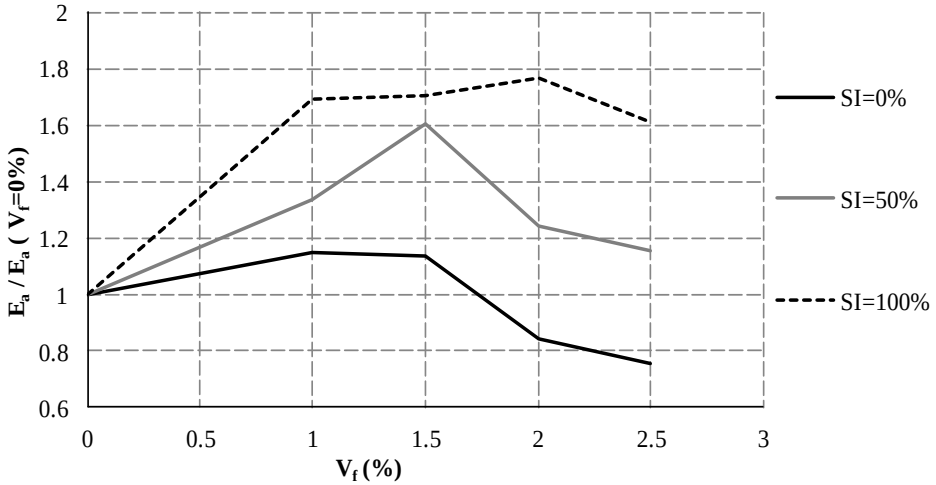


Figure 5.33: Ratio between the energy absorption in each column and that in the plain reinforced concrete column ($V_f = 0\%$) versus steel fibre volume fraction graph for Case Study 2(a)

It is interesting to see that the energy absorption ratio for the columns with SI=100% provides the best performance. This demonstrates that the fibres will provide higher energy absorption and ductility as the conventional reinforcement is reduced. Conversely, the response becomes less ductile if the fibres are provided in addition to

full conventional reinforcement (i.e. the "over-reinforced" brittle response discussed earlier). This suggest that there an optimum fibre content that can help provide best strength, ductility and energy absorption levels.

5.3.5 Comparison between FE results and analytical calculation

In this section, the results obtained from the FE analyses are compared with those calculated based on Eurocode 2 (2004). Adopting a rectangular compressive-stress block as recommended by Eurocode 2 (2004), the flexural capacity of the section is calculated as M_p, for a simultaneous axial force, $N \approx 0.2bhfc$. An additional (and simplified) rectangular tensile-stress block is added to calculate the M_p for SFRC sections, as suggested by Concrete Society TR-63 (2007).

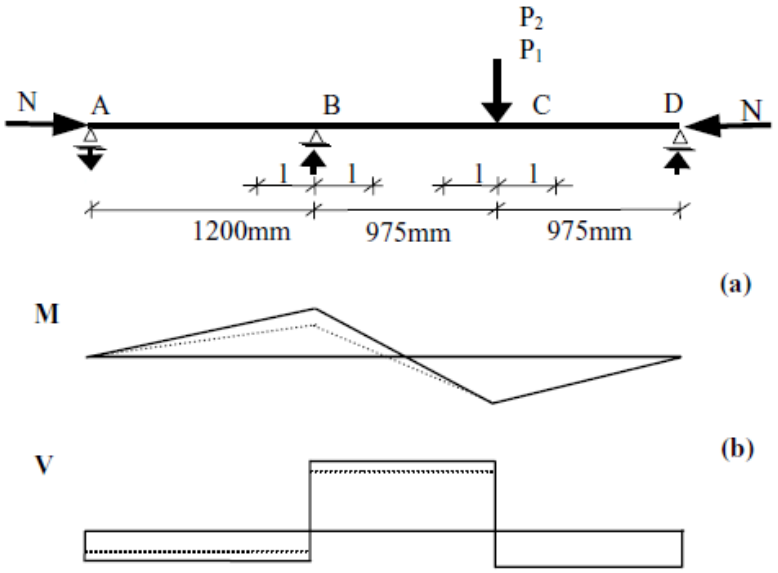


Figure 5.34: The loading condition, bending moment (M) and shear force (V) diagram from Case Study 2 (adapted from: Kotsovos et al, 2007)

V_f (%)	M_p (kNm)
0	54.01
1	58.12
1.5	60.14
2	62.13
2.5	64.12

Table 5.10: Section flexural capacity (M_p) calculated based on Eurocode 2

Figure 5.34 shows the bending moment and shear force diagram for the column, which can be established based on the values calculated for the M_p. This is achieved by

assuming that yielding occurs when either the reinforcement yields in tension or the concrete strain at the extreme compressive fibre attain a value of 0.002. The values calculated for these moments, regardless of the loading conditions, for each fibre ratio are summarised in Table 5.9.

Tables 5.11 to 5.13 present a summary of the values obtained from the FE analysis and the values calculated based on Eurocode 2 (2004) for column with $SI = 0\%$ to $SI = 100\%$. The parameters in the table can be defined as follows: the load at formation of the 1st plastic hinge ($P_{1p} = P_y = 2.67\ M_p$) and load at formation of the 2nd plastic hinge ($P_{2p} = 3.07 M_p$).

V_f	FE results		Values calculated based on Eurocode 2 (2004)		
(%)	P_{max}	δ_{Pmax}	$P_y = P_{1p}$	P_{2p}	P_{max}/P_{2p}
0	179.90	40.10	144.19	165.80	1.09
1	183.20	50.40	155.18	178.43	1.03
1.5	184.60	34.30	160.58	184.63	1.00
2	191.30	19.30	165.90	190.75	1.00
2.5	200.70	34.20	171.19	196.84	1.02

Table 5.11: Comparison of analysis results and calculated values for Case Study 2(a) column with $SI = 0\%$

V_f	FE results		Values calculated based on Eurocode 2 (2004)		
(%)	P_{max}	δ_{Pmax}	$P_y = P_{1p}$	P_{2p}	P_{max}/P_{2p}
0	176.10	39.50	144.19	165.80	1.06
1	183.70	34.50	155.18	178.43	1.03
1.5	187.20	24.20	160.58	184.63	1.01
2	195.60	19.20	165.90	190.75	1.03
2.5	200.60	19.20	171.19	196.84	1.02

Table 5.12: Comparison of analysis results and calculated values for Case Study 2(a) column with $SI = 50\%$

V_f	FE results		Values calculated based on Eurocode 2 (2004)		
(%)	P_{max}	δ_{Pmax}	$P_y = P_{1p}$	P_{2p}	P_{max}/P_{2p}
0	170.80	33.40	144.19	165.80	1.03
1	181.60	38.00	155.18	178.43	1.02
1.5	183.10	23.30	160.58	184.63	0.99
2	188.70	18.40	165.90	190.75	0.99
2.5	193.60	18.40	171.19	196.84	0.98

Table 5.13: Comparison of analysis results and calculated values for Case Study 2(a) column with $SI = 100\%$

Comparison between the results obtained from FE analysis and values calculated based on Eurocode 2 (2004) shows a good agreement with less than 10% discrepancy for the ratio P_{max}/P_{2p}as given in the tables.

5.4 Case Study 2(b): Parametric study analysed under combined axial force and reversed-cyclic loading

5.4.1 Strength

Figures 5.35, 5.36 and 5.37 presents the FE analysis obtained for Case Study 2(b) columns with *SI* = 0%, 50% and 100%, respectively. In addition, Figure 5.38 to 5.40 shows the load-deflection of the columns for each fibre volume fraction. Some of the significant loads and their deflections are summarised into Tables 5.14 to 5.16.

Under reversed-cyclic loading, continuous increase in the strength, (i.e P_{max}) is observed, as the fibre amount is increase. This behaviour is consistent throughout all the columns analysed by FE model in ABAQUS. Addition of steel fibres reduces the cracking by controlling the crack opening width. Due to the fibres bridging the cracks, a higher load is required in order to produce a similar deflection. Consequently, the amount of fibres contributes to the increase in the strength and stiffness of the SFRC structures.

In general, the yielding load (P_y) in the SFRC columns show enhancement with an average value of 19.7%; whilst, for $P_{max}/\ P_y$ ratio, the discrepancies in comparison to the control column is less than 14%, except for column $V_f = 2.5\%$ from the column with $SI = 0\%$. This column fails slightly after three number of cycles (N_c), due to the high fibre volume fraction, which increase the stiffness of the column leading it to deflect less, and consequently lose its ductility at an early stage. Therefore, for the column $V_f = 2.5\%$ ($SI = 0\%$), the $P_{max} = P_y$.

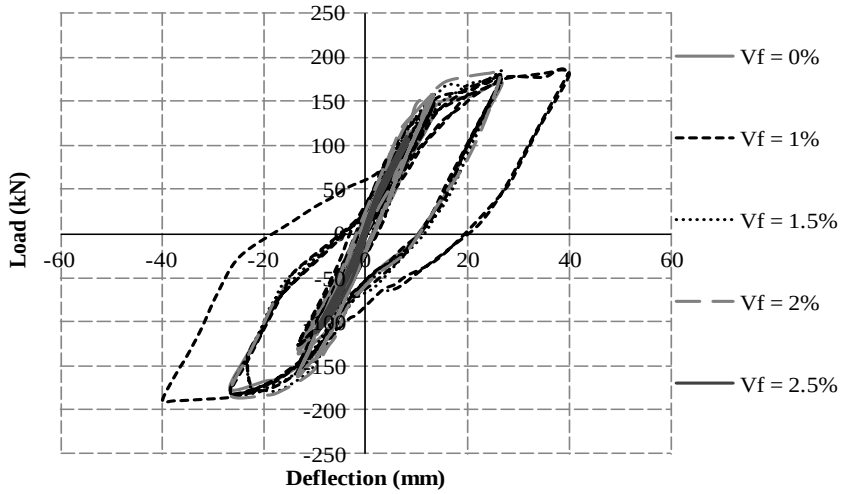


Figure 5.35: Load-deflection curve for Case Study 2(b), column with $SI = 0\%$

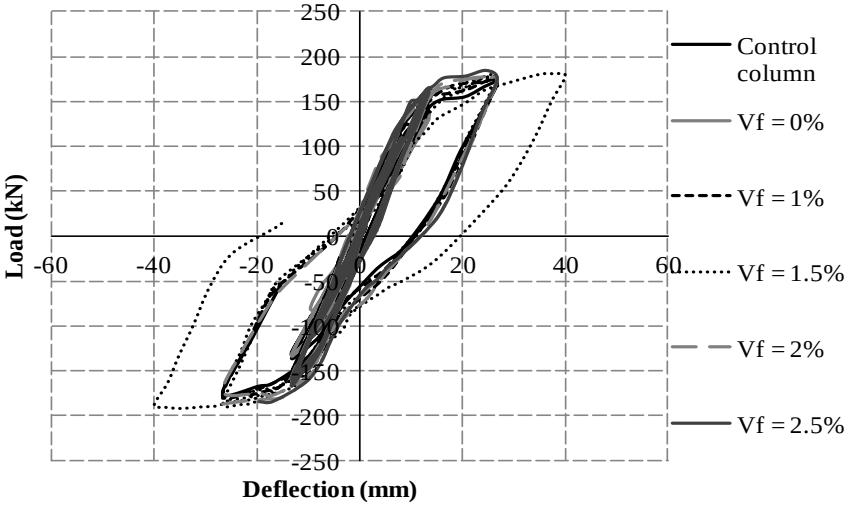


Figure 5.36: Load-deflection curve for Case Study 2(b), column with $SI = 50\%$

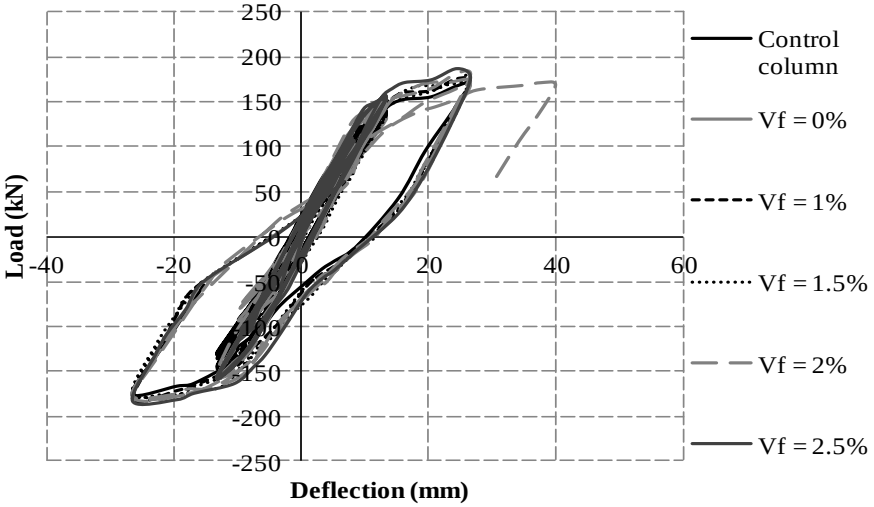


Figure 5.37: Load-deflection curve for Case Study 2(b), column with $SI = 100\%$

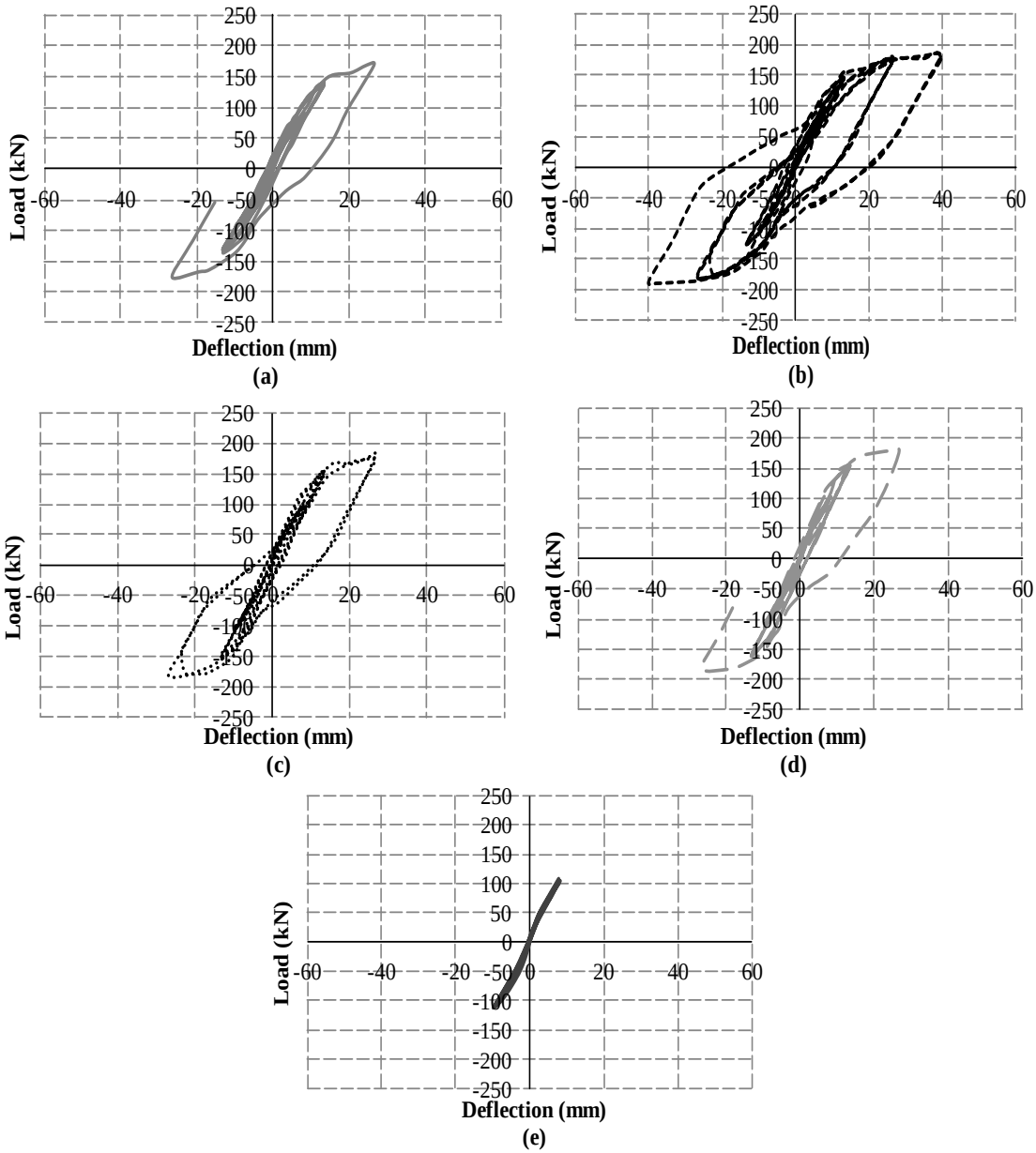


Figure 5.38: Load-deflection curve for Case Study 2(b) column with $SI = 0\%$ for each fibre fraction: (a) $V_f = 0\%$, (b) $V_f = 1\%$, (c) $V_f = 1.5\%$, (d) $V_f = 2\%$ and (e) $V_f = 2.5\%$

V_f (%)	N_c	P_y (kN)	δ_y (mm)	P_u (kN)	δ_u (mm)	P_{max} (kN)	δ_{Pmax} (mm)	$\mu = \frac{\delta_u}{\delta_y}$	$\frac{P_{max}}{P_y}$
0	6.86	91.4	8.0	170.3	26.6	170.3	26.6	3.33	1.86
1	10.46	98.3	8.0	183.2	40.0	187.4	38.8	5.01	1.91
1.5	7.97	101.7	8.0	174.1	26.6	182.1	26.6	3.33	1.79
2	6.86	104.7	8.0	180.6	26.6	181.0	24.5	3.33	1.73
2.5	3.15	107.7	8.0	106.6	8.3	107.7	8.0	1.04	1

Table 5.14: Result summary from load-deflection curve for Case Study 2(b) column with $SI = 0\%$

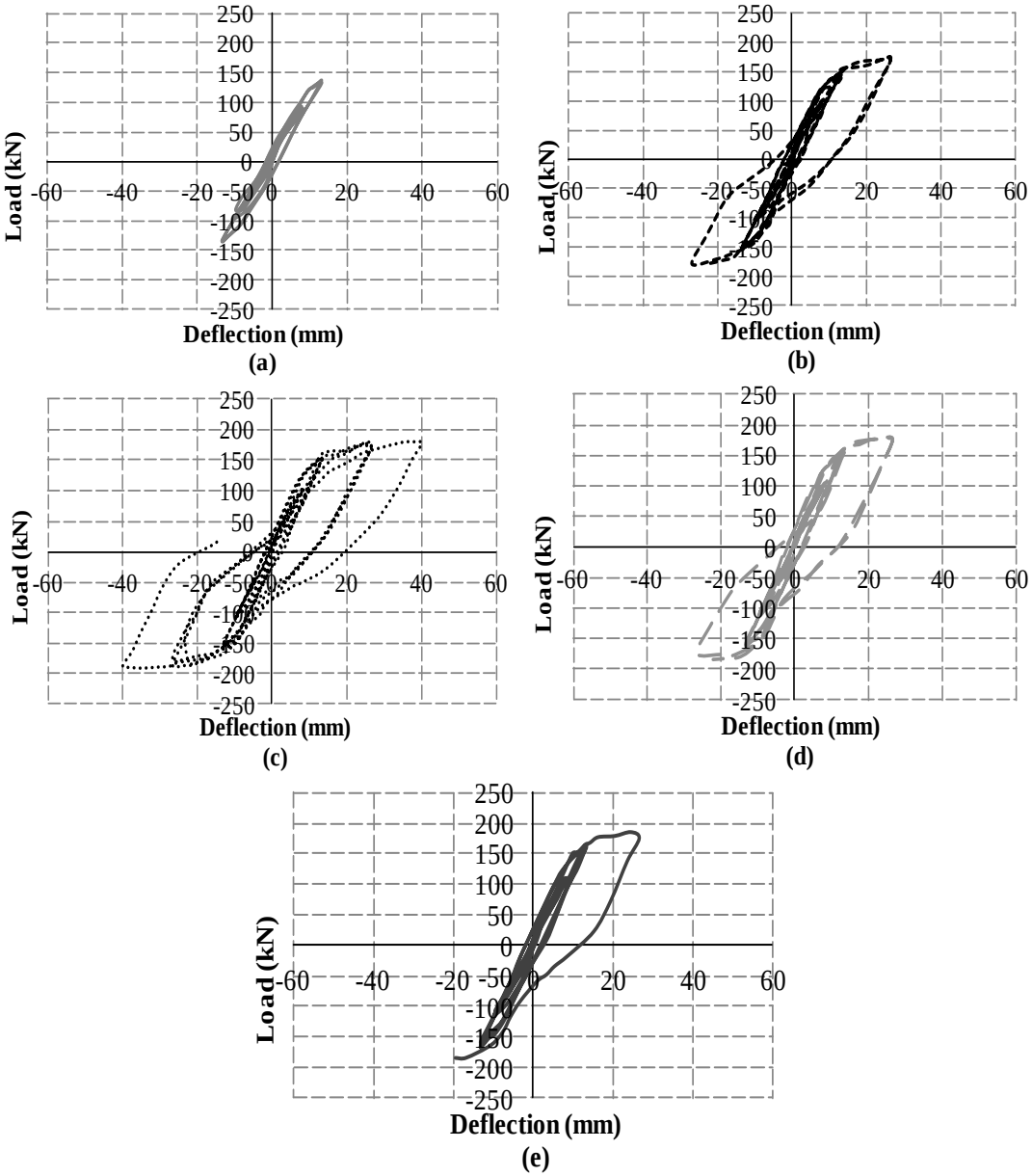


Figure 5.39: Load-deflection curve for Case Study 2(b) column with $SI = 50\%$ for each fibre fraction: (a) $V_f = 0\%$, (b) $V_f = 1\%$, (c) $V_f = 1.5\%$, (d) $V_f = 2\%$ and (e) $V_f = 2.5\%$

V_f (%)	N_c	P_y (kN)	δ_y (mm)	P_u (kN)	δ_u (mm)	P_{max} (kN)	δ_{Pmax} (mm)	$\mu = \frac{\delta_u}{\delta_y}$	$\frac{P_{max}}{P_y}$
CC	6.86	91.4	8.0	170.3	26.6	170.3	26.6	3.33	1.86
0	4.95	91.9	8.0	132.5	13.3	132.5	13.3	1.67	1.39
1	7.75	98.2	8.0	172.3	26.6	174.5	26.6	3.33	1.78
1.5	9.91	103.2	8.0	178.7	40.0	181.0	37.7	5.01	1.75
2	7.75	106.5	8.0	175.6	26.6	177.4	23.4	3.33	1.67
2.5	6.75	109.8	8.0	174.7	26.6	185.0	24.5	3.33	1.69

Table 5.15: Result summary from load-deflection curve for Case Study 2(b) column with $SI = 50\%$

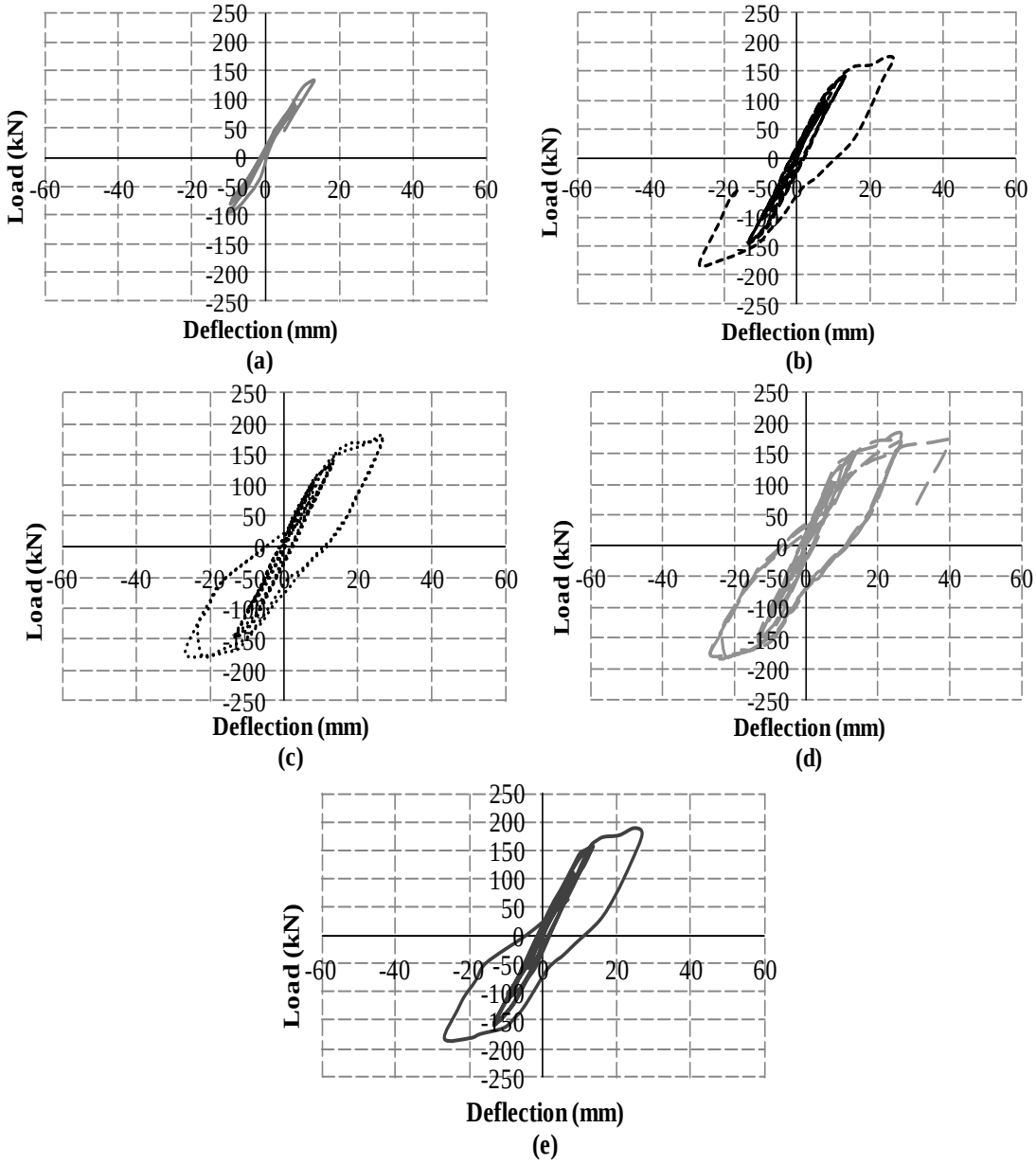


Figure 5.40: Load-deflection curve for Case Study 2(b) column with $SI = 100\%$ for each fibre fraction: (a) $V_f = 0\%$, (b) $V_f = 1\%$, (c) $V_f = 1.5\%$, (d) $V_f = 2\%$ and (e) $V_f = 2.5\%$

V_f (%)	N_c	P_y (kN)	δ_y (mm)	P_u (kN)	δ_u (mm)	P_{max} (kN)	δ_{Pmax} (mm)	$\mu = \frac{\delta_u}{\delta_y}$	$\frac{P_{max}}{P_y}$
CC	6.86	91.4	8.0	170.3	26.6	170.3	26.6	3.33	1.86
0	3.42	91	8.0	131.8	13.3	131.8	13.3	1.67	1.36
1	6.97	100.1	8.0	171.6	26.6	175.4	24.5	3.33	1.66
1.5	8.0	103.7	8.0	170.5	26.6	178.7	26.6	3.33	1.63
2	9	107.3	8.0	170.9	40.1	182.5	24.4	5.01	1.61
2.5	7.07	110.6	8.0	176.9	26.6	187.8	24.5	3.33	1.61

Table 5.16: Result summary from load-deflection curve for Case Study 2(b) column with $SI = 100\%$

5.4.2 Ductility

In terms of ductility, addition of fibres provide better ductility (i.e. μ) than that in the column with no fibres (but with same stirrups spacing). However, for one particular column with $V_f = 2.5\%$ (and with $SI = 0\%$), the failure occur at early stages of the analysis. In comparison to the control specimen, the μ of the SFRC columns show improvement in ductility (i.e μ = 5.01) for the columns with $SI = 0\%, 50\%$ and 100%, which are reached at $V_f = 1\%, 1.5\%$ and 2%, respectively. In addition, the remaining of the SFRC columns (except for the brittle column mentioned earlier) show similar μ with the control specimen.

N_c is the number of load cycles that are applied before failure. For all SFRC columns (except for column $V_f = 2.5\%$,with $SI = 0\%$) N_c is larger than that for $V_f = 0\%$ with the same stirrup spacing. The increase in N_c in relation to the column without fibre is up to 55%, 100% and 164% for the column with $SI = 0\%$, 50% and 100%, respectively. The optimum fibre volume fraction for the SFRC column in the different stirrup spacing is similar to that obtained for μ. This signifies the capability of steel fibres in bridging the cracks propagation and transmitting the load along the columns span, acting as part of the shear reinforcement. Therefore, an increase in N_c and μ are observed from the SFRC columns, and this is significantly higher, in comparison to the column in the same *SI* with no fibres. In addition, except for column discussed earlier that show low ductility performance, the remaining SFRC columns demonstrated similar or better performance, comparable to the control column ($SI = 0\%, V_f = 0\%$). Furthermore, the trend observed in the ductility shows that after optimum fibre volume fraction, the SFRC columns show decreased in N_c and μ. This suggests that the provision of fibres in addition to sufficient shear reinforcement can lead to brittleness as observed earlier in the monotonic-load case.

5.4.3 Cracking pattern

This section presents and discusses the principal strain contours, strain vectors and deformation shapes of the analysed columns taken at the final load level at failure under the reversed-cyclic loading. Based on these principal strain contours and vectors, the cracking pattern and mode of failure for the columns are determined.

5.4.3.1 Principal strain contours

To capture the cracking pattern developing in the columns, the range of maximum principal strain of columns with and without fibres is selected to be at 0.02 and 0.002 (i.e. the tensile cracking strain), respectively. Whereas a value of -0.0035 is adopted as the compressive cracking strain.

In almost all the columns analysed under reversed-cyclic loading, the cracking propagates at the two main critical regions, specifically at the intermediate support and the section in which the lateral load (P) is applied. In particular, for the columns with $V_f = 0\%$ (for column with $SI = 50\%$ and 100%) and $V_f = 2.5\%$ (for column with $SI = 100\%$), the intensive cracking occured at the location where the lateral load is applied. From each series, the cracks opening for the column with no fibres are intensive and broad, especially at the location where the lateral load is applied. The addition of steel fibres acts to reduce the crack opening, thus narrower cracks opening width and propagation are observed in the SFRC columns.

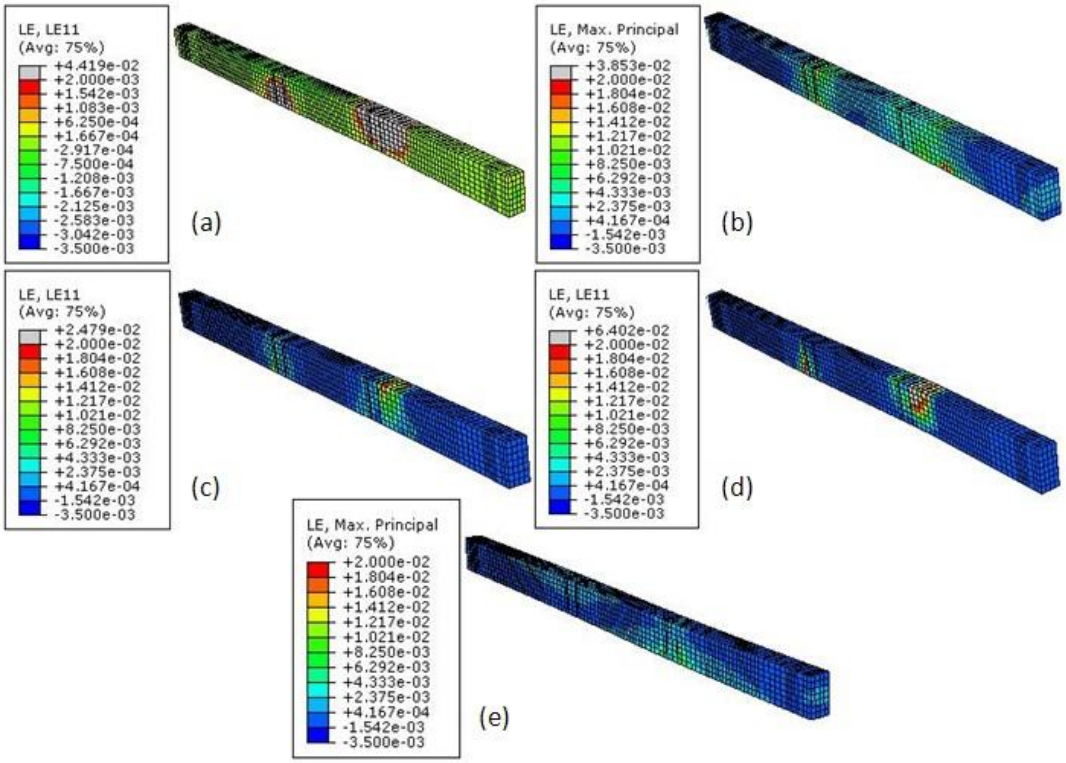


Figure 5.41: Principal strain contours for Case Study 2(b) column with $SI = 0\%$ for (a) $V_f = 0\%$, (b) $V_f = 1\%$, (c) $V_f = 1.5\%$, (d) $V_f = 2\%$ and (e) $V_f = 2.5\%$

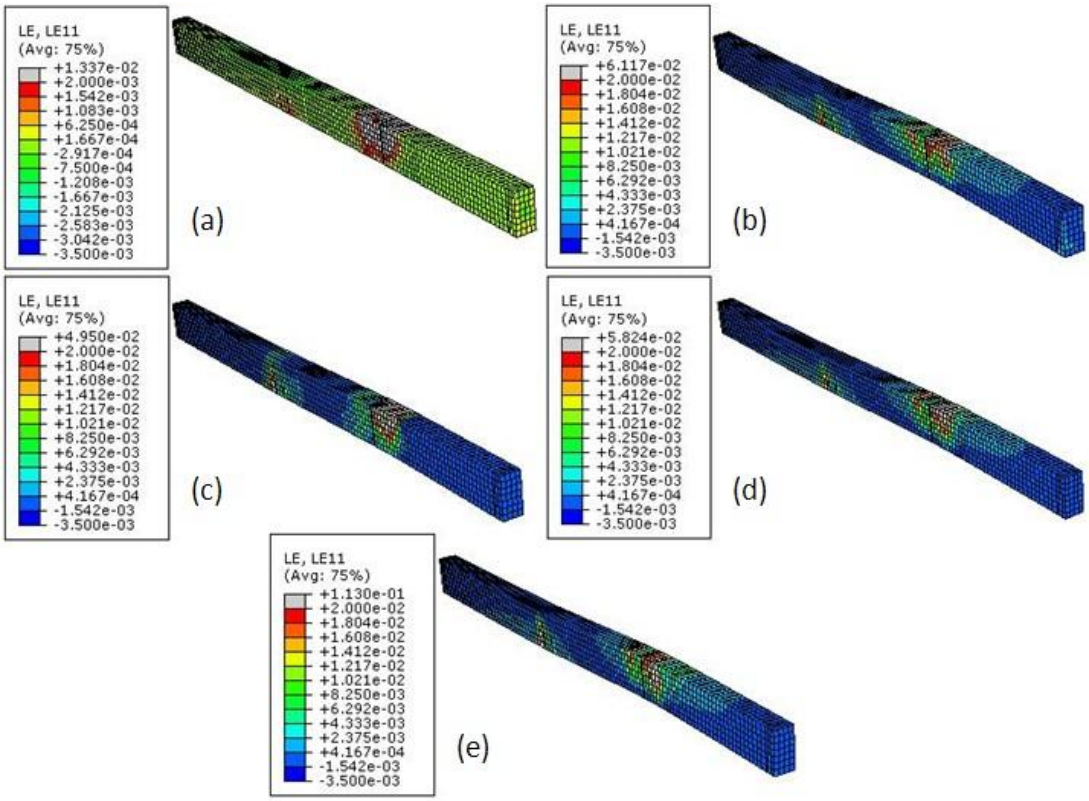


Figure 5.42: Principal strain contours for Case Study 2(b) column with $SI = 50\%$ for (a) $V_f = 0\%$, (b) $V_f = 1\%$, (c) $V_f = 1.5\%$, (d) $V_f = 2\%$ and (e) $V_f = 2.5\%$

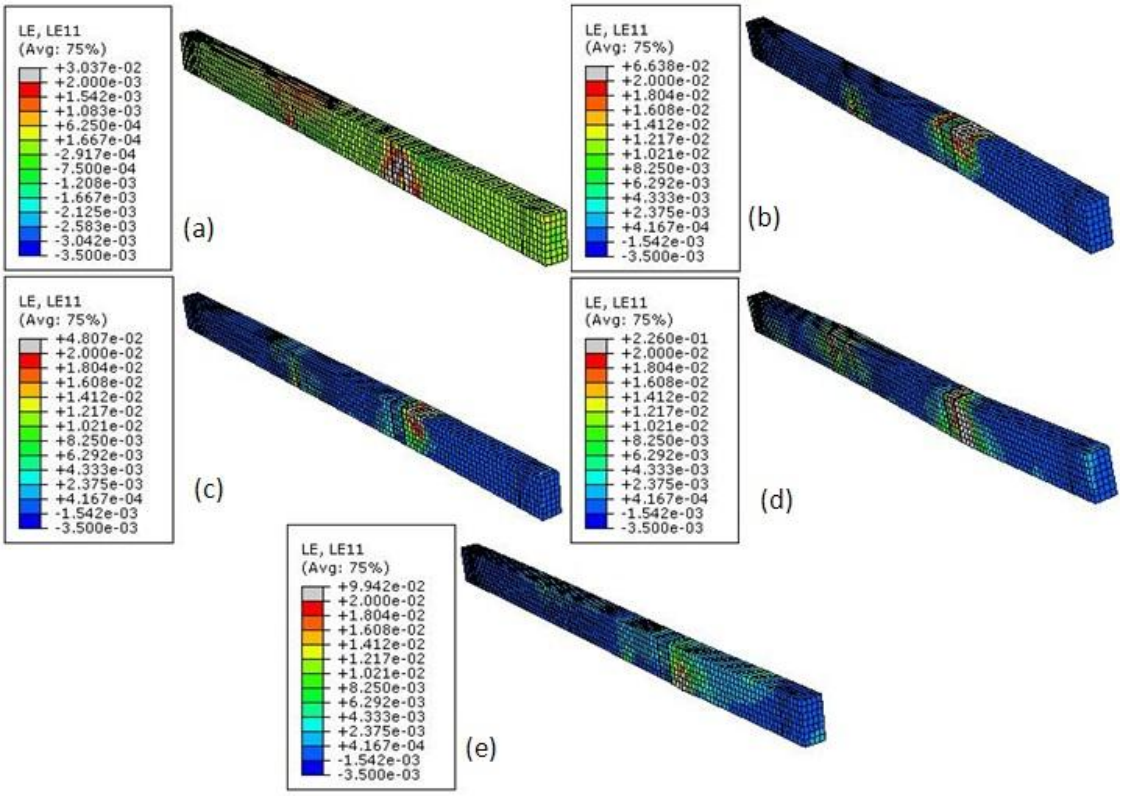


Figure 5.43: Principal strain contours for Case Study 2(b) column with $SI = 100\%$ for (a) $V_f = 0\%$, (b) $V_f = 1\%$, (c) $V_f = 1.5\%$, (d) $V_f = 2\%$ and (e) $V_f = 2.5\%$

The principal strain contour of the column $V_f = 2.5\%$ (column with $SI = 0\%$) that fails early after 3 cycles is presented in Figure 5.41(e). For this particular case, the condition of the column at failure is characterised with cracking that developed along the two continuous spans, and most of the principal strains have exceeded the tensile cracking strain.

5.4.3.2 Principal strain vectors

The crack propagation pattern in the columns can be clearly observed in Figures 5.44 to 5.46. The strain vectors can be adopted to conveniently indicate the cracking pattern for the columns. Based on this, it can be observed that, in most of the analysed, the failure is due to the cracks opening in these two regions: (i) intermediate support and (ii) the region where the lateral load (*P*) is applied. The extent of strain vectors as shown in Figure 5.44 (e) marks the cracking pattern of the column $V_f = 2.5\%$ that exhibited brittle (i.e. shear failure).

In the column with $SI = 50\%$, the addition of fibres reduces the crack, and facilitates the moment redistribution, thus allowing the SFRC columns to develop a second plastic hinge at the intermediate support. In contrast, the column with no fibres (i.e. column with $V_f = 0\%$) fails with intensive cracking at the mid-span of the second span of the column. In addition, for the column with $SI = 50\%$, the cracking is larger in the region where the lateral load (*P*) is applied.

Based on the cracking patterns observed, it is concluded that even in the severe loading type of reversed-cyclic loading (e.g. the one associated with seismic loading), at reduced shear reinforcement, steel fibres show capability of increasing the ductility of the columns. Furthermore, the cracking propagation is controlled through steel fibres pull-out resistance.

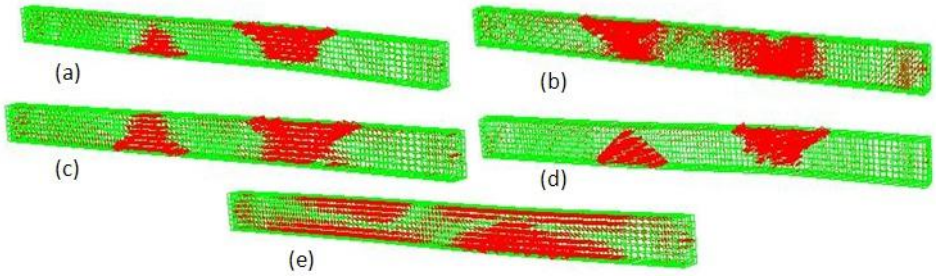


Figure 5.44: Principal strain vectors for Case Study 2(b) column with $SI = 0\%$ for (a) $V_f = 0\%$, (b) $V_f = 1\%$, (c) $V_f = 1.5\%$, (d) $V_f = 2\%$ and (e) $V_f = 2.5\%$

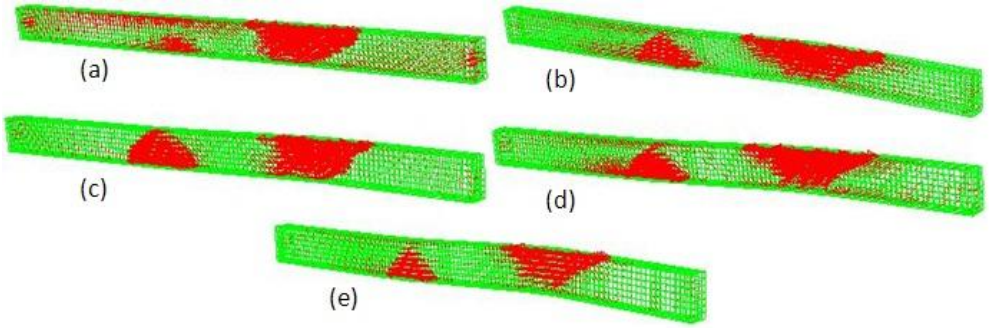


Figure 5.45: Principal strain vectors for Case Study 2(b) column with $SI = 50\%$ for (a) $V_f = 0\%$, (b) $V_f = 1\%$, (c) $V_f = 1.5\%$, (d) $V_f = 2\%$ and (e) $V_f = 2.5\%$

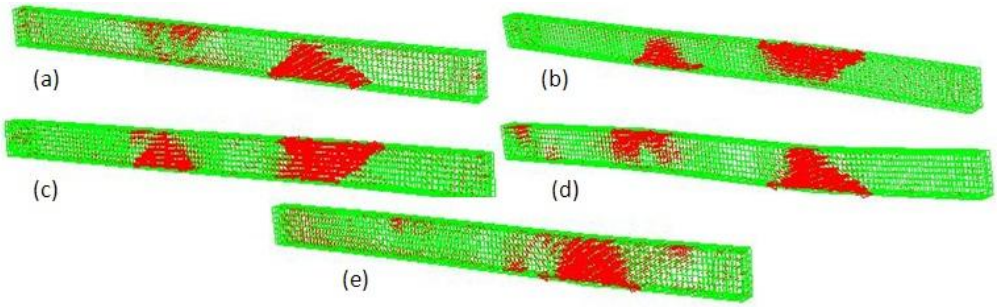


Figure 5.46: Principal strain vectors for Case Study 2(b) column with $SI = 100\%$ for (a) $V_f = 0\%$, (b) $V_f = 1\%$, (c) $V_f = 1.5\%$, (d) $V_f = 2\%$ and (e) $V_f = 2.5\%$

5.4.3.3 Deflected shapes

The deformation of the columns at the very last load level before failure is shown in the figures below. The deformation is related to the direction of the cyclic load (upward or downward) and load level before failure. Deflection at the intermediate support is presented for the columns which exhibit high principal strain in the intermediate support region as can be seen from Figure 5.47 (b) and (e), and Figure 5.49 (a) and (d). The columns in the column with $SI = 50\%$ fail in the similar load cycles' direction.

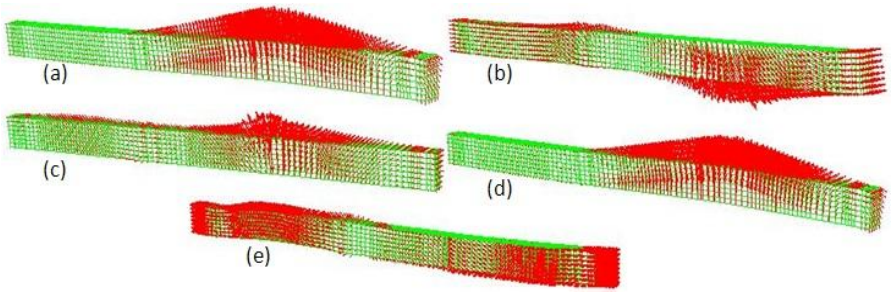


Figure 5.47: Deflected shapes for Case Study 2(b) column with $SI = 0\%$ for (a) $V_f = 0\%$, (b) $V_f = 1\%$, (c) $V_f = 1.5\%$, (d) $V_f = 2\%$ and (e) $V_f = 2.5\%$

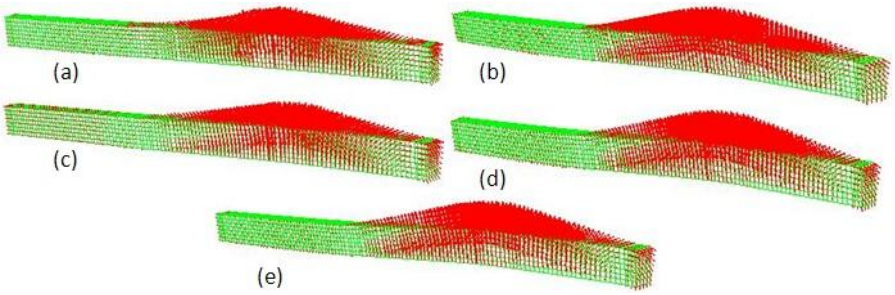


Figure 5.48: Deflected shapes for Case Study 2(b) column with $SI = 50\%$ for (a) $V_f = 0\%$, (b) $V_f = 1\%$, (c) $V_f = 1.5\%$, (d) $V_f = 2\%$ and (e) $V_f = 2.5\%$

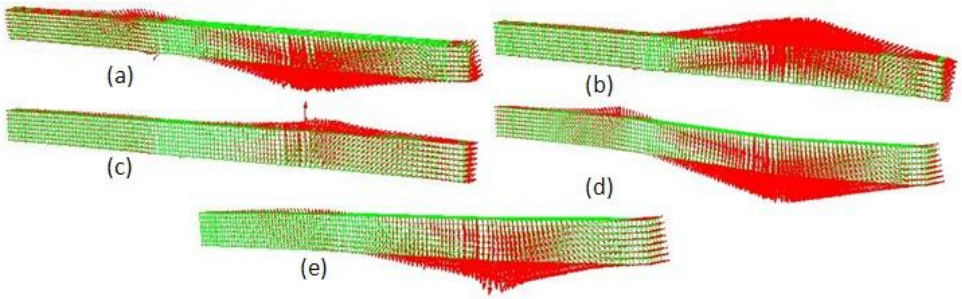


Figure 5.49: Deflected shapes Case Study 2(b) column with $SI = 100\%$ for (a) $V_f = 0\%$, (b) $V_f = 1\%$, (c) $V_f = 1.5\%$, (d) $V_f = 2\%$ and (e) $V_f = 2.5\%$

5.4.3 Comparative study with control specimen using non-dimensional ratios

5.4.4.1 Strength ratio

Figure 5.50 shows the ratio between the maximum load (P_{max}) and that in the control column ($P_{max,o}$). There is an upward trends observed in the $P_{max}/P_{max,o}$ ratio for the SFRC columns with the increased in stirrups spacing (i.e. columns with $SI = 50\%$ and $SI = 100\%$). In contrast, in the series with the original stirrups spacing (columns with $SI = 0\%$), the maximum load ratio shows a downward trend after $V_f = 1\%$. The

discrepancy is caused by the lower cycles analysed in the FE model, especially for $V_f = 2.5\%$, which failed at 3.15 number of cycles.

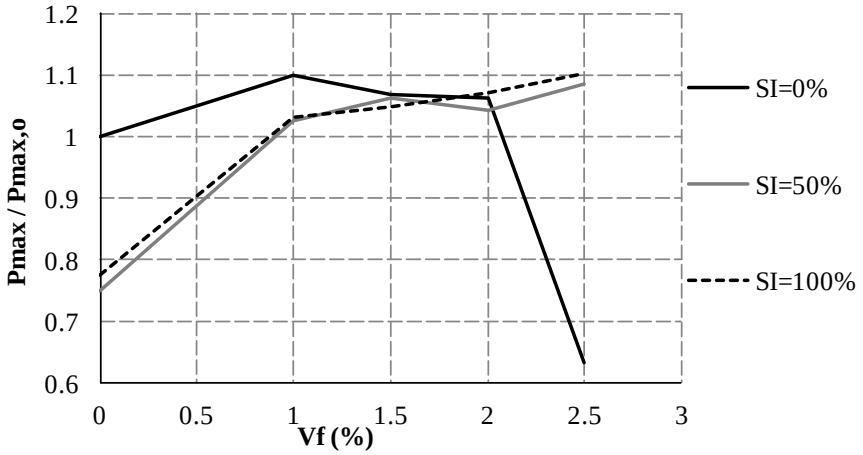


Figure 5.50: Ratio between the maximum load and that in the control column ($SI = 0\%, V_f = 0\%$) versus steel fibre volume fraction graph for Case Study 2(b)

5.4.4.2 Ductility ratio

Figure 5.51 shows the ratio between the ductility ratio in each column (μ) and that in the control column ($\mu_{,0}$) for the three series analysed using ABAQUS. The optimum ductility ratio for column with $SI = 0\%$, $SI = 50\%$ and $SI = 100\%$ is reached in the columns with a fibre volume ratio $V_f = 1\%$ $V_f = 1.5\%$ and $V_f = 2\%$, respectively.

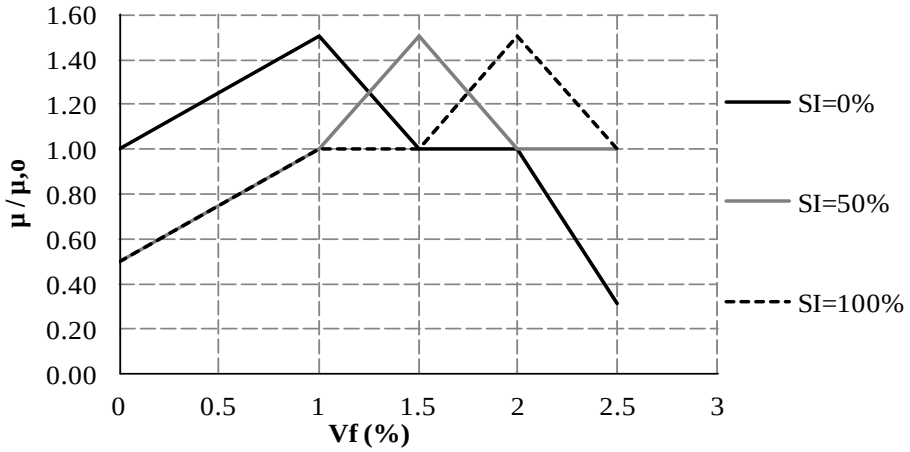


Figure 5.51: Ratio between the ductility ratio in each column and that in the control column ($SI = 0\%, V_f = 0\%$) versus steel fibre volume fraction graph for Case Study 2(b)

All the SFRC columns show better or similar performance except for brittle column with $V_f = 2.5\%$ column. Steel fibres improve the ductility of the columns through its

pull-out behaviour by bridging the crack opening from becoming wide, and partially absorbed further load applied on the column. Therefore, a higher load is required to produce a similar deflection in the structure. However, once the maximum load carrying capacity is exceeded or, the fibres bridging the cracking are pulled out, the cracks propagate rapidly with larger opening width. If the remaining fibres sustaining the load and bridging the crack are higher, the ductility will increased. On the other hand, if most of the fibres are pulled out after the peak load, the ductility of the structures will decreased.

5.4.4.3 Energy absorption ratio

The ratio between the energy absorption capacity in each column (E_a) and that in the control column ($E_{a,0}$) is presented in Figure 5.52. The highest energy absorption ratio for the column with $SI = 0\%$, $SI = 50\%$ and $SI = 100\%$ are observed from the fibre volume fraction of $V_f = 1\%$, $V_f = 1.5\%$ and $V_f = 2\%$, respectively. Therefore, it can be seen that the presence of fibres increases the energy absorption ratio appreciably. For all SFRC columns ($V_f \geq 1\%$), a higher energy absorption ratio is observed, except for $V_f = 2.5\%$ columns, which fails in brittle manner.

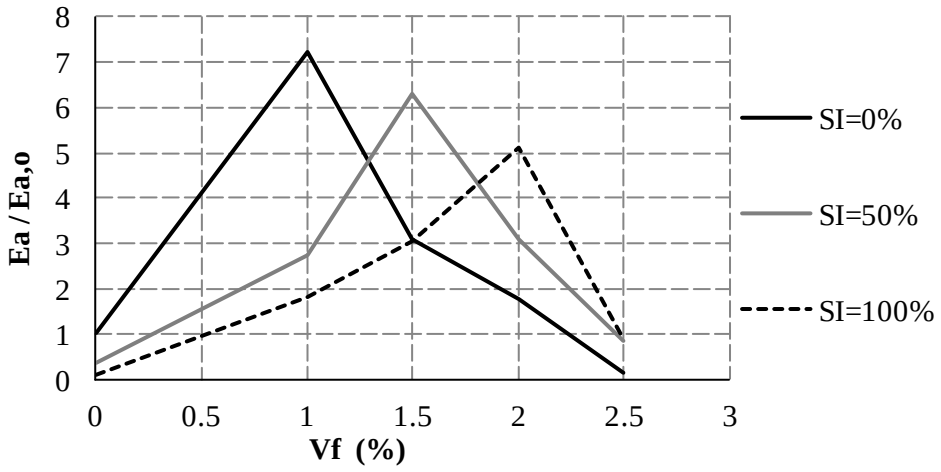


Figure 5.52: Ratio between the energy absorption in each column and that in the control column ($SI = 0\%, V_f = 0\%$) versus steel fibre volume fraction graph for Case Study 2(b)

The energy absorption ratio for columns with $V_f = 2.5\%$ (with $SI = 50\%$ and $SI = 100\%$) show a slight decrease of 10% to 15%. However, in the column with $SI = 0\%$, the absorption ratio for brittle failure column with $V_f = 2.5\%$ is calculated to be 0.55

only. Therefore, it can be concluded that steel fibres show considerable capability in increasing the energy absorption capacity of the columns, as more energy are required for the crack to propagate due to the steel fibres pull-out behaviour in resisting the crack width opening.

5.4.4.4 Number of cycles analysed ratio

The ratio between the maximum number of cycles before failure in each column (N_c) and that in the control column ($N_{c,o}$) analysed for two-span columns in reversed-cyclic loading is presented in Figure 5.53. The optimum fibres ratios for each series are similar as those discussed in section 5.4.3.2. However, it is interesting to note that the $N_c/N_{c,0}$ ratio of the optimum fibres volume fractions at $V_f = 1\%$ (for column with $SI = 0\%$), $V_f = 1.5\%$ (for column with $SI = 50\%$) and $V_f = 2\%$ (for column with $SI = 100\%$) show a downward pattern. The largest N_c for this parametric studies is achieved for the column with $SI = 0\%$ (with $V_f = 1\%$).

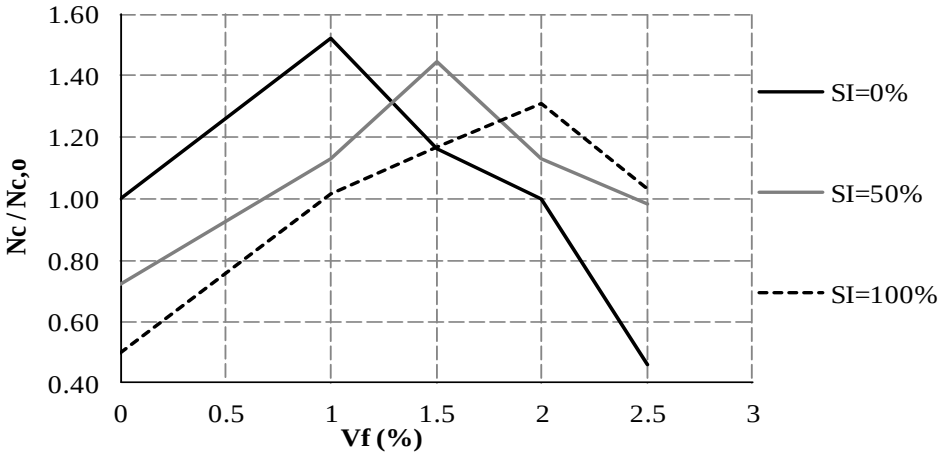


Figure 5.53: Ratio between the maximum number of cycles before failure in each column and that in the control column ($SI = 0\%, V_f = 0\%$) versus steel fibre volume fraction graph for Case Study 2(b)

5.5 Conclusions

Results of the parametric studies carried out on two-span continuous columns (i.e. statically indeterminate) with and without steel fibres (under both monotonic and cyclic loading) are presented and discussed in this chapter. Based on the results obtained, it can be concluded that the strength of the columns increases with the increase of amount

of fibres, regardless of the arrangement of stirrups and loading conditions. Furthermore, it is observed that the larger the stirrup spacing, the larger the enhancement as a consequence of the introduction of the fibres.

In term of the ductility, it can be seen that the stiffness and ductility of the columns improved with the addition of fibres. Although, the trend is consistent regardless of the stirrups spacing arrangement, there is an optimum fibre volume fraction observed for the columns with different stirrup spacing. The ductility of the column is observed to decrease after the fibres added exceed this optimum fibre volume fraction value. For the column with $SI = 0\%$, 50% and 100%, the optimum fibre volume fraction values are obtained at $V_f = 1\%$, $V_f = 1.5\%$ and $V_f = 2\%$, respectively. The energy absorption calculated also shows a similar pattern to that observed for the ductility ratio.

Furthermore, it can be observed that fibres help control the cracking and minimise crack width opening especially in the section between the intermediate support and the section where the lateral load (P) is applied. Most of the cracking develops at two main regions, which are intermediate support and the section where the lateral load (P) is applied. In the column with $SI = 100\%$, analysed in monotonic loading, it is clear that the inclusion of fibres improved the cracking pattern of the column, even at a low fibre volume fraction of 1%.

Therefore, based on the work carried out and presented here, it can be concluded that steel fibres have the capability to enhance the strength and ductility of the columns under both monotonic and revised-cyclic condition. The latter is particularly useful in seismic design considerations. Although a better ductility performance is observed with inclusion of fibres, this is true only up to certain fibre volume fraction. The optimum fibre volume fraction increases with the reduction of conventional shear reinforcement (i.e. with the increase in the stirrups spacing). The reduction in ductility when fibres are in provided in addition to full conventional reinforcement points to an “over-reinforced” behaviour similar to the one which is well known in RC design. Moreover, even if the ductility of the columns decreases, the cracking pattern observed is better than that in the column with no fibres. Thus, it is suggested that the use of steel fibres enhances the behaviour of the columns and provides a better strength, ductility, energy absorption as well controlling cracking propagation.

CHAPTER 6

CASE STUDY 3: BEAM-COLUMN JOINTS UNDER REVERSED-CYCLIC LOADING

6.1 Introduction

The present work aims at studying the effect of introducing steel fibres into the concrete mix in order to compensate for a reduced amount of conventional steel reinforcement (particularly shear reinforcement) and hence lessen congestion at critical regions of RC frames. The congestion is a particular issue for beam-column joints designed to withstand seismic loading as the code (e.g. Eurocode 8, 2004) requirements lead to a high amount of stirrups provided to protect critical regions of columns connected to these joints and within the joint itself. Potential enhancement to ductility, a key requirement in seismic design, is investigated as well as potential improvements to energy absorption and confinement. Different ratios of steel fibres are provided to replace reduced amounts of shear reinforcement (e.g. the latter is achieved by increasing spacing between the stirrups). The joints were subjected to reversed-cyclic loading (which is the key feature of seismic action) and both the overall structural behaviour and the local response at critical sections were studied. The work examines key structural behaviour and design issues such as strength (i.e. shear force and bending moment capacities), deformation (i.e. storey drift), ductility (i.e. ratio of maximum displacement to displacement at yield), stiffness, plastic hinges formation and cracking patterns.

This chapter discusses the third and final set of the case studies carried out in the present research work. Two types of beam-column joints, namely exterior (T-shape)

and interior (cross-shape) were selected and non-linear 3D FE analyses were carried out using ABAQUS (a full description of the material models and analysis procedures adopted is provided in Chapter 3 and the scope of all case studies is summarised in Section 3.4.3). The exterior beam-column joint investigated experimentally by Bayasi and Gebman (2002) under reversed-cyclic loading was selected as the basis of Case Study 3(a). The joint was initially calibrated – to ascertain the validity of the FE model used – and then parametric studies were carried out using different steel fibre ratios coupled with increased spacing of shear stirrups. For Case Study 3(b), the interior beam-column joint experimentally studied by Filiatrault et al. (1995) was adopted as the basis for this case study and ensuing parametric investigations. The joint was tested under reversed-cyclic loading (combined with axial load on the column), which was applied to mimic a seismic excitation.

6.2 Case Study 3(a): Exterior beam-column joint - Calibration with experimental data (Bayasi and Gebman, 2002)

6.2.1 Experimental setup

From six ½ - scale joints tested, one was selected and calibrated for this case study. Figure 6.1 shows the dimensions and reinforcement details of both the original full-scale beam-column joint designed in accordance to the Uniform Building Code (1997) and the ½ - scale specimen adopted for testing. The hoops (i.e. stirrups) spacing considered is 152 mm centre-to-centre uniformly applied throughout the beam and column. Hooked-end steel fibres of 30 mm length, 0.5 mm diameter and 2% ratio in volume were added to the joint concrete mixes in the experiment.

The uni-axial compressive (f_{ck}) of the concrete tested for the joint was 23.9 MPa. In addition, the longitudinal reinforcement applied were 12.7 mm and 15.9 mm in diameter with a yield stress (f_y) of 420 MPa, whilst, 9.5 mm diameter was used as transverse reinforcement with a yield stress of 420 MPa. Both types of steel reinforcement have the same modulus of elasticity (E_s) of 206 GPa. In the experimental work, the beam was subjected to a reversed-cyclic loading which was applied near the end of the free-end (cantilever) beam. The two ends of the column were restrained to wide-flange steel beam embedded into a concrete floor slab.

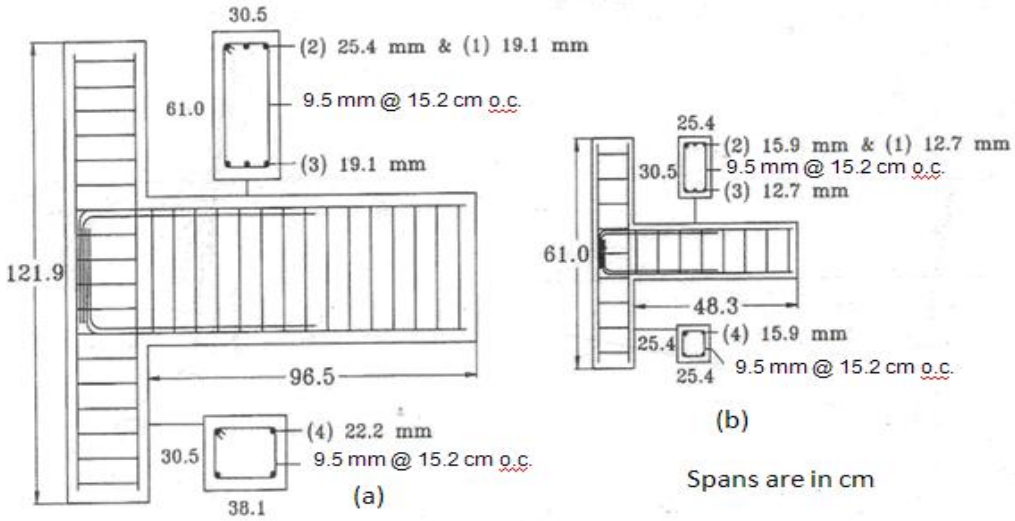


Figure 6.1: Dimensions and steel reinforcement details for (a) full-scale and (b) ½ - scale exterior beam-column joint (adopted from Bayasi and Gebman, 2002)

6.2.2 FE analysis input data

For purposes of calibration of the FE results against the experimental data, the ½ - scale beam-column joint was modelled using ABAQUS using the dimension shown in Figure 6.1b. Simply-supported boundary conditions were applied at both ends of the column. The tensile stress-strain diagrams for both SFRC and conventional reinforcement (used in longitudinal bars and shear stirrups) are depicted in Figures 6.2 and 6.3, respectively. The key points on the stress-strain diagrams are labelled as (A) to (F) and are summarised in Table 6.1. The uni-axial tensile strength of plain concrete is assumed to be 10% of f_{ck}. Additionally, the ultimate stress of the conventional steel reinforcement is assumed to be 460 MPa for both longitudinal and transverse bars.

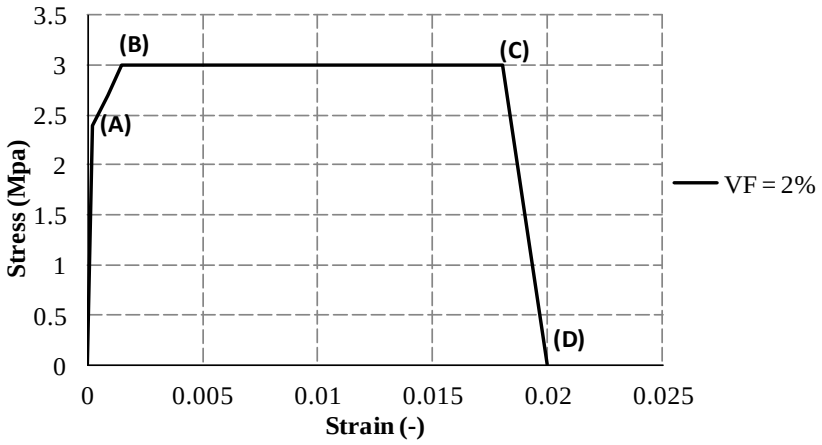


Figure 6.2: Tensile stress-stain diagram for SFRC adopted for the calibration work of the Bayasi and Gebman (2002) beam-column joints

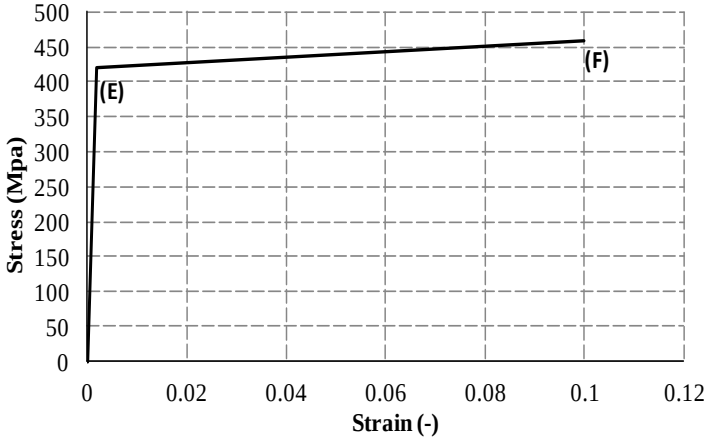


Figure 6.3: Stress-stain diagram for conventional steel reinforcement adopted for the calibration work of the Bayasi and Gebman (2002) beam-column joints

Point	Stress (MPa)	Strain (‰)
Origin	0	0
(A)	2.39	0.24
(B)	3	1.46
(C)	3	18
(D)	0	20
(E)	420	2.04
(F)	460	100

Table 6.1: Summary of key points on tress-strain diagrams adopted for the calibration work of Bayasi and Gebman (2002) beam-column joints

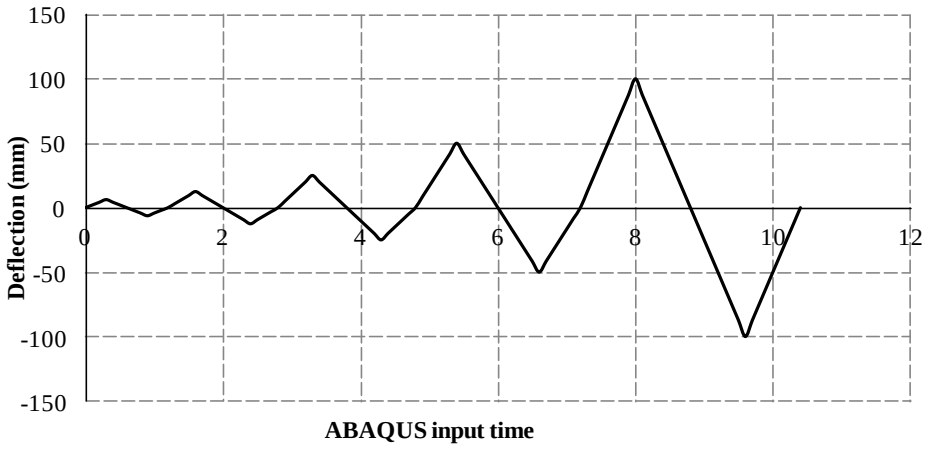


Figure 6.4: ABAQUS input data for reversed-cyclic loading

Lateral reversed-cyclic load is applied on the cantilever beam, at 430 mm from the column face. Steel plates of 20 mm thick are added at the support for the whole surface area of the column, and at loading point region along the beam width with 55 mm width

(this is to mimic experimental conditions and also avoid premature localised failure). The loading history input data adopted in this case study is shown in Figure 6.4. A sensitivity analysis was carried out to determine the most suitable FE mesh size and consequently an element size of 10 mm was adopted for the analysis as it yielded the most satisfactory agreement with the experimental load-deflection curve.

6.2.3 Results of calibration work

Figure 6.5 shows the analysis results obtained from the FE model and is compared with the test results. Table 6.2 summarised the key load and deflection values observed from the load-deflection curves. The non-linear FE analysis (using ABAQUS) was successful in modelling the analysis up to 3.83 cycles before it stopped signalling the failure of the specimen, compared to 5 cycles achieved experimentally.

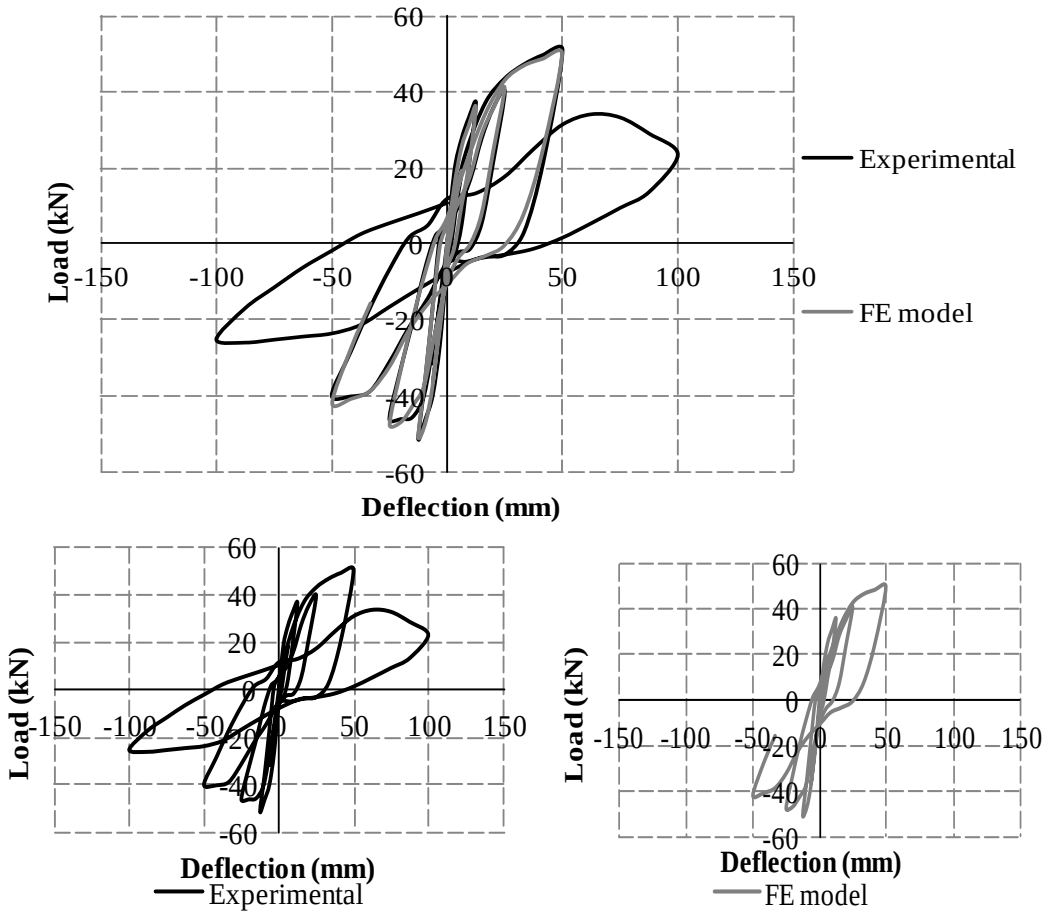


Figure 6.5: Load-deflection hysteresis loops for calibration work in Case Study 3(a)

Good agreement with experimental data can be seen in term of strength, especially the yield load (P_y) and maximum load sustained during the loading cycles (P_{max}).

However, the highest ductility predicted by the FE analysis is about half the maximum ductility achieved in the experiment. This is due to the difference in the number of cycles obtained (i.e. ~ 4 cycles in the FE analysis compared to 5 in the experiment). So the ductility levels were the same for the first 4 cycles, however the presence of the 5th cycle in the experimental data led to this discrepancy (with the FE predictions being on the safe side).

Beam-column joint	P_y (kN)	δ_y (mm)	P_u (kN)	δ_u (mm)	P_{max} (kN)	δ_{Pmax} (mm)	$\mu = \frac{\delta_u}{\delta_y}$	$\frac{P_{max}}{P_y}$
Experimental (at failure)	18.5	6.25	23.3	100	50.9	50	16.0	2.75
Experimental (at FE model failure)	18.5	6.25	50.9	50	50.9	50	8.0	2.75
FE model	19.3	6.25	50.0	49.6	50.0	49.6	7.94	2.59

Table 6.2: Results summary of load-deflection curve for calibration in Case Study 3(a)

The failure observed in the numerical analysis was confirmed by studying the kinetic energy graph shown in Figure 6.6, which highlights the sudden large jump in kinetic energy at failure indicating the presence of large/extensive cracks. This was further confirmed by examining the cracking pattern and deformed shape of the joint.

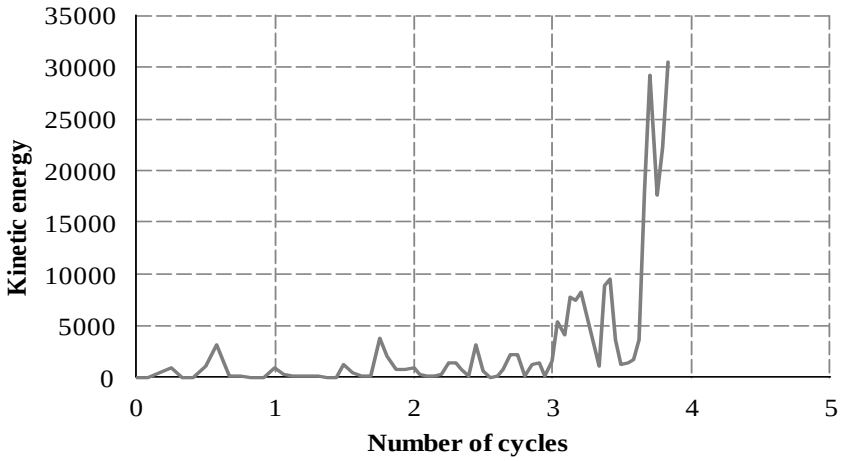


Figure 6.6: Kinetic energy graph for calibration work in Case Study 3(a)

From the preceding discussion it can be concluded that the FE model yields acceptable results and is thus adopted for the subsequent parametric studies in Case Study 3(a).

6.3 Case Study 3(a): Parametric study on exterior beam-column joint under reversed-cyclic loading

Parametric studies were carried out using non-linear FE analysis to examine the potential of steel fibres to compensate for reduction in shear reinforcement. To achieve this, the spacing between shear stirrups was increased, whilst the fibres were added. Therefore, joint specimens with spacing increase of *SI* = 0%, 50% and 100% were modelled while the fibre volume fractions considered were V_f = 0%, 1%, 1.5%, 2% and 2.5%.

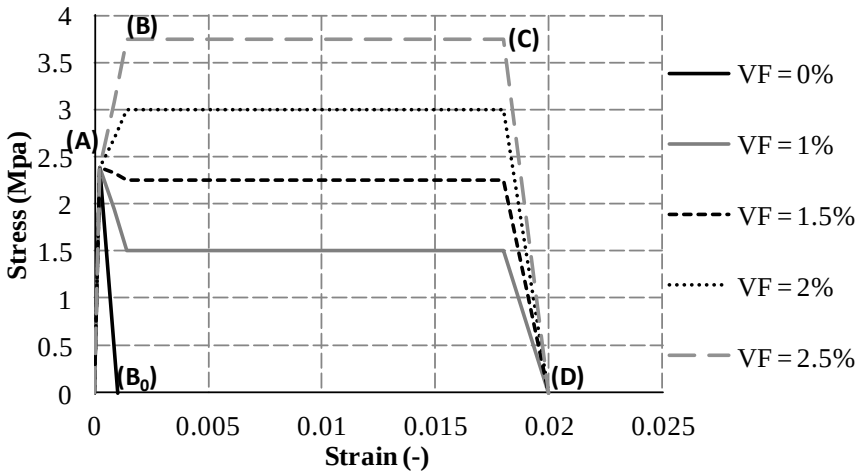


Figure 6.7: Stress-strain relations in tension for Case Study 3(a)

Point	Stress (MPa)	Strain (‰)
Origin	0	0
(A)	2.39	0.239
(B_0)	0	1

Table 6.3(a): Tensile strain-stress properties for plain concrete for Case Study 3(a)

Point	Strain (‰)	Stress, V_f =1% (MPa)	Stress, V_f =1.5% (MPa)	Stress, V_f =2% (MPa)	Stress, V_f =2.5% (MPa)
Origin	0	0	0	0	0
(A)	0.239	2.39	2.39	2.39	2.39
(B)	1.456	1.5	2.25	3	3.75
(C)	18	1.5	2.25	3	3.75
(D)	20	0	0	0	0

Table 6.3(b): Tensile strain-stress relation for SFRC for Case Study 3(a)

For FE modelling purposes, the tensile stress-strain diagrams for both plain and fibrous concrete are presented in Figure 6.7 (with key values summarised in Table 6.3). The stress-strain relation used for conventional steel bars is defined in Figure 6.3 and Table 6.1. The results obtained from the numerical analysis are discussed next.

6.3.1 Load-deflection curves

Load-deflection curves for all the specimens analysed in Case Study 3(a) under reversed-cyclic loading are presented in Figures 6.8 to 6.10. For clarity purposes, the curves are reproduced to show the response at every V_f value separately (Figures 6.11 to 6.13). The key values are summarised in Tables 6.4 to 6.6.

Taking the beam-column joint with conventional reinforcement and no fibres or increase in stirrups spacing (i.e. $V_f = 0\%$ and $SI = 0\%$) as the reference or control joint specimen (CJ), further comparisons were made with joints with varying fibre content and stirrup spacing as presented in Tables 6.5 and 6.6. In this manner, conclusions could be made on the potential of fibres to compensate for the increase in stirrup spacing (i.e. to restore the performance levels of the control specimen). The key structural parameters summarised in the tables are the yield load (P_y) and corresponding deflection (δ_y), the maximum load sustained during the loading cycles (P_{max}) and corresponding deflection (δ_{max}), the load at failure (P_u) and corresponding deflection (δ_u), the ductility ratio (μ) defined as $\mu = \frac{\delta_u}{\delta_y}$ and the number of cycles obtained before failure (N_c).

6.3.2 Strength

From the results presented in the preceding figures and tables, it can be seen that the steel fibres enhance the yield and strength characteristics for all specimens studied. For SFRC specimens without any increase in stirrups spacing (i.e. SI = 0%), P_y and P_{max} increased by up to 47% and 58%, respectively, depending on the amount of fibres provided. Increasing the stirrups spacing reduced the capability of the conventionally-reinforced concrete joint ($V_f = 0\%$) to sustain further loading, e.g. for joints with SI = 50%, a reduction of 18% in P_y and 11% in P_{max} compared to the control joint is

observed. Similarly, for joints with *SI* = 100% and no fibres the decrease in P_y and P_{max} is about 28% and 59%, respectively, of their control specimen counterparts.

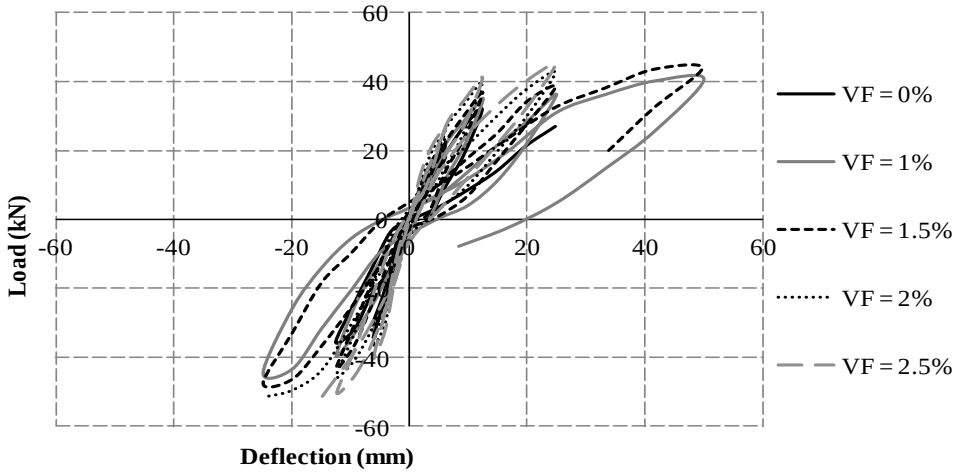


Figure 6.8: Load-deflection curve for Case Study 3(a) for specimens with *SI* = 0%

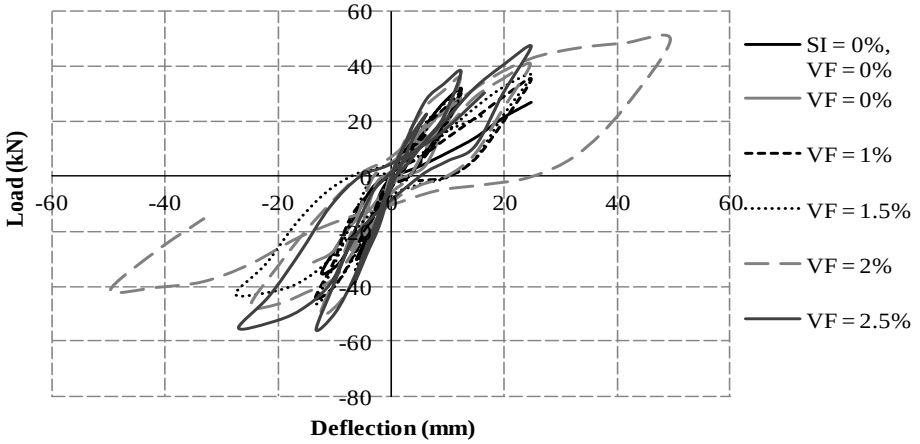


Figure 6.9: Load-deflection curve for Case Study 3(a) for specimens with *SI* = 50%

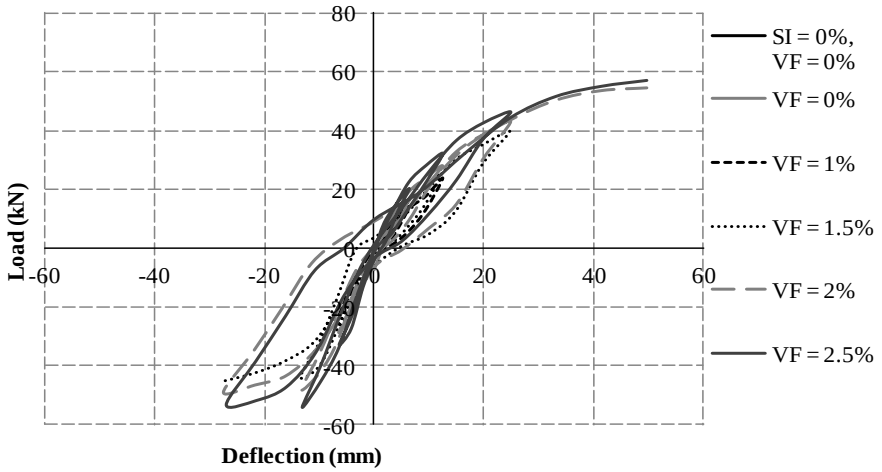


Figure 6.10: Load-deflection curves for Case Study 3(a) for specimens with *SI* = 100%

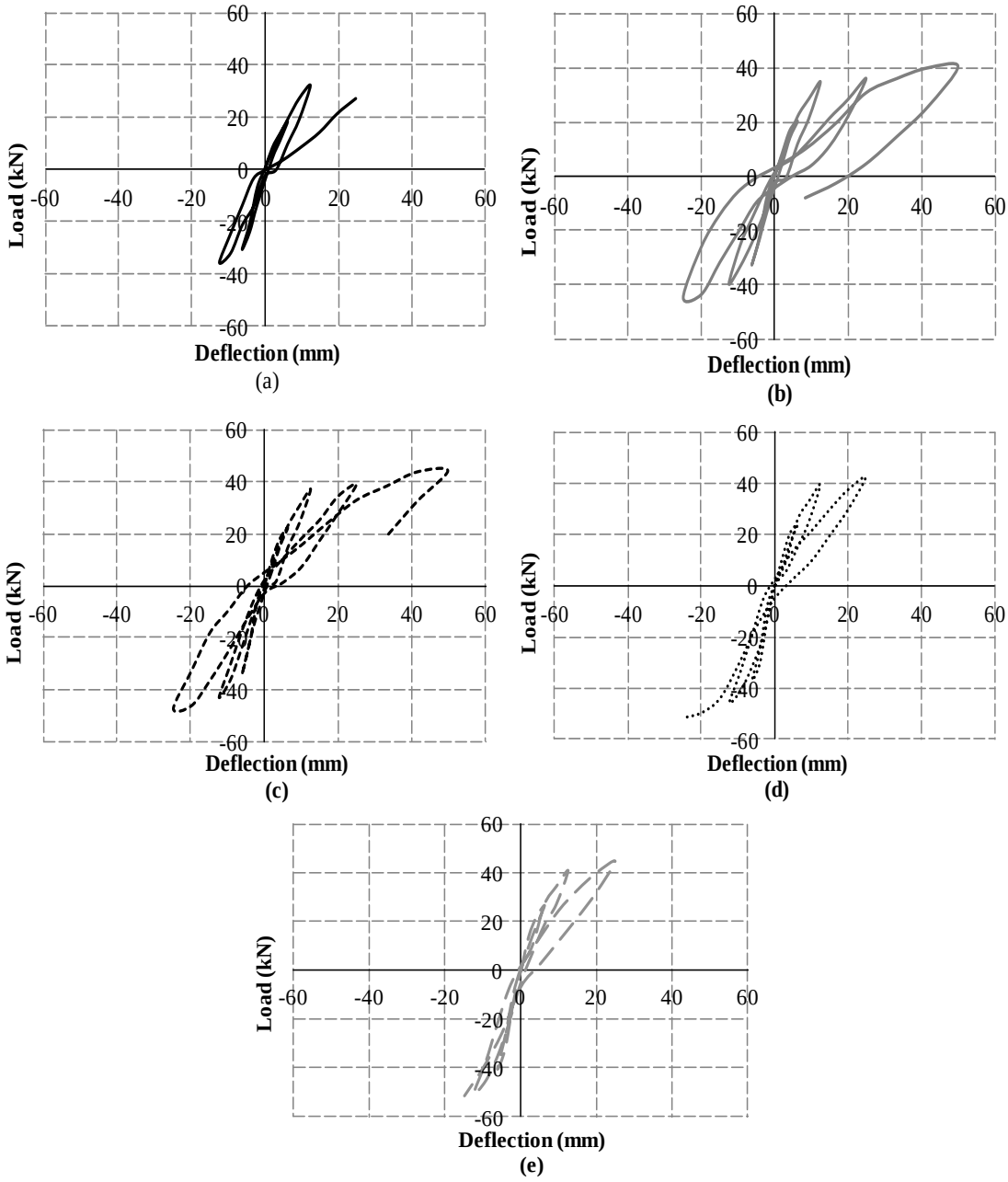


Figure 6.11: Load-deflection curve for Case Study 3(a) for specimens with *SI* = 0% and (a) $V_f = 0\%$, (b) $V_f = 1\%$, (c) $V_f = 1.5\%$, (d) $V_f = 2\%$ and (e) $V_f = 2.5\%$

V_f (%)	N_c	P_y (kN)	δ_y (mm)	P_u (kN)	δ_u (mm)	P_{max} (kN)	δ_{Pmax} (mm)	$\mu = \frac{\delta_u}{\delta_y}$	$\frac{P_{max}}{P_y}$
0	2.25	18.2	6.25	27	24.9	31.9	12.5	3.98	1.75
1	3.49	20.4	6.25	40.6	49.9	40.6	49.9	7.98	1.99
1.5	3.33	22.0	6.25	44.1	49.8	44.1	49.8	7.97	2.01
2	2.75	24.1	6.25	42.6	24.9	45.8	12.4	3.98	1.90
2.5	2.65	26.7	6.25	44.9	24.9	50.31	12.4	3.98	1.88

Table 6.4: Results summary for Case Study 3(a) for specimens with *SI* = 0%

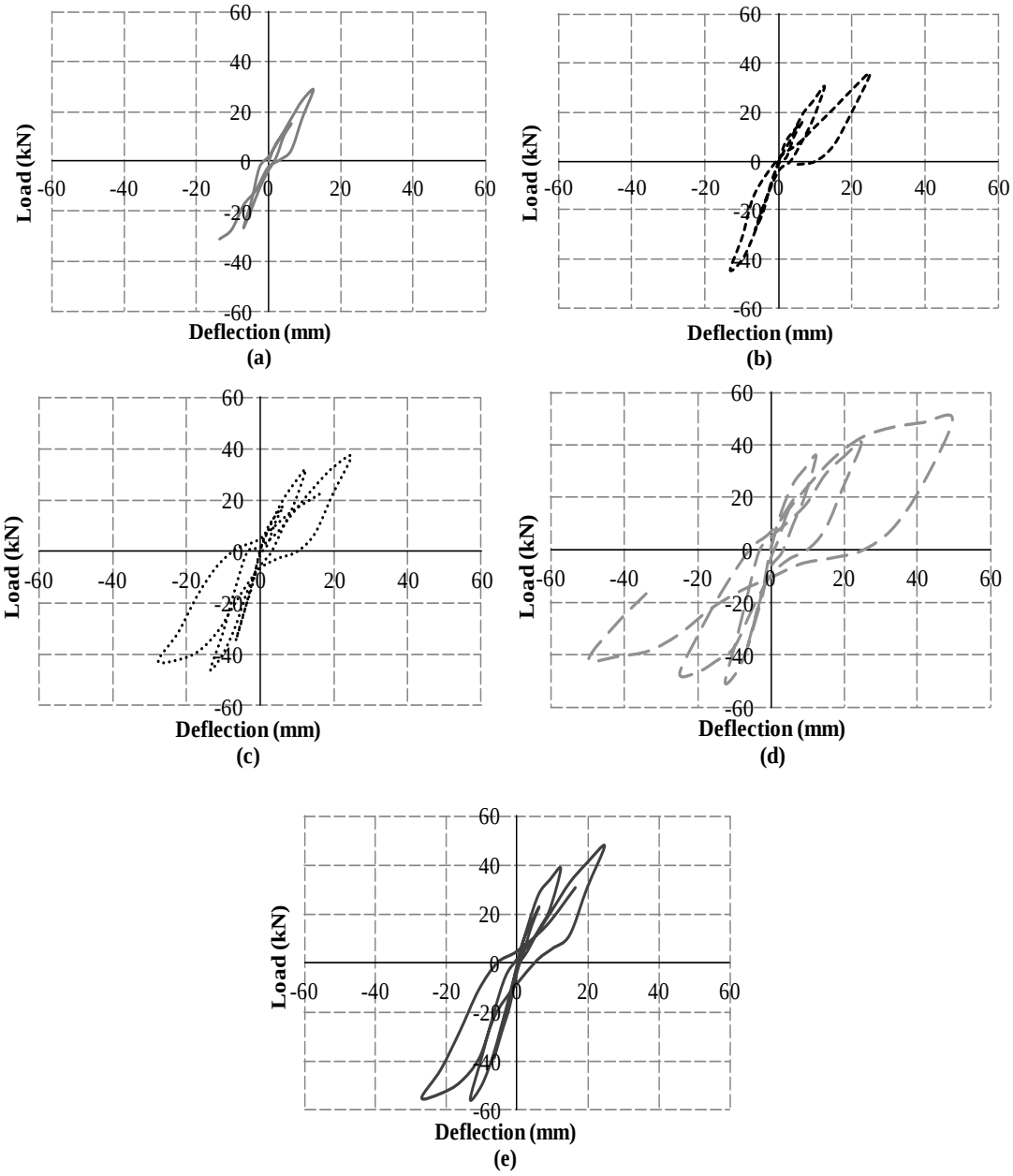


Figure 6.12: Load-deflection curve for Case Study 3(a) for specimens with *SI* = 50% and (a) $V_f = 0\%$, (b) $V_f = 1\%$, (c) $V_f = 1.5\%$, (d) $V_f = 2\%$ and (e) $V_f = 2.5\%$

V_f (%)	N_c	P_y (kN)	δ_y (mm)	P_u (kN)	δ_u (mm)	P_{max} (kN)	δ_{Pmax} (mm)	$\mu = \frac{\delta_u}{\delta_y}$	$\frac{P_{max}}{P_y}$
CJ	2.25	18.2	6.25	27	24.9	31.9	12.5	3.98	1.75
0	1.75	15.0	6.25	28.4	12.4	28.4	12.4	1.98	1.89
1	2.45	15.8	6.25	35.5	24.8	35.5	24.8	3.97	2.25
1.5	3.08	17.6	6.25	37.1	24.8	42.7	27.6	3.97	2.62
2	3.83	19.3	6.25	50.0	49.6	45.21	24.8	7.94	2.34
2.5	3.08	22.8	6.25	47.6	24.8	47.6	24.8	3.97	2.09

Table 6.5: Results summary for Case Study 3(a) for specimens with *SI* = 50% (CJ is the control joint specimen with V_f = 0% and *SI* = 0%)

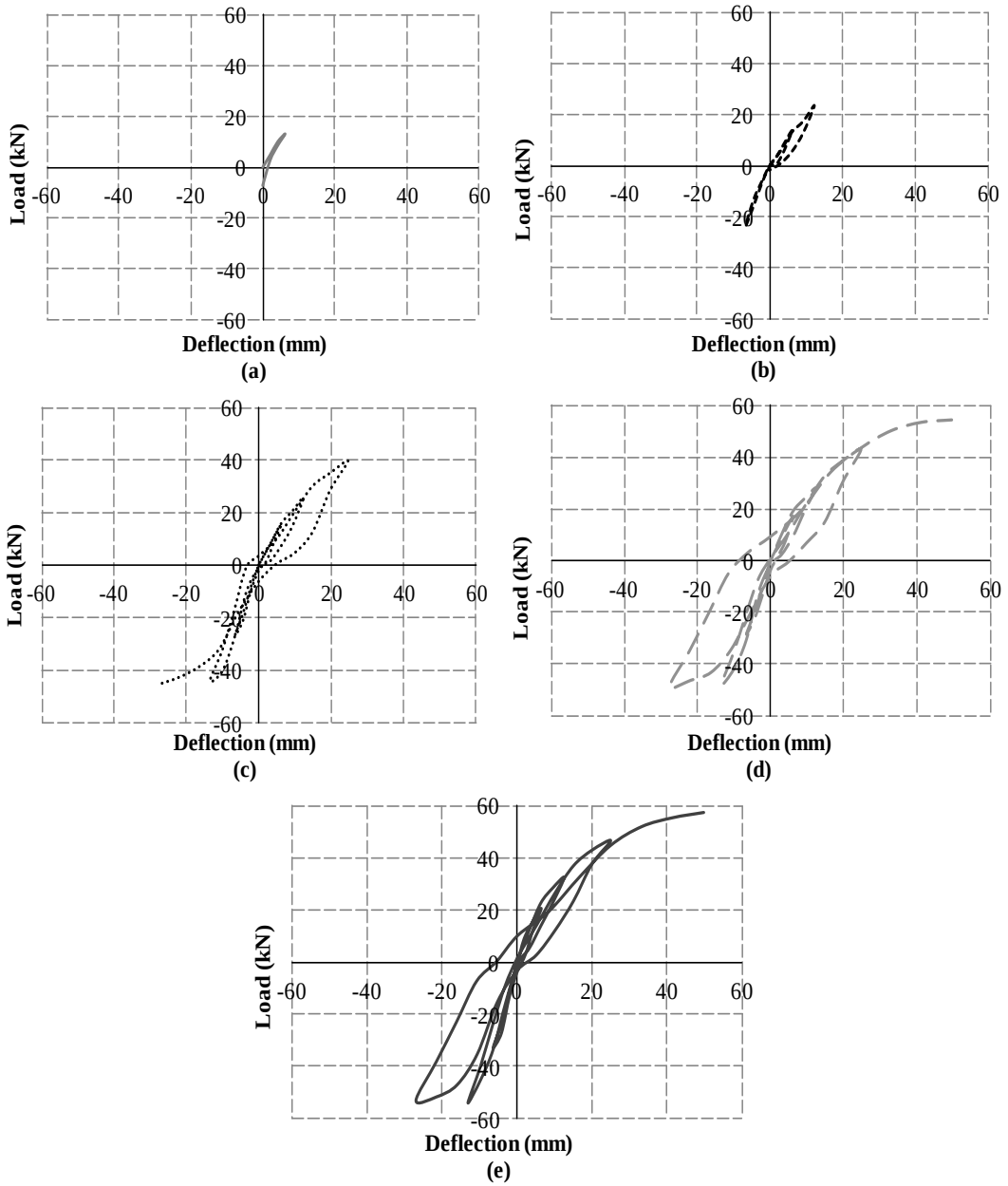


Figure 6.13: Load-deflection curve for Case Study 3(a) for specimens with *SI* = 100% and (a) $V_f = 0\%$, (b) $V_f = 1\%$, (c) $V_f = 1.5\%$, (d) $V_f = 2\%$ and (e) $V_f = 2.5\%$

V_f (%)	N_c	P_y (kN)	δ_y (mm)	P_u (kN)	δ_u (mm)	P_{max} (kN)	δ_{Pmax} (mm)	$\mu = \frac{\delta_u}{\delta_y}$	$\frac{P_{max}}{P_y}$
CJ	2.25	18.2	6.25	27.0	24.9	31.9	12.5	3.98	1.75
0	0.58	13.2	6.25	13.2	6.25	13.2	6.25	1	1
1	1.5	14.1	6.25	23.7	12.4	23.7	12.4	1.98	1.68
1.5	2.75	15.6	6.25	39.7	24.8	39.7	24.8	3.97	2.55
2	3.25	17.1	6.25	54.5	49.6	43.6	24.8	7.94	2.55
2.5	3.25	20.4	6.25	57.2	49.6	46.4	24.8	7.94	2.27

Table 6.6: Results summary for Case Study 3(a) for specimens with *SI* = 100% (CJ is the control joint specimen with V_f = 0% and *SI* = 0%)

On the other hand, the addition of the fibres substantially enhanced the values of P_y and P_{max} (e.g. P_{max} values increased by up to 76% and 33% in joints with *SI* = 50% and 100%, respectively). Similarly, P_y values increased by up to 52% and 55% in joints with *SI* = 50% and 100%, respectively. This shows that the steel fibres have the capability to improve the performance of the joints, through its crack bridging and pull-out behaviour even for the severe case of doubling the spacing of stirrups spacing.

Comparisons to the control joint (CJ) show that for SFRC joints with *SI* = 50% the yield load exceeded that of the control joint when fibres were provided at a volume fraction of $V_f = 2\%$ (for specimens with *SI* = 100%, $V_f = 2.5\%$ was needed). As regards the maximum load sustained, the control joint levels were exceeded when fibres were provided at $V_f = 1\%$ and $V_f = 1.5\%$ for joints with *SI* = 50% and 100%, respectively.

6.3.3 Ductility

The performance of the joints in terms of ductility is best observed considering the ductility ratio (μ) and the number of cycles attained before failure (N_c), as shown in Tables 6.4 to 6.6. The results indicate an enhancement to both parameters corresponding to an increase in fibre volume fraction. However, it is interesting to see that the trend is only true up to a certain *critical* fibre volume ratio, beyond which the behaviour becomes less ductile. It is also interesting to note that the higher the spacing between the stirrups, the higher the *critical* fibre volume ratio. This strongly suggests that the addition of fibres within an optimum range enhances ductility. However, if too many fibres are added in this seems to lead to a situation similar to the "over-reinforced" behaviour associated with RC design where too much reinforcement leads to a reduction – rather than an increase – in ductility.

For SFRC joints with *SI* = 0%, the maximum N_c and μ values were obtained at $V_f = 1\%$. (with μ for the joint with $V_f = 1\%$ is twice that of the joint without fibres). For SFRC joints with *SI* = 50%, the maximum N_c and μ values were obtained at $V_f = 2\%$ with μ twice that of the control specimen (while the ductility level of the control specimen was attained at $V_f = 1.5\%$). Similarly, for SFRC joints with *SI* = 100%, the maximum N_c and μ values were obtained at $V_f = 2\%$ with μ twice that of the control specimen (with the control joint ductility level attained at $V_f = 1.5\%$).

The results also demonstrate that that the ductility performance of the joints with increased stirrups spacing (but without fibres added to compensate) deteriorated rapidly and failed at $N_c = 1.75$ for the joint with *SI* = 50% and at $N_c = 0.58$ for the joint with *SI* = 100%. On the other hand, the addition of fibres increased the N_c and μ levels remarkably and, as stated earlier, the enhancement was better as the spacing increased. This suggests that fibres can be used to replace some of the conventional shear reinforcement, but should not be provided in excessive quantities as this will lead to a stiffer and deflects less joint (this largely due to the fibres role in bridging across cracks and limiting their opening). This is because the fibres contribute to the load-resisting mechanism by bridging across cracks and limiting their propagation. This will not allow the conventional reinforcement to yield, which is required for a ductile response (so the additional fibres will enhance strength but reduce ductility).

The crack control and confinement provided by the fibres will also lead to a stiffer response as the structure deflects less. This is most pronounced in the case when the fibres are provided in addition to full conventional shear reinforcement (i.e. $SI = 0\%$). To study this further, the FE-based principal strain contours and vectors for the joint with $SI = 0\%$ where studied at three levels of fibre content (i.e. $V_f = 0\%$, $V_f = 1\%$ and $V_f = 2\%$) and at different deflection points from yield to failure as presented in Figures 6.14 to 6.17. In order to observe crack patterns, the contour range was selected to coincide with the cracking tensile strain (i.e. 0.000239, see point A in Figure 6.7) and the ultimate compressive strain (i.e. -0.0035). Thus the areas highlighted in grey on the contours denote crack initiation. Principal strain vectors are also presented in the figures and they are also useful in indicating the pattern of crack formation.

The distribution of principal strains and vectors at yield (i.e. at $\delta_y = 6.25\,mm$), taken from the first cycle, is illustrated in Figure 6.14. The contours indicate that cracking has been reduced as fibre amount provided increases. This is supported by the graphs of principal strain vectors which also show that the crack formation is less in joints with higher fibre amounts. This confirms the role of fibres in controlling crack opening.

Figure 6.15 shows the distribution of the principal strains and vectors at the maximum deflection in the second load cycle (i.e. $\delta_2 = 12.5\,mm$). Again, it can be seen that the crack formation is limited with $V_f = 2\%$ as compared to the results of specimens with less amounts of fibre.

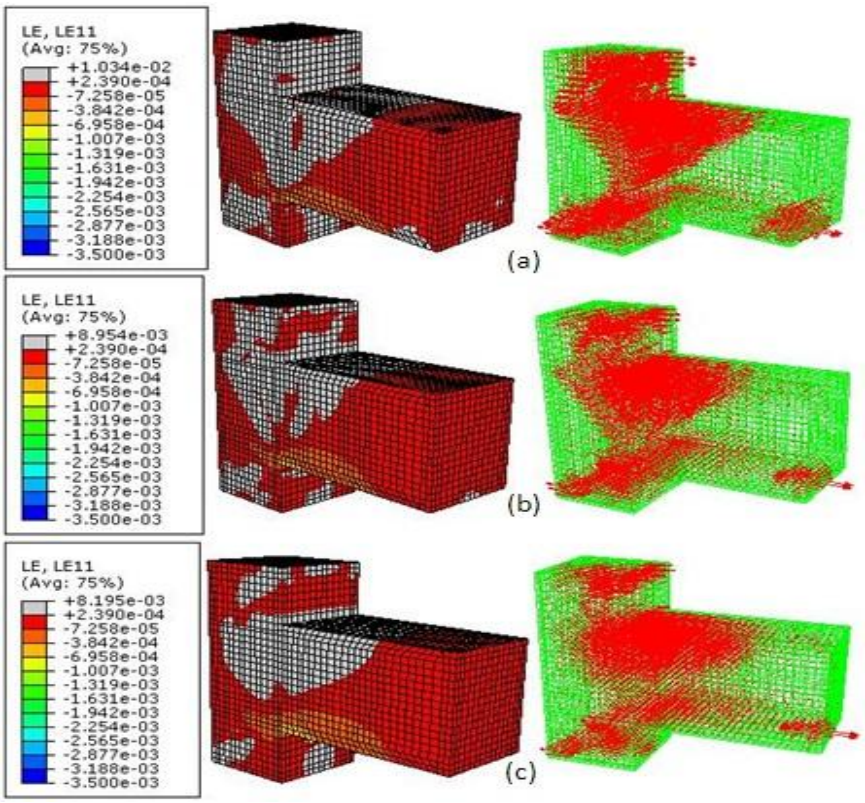


Figure 6.14: Principal strain contours and vectors for exterior joints with $SI = 0\%$ and (a) $V_f = 0\%$, (b) $V_f = 1\%$, (c) $V_f = 2\%$ at $\delta_y = 6.25\ mm$

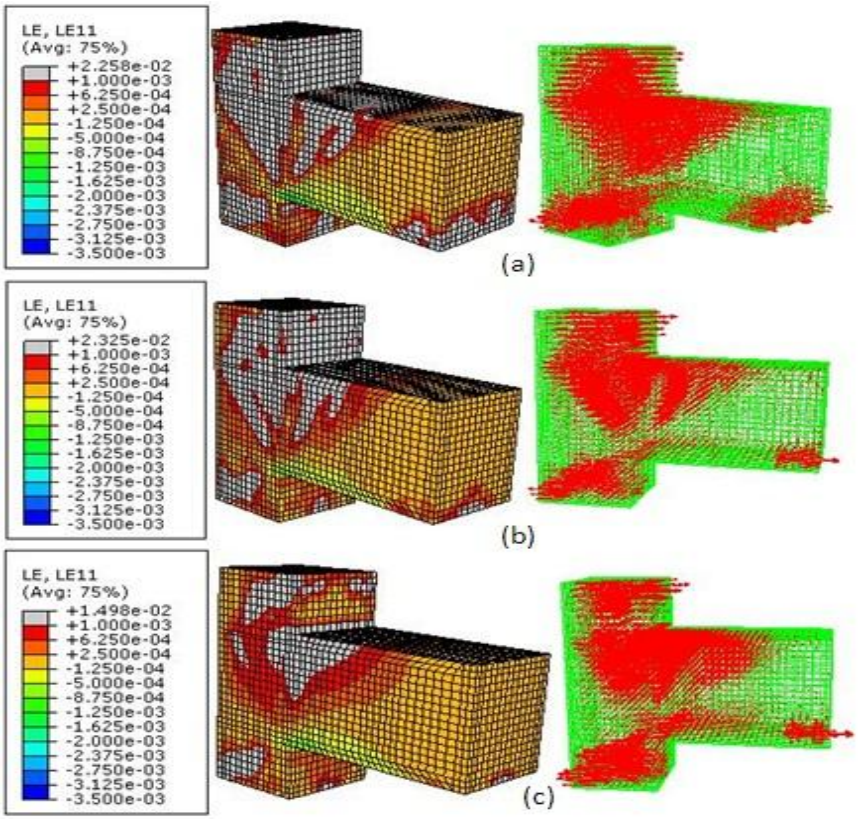


Figure 6.15: Principal strain contours and vectors for exterior joints with $SI = 0\%$ and (a) $V_f = 0\%$, (b) $V_f = 1\%$, (c) $V_f = 2\%$ at $\delta_2 = 12.5\ mm$

It should be noted that the grey area now is defined to highlight tensile strains higher than 0.001, which is the ultimate tensile strain for plain concrete (see point B_0 in Figure 6.7). Thus, the contours and vectors indicate that the crack opening has been controlled better as fibres content is increased.

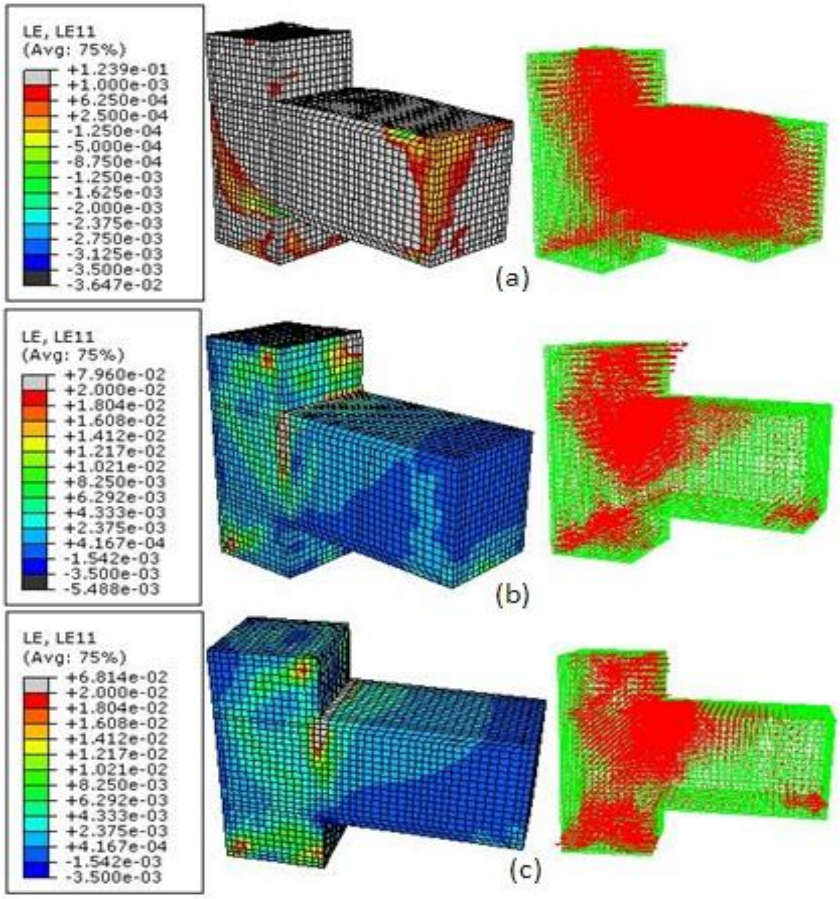


Figure 6.16: Principal strain contours and vectors for exterior joints with $SI = 0\%$ and (a) $V_f = 0\%$, (b) $V_f = 1\%$, (c) $V_f = 2\%$ taken at $\delta_3 = 24.9\ mm$

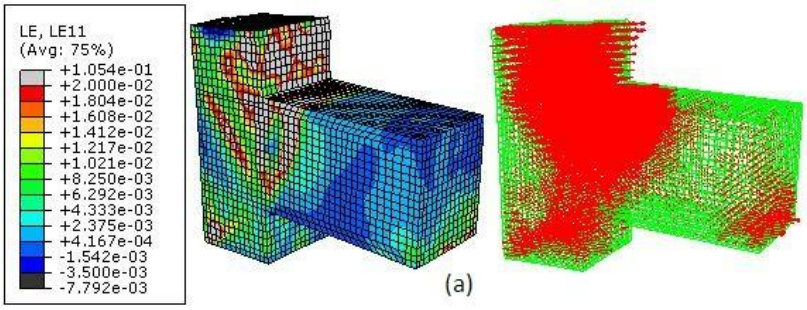


Figure 6.17: Principal strain contours and vectors for exterior joints with $SI = 0\%$ and (a) $V_f = 1\%$ at $\delta_4 = 49.9\ mm$

The strain distribution and vectors at the point of failure (i.e. ultimate deflection) are presented in Figures 6.16 and 6.17. The failure of specimens with $V_f = 0\%$ and $V_f = 2\%$ coincides with an ultimate deflection of $\delta_3 = 24.9\, mm$. The strain results for all specimens at this deflection level are presented in Figure 6.16 (for comparison purposes, the data for the joint with $V_f = 1\%$ was also included). On the other hand, Figure 6.17 depicts the strain results for the specimen with $V_f = 1\%$, which failed at an ultimate deflection of $\delta_4 = 49.9\, mm$.

It should be noted that the grey area now is defined to highlight tensile strains higher than 0.02, which is the ultimate tensile strain for SFRC associated with pull-out fibre (see point D in Figure 6.7). Thus, the contours and vectors indicate that the crack opening has been controlled better as fibres content is increased and that pull-out failure occurred in limited zones of the SFRC joints (compared to an extensive grey area on the joint without fibres showing that the latter experienced wider crack opening).

6.3.4 Cracking pattern

The principal stress and strain distributions contours for the beam-column joints are presented herein. The figures were constructed based on the condition of the joint at failure. The stress and strain contours illustrated in the figures provide insight into the process of cracking showing crack formation patterns. In addition, deflected shapes are also provided which give further information on both deformation and cracking.

6.3.4.1 Principal stress contours

Figures 6.18 to 6.20 depict the FE-based principal stress contours for the specimens modelled (i.e. joints with joints with $SI = 0\%$, 50% and 100% coupled with fibre volume fractions of $V_f = 0\%$, 1%, 1.5%, 2% and 2.5%). To understand the state of tensile stresses at failure, the contour intervals were selected so that the stress values exceeding the tensile strength of plain concrete (i.e. 2.39 MPa, see point A in Figure 6.7 and Table 6.3) are depicted in grey for specimens without fibres (i.e. $V_f = 0\%$) and for those exhibiting strain-softening trend (i.e. V_f =1% and 1.5%).

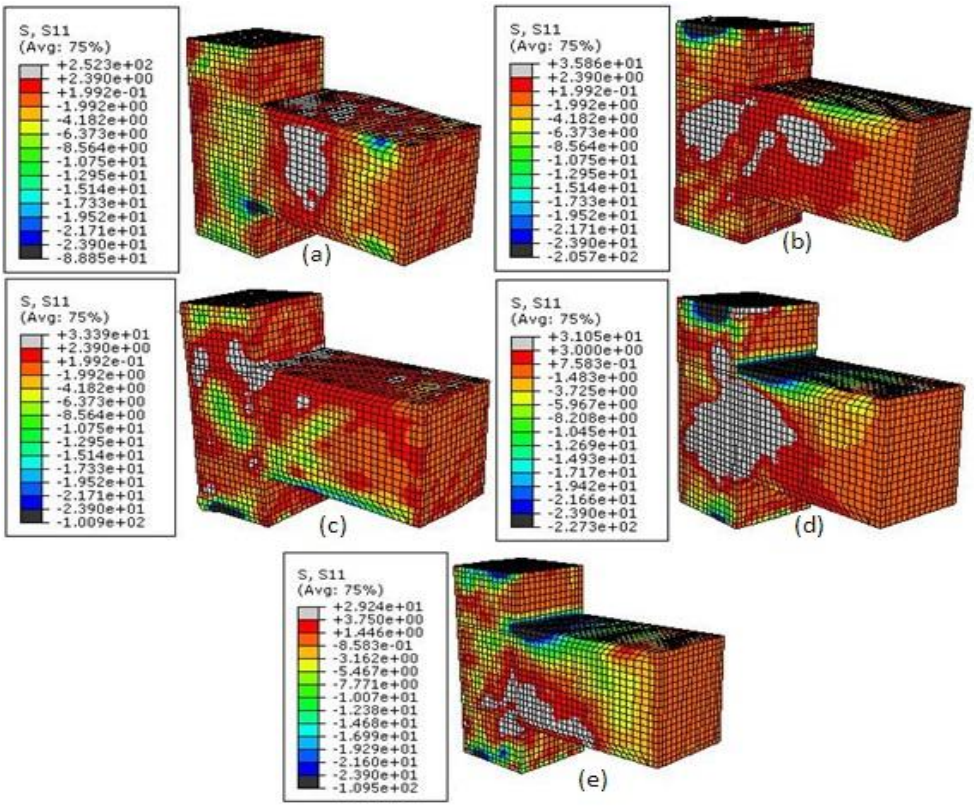


Figure 6.18: Principal stress contours for Case Study 3(a) joints with $SI = 0\%$ and (a) $V_f = 0\%$, (b) $V_f = 1\%$, (c) $V_f = 1.5\%$, (d) $V_f = 2\%$ and (e) $V_f = 2.5\%$

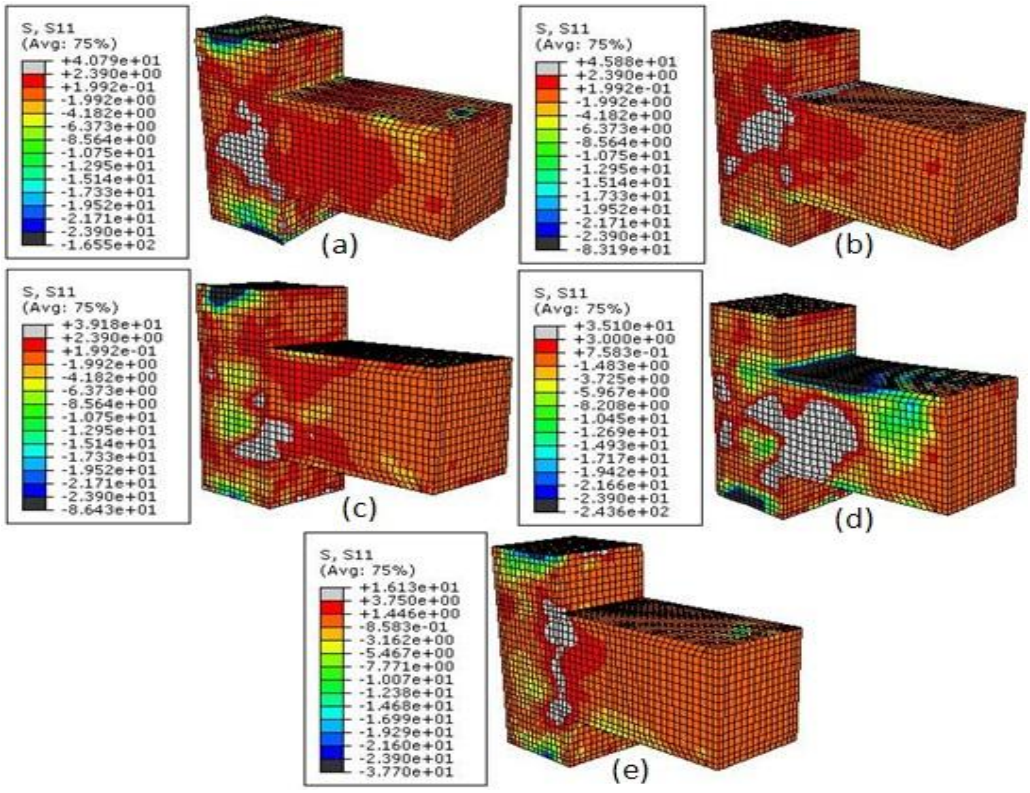


Figure 6.19: Principal stress contours for Case Study (a) joints with $SI = 50\%$ and (a) $V_f = 0\%$, (b) $V_f = 1\%$, (c) $V_f = 1.5\%$, (d) $V_f = 2\%$ and (e) $V_f = 2.5\%$

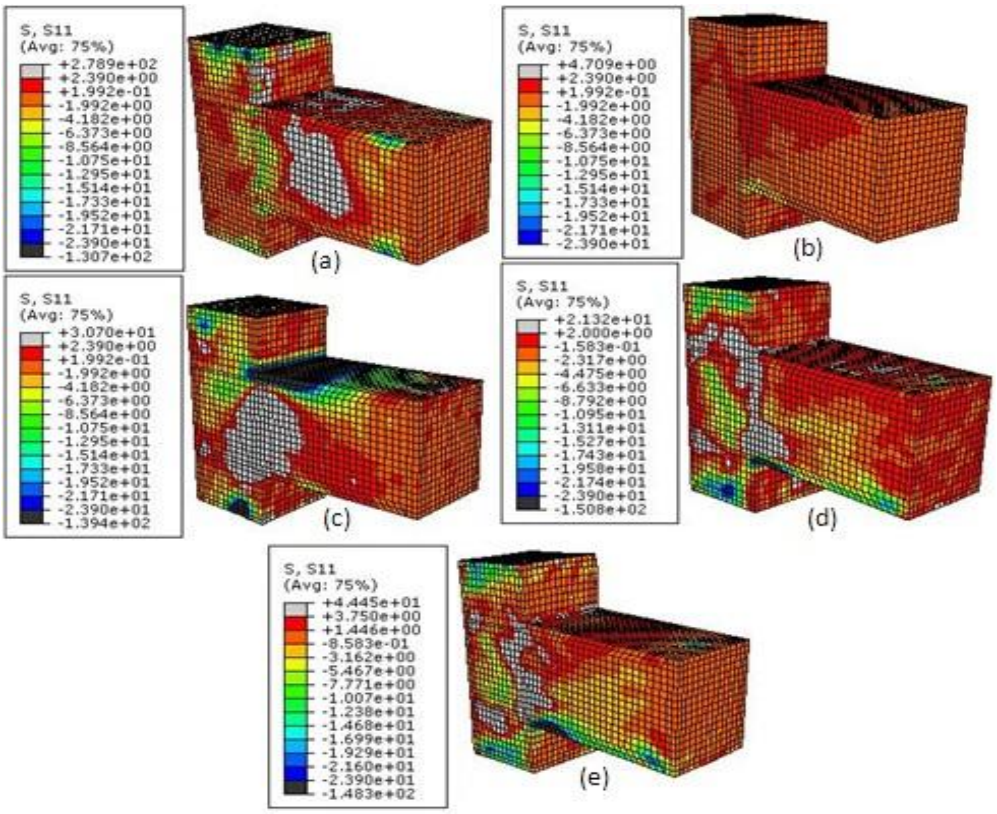


Figure 6.20: Principal stress contours for Case Study 3(a) joints with $SI = 100\%$ and (a) $V_f = 0\%$, (b) $V_f = 1\%$, (c) $V_f = 1.5\%$, (d) $V_f = 2\%$ and (e) $V_f = 2.5\%$

For SFRC specimens exhibiting strain-hardening (i.e. V_f =2% and 2.5%, see point B in Figure 6.7 and Table 6.3), the grey zones denote areas where the tensile stresses exceed the SFRC tensile strength of 3 MPa and 3.75 MPa for joints with V_f =2% and 2.5%, respectively. Similarly, to understand the state of compressive stresses at failure, the contours were arranged so that the stress values exceeding the ultimate compressive strength of plain concrete, i.e. -23.9 MPa, are highlighted in black.

The figures show at failure, the tensile strength of both plain concrete and SFRC have been exceeded. The compressive stress has also been exceeded in some cases. However, it must be noted that tensile and compressive failures are defined based on strains rather than stresses and thus the state of strains at failure is examined next.

6.3.4.2 Principal strain contours

The FE-based principal strain contours at failure are presented in the Figures 6.21 to 6.23 for all joint specimens modelled. To understand the failure mechanism, the strain contours are arranged so that the grey areas now highlight zones where the ultimate tensile strain has been exceeded. The latter are defined in Figure 6.7 and Table 6.3, see point D. Thus, the tensile cracking strain considered is 0.001 for plain concrete (i.e. $V_f = 0\%$) and the ultimate strain is taken as 0.02 for SFRC (i.e. $V_f = 1\%, 1.5\%, 2\%$ and 2.5%) and the grey contour intervals in parts (a) to (e) in Figures 6.21 to 6.23 follow this definition. Consequently, for SFRC specimens, the grey areas represent zones where pull-out failure of fibres occurred. Similarly, the ultimate compressive strain of -0.0035 is adopted to indicate crushing failure and the corresponding intervals are highlighted in black.

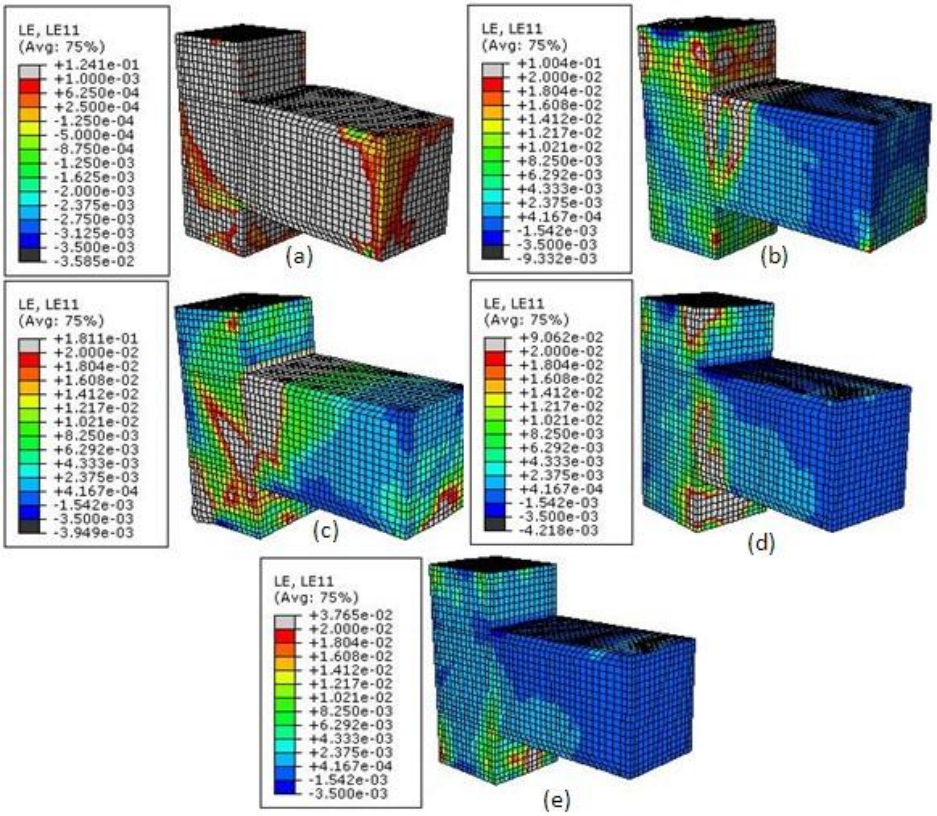


Figure 6.21: Principal strain contours for Case Study 3(a) joints with $SI = 0\%$ and (a) $V_f = 0\%$, (b) $V_f = 1\%$, (c) $V_f = 1.5\%$, (d) $V_f = 2\%$ and (e) $V_f = 2.5\%$

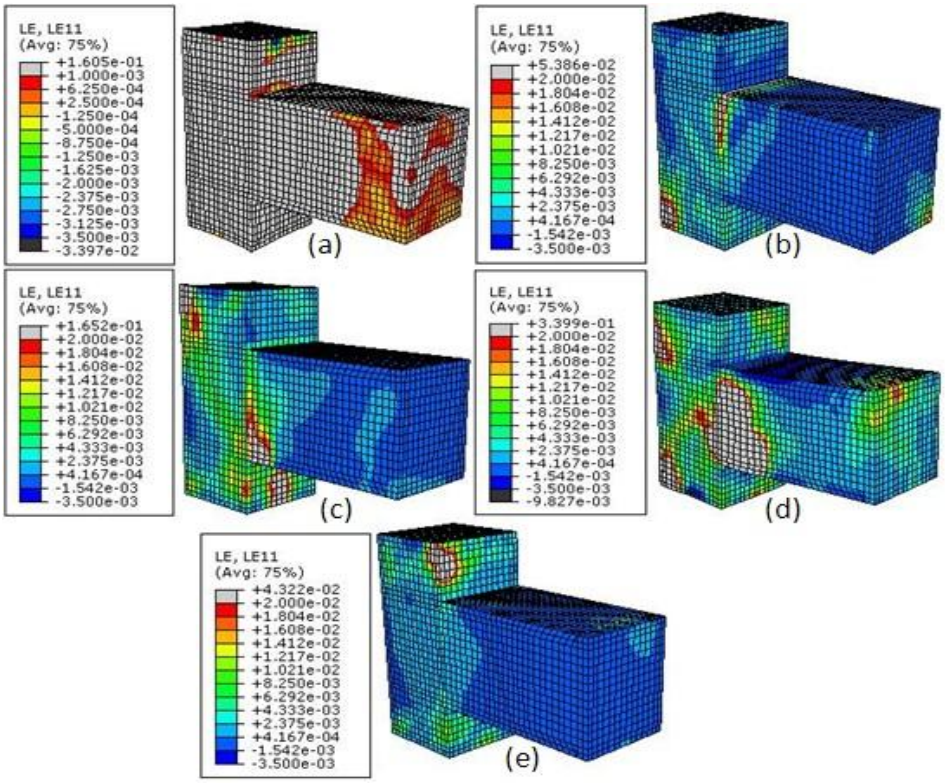


Figure 6.22: Principal strain contours for Case Study 3(a) joints with $SI = 50\%$ and (a) $V_f = 0\%$, (b) $V_f = 1\%$, (c) $V_f = 1.5\%$, (d) $V_f = 2\%$ and (e) $V_f = 2.5\%$

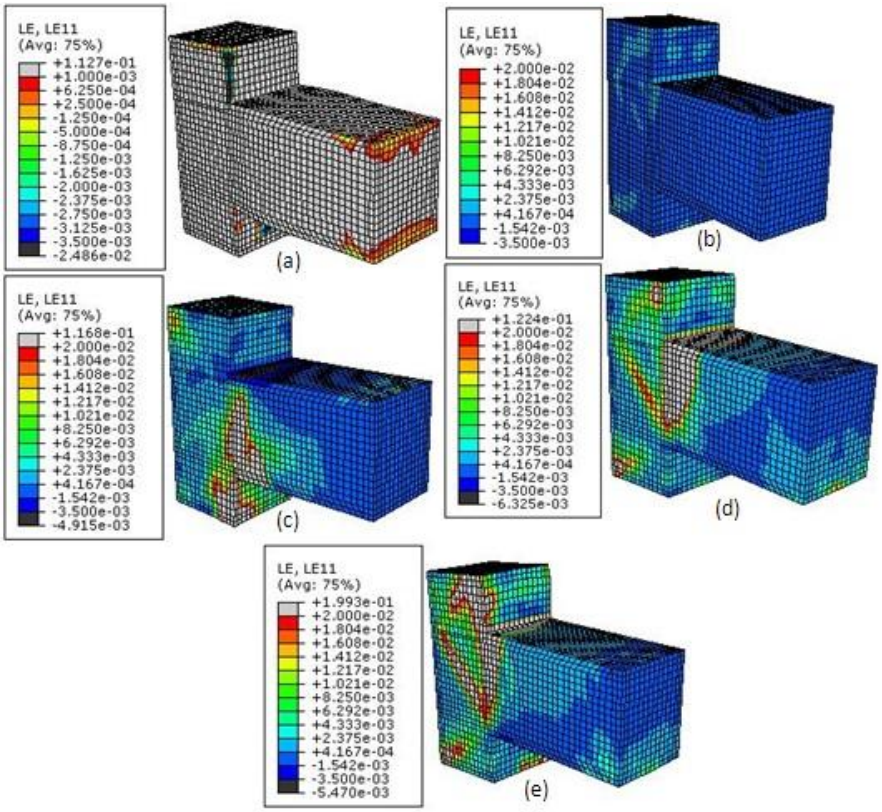


Figure 6.23: Principal strain contours for Case Study 3(a) joints with $SI = 100\%$ and (a) $V_f = 0\%$, (b) $V_f = 1\%$, (c) $V_f = 1.5\%$, (d) $V_f = 2\%$ and (e) $V_f = 2.5\%$

The figures show that all joints with no fibres (i.e. $V_f = 0\%$) suffered extensive cracking at failure. On the other hand, the addition of fibres resulted in a reduction in crack propagation on the SFRC joints. Pull-out failure (i.e. grey zones in parts (b) to (e) on the figures) has occurred in limited zones at the root of the cantilever beam and has not extended into the column or the joint itself in the majority of cases (and in all cases at the optimum fibre content). This indicates that plastic hinges will form at the end of the beam – and not on the column – which is of particular relevance to seismic design (i.e. capacity design based on strong column-weak beam philosophy, discussed in Chapter 3). Thus, it can be concluded that the addition of steel fibres to exterior beam-column joints reduces crack propagation and leads to pull-out failure limited to the end of the beams.

6.3.4.3 Principal strain vectors

The principal strain vectors for all joints modelled (i.e. with $SI = 0\%$, $SI = 50\%$ and $SI = 100\%$ coupled with $V_f = 0\%, 1\%, 1.5\%, 2\%$ and 2.5%) are depicted in Figures 6.24 to 6.26. The strain vectors give an indication of crack patterns. It can be seen that the addition of fibres led to a reduction in extent of cracking. It is also interesting to see that increasing the stirrups spacing has led to more extensive cracking (note that for the specimen with no such increase, the cracking is limited to the beam and does not extend to the column or joint as intended in seismic design). This demonstrates the potential for fibres to compensate for a reduction in conventional reinforcement.

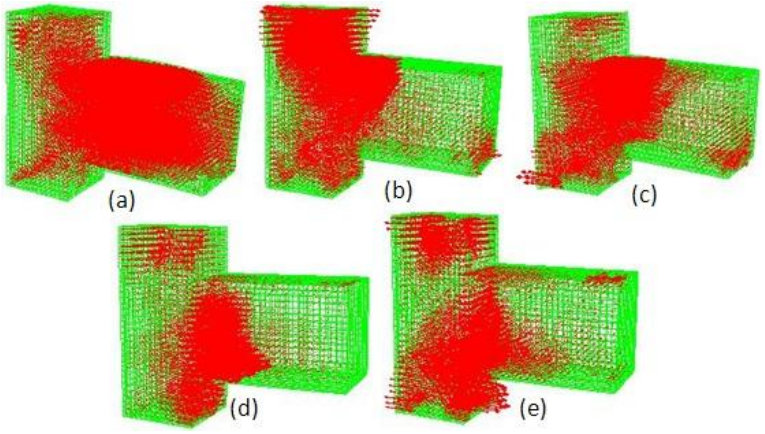


Figure 6.24: Principal strain vectors for Case Study 3(a) joints with $SI = 0\%$ and (a) $V_f = 0\%$, (b) $V_f = 1\%$, (c) $V_f = 1.5\%$, (d) $V_f = 2\%$ and (e) $V_f = 2.5\%$

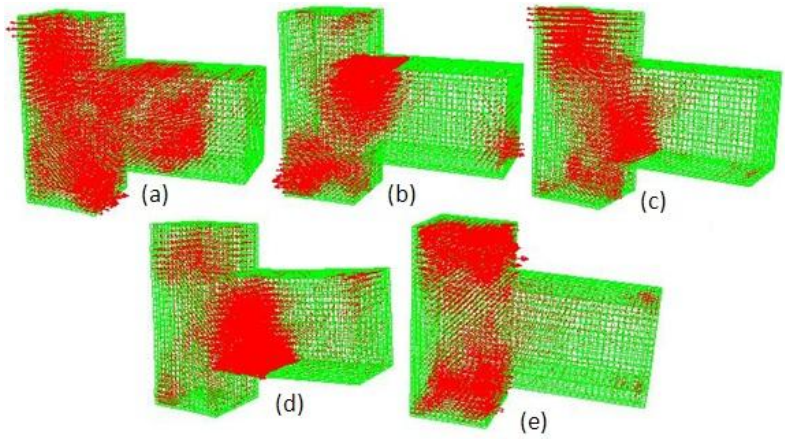


Figure 6.25: Principal strain vectors for Case Study 3(a) joints with $SI = 50\%$ and (a) $V_f = 0\%$, (b) $V_f = 1\%$, (c) $V_f = 1.5\%$, (d) $V_f = 2\%$ and (e) $V_f = 2.5\%$

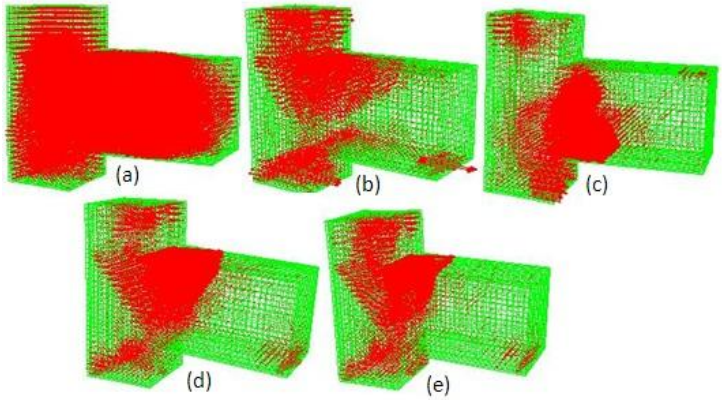


Figure 6.26: Principal strain vectors for Case Study 3(a) joints with $SI = 100\%$ and (a) $V_f = 0\%$, (b) $V_f = 1\%$, (c) $V_f = 1.5\%$, (d) $V_f = 2\%$ and (e) $V_f = 2.5\%$

6.3.4.4 Deflected shapes

The deformations of the exterior beam-column joints analysed in Case Study 3(a) at failure are depicted schematically in Figures 6.27 to 6.29. The diagrams show both downward and upward deflections (the latter associated with a reversed load cycle). The deformations are consistent with the cracking patterns discussed earlier.

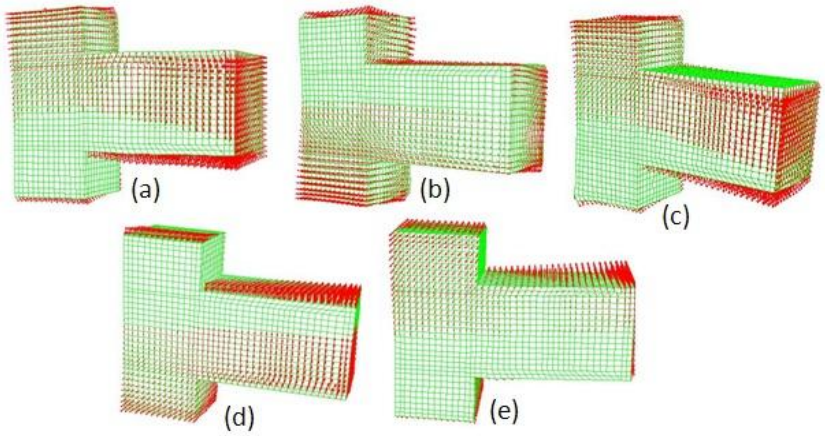


Figure 6.27: Deflected shapes for Case Study 3(a) joints with $SI = 0\%$ and (a) $V_f = 0\%$, (b) $V_f = 1\%$, (c) $V_f = 1.5\%$, (d) $V_f = 2\%$ and (e) $V_f = 2.5\%$

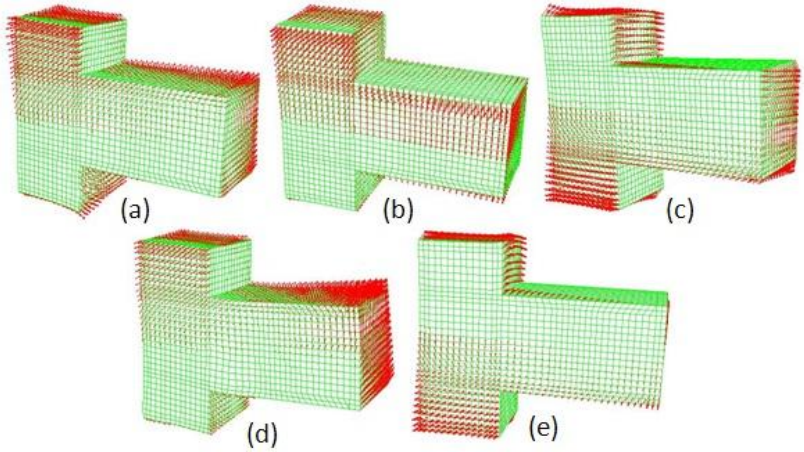


Figure 6.28: Deflected shapes for Case Study 3(a) joints with $SI = 50\%$ and (a) $V_f = 0\%$, (b) $V_f = 1\%$, (c) $V_f = 1.5\%$, (d) $V_f = 2\%$ and (e) $V_f = 2.5\%$

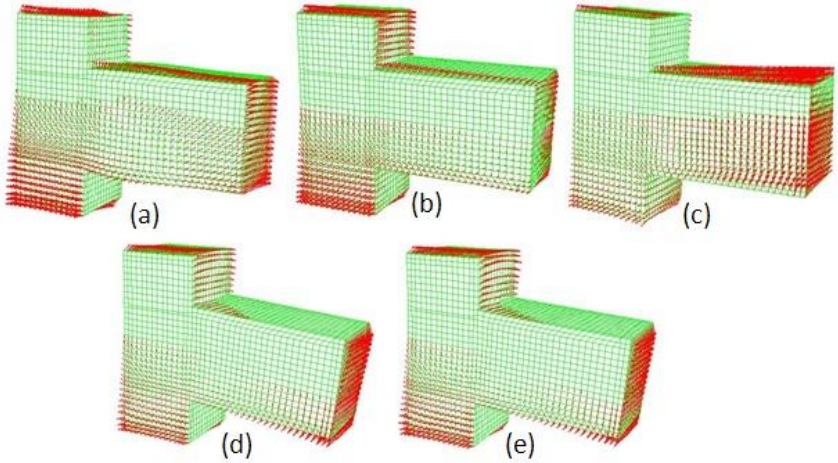


Figure 6.29: Deflected shapes for Case Study 3(a) joints with $SI = 100\%$ and (a) $V_f = 0\%$, (b) $V_f = 1\%$, (c) $V_f = 1.5\%$, (d) $V_f = 2\%$ and (e) $V_f = 2.5\%$

6.3.5 Comparative study with control specimen using non-dimensional ratios

In this section, an overall comparison is made between the control joint specimen (i.e. the one with no fibres and full conventional shear reinforcement) and the joints with various fibre dosages and reduced stirrup spacing. The values of the strength, ductility, energy absorption and number of cycles were normalised by dividing them by the corresponding values of the control specimen. In this manner, overall conclusions were made on the potential of fibres to compensate for reduction in conventional reinforcement. The normalised values of these key structural performance indicators (under cyclic loading) also provide an estimate of the potential enhancement to these parameters and the amount of fibres required to achieve them. Such findings are useful for loading types which are characterised by their cyclic nature, such as seismic loads.

6.3.5.1 Strength ratio

Figure 6.30 shows the ratio of the maximum load sustained (P_{max}) to that of the control joint ($P_{max,0}$), plotted against the steel fibre ratios. The graph shows that the strength consistently increases as more fibres are added. The joints with the least reduction in conventional reinforcement (i.e. lowest spacing increase) provided the highest strength increase. This suggests that increasing the reinforcement (whether conventional bars or fibres, or a mix of the two) will result in enhanced strength.

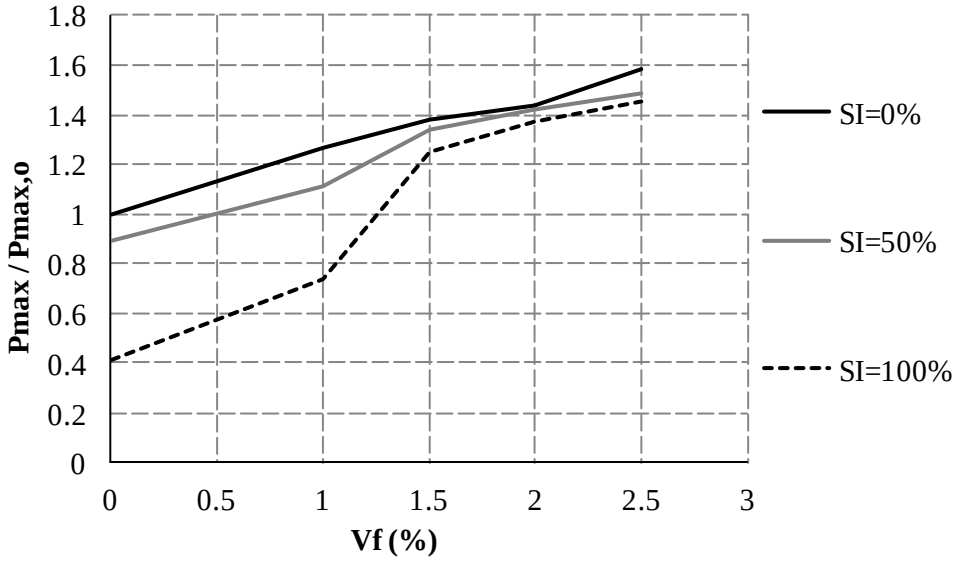


Figure 6.30: Ratio of maximum load to that of the control specimen ($SI = 0\%, V_f = 0\%$) versus fibre volume fraction for Case Study 3(a)

The strength level of the control specimen was restored with fibre contents of $V_f = 0.5\%$ and 1.3% for joints with $SI = 50\%$ and 100%, respectively. Higher fibre amounts led to the strength level of the control specimen been exceeded by up to 40~60%.

Another comparison presented is between the yield load of each joint (P_y) to that of the control specimen ($P_{y,0}$) as shown in Figure 6.31. It can be seen that there is a consistent upward trend with the load increasing as the amount of fibres provided is raised. The yield load ratio for joints with $SI = 50\%$ and $SI = 100\%$. The load levels of the control specimen were restored when fibres were added in sufficient amounts, i.e. $V_f = 1.7\%$ and 2.2% for joints with $SI = 50\%$ and $SI = 100\%$, respectively.

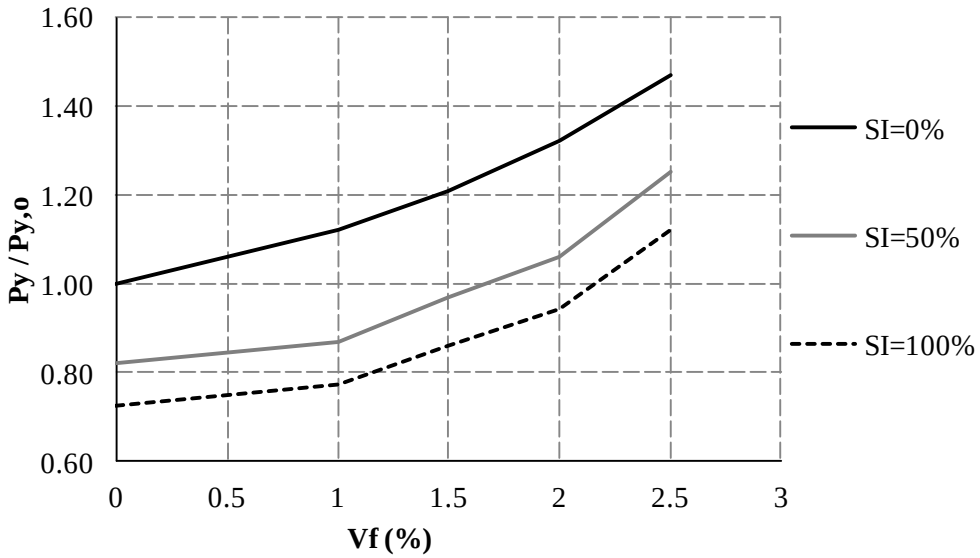


Figure 6.31: Ratio of yield load to that of the control specimen ($SI = 0\%, V_f = 0\%$) versus fibre volume fraction for Case Study 3(a)

6.3.5.2 Ductility ratio

The ductility ratio calculated for each joint (μ) and compared to that of the control joint specimen ($\mu_{,o}$) is presented in Figure 6.32. It is clear that for joints without increase in stirrups spacing (i.e. $SI = 0\%$) the ductility has doubled when fibres were provided at $V_f = 1\%$. However, increasing the fibre amount further beyond $V_f = 1.5\%$ led to a reduction rather than an increase in ductility.

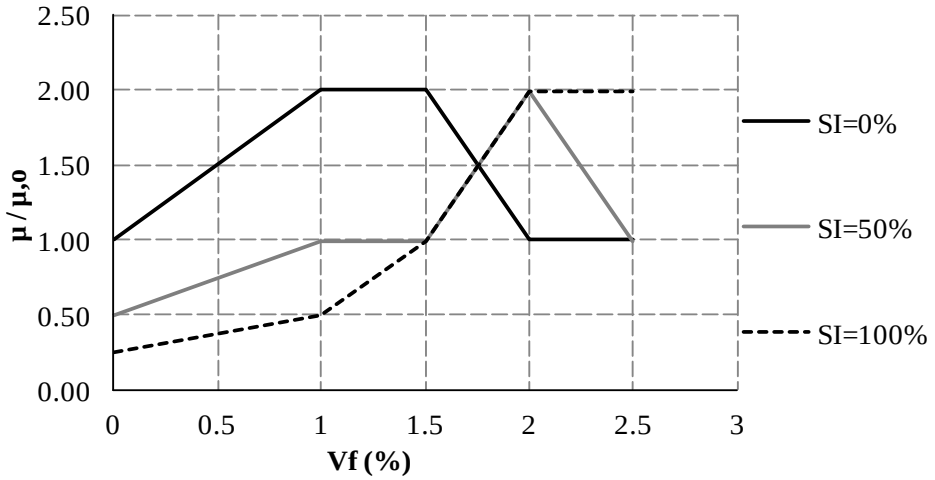


Figure 6.32: Ratio of ductility ratio to that of the control specimen ($SI = 0\%, V_f = 0\%$) versus fibre volume fraction for Case Study 3(a)

A similar trend was observed for the other joints with increased stirrups spacing as the addition of fibres within a certain threshold enhances ductility. The optimum amounts of fibres were found to be $V_f = 2\%$ for both joints with $SI = 50\%$ and $SI = 100\%$ (with ductility achieved being double that associated with the control specimen). However, a less-ductile response will result if fibres are provided beyond this threshold.

Therefore, it can be concluded that the addition of fibres in optimum amounts will lead to significant enhancement to ductility. This is of particular relevance to seismic design as ductility is one of the main considerations to ensure sufficient energy dissipation (energy absorption was also studied and the results are presented subsequently). Nevertheless, fibres should not be provided in excess of the optimum amounts as this will lead to a less-ductile response. Therefore, fibres could be provided to replace some of the conventional shear reinforcement (and thus lessen the congestion of shear reinforcement in critical regions), but should not be provided in addition to *full* conventional reinforcement as they will make the joint becomes stiffer and deflect less (this largely due to the fibres role in bridging across cracks and limiting their opening). This is similar to the "over-reinforced" brittle response associated with concrete members reinforced with excessive amounts of conventional reinforcement.

6.3.5.3 Energy absorption ratio

Figure 6.33 shows the ratio of the energy absorption calculated at each joint (E_a) to the control joint energy absorption ($E_{a,0}$). The trend is similar to the one observed earlier

for ductility with energy absorption increasing up to a certain peak and then dropping if excessive amounts are provided. The optimum fibre volume fractions were found to be $V_f = 1\%$ for joints with $SI = 0\%$ and $V_f = 2\%$ for both joints with $SI = 50\%$ and $SI = 100\%$. It should be noted that the enhancement in energy absorption due to fibres is significant (with absorption levels 4~10 times higher than those associated with the control specimen).

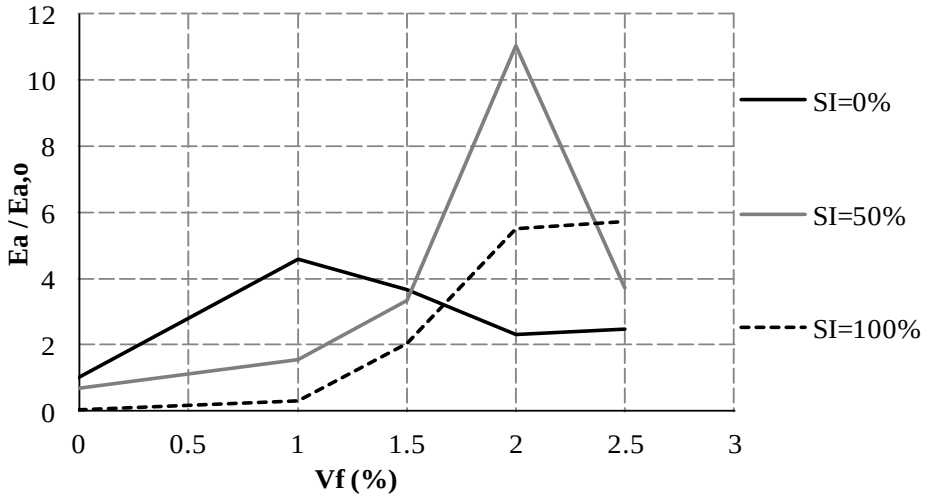


Figure 6.33: Ratio of energy absorption to that of the control specimen ($SI = 0\%, V_f = 0\%$) versus fibre volume fraction for Case Study 3(a)

6.3.5.4 Number of the cycles ratio

The ratio of the number of cycles achieved before failure for each beam-column joint (N_c) to the corresponding number of cycles for the control joint ($N_{c,0}$) is given in Figure 6.34. The data confirms the trend observed when examining ductility and energy absorption in the preceding sections (with optimum fibre amounts found to be $V_f = 1\%$ for joints with $SI = 0\%$ and $V_f = 2\%$ for joints with $SI = 50\%$ and $SI = 100\%$). Thus, it can be concluded that SFRC added in optimum amounts is capable of providing alternative shear resistance and achieving the strength, ductility and energy absorption levels required under reversed-cyclic loading (which the key feature of seismic loading). This indicates that SFRC can help reduce the conventional shear reinforcement and thus lessen the congestion of such reinforcement in the critical regions of beam-column joints, particularly for seismic design

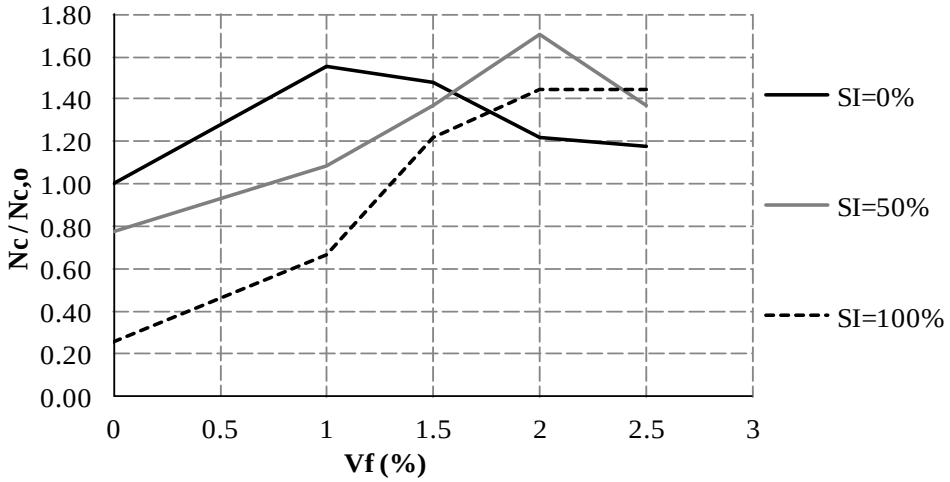


Figure 6.34: Ratio of number of cycles to that of the control specimen ($SI = 0\%, V_f = 0\%$) versus fibre volume fraction for Case Study 3(a)

6.4 Case Study 3(b): Interior beam-column joint - Calibration with experimental data (Filiatrault et al, 1995)

6.4.1 Experimental setup

Filiatrault et al (1995) carried out experiments to investigate interior beam-column joint specimens (with and without fibres) under earthquake excitation. The joints were selected to represent those located at the central region of the first floor of a prototype four-storey office building as shown in Figure 6.35.

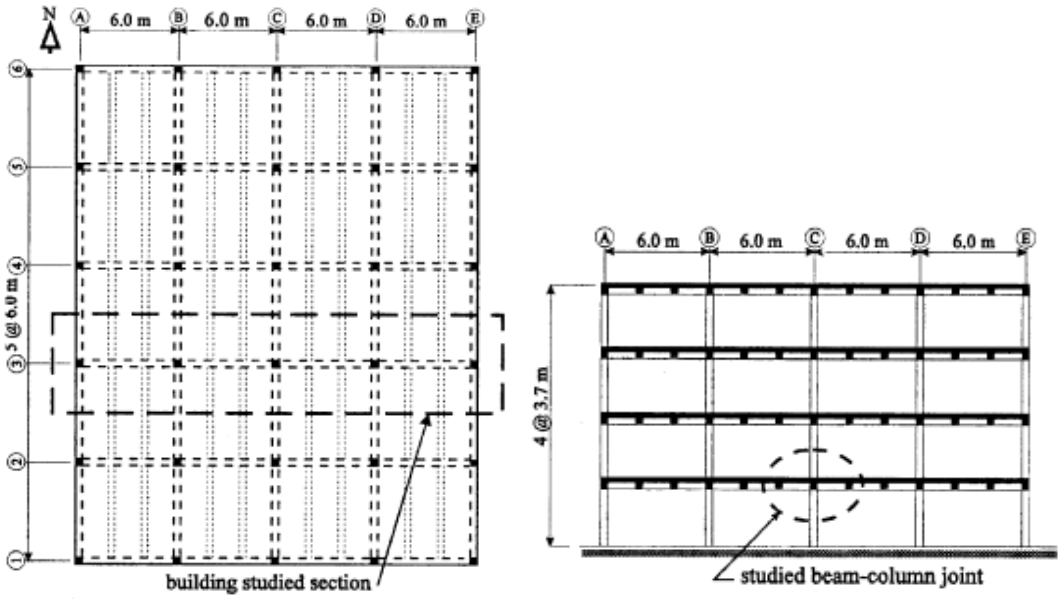


Figure 6.35: Prototype building (adapted from Filiatrault et al, 1995)

Three full-scale beam-column joint specimens (i.e. S1, S2 and S3) were tested to investigate the potential for fibres to compensate for a reduction in transverse hoops (i.e. increase in spacing between hoops to lessen congestion). Therefore, specimens were arranged to have the same the longitudinal reinforcement in the beam and column and to differ only in the transverse (i.e. shear reinforcement) arrangements. The idea was that one specimen would have full conventional seismic shear reinforcement, while the other two would have reduced conventional reinforcement with fibres being added as a replacement in one specimen and with no fibres in the other. Therefore, one of the joints specimens (S2) was designed with seismic detailing as recommended by the National Building Code of Canada (1990). Thus this specimen represents the joint with full conventional seismic reinforcement. The other two joint specimens (i.e. S1 and S3) were constructed incorporating the same relaxed hoop ties (i.e. stirrups) spacing, but with a SFRC mix cast in the critical region around the joint of specimen S3 (whereas no fibres were added to S1). Thus joint S1 represents the specimen with deficient seismic reinforcement, while S3 represents the SFRC joint with fibres added to replace the reduced conventional seismic reinforcement.

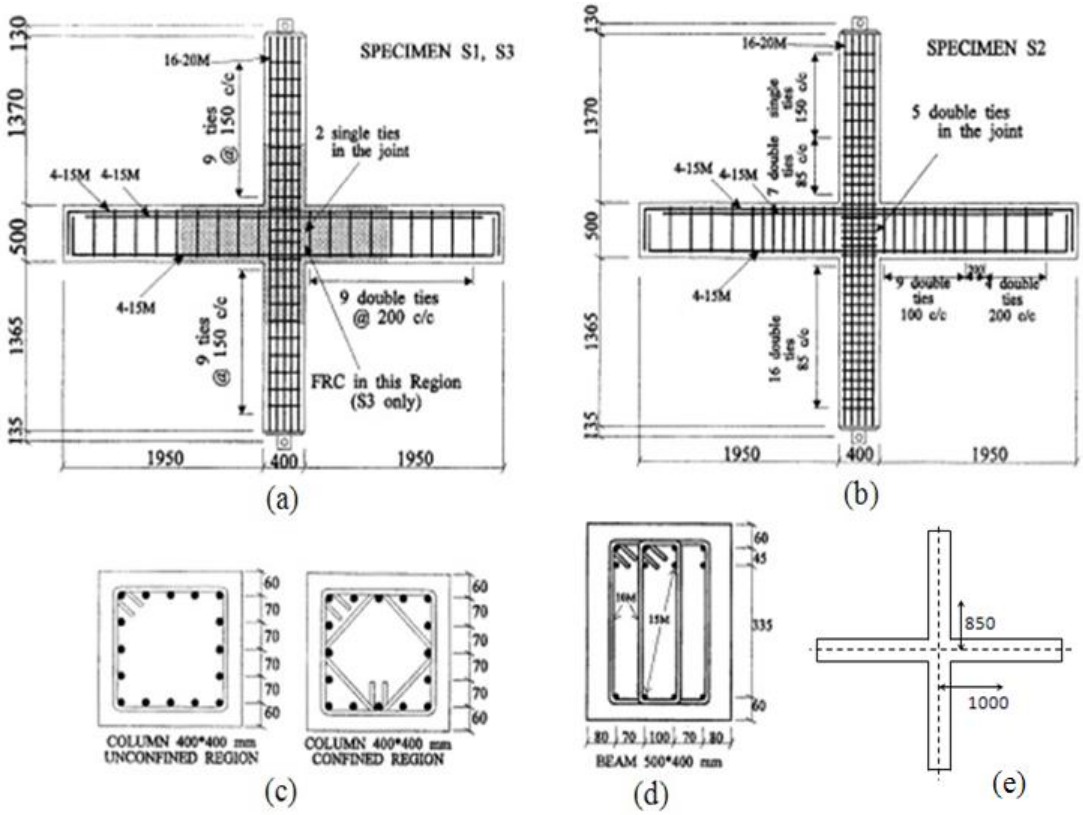


Figure 6.36: Details of the beam-column joints showing (a) specimens S1 and S3, (b) specimen S2, (c) column cross-section, (d) beam cross-section and (e) dimension for FRC (adapted from Filiatrault et al, 1995)

Figure 6.36 shows the dimensions and steel reinforcement arrangement for the three beam-column joint specimens investigated in the study. The steel fibres used in specimen S3 were hooked-end fibres with length of 50 mm, diameter of 0.5 mm and were added at a volume fraction of $V_f = 1.6\%$. The compressive strength for concrete used was 46 MPa, whilst the steel reinforcement yielded at 400 MPa. Both ends of the column were simply supported and were acted upon by a constant axial compressive load of 670 kN representing 100% gravity load of the 2nd floor of the central column of the prototype building.

The seismic excitation was simulated in the tests using an arrangement of hydraulic actuators, applied on the beams at 1.64 m and 1.96 m from the centre of the column cross-section (see Figure 6.37).

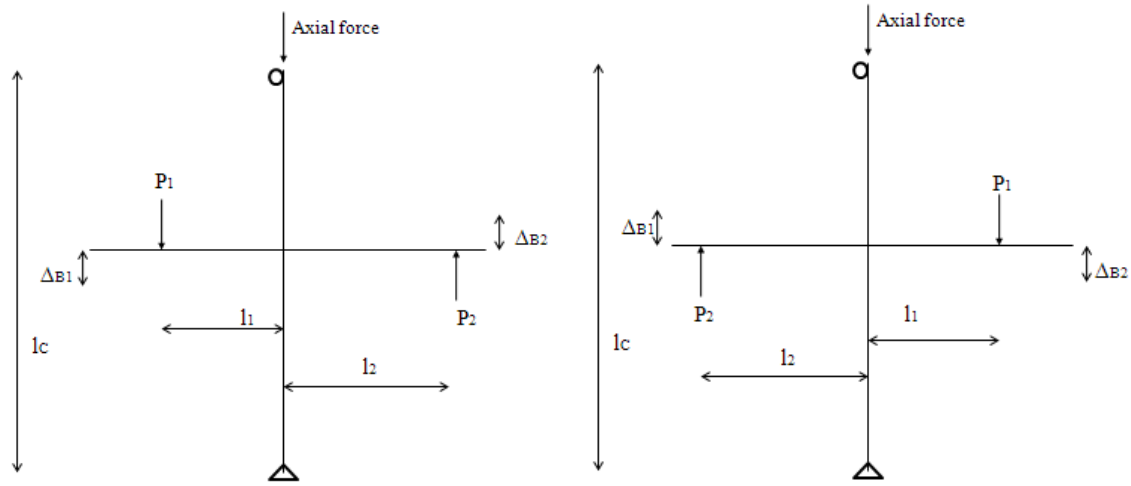


Figure 6.37: Loading arrangement of in cyclic (left) and reversed cyclic (right) loading

Reversed-cyclic loading was applied using a displacement-controlled procedure, while the axial load on the column was kept constant. The actuator forces and corresponding vertical displacements obtained were converted into equivalent storey shear force (V_{col}) and storey drift (Δ_{col}) using the equations below:

$$V_{col} = \left(\frac{P_1 l_1 + P_2 l_2}{l_c}\right) \quad (6.1)$$

$$\Delta_{col} = \left(\frac{\Delta_{B1} + \Delta_{B2}}{l_1 + l_2}\right) l_c \quad (6.2)$$

where P_1 and P_2 are the actuator forces, l_1 and l_2 are the distances of vertical actuators from the column centre, Δ_{B1} and Δ_{B2} are the vertical displacements at the loading points

and l_c is the total column height between supports (see Figure 6.37). The first load cycle in each direction was examined to determine the yield lateral drift (Δ_y) of the specimen. Subsequent cycles were defined using the drift ductility ratio (μ), i.e.:

$$\mu = \Delta_{max}/\Delta_y \quad (6.3)$$

where Δ_{max} is the maximum drift in the given cycle. In this manner, the structural responses of the specimens were studied at varying ductility levels.

6.4.2 FE analysis input data

For calibration purposes, all three beam-column joint specimens S1, S2 and S3 tested by Filiatrault et al. (1995) were adopted. Steel plates of 50 mm thickness were added at the supports at the column ends covering the column's cross-sectional area and were also added at the cyclic loading points on the beams extending along the breadth of the beam and with a width of 100 mm along the beam span. These small plates were added to mimic experimental conditions and avoid premature localised failure. The models developed for the subsequent non-linear FE analyses are depicted in Figure 6.38.

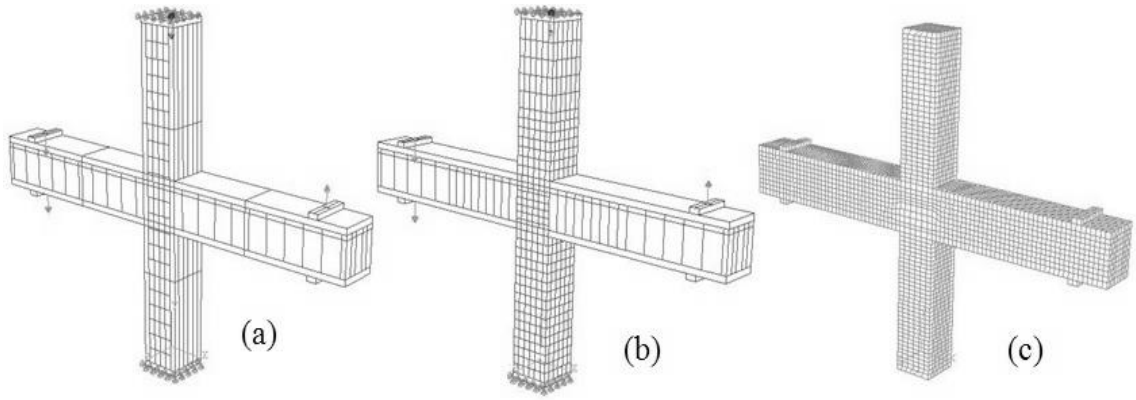


Figure 6.38: Beam-column joint modelled using ABAQUS with boundary condition and reinforcement details for specimens (a) S1 and S3, (b) S2 and (c) mesh adopted

Figures 6.39 and 6.40 show the tensile stress-strain diagrams for SFRC and steel bars, respectively, which were implemented into the FE model. The key values of stress and strain are summarised in Table 6.7. The Young's modulus of concrete is assumed to be 35GPa. To replicate the experimental layout, the SFRC region of the beam-column joint was taken to cover a distance of 1 m from the centreline of the column on both sides of the beams and 0.85 m from the beam centreline on both sides of the columns (see Figure 6.36 (e)).

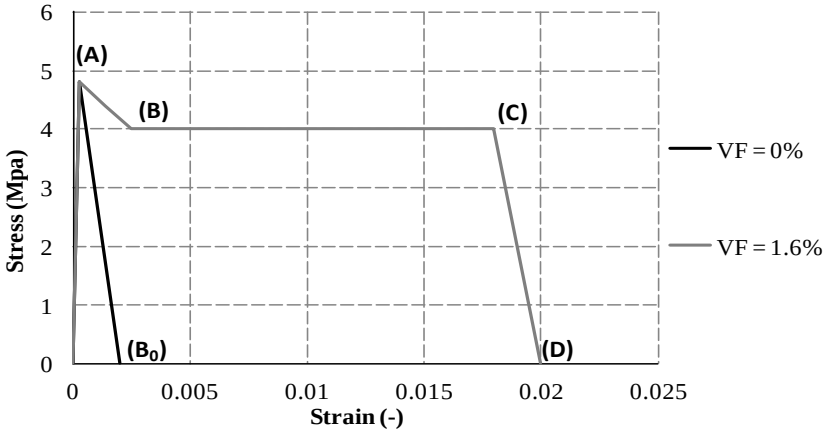


Figure 6.39: Tensile stress-strain diagram for plain and fibre-reinforced concrete adopted in the calibration work for Filiatrault et al. (1995) beam-column joints

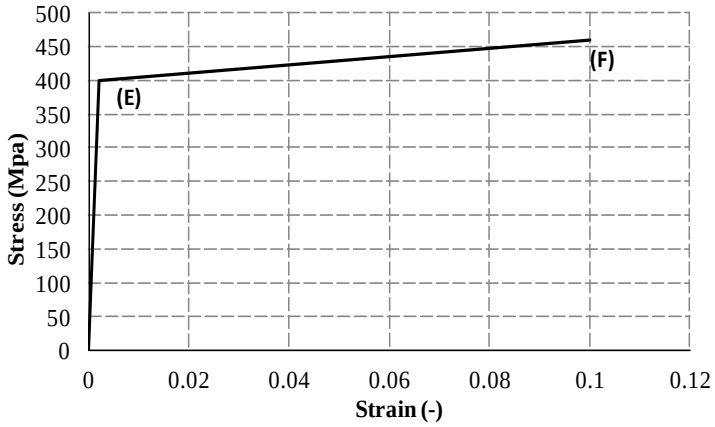


Figure 6.40: Stress-strain diagram for conventional steel reinforcement bars adopted in the calibration work for Filiatrault et al (1995) beam-column joints

Point	Stress (MPa)	Strain (‰)
Origin	0	0
(A)	4.8	0.24
(B_0)	0	2

Table 6.7(a): Tensile stress-strain properties for plain concrete

Point	Stress (MPa)	Strain (‰)
Origin	0	0
(A)	4.8	0.24
(B)	4	1.37
(C)	4	18
(D)	0	20
(E)	400	2
(F)	460	100

Table 6.7(b): Stress-strain properties adopted for the calibration work for Filiatrault et al (1995) beam-column joints

To streamline the FE modelling, the loading arrangement from the experimental work was simplified by assuming that $l_1 = l_2$ (refer to Figure 6.37). Therefore, it can be considered that $\Delta_{B1} = \Delta_{B2}$. Thus, the distance adopted in the FE analysis was taken as the average of the two lengths considered in the experimental work. The reversed-cyclic loading history adopted for the numerical modelling is shown in Figure 6.41. Initially, an axial force equal to 670 kN is applied at the top of the column gradually until the FE model time input is equal to 1, and kept constant beyond this point. The reversed-cyclic loading (see Figure 6.41) is applied using a displacement-based procedure using Δ_{B1} and Δ_{B2} at P_1 and P_2, respectively. A sensitivity analysis was carried out to determine the optimum FE mesh and consequently an element with width 50 mm was adopted. The loading history in the experiment was arranged so that the peaks co incise with multiples of the ductility ratio (μ) and this has been repeated in the FE calibration work as well.

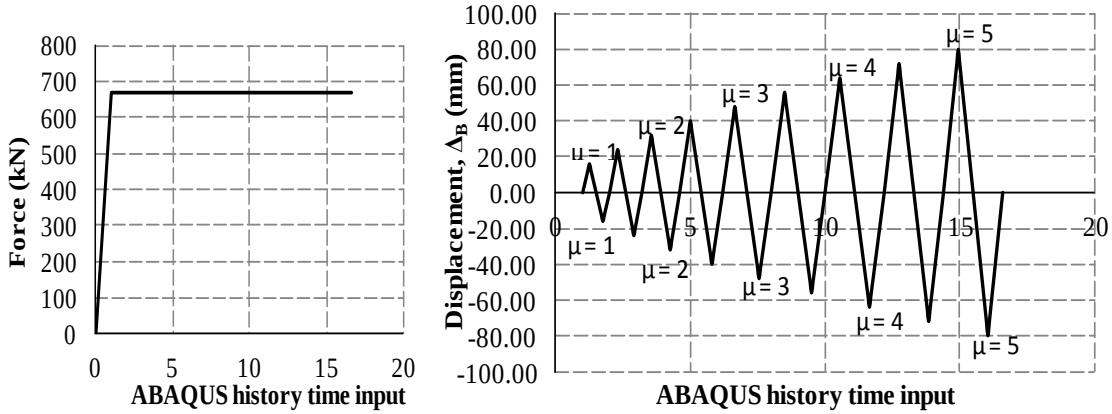


Figure 6.41: ABAQUS history input for calibration work

6.4.3 Results of calibration work

The FE model and analysis procedures have been calibrated by comparing their predictions with the experimental results as depicted in Figures 6.42 to 6.47. Reasonable agreement can be observed in the storey shear versus storey drift hysteresis loops for all specimens as shown in Figure 6.42 (Specimen S1), Figure 6.43 (Specimen S2) and Figure 6.44 (Specimen S3). The key points from these curves are summarised in Tables 6.8, 6.9 and 6.10 for the Specimens S1, S2 and S3, respectively. Based on the results given in the tables, it is evident that the yielding storey shear (V_y) and maximum storey shear capacity (V_{max}) for all specimens resulting from the FE analyses are almost the same as the ones found in the experimental work (discrepancy of less than 3.4%).

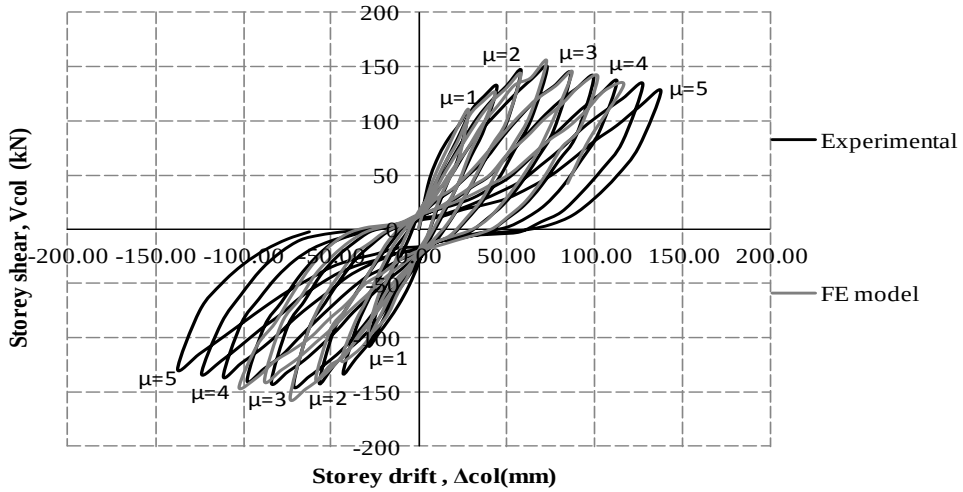


Figure 6.42: Storey shear-storey drift curves comparison for Specimen S1

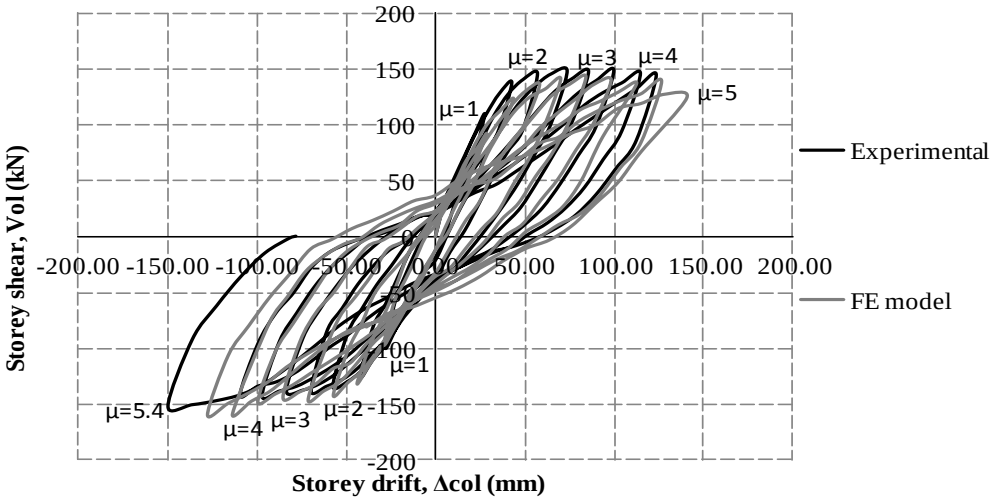


Figure 6.43: Storey shear-storey drift curves comparison for Specimen S2

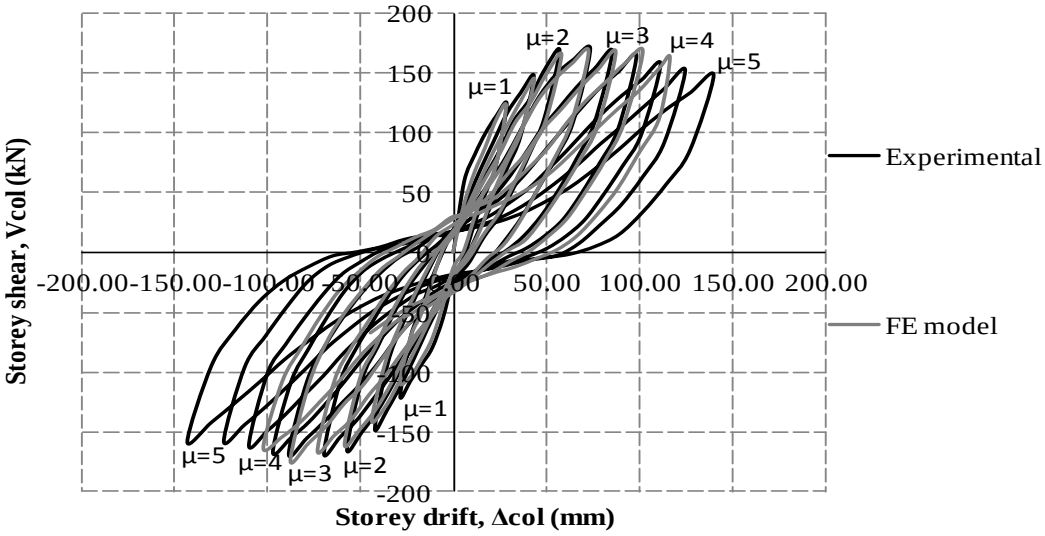


Figure 6.44: Storey shear-storey drift curves comparison for Specimen S3

V_f (%)	N_c	V_y (kN)	Δ_y (mm)	V_{max} (kN)	Δ_{Vmax} (mm)	V_u (kN)	Δ_u (mm)	$\mu = \frac{\Delta_u}{\Delta_y}$	$\frac{V_{max}}{V_y}$
Experiment	9.14	109.4	28.2	149.8	72.9	127.9	137.6	4.88	1.37
FE model	6.59	109.3	28.6	154.9	73.0	132.1	116.8	4.08	1.42

Table 6.8: Result summary from storey shear – storey drift curves (Specimen S1)

V_f (%)	N_c	V_y (kN)	Δ_y (mm)	V_{max} (kN)	Δ_{Vmax} (mm)	V_u (kN)	Δ_u (mm)	$\mu = \frac{\Delta_u}{\Delta_y}$	$\frac{V_{max}}{V_y}$
Experiment	7.75	109.4	27.6	148	73.8	144.3	123.8	4.49	1.35
FE model	8.82	92.4	28.8	143.1	84.3	124.2	140.8	4.9	1.55

Table 6.9: Result summary from storey shear – storey drift curve (Specimen S2)

V_f (%)	N_c	V_y (kN)	Δ_y (mm)	V_{max} (kN)	Δ_{Vmax} (mm)	V_u (kN)	Δ_u (mm)	$\mu = \frac{\Delta_u}{\Delta_y}$	$\frac{V_{max}}{V_y}$
Experiment	9.25	123.9	28.7	170.1	73.6	140.0	147.9	5.15	1.37
FE model	6.84	122.4	28.6	168.0	102.2	162.7	116.8	4.08	1.37

Table 6.10: Result summary from storey shear – storey drift curves (Specimen S3)

The only exception is Specimen S2, in which the FE-based value of V_y is about 15.5% lower than the corresponding value obtained from the test. Although good agreement is observed from the storey shear strength, however in terms of the ductility ratio calculated the FE-based results for Specimen S1 and S3 show up to 20% lower ductility than their experimental counterparts. This discrepancy can be explained by noting that the number of cycles (N_c) obtained in the numerical analyses for S1 and S3 is lower than the one found in the tests (for S2 the number of cycles discrepancy is small, ~9%). These differences are well within the accepted range of accuracy for concrete structures, with the FE predictions being on the safe side.

The failure point in the numerical analyses is characterised by a sudden large jump in kinetic energy that is usually associated with formation of large/extensive cracks indicating that the structure has lost its structural integrity. These sudden changes in kinetic energy are clearly visible in the energy graphs given in Figure 6.45 for Specimen S1, Figure 6.46 for Specimen S2 and Figure 6.47 for Specimen S3.

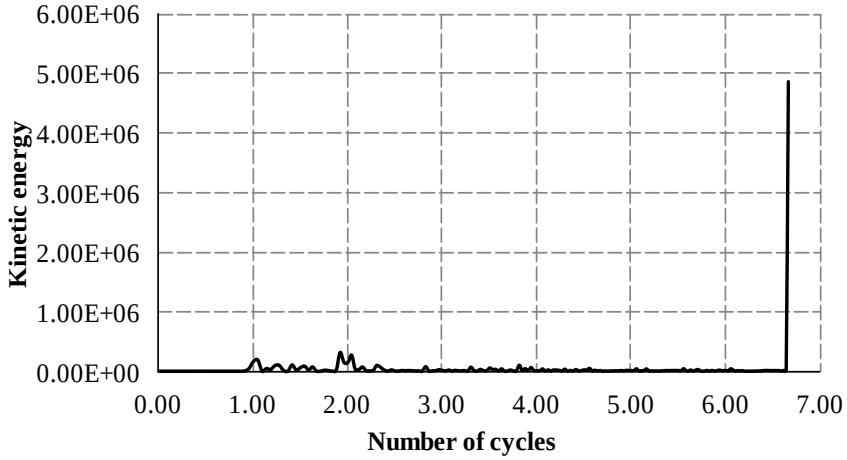


Figure 6.45: Kinetic energy graph for Specimen S1

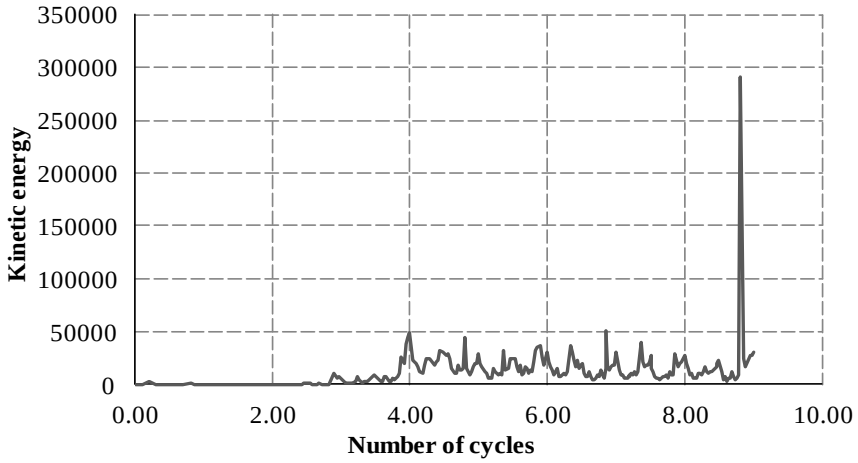


Figure 6.46: Kinetic energy graph for Specimen S2

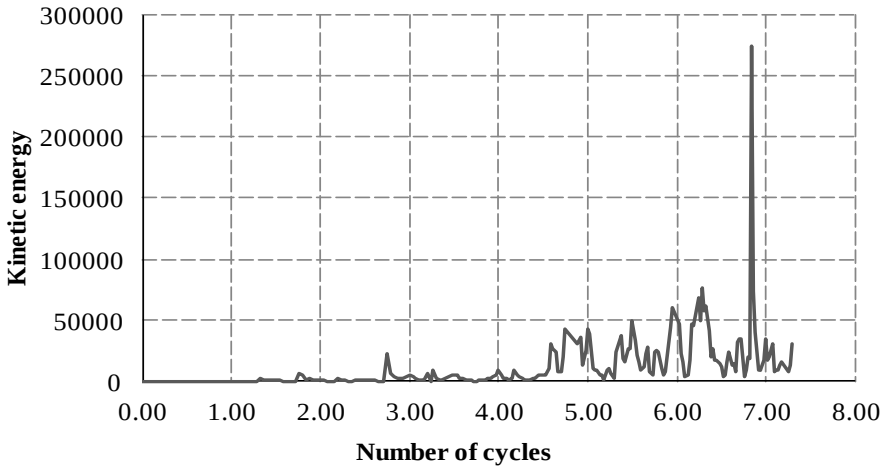


Figure 6.47: Kinetic energy graph for Specimen S3

The principal stresses and strains distribution, strain vectors and deformed shapes of Specimen S1, S2 and S3 taken at failure load level are illustrated in Figures 6.48, 6.49

and 6.50, respectively. The maximum and minimum levels on the contours of principal stresses were selected to coincide with the tensile and compressive strength of concrete (i.e. 4.8 MPa and -46 MPa, respectively). Similar consideration is adopted for the maximum principal strain contour levels at the joint, in which the tensile cracking strain is taken as 0.002 for plain concrete (and 0.02 representing pull-out failure for fibrous concrete, see point D in Figure 6.39 and Table 6.7) and the ultimate compressive strain as -0.0035. Using these contour settings, the cracking pattern can be determined from the principal strain distribution, which is highlighted in grey (tensile failure) or black (compressive failure).

Therefore, from Figures 6.48, 6.49 and 6.50 it can be seen that the crack opening at failure for Specimen S1 occur at the middle of the joint or connection of the beams and columns as evident from Figure 6.48 (b) and (c). In Figure 6.48 (c), the principal strain vector is marked by the red marks, which were found to have a high concentration at the centre of the joint and in a small region at bottom of the column. The vectors are also used an indicator of crack opening in the beam-column joints (interpreted in conjunction with the contours of principal strain distribution). The deflected shape of the joint at failure is depicted in Figure 6.48 (d).

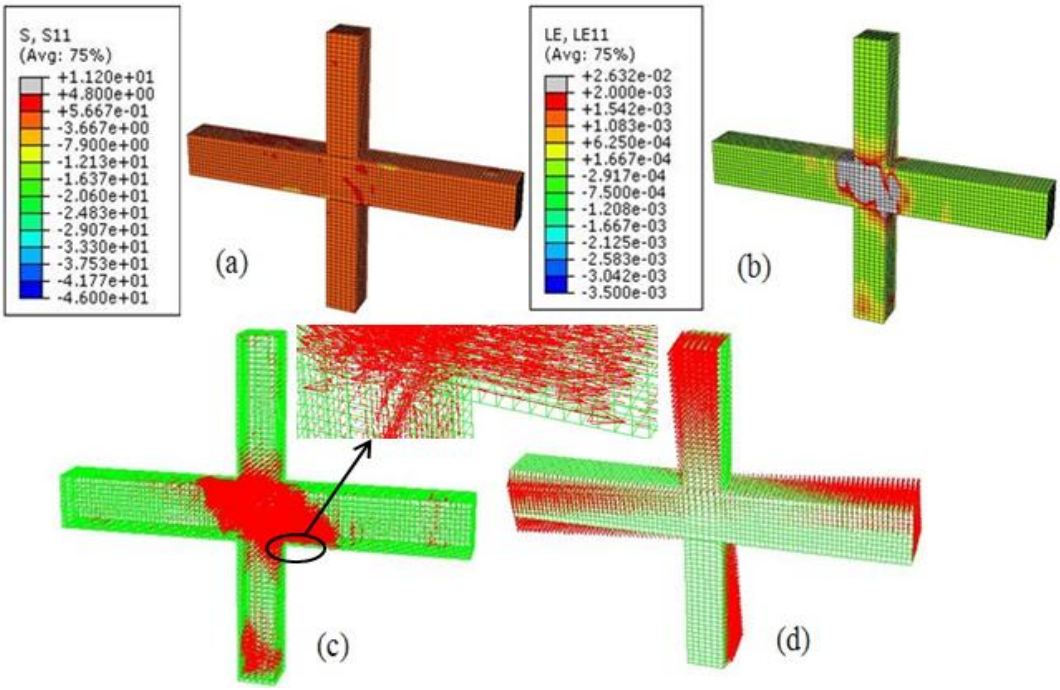


Figure 6.48: Principal (a) stress contour, (b) strain contour, (c) strain vectors and (d) deflected shape for Specimen S1

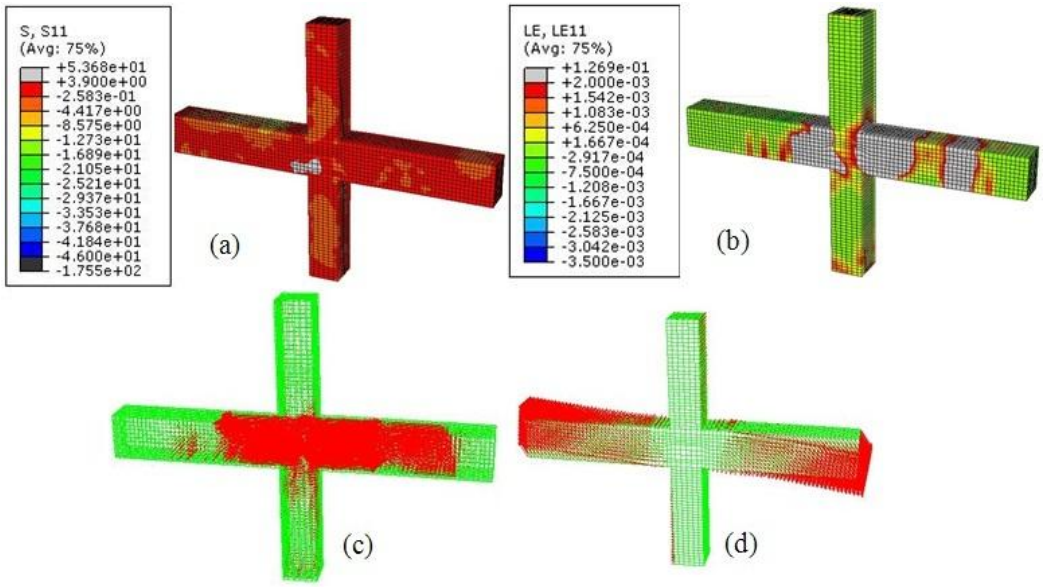


Figure 6.49: Principal (a) stress contour, (b) strain contour, (c) strain vectors and (d) deflected shape for Specimen S2

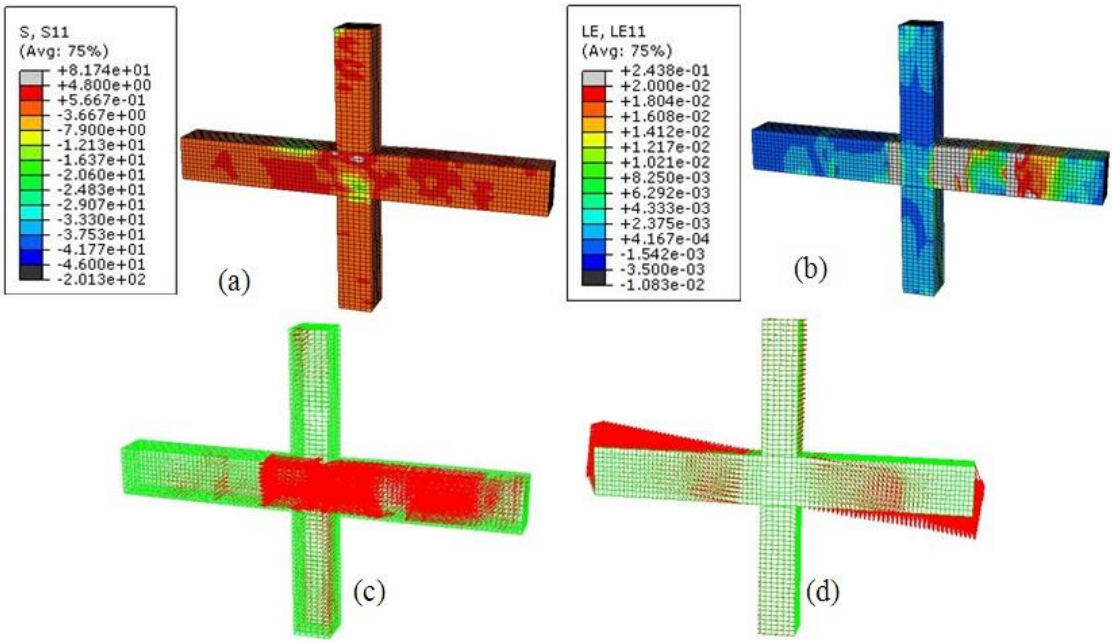


Figure 6.50: Principal (a) stress contour, (b) strain contour, (c) strain vectors and (d) deflected shape for Specimen S3

Based on the strains contours and vectors shown in Figure 6.49 (b) and (c), respectively, for Specimen S2, it can be concluded that plastic hinges develop at the roots of the beams adjoining the column.

The cracking pattern and deformed shape of Specimen S3 is considered from the principal stresses and strains distributions in Figure 6.50. Recalling that the conventional longitudinal and transverse reinforcement for Specimens S1 and S3 are the

same, but with fibres added to S3, it is clear that the addition of steel fibres at the joint region improved the cracking pattern of Specimen S3. This indicates that fibres are useful in bridging and controlling cracks at these regions under reversed-cyclic loading.

The ultimate tensile strain for SFRC is adopted as 0.02 to indicate pull-out failure and is highlighted in grey in Figure 6.50b. Thus, it can be concluded that plastic hinges develop at the end of the beams connected to the column on Specimen S3 and not within the column or the joint itself. This is a key requirement in seismic design (i.e. capacity design concept utilising strong column–weak beam philosophy as discussed in Chapter 3). Furthermore, the stress values are lower than the maximum compressive strength considered suggesting that no crushing failure has occurred.

6.5 Case Study 3(b): Parametric study on interior beam-column joint under reversed-cyclic loading

The results obtained from the FE analyses carried out for Specimen S2 (with full conventional seismic reinforcement but no fibres, i.e. $SI = 0\%$ and $V_f = 0\%$) was adopted as the basis of the work for the parametric studies in Case Study 3(b). Therefore, the results for Specimen S2 are referred to as the control joint specimen (CJ). Comparing the structural response of the control joint with that of the SFRC joints with reduced conventional seismic transverse reinforcement provided an insight into the potential for steel fibres to act as seismic reinforcement helping lessen the congestion of conventional transverse reinforcement.

In the present study, the amount of conventional transverse reinforcement was reduced in three ways as follows:

(i) increase in the stirrups spacing (i.e. $SI = 50\%$)

(ii) increase in the stirrups spacing (i.e. $SI = 100\%$)

(iii) decrease in the hoops area from double stirrups to single stirrups in the columns (so the stirrups provided at 45^o to the column sides, see Figure 6.36c, were removed)

The scenarios in (ii) and (iii) above lead to the same level of reduction in transverse reinforcement (i.e. amount halved). However, the removal of the inner stirrups provided

insight into the potential of fibres to compensate for the loss of confinement provided by the double-stirrup arrangement, which is an important consideration in seismic design detailing. The latter also requires the spacing between stirrups to be within certain limits to ascertain adequate confinement. Fibres provide enhancement to confinement by controlling crack opening as they bridge the cracks. The current investigation examined whether or not this confinement is sufficient to compensate for the reduced conventional hoops (either by relaxing spacing or using single stirrups).

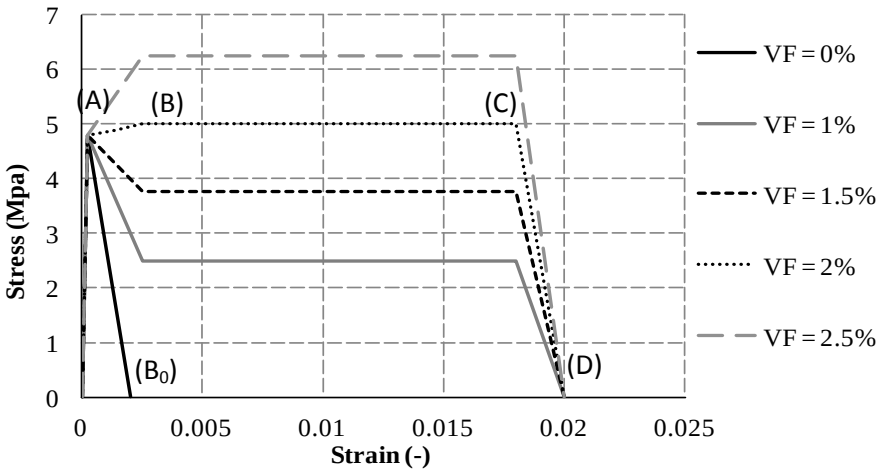


Figure 6.51: Stress-strain relations in tension for the Case Study 3(b)

Point	Stress (MPa)	Strain (‰)
0	0	0
(A)	4.8	0.24
(B_0)	0	2

Table 6.11(a): Tensile strain-stress properties for plain concrete in Case Study 3(b)

Point	Strain (‰)	Stress, V_f=1% (MPa)	Stress, V_f=1.5% (MPa)	Stress, V_f=2% (MPa)	Stress, V_f=2.5% (MPa)
0	0	0	0	0	0
(A)	0.24	4.8	4.8	4.8	4.8
(B)	2.5	2.5	3.75	5	6.25
(C)	18	2.5	3.75	5	6.25
(D)	20	0	0	0	0

Table 6.11(b): Tensile strain-stresses properties for SFRC in Case Study 3(b)

In order to make up for the loss in conventional reinforcement, fibres were added in varying amounts (i.e. $V_f = 0\%, 1\%, 1.5\%, 2\%$ and 2.5%) in all three scenarios

discussed above. The concrete stress-strain properties with and without steel fibres adopted for the parametric studies are shown in Figure 6.51 and summarised in Table 6.11. In addition, the values adopted for the conventional steel bars are similar to those defined in Figure 6.40 and Table 6.11 (b).

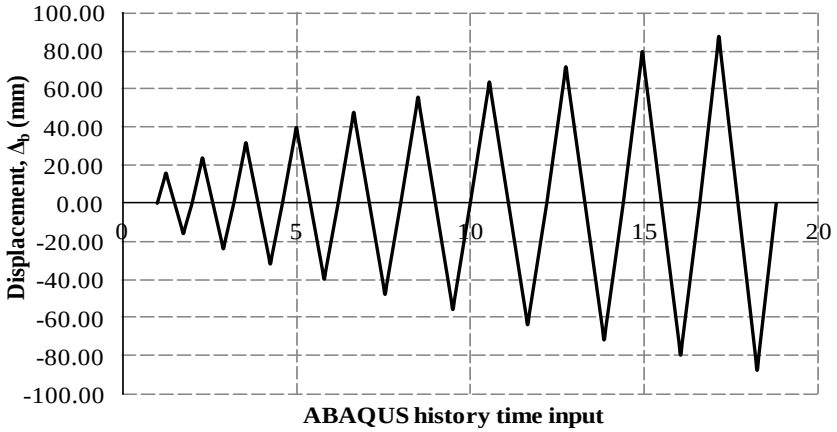


Figure 6.52: ABAQUS history input for the parametric study in the Case Study 3(b)

For the parametric study, the load history input data adopted is depicted in Figure 6.52. The output results are discussed next.

6.5.1 Storey shear-drift curves

The storey shear versus storey drift curves for Case Study 3(b) for interior beam-column joints with single stirrups (reduced from double-stirrups arrangement of Figure 6.36c), joints with increased stirrup spacing by 50% and 100% are presented in Figures 6.53, 6.54 and 6.55, respectively. The important values extracted from the analysis results are summarised in Tables 6.12 to 6.14. The structural parameters of the table can be defined as follows: V_y and Δ_y are the storey shear at yield and its respective storey drift, V_{max} and Δ_{max} are the maximum storey shear sustained during the loading cycles and its respective storey drift, Δ_u and V_u are the ultimate storey drift at failure and corresponding storey shear, μ is the ductility ratio defined as $\mu = \frac{\delta_u}{\delta_y}$ and N_c is the number of cycles obtained before failure. In addition, in order to investigate the structural response further, the storey shear-drift curves for each joint are plotted separately for every fibre volume fraction as given in Figures 6.56 to 6.58.

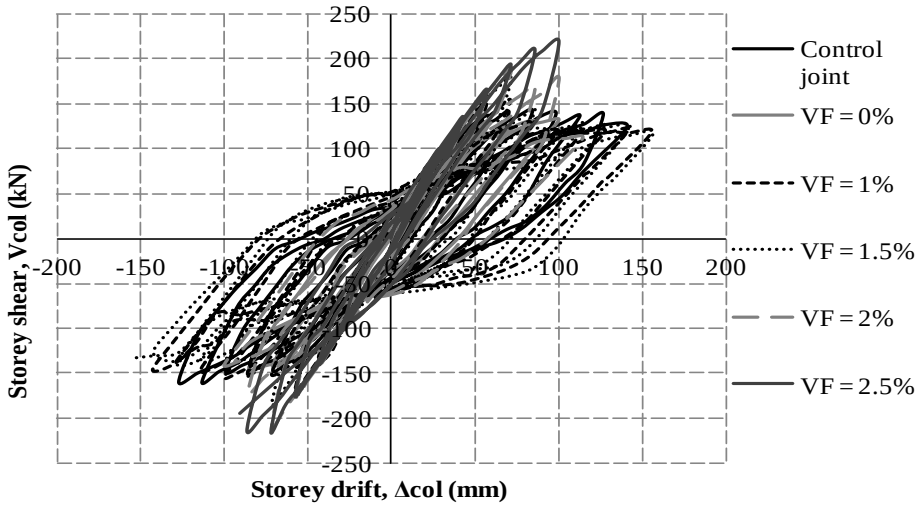


Figure 6.53: Storey shear-drift curve for Case Study 3(b) joints with single stirrups

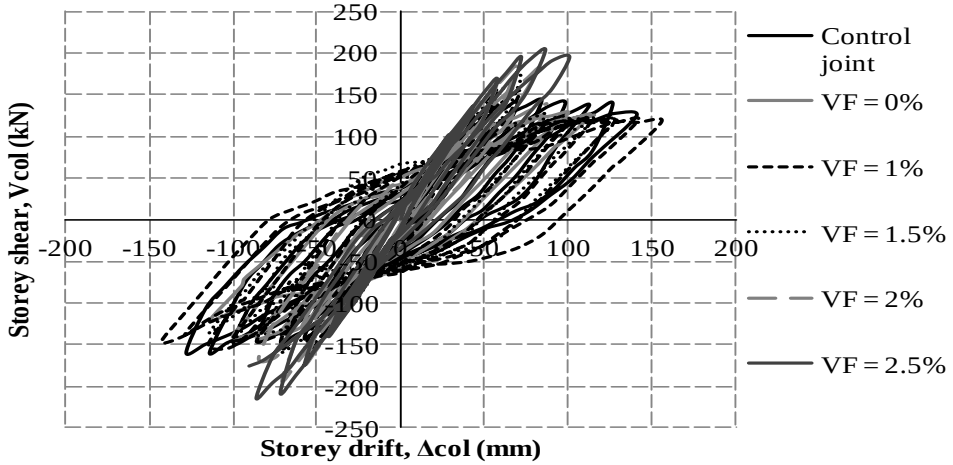


Figure 6.54 Storey shear-drift curve for Case Study 3(b) joints with $SI = 50\%$

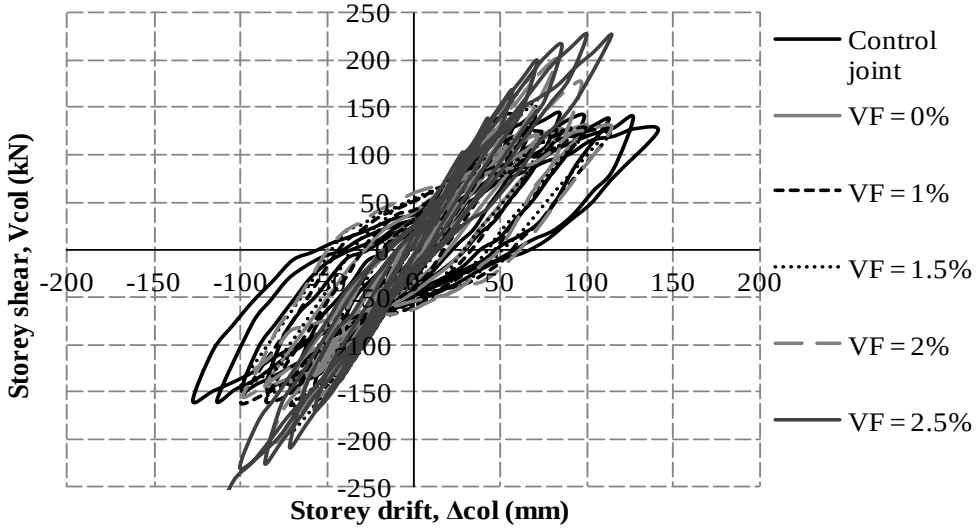


Figure 6.55: Storey shear-drift curve for Case Study 3(b) joints with $SI = 100\%$

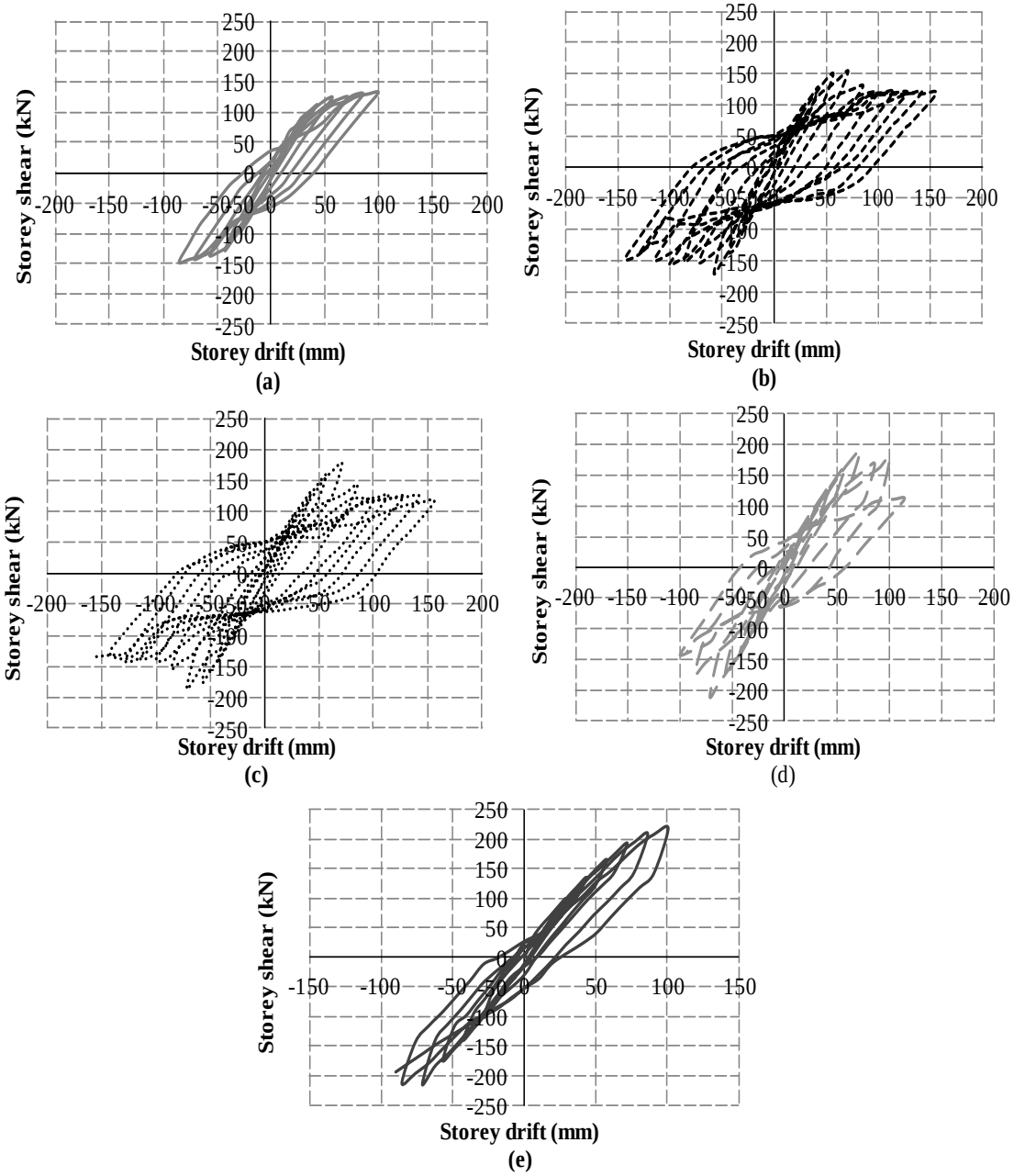


Figure 6.56: Storey shear-drift curve for Case Study 3(b) joints with single stirrups and (a) $V_f = 0\%$, (b) $V_f = 1\%$, (c) $V_f = 1.5\%$, (d) $V_f = 2\%$ and (e) $V_f = 2.5\%$

V_f (%)	N_c	V_y (kN)	Δ_y (mm)	V_{max} (kN)	Δ_{Vmax} (mm)	V_u (kN)	Δ_u (mm)	$\mu = \frac{\Delta_u}{\Delta_y}$	$\frac{V_{max}}{V_y}$
CJ	8.82	92.4	28.8	143.1	84.3	124.2	140.8	4.90	1.55
0	5.90	90.7	28.6	131.8	100	132	100.1	3.50	1.45
1	9.80	97.5	28.6	153.7	71.6	118	156.2	5.46	1.58
1.5	10.02	98.8	28.6	177.8	71.6	117	156.5	5.47	1.80
2	6.95	99.3	28.6	189.9	71.6	112	114.1	3.98	1.91
2.5	6.00	99.6	28.6	219.3	100	219	100.2	3.50	2.20

Table 6.12: Result summary from storey shear-drift curve for Case Study 3(b) joints with single stirrups

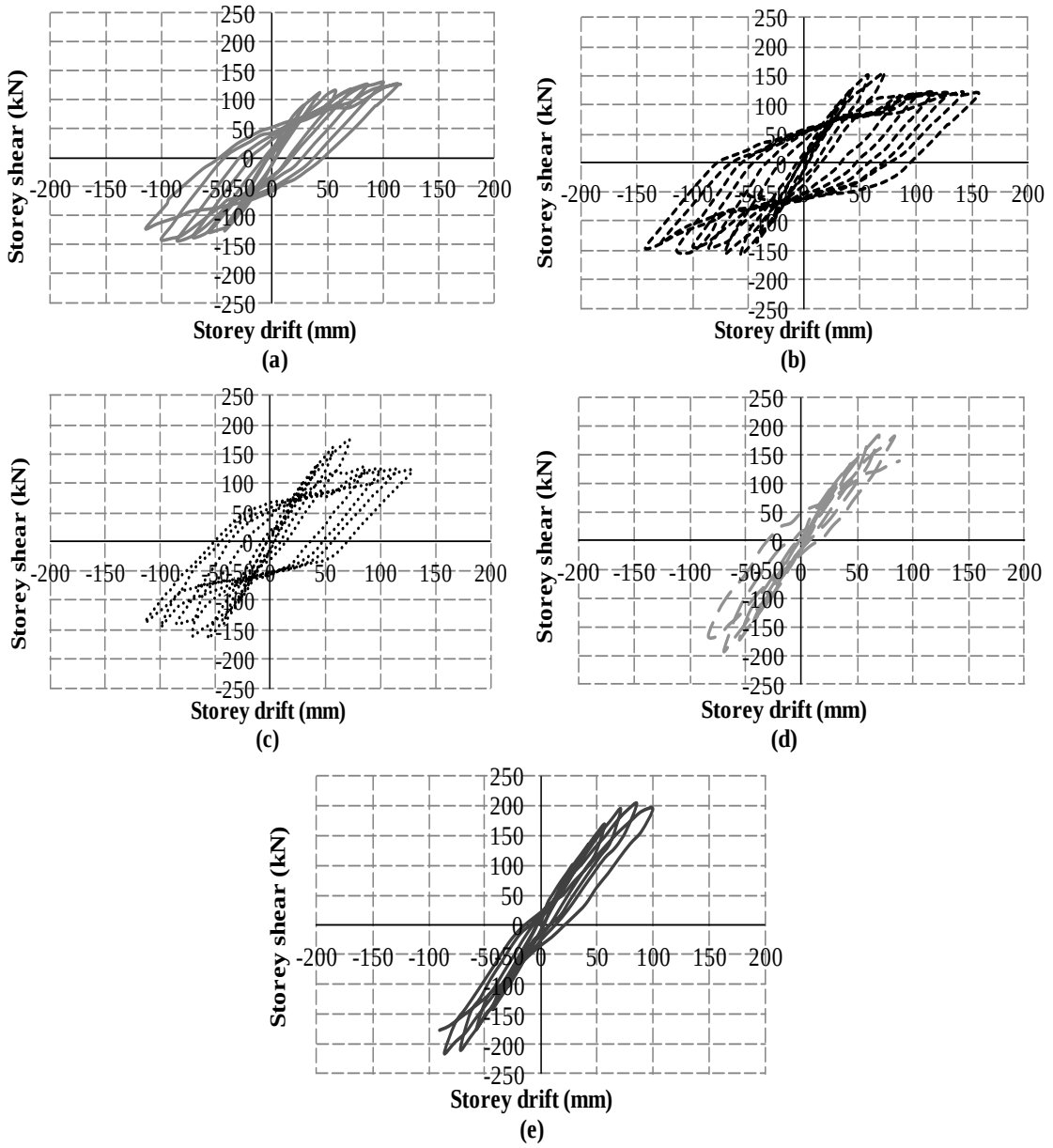


Figure 6.57: Storey shear-drift curve for Case Study 3(b) joints with $SI = 50\%$ and (a) $V_f = 0\%$, (b) $V_f = 1\%$, (c) $V_f = 1.5\%$, (d) $V_f = 2\%$ and (e) $V_f = 2.5\%$

V_f (%)	N_c	V_y (kN)	Δ_y (mm)	V_{max} (kN)	Δ_{Vmax} (mm)	V_u (kN)	Δ_u (mm)	$\mu = \frac{\Delta_u}{\Delta_y}$	$\frac{V_{max}}{V_y}$
CJ	8.82	92.4	28.8	143.1	84.3	124.2	140.8	4.90	1.55
0	7.50	90.2	28.6	129.6	100	128	127.2	4.44	1.44
1	9.84	97.8	28.6	154.4	71.6	118	156.2	5.46	1.58
1.5	7.89	99.2	28.6	172.5	71.6	121.2	128.7	4.50	1.74
2	5.50	100	28.6	193.1	70.4	140	87.55	3.06	1.93
2.5	5.98	101	28.6	215.4	85.9	195	100.2	3.50	2.13

Table 6.13: Result summary from storey shear-drift curve for Case Study 3(b) joints with $SI = 50\%$

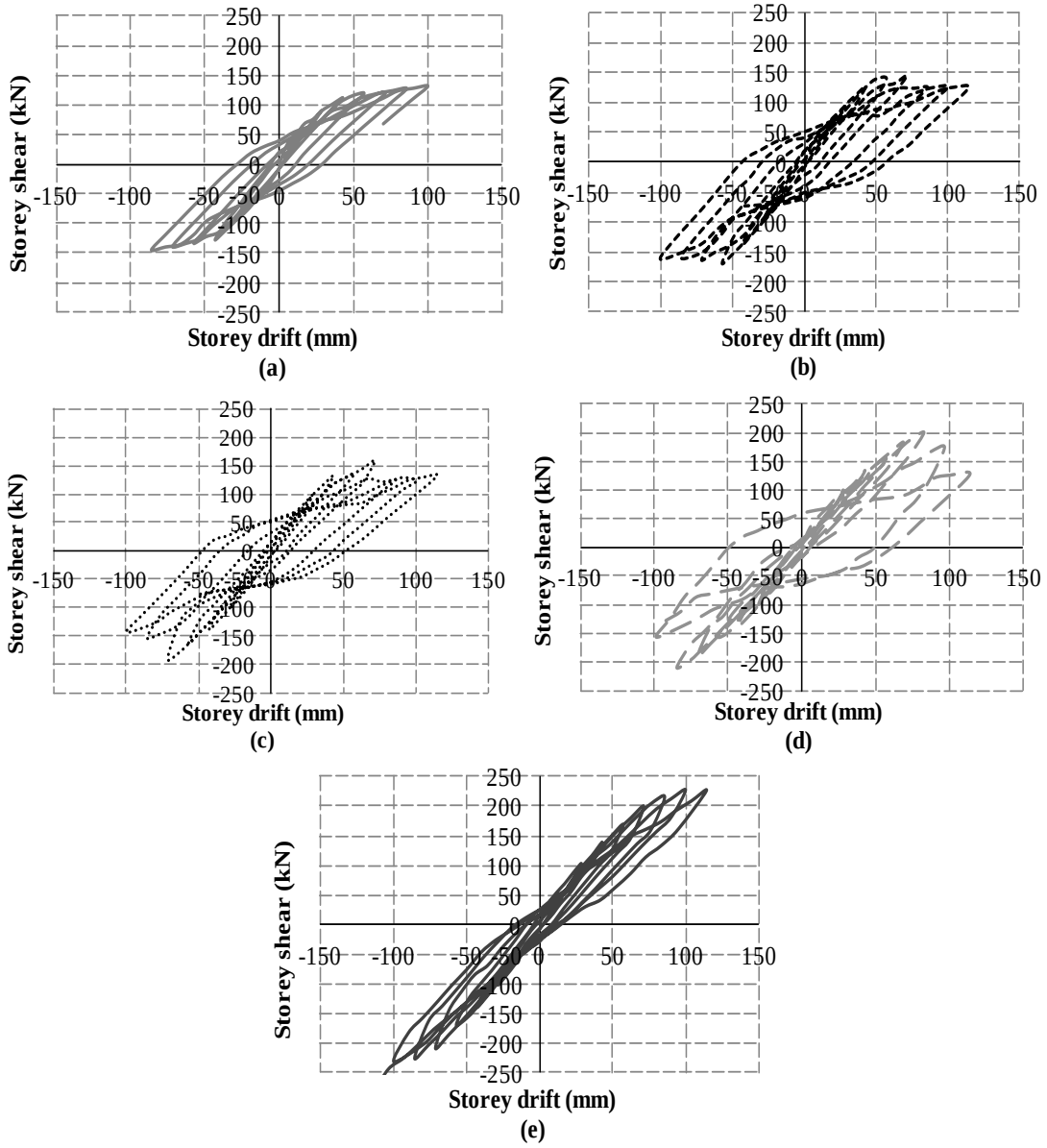


Figure 6.58: Storey shear-drift curve for Case Study 3(b) joints with $SI = 100\%$ and (a) $V_f = 0\%$, (b) $V_f = 1\%$, (c) $V_f = 1.5\%$, (d) $V_f = 2\%$ and (e) $V_f = 2.5\%$

V_f (%)	N_c	V_y (kN)	Δ_y (mm)	V_{max} (kN)	Δ_{Vmax} (mm)	V_u (kN)	Δ_u (mm)	$\mu = \frac{\Delta_u}{\Delta_y}$	$\frac{V_{max}}{V_y}$
CJ	8.82	92.4	28.8	143.1	84.3	124.2	140.8	4.90	1.55
0	5.60	89.9	28.6	131.2	100	131	100.1	3.50	1.46
1	6.84	93.6	28.6	146.1	71.6	132	114.2	4.00	1.56
1.5	6.86	96.5	28.1	158.3	71.6	132	114.4	4.07	1.64
2	6.98	98.53	28.1	187.8	73.9	128	114.4	4.07	1.91
2.5	8.30	99.25	27.5	214.9	85.9	225.3	114.5	4.16	2.13

Table 6.14: Result summary from storey shear-drift curve for Case Study 3(b) joints with $SI = 100\%$

6.5.2 Strength

In general, the figures show that the addition of steel fibres enhanced the strength of the SFRC joints. In comparison to the strength of the control joint, V_{max} increased by up to 53% (for joints with single stirrups), 43% (for joints with $SI = 50\%$) and 58% (for joints with $SI = 100\%$). The increase in V_y was up to 10% on average. For joints with single stirrups and joints with $SI = 50\%$ and 100% the original strength level of the control specimen is restored when fibres are provided at $V_f = 1\%$.

6.5.3 Ductility

The figures and tables data shows that the ductility ratio (μ) of the SFRC joints improves with the addition of fibres. However, the increase observed was only up to a certain (i.e. optimum) fibre volume fraction beyond which less ductile behaviour occurred. For instance in the joints with single stirrups the highest ductility increase was observed when fibres were added at $V_f = 1\% \sim 1.5\%$. Similarly, the optimum fibre contents were found to be at $V_f = 1\%$ for both joints with $SI = 50\%$ and 100%.

To study the structural response further, the FE-based principal strain contours and vectors taken at deflection levels of Δ_y, Δ_{max} and Δ_u are presented in Figures 6.59, 6.60 and 6.61, respectively. The samples were taken for the joints with $SI = 50\%$ at varying fibre content fractions (i.e. $V_f = 0\%, 1\%$ and 2%).

The principal strains distribution depicted in Figure 6.59 is taken in the first cycle at yield (i.e. $\Delta_y = 28.6$ mm). In order to observe crack patterns, the contour range was selected to coincide with the cracking tensile strain (i.e. 0.00024, see point A in Figure 6.51 and Table 6.11) and the ultimate compressive strain (i.e. -0.0035). Thus the areas highlighted in grey on the contours denote crack initiation. Principal strain vectors are also presented in the figures and they are also useful in indicating the pattern of crack formation. It can be seen that the principal strain for the joint with no fibres is the highest amongst all, while the strain has reduced as fibres amounts are increased indicating that crack control has been provided.

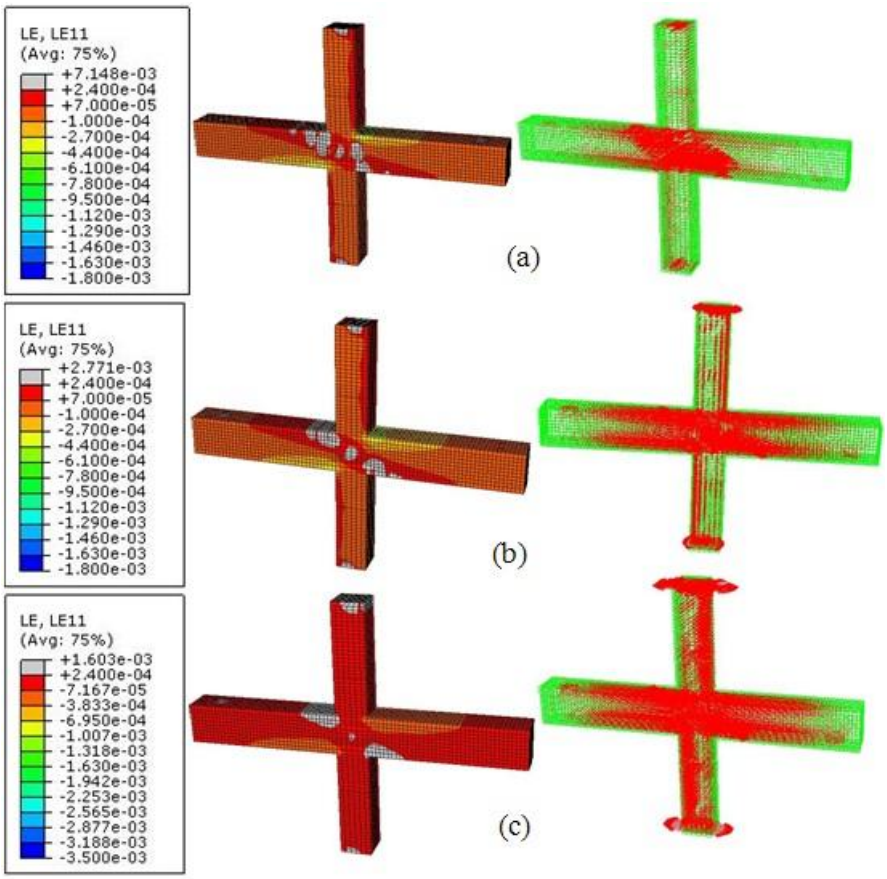


Figure 6.59: Principal strain contour and vectors for joints with $SI = 50\%$ and (a) $V_f = 0\%$, (b) $V_f = 1\%$, (c) $V_f = 2\%$ taken from storey drift at Δ_y= 28.6 mm

Figure 6.60 shows the distribution of the principal strains and vectors at the deflection associated with the maximum load sustained during the loading cycles (i.e. Δ_{max}= 69.4 mm). Again, it can bee seen that the crack formation is limited with $V_f = 2\%$ as compared to the results of specimens with less amounts of fibre. It should be noted that the grey area now is defined to highlight tensile strains higher than 0.002 for specimen without fibres (which is the ultimate tensile strain for plain concrete, see point B_0 in Figure 6.51), while for SFRC joints the grey area indicate regions with strain exceeding 0.01 which is about half the ultimate strain of SFRC. Also, the principal strain vectors were defined corresponded to its respective principal strain contours. Thus, the contours and vectors indicate that the crack opening has been controlled better as fibres content is increased. Extensive cracking at the ends of the beams can be seen for the joint without fibres (i.e. $V_f = 0\%$). Furthermore, the figures also show that the strains for the joint with $V_f = 2\%$ are lower than those for other joints with less or no fibres, confirming the role of steel fibres in controlling crack opening.

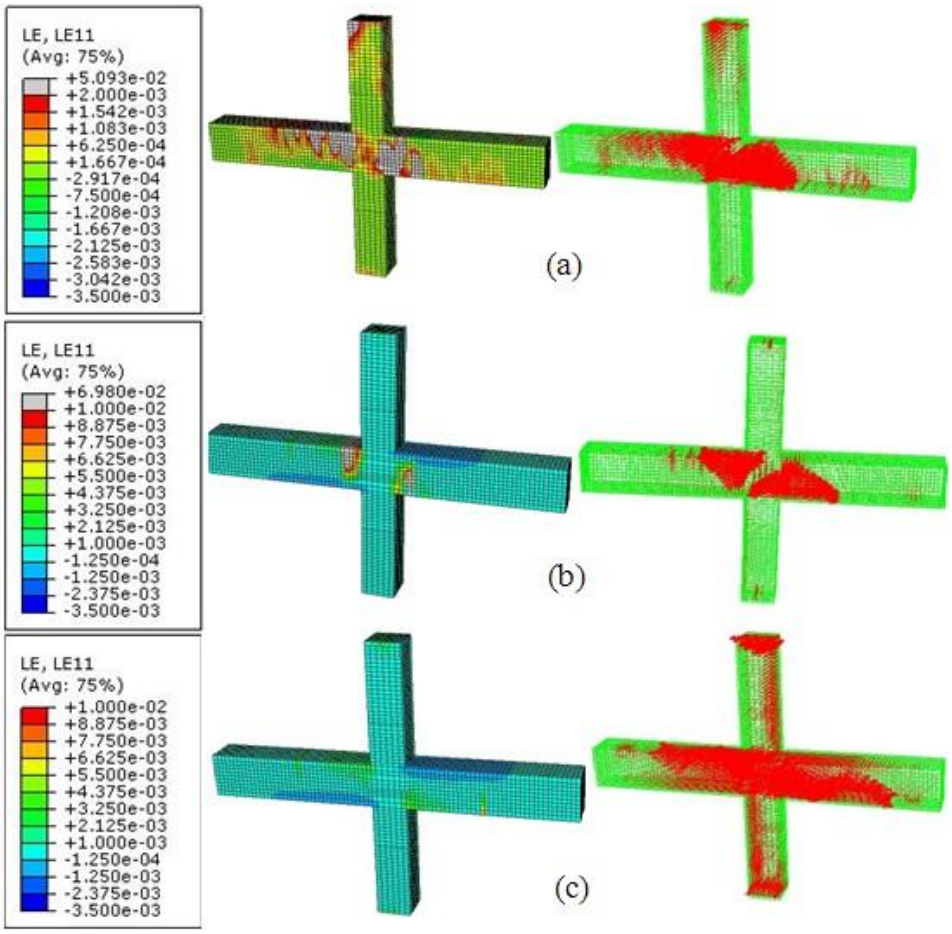


Figure 6.60: Principal strain contour and vectors for joints with $SI = 50\%$ and (a) $V_f = 0\%$, (b) $V_f = 1\%$, (c) $V_f = 2\%$ taken at Δ_{max}= 69.4 mm

The strain distribution and vectors at the point of failure (i.e. ultimate deflection Δ_u= 100.2 mm) are presented in Figure 6.61. It should be noted that the grey area now is defined to highlight tensile strains higher than 0.02, which is the ultimate tensile strain for SFRC associated with pull-out fibre (see point D in Figure 6.51). Thus, the contours and vectors indicate that the crack opening has been controlled better as fibres content is increased and that pull-out failure occurred in limited zones of the SFRC joints (compared to an extensive grey area on the joint without fibres showing that the latter experienced wider crack opening). It is interesting to see that for SFRC, pull-out failure occurred in limited zones at the ends of the beams.

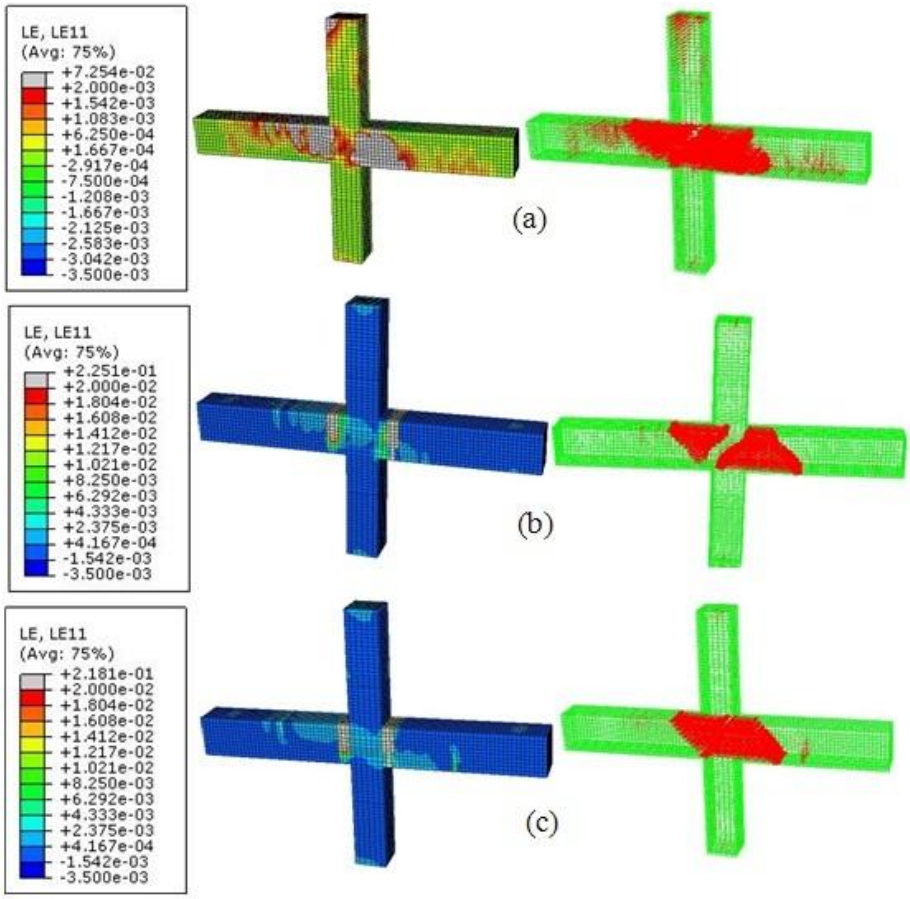


Figure 6.61: Principal strain contours and vectors for joints with $SI = 50\%$ and (a) $V_f = 0\%$, (b) $V_f = 1\%$, (c) $V_f = 2\%$ taken at $\Delta_u = 100.2$ mm

6.5.4 Cracking pattern

This section presents the principal stress and strain contours and vectors taken at failure for all joints to study the cracking pattern of the joints. In addition, the deflected shapes of the joints at failure are also discussed in this section.

6.5.4.1 Principal stress contours

The principal stress contours at failure for joints with single stirrups, $SI = 50\%$ and $SI = 100\%$ are depicted in Figures 6.62, 6.63 and 6.64, respectively. The data include all the fibre volume fractions investigated, i.e. $V_f = 0\%$, 1%, 1.5%, 2% and 2.5%. To understand the state of tensile stresses at failure, the contour intervals were selected so that the stress values exceeding the tensile strength of plain concrete (i.e. 4.8 MPa, see point A in Figure 6.51 and Table 6.11) are depicted in grey for specimens without fibres (i.e. $V_f = 0\%$). For those exhibiting strain-softening trend, i.e. V_f =1% and 1.5%, the

grey zone threshold values are 2.5 MPa and 3.75 MPa, respectively. For SFRC specimens exhibiting strain-hardening, the grey zones denote areas where the tensile stresses exceed 5 MPa and 6.25 MPa for joints with V_f =2% and 2.5%, respectively. These peaks were adopted from point B in Figure 6.51 and Table 6.11. Similarly, to understand the state of compressive stresses at failure, the contours were arranged so that the stress values exceeding the ultimate compressive strength of plain concrete, i.e. -46 MPa, are highlighted in black. The contours indicate that high stresses occur at the end of the beams adjoining the column. The strain (rather than stress) distribution is usually adopted to indicate tensile or compressive failure and is discussed next.

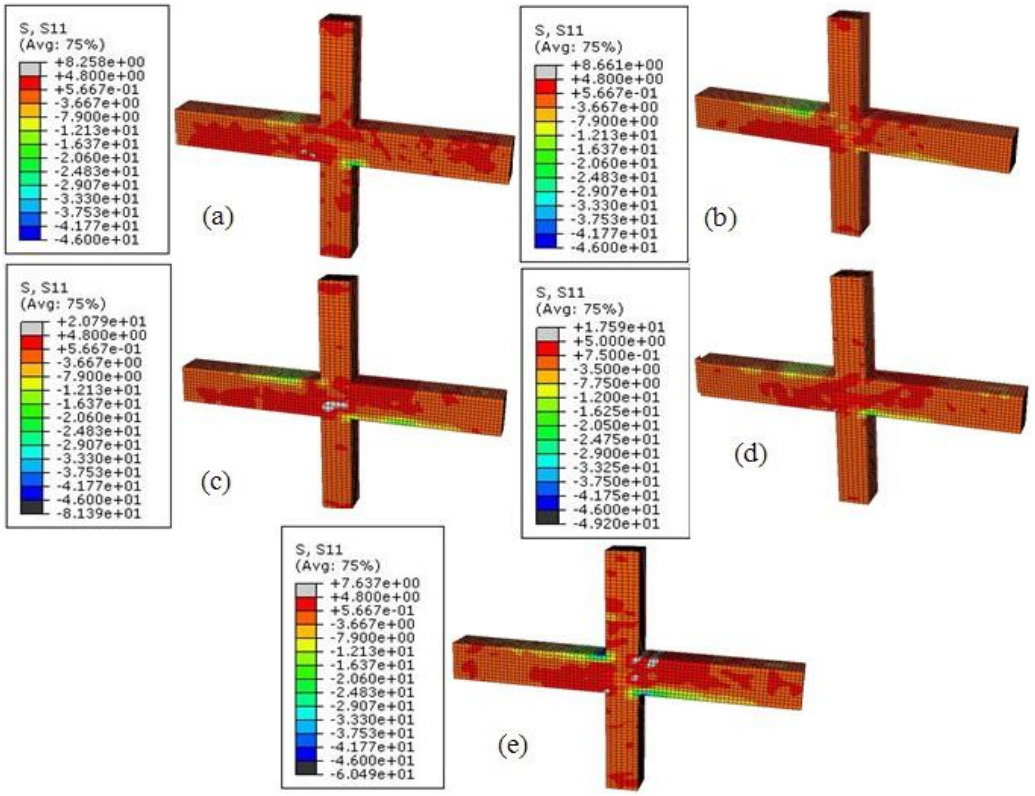


Figure 6.62: Principal stress contours for Case Study 3(b) joints with single stirrups and (a) $V_f = 0\%$, (b) $V_f = 1\%$, (c) $V_f = 1.5\%$, (d) $V_f = 2\%$ and (e) $V_f = 2.5\%$

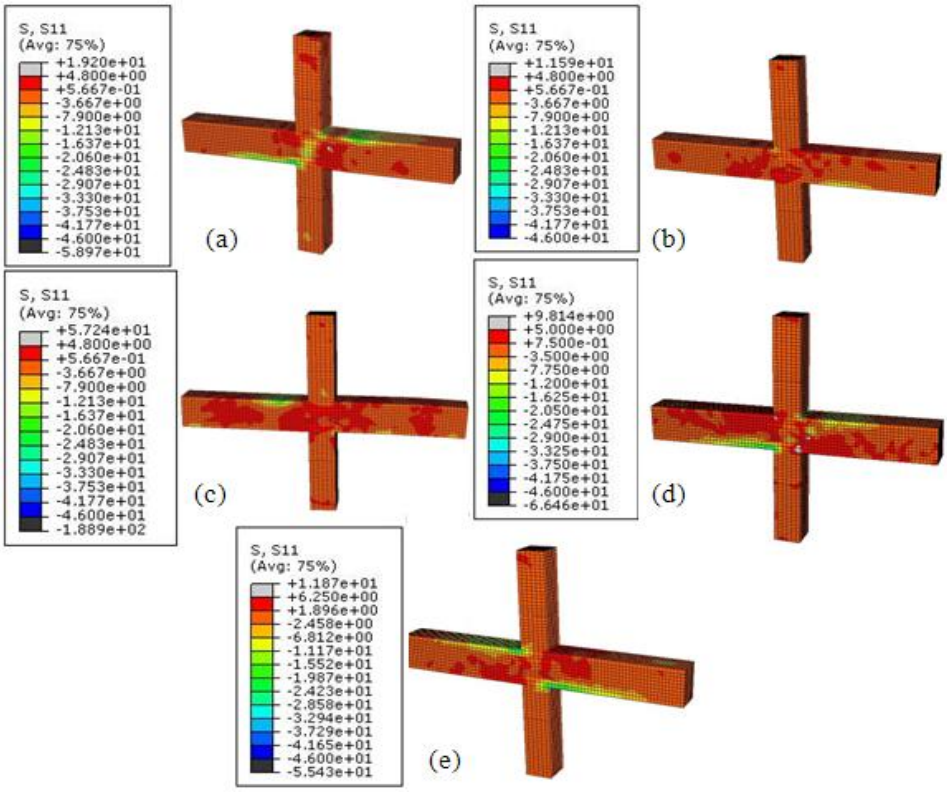


Figure 6.63: Principal stress contours for Case Study 3(b) joints with $SI = 50\%$ and (a) $V_f = 0\%$, (b) $V_f = 1\%$, (c) $V_f = 1.5\%$, (d) $V_f = 2\%$ and (e) $V_f = 2.5\%$

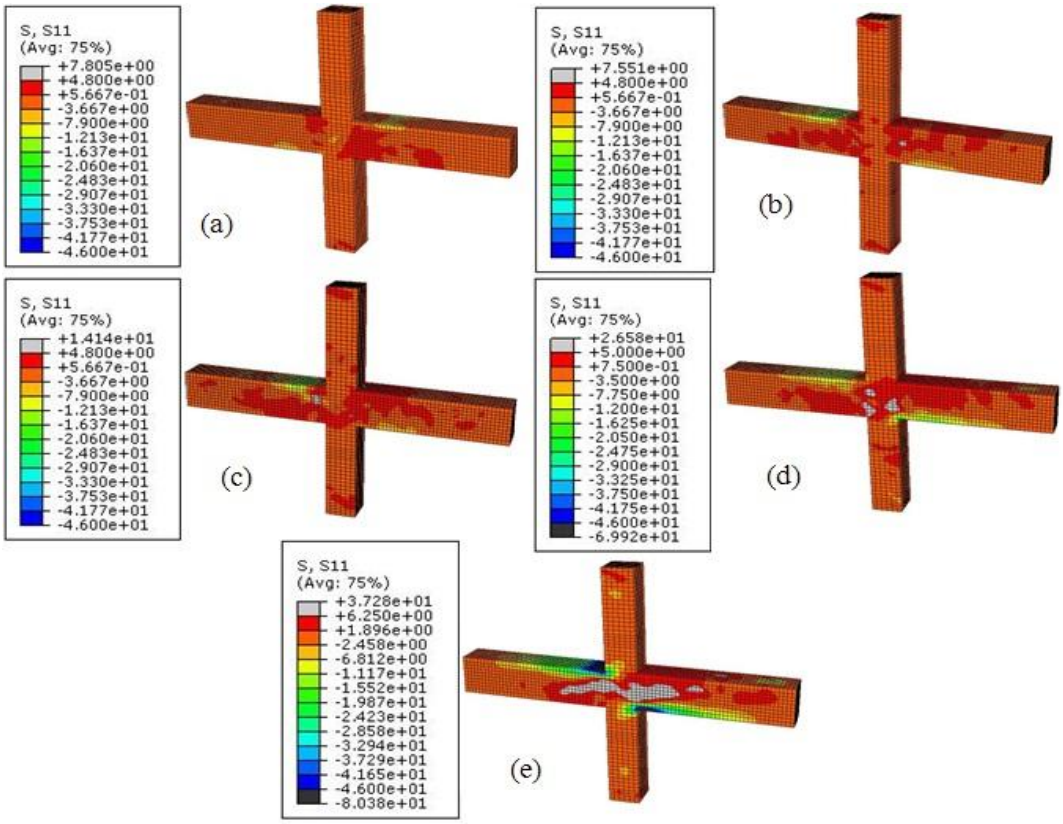


Figure 6.64: Principal stress contours for Case Study 3(b) joints with $SI = 100\%$ and (a) $V_f = 0\%$, (b) $V_f = 1\%$, (c) $V_f = 1.5\%$, (d) $V_f = 2\%$ and (e) $V_f = 2.5\%$

6.5.4.2 Principal strain contours

The FE-based principal strain contours at failure for all joints modelled are presented in Figures 6.65 to 6.67. The contours intervals were selected so that the strains exceeding the ultimate tensile strength of SFRC of 0.02 (see point D in Figure 6.51) were highlighted in grey, indicating pull-out failure. Similarly, strains higher than the ultimate compressive strain of -0.0035 were highlighted in black.

The contours indicate that for SFRC joints the zones suffering tensile failure (i.e. fibre pull-out failure) occurred in limited zones of the SFRC joints (compared to an extensive grey area on the joint without fibres – i.e. Part (a) of Figures 6.65, 6.66 and 6.67 – showing that the latter experienced wider crack opening). It is interesting to see that pull-out failure occurred at the ends of the beams and not within the column or joint itself. This indicates that plastic hinges formed at the end of the beams as desired in seismic design (i.e. strong column-weak beam philosophy, discussed in Chapter 3).

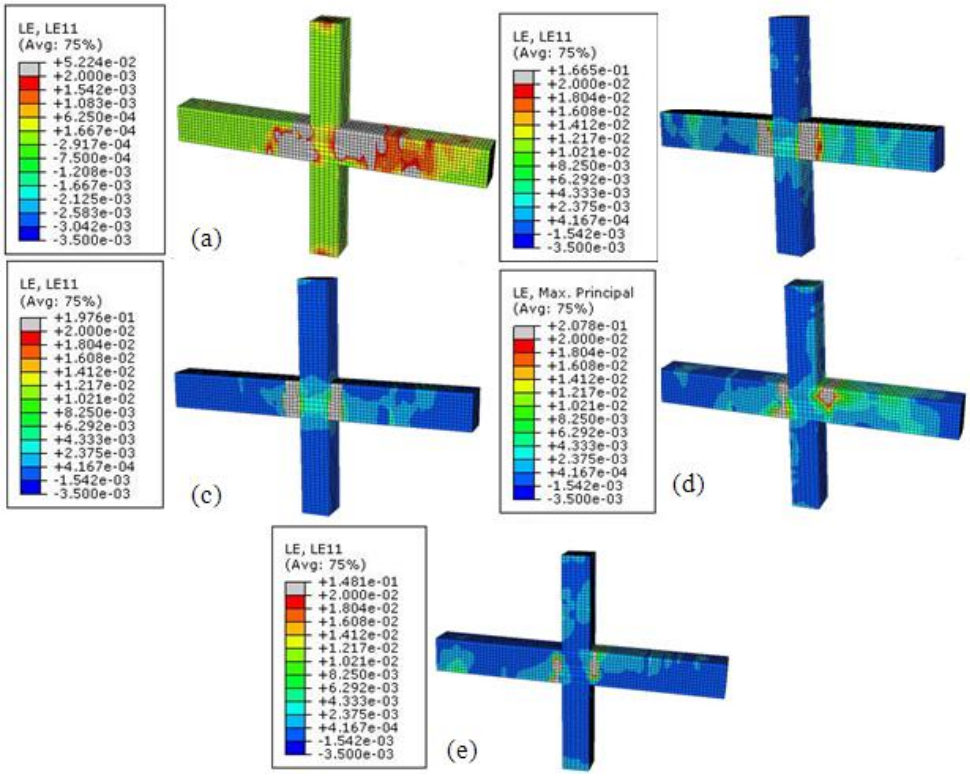


Figure 6.65: Principal strain contours for Case Study 3(b) joints with single stirrups and (a) $V_f = 0\%$, (b) $V_f = 1\%$, (c) $V_f = 1.5\%$, (d) $V_f = 2\%$ and (e) $V_f = 2.5\%$

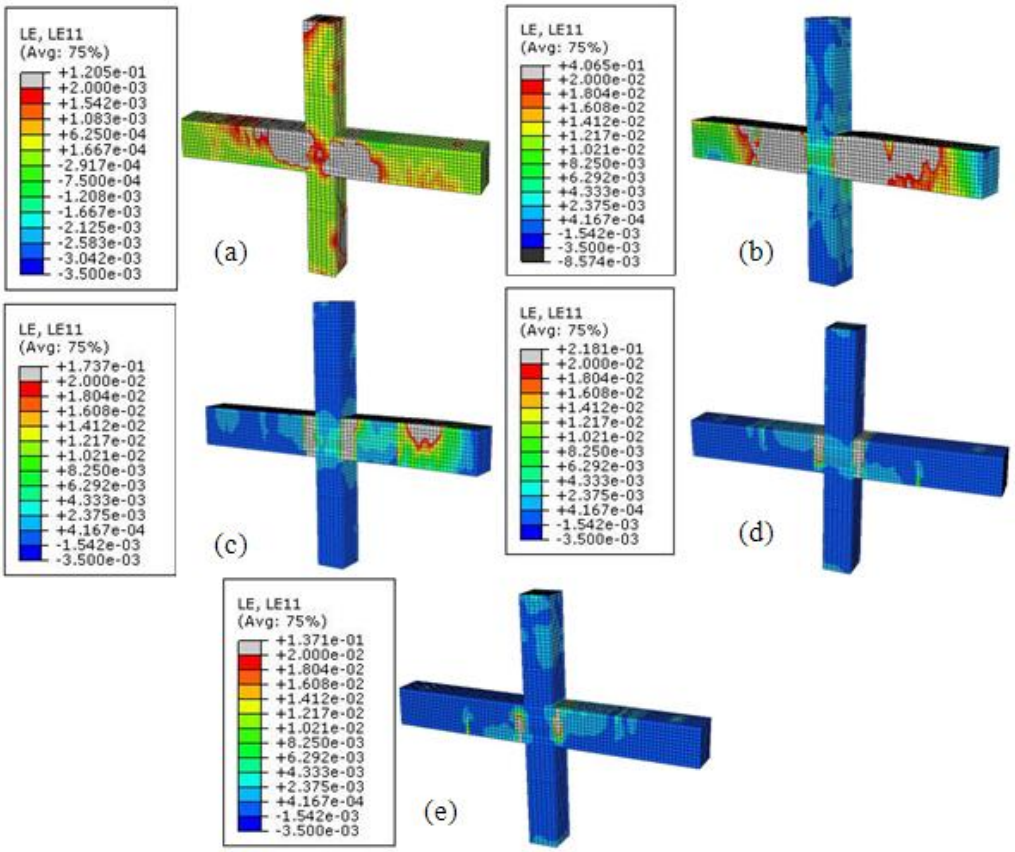


Figure 6.66: Principal strain contours for Case Study 3(b) joints with $SI = 50\%$ and (a) $V_f = 0\%$, (b) $V_f = 1\%$, (c) $V_f = 1.5\%$, (d) $V_f = 2\%$ and (e) $V_f = 2.5\%$

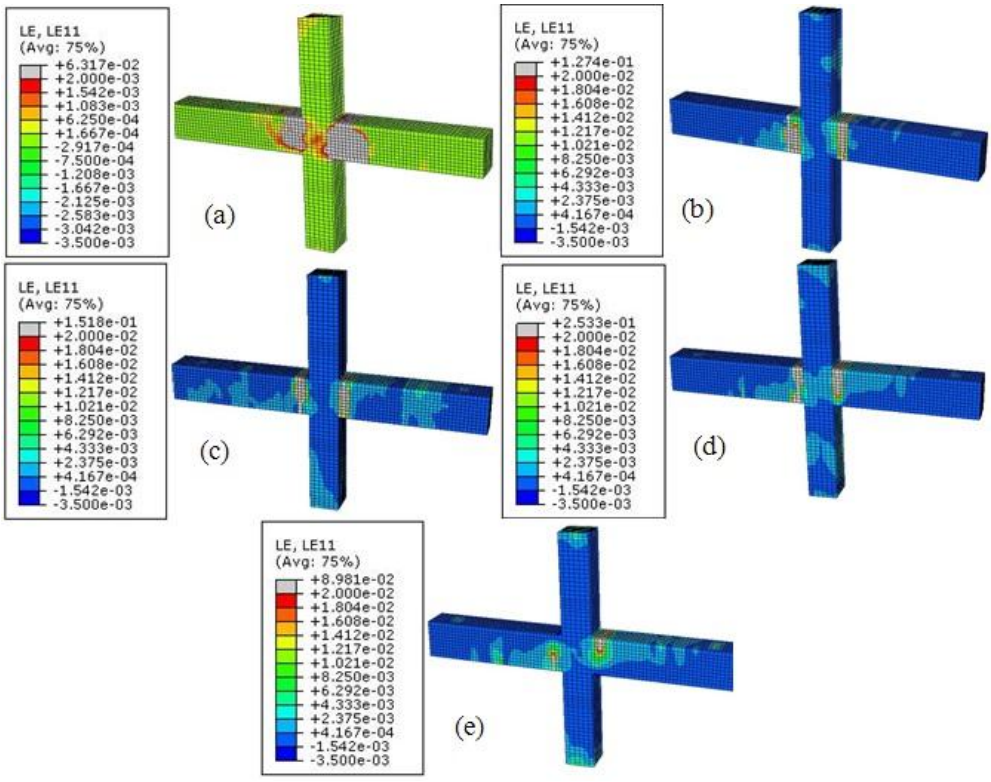


Figure 6.67: Principal strain contours for Case Study 3(b) joints with $SI = 100\%$ and (a) $V_f = 0\%$, (b) $V_f = 1\%$, (c) $V_f = 1.5\%$, (d) $V_f = 2\%$ and (e) $V_f = 2.5\%$

6.5.4.3 Principal strain vectors

Principal strain vectors at failure for all the joints are illustrated in Figures 6.68 to 6.70, which provide further indication of crack formation patterns. The graphs show that the increase in fibre content led to a reduction in the intensity of the strain vectors, which indicates that the addition of fibres resulted in better crack control.

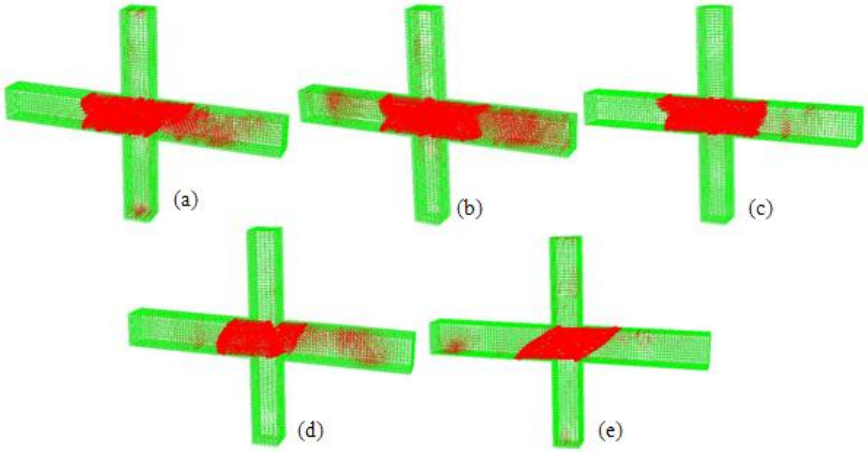


Figure 6.68: Principal strain vectors for Case Study 3(b) joints with single stirrups and (a) $V_f = 0\%$, (b) $V_f = 1\%$, (c) $V_f = 1.5\%$, (d) $V_f = 2\%$ and (e) $V_f = 2.5\%$

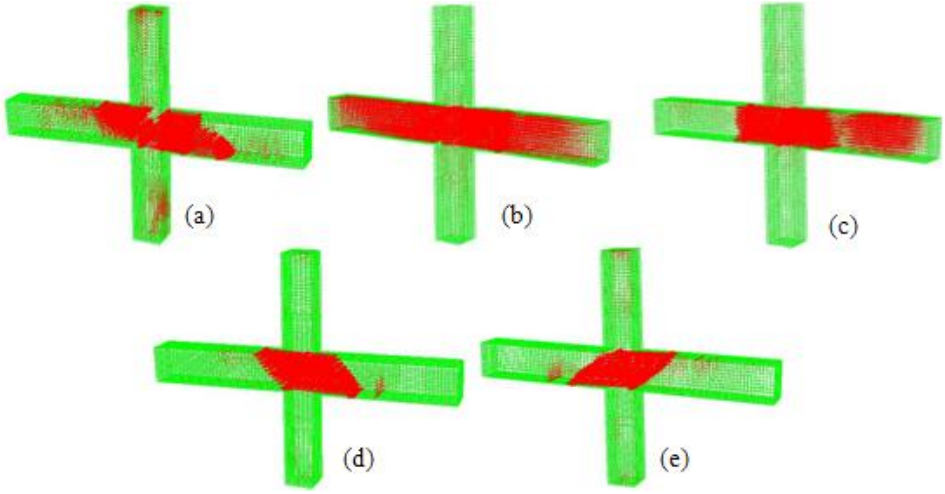


Figure 6.69: Principal strain vectors for Case Study 3(b) joints with $SI = 50\%$ and (a) $V_f = 0\%$, (b) $V_f = 1\%$, (c) $V_f = 1.5\%$, (d) $V_f = 2\%$ and (e) $V_f = 2.5\%$

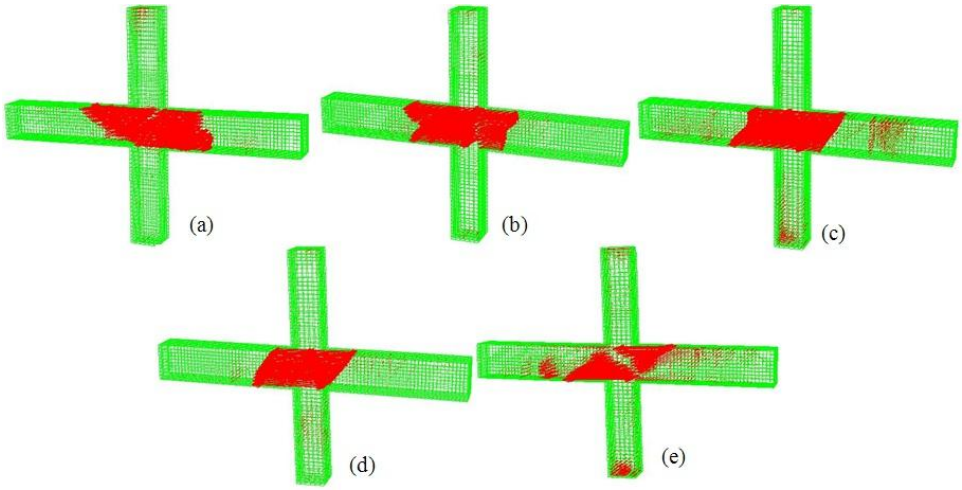


Figure 6.70: Principal strain vectors for Case Study 3(b) joints with $SI = 100\%$ and (a) $V_f = 0\%$, (b) $V_f = 1\%$, (c) $V_f = 1.5\%$, (d) $V_f = 2\%$ and (e) $V_f = 2.5\%$

6.5.4.4 Deflected shapes

The deformations of the interior beam-column joints modelled in Case Study 3(b) at failure are depicted schematically in Figures 6.71 to 6.73. The diagrams show both downward and upward deflections (the latter associated with a reversed load cycle). The deformations are consistent with the cracking patterns discussed earlier shown from principal strain contours and vectors.

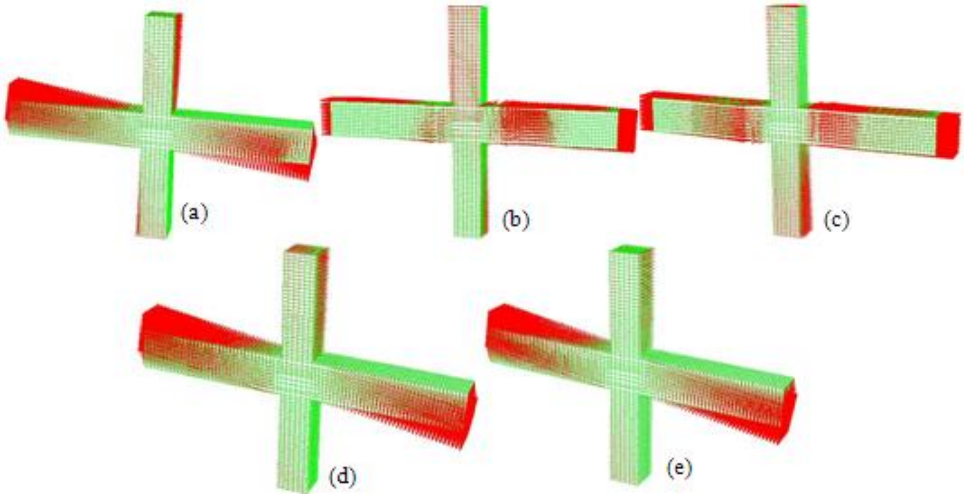


Figure 6.71: Deflected shapes for Case Study 3(b) joints with single stirrups and (a) $V_f = 0\%$, (b) $V_f = 1\%$, (c) $V_f = 1.5\%$, (d) $V_f = 2\%$ and (e) $V_f = 2.5\%$

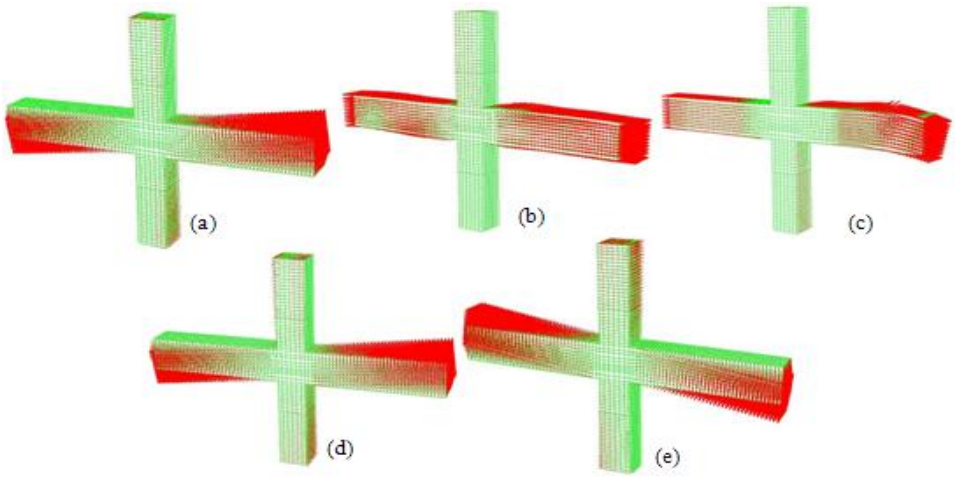


Figure 6.72: Deflected shapes for Case Study 3(b) joints with $SI = 50\%$ and (a) $V_f = 0\%$, (b) $V_f = 1\%$, (c) $V_f = 1.5\%$, (d) $V_f = 2\%$ and (e) $V_f = 2.5\%$

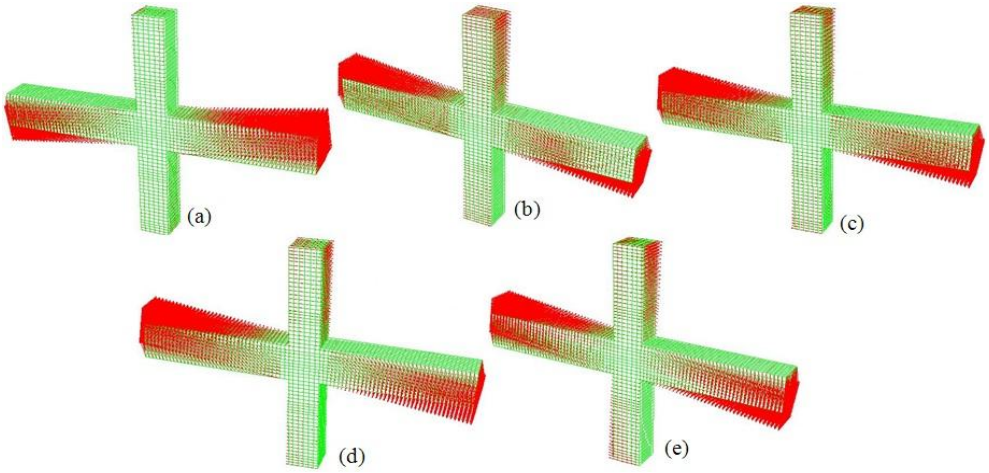


Figure 6.73: Deflected shapes for Case Study 3(b) joints with $SI = 100\%$ and (a) $V_f = 0\%$, (b) $V_f = 1\%$, (c) $V_f = 1.5\%$, (d) $V_f = 2\%$ and (e) $V_f = 2.5\%$

6.5.5 Comparative study with control specimen using non-dimensional ratios

In this section, an overall comparison is made between the control joint specimen (i.e. the one with no fibres and full conventional shear reinforcement) and the SFRC joints with fibres added to compensate for reduced transverse reinforcement (i.e. by either increasing stirrups spacing or providing single stirrups instead of double ones). The values of key structural performance indicators such as the strength, ductility, energy absorption and number of cycles were normalised by dividing them by the corresponding values of the control specimen. In this manner, overall conclusions were made on the potential of fibres to replace some of the conventional reinforcement (and thus help lessen congestion of the latter) and the fibre amounts required to achieve that.

6.5.5.1 Strength ratio

Figure 6.74 depicts the ratio of the maximum storey shear of a joint (V_{max}) to the corresponding value of the control joint specimen ($V_{max,o}$), plotted against steel fibre volume fraction. The graphs confirm the potential for fibres to enhance the strength of interior beam-column joints. The strength level of the control specimen was restored when fibres were added at $V_f = 0.5\%$ for both joints with single stirrups and those with $SI = 50\%$ and at $V_f = 1\%$ for joints with $SI = 100\%$. Further enhancements were achieved (exceeding control specimen level by ~50%) with higher fibre dosages.

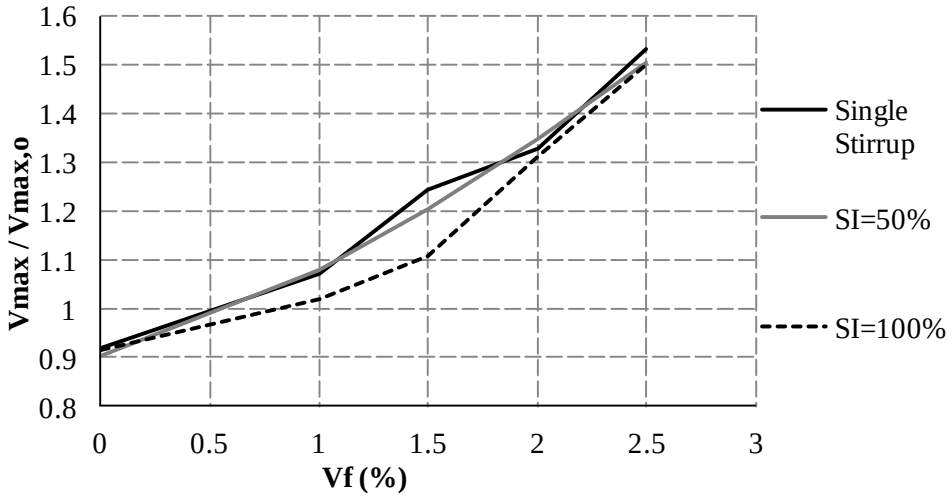


Figure 6.74: Ratio of maximum storey shear to that of the control joint versus fibre volume fraction graph for Case Study 3(b)

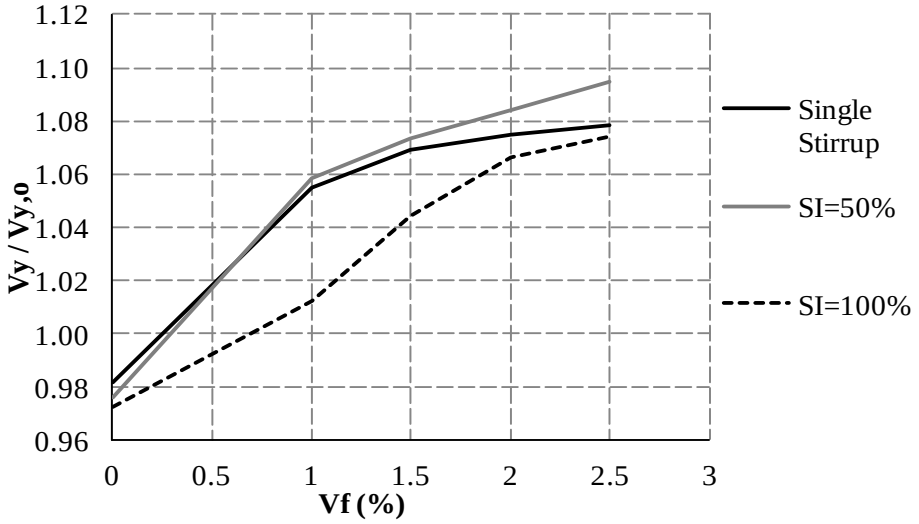


Figure 6.75: Ratio of storey shear at yield to that of the control joint versus fibre volume fraction graph for Case Study 3(b)

Similarly results for normalised yield loads (i.e. $V_y / V_{y,o}$) were obtained as illustrated in Figure 6.75. Again it is clear that fibres enhance the yield load value and are capable of restoring the initial levels associated with the control specimen.

6.5.5.2 Ductility ratio

Figure 6.76 presents the ductility ratio values (normalised by dividing by the corresponding ductility ratios of the control specimen) for the interior joint Case Study 3(b). It can be seen from the graphs that the addition of fibres improves ductility to a certain level beyond which additional fibres lead to less rather than more ductility. This is a finding that has been realised earlier when examining the interior joint of Case Study 3(a). The optimum fibre volume fraction was found to be $V_f = 1\%$ for all joints. The ductility level of the control specimen (i.e. the one with full conventional transverse reinforcement and no fibres) was restored for both joints with single stirrups and those with $SI = 50\%$ (with the control specimen level actually exceeded by ~10%).

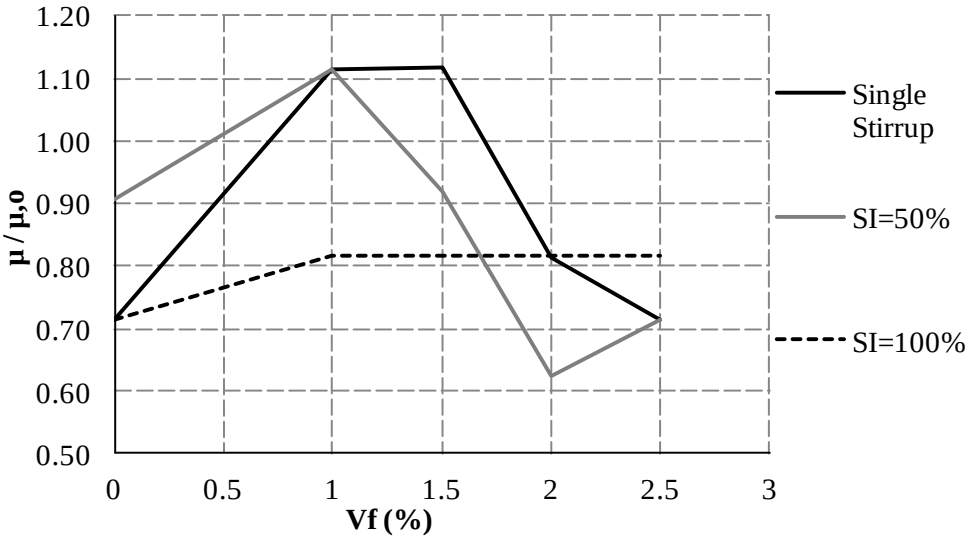


Figure 6.76: Ratio between the ductility ratio of each joint and that of the control joint versus fibre volume fraction for Case Study 3(b)

However, the ductility level of the control specimen could not be restored for the joint with $SI = 100\%$, even when fibres were provided at dosages as high as $V_f = 2.5\%$ (only about 80% of the control specimen ductility level was restored). This indicates the severity of conventional steel reduction in this case where the spacing between the stirrups has been doubled. This is also shows that, from a ductility performance viewpoint, this case is worse than using single stirrups (instead of double ones, see

Figure 6.36c) as a way of reducing transverse reinforcement congestion. The double-stirrups arrangement is usually provided to enhance confinement. This shows that fibres can provide sufficient confinement to allow the use of single stirrups. On the other hand, the loss in confinement due to doubling the spacing of stirrups is too severe to be restored using fibres.

As ductility is an important consideration in seismic design, therefore it can be concluded that the steel congestion can be best alleviated by using single stirrups coupled with fibres added in optimum quantities.

6.5.5.3 Energy absorption ratio

The energy absorption capacity calculated for the interior beam-column joints (E_a) was normalised by the energy absorption of the control joint ($E_{a,0}$) and presented in Figure 6.77. The optimum fibre contents were found to be $V_f = 1.5\%$ for joints with single stirrups and $V_f = 1\%$ for both joints with $SI = 50\%$ and 100%. The energy absorption level of the control specimen was restored for all joints except the ones with $SI = 100\%$, suggesting that this high increase in stirrup spacing is too extreme and cannot be resolved by adding steel fibres. These are important findings, particularly since energy absorption is a key mechanism in the seismic response of structures.

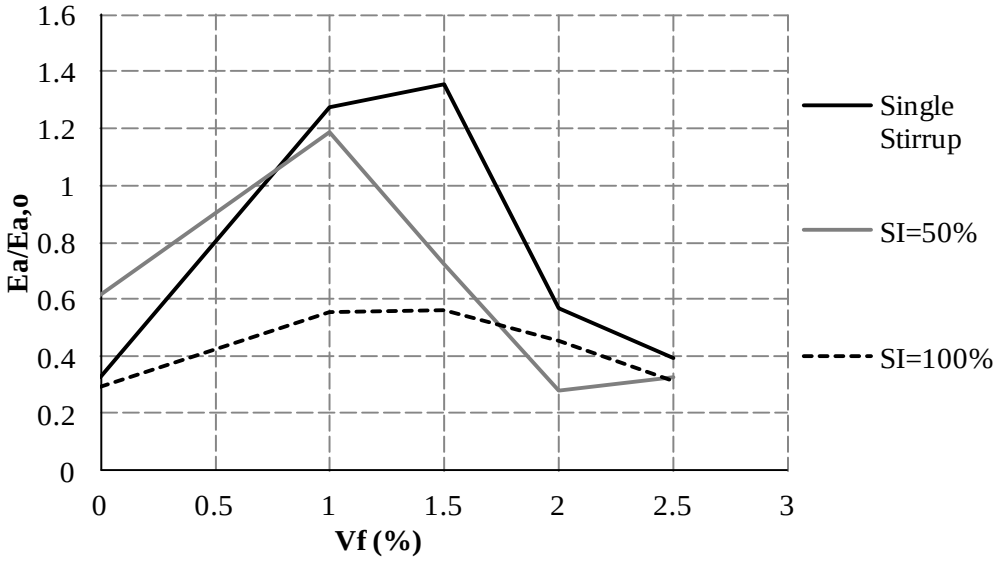


Figure 6.77: Ratio between the energy absorption of each joint and that of the control joint versus fibre volume fraction for Case Study 3(b)

6.5.5.4 Number of cycles

The ductility and energy absorption trends discussed earlier were confirmed by examining the normalised ratio of the maximum number of cycles (i.e. $N_c/N_{c,0}$) obtained as depicted in Figure 6.78. Therefore, similar conclusions can be made with regards to optimum fibre contents required to restore the control specimen performance and the severity of the case with doubling the stirrups spacing (i.e. $SI = 100\%$).

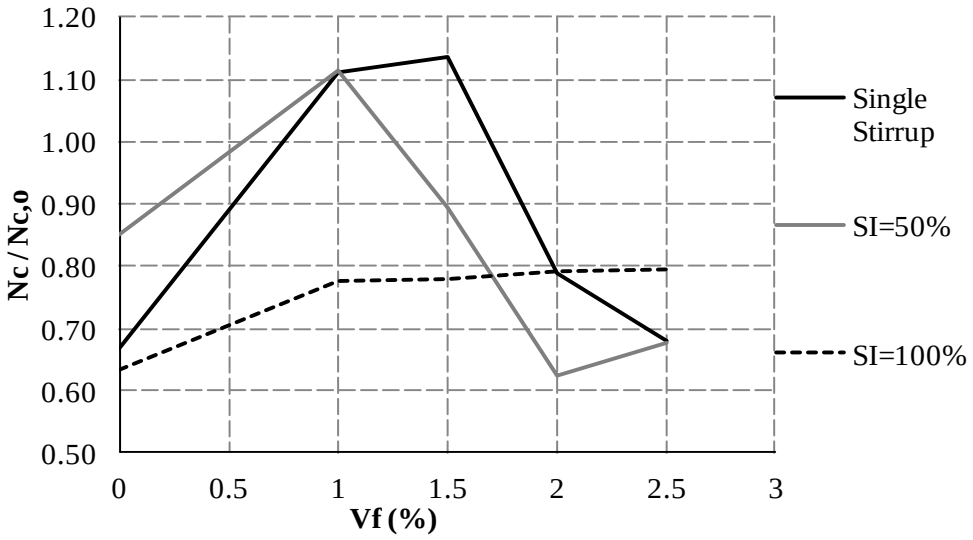


Figure 6.78: Ratio between the maximum number of cycles of each joint and that of the control joint versus fibre volume fraction for Case Study 3(b)

6.6 Conclusions

Two types of beam-column joints, namely exterior and interior joints, were investigated under reversed-cyclic loading (which is the key feature of seismic action). To achieve this, two case studies – one representing each joint type – were selected. Initially, the predictions of non-linear FE analysis were calibrated using existing experimental data to ascertain the accuracy of the numerical results. Once reasonable agreement between the experimental and numerical results was achieved, full parametric studies were carried out to examine the potential for steel fibres to compensate for a reduction in conventional transverse reinforcement (suggested to lessen congestion of such reinforcement, especially in seismic design). Key structural response indicators such as strength, cracking, ductility and energy absorption were studied. A comparative study was carried out between the responses of SFRC joints and the corresponding ones for

the control joint specimen (i.e. the one with full conventional transverse reinforcement and no fibres). Based on the results of these investigations, the following conclusions and recommendation are made:

- Fibres were also effective in controlling crack propagation. Pull-out failure was found to be at the ends of the beams adjoining the columns (and not within the columns or joint itself), which indicates that plastic hinges will form at these locations. This is useful for seismic design as the joint is detailed so that the plastic hinges form at these locations (i.e. strong column-weak beam arrangement related to capacity design concept, as discussed in Chapter 3).
- Addition of steel fibres to the structures improves the strength with the latter increasing consistently as the amount of fibres is increased.
- The addition of fibres in *optimum* amounts will lead to significant enhancement to ductility. This is of particular relevance to seismic design as ductility is one of the main considerations to ensure sufficient energy dissipation (energy absorption was also studied and the results were consistent with ductility findings). Nevertheless, fibres should not be provided in excess of the optimum amounts as this will lead to a less-ductile response. This can be explained by noting that as the fibre content is increased, the beam becomes stiffer and deflects less (this largely due to the fibres role in bridging across cracks and limiting their opening). This is similar to the "over-reinforced" brittle response associated with concrete members reinforced with excessive amounts of conventional reinforcement.
- For exterior joints, the optimum fibre dosages to enhance ductility were found to be $V_f = 2\%$ for both joints with $SI = 50\%$ and $SI = 100\%$ (with ductility achieved being double that associated with the control joint). The ductility level of the control specimen was restored with fibres added at $V_f = 1.5\%$.
- For interior joints, the ductility level of the control specimen was restored for both joints with single stirrups and those with $SI = 50\%$ when fibres were added with $V_f = 1\%$. However, the ductility level of the control specimen could not restored for the joint with $SI = 100\%$, even when fibres were provided at dosages as high as $V_f = 2.5\%$. This indicates the severity of conventional steel reduction in this case where the spacing between the stirrups has been doubled. This is also shows that, this arrangement is worse than using single stirrups

(instead of double ones, see Figure 6.36c) as a way of reducing transverse reinforcement congestion. The double-stirrups arrangement is usually provided to enhance confinement. This shows that fibres can provide sufficient confinement to allow the use of single stirrups. However the loss in confinement due to doubling the spacing of stirrups is too severe to be restored using fibres.

- A similar trend to that associated with ductility and energy absorption was found when the maximum number of cycles obtained was considered.

In summary, it can be concluded that fibres provided in optimum amounts have the potential to replace some of the conventional transverse reinforcement and thus allow for a relaxation in steel congestion often experienced in seismic detailing of beam-column joints.

CHAPTER 7

RECOMMENDATIONS FOR DESIGN

7.1 Introduction

This chapter presents selected results obtained from Case Studies 1, 2 and 3 in 3D surface and 2D contour diagrams. The two key parameters selected to be discussed herein were the ductility ratio (μ) and the load-carrying capacity (P_{max}). These parameters were plotted in 3D surface diagrams against the stirrups content ratio (r_{sw}) and fibre volume fraction (V_f). This was intended to provide an enhanced visual representation of the trends associated with these important parameters. For convenience, the diagrams were also reproduced in a simpler 2D contour diagram version.

In the present research work, the reduction in conventional shear reinforcement was implemented by increasing the stirrups spacing (SI). Nevertheless, current design codes of practice such as Eurocode 2 (2004) express the equations for transverse reinforcement in terms of the ratio between the stirrups area (A_{sw}) and their spacing (S). Therefore, it is more convenient to express SI in terms of the ratio of the stirrups content (r_{sw}). The latter is defined as the ratio of the stirrups area and spacing (used in the parametric studies) normalised by the corresponding ratio at full shear reinforcement and no fibre content (denoted by a zero subscript), i.e. $r_{sw} = (A_{sw}/S)/(A_{sw}/S)_0$. Table 7.1 shows the relationship between the two parameters SI and r_{sw} for the values used in the present study.

SI (%)	Stirrups area (A_{sw})	r_{sw}
0	Full	1
50	Full	0.67
100	Full	0.5
200	Full	0.33
0	Half	0.5
∞	No stirrups	0

Table 7.1: Relationship between *SI* and r_{sw}

The 3D surface and 2D contour diagrams for the ductility ratio (μ) and load-carrying capacity (P_{max}) for every case study carried out in the current work are presented next.

7.2 Case Study 1: Simply-supported beams

Figures 7.1 to 7.3 present the 3D surface and 2D contour diagrams of μ and P_{max} obtained for Case Studies 1(a)-M, 1(a)-C and 1(b), respectively. From the 3D figures, it can be seen that the maximum values of μ occurs between $V_f = 1\%$ and $V_f = 2\%$. For instance, in Case Study 1(a)-M (see Figure 7.1(a)), there were two maxima: one at $r_{sw} = 1$ and $V_f = 1\%$, and the other at $r_{sw} = 0.67$ and $V_f = 2\%$. On the other hand, the P_{max} values show an upward trend as depicted in the Figures 7.1(c), 7.2(c) and 7.3(c), which indicates that the strength consistently increases as the ratio of both stirrups and fibres contents were increased. These trends were also visible in the respective 2D contour plots.

Based on the 2D contour diagram for Case Study 1(a)-M shown in Figures 7.1(b) and (d), it was found that $\mu = 7.5$ can be maintained from the point $r_{sw} = 1$ and $V_f = 0\%$ to $r_{sw} = 0.55$ and $V_f = 1.9\%$. A dashed straight line was added onto the figure to represent this potential design recommendation. Therefore, it can be concluded that adding steel fibres to the concrete mix at a volume fraction of 1.9% can substitute for a reduction of 45% in the conventional shear reinforcement and restore the original ductility level associated with full shear reinforcement and no fibres (i.e. control beam specimen). The dashed line is now

suggested as the proposed one for design purposes (henceforth this will be referred to as the proposed line) in the current work.

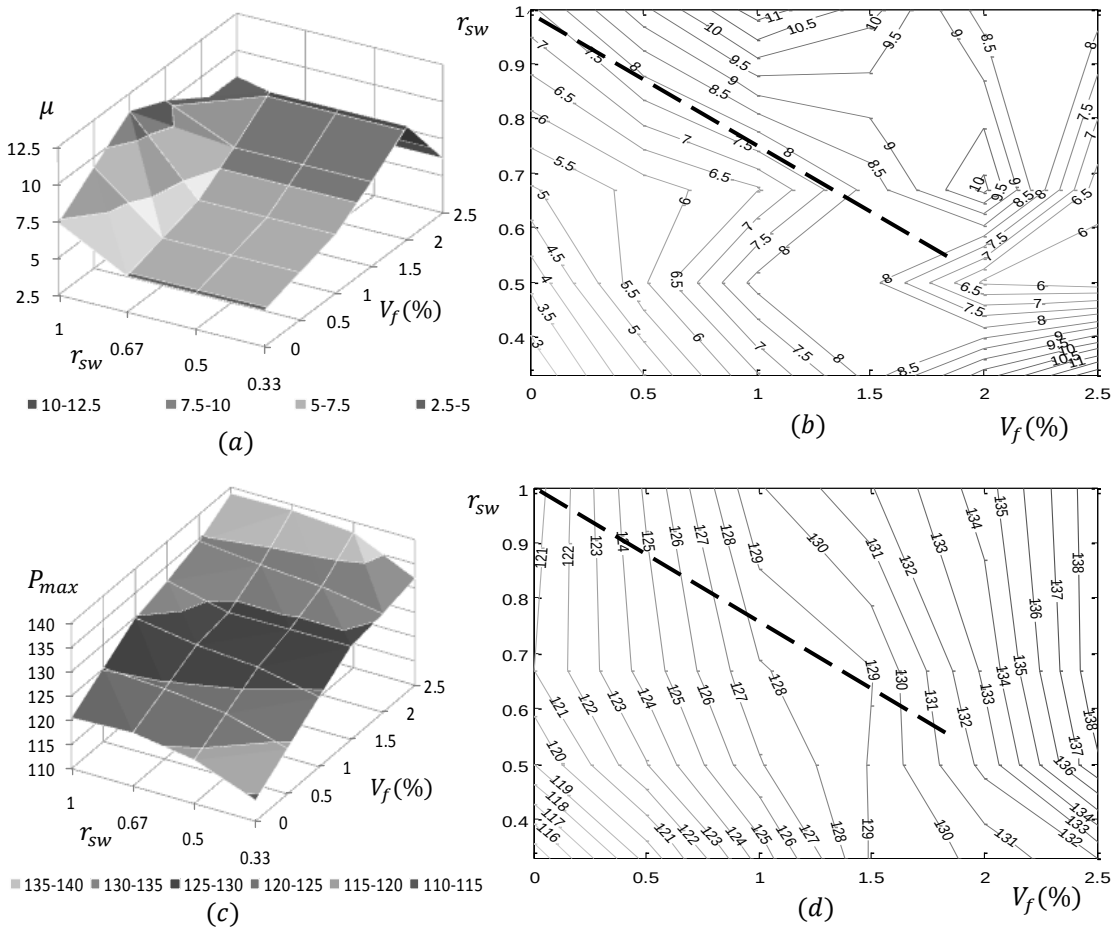


Figure 7.1: Ductility ratio (μ) in (a) 3D surface and (b) 2D contour diagrams; and Maximum load-carrying capacity (P_{max}) in (c) 3D surface and (d) 2D contour diagrams expressed in terms of r_{sw} and V_f for Case Study 1(a)-M

To ensure that the ductility values associated with the proposed line are achieved at acceptable strength levels, the same line (i.e. linking point $r_{sw} = 1$ and $V_f = 0\%$ to $r_{sw} = 0.55$ and $V_f = 1.9\%$) was also plotted on the 2D contours for P_{max} as depicted in Figure 7.1(d). It was found that P_{max} values along this dashed line were larger than those for the control beam specimen with full shear reinforcement and no fibres (i.e. $r_{sw} = 1$ and $V_f = 0\%$). Therefore, the substitution of reduced stirrups by adding steel fibres along this proposed line yields the same ductility level and a larger load-carrying capacity than that found in the control beam specimen. This confirms the potential for the proposed line to be

adopted as a design tool to determine the amount of fibres required to compensate for a given reduction in conventional transverse reinforcement.

Similalry, the line proposed in Figures 7.1(b) and (d) can also be adopted for Case Study 1(a)-C, which focused on simply-supported SFRC beams under reversed-cylcic loading, as illustrated in Figures 7.2(b) and (d). The 3D surface diagram presented in Figure 7.2(a) shows that the maximum μ value occurs in beams with V_f between 1% and 2%. At $r_{sw} = 0.55$ and $V_f = 1.9\%$, both μ and P_{max} were found to be significantly higher than their respective control beam specimen values (see Figures 7.2 (b) and (d)). Thus, it can be concluded that the proposed design line is valid for Case Study 1(a)-C as well.

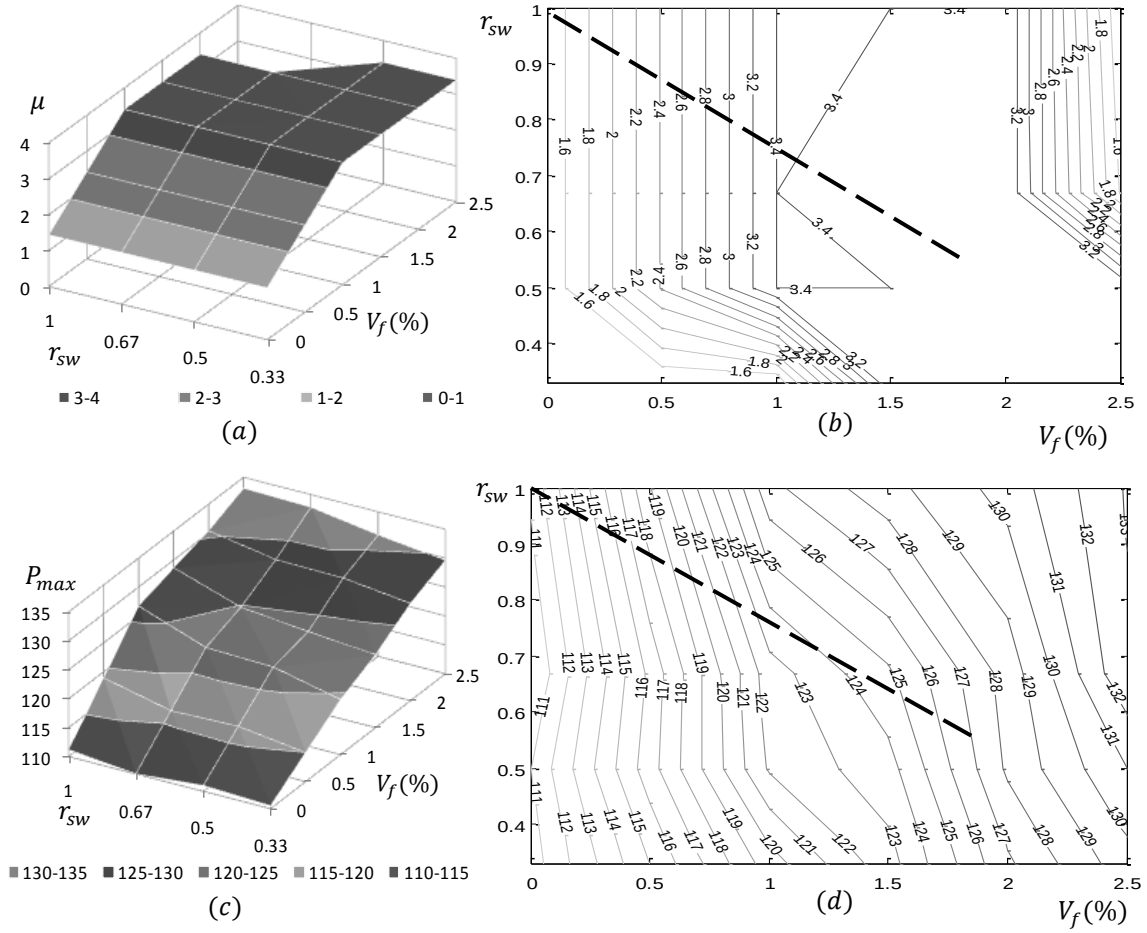


Figure 7.2: Ductility ratio (μ) in (a) 3D surface and (b) 2D contour diagrams; and Maximum load-carrying capacity (P_{max}) in (c) 3D surface and (d) 2D contour diagrams expressed in terms of r_{sw} and V_f for Case Study 1(a)-C

In Figure 7.3(a), for Case Study 1(b) which represents simply-supported SFRC beams initially designed to incorporate a shear mode of failure under monotonic loading, the maximum μ value was observed to be between $V_f = 1.5\%$ and 2%. For the SFRC beams with no stirrups (i.e. $r_{sw} = 0$), it was found that the addition of fibres at $V_f = 1.75\%$ restored the ductility ratio to 1.3 and by increasing the fibre content the ductility ratio of the SFRC beams were improved. For design purposes, the proposed line derived in the previous case studies was added onto Figures 7.3(b) and (d). It was observed, that any (r_{sw}, V_f) pair under the proposed line yields ductility ratio and load-carrying capacity values larger than those for the control beam specimen. This confirms that the proposal is also valid for the present case.

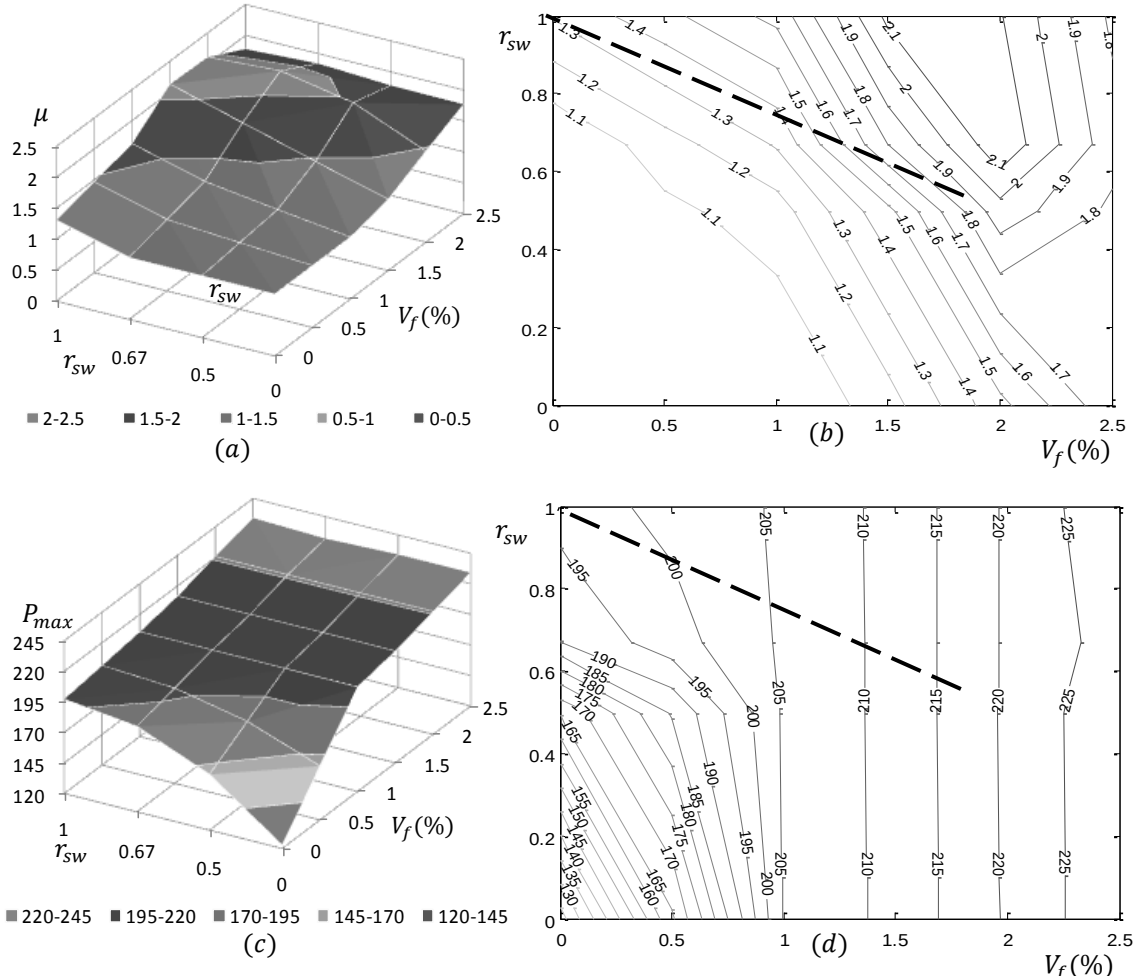


Figure 7.3: Ductility ratio (μ) in (a) 3D surface and (b) 2D contour diagrams; and Maximum load-carrying capacity (P_{max}) in (c) 3D surface and (d) 2D contour diagrams expressed in terms of r_{sw} and V_f for Case Study 1(b)

7.3 Case Study 2: Two-span continuous columns

In Case Study 2(a), for statically-indeterminate SFRC columns under monotonic loading, μ peaks at $V_f = 1.5\%$ and $r_{sw} \geq 0.67$ as shown in Figures 7.4(a) and (b). Similarly, Figures 7.4(c) and (d) indicate an upward trend in P_{max} within the range of 170 ~ 200 kN.

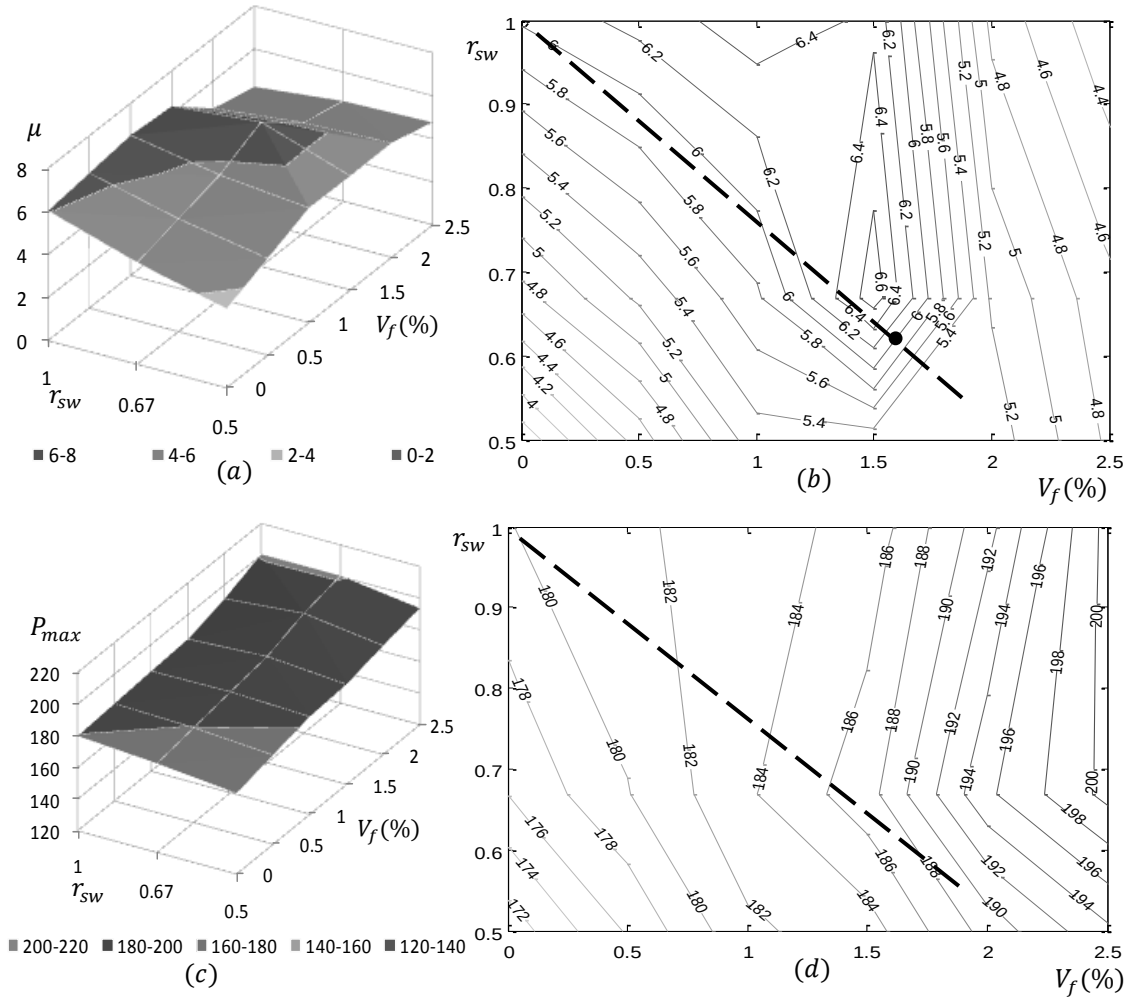


Figure 7.4: Ductility ratio (μ) in (a) 3D surface and (b) 2D contour diagrams; and Maximum load-carrying capacity (P_{max}) in (c) 3D surface and (d) 2D contour diagrams expressed in terms of r_{sw} and V_f for Case Study 2(a)

The proposed line established in previous case studies was added to Figures 7.4(b) and (d), however it was found that it was valid only up to $V_f = 1.6\%$. Therefore, in the present case the addition of fibres should be limited to 1.6% in order to ensure that sufficient ductility ratios can be achieved (i.e. to restore the original level of $\mu = 6$ associated with the control

specimen with full shear reinforcement and no fibres). In terms of strength, the full original proposed line was acceptable as increasing V_f consistently led to an increase in P_{max} beyond the target level observed in the control column specimen.

For the case of statically-indeterminate SFRC columns analysed under reversed-cyclic loading, i.e. Case Study 2(b), the results are depicted in Figures 7.5(a) to (d). It was found that the maximum μ value occurs at two points, namely: $V_f = 1\%$, $r_{sw} = 1$ and $V_f = 1.5\%$, $r_{sw} = 0.67$. In terms of the strength, Figures 7.5(c) and (d) show an enhancement in P_{max} as V_f increases (within the range of 155 ~ 185 kN).

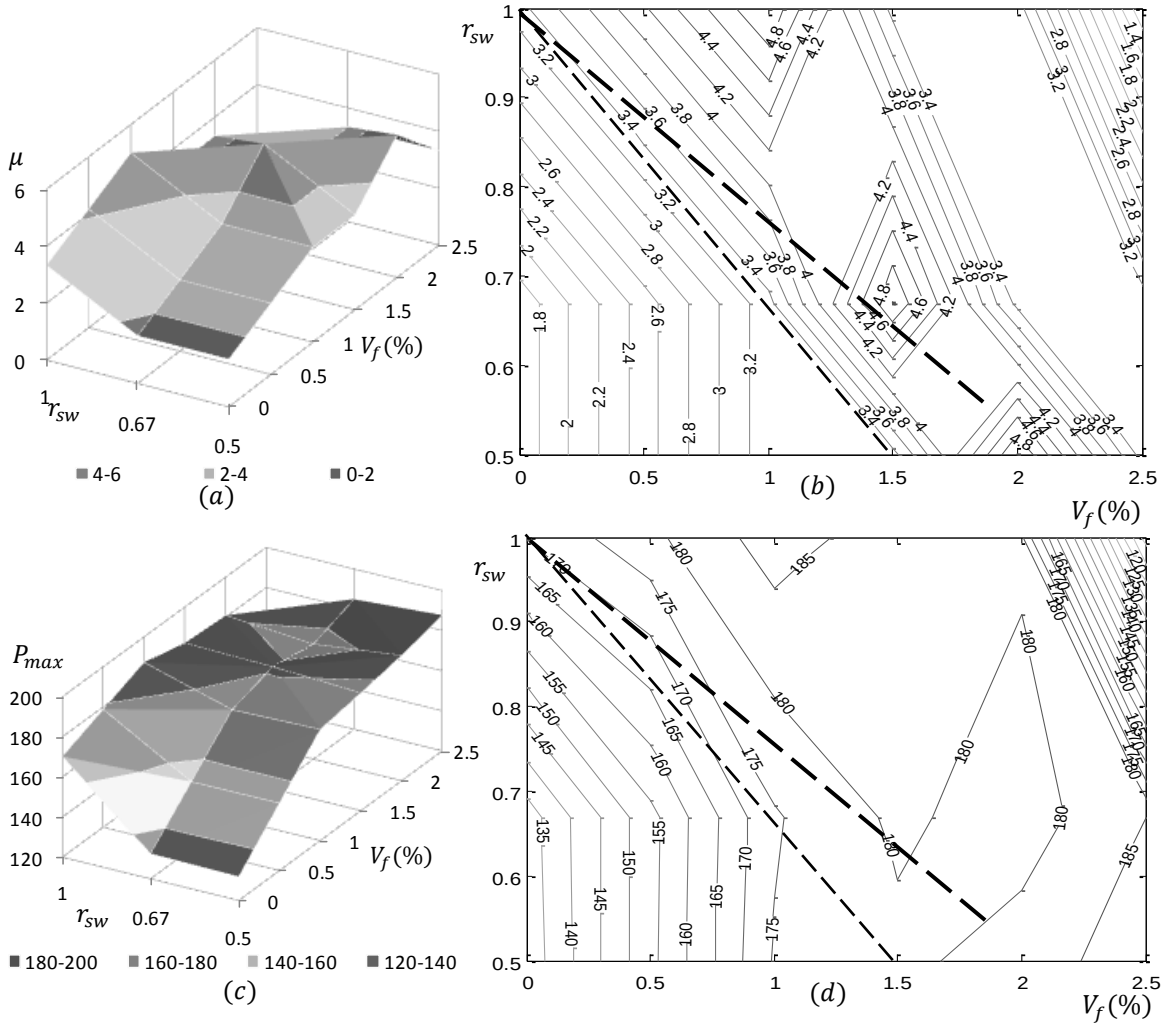


Figure 7.5: Ductility ratio (μ) in (a) 3D surface and (b) 2D contour diagrams; and Maximum load-carrying capacity (P_{max}) in (c) 3D surface and (d) 2D contour diagrams expressed in terms of r_{sw} and V_f for Case Study 2(b)

The maximum values of $\mu = 3.3$ and P_{max}= 170 kN observed in the control column specimen were maintained along a line extending from point $r_{sw} = 1$ and $V_f = 0\%$ to $r_{sw} = 0.5$ and $V_f = 1.5\%$, depicted as a thin dashed line on Figures 7.5(b) and (d). On the other hand, the original proposed line (derived in previous case studies linking point $r_{sw} = 1$ and $V_f = 0\%$ to $r_{sw} = 0.55$ and $V_f = 1.9\%$), was also added to the figures in thick dashed format for clarity. The latter proposed line yields μ and P_{max} values exceeding the ones associated with the control column specimen. Thus it can be adopted for design purposes (alternatively, the more economical "thin dashed" line can also be used).

7.4 Case Study 3 Beam-column joints

Figures 7.6 and 7.7 present the 3D surface and 2D contour diagrams for μ and P_{max} associated with Case Studies 3(a) and 3(b), for SFRC external and internal beam-column joints, respectively. From Figures 7.6(a) and (b), it was found that μ decreases for joints with $V_f > 1.75\%$ and $r_{sw} \geq 0.67$. However, for joints with $r_{sw} = 0.5$, μ continued to improve with an increase in V_f up to 2% ~ 2.5%. From the contour plots, it can be seen that the ductility ratio associated with the control joint specimen of μ = 4 can be restored with fibres at $V_f = 1\%$ and $r_{sw} = 0.67$. Similarly, the peak P_{max}= 32 kN of the control specimen can be maintained with $V_f = 1.25\%$ and $r_{sw} = 0.5$ (refer to Figures 7.6(d)).

The proposed line established in the previous case studies (linking point $r_{sw} = 1$ and $V_f = 0\%$ to $r_{sw} = 0.55$ and $V_f = 1.9\%$) was plotted on Figures 7.6(b) and (d). Consequently, it was found that μ and P_{max} values along this line were higher than those obtained from the control joint specimen. Thus, it can be concluded that the design recommendation of the proposed line is appropriate for Case Study 3(a).

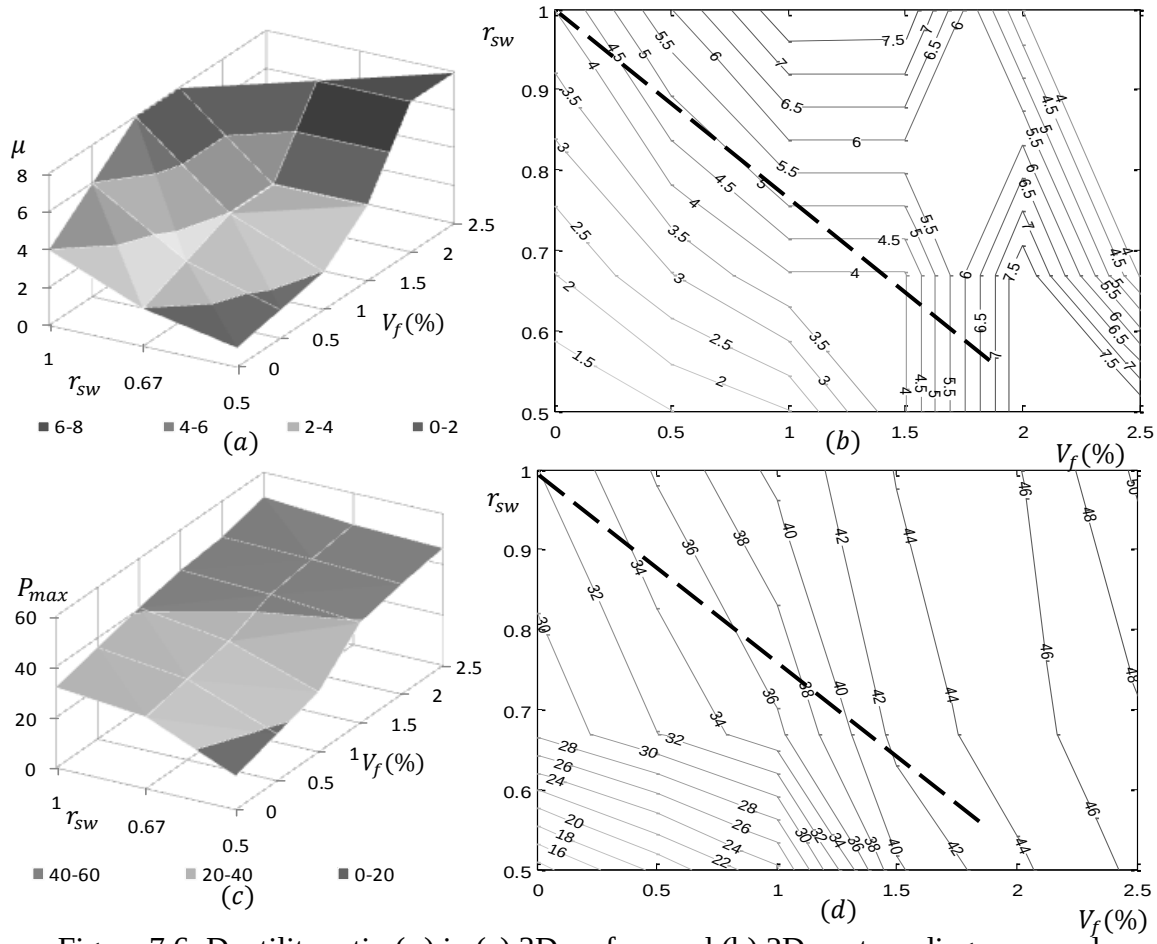


Figure 7.6: Ductility ratio (μ) in (a) 3D surface and (b) 2D contour diagrams; and Maximum load-carrying capacity (P_{max}) in (c) 3D surface and (d) 2D contour diagrams expressed in terms of r_{sw} and V_f for Case Study 3(a)

In Case Study 3(b), the interior RC joint with full seismic detailing ($r_{sw} = 1$) was considered as the control joint specimen. The parametric studies that were carried out in this particular case study only considered the joints with the reduction in the conventional shear reinforcement, and the steel fibres were added to these joints only. This explains the empty space on the top part of the 3D surface and 2D contour diagrams, see Figures 7.7(b) and (d), which was due to the unavailability of the data in this region (i.e. no fibres were added to the joint with full seismic detailing). The meaningful portion of the diagrams was observed between $r_{sw} = 0.5$ and 0.67. Therefore, further work is required to populate this region before relevant design recommendations can be proposed for SFRC interior joints. Nevertheless, based on the results obtained in the present work depicted in Figures 7.7(a)

and (b), it was found that the optimum V_f for Case Study 3(b) was between 1% and 1.5% for $r_{sw} = 0.67$ and $r_{sw} = 0.5$, respectively (for the single stirrups seismic arrangement case). Figures 7.7(c) and (d) show that P_{max} values yield a consistent enhancement as V_f values were increased, regardless of the value of r_{sw}.

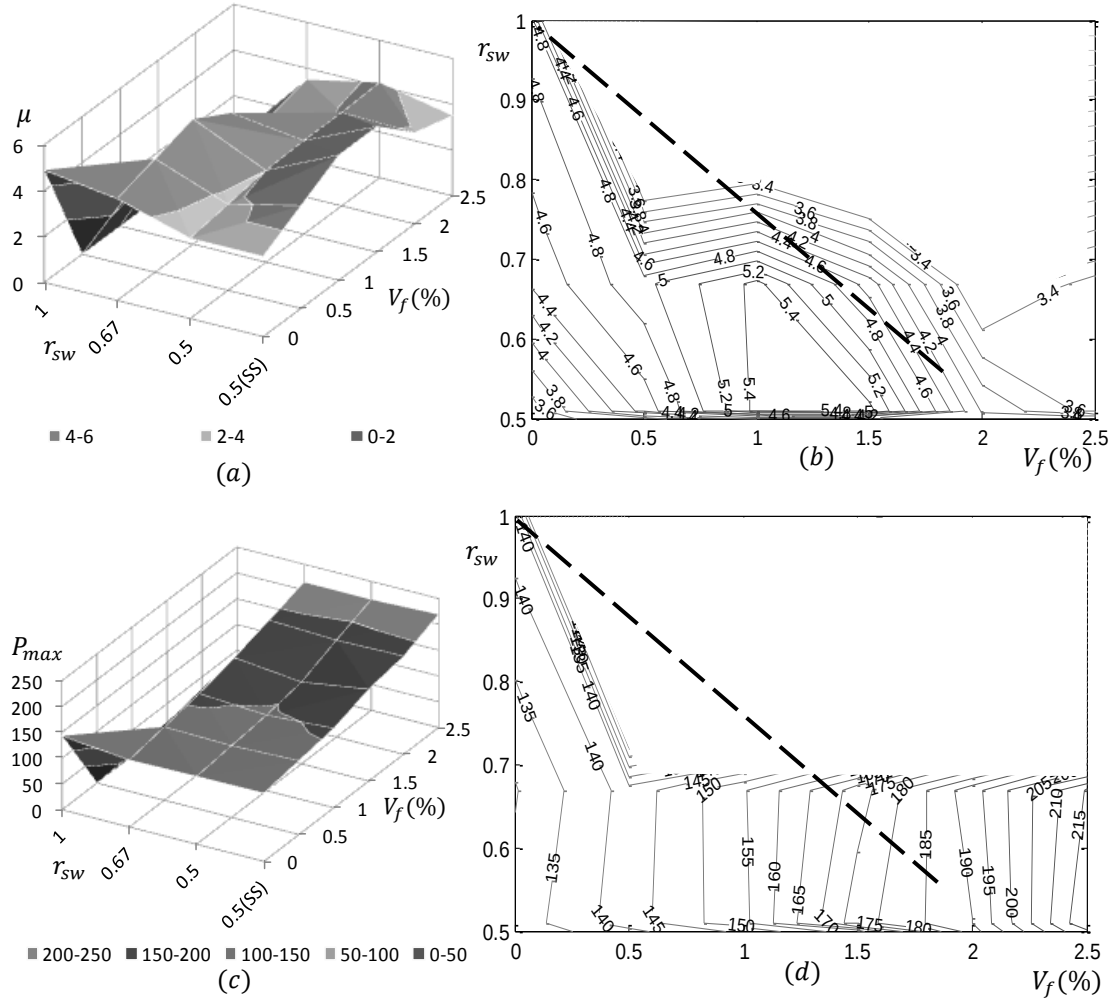


Figure 7.7: Ductility ratio (μ) in (a) 3D surface and (b) 2D contour diagrams; and Maximum load-carrying capacity (P_{max}) in (c) 3D surface and (d) 2D contour diagrams expressed in terms of r_{sw} and V_f for Case Study 3(b)

The proposed line derived previously was added onto Figures 7.7(b) and (d) to check its validity as a design recommendation for the present case study. The initial data available so far suggest that the ductility and strength levels associated with the control specimen (of μ = 4.8 and P_{max}= 140 kN) can be restored along the proposed line. However, further work is needed before definitive design recommendations can be arrived at.

7.5 Summary of design recommendations

The results obtained from the three case and parametric studies were plotted in 3D surface and 2D contour diagrams and discussed in the chapter. Subsequently, a design criterion was proposed based on the most critical parameters for seismic design, namely ductility and strength. The design recommendation is defined by a straight line linking points $r_{sw} = 1$, $V_f = 0\%$ to $r_{sw} = 0.55$, $V_f = 1.9\%$. Thus, the proposed line can be expressed as follows:

$$V_f(\%) = 4\,(1 - r_{sw})$$

where V_f is the volume fraction of fibres required to replace a given reduction in conventional transverse reinforcement expressed in terms of the ratio of the stirrups content $r_{sw} = (A_{sw}/S)/(A_{sw}/S)_0$. Recall that A_{sw} is the cross-sectional area of the stirrup and S is the spacing between the stirrups, while the zero subscript denotes the initial arrangement before any reduction in conventional shear reinforcement is applied. Therefore, r_{sw} ranges between 0 and 1.

It was found that the proposed line is appropriate for all case studies, except for Case Study 2(a) for statically-indeterminate columns under monotonic loading, where the line was found to be valid only up to $V_f = 1.6\%$. Therefore, it is recommended that the valid range of V_f in the above design equation should be between 0 and 1.6%. This suggests that the stirrups content can be linearly reduced by up to 40%, provided up to 1.6% of fibre volume fraction is added. In addition, it must be borne in mind that further studies should be performed for Case Study 3(b) for interior beam-column joints before establishing a definitive design equation.

CHAPTER 8

CONCLUSIONS AND RECOMMENDATIONS

8.1 Summary of research work

The present work is aimed at investigating the behaviour of SFRC structures under monotonic and reversed-cyclic loading (the latter being the key feature in seismic behaviour). Non-linear FE analysis was adopted in order to carry out the case and parametric studies. A summary of the research work discussed in this thesis and its limitations is presented below:

- 3D non-linear FE analyses were carried out using the commercial FE software package ABAQUS (2007). The RC structures were modelled using solid continuum 3D elements for concrete, while longitudinal bars and stirrups were modelled using 1D truss bar elements.
- The effect of steel fibres was introduced by altering the tensile stress-strain relationship of plain concrete across a crack and also by adjusting the shear response parallel to a crack.
- The SFRC constitutive model proposed by Lok and Xiao (1999) was selected to be used in the current work. This is a generic model which covers the definition of all significant properties for steel fibres (e.g. fibre volume fractions, aspect ratio, orientation and bond strength factor) and has a similar shape as the model proposed by RILEM TC 162-TDF Recommendation (2000, 2003). Furthermore, the Lok and Xiao model produced good predictions when compared with respective experimental data as discussed in Appendix A (a maximum of 10% discrepancy was observed between the Lok and Xiao model predictions and

experimental results). In addition, for numerical stability purposes, a gradual slope was introduced at the end of the stress-strain relationship (i.e. between strain values of 0.18 and 0.20) instead of original sharp vertical drop in the Lok and Xiao model.

- The SFRC constitutive model was implemented into ABAQUS software through its "brittle cracking" concrete model. This is a basic model that assumes a linear behaviour in compression, but the FE analyses results obtained from this model are able to provide good predictions against experimental results. This is due to the fact that the failure in the structural elements examined was governed by the tensile (i.e. bending) or diagonal-tension behaviour. Furthermore, initial calibration work showed that the model was capable of predicting the response of RC beams undergoing both ductile and brittle modes of failure. The effect of the fibres was added in the "tension stiffening" properties of this model (which describes the post-cracking tensile stress-strain relationship).
- The parametric studies in the current work were based on three case studies: Case Study 1, focussed on simply-supported beams (adopting the experimental work carried out by Campione and Mangiavillano, 2008; and Campione et al., 2006); Case Study 2, on two-span continuous columns (tested by Kotsovos et al., 2007); and Case Study 3, on exterior (Bayasi and Gebman, 2002) and interior (Filiatrault et al., 1995) beam-column joints. This research has extended the experimental work preformed by these researchers by carrying out full parametric studies using FE analyses.
- Both monotonic and reversed-cyclic loading types were conducted in all of the case studies (except for Case Study 3, in which only reversed-cyclic loading was considered). The reversed-cyclic loading was applied on the structures in order to examine their response to seismic loading.
- Two parameters were considered in the case studies: (i) the reduction in the amount of the conventional shear reinforcement and (ii) the increase in the amount of fibres. The reduction in conventional reinforcement was achieved mainly by gradually increasing the stirrups spacing (and also by reducing the double-hoop arrangement commonly used in joint seismic detailing). Five fibre volume fractions were considered in the present work, namely: 0%, 1%, 1.5%, 2% and 2.5%.

- The type of fibres considered in the present work was hooked-end steel fibres with the aspect ratio being kept the same as the one used in the corresponding experimental investigations.
- The compressive strength of plain concrete (i.e. with no fibres) considered was that of normal-strength concrete with f_{ck} between 23 MPa and 41 MPa.
- The FE models used were calibrated against existing experimental results, before subsequent parametric studies were carried out. The FE-based predictions correlated closely with the experimental data thus confirming the validity of the results obtained.
- The failure of the FE models was determined either by the identification of an abrupt high jump in the kinetic energy of the structures (taken to indicate large/extensive cracks) or by the simple termination of the analysis.
- The crack propagation of the structures was determined based on the analysis of the strain contours and vectors diagrams obtained from ABAQUS.
- The load-deflection curves were plotted based on the FE analysis results. From the curves, the key parameters (e.g. P_{max}, μ, N_c and E_a) of the SFRC structures were investigated and discussed.
- Finally, the FE analysis results obtained were plotted in 3D surface and 2D contour diagrams in order to propose design recommendations based on the current study.

8.2 Summary of conclusions

Specific observations and conclusions related to each case study were given within the body of the thesis. Henceforth, the main points alongside important conclusions are summarised here:

- The inclusion of the fibres into the RC structures increased the stiffness. This was notable from the load-deflection curves plotted in all the case and parametric studies. For instance in Case Study 1(a)-M, the stiffness in the SFRC beams was increased by 37% for beams with $SI = 0\%$ and $V_f = 2.5\%$, whereas in Case Study 3(a), the increase in the SFRC joint stiffness was up to 44% for the same SI and V_f values. It was noted that as the fibre content increases, the

crack opening was restrained by the fibres causing the structures to become stiffer and to deflect less.

- The maximum load carrying capacity (P_{max}) of the SFRC structures consistently increased with the increase in fibre content. The enhancement in P_{max} was more pronounced in the SFRC structures with a reduction in conventional shear reinforcement. For example in Case Study 3(a), at $SI = 100\%$ and $V_f = 2.5\%$ the P_{max} value of the joint was found to be 46.4 kN which was about 45% higher than that obtained in the control joint specimen (i.e. $P_{max} = 31.9\ kN$). The anchorage mechanism of the fibres limits the crack opening, thus higher load was required to pull-out the fibres and develop cracking. The enhancement in the strength of the SFRC structures was also confirmed by comparing the FE results against the design code predictions.
- The residual (i.e. post-peak) strength of the SFRC structures examined in the case and parametric studies were found to be at least 85% of the corresponding maximum load carrying capacities. This indicates that there is no significant post-peak softening response. This is beneficial in practice as it means that the post-peak ductility achieved coincides with an adequate residual strength level.
- Steel fibre volume fractions of 2% and 2.5% led to a post-yielding "peaked" or "spiked" trend that was observed on the relevant load-deflection curves. This behaviour occurred only for SFRC constitutive models exhibiting tensile strain hardening characteristics. The "peaked" load observed in the present work was up to 27% (with $V_f = 2.5\%$) higher than the residual load.
- The addition of fibres improved the ductility of the structures which is desirable in design. This improvement was more pronounced for the structures which were initially designed to undergo shear failure (i.e. up to 60% of the beam with full conventional reinforcement and $V_f = 2.5\%$). For the SFRC structures with a reduction in shear reinforcement, the ductility observed was significantly higher than that of the same structures with no fibres. For example, in Case Study 2(a), the ductility ratio (μ) of columns with $SI = 50\%$, $V_f = 0\%$ and 1.5% were 4.72 and 6.71, respectively. This shows that the addition of fibres improved μ by about 42%. This can be explained by recalling the fibres' role in bridging across cracks and limiting their opening. Consequently, crack propagation was delayed leading to enhanced ductility of the SFRC structures.

- Interestingly, in each case study, an optimum fibre volume fraction was found beyond which additional fibres led to less rather than more ductility. The present work highlights that this was due to the crack control mechanism introduced by higher amount of fibres, causing the structure to become stiffer and thus deflect less. This is similar to the "over-reinforced" structural response found in conventional RC design when excessive flexural reinforcement is provided prohibiting the steel from yielding. The optimum value was found to be dependent on the reduction in transverse shear reinforcement (i.e. the spacing between the stirrups) in each parametric study. The higher the spacing between the stirrups, the higher the optimum fibre content associated with the maximum ductility. This indicates that providing excessive amounts of fibres in addition to sufficient amounts of transverse reinforcement leads to brittle rather than ductile behaviour. Conversely, fibres can replace reduced amounts of conventional shear reinforcement by restoring the required ductility levels.
- Fibres enhanced confinement and led to better controlled crack propagation as well as reduced degradation effects under reversed-cyclic loading (thus enhancing the seismic structural response). This was observed in the results obtained for Case Study 3(b), for internal beam-column joints with stirrups spacing increases between $SI = 100\%$ and 0% (Single Stirrup arrangement).
- Sufficient amounts of fibres changed the mode of failure of the structure from brittle to a more ductile manner (i.e. from shear to bending failure). The anchorage mechanism and pull-out behaviour of the SFRC controlled the crack once it was initiated. This delayed the crack propagation causing the structures to fail in a more ductile manner.
- SFRC structures yielded higher energy absorption capabilities compared to their counterparts with similar amounts of stirrups (either full or reduced shear reinforcement) but with no fibres. The enhancement in energy absorption was particularly significant in the case of SFRC structures under reversed-cyclic loading. For example, in Case Studies 2(b) and 3(b), for the SFRC specimens with $SI = 50\%$, the maximum energy absorption capacity (E_a) was observed at $V_f = 1.5\%$ and 1% with an increase in E_a by up to 160% and 92%, respectively (compared to the same structures with no fibres).

- Fibres allowed for a reduction of the shear reinforcement while maintaining the ductility ratio, load-carrying capacity, energy absorption as well as controlling the crack propagation. This supports earlier investigations on the potential of using fibres as part of the conventional shear reinforcement particularly for the case of the structures designed to accommodate seismic detailing. This is because the demands on the latter often lead to congestion of conventional transverse reinforcement. Also, under seismic conditions, there is a higher need for sufficient amounts of ductility and energy absorption to be available and this is particularly one of the key advantages of adding fibres.
- Fibres improved the structural response under both serviceability and ultimate limit states which is significant in terms of design considerations.
- The reduction in the stirrups content by up to $r_{sw} = 0.6$ (i.e. 40%) can be compensated by adding fibres by up to 1.6%. This proposal was sufficient for all of the case and parametric studies investigated in the present research work. For the particular Case Study 3(b), further work is required before setting a design recommendation.

8.3 Recommendations for future work

In the course of this research, some topics have been identified which require further investigation. The following areas are suggested to extend the present work by:

- Studying the effect of different steel fibre shapes (i.e. twin cone, crimped) and how it compares to the findings of the present work. The effect of the fibre shapes can be conveniently defined by modifying the bond strength properties.
- Considering different fibre aspect (i.e. length/diameter) ratios and comparing their effects when provided at a range of fibre volume fractions.
- Extending the current static cyclic numerical analysis of SFRC joints by carrying out dynamic analysis using different natural earthquake records. This can be carried out by modelling some SFRC structures initially designed to Eurocode 8 (2004), for seismic design, before adding steel fibre to compensate the reduction in conventional transverse reinforcement.

- Carrying out experimental work on SFRC beam-column joints under cyclic loading. The joints will be initially designed to Eurocode 8 (2004) before replacing some of the conventional transverse reinforcement with fibres.
- Proposing equations for SFRC joints shear strength by extending the existing equations in Eurocode 8 (2004) for RC joints. This will be based on results obtained from the parametric studies to allow for the effect of fibres.
- Adjusting the equations in Eurocode 8 (2004) for seismic design relating to confinement (in particular the limits on the stirrups spacing) and ductility curvature requirements (see clause 5.4.3.2.2, Eurocode 8, 2004). These amendments will include a relaxation factor (of the spacing) based on the amount of steel fibres added.
- Adopting damaged-plasticity concrete models to study the behaviour of SFRC structures by means of dynamic analysis.
- Investigating the redistribution of internal forces in statically indeterminate SFRC structures.
- Considering different loading conditions, structure configurations (i.e. dimensions and steel reinforcement) and expanding the span-to-section-depth ratio especially for the case of SFRC beam-column joints.
- Investigating the effect of varying the extent of the SFRC zone within a structure (i.e. whether fibres should only be added at the joint region, throughout the beam or column region, or throughout the whole frame structure).
- Extending the current work to propose design recommendations to determine the optimum fibre amount that corresponds to a prescribed reduction in conventional shear reinforcement (ideally in the form of design charts/equations for use by practising engineers). This is particularly important for the case of beam-column joints.

In addition, further topics that can be explored by carrying out a study considering both experimental and numerical work are suggested as follows:

- Studying the seismic behaviour of steel fibres added to high-strength concrete, as the latter is more brittle than ordinary concrete and thus the fibres can potentially help to enhance its ductility.

- Investigating the impact response of SFRC structures, as fibres have been found to enhance energy absorption.
- Studying the fire resistant behaviour of SFRC structural elements, particularly the effect of fibres on reducing concrete spalling.
- Examining other types of fibres such as plastic and natural fibres and hybrid arrangements of different fibre types.

REFERENCES

ABAQUS Version 6.7 Documentation, 2007. [Online]. Available at http://www.engine.brown.edu:2080/v6.7/index.html.

ACI 544.2R Committee Report, 1988. Measurement of Properties of Fibre Reinforced Concrete. *ACI Structural Journal,* 85; p. 583-593.

ACI 544.4R Committee Report, 1988. Design Considerations for Steel Fibre Reinforced Concrete. *ACI Structural Journal,* 85; p. 563-580.

Anon[a], 2002. Getting Started with ABAQUS/Explicit, Interactive Version, Version 6.3. U.S.A: Hibbit, Karlsson and Sorensen, Inc.

Anon[b], 2002. Getting Started with ABAQUS/Standard, Interactive Version, Version 6.3. U.S.A: Hibbit, Karlsson and Sorensen, Inc.

Barragán, B.E., Gettu, R., Martín, M.A., and Zerbino, R.L., 2003. Uni-axial Tension Test for Steel Fibre-Reinforced concrete – A Parametric Study. *Cement & Concrete Composites, ELSEVIER,* 25; p. 767-777.

Barros, J.A.O., and Figueiras, J.A., 1999. Flexural behavior of SFRC: Testing and modelling. *Journal of Materials in Civil Engineering, ASCE,* 11(4); p. 331 – 339.

Barros, J.A.O., and Figueiras, J.A., 2001. Model for the Analysis of Steel Fibre Reinforced Concrete Slabs on Grade. *Computers and Structures, PERGAMON,* 79; p. 97 – 106.

Barros, J.A.O., Cunha, V.M.C.F., Ribeiro, A.F., and Antune, J.A.B., 2005. Post-Cracking Behaviour of Steel Fibre-Reinforced Concrete. *Materials and Structures, RILEM,* 38; p. 47-56.

Bayasi, Z., and Gebman, M., 2002. Reduction of Lateral Reinforcement in Seismic Beam-Column Connection via Application of Steel Fibres. *ACI Structural Journal*; p. 772-780.

Bencardino, F., Rizzuti, L., Spadea, G., and Ramnath, N.S., 2008. Stress-Strain Behavior of Steel Fiber-Reinforced Concrete in Compression. *Journal of Materials in Civil Engineering, ASCE,* 20(3); p. 255 – 262.

Booth, E., and Key, D., 2006. Earthquake Design Practice for Buildings. 2nd ed. London: Thomas Telford.

Booth, E., 2009. Design of Concrete Building to Eurocode 8. [Class handouts] London; Imperial College London.

Bresler, G., and Scordelis, A.C., 1963. Shear Strength of Reinforced Concrete Beams. *ACI Journal,* 60; p. 51-74.

British Standard Institution, 2004. Eurocode 2: Design of Concrete Structures - Part 1: General Rules and Rules for Buildings. *British Standard*, DD ENV1992-1-1.

British Standard Institution, 2004. Eurocode 8: Design of Structures for Earthquake Resistance – Part 1: General Rules, Seismic Actions and Rules for Buildings. *Bristish Standard*, BS EN 1998-1.

Buchholdt, H.A., 1997. Structural Dynamics for Engineers. London: Thomas Telford.

Campione, G., Cucchiara, C., and La Mendola, L., 2003. Role of fibres and stirrups on the experimental behaviour of reinforced concrete beams and flexure and shear. International Conference on Composites in Construction.

Campione, G., La Mendola, L., and Papia, M., 2006. Shear strength of steel fibre reinforced concrete beams with stirrups. *Structural Engineering and Mechanics*, Vol 24 (1); p. 107 – 136.

Campione, G., and Mangiavillano, M.L., 2008. Fibrous reinforced concrete beams in flexure: Experimental investigation, analytical modelling and design considerations. *Engineering Structures 30*; p. 2970 – 2980.

Casanova, P., and Rossi, P., 1997. Analysis and Design of Steel Fibre Reinforced Concrete Beams. *ACI Structural Journal*, 94; p. 594 – 602.

Cho, S.H., and Kim, Y.I., 2003. Effects Steel Fibres on Short Beams Loaded in Shear. *ACI Structural Journal*, 100(79); p. 765 – 774.

Chopra, A.K., 2007. Dynamics of Structures: Theory and Applications to Earthquake Engineering. Third Edition, United States of America: Pearson Prentice Hall.

Conise Eurocode 2, 2006. The Concrete Centre.

Concrete Society, 2007. Guidance for the Design of Steel-Fibre-Reinforced Concrete. Techincal Report No. 63. *Cement and Concrete Industry.*

Cook, R.D., 1995. Finite element modelling for stress analysis. United States of America: John Wiley & Sons, Inc.

Cotsovos, D., 2004. Numerical Modelling of Structural Concrete under Dynamic (Earthquake and Impact) Loading. London: Imperial College, London.

Craig, R.J., Mahadev, S., Patel, C.C., Viteri, M., and Kertesz, C., 1984. Behaviour of Joints Using Reinforced Fibrous Concrete. *Fibre Reinforced Concrete, Proceedings of the International Symposium, SP-81, G.F.Hoff, ed., American Concrete Institute,* Farmington Hills, Mich.; p. 125 – 167.

Crowther, D., 2009. Fibre-reinforced concrete-origin of the spcies. Tunnels and Tunneling, CONCRETE; p. 22 – 24.

Destrée, 2001. Steel fibre reinforcement for suspended slabs. *CONCRETE;* p. 58 – 59.

El-Niema, E.I., 1991. Reinforced Concrete Beams with Steel Fibres under Shear. *ACI Structural Journal*, 88; p. 178 -183.

Fardis, M. et al, 2005. Designers' Guide to EN 1998-1 and EN 1998-5 Eurocode 8: General Rules, Seismic Actions, Design Rules for buildings, Foundations and Retaining Structures. London: Thomas Telford.

Filiatrault, A., Ladicani, K., and Massicotte, B., 1994. Seismic Performance of Code-Designed Fiber Reinforced Concrete Joints. *ACI Structural Journal;* p. 564-571.

Filiatrault, A., Pineau, S., and Houde, J., 1995. Seismic Behaviour of Steel Fiber-Reinforced Concrete Interior Beam-Column Joints. *ACI Structural Journal;* p. 543-552.

Gefken, P.R., and Ramey, M.R., 1989. Increased Joint Hoop Spacing in Type 2 Seismic Joints Using Fiber Reinforced Concrete. *ACI Structural Journal;* p.168-172.

Hannant, D.J., 1978. Fibre Cements and Fibre Concretes. John Wiley & Sons, Ltd.

Henager, C.H., 1977. Steel Fibrous, Ductile Joint for Seismic-Resistant Structures. Reinforced Concrete Structures in Seismic Zones. SP-53, N.M. Hawkins, ed., *American Concrete Institute, Farmington Hills, Mich.,* p. 371-386.

Hillerborg, A., 1990. Application of the fictitious crack model to different types of materials. International Journal of Fracture, 51; p. 95 – 102, (1991).

Hughes, G. and Spiers, D.M., 1982. An Investigation on the Beam Impact Problem. *Cement and Concrete Association,* Technical Report 546.

Johnston, C.D., 2001. Fibre-Reinforced Cements and Concretes. Advances in Concrete Technology, Volume 3. Canada: Gordon and Breach Science Publisher.

Jindal R.L., and Hassan, K.A., 1984. Behaviour of Steel Fibre Reinforced Concrete Beam-Column Connections. Fibre *Reinforced Concrete, Proceedings of the International Symposium, SP-81, G.F.Hoff, ed., American Concrete Institute,* Farmington Hills, Mich.; p. 107 – 123.

Jiuru, T., Chaobin, H., Kaijian, Y., and Yongcheng, Y., 1992. Seismic Behaviour and Shear Strength of Framed Joints Using Steel Fibre Reinforced Concrete. *Journal of Structural Engineering, ASCE,* 118 (2); p. 341-358.

Khaloo, A.R., and Afshari, M., 2005. Flexural Behaviour of Small Steel Fibre-Reinforced Concrete Slabs. *Cement & Concrete Composites, ELSEVIER,* 27; p. 141 – 149.

Kotsovos, G., Zeris, C., and Kotsovos, M., 2007. The Effect of Steel Fibres on the Earthquake-Resistance Design of Reinforced Concrete Structures. *Materials and Structures, RILEM,* 40; p. 175-188.

Kotsovos, M.D. and Pavlović, M.N., 1995. Structural concrete, Finite-element analysis for limit-state design. London. Thomas Telford.

Kwak, Y.K, Eberhard, M.O, Kim, W.S., and Kim, J., 2002. Shear Strength of Steel Fibre-Reinforced Concrete Beams without Stirrups. *ACI Structural Journal, Technical Paper*, No. 99-S55; p. 530 – 538.

Kwak, H.G., Filippou, F.C., 1990. Finite Element Analysis of Reinforced Concrete Structures under Monotonic Loads, *UCB/SEMM-90/14*. University of California Berkeley.

Lee, H.H., 2007. Shear strength and behaviour of steel fibre reinforced concrete columns under seismic loading, *Engineering Structures, ELSEVIER*, 29; p. 1253 – 1262.

Lim, T.Y., Paramasivam, P., and Lee, S.L, 1987. Analytical Model for Tensile Behaviour of Steel-Fibre Concrete, *ACI Materials Journal, Technical Paper, No 84-M30*; p. 286 – 298.

Lim, T.Y., Paramasivam, P., and Lee, S.L, 1987. Bending Behaviour of Steel-Fibre Concrete Beams, *ACI Strutural Journal, Technical Paper, No 84-S54*; p. 524 – 536.

Lok, T.S., and Pei, J.S., 1996. Flexural Behavior of Steel Fiber-Reinforced Concrete. *Journal of Materials in Civil Engineering, ASCE*, 10(2); p. 86 – 97.

Lok, T.S., and Xiao, J.R., 1999. Flexural Strength Assessment of Steel Fiber-Reinforced Concrete. *Journal of Materials in Civil Engineering, ASCE,* 11(3); p. 188 – 196.

Mansur, M.A., Ong, K.C.G., and Parasiivam, P., 1986. Shear Strength of Fibrous Concrete Beams without stirrups. *Journal of Structural Engineering*, Vol. (112); p. 2066 – 2079.

Mansur, M.A., and Ong, K.C.G., 1991. Behaviour of Reinforced Concrete Deep Beams in Shear. *ACI Structural Journal*, 88; p. 98 – 105.

Murugappan, K., Tan, K.H., and Paramasivam, P., 1994. Finite element formulation for the analysis of reinforced fibrous concrete beams. *Finite Element in Analysis and Design, ELSEVIER*, 18; p. 67-74.

Narayanan, R., and Darwish, I.Y.S., 1987. Use of Steel Fibres as Shear Reinforcement. *ACI Structural Journal*, 84; p. 216 – 227.

National Research Council, 2007. Guide for the Design and Construction of Fibre-Reinforced Concrete Structures. *CNR-DT 204/2006.*

Noghabai, K., 2000. Beams of Fibrous Concrete in Shear and Bending: Experiment and Model. *Journal of Structural Engineering, ASCE*, 126; p. 243-251.

Oh, B.H., Lim, D.H., Yoo, S.W., and Kim, E.S., 1998. Shear behaviour and shear analysis of reinforced concrete beams containing steel fibres. *Magazine of Concrete Research*, 50, No. 4; p. 283-291.

Olesen, J.F., 2001. Fictitious crack propagation in Fibre-Reinforced Concrete Beams. *Journal of Engineering Mechanics, ASCE,* 127(3); p. 272 – 281.

Ozcan, D.M., Bayraktar, A., Sahin, A, Haktanir, T., and Turker, T., 2009. Experimental and Finite Element Analysis on the Steel Fibre-Reinforced Concrete (SFRC) Beams Ultimate Behaviour. *Construction and Building Materials, ELSEVIER*, 23; p. 1064-1077.

RILEM Technical Committees, 2000. RILEM TC 162-TDF: Test and Design Methods for Steel Fibre-Reinforced Concrete, Recommendation: σ@ε Design Method. *Materials and Structures, RILEM*, 33; 75-81.

RILEM Technical Committees, 2002. RILEM TC 162-TDF: Test and Design Methods for Steel Fibre-Reinforced Concrete, Design of Steel Fibre-Reinforced Concrete using the σ@*w* Method: Principles and Application. *Materials and Structures, RILEM,* 35; p. 262-278.

RILEM Technical Committees, 2003. RILEM TC 162-TDF[a]: Test and Design Methods for Steel Fibre-Reinforced Concrete, Final Recommendation: σ@ε Design Method. *Materials and Structures, RILEM*, 36; p. 560-567.

RILEM Technical Committees, 2003. RILEM TC 162-TDF[b]: Test and Design Methods for Steel Fibre-Reinforced Concrete, Round-robin analysis of the RILEM TC 162-TDF beam-bending test: Part 1 – Test method evaluation. *Materials and Structures, RILEM,* 36; p. 609 -620.

RILEM Technical Committees, 2003. RILEM TC 162-TDF[c]: Test and Design Methods for Steel Fibre-Reinforced Concrete, Round-robin analysis of the RILEM TC 162-TDF beam-bending test: Part 2 – Approximation of δ from the CMOD response. *Materials and Structures, RILEM,* 36; p. 621 -630.

Robins, P., Austin, S., and Jones, P., 2002. Pull-out Behaviour of Hooked Steel Fibres. *Materials and Structures, RILEM,* 35; p. 4343-442.

Sharma, A.K., 1986. Shear Strength of Steel Fibre Reinforced Concrete Beams. *ACI Journal,* 83; p. 624 – 628.

Shah, S.P., and Rangan, B.V., 1971. Fibre Reinforced Concrete Properties. *ACI Journal,* 68; p. 126-135.

Structural Concrete, 1999. *Federation Internationale du beton (fib*); volumes 1 – 4.

Swamy, R.N., and Lankard, D.R., 1974. Some Practical Applications of Steel Fibre-Reinforced Concrete. *Proceedings,* Part 1; p. 235 – 256.

Swamy, R.N., and Al-Ta'an, S.A., 1981. Deformation and Ultimate Strength in Flexure of Reinforced Concrete Beams Made with Steel Fibre Concrete. *ACI Journal,* 78(36); p. 395 – 405.

Swamy, R.N., 1984. Concrete Technology and Design, New Reinforced Concrete. Volume 2. London: Blackie & Son Ltd.

Swamy, R.N., and Bahia, M., 1985. The Effectiveness of Steel Fibres as Shear Reinforcement. *Concrete International*; p. 35 – 40.

Sukontasukkul, P., 2004. Tensile Behaviour of Hybrid Fibre-Reinforced Concrete. *Advances in Cement Research, Thomas Telford Ltd,* 3; p. 115-122.

Tlemat[a], H., Pilakoutas, K., and Neocleous, K., 2006. Stress-strain Characteristic of SFRC using Recycled Fibres. *Materials and Structures, RILEM,* 39; p. 365-377.

Tlemat[b], H., Pilakoutas, K., and Neocleous, K., 2006. Modelling of SFRC using Inverse Finite Element Analysis. *Materials and Structures, RILEM*, 39; p. 221-233.

Tlemat[c], H., Pilakoutas, K., and Neocleous, K., 2006. Design Issues for Concrete Reinforced with Steel Fibres, Including Fibres Recovered from Recycled Tires. *Journal of Materials in Civil Engineering, ASCE*, 18(5); p. 677 – 685.

Trottier, J.F., and Banthia, N., 1994. Toughness Characterization of Steel Fiber-Reinforced Concrete. *Journal of Materials in Civil Engineering, ASCE*, 6(2); p. 264 – 289.

Uniform Building Code, 1997. Structural Engineering Design Provision. Vol 2.

Yazici, S., İnan, G., Tabak, V., 2007. Effect of aspect ratio and volume fraction of steel fibre on the mechanical properties of SFRC. *Construction and Building Materials, ELSEVIER*, 21, p. 1250 – 1253.

Zienkiewicz O. C. And Taylor R. L., 1989. The finite element method. Vol. 1. Basic formulations and linear problems. London: McGraw-Hill.

APPENDIX A

MODEL CALIBRATION WORK

A.1 Background

A series of analyses were carried out using ABAQUS and SFRC constitutive models as discussed in Chapter 3. The analyses were carried out to select and calibrate the most appropriate SFRC (see Section 3.3) and ABAQUS (see Section 3.4) models to be adopted in the subsequent parametric studies for Case Studies 1, 2 and 3. This section discusses all the calibration work performed including a comparative study between numerical and experimental results.

Initially calibrations on RC beams (i.e. without fibres) were carried out using experimental data on beams undergoing both ductile and brittle responses (i.e. Hughes and Spiers (1982) and Bresler and Scordelis (1963), respectively). These analyses were carried out to ensure that the FE analysis software and associated constitutive model adopted for concrete (fully described in Chapter 3) is capable of yielding good predictions for RC structures. The results of the ductile beams are presented in Section A.2, while the responses of the brittle beams are discussed in Section A.3.

Subsequently, further analyses were carried out to calibrate the SFRC constitutive models considered in the light of existing experimental data (at both material and structural levels). With regards to investigations at the material level, experimental work by Barros et al (2005), Tlemat[a;b] et al (2006), Barros and Figueiras (1999), and Trottier and Banthia (1994) was considered as presented in Sections A.4 to A.7, respectively. Similarly, SFRC beams tested by Cho and Kim (2003), Oh et al (1998),

and Sharma (1986) were analysed for cases at the structural level as discussed in Sections A.8 to A.10, respectively.

A.2 Ductile failure: Hughes and Speirs (1982)

A.2.1 Experimental data and analysis procedure

A simply supported reinforced concrete beam (specimen C2) investigated by Hughes and Speirs (1982) is selected herein. The beam dimension, longitudinal and transverse reinforcement are illustrated in Figure A.1. The uni-axial compressive (f_{ck}) and tensile (f_{tk}) strength of the concrete used for the specimen are approximately 45 MPa and 3 MPa, respectively. Furthermore, the modulus of elasticity (E_s), the yield stress (f_y), and the ultimate strength (f_u) of both the longitudinal and transverse reinforcement bars used are 206 GPa, 460 MPa and 560 MPa, respectively. During the experiment, the reinforced concrete beam is subjected to a point load which is applied on the centre of the specimens' span.

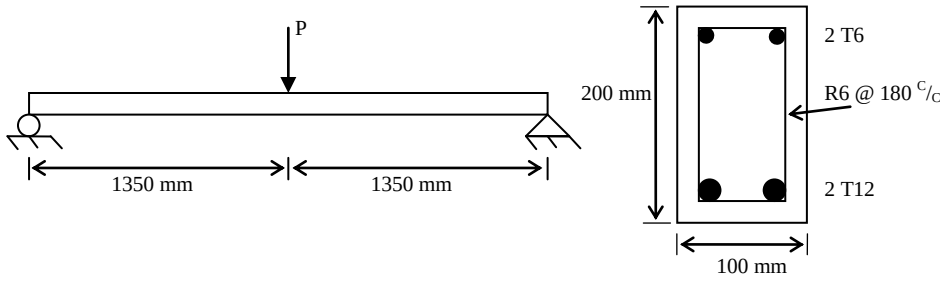


Figure A.1: Dimension and loading condition of specimen C2 (Modified from: Hughes and Speirs, 1982)

By taking into consideration the symmetrical arrangement of the beam, only one quarter of the beam with dimension of 50 x 200 x 1350 mm is modelled. The tensile cracking strain is assumed to be 0.001. The beam is assumed to have full shear retention ($\rho_{close} = 1.0$) throughout the analysis. The analysis is carried out using the brittle cracking model and the element size adopted for the analysis is 20 mm.

A.2.2 Discussion of ABAQUS simulation results

A reasonable comparison of load-deflection curve is achieved as shown in Figure A.2. The ABAQUS produced results with slightly higher stiffness (4%) as compared to the experimental data. The post-cracking result analysed by ABAQUS show a softening behaviour after 25 mm deflection, however, it is still in an acceptable range which is less than 10% deviation. From the figure below, it can be concluded that ABAQUS is capable of modelling conventional reinforced concrete structure in ductile failure.

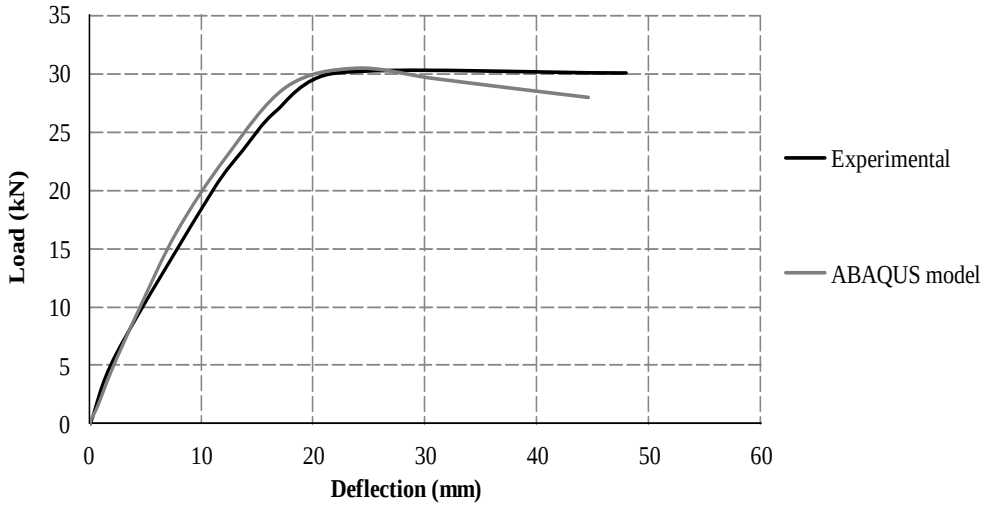


Figure A.2: Results comparison graph for specimen C2 (Hughes and Speirs, 1982)

A.3 Brittle failure: Bresler and Scordelis (1963)

A.3.1 Experimental data and analysis procedure

An over-reinforced concrete beam without stirrups reported as beam OA-1 tested by Bresler and Scordelis (1963) is chosen for comparison to investigate the effectiveness of ABAQUS in modelling a brittle failure of a reinforced concrete beam. Figure A.3 illustrates the dimension and longitudinal reinforcement of the beam. The uni-axial compressive (f_{ck}) strength is given as 22.5 MPa. High strength steel (f_y = 555 MPa, f_u = 958 MPa) was used for the tension reinforcement to prevent ductile failure. The beam failed in shear at 334 kN (6.6 mm of mid span deflection) without yielding of the tension bars.

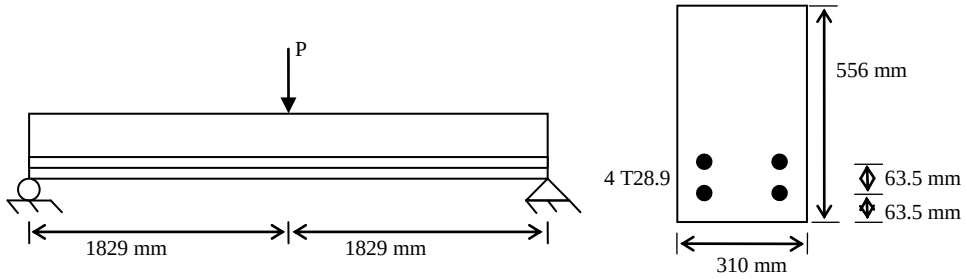


Figure A.3: Dimension and loading condition of beam OA-1 (Modified from: Bresler and Scordelis, 1963)

The tensile strength is taken as 10 % of compressive strength, 2.25 MPa, whereas, the tensile cracking strain is assumed as 0.002. This beam is assumed to have full shear retention factor ($\rho_{close} = 1.0$) at the beginning of the analysis, and losses completely when the crack opening strain reached tensile cracking strain of 0.002.

A.3.2 Discussion of ABAQUS simulation results

Analysis is carried using element size of 30 mm. Good agreement with the experimental result is achieved as shown in Figure A.4. The load carrying capacity predicted by ABAQUS is 5% lower than the one obtained trough experimental work. This demonstrates that ABAQUS also give good results in replicating the load-deflection curve for the beam behaves in brittle manner (with no stirrups).

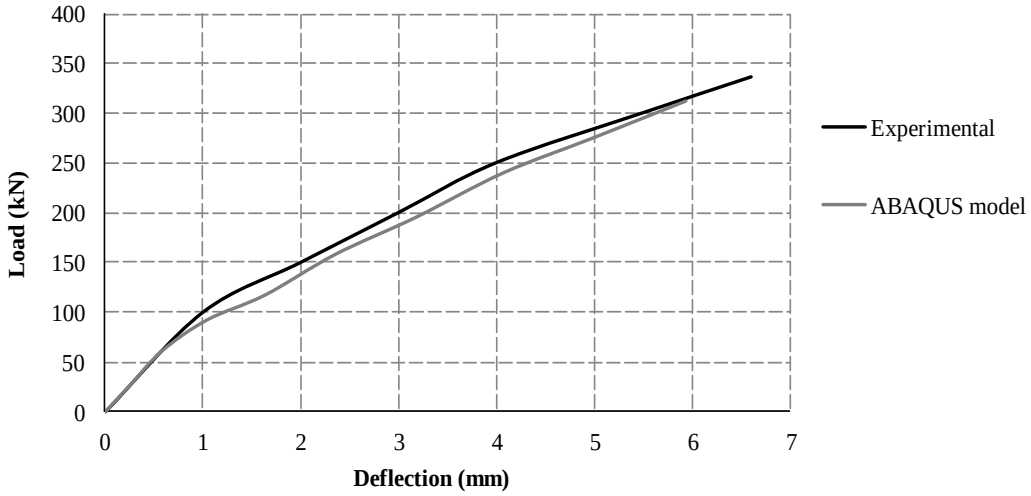


Figure A.4: Results comparison graph for beam OA-1 (Bresler and Scordelis, 1963)

A.4 Three-point bending test (tensile failure): Barros et al (2005)

A.4.1 Experimental data and analysis procedure

Two SFRC notched beams tested under 3-point bending test are selected for calibration as shown in Figure A.5. Barros et al (2005) considered two types of steel fibres for the testing, which are Dramix RC 80/60 BN and RC 65/60 BN. The details of these steel fibres are defined fully in Table A.1. The uni-axial compressive strength (f_c) and elasticity modulus (E_c) of the beams are 25 MPa and 29250 MPa, respectively. For calibration purposes, the material model proposed by Lok and Pei (1998) and Lok and Xiao (1999) are applied into ABAQUS to model the behaviour of SFRC.

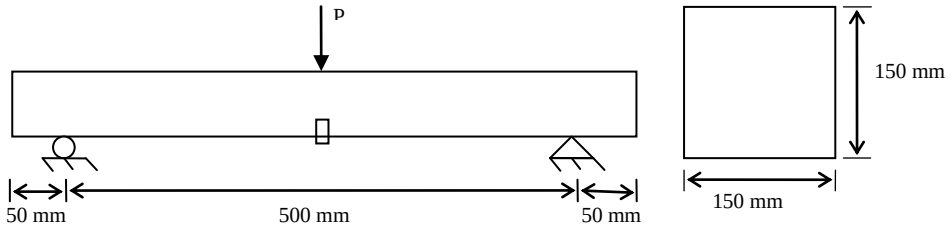


Figure A.5: Dimension and loading condition of the notched beam (Modified from: Barros et al, 2005)

Fibre type Dramix	Length (l) [mm]	Diameter (d) [mm]	Tensile strength [N/mm^2]	Fibre volume (v_f) [%]
RC 65/60 BN	60	0.92	1100	0.58
RC 80/60 BN	60	0.75	1100	0.40

Table A.1: Summary of geometry, tensile strength and fibre content for each type of steel fibres (Modified from: Barros et al, 2005)

The ABAQUS concrete smeared cracking (SC), brittle cracking (BC) and damaged plasticity (DP) models were compared to assess the performance of each model. The tension softening of the concrete after cracking is simulated by a multi-linear descending curve, which is presented in Figures A.6 and A.7 for RC 65/60 BN and RC 80/60 BN, respectively. In this analysis, the bond stress values assumed for RC 65/60 BN and RC 80/60 BN beams are 7.1 Mpa and 3.57 Mpa, respectively. A mesh size of 25 mm is chosen to be applied for the analyses.

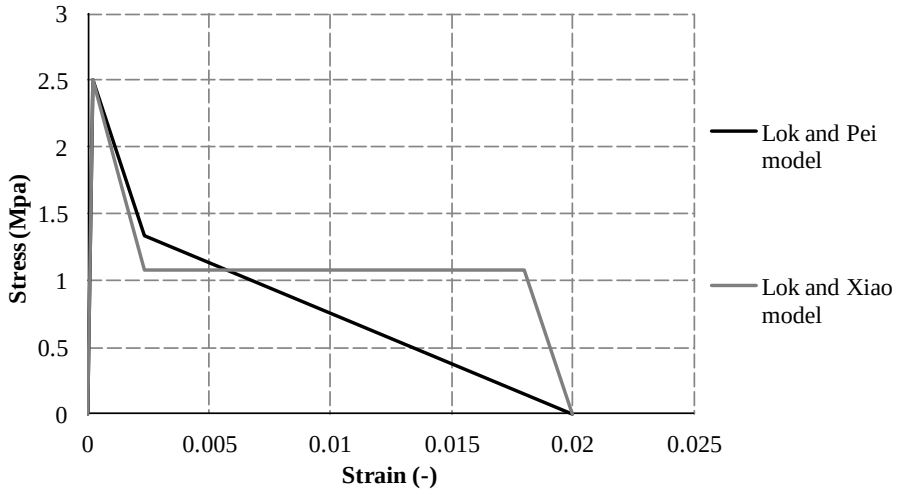


Figure A.6: Tensile stress-strain diagram for Barros et al (2005) SFRC beams for RC 65/60 BN (v_f = 0.58%)

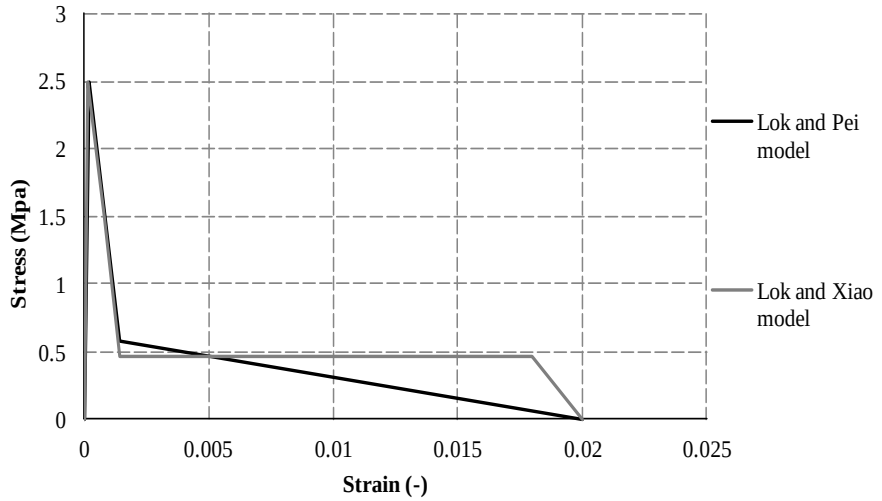


Figure A.7: Tensile stress-strain diagram for Barros et al (2005) SFRC beams for RC 80/60 BN (with v_f = 0.4%)

A.4.2 Discussion of ABAQUS simulation results

The results for the beams, reinforced with steel fibres types of RC 65/50 and RC 80/60 are illustrated in Figure A.8 and Figure A.9, respectively. The graphs show that for both types of steel fibres, the results predicted by FE models in ABAQUS were slightly stiffer compared to experiment results. Generally, the pattern for both curves analysed in BC model, fairly follows the experiment curve with a displacement failure occurred slightly higher than evaluated by the experimental work.

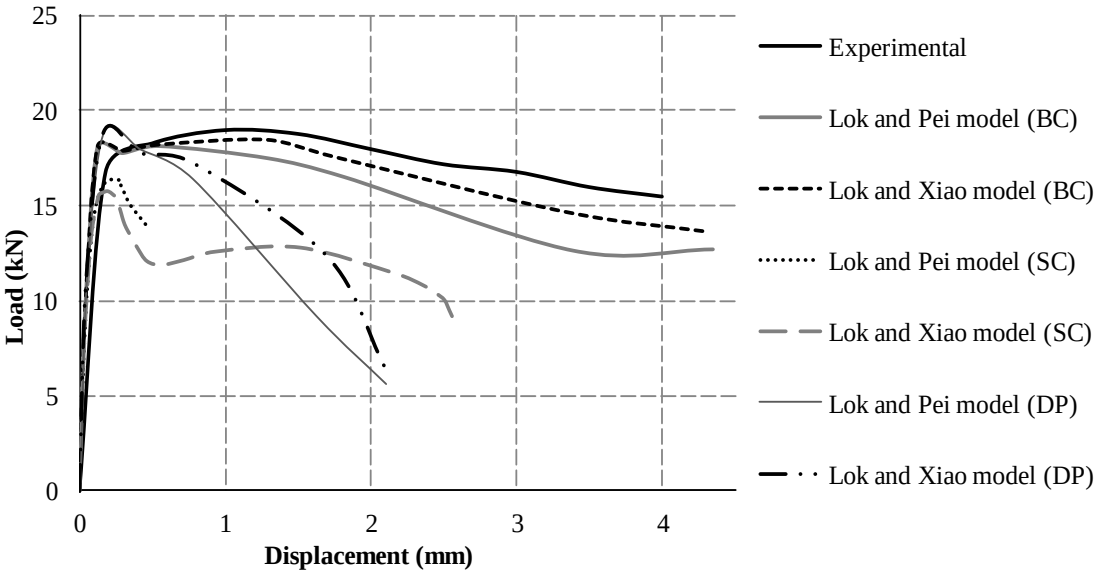


Figure A.8: Comparison graph for SFRC beam RC 65/60(v_f = 0.58%)

Figure A.8 shows that the results obtained from SC and DP concrete models observed localised failure, and the post-cracking behaviour inclined towards softening behaviour. SC model underestimated the load bearing capacity of the beams by 10%, whilst the load bearing capacity modelled by BC and DP is slightly higher as compared to the experimental value up to 5% and 11%, respectively. Furthermore, it can be seen that the results analysed by BC exhibits more reasonable results compared with results analysed by concrete SC and DP. Comparison on SFRC constitutive model shows that the results obtained from Lok and Xiao (BC) model demonstrates better post-cracking behaviour and agrees well with the experimental result.

Similar pattern is observed in Figure A.9, as the best results were obtained from the BC models. Figure A.9 (b) depicts the clear responses of the load-deflection curves up to displacement equal to 1.5 mm. SC and DP suffered localised failure, in which the post-cracking behaviour of SC model is the lowest. Whereas for DP, the post-cracking behaviour after the "necking" exhibits hardening behaviour, even higher than the results analysed by BC. Even so, the results for Lok and Xiao model analysed in each case exhibits higher post-cracking load and are closer to the experimental result. Thus it can be concluded that Lok and Xiao model produces a good load-deflection response in comparison with the experimental result.

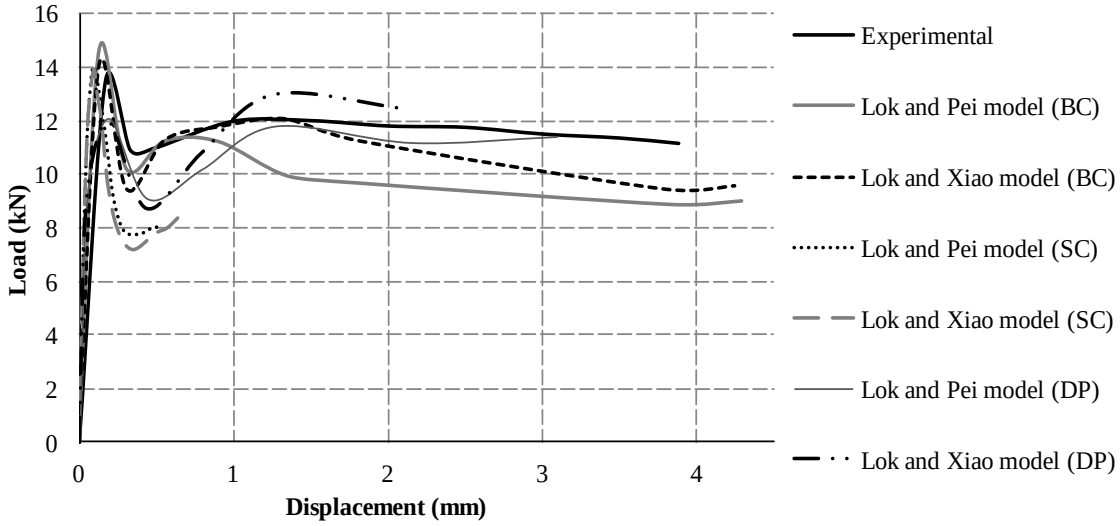


Figure A.9: Comparison graph for SFRC beam RC 80/60 (v_f = 0.4%)

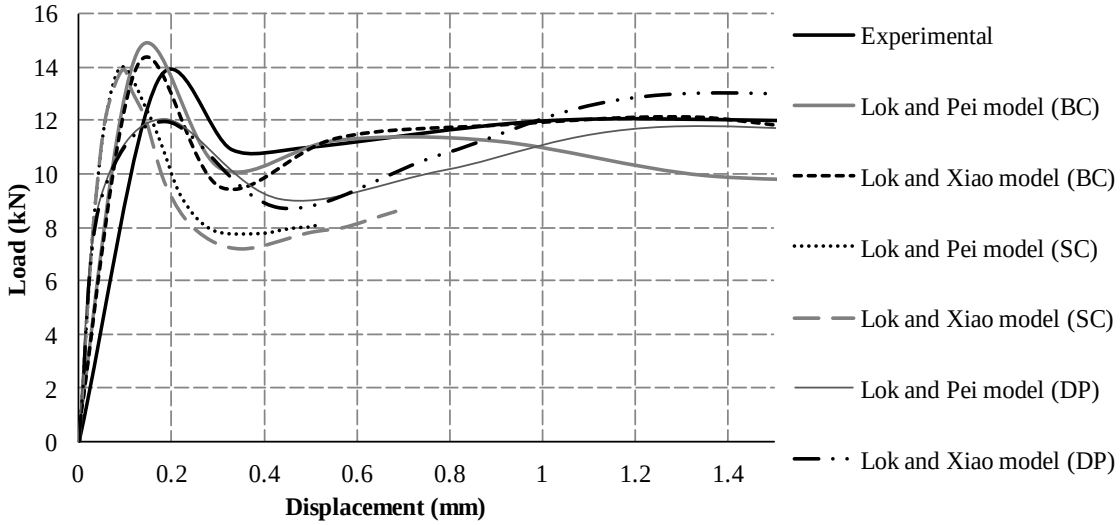


Figure A.9 (b): Comparison graph for SFRC beam RC 80/60 (v_f = 0.4%) until displacement = 1 mm

A.5 Four-point bending test (tensile failure): Tlemat[a;b] et al (2006)

A.5.1 Experimental data and analysis procedure

Based on experimental work carried out by Tlemat[a] et al (2006) and Tlemat[b] et al (2006), two SFRC small beam specimens were selected and modelled using ABAQUS (see Figure A.10). There are two types of fibrous concrete considered in this study, namely industrialised steel fibre (ISF) types 1 (twin-cone) and 2 (hooked-end). The details of these steel fibres are given in Table A.2. The plain concrete has compressive

strength of 51.5 MPa. For calibration purposes, three SFRC material models suggested by Tlemat[b] et al (2006), Lok and Pei (1998) and Lok and Xiao (1999) are adopted into ABAQUS to model the behaviour of SFRC.

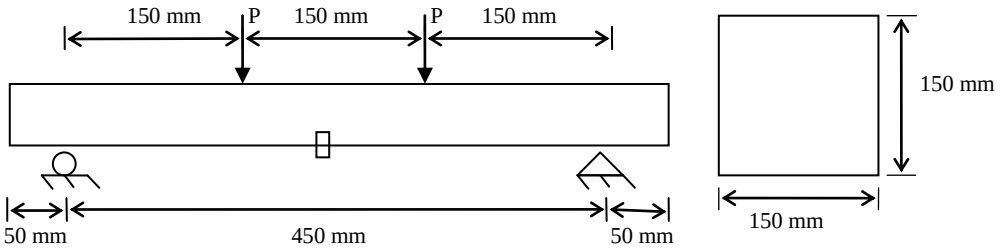


Figure A.10: Dimension and loading condition of the beams (Modified from: Tlemat[b] et al, 2006)

Fibre type	Length (l) [mm]	Diameter (d) [mm]	Tensile strength [N/mm^2]	Fibre volume (v_f) [%]
ISF-1	50	1.00	1050	6.0
ISF-2	50	1.05	1000	6.0

Table A.2: Summary of geometry, tensile strength and volume percentage for each type of fibre (Adapted from: Tlemat[a] et al, 2006)

Two approaches were used to model the behaviour of the SFRC beam, namely smeared cracking concrete model and brittle cracking model. The compressive behaviour for this analysis is investigated by using the values recommended by Kupfer et al (1973) as implemented by Tlemat[b] et al (2006) for the analyses. The tensile behaviour for SFRC material model shown in Figures A.11 and A.12 for ISF-1 and ISF-2, respectively, were utilised for the analysis. Bond stress value of 3 MPa is adopted for both types of steel fibres. Failure ratio in concrete smeared cracking is taken as 1.15 as suggested by Tlemat[b] et al, 2006. In addition, it was assumed that the beam have full shear retention (ρ_{close} = 1.0) with an appropriately large value for $\varepsilon_{\max}$ since this provide more stable results. Mesh size of 25 mm is adopted, as it was found showing good comparison with the experimental results.

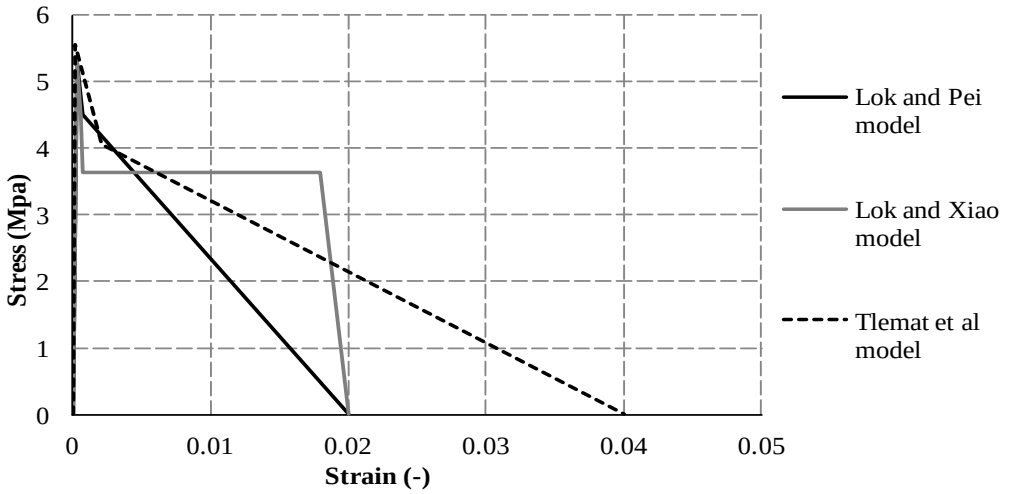


Figure A.11: Tensile stress-strain diagram for ISF-1 with $v_f = 6\%$

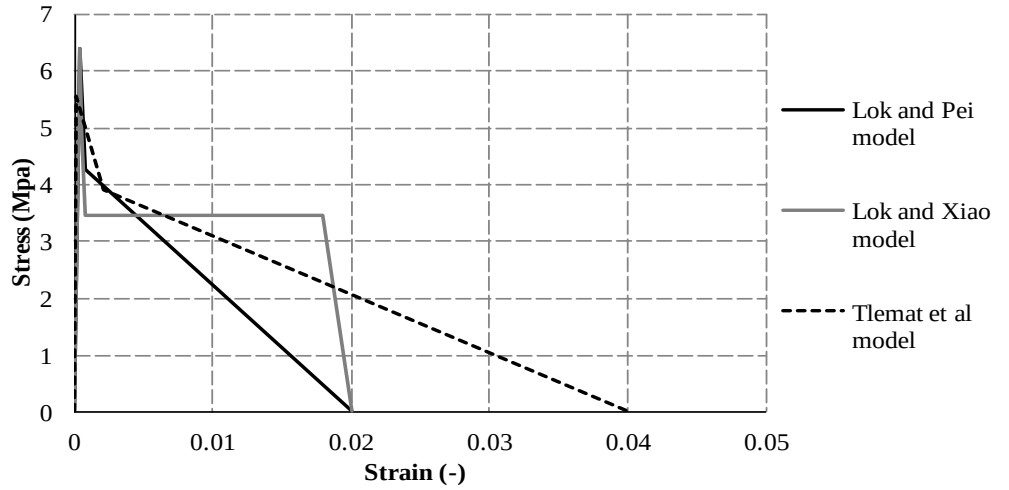


Figure A.12: Tensile stress-strain diagram for ISF-2 with $v_f = 6\%$

A.5.2 Discussion of ABAQUS simulation results

The load versus deflection at mid span results for beam ISF-1 and ISF-2 are presented in Figures A.13 to A.14. For analyses using SC model, the best performance are observed from both Tlemat[b] et al and Lok and Xiao models. From the analyses carried out, Tlemat[b] et al (2006) model produced a good agreement for this comparison as the model was developed based on the same experiments (and for high fibre content of 6%). All the results obtained from FE model in ABAQUS using SC model underestimated the load bearing capacity, with the closest to the experimental value exhibited by Tlemat[b] et al model.

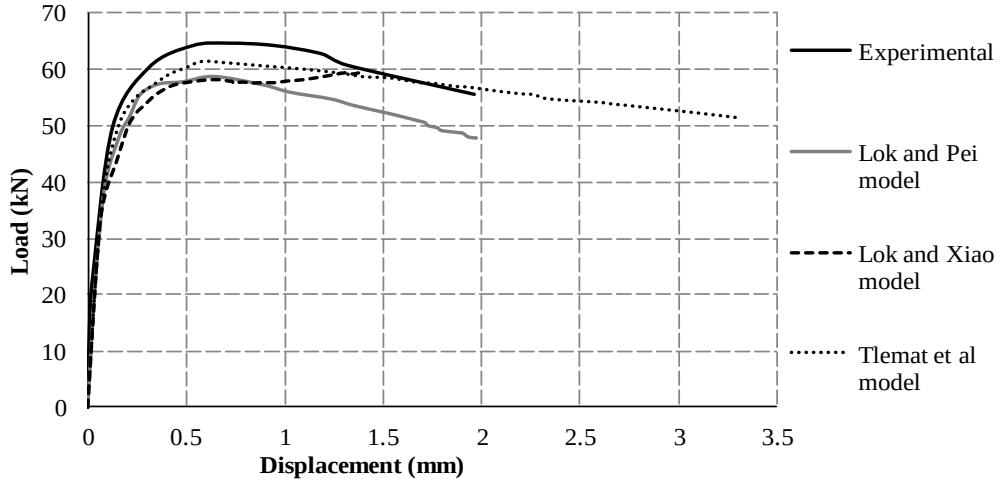


Figure A.13: ISF-1 results graph using SC concrete model (v_f = 6%)

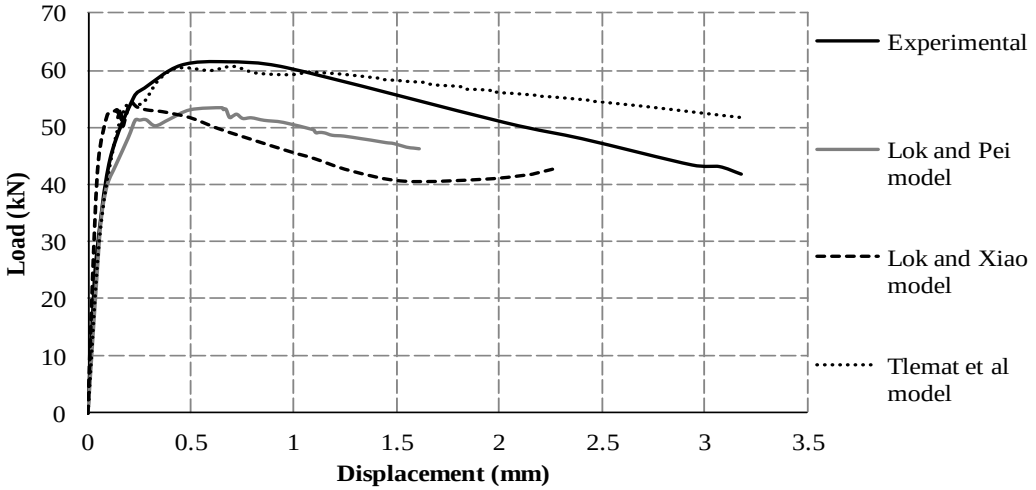


Figure A.14: ISF-2 results graph using SC concrete model (v_f = 6%)

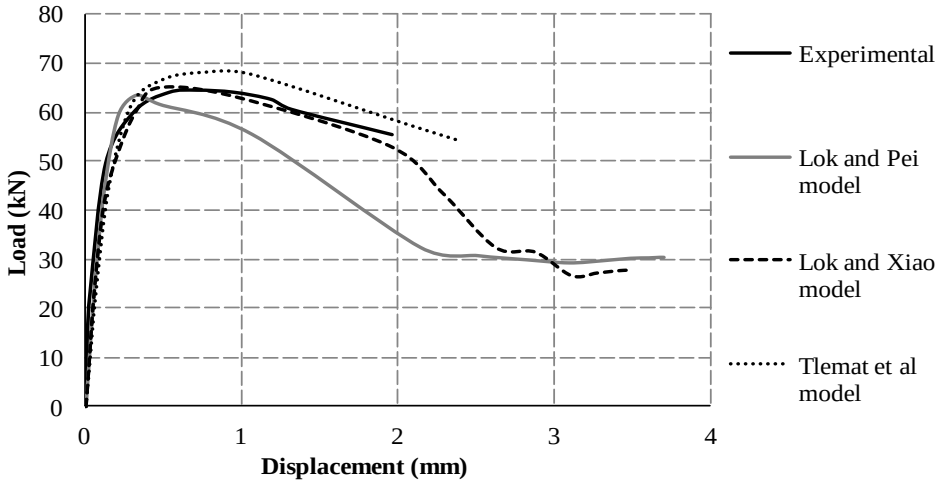


Figure A.15: ISF-1 results graph using BC concrete model (v_f = 6%)

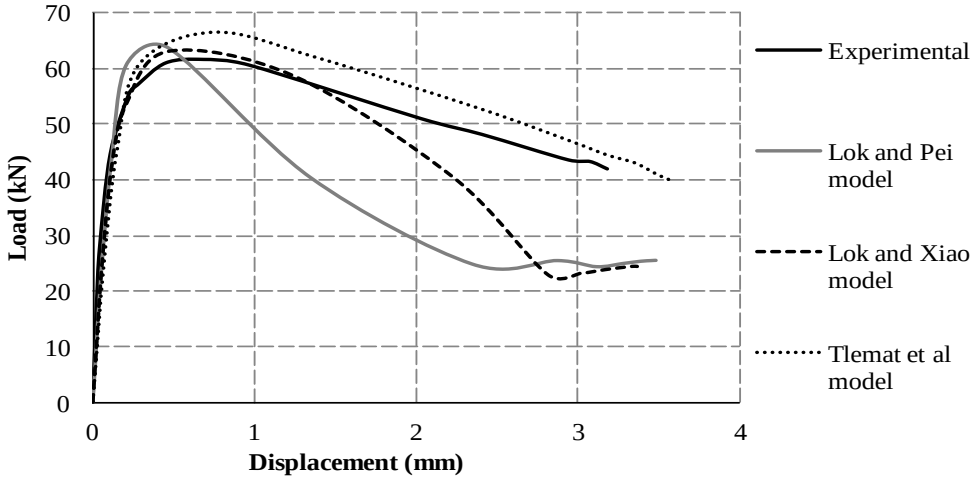


Figure A.16: ISF-2 results graph using BC concrete model (v_f = 6%)

The results produced by ABAQUS with BC model exhibits good agreement with the experimental result, especially from the model proposed by Lok and Xiao. This is observed in both cases of ISF-1 (see Figure A.15) and ISF-2 (see Figure A.16) beams. Whilst, the results analysed using Lok and Pei model show higher load bearing capacity, but very low softening behaviour in the post-cracking region. The Tlemat[b] et al model, ABAQUS analyses predicted a very similar pattern with the experimental result, however, the load in the post-cracking region is higher in both SFRC beams.

Both Lok and Pei model and Lok and Xiao model exhibited reasonable results for both beam ISF-1 and ISF-2 (although the model was developed for fibre range content of 0.5% to 3%). Therefore it can be concluded that both Lok and Pei model and Lok and Xiao model are applicable to analyse different properties of steel fibres with high fibre concentration up to 6 %, nonetheless Lok and Xiao model provided a better agreement to the experimental result.

A.6 Three-point bending test (tensile failure): Barros and Figueiras (1999)

A.6.1 Experimental data and analysis procedure

Two SFRC beams, each from specimens mixes s3 and s4 (Barros and Figueiras, 1999), are modelled under a 3-point flexure scheme. Figure A.17 exhibits the dimensions and loading condition of the beams. Two types of steel fibres were adopted for the investigation, specifically ZP 30/.50 and ZX 60/.80 for s3 and s4, respectively. The

details of steel fibres adopted in these beams are summarised in Table A.3. The average compression strength for series s3 and s4 is 32.9 MPa and 31.2 MPa, respectively.

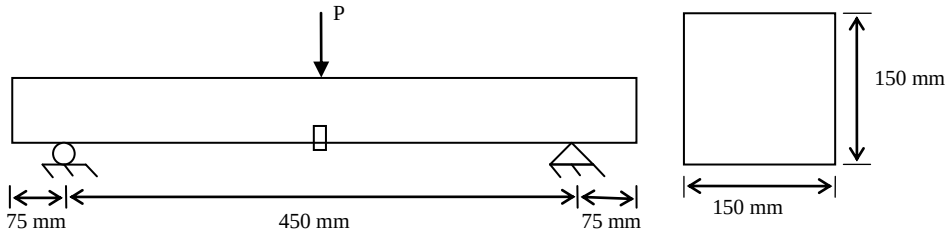


Figure A.17: Dimension and loading condition of the beams (Modified from: Barros and Figueiras, 1999)

Fibre type Dramix	Length (l) [mm]	Diameter (d) [mm]	Tensile strength [N/mm^2]	Fibre volume (v_f) [%]
ZP 30/.50	30	0.5	1250	0.77
ZX 60/.80	60	0.8	1100	0.77

Table A.3: Summary of geometry, tensile strength and fibre content for each type of fibre (Barros and Figueiras, 1999)

A brittle cracking concrete model is implemented in ABAQUS with material properties defined based on values obtained from the experimental data, and the Lok and Pei (1998), Lok and Xiao (1999) and Barros and Figueiras (2001) material models shown in Figures A.18 and A.19. Two different bond stress values are adopted into Lok and Pei and Lok and Xiao models: 3.57 Mpa for the beam with ZX30/.50 fibres, and 7.1 Mpa for the one with ZX60/.80 fibres. A rectangular 25 mm mesh size is implemented for the analysis.

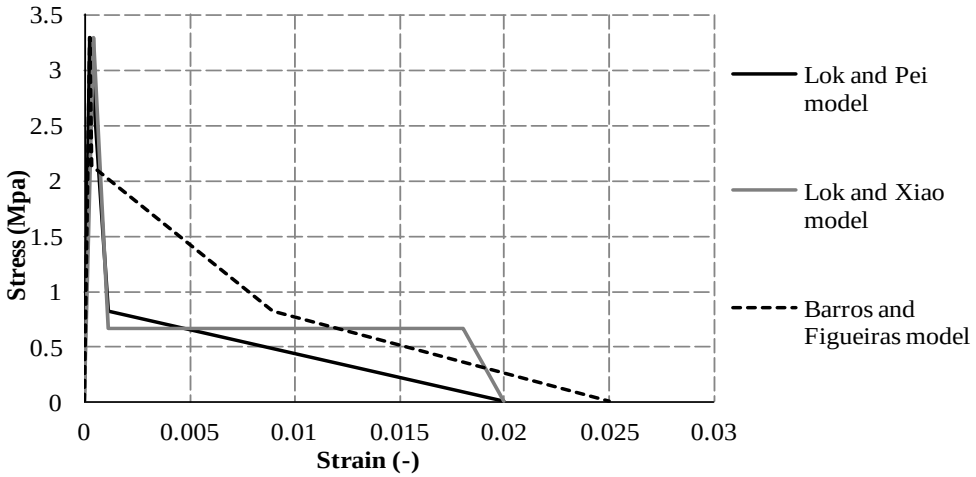


Figure A.18: Tensile stress-strain diagram for Barros and Figueiras (1999) ZP 30/.50 SFRC beams (v_f = 0.77%)

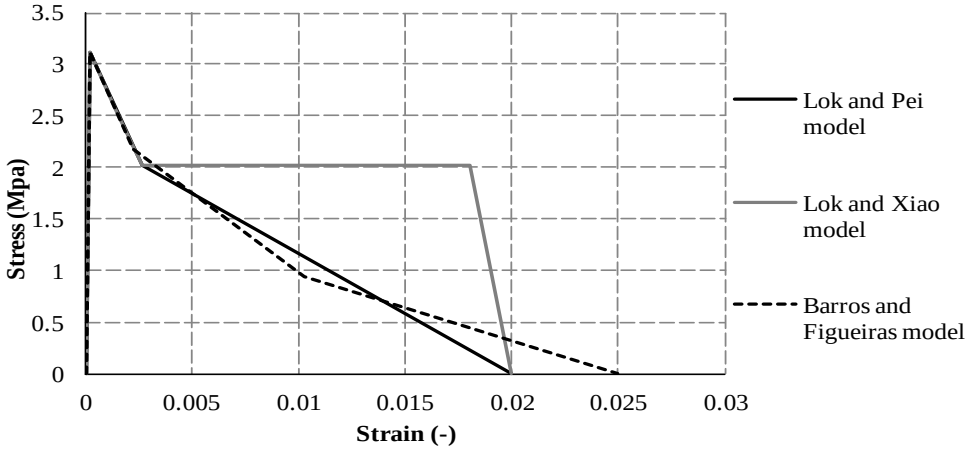


Figure A.19: Tensile stress-strain diagram for Barros and Figueiras (1999) ZX 60/.80 SFRC beams (v_f = 0.77%)

A.6.1 Discussion of ABAQUS simulation results

Results are represented in Figures A.20 and A.21. Figure A.20 exhibits good agreement between ABAQUS and experimental results up to 4mm displacement. The load at the initial yielding is slightly lower than experimental value. Again, the best agreement is observed from Lok and Xiao model.

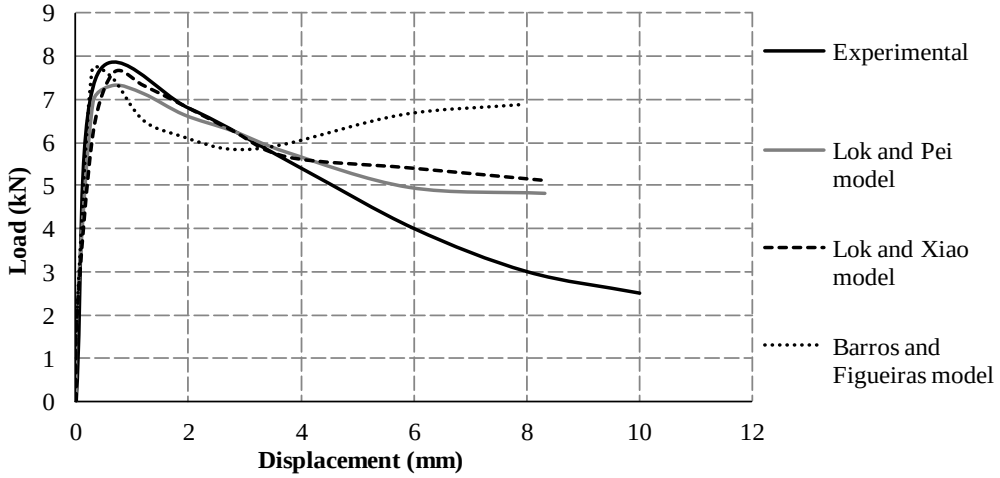


Figure A.20: Comparison graph for specimen ZP 30/.50 (v_f = 0.77%)

The results from the FE models for SFRC beam with ZX 60/.80 show very good agreement with the experimental results in the entire range (see Figure A.21). The curve based on Lok and Xiao model follows the experimental curve well up to displacement of 7 mm, being the best one to map the experimental results.

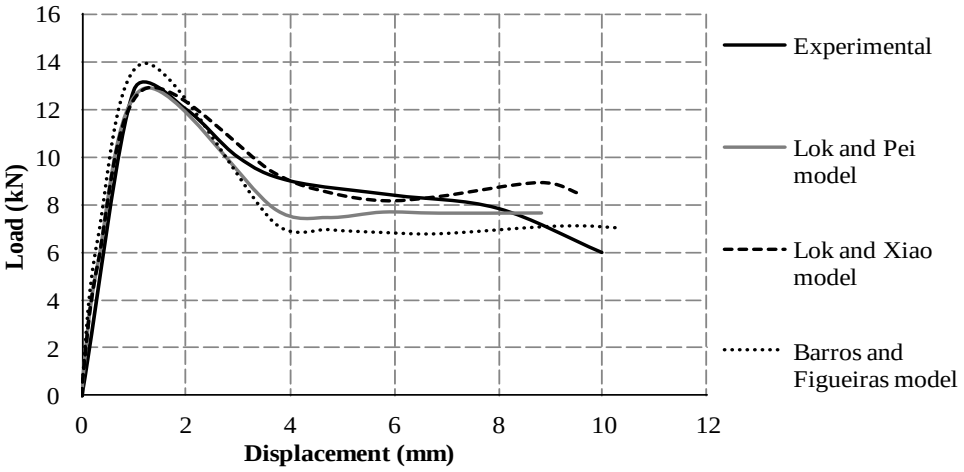


Figure A.21: Comparison graph for specimen ZX 60/.80 (v_f = 0.77%)

A.7 Four-point bending test (tensile failure): Trottier and Banthia (1994)

A.7.1 Experimental data and analysis procedure

A hooked-end SFRC beam (labelled as F1) with normal concrete strength investigated by Trottier and Banthia (1994) under flexural test is selected for analysis comparison (see Figure A.22). The properties of steel fibres utilised in the study are given in Table A.4. The plain concrete has compressive strength of 40 MPa. For calibration purposes, material model suggested by Lok and Pei (1998) and Lok and Xiao (1999) are applied into ABAQUS to model the behaviour of this SFRC beam.

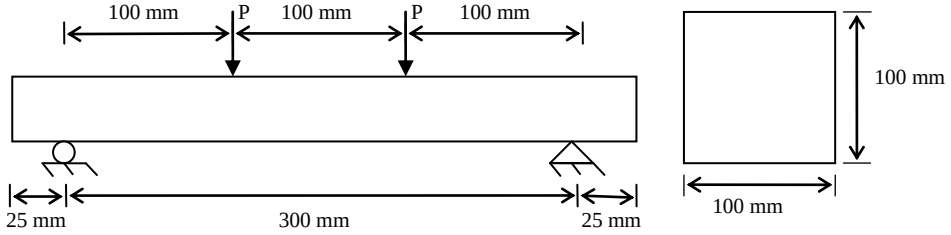


Figure A.22: Dimension and loading condition of the beams (Modified from: Trottier and Banthia, 1994)

Fibre type	Length (l) [mm]	Diameter (d) [mm]	Tensile strength [N/mm^2]	Fibre volume (v_f) [%]
Hooked-end (F1)	60	0.8	1115	0.51

Table A.4: Summary of geometry, tensile strength and fibre content for F1 steel fibre (Trottier and Banthia, 1994)

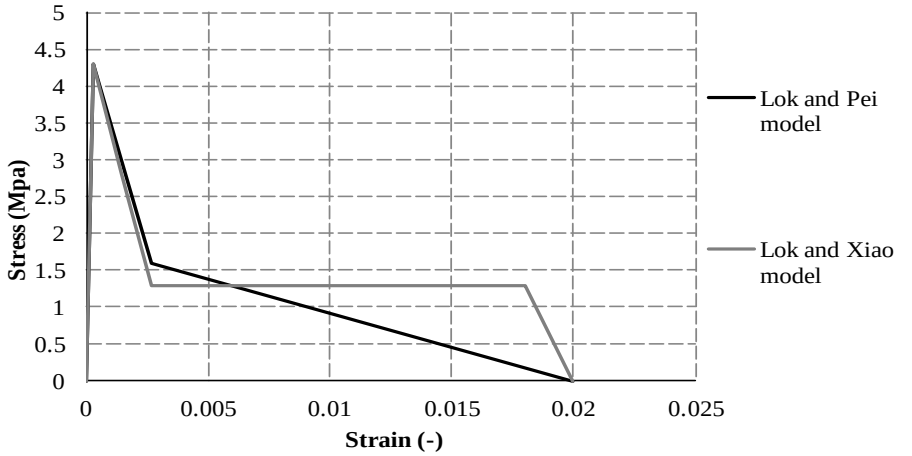


Figure A.23: Tensile stress-strain diagram for Trottier and Banthia (1994) SFRC beams using Lok and Pei (1998) model with v_f = 0.51%

Two approaches are used to analyse the beam, in which, it is modelled as 2D-plane stress (CPS4R) and 3D-solid element (C3D8R). Values from Figure A.23 and values from experimental data are defined in the material properties (based on the bond stress value of 7.1Mpa). The mesh size applied was10 mm.

A.7.2 Discussion of ABAQUS Simulation Results

The analysis of 3D element shows more sensible results compared to the 2D element analysis results. The general behaviour of 2D curves follow the pattern of experimental curve, however, the post-cracking load along the curve is underestimated.

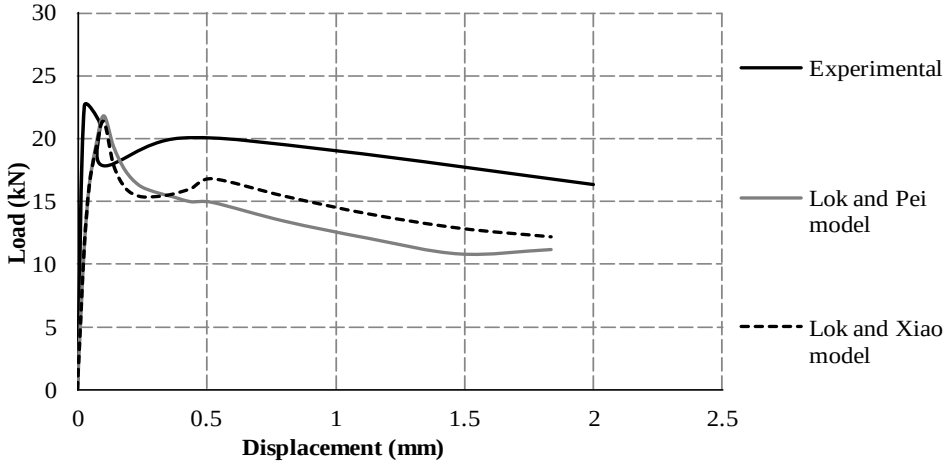


Figure A.24: Comparison graph for specimen F1 (v_f =0.51%) using 2D element

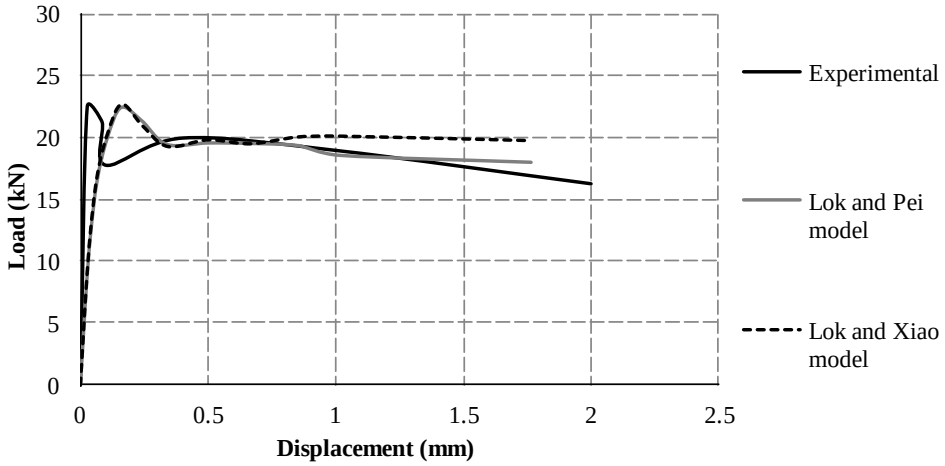


Figure A.25: Comparison graph for specimen F1 (v_f =0.51%) using 3D element

A.8 Four-point bending test: Cho and Kim (2003)

A.8.1 Experimental data and analysis procedure

Three simply supported reinforced concrete beams (batch SFC-30) investigated by Cho and Kim (2003) are selected herein (see Figure A.26). The beams have similar properties except for the volume concentration of steel fibres. The properties of steel fibres and concrete strength utilised in the study are given in Table A.5. Furthermore, the elasticity modulus (E_s), the yield stress (f_y), and the ultimate strength (f_u) of both the longitudinal and transverse reinforcement bars used are 200 GPa, 400 MPa and 600 MPa, respectively. During the experiment, the reinforced concrete beam is subjected to a four point test.

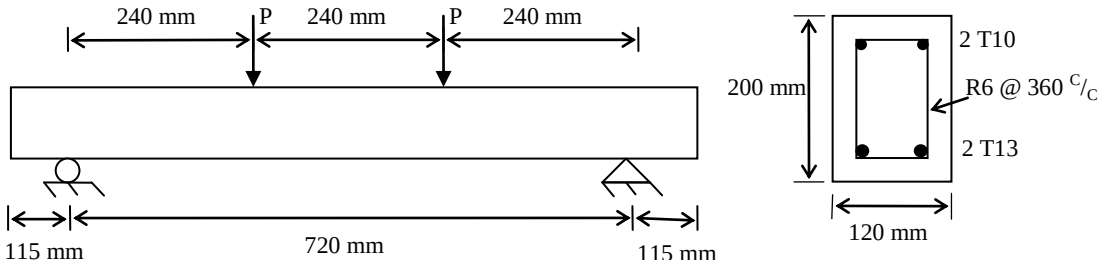


Figure A.26: Dimension and loading condition of SFRC batch SFC-30 (Modified from Cho and Kim, 2003)

Fibre type	Length (l) [mm]	Diameter (d) [mm]	Fibre volume (v_f) [%]	Compressive strength (f_{ck}) [mm]	Tensile strength (f_{tk}) [mm]
Hooked-end	36	0.6	1.0	25.3	2.99
Hooked-end	36	0.6	1.5	23.9	2.93
Hooked-end	36	0.6	2.0	28.8	3.19

Table A.5: Summary of geometry and fibre content for F1 steel fibre (Cho and Kim, 2003)

Figures A.27 to A.29 show the materials models applied into the FE models in ABAQUS. In general, it can be assumed that the higher the volume of fibres, the higher the bond stress developed between fibre and concrete. However, for the analyses, the value of bond stress is kept constant at 3.57 MPa, as this is the average value investigated and proposed by other researchers (Swamy et al, 1981; Hannant, 1978).

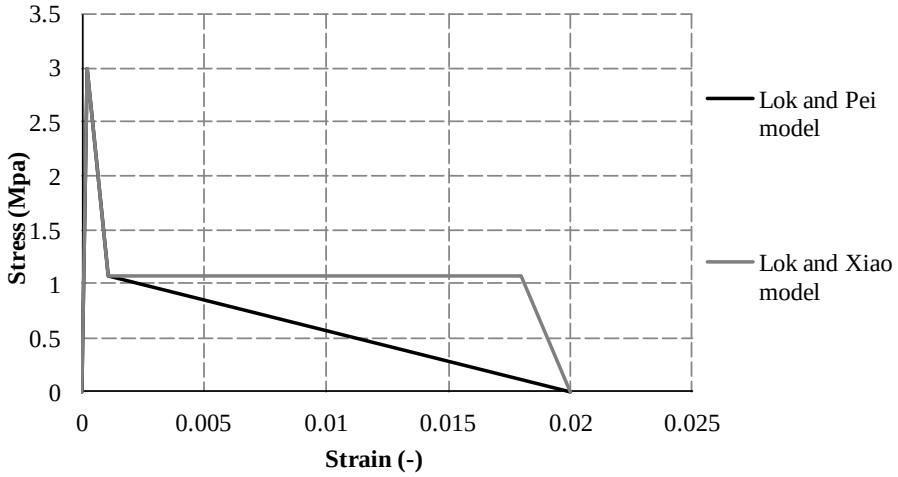


Figure A.27: Material models values applied into ABAQUS for beam (v_f =1.0%)

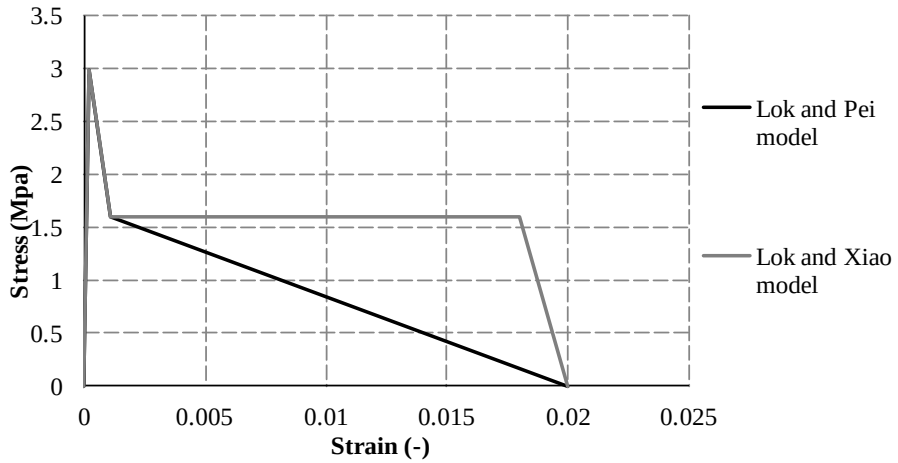


Figure A.28: Material models values applied into ABAQUS for beam (v_f =1.5%)

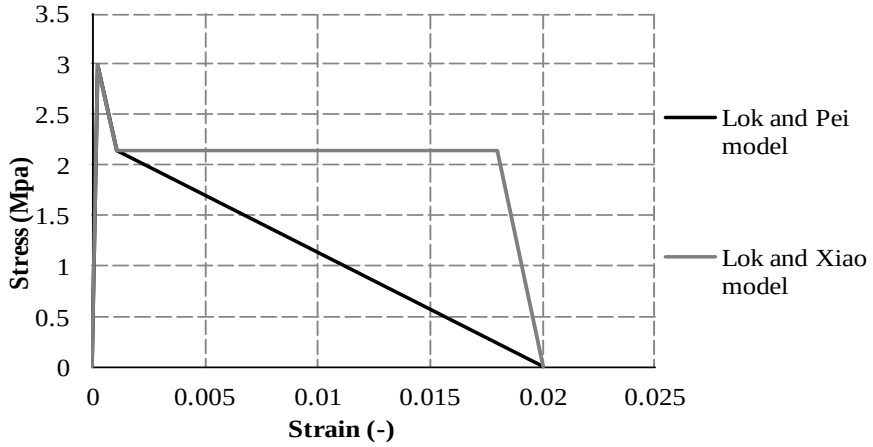


Figure A.29: Material models values applied into ABAQUS for beam (v_f =2.0%)

A.8.2 Discussion of ABAQUS simulation results

Figures below shows that the results simulated by ABAQUS for SFC-30 beam at its assorted percentages volume of fibre content agrees well with the results observed in the experimental work. The numerical results replicate very well the experimental data. The Lok and Xiao model again very appropriate to reproduce the experimental results.

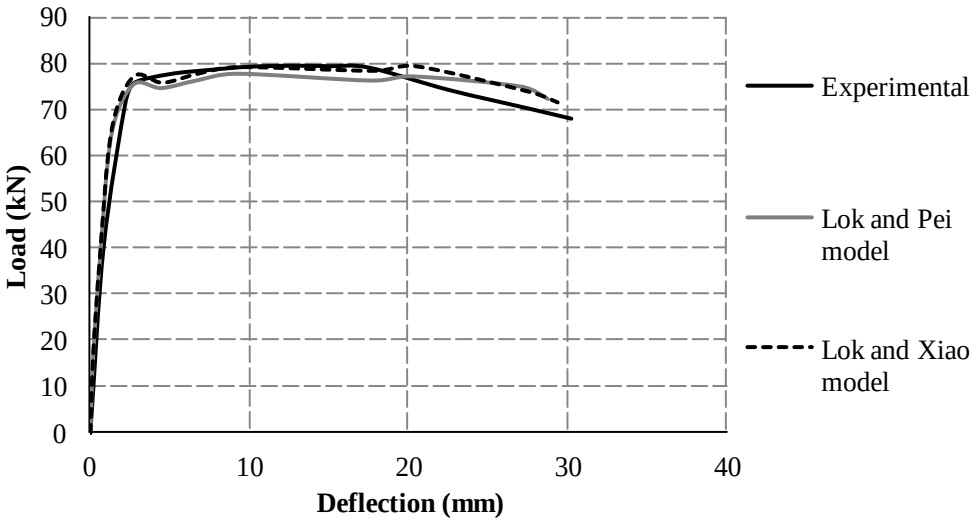


Figure A.30: Comparison results for beam SFC-30 with v_f =1.0%

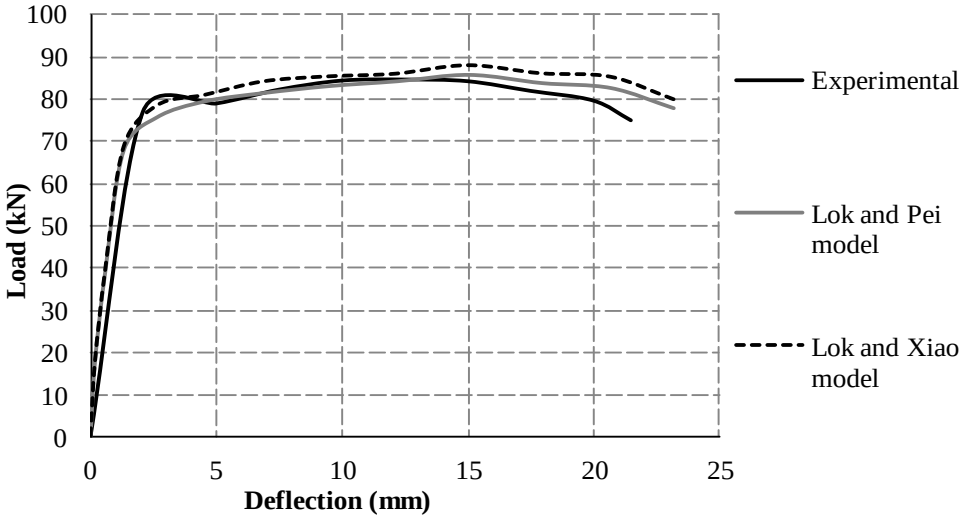


Figure A.31: Comparison results for beam SFC-30 with v_f =1.5%

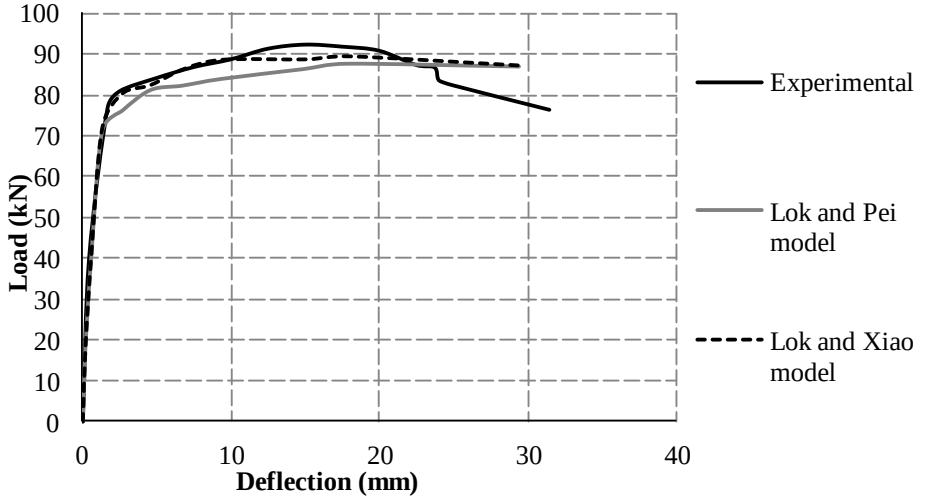


Figure A.32: Comparison results for beam SFC-30 with v_f =2.0%

A.9 Four-point bending test: Oh et al (1998)

A.9.1 Experimental data and analysis procedure

Two simply supported SFRC beams (specimen S0.5V1 and S0.5V2) tested by Oh et al (1998) are modelled into ABAQUS (see Figure A.33). The properties of steel fibres and its respective uni-axial compressive and tensile strength are summarised into Table A.6. In addition, the elasticity modulus (E_s), the yield stress (f_y), and the ultimate strength (f_u) of both the longitudinal and transverse reinforcement bars used are 200 GPa, 460 MPa and 560 MPa, respectively. The beams are tested in a 4-point scheme.

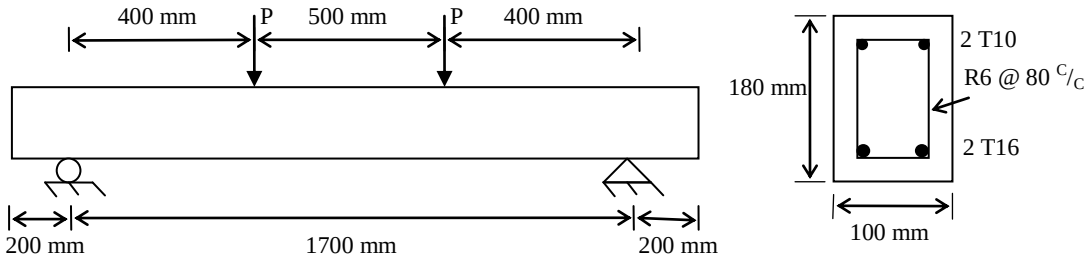


Figure A.33: Dimension and loading condition of SFRC S0.5V1 and S0.5V2 beams (Oh et al, 2009)

Fibre type	Length (l) [mm]	Diameter (d) [mm]	Fibre volume (v_f) [%]	Compressive strength (f_{ck}) [mm]	Tensile strength (f_{tk}) [mm]
Round-straight	42	0.7	1.0	38.7	4.0
Round-straight	42	0.7	2.0	42.4	5.1

Table A.6: Summary of geometry, tensile strength and fibre content for F1 steel fibre (Oh et al, 2009)

The analysis is carried out using the brittle cracking model. Figures A.34 and A.35 shows the materials models applied into ABAQUS by means of the brittle model and a mesh size of 20 mm.

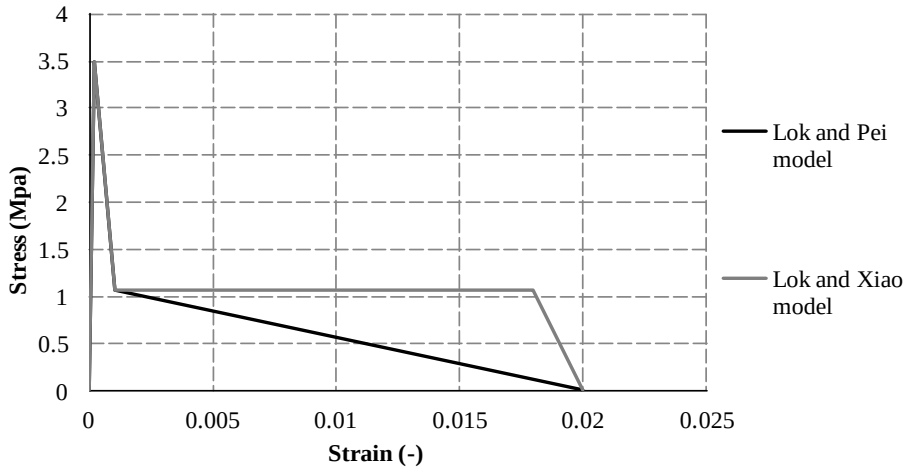


Figure A.34: Material models values applied into ABAQUS for beam S0.5V1 (v_f =1.0%)

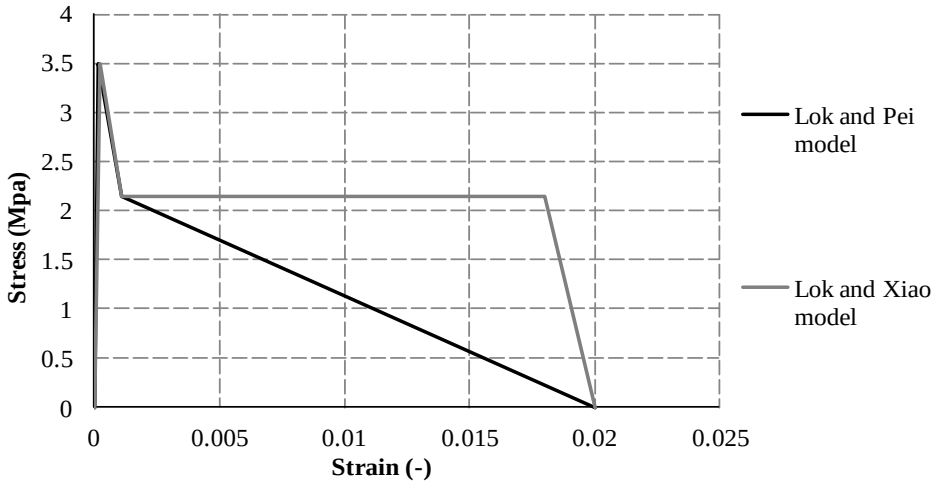


Figure A.35: Material models values applied into ABAQUS for beam S0.5V2 (v_f =2.0%)

A.9.2 Discussion of ABAQUS simulation results

The results obtained from the analyses are shown in Figures A.36 to A.37. It can be seen that, for both cases of the beams, ABAQUS estimated is slightly stiffer stiffness; however, the curves pattern almost similar to the experimental curves. It can be seen that the post-cracking behaviour for both type of beams agrees well with the experimental results.

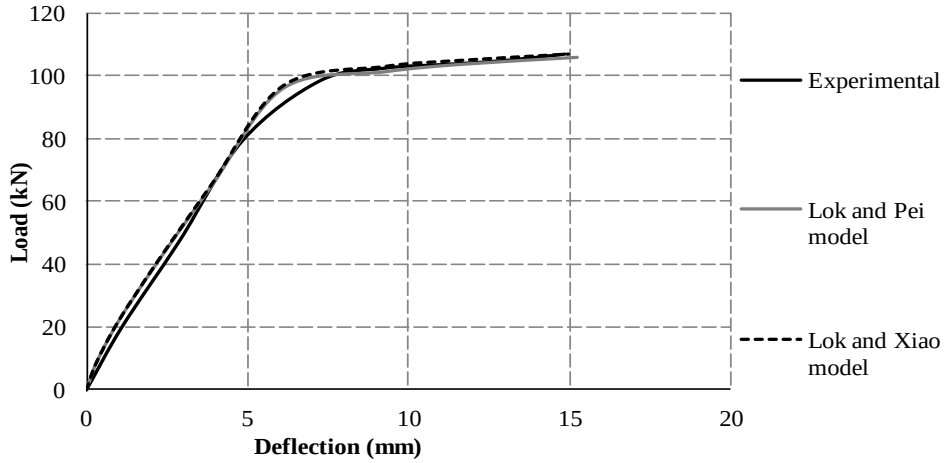


Figure A.36: Comparison results for beam S0.5V1 with v_f =1.0%

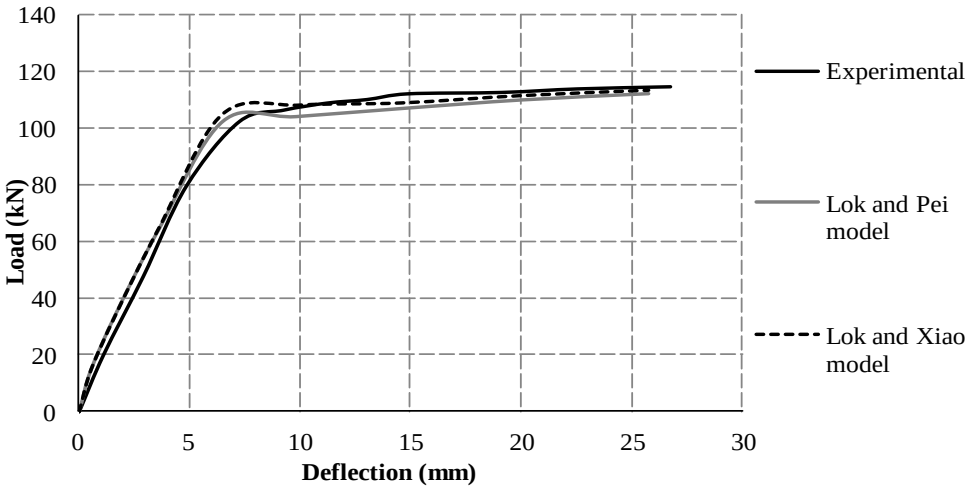


Figure A.37: Comparison results for beam S0.5V2 with v_f =2.0%

A.10 Four-point bending test: Sharma (1986)

A.10.1 Experimental data and analysis procedure

Figure A.38 shows a SFRC beam (D-3F) tested by Sharma (1986), which is selected and modelled using ABAQUS. The value for the elasticity modulus (E_s), the yield stresses (f_y), and the ultimate strength (f_u) of both the longitudinal and transverse reinforcement bars used are 200 GPa, 400 MPa and 460 MPa, respectively. During the experiment, the reinforced concrete beam is subjected to 4-point bending test.

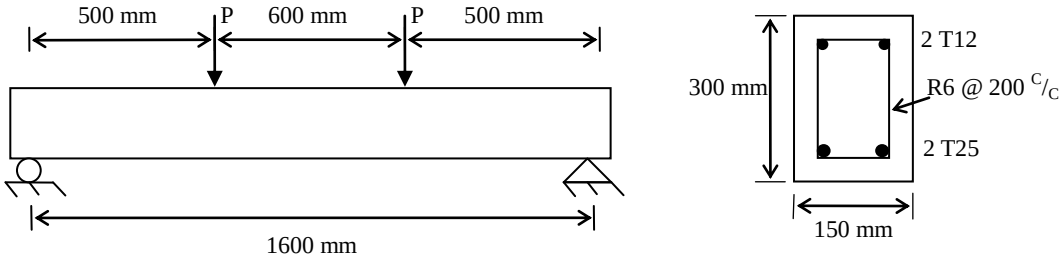


Figure A.38: Beam dimensions and reinforcement detailing (Modified from Sharma, 1986)

Fibre type	Length (l) [mm]	Diameter (d) [mm]	Fibre volume (v_f) [%]	Compressive strength (f_{ck}) [mm]	Tensile strength (f_{tk}) [mm]
Hooked-end	50	0.6	0.96	47.7	5.8

Table A.7: Summary of geometry, tensile strength, fibre content and concrete strength of the beam (Sharma, 1986)

Figure A.39 shows the materials models applied into ABAQUS obtained from a bond stress value of 3.57 Mpa. Brittle cracking and damaged plasticity model through the 3D solid elements are used with a mesh size of 20 mm. The analysis is carried out using dynamic, explicit procedure.

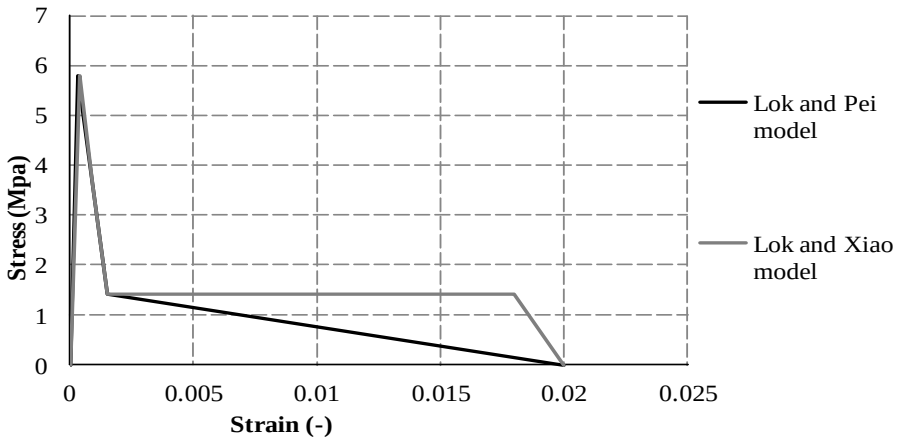


Figure A.39: Material models values applied into ABAQUS for beam DF3

A.10.2 Discussion of ABAQUS simulation results

The result comparison in Figure A.40 shows that Lok and Pei (1998) and Lok and Xiao (1999) models slightly overestimated the load of the beam up to the deflection of 4mm for brittle cracking model and up to 2.5 mm for damage plasticity model. Beyond these deflection points, the estimated results exhibit good reasonable agreement with experimental result for brittle cracking model, whilst the loads predicted by damaged plasticity model is lower by about 40%. This is probably due the value of Young's modulus of the concrete is overestimated, when conducting the analysis. Based on the results, again it could be observed that good agreement could be seen from the brittle cracking model and Lok and Xiao model.

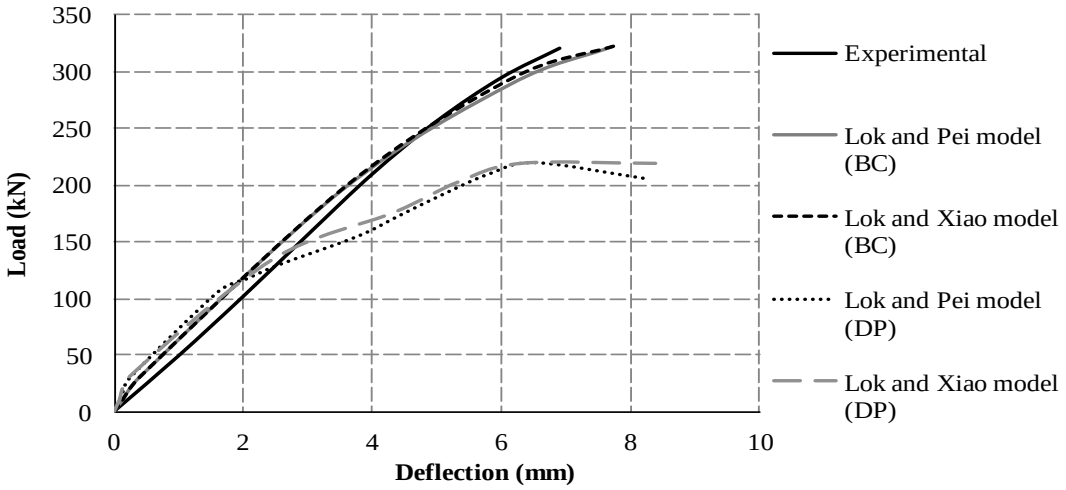


Figure A.40: Comparison results between experimental and numerical simulation for beam DF3

A.11 Conclusions

Based on the FE modelling results for the calibration work presented herein, it can be seen that the numerical predictions are in good agreement with their experimental counterparts (even in instances when there was some slight difference, the discrepancy was always on the safe side as the FE-based results did not over-estimate the actual strength values). The best results were obtained from the brittle cracking model, confirming the ability of this model to efficiently capture the essential features of concrete behaviour, namely brittleness and cracking (both driven by tensile behaviour). Furthermore, the SFRC model proposed by Lok and Xiao (1999) incorporated into the brittle cracking model was found to yield predictions that are in good agreement with experimental data. Therefore, these SFRC and ABAQUS models were adopted for subsequent parametric studies in the present research work.

APPENDIX B

DESIGN CALCULATION

B.1 Shear capacity

The shear capacity of the RC beam is calculated based on the equations recommended by Eurocode 2 (2004). Figure B.1 shows the strut inclination method used by the Eurocode 2 (2004).

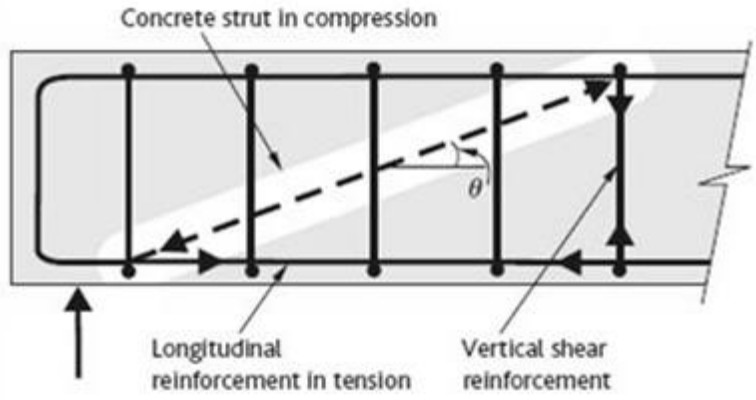


Figure B.1: Strut inclination method (Reproduced from Eurocode 2, 2003)

The equations recommended for the shear capacity check are reproduced here and full definition of the parameters can be obtained from Eurocode 2 (2004). The resistance of the members without shear reinforcement is:

$$V_{rd,c} = \left(\frac{0.18}{\gamma_c}\right) k(100\rho_l f_{ck})^{1/3} bd \geq 0.035(k)^{3/2}(f_{ck})^{1/2} bd \quad \text{(B.1)}$$

where $k = 1 + (200/d)^{1/2} \leq 2$ (d in mm) and $\rho_l = (A_{sl}/b * d) \leq 0.02$.

The capacity of concrete section acting as a strut is calculated as:

$$V_{rd,max} = \frac{b*z*v*f_{cd}}{(cot\theta+tan\theta)} \geq V_{ed} \quad \text{(B.2)}$$

For vertical links (i.e. $\alpha = 90°$ and $\cot\alpha = 0$) shear reinforcement (A_{sw}/s) required, the equation is given as below:

$$V_{rd,s} = (A_{sw}/s)zf_{ywd}(cot\theta + cot\alpha)sin\alpha \quad \text{(B.3)}$$

Thus, the shear capacity for combination of RC structures with shear reinforcement is:

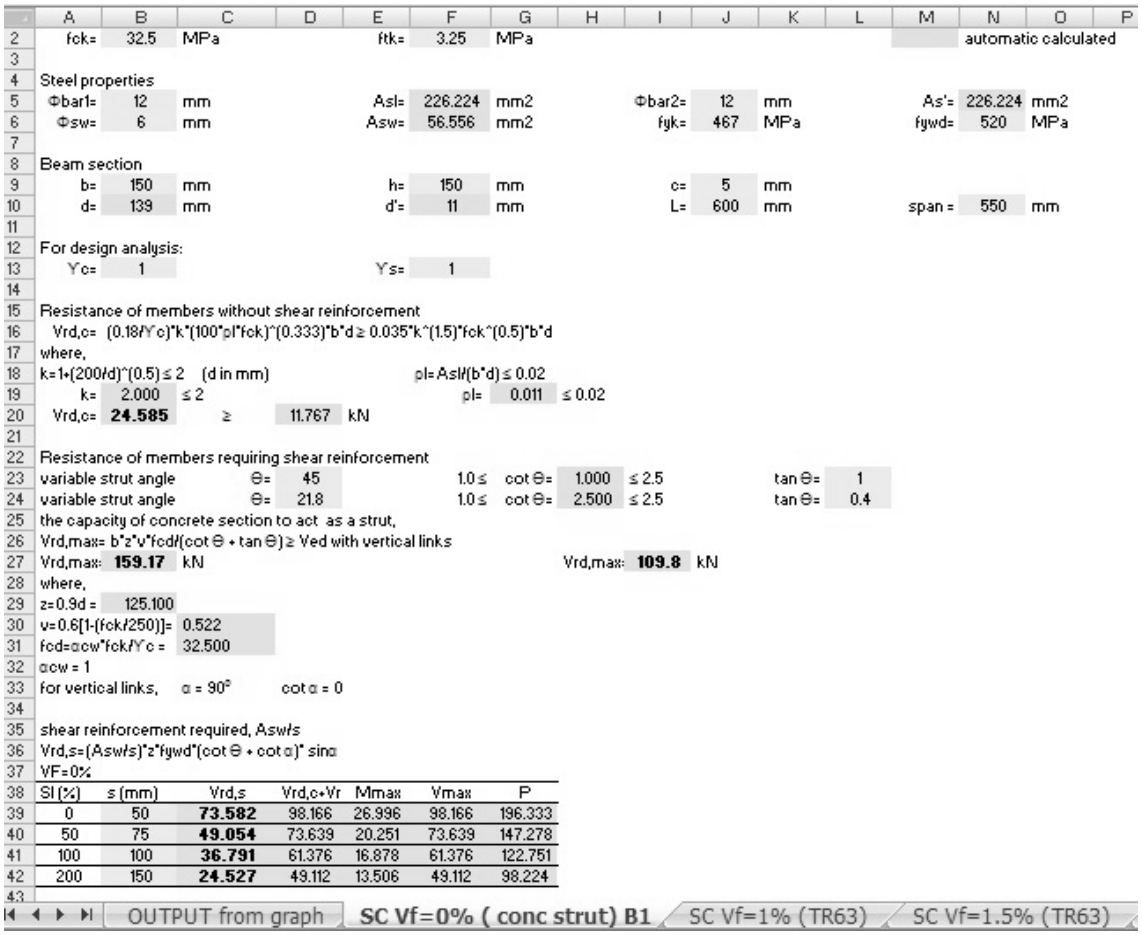
$$V_{rd,t} = V_{rd,c} + V_{wd} \quad \text{(B.4)}$$

For the SFRC beam, the effect of steel fibres is considered based on the equation suggested by Concrete Society TR-63 (2007). This recommendation is based on the Eurocode 2 (2004), and it is stated that for element with addition of steel fibres, the fibrous concrete effect (v_{fd}) is just added to the shear reinforcement equation as shown below:

$$V_{rd,c} = \left[\left(\frac{0.18}{\gamma_c}\right) k(100\rho_l f_{ck})^{1/3} + v_{fd}\right] bd \quad \text{(B.5)}$$

where $v_{fd} = 0.7 * k_f * k * \tau_{fd}$. Full definition of the parameters is explained in Concrete Society TR-63 (2007).

These equations are then applied into the Microsoft Excel Worksheet and some of the screenshot of the spreadsheets are shown in Figure B.2 and B3.



fck= 32.5 MPa ftk= 3.25 MPa automatic calculated

Steel properties

Φbar1= 12 mm Asl= 226.224 mm2 Φbar2= 12 mm As'= 226.224 mm2

Φsw= 6 mm Asw= 56.556 mm2 fyk= 467 MPa fywd= 520 MPa

Beam section

b= 150 mm h= 150 mm c= 5 mm

d= 139 mm d'= 11 mm L= 600 mm span = 550 mm

For design analysis:

Yc= 1 Ys= 1

Resistance of members without shear reinforcement

Vrd,c= (0.18/Yc)*k*(100*pl*fck)^(0.333)*b*d ≥ 0.035*k^(1.5)*fck^(0.5)*b*d

where,

k=1+(200/d)^(0.5) ≤ 2 (d in mm) pl=Asl/(b*d) ≤ 0.02

k= 2.000 ≤ 2 pl= 0.011 ≤ 0.02

Vrd,c= **24.585** ≥ 11.767 kN

Resistance of members requiring shear reinforcement

variable strut angle Θ= 45 1.0 ≤ cot Θ= 1.000 ≤ 2.5 tan Θ= 1

variable strut angle Θ= 21.8 1.0 ≤ cot Θ= 2.500 ≤ 2.5 tan Θ= 0.4

the capacity of concrete section to act as a strut,

Vrd,max= b*z*v*fcd/(cot Θ + tan Θ) ≥ Ved with vertical links

Vrd,max= **159.17** kN Vrd,max= **109.8** kN

where,

z=0.9d = 125.100

v=0.6[1-(fck/250)]= 0.522

fcd=αcw*fck/Yc = 32.500

αcw = 1

for vertical links, α = 90° cot α = 0

shear reinforcement required, Asw/s

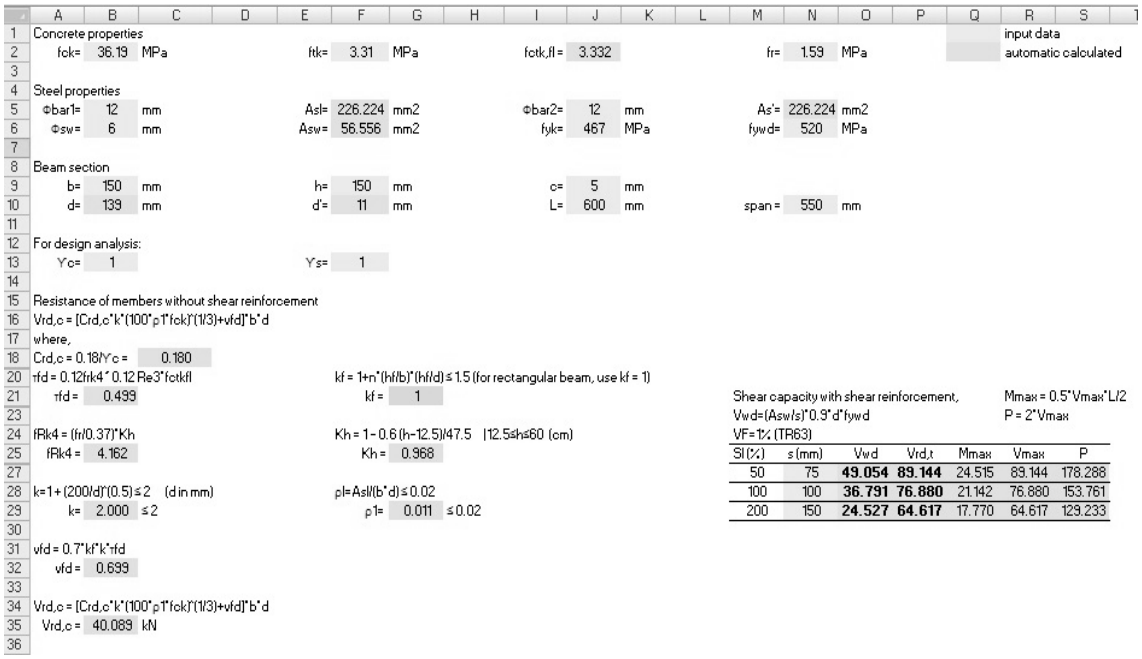
Vrd,s=(Asw/s)*z*fywd*(cot Θ + cot α)* sinα

VF=0%

Sl (%)	s (mm)	Vrd,s	Vrd,c+Vr	Mmax	Vmax	P
0	50	**73.582**	98.166	26.996	98.166	196.333
50	75	**49.054**	73.639	20.251	73.639	147.278
100	100	**36.791**	61.376	16.878	61.376	122.751
200	150	**24.527**	49.112	13.506	49.112	98.224

OUTPUT from graph | SC Vf=0% (conc strut) B1 | SC Vf=1% (TR63) | SC Vf=1.5% (TR63)

Figure B.2: Spreadsheet shear capacity calculation screenshot for the RC beams



Concrete properties

fck= 36.19 MPa ftk= 3.31 MPa fctk,fl= 3.332 fr= 1.59 MPa input data

automatic calculated

Steel properties

Φbar1= 12 mm Asl= 226.224 mm2 Φbar2= 12 mm As'= 226.224 mm2

Φsw= 6 mm Asw= 56.556 mm2 fyk= 467 MPa fywd= 520 MPa

Beam section

b= 150 mm h= 150 mm c= 5 mm

d= 139 mm d'= 11 mm L= 600 mm span = 550 mm

For design analysis:

Yc= 1 Ys= 1

Resistance of members without shear reinforcement

Vrd,c = [Crd,c*k*(100*ρ1*fck)^(1/3)+vfd]*b*d

where,

Crd,c = 0.18/Yc = 0.180

rfd = 0.12rfk4^0.12 Re3*fctkfl kf = 1+n*(hf/b)*(hf/d) ≤ 1.5 (for rectangular beam, use kf = 1)

rfd = 0.499 kf = 1

fRk4 = (fr/0.37)*Kh Kh = 1 - 0.6 (h-12.5)/47.5 |12.5≤hs≤60 (cm)

fRk4 = 4.162 Kh = 0.968

k=1+(200/d)^(0.5) ≤ 2 (d in mm) ρl=Asl/(b*d) ≤ 0.02

k= 2.000 ≤ 2 ρ1= 0.011 ≤ 0.02

vfd = 0.7*kf*k*rfd

vfd = 0.699

Vrd,c = [Crd,c*k*(100*ρ1*fck)^(1/3)+vfd]*b*d

Vrd,c = 40.089 kN

Shear capacity with shear reinforcement, Mmax = 0.5*Vmax*L/2

Vwd=(Asw/s)*0.9*d*fywd P = 2*Vmax

VF=1% (TR63)

Sl (%)	s (mm)	Vwd	Vrd,t	Mmax	Vmax	P
50	75	**49.054**	**89.144**	24.515	89.144	178.288
100	100	**36.791**	**76.880**	21.142	76.880	153.761
200	150	**24.527**	**64.617**	17.770	64.617	129.233

Figure B.3: Spreadsheet shear capacity calculation screenshot for the SFRC beams

B.2. Bending moment capacity

The bending moment capacity of the RC beam can be calculated based on the stress distribution shown in Figure B.4. The maximum compressive concrete strain (i.e. $\varepsilon_c = 0.0035$) adopted the value recommended by the Eurocode 2 (2004).

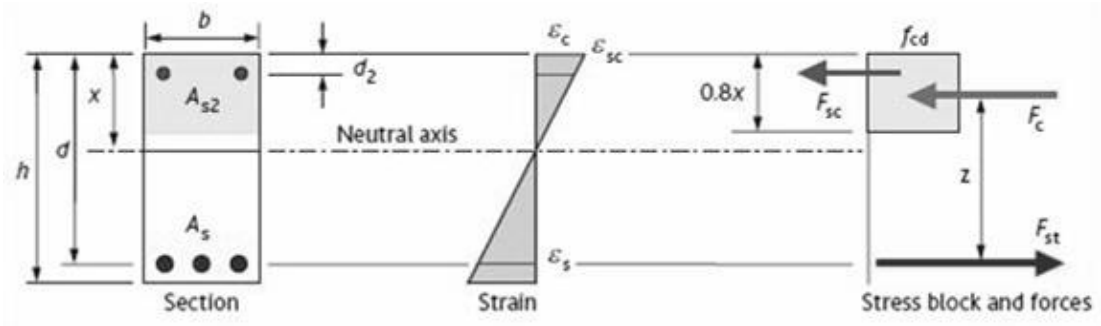


Figure B.4: Flexural section analysis for RC beam (Reproduced from Eurocode 2, 2003)

The steel bar reinforcement in the compression zone is assumed to be in elastic range, thus:

$$F_{sc} = A_{s2}\varepsilon_{sc}E_s \quad \text{(B.6)}$$

Whilst the steel reinforcement bar in tension is assumed to be yielded, therefore:

$$F_{st} = A_s(f_{yk}/\gamma_s) \quad \text{(B.7)}$$

Compressive force acting in the compression zone, x is taken as:

$$F_c = 0.85\left(\frac{f_{ck}}{\gamma_c}\right)b(0.8x) \quad \text{(B.8)}$$

Taken equilibrium condition, the x value is obtained from the sums of forces:

$$\sum F = F_c + F_{sc} - F_{st} = 0 \quad \text{(B.10)}$$

Then, the bending moment capacity is calculated using the following equation:

$$M = F_c(d - 0.333x) + F_{sc}(d - d_2)$$

In order to calculate the effect of the steel fibres in the bending moment capacity, Concrete Society TR-63 (2007), suggested the stress and strain block distribution as shown in Figure B. 5.

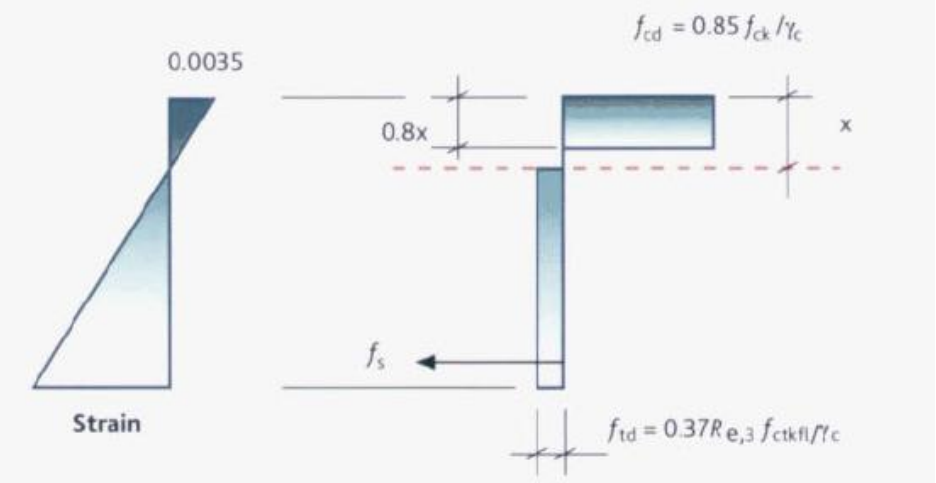


Figure B.5: Flexural section analysis for SFRC beam (Reproduced from Concrete Society TR-63, 2007)

To account the effect of steel fibres, additional force is required which can be calculated from the following equations:

$$F_{td} = 0.37R_{e,3}\left(f_{ctkl,fl}/\gamma_c\right)b(d-x) \quad \text{(B.11)}$$

where $R_{e,3} = (f_r/k_h)/(0.37f_{ctk,fl}$. Similar to the previous step, the x value is obtained from the sums of forces as follows:

$$\sum F = F_c + F_{sc} - F_{st} - F_{td} = 0 \quad \text{(B.12)}$$

Therefore, the bending moment capacity for the SFRC beam is calculated using the equation below:

$$M = F_c(d-0.4x) + F_{sc}(d-d_2) - F_{td}(d-0.5h-0.5x) \quad \text{(B.13)}$$

To ease the estimation of the *x* value, these equations are applied into Microsoft Excel spreadsheet, and Figures B.6 and B.7 show the screenshot taken for the spreadsheet for RC and SFRC beams.

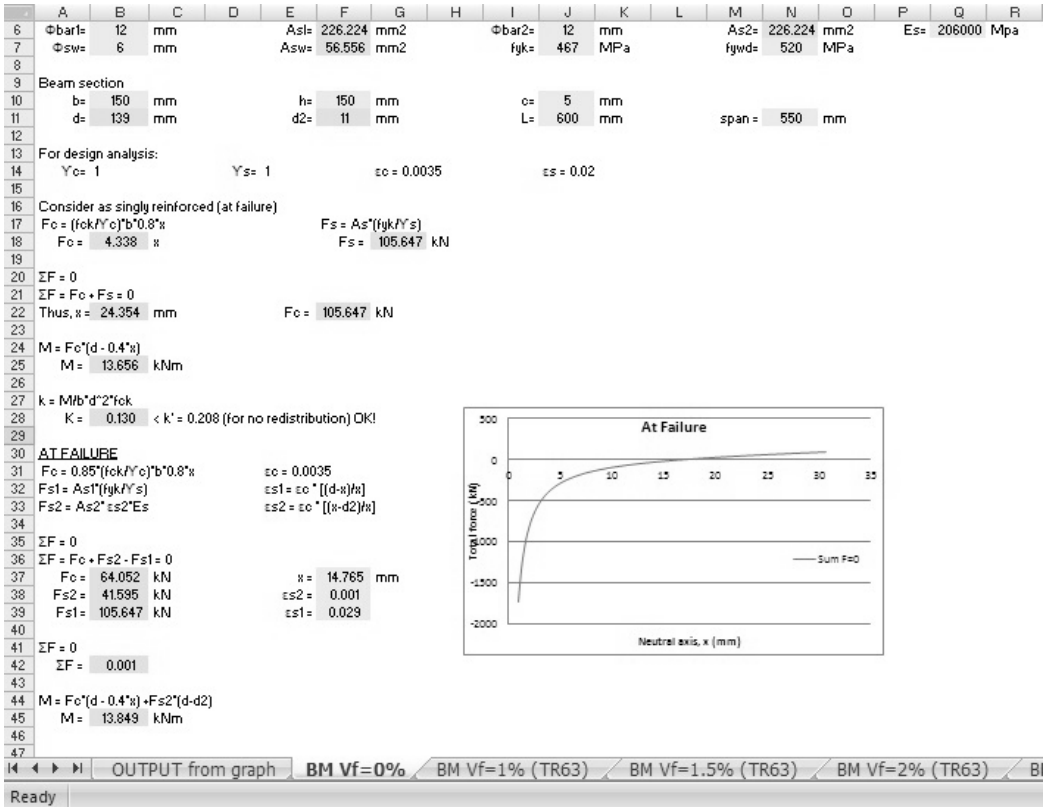


Figure B.6: Spreadsheet bending moment capacity calculation screenshot for the RC beams

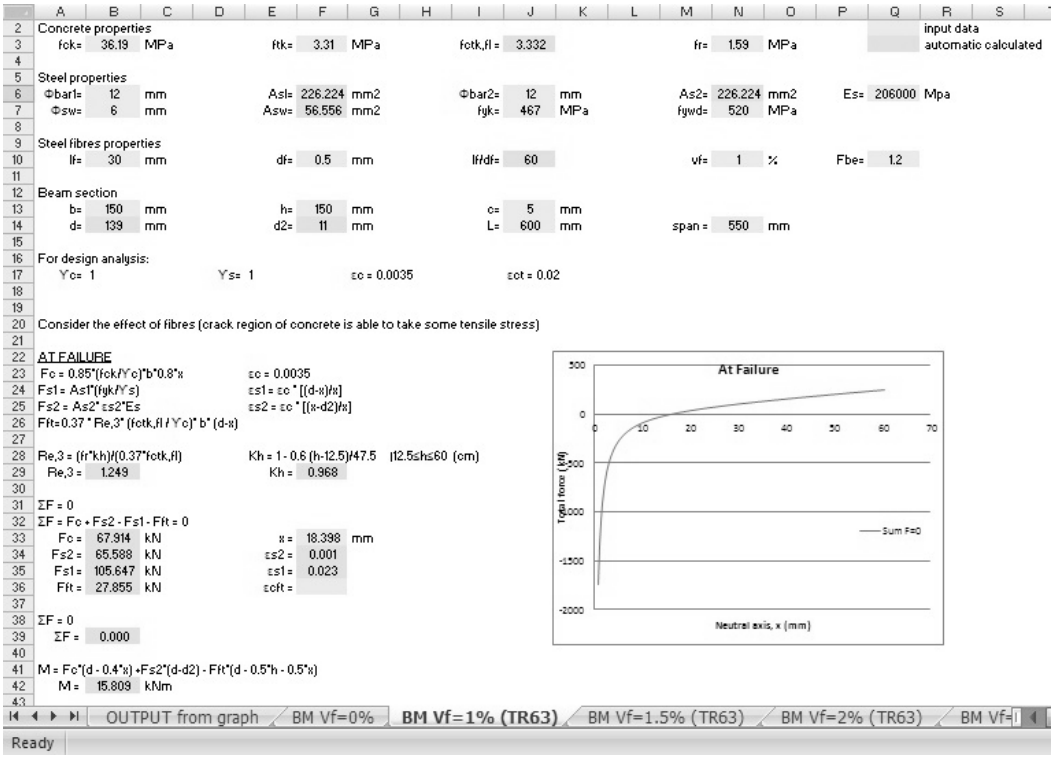


Figure B.7: Spreadsheet bending moment capacity calculation screenshot for the SFRC beam